Inaugural dissertation

for

obtaining the doctoral degree

of the

Combined Faculty of Mathematics, Engineering and Natural Sciences

of the

Ruprecht – Karls – University

Heidelberg

Presented by

M.Sc. Gemma Pidelaserra Martí

born in: Barcelona

Oral examination: 15th December 2023

Exploring the Interplay of Oncolytic Measles Vaccines with the Cancer-Immunity Cycle

Referees:

Prof. Dr. Ralf Bartenschlager

Prof. Dr. Dr. Christine E. Engeland

Dedicated to / Dedicada a

Miquel Pidelaserra Mas

Maria Mercè Martí Campaña

Written in tribute to / Escrita en homenatge a

Esteve Pidelaserra Surià

Eulàlia Mas Cortés

Joan Martí Fortuny

Montserrat Campaña Castellano

Abstract

Oncolytic vaccine strains of measles virus (MeVac) are studied as novel cancer therapeutics. By preferentially lysing tumor cells, these attenuated viruses induce systemic antitumor immunity. However, MeVac virotherapy alone is insufficient to achieve high rates of complete tumor remissions. Thus, in this study I aimed at identifying immunological mechanisms that limit or restrict the therapeutic potential of oncolytic MeVac.

Following the cancer-immunity cycle, I first focused on antigen presentation and T cell priming. I hypothesized that the immune response elicited by MeVac virotherapy is limited by impaired antigen processing, common in tumor cells, and reasoned that delivering pre-processed antigens to the tumor via MeVac vectors could circumvent this limitation. Using a murine system and chicken ovalbumin as model antigen, I showed that dendritic cells and tumor cells exposed to MeVac vectors encoding antigen-derived epitope variants present the encoded epitopes, especially when exposed to MeVac encoding six epitope copies targeted to the proteasome. Increased epitope presentation enhanced priming of naïve OT-I T cells and activation of cognate cytotoxic T lymphocytes. Thus, I proved the concept of using MeVac encoding antigen-derived epitope variants for T cell priming and activation. This project is now continued in the human context.

Subsequently, I focused on T cell migration and effector function. Based on efficacy and tumor gene expression data from previous studies, I hypothesized that the efficacy of MeVac virotherapy is limited by insufficient intratumoral expression of specific chemokines and cytotoxic molecules. To assess whether intratumoral overexpression of these molecules improves therapeutic efficacy, I conducted gain of function (GOF) efficacy studies in immunocompetent models of murine melanoma and colon adenocarcinoma. GOF studies with MeVac vectors encoding murine CXCL9, CXCL10, CCL19, or CCL21a, which I generated and characterized, showed that these chemokines do not limit the therapeutic efficacy of oncolytic MeVac. Loss of function studies will reveal whether these molecules are essential for MeVac virotherapy despite not being limiting. The identified cytotoxic molecules will be investigated following the same experimental approach.

MeVac virotherapy often results in PD-L1 upregulation on tumor cells. To address whether the PD-1/PD-L1 pathway restricts the efficacy of MeVac virotherapy, I investigated the combination of MeVac with PD-1/PD-L1 blockade in two systems. In an immunocompetent model of murine colon adenocarcinoma, I found that MeVac vectors encoding antibody-like molecules against PD-1 or PD-L1 induce stronger antitumor immune memory compared to MeVac alone. However, this effect was insufficient to improve therapeutic efficacy. In an immunocompetent model of murine pancreatic ductal adenocarcinoma (PDAC), local MeVac plus systemic anti-PD-1 antibody treatment was more effective than either monotherapy. In this model, I showed that MeVac was the main driver of systemic antitumor immunity, but required combination with anti-PD-1 to transiently induce an immune activation gene signature in the tumor. This study provides the basis for a Phase I clinical trial of MeVac plus Pembrolizumab in PDAC patients, currently in preparation.

While this work was conducted in wild-type mice, I also established CD46tg mice as a novel animal model to study oncolytic MeVac therapy. My investigations are the first to show that these mice develop systemic tumor-specific and measles virus-specific immunity upon intratumoral MeVac treatment. In gene expression studies, I identified a MeVac-induced tumor immune gene signature that warrants further investigation. Finally, I worked towards the establishment of patient-derived *ex vivo* tumor slice cultures as a platform to study early effects of oncolytic MeVac in a setting that preserves the patient-specific tumor heterogeneity and microenvironment.

Overall, identifying limiting factors of MeVac virotherapy will lead to the rational development of combination approaches that tackle treatment resistance. Furthermore, the refined models that I have established will increase the robustness of preclinical findings, thus improving translation into clinical research.

The addendum describes a preclinical study that I conducted to test the cellular immune response of MeVac-susceptible mice to a MeVac-based vaccine candidate against COVID-19.

Zusammenfassung

Onkolytische Masern-Impfviren (MeVac) werden als neuartige Krebstherapeutika untersucht. Diese attenuierten Viren infizieren bevorzugt Tumorzellen und können dadurch eine systemische Antitumor-Immunantwort induzieren. Allerdings reicht die MeVac-Therapie alleine nicht aus, um hohe Raten an kompletten Tumor-Remissionen zu erreichen. Deshalb habe ich im Rahmen dieser Arbeit versucht, molekulare Mechanismen zu identifizieren, die das therapeutische Potential der MeVac-induzierten Immunantwort limitieren.

Dem Konzept des *"Cancer-Immunity Cycle"* folgend fokussierte ich mich zunächst auf Antigen-Präsentation und T-Zell-Priming. Ich postulierte, dass die MeVac-induzierte Antitumor-Immunantwort durch mangelhafte Antigen-Prozessierung, wie sie in Tumorzellen verbreitet ist, limitiert sein könnte und dass MeVac-Vektoren, die zur Expression präprozessierter Antigene im Tumor führen, diese Limitation überwinden könnten. In einem murinen System mit Hühner-Ovalbumin als Modell-Antigen konnte ich zeigen, dass dendritische Zellen und Tumorzellen, die mit diesen MeVac-Vektoren behandelt wurden, die kodierten Epitope präsentierten, insbesondere nach Behandlung mit Vektoren, die sechs an das Proteasom adressierte Epitop-Kopien kodieren. Eine vermehrte Epitop-Präsentation verstärkte das Priming naiver OT-I T-Zellen und die Aktivierung Epitop-spezifischer zytotoxischer T-Lymphozyten. Meine Ergebnisse stellen einen Machbarkeitsnachweis für die Verwendung Epitop-kodierender MeVac-Varianten zum *Priming* und zur Aktivierung spezifischer T-Zellen dar. Dieses Projekt wird nun im humanen Kontext fortgesetzt.

Anschließend fokussierte ich mich auf T-Zell-Migration und –Effektor-Funktionen. Basierend auf Daten zur therapeutischen Effizienz und intratumoralen Genexpression aus vorherigen Arbeiten postulierte ich, dass die Wirksamkeit der MeVac-Virotherapie durch unzureichende intratumorale Expression spezifischer Chemokine und zytotoxischer Moleküle limitiert sein könnte. Um festzustellen, ob die intratumorale Überexpression dieser Moleküle die Wirksamkeit verbessert, führte ich *gain of function (GOF)*-Wirksamkeitsstudien in immunkompetenten Mausmodellen des Melanoms und kolorektalen Karzinoms durch. Hierzu verwendete ich MeVac-Vektoren, die murines CXCL9, CXCL10, CCL19 oder CCL21a kodieren, welche ich generiert und charakterisiert habe. Diese Studien zeigten, dass diese Chemokine für die Wirksamkeit von onkolytischen MeVac nicht limitierend sind. *Loss of function*-Studien werden zeigen, ob diese Moleküle zwar nicht limitierend, jedoch essentiell sind für die MeVac-Virotherapie. Die von mir identifizierten zytotoxischen Moleküle werden mit demselben experimentellen Ansatz untersucht.

MeVac-Virotherapie führt häufig zur Hochregulation von PD-L1 auf Tumorzellen. Um festzustellen, ob der PD-1/PD-L1-Signalweg die Wirksamkeit der MeVac-Virotherapie begrenzt, untersuchte ich die Kombination von MeVac mit PD-1/PD-L1-Blockade in zwei experimentellen Systemen. In einem immunkompetenten Mausmodell des Kolonkarzinoms fand ich heraus, dass MeVac-Vektoren, die Antikörper-artige Moleküle gegen PD-1 oder PD-L1 kodieren, ein stärkeres Antitumor-Immun-Gedächtnis induzieren im Vergleich zu unmodifizierten MeVac. Allerdings war dieser Effekt unzureichend, um die therapeutische Wirksamkeit zu steigern. In einem immunkompetenten Modell des Pankreaskarzinoms (PDAC) war die lokale MeVac-Behandlung plus systemischer anti-PD-1-Antikörper wirksamer als die jeweiligen Monotherapien. In diesem Modell konnte ich zeigen, dass MeVac der Haupt-Treiber der systemischen Antitumor-Immunantwort ist, die Kombination mit anti-PD-1 jedoch nötig ist, um eine transiente Immunaktivierungs-Gensignatur im Tumor zu induzieren. Diese Studie bildet die Grundlage für eine klinische Phase I-Studie mit MeVac plus Pembrolizumab für PDAC-Patienten, die aktuell vorbereitet wird.

Während diese Studien in Wildtyp-Mäusen durchgeführt wurden, etablierte ich zusätzlich ein CD46-transgenes Mausmodell für Untersuchungen zur onkolytischen Virotherapie. Zum ersten Mal konnte ich zeigen, dass diese Mäuse nach intratumoraler MeVac-Behandlung systemische Antitumor- und Masern-spezifische Immunantworten entwickeln. In Genexpressionsanalysen identifizierte ich eine MeVac-induzierte Genexpressions-Signatur, die weitere Untersuchungen

fordert. Schließlich arbeitete ich an der Etablierung von Patienten-abgeleiteten *ex vivo*-Tumorschnittmodellen als Plattform zur Untersuchung der frühen Effekte von onkolytischen MeVac in einem Modell, das Tumorheterogenität widerspiegelt und das Patienten-spezifische Tumormikromilieu erhält.

Zusammenfassend ist festzustellen, dass die Erkennung von Faktoren, welche die Wirksamkeit der MeVac-Virotherapie begrenzen, zur rationalen Entwicklung von Kombinationstherapien beiträgt, um Therapieresistenzen zu überwinden. Des Weiteren werden die verbesserten Modelle, die ich etabliert habe, die Aussagekraft präklinischer Ergebnisse steigern, so dass die Translation in die klinische Forschung verbessert wird.

Das Addendum beschreibt eine präklinische Studie, die ich in MeVac-suszeptiblen Mäusen durchgeführt habe, um die zelluläre Immunantwort auf einen MeVac-basierten Impfstoff-Kandidaten gegen COVID-19 zu testen.

Resum

Les soques vacunals del virus del xarampió (MeVac) [i] són oncolítiques i s'estan estudiant com a nova teràpia contra el càncer. A part de destruir cèl·lules canceroses per mitjà de la lisi cel·lular, aquests virus atenuats activen la resposta immunitària adaptativa primària (*priming*) contra el tumor a nivell sistèmic. No obstant això, la viroteràpia amb MeVac és insuficient per aconseguir taxes elevades de regressió tumoral completa. Per tant, en aquest estudi aspiro a identificar mecanismes moleculars que limiten el potencial terapèutic de la resposta immunitària desencadenada per les MeVac oncolítiques.

Seguint el cicle immunitari del càncer, primer m'he centrat en la presentació d'antígens i el *priming* de cèl·lules T. He hipotetitzat que la resposta immunitària desencadenada per la viroteràpia amb MeVac es veu limitada per un processament d'antígens defectuós, habitual en cèl·lules tumorals. En conseqüència, he raonat que aquesta limitació es podria superar amb l'administració intratumoral, per mitjà de vectors MeVac, d'antígens preprocessats. Utilitzant un sistema murí i ovoalbúmina de pollastre com a model d'antigen, he demostrat que les cèl·lules dendrítiques i les cèl·lules tumorals exposades a vectors MeVac dissenyats per codificar antígens preprocessats (els quals consisteixen en diverses variants d'un epítop derivat de l'ovoalbúmina) presenten l'epítop codificat en el vector, especialment quan s'exposen a vectors MeVac que codifiquen sis còpies de l'epítop dirigides al proteasoma. A més, he observat que l'increment en la presentació d'antígens potencia el *priming* de les cèl·lules T *naïve* OT-I i l'activació dels limfòcits T citotòxics específics per a l'epítop codificat en el vector MeVac. Així doncs, he demostrat el concepte d'utilitzar vectors MeVac que codifiquen antígens preprocessats per promoure el *priming* i l'activació de cèl·lules T. Actualment aquest projecte s'està continuant en el context humà.

A continuació, m'he centrat en el trànsit de les cèl·lules T i la seva funció efectora. Basant-me en dades d'eficàcia i d'expressió gènica tumoral, obtingudes en estudis previs, he hipotetitzat que l'eficàcia de la viroteràpia amb MeVac es veu limitada per un nivell d'expressió intratumoral insuficient de determinades quemocines i molècules citotòxiques. Per analitzar si la sobreexpressió d'aquestes molècules al tumor millora l'eficàcia de la viroteràpia amb MeVac, he dut a terme estudis de guany de funció (GOF) [ii] en models immunocompetents de melanoma murí o d'adenocarcinoma de còlon murí. Els estudis de GOF amb vectors MeVac, generats i caracteritzats per mi, que codifiquen la variant murina de les quemocines CXCL9, CXCL10, CCL19, o CCL21a, han demostrat que aquestes quemocines no limiten l'eficàcia terapèutica de les MeVac oncolítiques. Estudis de pèrdua de funció revelaran si aquestes molècules són essencials per a la viroteràpia amb MeVac malgrat no limitar-la. Les molècules citotòxiques que he identificat seran estudiades seguint el mateix procediment experimental.

La viroteràpia amb MeVac habitualment augmenta l'expressió de la molècula PD-L1 en cèl·lules tumorals. Per determinar si la via de senyalització PD-1/PD-L1 restringeix l'eficàcia d'aquesta viroteràpia, he investigat la seva combinació amb inhibidors de la PD-1 o PD-L1 en dos sistemes experimentals. En un model immunocompetent d'adenocarcinoma de còlon murí, he observat que el tractament amb vectors MeVac dissenyats per codificar inhibidors de la PD-1 o PD-L1 (essent aquests inhibidors molècules similars a anticossos) indueix una memòria immunològica antitumoral més potent que la monoteràpia amb MeVac. No obstant, aquest efecte ha demostrat ser insuficient per millorar l'eficàcia de la viroteràpia. En un model immunocompetent d'adenocarcinoma ductal pancreàtic (PDAC) [iii] murí, la viroteràpia local amb

[i] **MeVac** és una abreviatura derivada de l'anglès que significa "soca vacunal del virus del xarampió" [en anglès: *measles virus vaccine strain*].

[ii] **GOF** és una abreviatura derivada de l'anglès que significa "guany de funció" [en anglès: *gain of function*].

[iii] **PDAC** és una abreviatura derivada de l'anglès que significa "adenocarcinoma ductal pancreàtic" [en anglès: *pancreatic ductal adenocarcinoma*].

MeVac més la teràpia sistèmica amb anticossos contra la PD-1 ha millorat l'eficàcia de les respectives monoteràpies. En aquest model, he demostrat que la viroteràpia amb MeVac és la principal impulsora de la immunitat antitumoral sistèmica però requereix la combinació amb anticossos contra la PD-1 per induir, de manera transitòria, un patró gènic d'immunoactivació al tumor. Aquest estudi proporciona la base per un assaig clínic de Fase I que analitzarà la combinació de Pembrolizumab amb la viroteràpia amb MeVac en pacients que pateixen PDAC. Actualment, aquest assaig clínic està en fase de preparació.

Mentre que aquests estudis s'han realitzat en ratolins *wild-type*, també he establert ratolins CD46tg com a nou model animal de la teràpia amb MeVac oncolítiques. Per primera vegada, he demostrat que aquests ratolins desenvolupen immunitat sistèmica contra el tumor i contra el virus del xarampió després de tractament intratumoral amb MeVac. En estudis d'expressió gènica, he identificat un patró gènic d'immuno-activació en tumors tractants amb MeVac que justifiquen investigacions futures. Finalment, he iniciat estudis per establir cultius *ex vivo* de seccions tumorals derivades de pacients com a plataforma en la qual estudiar els efectes inicials de les MeVac oncolítiques en un sistema que reflecteixi l'heterogeneïtat del tumor i preservi el microambient tumoral específic del pacient.

En general, la identificació de factors limitats de la viroteràpia amb MeVac contribuirà al desenvolupament racional de combinacions terapèutiques que combatin la resistència als tractaments actuals. Optimitzar els models experimentals augmentarà la robustesa dels descobriments preclínics, fet que millorarà la promoció d'aquests estudis cap a investigacions translacionals i clíniques.

L'apèndix descriu un estudi preclínic que he dut a terme per investigar la resposta immunològica a una vacuna contra la COVID-19 basada en un vector MeVac.

Contents

Abbreviations

Note: For abbreviations on growth media refer to Table 9.

ACK	Ammonium-Chloride-Potassium
ACKR	Atypical chemokine receptor
AdV	Adenovirus
AF700	Alexa Fluor™ 700
ALI	Air-liquid interface
APC	Antigen presenting cell (biological context) / Allophycocyanin (flow cytometry)
ATCC	American Type Culture Collection
ATP	Adenosine triphosphate
ATU	Additional transcription unit
BCA	Bicinchoninic acid
BCIP	5-bromo-4-chloro-3-indolyl-phosphate
BiTE	Bispecific T cell engager
BMDM	Bone marrow-derived macrophage
bp	Basepairs
BSA	Bovine serum albumin
BV650	Brilliant Violet™ 650
CAG	Human cytomegalovirus immediate early enhancer and chicken β-actin promoter
CAR	Chimeric antigen receptor
CCL	C-C motif ligand
CCR	C-C chemokine receptor
CD	Cluster of differentiation
CD46tg	Human CD46-transgenic mice (from the MY II strain)
CDS	Coding sequence
CEA	Carcinoembryonic antigen
CEF	Chicken embryo fibroblast

CMCP	Center for Model System and Comparative Pathology
CMV	Cytomegalovirus
ConA	Concanavalin A
Cq	Quantification cycle
CTL	Cytotoxic T lymphocyte
CTLA-4	Cytotoxic T lymphocyte antigen 4
CXCL	C-X-C motif ligand
CXCR	C-X-C chemokine receptor
DAMPs	Danger-associated molecular patterns
DAPI	4’,6-diamidino-2-phenylindole
DC	Dendritic cell
DC-SIGN	Dendritic cell-specific ICAM-grabbing non-integrin
DKFZ	Deutsches Krebsforschungszentrum (German Cancer Research Center)
DMH	Dimethylhydrazine
DMSO	Dimethyl sulfoxide
DNA	Deoxyribonucleic acid
dNTP	Deoxynucleotide triphosphate
D-PBS	Dulbecco’s phosphate-buffered saline
DPP4	Dipeptidylprotease 4
ECM	Extracellular matrix
EDTA	Ethylenediaminetetraacetic acid
EF1	Eukaryotic translation elongation factor 1
e.g.	*exempli gratia* (for example)
eGFP	Enhanced green fluorescent protein
ELISA	Enzyme-linked immunosorbent assay
ELISpot	Enzyme-linked immunosorbent spot
EMA	European Medicines Agency

ERCC	External RNA Controls Consortium
et al.	*et alia* (and others)
F	Measles virus fusion protein
FF	Free-floating
FACS	Fluorescence-activated cell sorting
Fc	Fragment crystallizable
FCS	Fetal calf serum
FDA	United States Food and Drug Administration
FFPE	Formalin-fixed paraffin-embedded
FISH	Fluorescence *in situ* hybridization
FITC	Fluorescein Isothiocyanate
FMOi	Fluorescence minus one, plus isotype control
GFP	Green fluorescent protein
GM-CSF	Granulocyte-macrophage colony-stimulating factor
GOF	Gain of function
GPCR	G protein-coupled receptor
H	Measles virus hemagglutinin protein
HBV	Hepatitis B virus
HEPES	4-(2-Hydroxyethyl)piperazine-1-ethanesulfonic acid
HIV	Human immunodeficiency virus
HMGB1	High mobility group protein B1
HSV	Herpes simplex virus
HSV1/HSV2	Herpes simplex virus type 1 / Herpes simplex virus type 2
ICB	Immune checkpoint blockade
i.e.	*id est* (that is)
IFN-α/β/γ	Interferon alpha / Interferon beta / Interferon gamma
IgG	Immunoglobulin G

IHC	Immunohistochemistry
IL	Interleukin
i.p.	Intraperitoneal
ISGs	Interferon-stimulated genes
i.t.	Intratumoral
i.v.	Intravenous
kbp	kilo-base pairs
L	Measles virus large protein
LOF	Loss of function
M	Measles virus matrix protein
mAb	Monoclonal antibody
MDA-5	Melanoma differentiation-associated protein 5
MDSCs	Myeloid-derived suppressor cells
MERS-CoV	Middle east respiratory syndrome coronavirus
MeV	Measles virus (wild-type, pathogenic strain)
MeVac	Measles virus vaccine strain
MFI	Median fluorescence intensity
MHC	Major histocompatibility complex class I (MHC-I) or class II (MHC-II)
miRNA	MicroRNA
MMP	Matrix metalloproteinase
MOI	Multiplicity of infection
NCBI	National Center for Biotechnology Information
NCT	National Center for Tumor Diseases
NDV	Newcastle disease virus
NEB	New England Biolabs
NIS	Sodium-iodide symporter
NK cell	Natural killer cell

ORF	Open reading frame
OV	Oncolytic virus
OVA	Ovalbumin
P	Measles virus phosphoprotein
PAMPs	Pathogen-associated molecular patterns
PBMCs	Peripheral blood mononuclear cells
PBS-T	Phosphate-buffered saline with Tween 20
PCR	Polymerase chain reaction
PDAC	Pancreatic ductal adenocarcinoma
PD-1	Programmed cell death 1
PD-L1	Programmed cell death 1 ligand 1
PDTF	patient-derived tumor fragment
PE	Phycoerythrin
PerCP-Cy5.5	Peridinin Chlorophyll Protein – Cyanine 5.5
PFA	Paraformaldehyde
p. i.	Post infection / Post inoculation
PMA	Phorbol 12-myristate 13-acetate
PMDA	Pharmaceuticals and Medical Devices Agency
PRR	Pattern recognition receptor
PV	Poliovirus
PVDF	Polyvinylidene difluoride
PVRL-4	Poliovirus receptor-like 4
qPCR	Quantitative Polymerase Chain Reaction
RIG-I	Retinoic acid-inducible gene I
RLE	Relative log expression
RNA	Ribonucleic acid (Not introduced 1.3.2.3 Cancer Vaccines)
RNP	Ribonucleoprotein

RNS	Reactive nitrogen species
ROS	Reactive oxygen species
RT	Room temperature (in the context of incubations) / Reverse transcription
RUV	Remove unwanted variation
RV	Reovirus
SA	Streptavidin
SARS	Severe acute respiratory syndrome
SARS-CoV-1	Severe acute respiratory syndrome coronavirus 1
SARS-CoV-2	Severe acute respiratory syndrome coronavirus 2
s.c.	subcutaneous
scFv	Single-chain fragment variable
scFv-Fc	Single-chain fragment variable (scFv) linked to an immunoglobulin fragment crystallizable (Fc) region
SDS-PAGE	Sodium dodecyl sulfate polyacrylamide gel electrophoresis
SLAM	Signaling lymphocyte activation molecule
TAA	Tumor-associated antigen
TBE	Tris-borate-EDTA
TBS-T	Tris-buffered saline with Tween 20
TCR	T cell receptor
TDLN	Tumor-draining lymph node
T_{EFF}	T effector cell
T_H1	T helper type 1 cell
TILs	Tumor-infiltrating lymphocytes
TLR	Toll-like receptor
TLS	Tertiary lymphoid structure
TMB	3,3’,5,5’-tetramethylbenzidine
TME	Tumor microenvironment
TNF	Tumor necrosis factor

TRAIL	Tumor necrosis factor-related apoptosis-inducing ligand
T_{REG}	T regulatory cell
T-VEC	Talimogene laherparepvec
uPAR	urokinase plasminogen activator receptor
UWH	Universität Witten/Herdecke (Witten/Herdecke University)
V_H	Variable domain of an immunoglobulin heavy chain
V_L	Variable domain of an immunoglobulin light chain
VP1/VP2/VP3	Virus passage 1 / Virus passage 2 / Virus passage 3
VSV	Vesicular stomatitis virus
XTT	2,3-bis-(2-methoxy-4-nitro-5-sulfophenyl)-2H-tetrazolium-5-carboxanilide

.

1 Introduction

1.1 Cancer – An Unmet Medical Need

Cancer is a large group of diseases arising from malignant cell transformation. These diseases share an ever growing number of common features, such as invasiveness and uncontrolled cell growth, collectively known as the "Hallmarks of Cancer" [1]. However, they are also extremely diverse. This diversity hampers cancer prevention and diagnosis as well as the development of treatments that prove highly efficacious for a large proportion of patients. In fact, despite several therapeutic breakthroughs, cancer diseases are still one of the leading causes of mortality worldwide, accounting for almost 10 million deaths across 185 countries in 2020 [2]. The oncology field is therefore in urgent need for improvements in all directions: prevention, diagnosis, and treatment.

1.2 The Immune System and Cancer

The immune system has the ability to recognize and kill tumor cells. This phenomenon, referred to as cancer immunosurveillance, comprises both innate and adaptive immune responses [3]. Natural killer (NK) cells are the cytotoxic effector cells of the innate immune system, whereas cytotoxic T lymphocytes (CTLs), mainly of CD8+ T cell lineage, are the most powerful effector cells of adaptive antitumor immunity [4,5].

1.2.1 The Cancer-Immunity Cycle

The "cancer-immunity cycle" was conceptualized in 2013 as a simplified framework of the sequential steps required for the development of CTL-mediated antitumor immune responses [6,7]. This cycle starts with the release of tumor antigens from tumor cells that are dying in an immunogenic manner (Figure 1, Step 1). The released antigens are captured by antigen presenting cells (APCs) located at the tumor site, mainly dendritic cells (DCs). In parallel, the immunostimulatory signals released during immunogenic tumor cell death promote DC maturation (Figure 1, Step 2). Mature DCs process the captured antigens and present antigen-derived peptides on major histocompatibility complex (MHC) molecules. Since the captured antigens are exogenous to the DCs, they are classically processed via the endosomal pathway and presented on MHC class II (MHC-II) molecules. However, they can also be processed via the vacuolar or cytosolic pathways and presented on MHC class I (MHC-I) molecules, a phenomenon known as antigen cross-presentation[8]. This phenomenon is important for subsequent priming of tumor-specific CD8+ naïve T cells [9]. Besides enhanced antigen presentation properties, mature DCs acquire a migratory phenotype and traffic to the tumor-draining lymph node (TDLN) following C-C motif ligand (CCL)19 and CCL21 chemokine gradients [10]. There, they prime cognate naïve T cells (Figure 1, Step 3). This

process requires three signals, namely antigen presentation, costimulation, and an appropriate cytokine milieu, all of which are provided by mature DCs [11]. In addition, cross-priming of CD8+ T cells requires the support of CD4+ helper T cells [9]. A subset of primed CD8+ T cells differentiates into effector CD8+ CTLs and traffics to the tumor site via chemotaxis, for instance following C-X-C motif ligand (CXCL)9 and CXCL10 chemokine gradients (Figure 1, Step 4) [12]. Upon recruitment, CD8+ CTLs infiltrate the solid tumor (Figure 1, Step 5). There, they recognize tumor cells presenting the cognate epitope (peptide) on MHC-I molecules. This recognition activates CTL-mediated cytotoxic effector functions (Figure 1, Step 6). Contrary to priming, CTL activation requires very little, if any, costimulation. CTL-mediated cytotoxicity comprises granule-mediated and receptor-mediated mechanisms [13,14]. The first consists in the release of perforin and granzymes from lytic granules present in CTLs into the extracellular space. Upon release, perforin forms pores in the target cell membrane, eventually leading to necrosis [15]. Granzymes are taken up by target cells and induce apoptosis [14]. The second mechanism involves members of the tumor necrosis factor (TNF) family. Activated CTLs upregulate TNF family ligands, such as Fas ligand, TNF-α [16], lymphotoxins [17,18], and TNF-related apoptosis-inducing ligand (TRAIL). Binding of these ligands to the corresponding receptors, expressed on target cells, triggers target cell death. Activated CTLs also secrete interferon (IFN)-γ. Among other functions, this pleiotropic cytokine enhances CTL effector function and activates additional cytotoxic effector cells [19]. Ultimately, CTL-mediated killing of tumor cells leads to the release of tumor antigens, thereby starting a new round of the cancer-immunity cycle. Subsequent rounds of this cycle increase the breadth and depth of the antitumor immune response, for instance by priming immunity against additional tumor antigens emerging from acquired mutations.

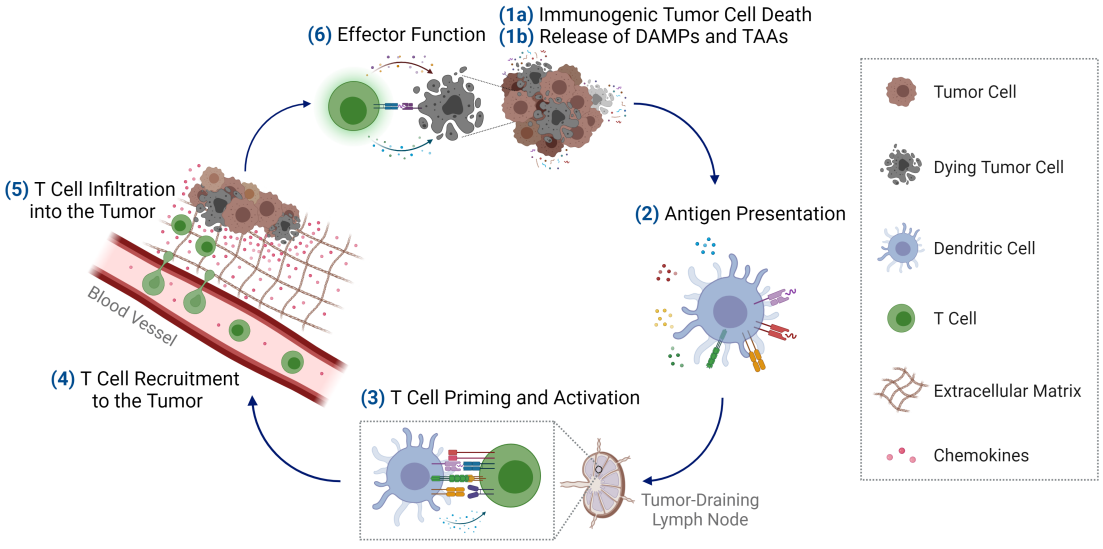

Figure 1. The cancer-immunity cycle. The main steps towards the development of T cell-mediated antitumor immunity, known as the cancer-immunity cycle, are depicted. Schematic created with BioRender.com.

1.2.2 Immune Evasion – A Hallmark of Cancer

In clinical reality, the full potential of the cancer-immunity cycle is limited by a plethora of mechanisms that suppress or evade the antitumor immune response. Given its contribution to cancer progression, immune evasion is considered a "Hallmark of Cancer" [20]. The process of cancer immunoediting, the tumor immune phenotype, and the upregulation of inhibitory immune checkpoints are decisive in the acquisition of this hallmark.

1.2.2.1 Cancer Immunoediting

Tumors evolve under selective pressure exerted by the immune system. This process is known as cancer immunoediting and consists of three phases: elimination, equilibrium, and escape [3]. Initially, many nascent tumors are completely eradicated through innate and adaptive cytotoxic immune responses, including CTL-mediated responses triggered by the cancer-immunity cycle (elimination phase). However, in some tumors the acquisition of genetic or epigenetic changes leads to tumor cell variants that escape immunological recognition or elimination, and thus persist. In that case, the elimination phase fails and a dynamic equilibrium between the immune system and the tumor cells is established (equilibrium phase). Subsequent immune responses are triggered against the previously resistant variants, but again new variants appear and are selected. This equilibrium continues until the immune system kills all tumor cells (retroceding to the elimination phase) or until immune-resistant tumor cell variants expand in an uncontrolled manner (evasion phase) [21].

1.2.2.2 Tumor Immune Phenotype

The progression of solid tumors is influenced by the tumor microenvironment (TME), a complex network of malignant and non-malignant cells surrounded by the extracellular matrix (ECM). Cancer cells often reprogram non-malignant cells from the TME (e.g. fibroblasts, pericytes, endothelial cells, immune cells) to support tumor progression, for instance by promoting angiogenesis, providing growth factors, or inducing immunosuppression[22]. Based on the degree of local inflammation, tumors are classified into immunologically "hot" (inflamed) and immunologically "cold" (non-inflamed)[23,24]. Understanding how the tumor immune phenotype shapes antitumor immunity provides insights into potential limiting steps of the cancer-immunity cycle.

Inflamed "hot" tumors are broadly infiltrated by immune effector cells, such as NK cells, CTLs, and CD4+ helper type 1 T cells (T_H1). Moreover, they contain high levels of pro-inflammatory cytokines, for instance interleukin (IL)-1β, IL-12, interferon (IFN)-α, IFN-β, IFN-γ, and TNF-α[23]. Although this profile is indicative of pre-existing antitumor immunity, in these tumors the cancer-immunity cycle might be suppressed at the effector phase, for instance via T cell exhaustion.

Non-inflamed “cold” tumors are sub-classified into three immune phenotypes: immune-suppressed, immune-excluded, and immune-deserted. Immune-suppressed tumors are largely infiltrated by tolerogenic immune cells, such as regulatory T cells (T_{REG}) cells, M2 anti-inflammatory macrophages, and myeloid-derived suppressor cells (MDSCs) [25]. These cells induce immunosuppression via multiple mechanisms, including metabolic reprogramming, production of reactive oxygen and nitrogen species (ROS, RNS), and secretion of pro-tumorigenic cytokines, such as IL-4, IL-10, IL-13, and transforming growth factor (TGF)-β [26]. Under these conditions, DCs do not receive the immunostimulatory signals required for maturation and rather acquire a tolerogenic phenotype, subsequently priming T_{REG} cells and inducing immune tolerance. Immune-excluded tumors contain immune effector cells, but those are located at the invasive tumor margin and do not infiltrate the tumor core [23,24]. Immune-deserted tumors are characterized by low abundance or absence of effector and regulatory immune cells, both at the tumor margin and tumor core [23]. Overall, multiple mechanisms impair the cancer-immunity cycle in non-inflamed “cold” tumors. In immune-deserted and immune-suppressed tumors, the cycle might not be triggered, for instance due to absence of intratumoral immune cells or to presence of regulatory and tolerogenic cells. In immune-excluded tumors, the cycle might be impaired at the trafficking and invasion phases, for instance by physical barriers or dysregulated chemokine signaling.

1.2.2.3 Immune Checkpoints

The cancer-immunity cycle is also regulated by immune checkpoints [27]. These are co-receptors expressed on effector and/or regulatory immune cells that provide stimulatory or inhibitory signals upon interacting with the corresponding ligands, commonly expressed on APCs but also on other cell types. Stimulatory immune checkpoints (e.g. CD28, OX40, 4-1BB) support immune cell activation. Conversely, inhibitory immune checkpoints prevent immune cell hyperactivation and promote self-tolerance. Among those, cytotoxic T lymphocyte antigen 4 (CTLA-4) and programmed cell death 1 (PD-1) are the most studied. CTLA-4 acts predominantly in lymphoid organs and regulates early stages of the cancer-immunity cycle, such as T cell priming and differentiation into regulatory (T_{REG}) or effector (T_{EFF}) T cells [28]. It is constitutively expressed on T_{REG} cells and strongly induced on T_{EFF} cells upon antigen stimulation. PD-1 is upregulated on CTLs and NK cells upon antigen encounter and acts later, mainly at the periphery [28]. It modulates the effector phase of the cycle by promoting CTL and NK cell exhaustion, thus dampening their cytotoxic functions, particularly during chronic viral infection and cancer.

1.3 Cancer Immunotherapy

The identification of molecular mechanisms driving cancer immune evasion has fostered the development of immunotherapy as the fifth pillar of cancer treatment complementing surgery, radiotherapy, chemotherapy, and molecularly-targeted therapy. Cancer immunotherapy aims at inducing or enhancing immune-mediated killing of tumor cells [29]. This field comprises a wide spectrum of approaches including cytokine therapy [30], antibody therapy [31], adoptive cell therapy [32,33], cancer vaccines [34], and oncolytic virotherapy [35].

1.3.1 Recent Breakthroughs (2010 – 2020)

The past decade has marked a major breakthrough for cancer immunotherapy. Within just eight years, we have witnessed the first United States Food and Drug Administration (FDA) approvals of DC-based therapeutic cancer vaccines (Sipuleucel-T, 2010) [36], immune checkpoint blockades (Ipilimumab, 2011) [37], oncolytic viruses (Talimogene Laherparepvec, 2015) [38], and chimeric antigen receptor (CAR) T cells (Tisagenlecleucel, 2017) [39] for the treatment of cancer. Although the overall clinical responses are far from optimal, each of these therapies has provided substantial clinical benefits to subgroups of patients suffering from tumors refractory to previous standard-of-care treatments. Paying tribute to the unprecedented therapeutic benefit of immune checkpoint blockades, James P. Allison and Tasuku Honjo were jointly awarded the 2018 Nobel Prize in Physiology or Medicine "*for their discovery of cancer therapy by inhibition of negative immune regulation*" [40]. Together, these milestones have established cancer immunotherapy as a real treatment option for cancer patients.

1.3.2 Current State and Challenges

1.3.2.1 Cytokine and Antibody Therapy

Cytokine administration was the first type of immunotherapy but is hampered by short half-lives and treatment-related adverse events, particularly upon systemic treatment [30]. Antibody therapy comprises several strategies, such as tumor-targeting monoclonal antibodies (mAbs) (*e.g.* Rituximab, anti-CD20 mAb [41]), antibody-drug conjugates, and bispecific T cell engagers (BiTEs) (*e.g.* Blinatumomab [42]). However, antigen escape hampers response to these treatment modalities [43].

Based on the physiological role of immune checkpoints, the idea of enhancing T cell-mediated antitumor immunity by treating cancer patients with (i) agonistic mAbs targeted to stimulatory co-receptors or (ii) antagonistic mAbs targeted to inhibitory co-receptors emerged as a promising strategy to fight cancer. Whereas the first approach is under clinical investigation [44], the latter, included under the broader concept of immune checkpoint blockade (ICB), received clinical approval in 2011 with Ipilimumab (anti-CTLA-4 mAb) [37]. As of October 2023, the FDA has approved

nine ICB mAbs for the treatment of several tumor entities [45–47]. Those target inhibitory co-receptors (CTLA-4, PD-1, lymphocyte activation gene 3 (LAG-3)) or the corresponding ligands (PD-1 ligand 1 (PD-L1)). ICB has revolutionized cancer immunotherapy by conferring durable responses to cancer patients previously considered untreatable. Responses in patients with advanced melanoma or non-small-cell lung cancer are among the most remarkable examples [37,48,49]. However, long-term responses are limited to subsets of patients and influenced by numerous factors. For instance, immunological mechanisms of resistance to ICB include low tumor antigenicity, upregulation of other inhibitory immune checkpoints, and absence of intratumoral immune effector cells [45].

1.3.2.2 Adoptive Cell Therapy

Adoptive cell therapy consists in the infusion of immune effector cells to the patient, such as tumor-infiltrating lymphocytes (TILs), T cell receptor (TCR)-transgenic T cells, CAR T cells, and CAR NK cells [32,33]. Several CAR T cell products have received FDA approval for the treatment of hematological malignancies, but the results have been less promising in solid tumors. Reasons for lack of response include immunosuppressive TMEs, low efficiency of cell trafficking to the tumor, and poor persistence of the infused cells. Defects in the antigen processing and presentation machinery, common in tumor cells, hamper the efficacy of TCR-based therapies, whereas antigen escape via immunoediting is a major challenge of CAR-based therapies. Modular CAR T cells are a promising strategy to circumvent this limitation [50,51].

1.3.2.3 Cancer Vaccines

Cancer vaccines are active immunotherapies that educate the patient's immune system to trigger the cancer-immunity cycle. They can be prophylactic or therapeutic and are classified into antigen-specific and antigen-agnostic [34]. Antigen-specific vaccines are designed to deliver specific tumor antigens to the patient, together with adjuvants. The chosen antigens are administered directly (deoxyribonucleic acid [DNA], ribonucleic acid [RNA], or peptide vaccines) or loaded *ex vivo* onto DCs, subsequently infused into the patient (*e.g.* Sipuleucel-T, FDA-approved for the treatment of prostate cancer [36]). These vaccines enhance antigen presentation and DC maturation *in situ*, thus supporting the cancer-immunity cycle from the second step onwards. Antigen-agnostic vaccines have a broader antigen coverage. They consist of non-proliferative (*e.g.*, irradiated) tumor cells (sometimes engineered to secrete GM-CSF, *e.g.*, GVAX [52,53]) delivered to patients together with adjuvants. Death of the infused cells in the immunogenic context conferred by the adjuvant triggers the cancer-immunity cycle. Of note, by promoting immunogenic tumor cell death, radiotherapy and some chemotherapies also induce antigen-agnostic tumor vaccination effects [54,55]. Moreover, by preferentially lysing tumor cells, certain viruses act as antigen-agnostic cancer vaccines. Their therapeutic application in the treatment of cancer is referred to as oncolytic virotherapy.

1.4 Oncolytic Virotherapy

In the mid 1900s, clinical case reports described transient regressions of hematological malignancies during naturally acquired virus infections [56]. These observations suggested that certain viruses can eliminate tumor cells and fostered their study as cancer therapeutics. However, administration of pathogenic viruses raised major safety concerns. Thus, investigations soon shifted to safer approaches that employed (i) viruses for which humans are not a natural host or (ii) attenuated strains of pathogenic viruses. These investigations demonstrated that some non-pathogenic (for humans) viruses preferentially infect and replicate in human tumor cells, resulting in tumor cell lysis, whereas healthy cells remain spared. These viruses were therefore referred to as "oncolytic" and their administration to patients for the treatment of cancer was termed "oncolytic virotherapy" [57]. To date, a broad range of viruses with oncolytic properties (inherent to the virus or acquired via genetic engineering) are under preclinical and, in some cases, clinical investigation [35]. In alphabetical order, the most studied ones are adenovirus (AdV), herpes simplex virus (HSV), measles virus vaccine strains (MeVac), Newcastle disease virus (NDV), parvovirus (H-1PV), poliovirus (PV), reovirus (RV), vaccinia virus (VACV), and vesicular stomatitis virus (VSV).

1.4.1 Oncoselectivity

Oncolytic viruses (OVs) are oncoselective, *i.e.* they preferentially infect and replicate in tumor cells. This property, which can be conferred both on the entry and post-entry level, is guided by tumor evolution: some of the genetic alterations acquired by tumor cells, presumably selected for their tumorigenic or immune evasion effects, render tumor cells more susceptible and permissive to viruses. For instance, tumor cells often overexpress certain viral entry receptors, such as CD155 (PV entry receptor), thus becoming more susceptible to the corresponding virus [58]. As another example, tumor cells commonly acquire defects in the type I IFN pathway, probably selected to avoid its anti-proliferative signals [59]. Since this pathway is a major defense mechanism against viral infections, the acquired defects prevent tumor cells from developing an innate antiviral immune response. In this case, viral replication is limited in healthy cells but supported in tumor cells [60].

Deleting or disrupting viral virulence genes via genetic engineering may also confer oncoselectivity (in addition to attenuation), particularly when the function of the disrupted viral gene is complemented by mutations acquired by tumor cells. Two classical examples are (i) the deletion of the gene encoding viral thymidine kinase (*e.g.* in oncolytic HSV [61]), the function of which is complemented by host thymidine kinase, commonly overexpressed in tumor cells, and (ii) the disruption of the *E1A* gene of AdV, the function of which is complemented by loss-of-function mutations in the tumor-suppressor gene *RB1* (encoding retinoblastoma protein), also common in tumor cells [62].

Other genetic engineering approaches that render viruses oncoselective include the modification of virus tropism towards surface antigens overexpressed on tumor cells [63], the usage of tumor-specific promoters to drive the expression of certain viral genes [64], and the post-transcriptional modulation of viral replication by cell-specific microRNAs (miRNAs) [65].

1.4.2 Modes of Action

The antitumor properties of OVs, namely oncoselectivity and lytic viral replication, trigger (i) direct oncolysis and (ii) tumor vaccination effects [66]. This dual mechanism of action starts with the lytic viral replication cycle, a consequence of which is the lysis of the infected cell. In the context of oncolytic virotherapy, the lysed cell is predominantly a tumor cell, since OVs preferentially replicate in those. Besides reducing the tumor mass, this phenomenon, referred to as "direct oncolysis" promotes the release of tumor-associated antigens (TAAs) into the TME. OV-mediated tumor cell death is often accompanied by the release of danger-associated molecular patterns (DAMPs) and is therefore immunogenic [67]. Moreover, since the dying tumor cell is infected, its lysis leads to the release of OV-derived pathogen-associated molecular patterns (PAMPs). Tumor cell lysis in such an immunogenic context supports the induction of adaptive antitumor immunity by representing the first step of the cancer-immunity cycle [68]. Ultimately, this cycle leads to CTL-mediated killing of both infected and, more importantly, uninfected tumor cells, thus further reducing (and perhaps even eliminating) the tumor mass.

Of note, the specificity of the CTL response triggered by OVs is shaped *in situ* based on the broad spectrum of TAAs released from the lysed tumor cells [68]. This antigen-agnostic effect offers the opportunity of developing immune responses against unknown TAAs which would not have been included in antigen-specific cancer vaccines. Despite being shaped *in situ*, the antitumor immune response elicited by OVs acts on a systemic level and has abscopal effects. As a remarkable example, in a phase III clinical trial melanoma patients receiving local virotherapy with oncolytic HSV-1 encoding granulocyte-macrophage colony-stimulating factor (GM-CSF) experienced partial or total remission of some OV-injected and some non-OV-injected melanoma lesions [69].

Besides triggering the cancer-immunity cycle, which focuses on DCs and CTLs, the pro-inflammatory state conferred by OV-mediated tumor cell death supports other antitumor immune mechanisms, such as activation of additional immune effector cells (*e.g.*, NK cells) and macrophage re-polarization from a pro-tumorigenic (M2) to an anti-tumorigenic (M1) phenotype [70]. Together with the cancer-immunity cycle, these mechanisms turn "cold" (non-inflamed) tumors "hot" (inflamed). However, OV-induced intratumoral inflammation also supports the development of antiviral immunity. The contribution of antiviral immunity to the efficacy of oncolytic virotherapy is a topic of intense debate [71].

The immunological effects of OVs are enhanced by inserting transgenes encoding immunomodulators in the viral genome, a process known as “arming”. OVs have been engineered to encode TAAs, cytokines, BiTEs, and ICBs, among other molecules [35]. In solid tumors, this approach, which links transgene expression with viral replication, allows targeted production of the encoded molecule within the tumor mass (site of viral replication), thus reducing the risk of toxicities associated with systemic delivery of immunomodulators. Moreover, this strategy provides a constant supply of the encoded molecule as long as there is viral replication, thereby prolonging the effect of immunomodulators with short half-lives, such as cytokines. Besides immunomodulators, other types of therapeutic payloads have been encoded in OVs to confer additional modes of action, such as metabolism regulation [72] or disruption of the extracellular matrix [73]. The therapeutic effects of OVs are also enhanced by combination treatments that do not necessarily involve virus “arming". For instance, OVs have been combined with radiotherapy, chemotherapy, and other cancer immunotherapies, such as CAR T cells and ICBs [35].

1.4.3 Clinical Application

Globally, three OVs have been granted approval for cancer therapy. In 2005, China approved H101 (Oncorine®, an attenuated and oncolytic serotype 5 AdV) in combination with chemotherapy for the treatment of nasopharyngeal carcinoma [74]. Ten years later, in 2015, the FDA and the European Medicines Agency (EMA) approved talimogene laherparepvec (T-VEC, Imlygic®) for the treatment of advanced melanoma [38]. Soon afterwards this OV was approved in Australia (2016) and Israel (2017). T-VEC is an attenuated and oncolytic type I HSV that encodes human GM-CSF, a molecule known to promote APC maturation [75]. This OV has also been evaluated in combination with ICB, but the results from a Phase III study in advanced melanoma do not support approval of the combination approach [76]. Current clinical trials in melanoma patients investigate the usage of T-VEC in a neoadjuvant setting (NCT04427306 [iv], NCT04330430, NCT03842943). More recently, in 2021, the Japanese Pharmaceuticals and Medical Devices Agency (PMDA) approved teserpaturev (G47Δ, Delytact®, an attenuated and oncolytic type I HSV) for the treatment of malignant glioma based on the results from a phase I/II trial [77] and a phase II trial [78]. At present, G47Δ is under clinical investigation for the treatment of prostate cancer (JRCTs033210603 [v]), malignant pleural mesothelioma (UMIN000034063 [vi]), and recurrent olfactory neuroblastoma (UMIN000011636) [79].

[iv] Here and further, the letters NCT followed by an eight digit number correspond to the identifier of a clinical trial registered in the National Library of Medicine (https://clinicaltrials.gov/).
[v] The letters JRCTs followed by a nine digit number correspond to the identifier of a clinical trial registered in the Japan Registry of Clinical Trials (JRCTs) (https://rctportal.niph.go.jp/en).
[vi] The letters UMIN followed by a nine digit number correspond to the identifier of a clinical trial registered in the University Hospital Medical Information Network (UMIN) (https://www.umin.ac.jp/ctr/).

1.5 Measles Virus (MeV)

Among the large panel of OVs under investigation, my thesis focuses on measles virus vaccine strains (MeVac), which are attenuated strains of wild-type measles virus (MeV).

1.5.1 Measles Disease

Measles virus (MeV) is a human-restricted pathogen that causes measles, a highly contagious disease characterized by flu-like symptoms, Koplik's spots, and skin rash [80]. MeV initially replicates in lymphoid tissues in the respiratory tract and then disseminates systemically, also infecting epithelial cells. MeV infection of immune cells induces immunosuppression, thus decreasing protection from secondary infections with potentially fatal outcome [81]. Albeit rare, central nervous system complications can occur, including fatal subacute sclerosing panencephalitis [82]. Measles incidence has been drastically reduced since the introduction of safe and effective vaccines [83]. However, this disease remains a public health issue in regions with limited vaccine coverage.

1.5.2 MeV Structure

MeV is a pleomorphic and enveloped virus of 100 – 300 nm belonging to the *Mononegavirales* order, *Paramyxoviridae* family, and *Morbillivirus* genus. It has a non-segmented negative-sense single-strand RNA [(-)ssRNA] genome of 15894 nucleotides (nt). The MeV genome starts and ends with non-coding sequences (leader and trailer) and contains six genes (*N*, *P*, *M*, *F*, *H*, *L*) [84] that encode six structural (N, P, M, F, H, L) [85] and two non-structural (C, V) [86,87] proteins (Figure 2 A). The genes are spaced by non-coding intergenic sequences of different length that, together with the leader and trailer regions, regulate genome replication, transcription, and packaging [88]. The essential components of the MeV particle are the viral genome, the structural viral proteins, and a lipid bilayer (Figure 2 B). Multiple nucleoproteins (N) bind to the viral genome to form a helical structure, the nucleocapsid [89]. For assembly of functional MeV particles, the length of the MeV genome has to be a multiple of six, presumably because each N protein binds to six nucleotides [90]. This phenomenon, referred to as "rule of six", must be considered during MeV genetic engineering. The large (L) protein is an RNA-dependent RNA polymerase that requires phosphoprotein (P) as co-factor for catalyzing viral gene replication and transcription. Together, L and P constitute the polymerase complex, which binds to the nucleocapsid, thus forming the ribonucleoprotein (RNP)[91]. The RNP is enclosed in an envelope derived from the host cell plasma membrane. This envelope is composed of a lipid bilayer, host cell membrane proteins, and two viral transmembrane glycoproteins: hemagglutinin (H), assembled in tetramers [92], and fusion (F), assembled in trimers [93]. Matrix (M) proteins line the inner layer of the viral envelope and interact with the RNP [94]. In addition, the viral particle contains host cell factors trapped during particle assembly [95].

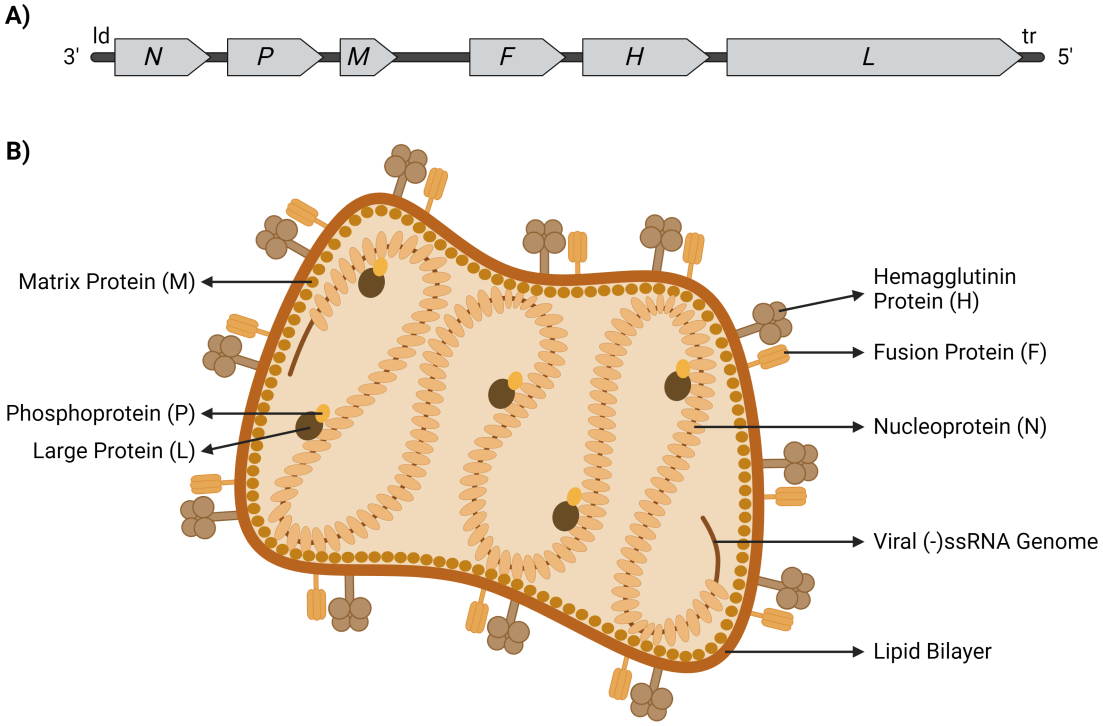

Figure 2. Measles virus (MeV) genome and structure. (A) Schematic of the MeV negative sense single-strand RNA genome. The MeV genome harbors six genes, each encoding one structural protein. In addition, MeV *P* encodes two non-structural proteins known as C and V (not shown). The genes are spaced by non-coding regulatory regions. The genome is flanked by 3' leader (ld) and 5' trailer (tr) non-coding regulatory regions. **(B)** Schematic of the MeV virion. The MeV genome is encapsulated by nucleoproteins (N), forming the nucleocapsid. The viral polymerase (large protein, L) and its co-factor (phosphoprotein, P) are associated with the nucleocapsid, forming the ribonucleoprotein (RNP). The RNP is enveloped in a lipid bilayer derived from the host cell plasma membrane that contains MeV hemagglutinin (H) and fusion (F) proteins assembled in tetramers and trimers, respectively. The matrix protein (M) lines the inner layer of the viral envelope and interacts with the RNP. **(A-B)** Created with BioRender.com.

1.5.3 MeV Replication Cycle

To date, two MeV entry receptors are known: Nectin-4 [96,97], also called poliovirus receptor-like 4 (PVRL-4), expressed on the basolateral surface of epithelial cells, and CD150 [98], also called signaling lymphocyte-activation molecule (SLAM), expressed on activated lymphocytes, DCs, macrophages, and monocytes. Additionally, measles virus vaccine strains also employ CD46 as entry receptor [99]. DC-SIGN mediates MeV attachment to target cells but is not a MeV entry receptor [100]. MeV attaches to the viral entry receptor via H. This interaction induces conformational changes in F, resulting in fusion of the viral envelope with the target cell membrane [101]. The RNP is then released into the cytoplasm of the host cell. There, the virus genome serves as template for replication and translation. Both processes are catalyzed by the viral polymerase complex (L and P), present in the RNP [91]. Viral gene transcription is initiated at the 3' end of the genome and guided by gene start and gene stop sequences that flank each transcription unit. Failure to recognize the start sequence of the next transcription unit results in polymerase dissociation from the viral genome. Transcription is then terminated and can only be re-initiated at the 3' end of the genome. This

phenomenon results in a transcriptional gradient: the closer to the leader sequence, the more transcripts are generated [102]. Viral mRNAs are translated using the host cell machinery. The structural proteins are translated from the respective transcript (MeV *N*, *P*, *M*, *F*, *H*, *L* mRNA). The non-structural proteins C and V are translated from the MeV *P* transcript via an alternative open reading frame (ORF) or RNA editing, respectively [86,87]. In parallel, the viral genome is replicated in a two-step process: (-)ssRNA (genome) is transcribed into (+)ssRNA (anti-genome) and subsequently replicated into (-)ssRNA (genome). The new MeV genomes are assembled into RNPs and used as template for further transcription and replication or transported to the host cell membrane for particle assembly. H and F undergo post-translational modifications and are inserted into the host cell membrane as glycoproteins. This phenomenon triggers the fusion of infected cells (expressing H and F) with neighboring cells (expressing the MeV entry receptor), thereby mediating the typical cytopathic effect of MeV infection, the formation of large multinucleated syncytia, which eventually burst [103]. Moreover, the presence of H and F on the host cell membrane ensures that these proteins are part of the MeV envelope, which is acquired during viral particle budding. The MeV replication cycle takes place exclusively in the cytoplasm of the host cell and is supported by C and V (particularly in wild-type pathogenic MeV strains), which regulate viral replication and antagonize the antiviral interferon response triggered by the host cell [104].

1.5.4 MeV Attenuation

In 1954, wild-type MeV was isolated from the blood of a 13 year-old boy named David Edmonston who presented clinical symptoms of measles disease [105]. Serial passaging of the pathogenic isolate, mainly in tissue cultures of chicken embryo fibroblasts (CEFs), led to the acquisition of mutations in all MeV genes and resulted in several closely-related attenuated MeV strains, such as Edmonston B, Schwarz/Moraten, and Edmonston/Zagreb [83]. Compared to wild-type MeV, these attenuated strains showed limited replication in many human tissues. The molecular determinants of attenuation, which remain incompletely characterized, include mutations in the MeV *P* gene that render the virus more sensitive to the antiviral response of the host cell by altering the protein sequence of the virulence factors C and V [106,107]. Specific non-synonymous mutations in the MeV *H* gene confer attenuated MeV strains the capacity to use CD46, a complement-regulatory protein expressed on all nucleated cells, as preferential entry receptor in addition to CD150 and Nectin-4 [99]. Since the 1960s, live-attenuated MeV strains derived from the wild-type MeV Edmonston isolate or other local isolates have been, and still are, administered to billions of people as prophylactic vaccines against measles disease [108]. These vaccines have proven effective and hold an excellent safety record throughout decades of vaccination, with no observed reversion to pathogenicity [108]. Since the live-attenuated MeV strains are employed in vaccination, they are also referred to as measles virus vaccine strains (MeVac).

1.6 Oncolytic Virotherapy with Measles Virus Vaccines

In the 1970s and 1980s, clinical case reports described tumor regressions in patients suffering from Burkitt's lymphoma [109], acute lymphoblastic leukemia [110], and Hodgkin's lymphoma [111] during naturally-acquired MeV infection. These observations prompted the study of pathogenic MeV as a potential cancer therapeutic. Safety concerns shifted the focus to the live attenuated MeV strains used for measles vaccination (MeVac), which also proved oncolytic while being safe [112].

Among all OVs, MeV/MeVac offers the advantage of a fully cytosolic replication cycle, thus precluding insertional mutagenesis. Moreover, the MeV/MeVac particle can accommodate large genomes. At present, MeVac genomes containing up to 5000 nucleotides of foreign RNA (ca. 30% of the unmodified MeVac genome size) in addition to all viral genes and regulatory sequences have been incorporated into functional MeVac particles [113]. Manipulation of the MeV/MeVac genome via conventional cloning techniques is feasible, particularly since the development of a reverse genetics system for the rescue of MeV/MeVac particles from anti-genomic MeV/MeVac cDNA [114,115]. Besides these aspects, using MeVac instead of wild-type MeV provides the indispensable advantage of an excellent safety profile.

1.6.1 MeVac Oncoselectivity

As with other OVs, MeVac preferentially infects and replicates in tumor cells, resulting in tumor cell lysis, whereas healthy cells remain spared. This oncoselective property is conferred at the entry and post-entry levels. Although MeVac can enter human cells via CD150 and Nectin-4, it mainly does so via CD46, a negative regulator of the complement system expressed on all human nucleated cells. A certain CD46 density is needed for strong cytopathic effects following MeVac infection, thus protecting healthy cells from MeVac-mediated cytotoxicity [116]. Notably, CD46 is overexpressed on a plethora of tumor entities, probably as a result of selective pressure to evade immune responses mediated by the complement system. This overexpression increases the susceptibility of the cells to MeVac and predisposes them to stronger cytotoxicity following infection [117–119]. Importantly, MeVac is more sensitive to the antiviral defense mechanisms of host cells (including the type I IFN response) than wild-type MeV. Thus, healthy cells, which are IFN-competent, counteract MeVac infection and restrict MeVac replication. Conversely, malignant cells often acquire defects in the type I IFN response, presumably selected to avoid its anti-proliferative signals, and are therefore more permissive to MeVac replication [120–122]. Additional mechanisms regulating preferential MeVac replication in malignant cells are under investigation (Schäfer *et al.*, in revision).

1.6.2 MeVac and the Cancer-Immunity Cycle

More than two decades of research have shown that MeVac oncolytic virotherapy supports all phases of the cancer-immunity cycle [123]. This cycle starts with MeVac infection and replication in tumor cells, which leads to sensing of MeVac-derived PAMPs, in particular sensing of MeVac RNA by two cytosolic pattern recognition receptors (PRRs): retinoic acid-inducible gene I (RIG-I) and melanoma differentiation-associated protein 5 (MDA-5) [124]. The signaling cascades triggered by these interactions lead to type I IFN (IFN-α, IFN-β) production in tumor cells [125,126]. In turn, these molecules activate the type I IFN response in an autocrine or paracrine manner, resulting in expression of IFN-stimulated genes (ISGs) [126]. Tumor-derived IFN-α and IFN-β might not act in an autocrine manner, as tumor cells are often unresponsive to type I IFN signaling. However, they may still act in a paracrine manner on non-malignant cells located at the tumor site. MeVac infection and replication in tumor cells also results in cellular stress and production of DAMPs, including higher intracellular levels of 70 kDa heat shock protein (HSP70) [125], membrane translocation of calreticulin[127], release of adenosine triphosphate (ATP) [127], and release of high mobility group protein B1 (HMGB1)[128]. Thus, MeVac induces immunogenic tumor cell death [129] (Figure 3, Step 1).

Sensing of pro-inflammatory and immunogenic molecules released during MeVac-mediated oncolysis alters the phenotype of non-malignant cells in the tumor bed. Moreover, these cells might also sense PAMPs derived from direct MeVac infection, as they also express the MeVac entry receptor CD46 (infection is possible, but viral replication should be limited by the functional antiviral mechanisms). Among all intratumoral cell populations, DCs are of particular interest. *Ex vivo* studies have shown that exposure of human DCs to MeVac or to lysates from MeVac-infected tumor cells enhances their phagocytic activity [125,130] (Figure 3, Step 2). Phagocytosis does not only lead to TAA uptake, but also to capture of PAMPs, DAMPs, and other tumor cell components, that can then be sensed by endosomal Toll-like receptors (TLRs). For instance, plasmacytoid DCs sense MeVac ssRNA derived from MeVac-infected tumor cells via TLR7 [130]. Signaling via TLR7 contributes to the pro-inflammatory response.

Together, (i) sensing of DAMPs, PAMPs, and pro-inflammatory molecules, released during MeVac-mediated oncolysis, via cell surface receptors, (ii) sensing of phagocytosed material (DAMPs, PAMPs, TAAs, other tumor cell components) via endosomal receptors, and (iii) sensing of MeVac PAMPs, derived from direct infection, via cytosolic receptors, triggers DC maturation [131] (Figure 3, Step 3). In the context of MeVac virotherapy, human DC maturation is characterized by upregulation of surface co-stimulatory molecules (CD40, CD80, CD83, CD86) [125,128,130,132], MHC-II molecules (HLA-DR) [125], and death receptor ligands (TRAIL) [132] as well as increased secretion of the pro-inflammatory cytokines IFN-α, IL-1β, IL-6, heterodimeric IL-12 (IL-12p70), and TNF-α [125,130,132].

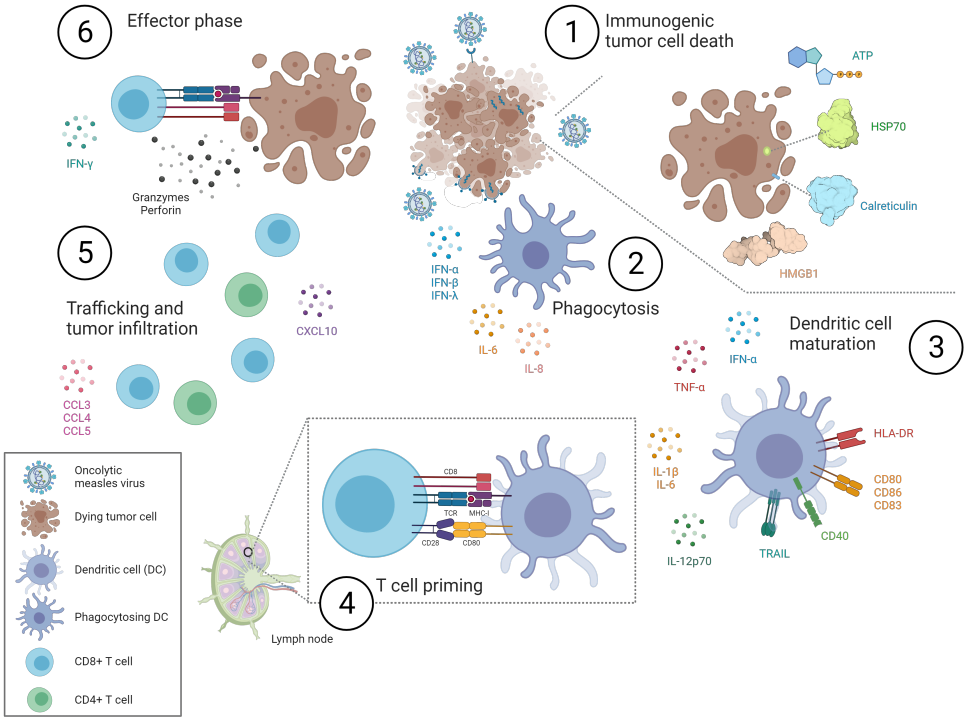

Figure 3. MeVac-mediated oncolysis and the cancer-immunity cycle. Molecules supporting specific steps of the cancer-immunity cycle during MeVac immunotherapy are depicted. Reproduced from Pidelaserra-Martí and Engeland with permission[123]. Created with BioRender.com.

Mature DCs process and present antigen more efficiently than immature DCs. Moreover, they acquire a migratory phenotype and traffic to the TDLN, where they prime cognate T cells. The interaction of DCs with T cells upon MeVac virotherapy has been studied in *ex vivo* co-cultures of human cells [125,130]. Priming has not been addressed, since the T cells were not naïve. Moreover, the studies have not investigated antigen presentation in a direct manner (*e.g.*, staining MHC::peptide complexes), but rather indirectly by determining activation of cognate T cells. These studies showed that DCs exposed to lysates from MeVac-infected tumor cells activate tumor-specific T cells, as detected by increased T cell proliferation [125] and IFN-γ release [130]. From these results, it is inferred that MeVac therapy promotes DC (cross-)presentation of TAA-derived epitopes to cognate T cells.

Priming of tumor-specific T cells during MeVac therapy has been inferred from two *in vivo* studies [133,134]. In these studies, mice received transplantable syngeneic tumor cells and, after tumor establishment, were treated with MeVac or carrier fluid. *Ex vivo* restimulation experiments showed increased tumor reactivity in splenocytes from MeVac-treated mice compared to controls, suggesting that tumor-specific immune cells had been primed *in vivo* (Figure 3, Step 4).

Regarding long-term responses, one re-challenge study showed that most (3 of 4) mice experiencing complete tumor remissions upon MeVac therapy reject secondary tumor engraftment at a distal site [135]. This points towards MeVac-mediated priming of antitumor immune memory. However, these results were obtained with very few mice and remain to be corroborated in additional studies.

Following the cancer-immunity cycle, primed T cells traffic to the tumor and infiltrate the tumor mass. Although the molecular mechanisms driving T cell infiltration into MeVac-treated tumors remain unknown, *in vitro* and xenograft studies argue for the involvement of CCL5 and CXCL10, since these T cell attractants are secreted at higher levels upon MeVac virotherapy compared to control treatment [126–128]. Increased secretion of CCL5 and CXCL10 is consistent with activation of the type I IFN response, since these chemokines are encoded by ISGs (Figure 3, Step 5).

At the tumor site, CTLs recognize tumor cells presenting cognate epitope on MHC-I molecules. MeVac virotherapy contributes to this step by enhancing antigen presentation on tumor cells. *In vitro*, MeVac infection was shown to increase the mRNA levels of *HLA-A*, *HLA-B*, and *TAP* in tumor cells, the protein products of which are involved in MHC-I antigen presentation. Increased antigen presentation was also confirmed on the protein level [126]. Recognition of cognate MHC-epitope complexes on tumor cells results in CTL activation, as determined by IFN-γ secretion [128]. Ultimately, activated CTLs kill target cells via cytotoxic effector functions. In the context of MeVac virotherapy, this phenomenon comprises CTL upregulation of the degranulation marker CD107 [128]. This is indicative of granule-mediated cytotoxicity via granzyme and perforin release. Importantly, the cytotoxic effector phase targets both infected and non-infected tumor cells, thus further reducing the tumor mass as compared to oncolysis alone (Figure 3, Step 6).

Besides DCs and T cells, MeVac virotherapy also influences the intratumoral abundance and phenotype of other cell types. For instance, it promotes intratumoral infiltration of innate immune cells [136,137]. Xenograft studies argue for the involvement of CCL3 and CCL4 in this process, since MeVac virotherapy increases the levels of these myeloid cell attractants at the tumor site [127]. Regarding immune cell phenotype, MeVac induces NK cell activation and cytotoxicity[128], neutrophil activation [138], and macrophage repolarization towards an anti-inflammatory M1 phenotype [139]. Anti-angiogenic properties have also been described, although only in one xenograft study [137].

The intrinsic immunological effects of MeVac can be enhanced by encoding immunomodulators in the viral genome. MeVac has been engineered to encode TAAs [140], TLR2 agonists [141], BiTEs [142], cytokines/chemokines [133,135–137,143,144], co-stimulatory molecules [135,145], and ICBs [134,146]. Moreover, MeVac has been combined with systemic delivery of ICB mAbs [134,147]. Pro-drug convertases and human sodium-iodide symporter (NIS) have been encoded in MeVac vectors to improve the therapeutic effects of combining virotherapy with chemotherapy or radiotherapy [148].

Overall, MeVac virotherapy is emerging as a promising cancer immunotherapy. Early phase clinical trials have demonstrated its safety and tolerability [149]. Ongoing trials will determine whether the therapeutic effects observed in preclinical studies translate to clinical practice.

2 Hypotheses and Aims

MeVac virotherapy, *i.e.,* the usage of oncolytic measles virus vaccine strains (MeVac) for the treatment of cancer, is under preclinical and clinical investigation as an option for cancer treatment. Previous research has shown that MeVac preferentially infects and replicates in tumor cells, leading to tumor cell lysis. Moreover, MeVac-induced tumor cell death is immunogenic and triggers T cell-mediated antitumor immunity, following the cancer-immunity cycle. However, this dual mechanism of action (direct cytotoxicity and immunomodulation) is insufficient to achieve high rates of complete tumor remissions, both in preclinical studies and clinical settings.

My study is based on the hypothesis that certain mechanisms limit or restrict the therapeutic potential of MeVac-induced antitumor immunity. I therefore aimed at identifying these mechanisms. Upon literature search and analysis of tumor immune gene expression datasets available at our research group, I hypothesized that the antitumor immune response triggered by MeVac virotherapy is limited or restricted at three phases of the cancer-immunity cycle: (i) the priming phase, by impaired antigen processing and presentation, (ii) the intratumoral T cell recruitment phase, by insufficient chemokine signaling, and (iii) the effector phase, by PD-1/PD-L1-mediated immunosuppression.

During my doctoral studies, I aimed at investigating the contribution of these mechanisms to the efficacy of MeVac virotherapy by exploring the interplay of MeVac with specific steps of the cancer-immunity cycle at the cellular and molecular level (Figure 4). To that aim, I conducted gain of function studies employing MeVac not only as therapeutic agent, but also as vehicle to deliver processed antigens to DCs and tumor cells (aiming at enhancing MeVac-induced T cell priming and activation) or to deliver chemokines to the tumor site (aiming at enhancing MeVac-induced intratumoral T cell recruitment). To study the contribution of the PD-1/PD-L1 pathway, I conducted loss of function studies by blocking this signaling axis with MeVac-encoded antibody-like molecules targeted to PD-1 or PD-L1, or with anti-PD-1 antibodies administered systemically in combination with local virotherapy.

Throughout my studies, I employed several MeVac variants encoding antigens, antigen-derived epitopes, or immunomodulators. I generated and characterized the viruses encoding chemokines and cytotoxic molecules, whereas the other virus variants were available at our research group. Furthermore, I also aimed at refining the preclinical models of MeVac virotherapy by optimizing current models (establishing a MeVac purification protocol and generating novel tumor cell lines) and by establishing novel models (CD46tg mice and patient-derived *ex vivo* tumor slice cultures).

The specific biological and technical aims of my studies are detailed on the next page.

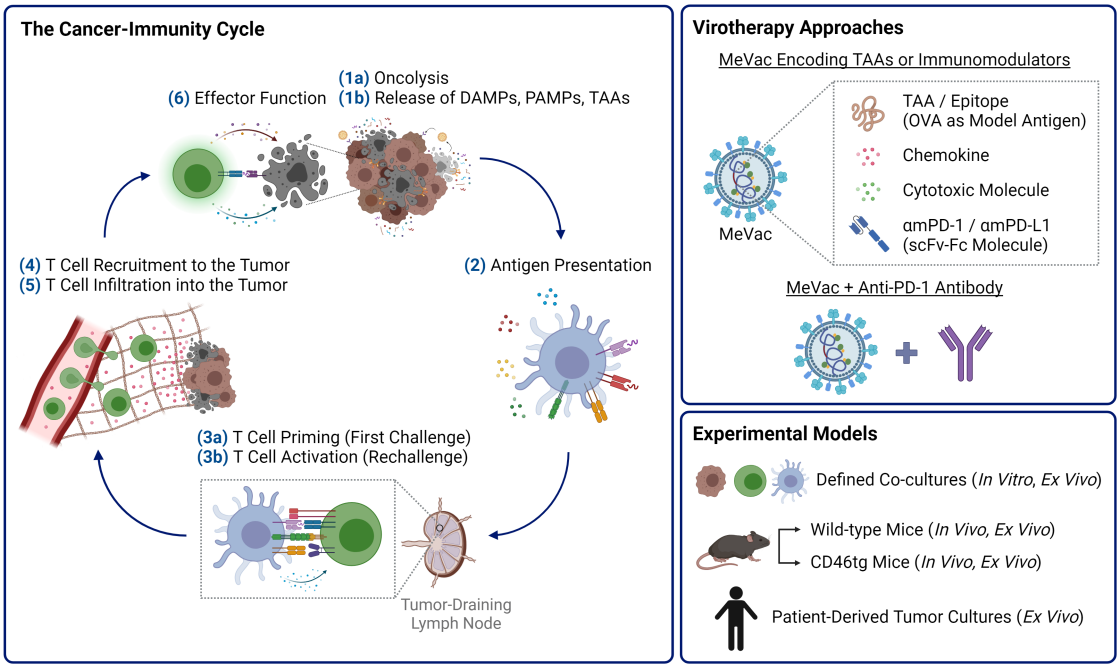

Figure 4. Conceptual representation of my doctoral studies. During my doctoral studies, I have investigated T cell-mediated antitumor immunity in the context of MeVac virotherapy, aiming at identifying limiting factors of this therapeutic approach. To that aim, I have explored the interplay of oncolytic MeVac with specific steps of the cancer-immunity cycle. First, I have addressed the concept of oncolytic vaccination with MeVac vectors encoding pre-processed antigens. Next, using different experimental models and virotherapy approaches, I have investigated whether and how chemokine overexpression or PD-1/PD-L1 blockade alters the efficacy and immunomodulatory properties of MeVac virotherapy. Finally, I have established CD46-transgenic (CD46tg) mice and patient-derived *ex vivo* tumor slice cultures as novel systems for the study of MeVac virotherapy. Schematic created with BioRender.com.

Biological Aims

- To determine whether DCs and tumor cells exposed to MeVac encoding antigen-derived epitope variants prime and activate cognate T cells
- To identify molecular mechanisms potentially limiting intratumoral T cell recruitment in the context of MeVac virotherapy
- To assess whether the identified mechanisms, namely distinct chemokine signaling pathways, modulate the efficacy of MeVac virotherapy
- To determine whether the PD-1/PD-L1 axis restricts the efficacy of MeVac virotherapy
- To characterize the local and systemic immunomodulatory effects of MeVac virotherapy in combination with PD-1/PD-L1 blockade
- To investigate the local and systemic immunomodulatory effects of MeVac virotherapy in tumor-bearing CD46tg mice

Technical Aims

- To establish a protocol for MeVac purification
- To generate and characterize MeVac variants encoding chemokines or cytotoxic molecules
- To generate and characterize murine tumor cell lines with ectopic expression of human CD46
- To establish CD46tg mice and patient-derived *ex vivo* tumor slice cultures as novel models of MeVac virotherapy

3 Materials and Methods

3.1 Materials

3.1.1 Oligonucleotides

Table 1. Oligonucleotides. All oligonucleotides were synthesized by Eurofins Genomics. **Bold:** Kozak sequence; Underlined: restriction enzyme (MluI, PauI/BssHII, BtgI) target site.

Name	Sequence (5' → 3')
mCCL5_Fw_MluI	GCTAACGCGT**GCCACC**ATGAAGATCTCTGCAGC
mCCL5_Rv_PauI	GCATGCGCGCCTAGCTCATCTCCAAATAG
mCCL19_Fw_MluI	GCTAACGCGT**GCCACC**ATGGCCCCCCGTG
mCCL19_Rev_PauI	GCATGCGCGCTTATCAAGACACAGGGCTC
mCCL21_Fw_MluI	GCTAACGCGT**GCCACC**ATGGCTCAGATGATGACTC
mCCL21_Rev_PauI	GCATGCGCGCCTATCCTCTTGAGGGCTG
mCXCL9_Fw_MluI	GCTAACGCGT**GCCACC**ATGAAGTCCGCTGTTC
mCXCL9_Rv_PauI	GCATGCGCGCTTATTATGTAGTCTTCCTTGAACG
mCXCL13_Fw_MluI	GCTAACGCGT**GCCACC**ATGAGGCTCAGCACAGC
mCXCL13_Rev_PauI	GCATGCGCGCTCAGGCAGCTCTTCTCTTAC
mL13A_Fw	GGCTGCCGAAGATGGCGGAG
mL13A_Rv	GCCTTCACAGCGTACGACCACC
mLIGHT_Fw_MluI	GCTAACGCGT**GCCACC**ATGGAGAGTGTGGTACAG
mLIGHT_Rv_PauI	GCATGCGCGCTCAGACCATGAAAGCTC
mLTa_Fw_MluI	GCTAACGCGT**GCCACC**ATGACACTGCTCGGC
mLTa_Rv_PauI	GCATGCGCGCTTACTACAGTGCAAAGGCTCC
mTNF_Fw_MluI	GCTAACGCGT**GCCACC**ATGAGCACAGAAAGCATG
mTNF_Rv_BtgI	CGATCCGCGGTCACAGAGCAATGACTCC
MeV N-241	TTACCACTCGATCCAGACTTC
MeV N-331+	CCTATTAGTGCCCCTGTTAGTTT
MeV P-3287	TTGCCAAGTTCCACCAGATGCT
MeV M-3478+	ATGTCCCATGCCGACTTGTCGAA
pCAG_P2A_hCD46_F	GGAAAACCCTGGGCCCATGG
pCAG_hCD46_R	GAGCTCGAGTCACAGGCTGG
pJET1.2 for	CGACTCACTATAGGGAGAGCGGC
pJET1.2 rev	AAGAACATCGATTTTCCATGGCAG
oIMR3657 (for transgene)	GCCTGTGAGGAGCCACCAA
oIMR3658 (for transgene)	CGTCATCTGAGACAGGTAG
oIMR7338 (for internal control)	CTAGGCCACAGAATTGAAAGATCT
oIMR7339 (for internal control)	GTAGGTGGAAATTCTAGCATCATCC

3.1.2 DNA Cloning Vectors

Table 2. DNA cloning vectors. pcMeVac and derivatives allow for rescue using the RNA polymerase II system. Plasmids without an indicated source were generated by myself. **ATU:** additional transcription unit, **CAG promoter:** human cytomegalovirus immediate early enhancer and chicken β-actin promoter, **CDS:** coding sequence, **EF1 promoter:** eukaryotic translation elongation factor 1α (EF-1α) promoter.

Name	Description and Source
pEX-A128 mLT-β	pEX-A128 vector containing the Kozak sequence + murine LT-β CDS as an MluI-MluI fragment in rule of six for insertion into the MeVac genome Source: Eurofins Genomics
pJET1.2/blunt	DNA cloning vector (linearized) GenBank number: EF694056.1 Source: Thermo Fisher Scientific, Ref. K1231
pJET IgG-Fc *C.m.* [150]	pJET1.2/blunt vector encoding the Fc region of hamster (*Cricetulus migratorius*) IgG Source: R. Veinalde (DKFZ, Heidelberg)
pJET mCCL5	pJET1.2/blunt vector containing the Kozak sequence + murine CCL5 CDS as an MluI-PauI fragment in rule of six for insertion into the MeVac genome
pJET mCCL19	pJET1.2/blunt vector containing the Kozak sequence + murine CCL19 CDS as an MluI-PauI fragment in rule of six for insertion into the MeVac genome
pJET mCCL21a	pJET1.2/blunt vector containing the Kozak sequence + murine CCL21a CDS as an MluI-PauI fragment in rule of six for insertion into the MeVac genome
pJET mCXCL9	pJET1.2/blunt vector containing the Kozak sequence + murine CXCL9 CDS as an MluI-PauI fragment in rule of six for insertion into the MeVac genome
pJET mCXCL10 [135,145] (also designated pJET 1.2 mIP-10)	pJET1.2/blunt vector containing the Kozak sequence + murine CXCL10 CDS as an MluI-AscI fragment in rule of six for insertion into the MeVac genome Source: R. Veinalde (DKFZ, Heidelberg)
pJET mCXCL13	pJET1.2/blunt vector containing the Kozak sequence + murine CXCL13 CDS as an MluI-PauI fragment in rule of six for insertion into the MeVac genome
pJET mLIGHT	pJET1.2/blunt vector containing the Kozak sequence + murine LIGHT CDS as an MluI-PauI fragment in rule of six for insertion into the MeVac genome
pJET mLT-α	pJET1.2/blunt vector containing the Kozak sequence + murine LT-α CDS as an MluI-PauI fragment in rule of six for insertion into the MeVac genome
pJET mTNF-α	pJET1.2/blunt vector containing the Kozak sequence + murine TNF-α CDS as an MluI-BtgI fragment in rule of six for insertion into the MeVac genome

Table 2 (continued). DNA cloning vectors. pcMeVac and derivatives allow for rescue using the RNA polymerase II system. Plasmids without an indicated source were generated by myself. **ATU:** additional transcription unit, **CAG promoter:** human cytomegalovirus immediate early enhancer and chicken β-actin promoter, **CDS:** coding sequence, **EF1 promoter:** eukaryotic translation elongation factor 1α (EF-1α) promoter.

Name	Description and Source
pcMeVac [151]	Vector containing the MeVac (Schwarz strain) antigenome under the control of a cytomegalovirus promoter Source: S. Bossow (DKFZ, Heidelberg)
pcMeVac P-ATU [135]	Vector containing the MeVac (Schwarz strain) antigenome with an additional transcription unit (ATU) downstream of the MeVac P CDS; derived from pcMeVac Source: J. Albert, S. Bossow (DKFZ, Heidelberg)
pcMeVac P-IgG-Fc *C.m.*	Vector containing the MeVac (Schwarz strain) antigenome with the Kozak sequence and a sequence encoding the Fc region of hamster (*Cricetulus migratorius*) IgG inserted in an ATU downstream of the MeVac P CDS; derived from pcMeVac P-ATU
pcMeVac P-mCCL5	Vector containing the MeVac (Schwarz strain) antigenome with the Kozak sequence and murine CCL5 CDS inserted in an ATU downstream of the MeVac P CDS; derived from pcMeVac P-ATU
pcMeVac P-mCCL19	Vector containing the MeVac (Schwarz strain) antigenome with the Kozak sequence and murine CCL19 CDS inserted in an ATU downstream of the MeVac P CDS; derived from pcMeVac P-ATU
pcMeVac P-mCCL21a	Vector containing the MeVac (Schwarz strain) antigenome with the Kozak sequence and murine CCL21a CDS inserted in an ATU downstream of the MeVac P CDS; derived from pcMeVac P-ATU
pcMeVac P-mCXCL9	Vector containing the MeVac (Schwarz strain) antigenome with the Kozak sequence and murine CXCL9 CDS inserted in an ATU downstream of the MeVac P CDS; derived from pcMeVac P-ATU
pcMeVac P-mCXCL10	Vector containing the MeVac (Schwarz strain) antigenome with the Kozak sequence and murine CXCL10 CDS inserted in an ATU downstream of the MeVac P CDS; derived from pcMeVac P-ATU
pcMeVac P-mCXCL13	Vector containing the MeVac (Schwarz strain) antigenome with the Kozak sequence and murine CXCL13 CDS inserted in an ATU downstream of the MeVac P CDS; derived from pcMeVac P-ATU
pcMeVac P-mLIGHT	Vector containing the MeVac (Schwarz strain) antigenome with the Kozak sequence and murine LIGHT CDS inserted in an ATU downstream of the MeVac P CDS; derived from pcMeVac P-ATU

Table 2 (continued). DNA cloning vectors. pcMeVac and derivatives allow for rescue using the RNA polymerase II system. Plasmids without an indicated source were generated by myself. **ATU:** additional transcription unit, **CAG promoter:** human cytomegalovirus immediate early enhancer and chicken β-actin promoter, **CDS:** coding sequence, **EF1 promoter:** eukaryotic translation elongation factor 1α (EF-1α) promoter.

Name	Description and Source
pcMeVac P-mLT-α	Vector containing the MeVac (Schwarz strain) antigenome with the Kozak sequence and murine LT-α CDS inserted in an ATU downstream of the MeVac P CDS; derived from pcMeVac P-ATU
pcMeVac P-mLT-β	Vector containing the MeVac (Schwarz strain) antigenome with the Kozak sequence and murine LT-β CDS inserted in an ATU downstream of the MeVac P CDS; derived from pcMeVac P-ATU
pcMeVac P-mTNF-α	Vector containing the MeVac (Schwarz strain) antigenome with the Kozak sequence and murine TNF-α CDS inserted in an ATU downstream of the MeVac P CDS; derived from pcMeVac P-ATU
pcDI dsRed	Vector containing the CDS for a variant of the *Discosoma* red fluorescent protein under the control of a cytomegalovirus promoter Source: S. Bossow (DKFZ, Heidelberg)
pcDIMER-L [151]	Vector containing the MeVac L CDS (Schwarz strain) under the control of a cytomegalovirus promoter Source: S. Bossow (DKFZ, Heidelberg)
pcDIMER-N [151]	Vector containing the MeVac N CDS (Schwarz strain) under the control of a cytomegalovirus promoter Source: S. Bossow (DKFZ, Heidelberg)
pcDIMER-P [151]	Vector containing the MeVac P CDS (Schwarz strain) under the control of a cytomegalovirus promoter Source: S. Bossow (DKFZ, Heidelberg)
pCG-N	Vector containing the MeVac N CDS (Edmonston B-derived strain) under the control of a cytomegalovirus promoter Source: R. Cattaneo (Mayo Clinic, Rochester)
pCAG-Puro-P2A-hCD46-SMAR (in the thesis: “pCAG-SMAR”)	Plasmid-S/MAR (pS/MAR) vector [152] containing the CDS for human CD46 (isoform BC1) and the S/MAR sequence from the human interferon-β gene cluster under the control of the CAG promoter Source: M. Bozza (DKFZ, Heidelberg)
pCAG-Puro-P2A-hCD46-SMARter-NP (in the thesis: “pCAG-Nano”)	Nano-S/MAR (nS/MAR) vector [152,153] containing the CDS for human CD46 (isoform BC1) and the S/MAR sequence from the human interferon-β gene cluster under the control of the CAG promoter Source: M. Bozza (DKFZ, Heidelberg)
pEF1-Puro-P2A-hCD46-SMARter-NP (in the thesis: “pEF1-Nano”)	Nano-S/MAR (nS/MAR) vector [152,153] containing the CDS for human CD46 (isoform BC1) and the S/MAR sequence from the human interferon-β gene cluster under the control of the EF1 promoter Source: M. Bozza (DKFZ, Heidelberg)

3.1.3 NCBI Reference Sequences

Table 3. NCBI reference sequences. The coding sequences (CDS) inserted in pJET1.2/blunt and pcMeVac P-ATU plasmids for expression of murine chemokines or cytotoxic molecules correspond to the CDS regions of the NCBI mRNA (NM) reference sequences indicated in this table.
NCBI: National Center for Biotechnology Information (https://www.ncbi.nlm.nih.gov/).

Protein	NCBI mRNA (NM) Reference Sequence
Murine CCL5	NM_013653.3 (CDS = nucleotides 58 to 333)
Murine CCL19	NM_011888.4 (CDS = nucleotides 229 to 555)
Murine CCL21 (isoform A)	NM_011124.4 (CDS = nucleotides 74 to 475)
Murine CXCL9	NM_008599.4 (CDS = nucleotides 57 to 437)
Murine CXCL10	NM_021274.2 (CDS = nucleotides 76 to 372)
Murine CXCL13	NM_018866.3 (CDS = nucleotides 46 to 375)
Murine LIGHT	NM_019418.4 (CDS = nucleotides 114 to 833)
Murine LT-α	NM_010735.2 (CDS = nucleotides 203 to 811)
Murine LT-β	NM_008518.2 (CDS = nucleotides 16 to 936)
Murine TNF-α (isoform 1)	NM_013693.3 (CDS = nucleotides 168 to 875)

3.1.4 Amino Acids, Peptides, and Proteins (except enzymes and antibodies)

Table 4. Amino acids, peptides, and proteins (except enzymes and antibodies).

Name	Source
Bovine Serum Albumin (BSA)	Sigma-Aldrich (Merck), Ref. A9418
Concanavalin A from *Canavalia ensiformis* (ConA)	Sigma-Aldrich (Merck), Ref. C2010
L-Glutamine (200 mM)	Thermo Fisher Scientific, Ref. 25030149
Measles Virus Vaccine Strain (MeVac) Bulk Antigen	Virion Serion, Ref. BA102VS-S
Mouse Interleukin-2 (IL-2)	Miltenyi Biotec, Ref. 130-120-332
Mouse Programmed Cell Death 1 (PD-1) Protein, His-tagged	Sinobiological, Ref. 50124-M08H
Non-Essential Amino Acids (100X)	Thermo Fisher Scientific, Ref. 11140035
SIINFEKL (chicken ovalbumin amino acids 257 to 264), H-2K^{b}-restricted	M. Koch (DKFZ, Heidelberg)

3.1.5 Enzymes

Table 5. Enzymes. **NEB:** New England Biolabs, **U:** units.

Name	Manufacturer
Alkaline Phosphatase (rAPid) (1 U/µL) as component of the Rapid DNA Dephos & Ligation kit	Roche (Merck), Ref. 04898117001
Alkaline phosphatase linked to streptavidin (AKP-SA)	BD Pharmingen™, Ref. 554065
Collagenase type I	Thermo Fisher Scientific, Ref. 17100017
DNA Polymerase (Q5® High-Fidelity) (2000 U/mL)	NEB, M0491
DNA Polymerase (One*Taq*®) (5000 U/mL)	NEB, M0480
DNA Polymerase (AmpliTaq Gold™), component of the *Power* SYBR® Green PCR Master Mix	Thermo Fisher Scientific, Ref. 4367659
Deoxyribonuclease I (DNase I) (2.7 U/µL), component of the RNase-Free DNase Set	QIAGEN, Ref. 79254
Horseradish peroxidase linked to streptavidin (HRP-SA)	BD™ ELISPOT, Ref. 557630
Proteinase K (800 U/mL)	NEB, Ref. P8107
Restriction enzyme (AscI) (10 U/µL)	NEB, Ref. R0558
Restriction enzyme (BtgI) (10 U/µL)	NEB, Ref. R0608
Restriction enzyme (HindIII-HF) (20 U/µL)	NEB, Ref. R3104
Restriction enzyme (MauBI) (5 U/µL)	Thermo Fisher Scientific, Ref. ER2081
Restriction enzyme (MluI) (10 U/µL)	NEB, Ref. R0198
Restriction enzyme (PauI or BssHII) (10 U/µL)	Thermo Fisher Scientific, Ref. ER1091
Ribonuclease H (RNase H) (5 U/µL)	NEB, Ref. M0297
T4 DNA Ligase (5 U/µL), component of the Rapid DNA Dephos & Ligation kit	Roche (Merck), Ref. 04898117001
T4 DNA Ligase (5 U/µL), component of the CloneJET PCR Cloning kit	Thermo Fisher Scientific, Ref. K1231
Trypsin (0.05%, w/v) – EDTA with phenol-red	Thermo Fisher Scientific, Ref. 25300054

3.1.6 Antibodies

Table 6. Antibodies. FC: flow cytometry, **Fluorochromes:** AF700 (Alexa Fluor™ 700), APC (Allophycocyanin), APC-Cy7 (Allophycocyanin – Cyanine 7), BV650 (Brilliant Violet™ 650), FITC (Fluorescein Isothiocyanate), PE (Phycoerythrin), PerCP-Cy5.5 (Peridinin Chlorophyll Protein – Cyanine 5.5).

Name and Description	Application	Manufacturer
AF700 rat anti-mouse **CD3** Clone: 17A2, Isotype: Rat IgG2b,κ	FC 1:100	BD Ref. 561388
AF700 rat IgG2b,κ (isotype control) Clone: RTK4530, Isotype: Rat IgG2b,κ	FC 1:250	BioLegend Ref. 400628
APC mouse anti-human **CD46** Clone: TRA-2-10, Isotype: Mouse IgG1,κ	FC 1:100	BioLegend Ref. 352405
APC mouse IgG1,κ (isotype control) Clone: MOPC-21, Isotype: Mouse IgG1,κ	FC 1:100	BioLegend Ref. 400120
APC rat anti-mouse **CD8a** Clone: 53-6.7, Isotype: Rat IgG2a,κ	FC 1:100	BD Ref. 553035
APC rat IgG2a,κ (isotype control) Clone: R35-95, Isotype: Rat IgG2a,κ	FC 1:100	BD Ref. 553932
APC-Cy7 rat anti-mouse **CD4** Clone: GK1.5, Isotype: Rat IgG2b,κ	FC 1:100	BD Ref. 552051
APC-Cy7 rat IgG2b,κ (isotype control) Clone: A95-1, Isotype: Rat IgG2b,κ	FC 1:100	BD Ref. 552773
BV650 rat anti-mouse **CD19** Clone: 6D5, Isotype: Rat IgG2a,κ	FC 1:100	BioLegend Ref. 115541
BV650 rat IgG2a,κ (isotype control) Clone: RTK2758, Isotype: Rat IgG2a,κ	FC 1:100	BioLegend Ref. 400541
FITC rat anti-mouse **CD62L** Clone: MEL-14, Isotype: Rat IgG2a,κ	FC 1:100	BioLegend Ref. 104406
FITC rat IgG2a,κ (isotype control) Clone: RTK2758, Isotype: Rat IgG2a,κ	FC 1:100	BioLegend Ref. 400505
PE Armenian hamster anti-mouse **CD69** Clone: H1.2F3, Isotype: Armenian Hamster IgG	FC 1:100	BioLegend Ref. 104508
PE Armenian hamster IgG (isotype control) Clone: HTK888, Isotype: Armenian Hamster IgG	FC 1:100	BioLegend Ref. 400907
PE mouse anti-mouse **H-2K^{b} bound to SIINFEKL** Clone: 25-D1.16, Isotype: Mouse IgG1,κ	FC 1:100	BioLegend Ref. 141604
PE mouse IgG1,κ (isotype control) Clone: MOPC-21, Isotype: Mouse IgG1,κ	FC 1:100	BioLegend Ref. 400111
PE rat anti-mouse/human **CD44** Clone: IM7, Isotype: Rat IgG2b,κ	FC 1:100	BioLegend Ref. 103024
PE rat IgG2b,κ (isotype control) Clone: RTK4530, Isotype: Mouse IgG2b,κ	FC 1:400	BioLegend Ref. 400607

Table 6 (continued). Antibodies. The Armenian hamster anti-mouse CD279 (PD-1) antibody, clone J43, was employed at different dilutions as competitor of virus-encoded αmPD-1 in the competitive binding assay (Figure 16) and as standard in the anti-mouse PD-1 ELISA (Figure 17). The human anti-mouse/human PD-L1 antibody Atezolizumab was employed at different dilutions as competitor of virus-encoded αmPD-L1 in the competitive binding assay (Figure 16). **CB:** competitive binding assay, **diff. dil.**: different dilutions, **ELISA:** Enzyme-linked immunosorbent assay, **ELISpot:** Enzyme-linked immunosorbent spot, **FC:** flow cytometry, **IHC:** immunohistochemistry, **T:** treatment (*in vivo*), **Fluorochromes:** AF700 (Alexa Fluor™ 700), APC (Allophycocyanin), APC-Cy7 (Allophycocyanin – Cyanine 7), BV650 (Brilliant Violet™ 650), FITC (Fluorescein Isothiocyanate), PE (Phycoerythrin), PerCP-Cy5.5 (Peridinin Chlorophyll Protein – Cyanine 5.5).

Name and Description	Application	Manufacturer
PerCP-Cy5.5 mouse anti-mouse **CD45.2** Clone: 104, Isotype: Mouse IgG2a,κ	FC 1:100	BD Ref. 552950
PerCP-Cy5.5 mouse IgG2a,κ (isotype control) Clone: MOPC-173, Isotype: Mouse IgG2a,κ	FC 1:50	BioLegend Ref. 400251
PerCP-Cy5.5 rat anti-mouse **CD3** molecular complex Clone: 17A2, Isotype: Rat IgG2b,κ	FC 1:100	BD Pharmingen™ Ref. 560527
PerCP-Cy5.5 rat IgG2b,κ (isotype control) Clone: A95-1, Isotype: Rat IgG2b,κ	FC 1:100	BD Pharmingen™ Ref. 550764
Rat anti-mouse **CD16/CD32**, purified (Mouse BD Fc Block™) Clone: 2.4G2, Isotype: Rat IgG2b,κ	FC 1:100	BD Pharmingen™ Ref. 553141
Rabbit anti-mouse **CD3** Clone: SP7, Isotype: Rabbit IgG	IHC (primary) 1:100	Fisher Scientific (Epredia™) Ref. RM-9107-S1
Anti-rabbit **IgG** conjugated to nanopolymers of alkaline phosphatase (AP) Polyview® Plus AP reagent, anti-rabbit Clone: Not specified, Isotype: Not specified	IHC (secondary) 100 µL	Enzo Life Sciences Ref. ENZ-ACC110-0150
Rat anti-mouse **IFN-γ** Clone: R4-6A2, Isotype: Rat IgG1,κ	ELISpot (coating) 1:200	BD Pharmingen™ Ref. 551216
Biotin rat anti-mouse **IFN-γ**, conjugated to biotin Clone: XMG1.2, Isotype: Rat IgG1,κ	ELISpot (detection) 1:500	BD Pharmingen™ Ref. 554410
Mouse IFN-γ ELISpot pair (RRID: AB_2868948) 1) Anti-mouse **IFN-γ** (coating) Part number: 51-2525KZ, Isotype: Not specified 2) Biotin anti-mouse **IFN-γ** (detection) Part number: 51-1818KA, Isotype: Not specified	ELISpot (coating) 1:200 ELISpot (detection) 1:250	BD™ ELISPOT Ref. 551881
Armenian hamster anti-mouse **CD279 (PD-1)** Clone: J43, Isotype: Armenian Hamster IgG, Concentration: 1 mg/mL	CB at diff. dil. ELISA at diff. dil. T (1:2)	Thermo Fisher Scientific (eBioscience™) Ref. 16-9985-85
Armenian hamster anti-mouse **CD279 (PD-1)** Clone: J43, Isotype: Armenian Hamster IgG, Concentration: 7.53 mg/mL, Quality: *InVivo*Plus™	T (1:15)	BioXCell Ref. BP0033-2
Biotin goat anti-Syrian/Armenian hamster **IgG (H+L)** Clone: Polyclonal, Isotype: Goat IgG	ELISA (secondary) 1:20000	Thermo Fisher Scientific Ref. 31750
Humanized anti-mouse/human **PD-L1** (Atezolizumab) Isotype: Human IgG1	CB at diff. dil.	Source: Heidelberg University Hospital

3.1.7 Kits

Table 7. Kits. XTT: 2,3-bis-(2-methoxy-4-nitro-5-sulfophenyl)-2H-tetrazolium-5-carboxanilide.

Name	Manufacturer
Bicinchoninic acid (BCA) Protein Assay kit	Novagen (Merck), Ref. 71285-3
CloneJET PCR Cloning kit	Thermo Fisher Scientific, Ref. K1231
Colorimetric Cell Viability kit III (XTT)	PromoCell, Ref. PK-CA20-300-1000
DuoSet ELISA Ancillary Reagent Kit 2	R&D Systems, Ref. DY008B
Maxima H Minus First Strand cDNA Synthesis kit	Thermo Fisher Scientific, Ref. K1651
Mouse CCL5/RANTES DuoSet ELISA kit	R&D Systems, Ref. DY478
Mouse CCL19/MIP-3 beta DuoSet ELISA kit	R&D Systems, Ref. DY440
Mouse CCL21/6Ckine DuoSet ELISA kit	R&D Systems, Ref. DY457
Mouse CXCL9/MIG ELISA kit	Thermo Fisher Scientific, Ref. EMCXCL9
Mouse CXCL10/IP-10 ELISA kit	Thermo Fisher Scientific, Ref. BMS6018
Mouse CXCL13/BLC/BCA-1 DuoSet ELISA kit	R&D Systems, Ref. DY470
Mouse IFN gamma uncoated ELISA kit	Thermo Fisher Scientific, Ref. 88-7314-22
Pan T Cell Isolation kit II, mouse	Miltenyi Biotec, Ref. 130-095-130
Power SYBR® Green PCR Master Mix	Thermo Fisher Scientific, Ref. 4367659
QIAprep Spin Miniprep kit	QIAGEN, Ref. 27104
QIAquick Gel Extraction kit	QIAGEN, Ref. 28704
QIAshredder kit	QIAGEN, Ref. 79654
Rapid DNA Dephos & Ligation kit	Roche (Merck), Ref. 04898117001
RNeasy Plus Mini Kit	QIAGEN, Ref. 74134
RNeasy Protect Mini kit	QIAGEN, Ref. 74124
RNase-Free DNase Set	QIAGEN, Ref. 79254
Venor™ GeM mycoplasma detection kit	Sigma-Aldrich (Merck), Ref. MP0025

3.1.8 Recombinant Measles Viruses (Vaccine Strains)

Table 8. Recombinant measles viruses. Viruses without an indicated source were generated by myself. Some viruses have an alternative name used in other contexts (other theses, laboratory documentation, some publications). The alternative names are indicated in grey and preceded by "or". **ATU:** additional transcription unit; **BiTE:** bispecific T cell engager; **CDS:** coding sequence; **CEA:** carcinoembryonic antigen; **scFv-Fc:** single-chain fragment variable (scFv) linked to an immunoglobulin fragment crystallizable (Fc) region; **V_H:** variable domain of an immunoglobulin heavy chain; **V_L:** variable domain of an immunoglobulin light chain.

Name	Description and Source
$MeVac_{Schw}$ [151]	MeVac (Schwarz strain), unmodified Source: J. Albert (DKFZ, Heidelberg), L. Küther (UWH, Witten)
MeVac eGFP [135] or MeVac ld-eGFP	MeVac (Schwarz strain) encoding enhanced green fluorescent protein (eGFP) (GFP originally from *Aequorea victoria*) in an ATU upstream of the N CDS Source: J. Albert, J. M. Derani, M. S. C. Finkbeiner, Ž. Modic (DKFZ, Heidelberg), L. Küther (UWH, Witten)
MeVac OVA [154] or MeVac H-mOVA	MeVac (Schwarz strain) encoding full-length chicken ovalbumin (OVA) in an ATU downstream of the H CDS Source: J. Albert, E. Busch (DKFZ, Heidelberg)
MeVac SIINFEKL [154,155] or MeVac ld-OVA	MeVac (Schwarz strain) encoding the OVA-derived peptide SIINFEKL ($OVA_{257-264}$) in an ATU upstream of the N CDS Source: J. Albert, K. D. Kubon (DKFZ, Heidelberg)
MeVac Igκ SIINFEKL [154,155] or MeVac ld-Igκ-OVA	MeVac (Schwarz strain) encoding a fusion peptide in an ATU upstream of the N CDS. From N-terminus to C-terminus, the fusion peptide is composed of the murine Igκ signal peptide and the OVA-derived peptide SIINFEKL ($OVA_{257-264}$) Source: J. Albert, K. D. Kubon (DKFZ, Heidelberg)
MeVac Ub-AAY-[SIINFEKL-AAY]$_1$ [154] or MeVac ld-Ub-OVA 1x	MeVac (Schwarz strain) encoding ubiquitin fused to the OVA-derived peptide SIINFEKL ($OVA_{257-264}$) in an ATU upstream of the N CDS; amino acids AAY are encoded to promote proteasomal cleavage of the fusion peptide Source: J. Albert, J. K. M. Mayer (DKFZ, Heidelberg)
MeVac Ub-AAY-[SIINFEKL-AAY]$_2$ [154] or MeVac ld-Ub-OVA 2x	MeVac (Schwarz strain) encoding ubiquitin fused to two copies of the OVA-derived peptide SIINFEKL ($OVA_{257-264}$) in an ATU upstream of the N CDS; amino acids AAY are encoded to promote proteasomal cleavage of the fusion peptide Source: J. Albert, J. K. M. Mayer (DKFZ, Heidelberg)
MeVac Ub-AAY-[SIINFEKL-AAY]$_6$ [154,155] or MeVac ld-Ub-OVA 6x	MeVac (Schwarz strain) encoding ubiquitin fused to six copies of the OVA-derived peptide SIINFEKL ($OVA_{257-264}$) in an ATU upstream of the N CDS; amino acids AAY are encoded to promote proteasomal cleavage of the fusion peptide Source: J. Albert, K. D. Kubon (DKFZ, Heidelberg)
MeVac mCCL5 or MeVac_P-ATU_mCCL5	MeVac (Schwarz strain) encoding murine CCL5 in an ATU downstream of the P CDS
MeVac mCCL19 or MeVac_P-ATU_mCCL19	MeVac (Schwarz strain) encoding murine CCL19 in an ATU downstream of the P CDS
MeVac mCCL21a or MeVac_P-ATU_mCCL21a	MeVac (Schwarz strain) encoding murine CCL21a in an ATU downstream of the P CDS

Table 8 (continued). Recombinant measles viruses. Viruses without an indicated source were generated by myself. Some viruses have an alternative name used in other contexts (other theses, laboratory documentation, some publications). The alternative names are indicated in grey and preceded by "or". **ATU:** additional transcription unit; **BiTE:** bispecific T cell engager; **CDS:** coding sequence; **CEA:** carcinoembryonic antigen; **scFv-Fc:** single-chain fragment variable (scFv) linked to an immunoglobulin fragment crystallizable (Fc) region; **V_H:** variable domain of an immunoglobulin heavy chain; **V_L:** variable domain of an immunoglobulin light chain.

Name	Description and Source
MeVac mCXCL9 or MeVac_P-ATU_mCXCL9	MeVac (Schwarz strain) encoding murine CXCL9 in an ATU downstream of the MeVac P CDS
MeVac mCXCL10 or MeVac_P-ATU_mCXCL10	MeVac (Schwarz strain) encoding murine CXCL10 in an ATU downstream of the P CDS
MeVac mCXCL13 or MeVac_P-ATU_mCXCL13	MeVac (Schwarz strain) encoding murine CXCL13 in an ATU downstream of the P CDS
MeVac mLIGHT or MeVac_P-ATU_mLIGHT	MeVac (Schwarz strain) encoding murine LIGHT in an ATU downstream of the P CDS
MeVac mLT-α or MeVac_P-ATU_mLTα	MeVac (Schwarz strain) encoding murine LT-α in an ATU downstream of the P CDS
MeVac mLT-β or MeVac_P-ATU_mLTβ	MeVac (Schwarz strain) encoding murine LT-β in an ATU downstream of the P CDS
MeVac mTNF-α or MeVac_P-ATU_mTNFα	MeVac (Schwarz strain) encoding murine TNF-α in an ATU downstream of the P CDS
MeVac IgG-Fc *C.m.* or MeVac_P-ATU_IgG-Fc-*C.m.*	MeVac (Schwarz strain) encoding the Fc region of hamster (*Cricetulus migratorius*) IgG in an ATU downstream of the P CDS
$MeVac_{HblαCEA}$ FmIL-12 [135] or MeVac P-FmIL-12 Hbl-αCEA	MeVac (Schwarz strain) encoding a murine IL-12 fusion protein (FmIL-12) in an ATU downstream of the P CDS and with the H protein fully retargeted to human CEA Source: R. Veinalde (DKFZ, Heidelberg)
$MeVac_{HblαCEA}$ αmPD-1 [150]	MeVac (Schwarz strain) encoding an scFv-Fc molecule targeting murine PD-1 in an ATU downstream of the H CDS and with the H protein fully retargeted to human CEA; the scFv fragment contains the V_H and V_L domains from the hamster anti-mouse PD-1 antibody J43 and is linked to the Fc region of hamster IgG Source: R. Veinalde (DKFZ, Heidelberg)
$MeVac_{HblαCEA}$ IgG-Fc *C.m.* [150]	MeVac (Schwarz strain) encoding the Fc region of hamster (*Cricetulus migratorius*) IgG in an ATU downstream of the H CDS and with the H protein fully retargeted to human CEA Source: R. Veinalde (DKFZ, Heidelberg)
$MeVac_{HblαCEA}$ αmPD-L1 [135] or MeVac H-anti-PD-L1 Hbl-αCEA	MeVac (Schwarz strain) encoding an scFv-Fc molecule targeting human and murine PD-L1 in an ATU downstream of the H CDS and with the H protein fully retargeted to human CEA; the scFv fragment contains the V_H and V_L domains from Atezolizumab and is linked to the Fc region of human IgG1 Source: R. Veinalde (DKFZ, Heidelberg)
$MeVac_{HblαCEA}$ IgG1-Fc [135] or MeVac H-IgG1Fc Hbl-αCEA	MeVac (Schwarz strain) encoding the Fc region of human IgG1 in an ATU downstream of the H CDS and with the H protein fully retargeted to human CEA Source: R. Veinalde (DKFZ, Heidelberg)

Table 8 (continued). Recombinant measles viruses. Viruses without an indicated source were generated by myself. Some viruses have an alternative name used in other contexts (other theses, laboratory documentation, some publications). The alternative names are indicated in grey and preceded by "or". **ATU:** additional transcription unit; **BiTE:** bispecific T cell engager; **CDS:** coding sequence; **CEA:** carcinoembryonic antigen; **scFv-Fc:** single-chain fragment variable (scFv) linked to an immunoglobulin fragment crystallizable (Fc) region; **V_H:** variable domain of an immunoglobulin heavy chain; **V_L:** variable domain of an immunoglobulin light chain.

Name	Description and Source
$MeVac_{Edm}$ [156] or MVtag, or NSe	MeVac (Edmonston B-derived strain) Edmonston B-derived strain: Edmonston B strain engineered to exhibit unique NarI and SpeI target sites in the virus antigenome. Also designated NSe (NarI SpeI eliminated) Source: C. E. Engeland (DKFZ, Heidelberg)
MeVac BiTE(mCD3xhCD20) [142] or MV-mCD3xCD20	MeVac (Edmonston B-derived strain) encoding a BiTE targeting murine CD3 and human CD20 in an ATU downstream of the H CDS Source: J. P. W. Heidbuechel, T. Speck (DKFZ, Heidelberg)
MeVac BiTE(mCD3xhCEA) [142] or MV-mCD3xCEA	MeVac (Edmonston B-derived strain) encoding a BiTE targeting murine CD3 and human CEA in an ATU downstream of the H CDS Source: J. P. W. Heidbuechel, T. Speck (DKFZ, Heidelberg)
MV-NIS [157]	MeVac (Edmonston B-derived strain) encoding the human sodium iodide symporter (NIS) in an ATU downstream of the H CDS Source: Imanis Life Sciences, Ref. OV1003

3.1.9 Growth Media for Bacterial and Mammalian Cell Culture

Table 9. Growth media. NEB: New England Biolabs.

Name	Manufacturer
Dulbecco's Modified Eagle Medium, high glucose, GlutaMAX™ supplement (DMEM)	Thermo Fisher Scientific, Ref. 61965-026
Dulbecco's Modified Eagle Medium, 1 g/L glucose, GlutaMAX™ supplement, pyruvate (DMEM low glucose)	Thermo Fisher Scientific, Ref. 21885-025
Lysogeny Broth medium (LB)	Carl-Roth, Ref. X964
Lysogeny Broth medium with Agar (LB-Agar)	Carl-Roth, Ref. X965
Minimum Essential Medium Eagle alpha modification (α-MEM)	Sigma-Aldrich (Merck), Ref. M4526
OptiPRO™ serum-free medium (OptiPRO SFM)	Thermo Fisher Scientific, Ref. 12309019
OptiMEM™ reduced serum medium, GlutaMAX™ supplement (OptiMEM)	Thermo Fisher Scientific, Ref. 51985-034
Roswell Park Memorial Institute 1640 medium, GlutaMAX™ supplement (RPMI)	Thermo Fisher Scientific, Ref. 61870-044
Super optimal broth with catabolite repression medium (SOC)	NEB, Ref. B9020S

3.1.10 Cell Lines

Table 10. Cell lines. **CMV:** cytomegalovirus.

Name	Description	Source
B16-F0 [158]	Murine melanoma cell line derived from a spontaneous melanoma in a C57BL/6J mouse.	D. M. Nettelbeck (DKFZ, Heidelberg)
B16-hCD46 (pCAG-SMAR)	B16-F1 cell line with stable expression of human CD46. Generated by transfection of B16-F1 cells with the pCAG-Puro-P2A-hCD46-SMAR vector (Table 2).	Present thesis (see 4.7.2)
B16-hCD46 (pEF1-Nano)	B16-F1 cell line with stable expression of human CD46. Generated by transfection of B16-F1 cells with the pEF1-Puro-P2A-hCD46-SMARter-NP vector (Table 2).	Present thesis (see 4.7.2)
B16-hCD20 [159]	B16-F1 cell line with stable expression of human CD20. Generated by transduction of B16-F1 cells with a lentiviral vector encoding human CD20 under the control of the human CMV promoter.	C. Großardt (DKFZ, Heidelberg)
B16-hCD20-hCD46 (lenti) [142]	B16-F1 cell line with stable expression of human CD20 and human CD46. Generated by transduction of B16-hCD20 cells with a lentiviral vector encoding human CD46 under the control of the human CMV promoter followed by single cell sorting for human CD46 expression. Clonal cell line #2D was employed in the present thesis.	J. P. W. Heidbuechel (DKFZ, Heidelberg)
B16-hCD20-hCD46 (pCAG-SMAR)	B16-F1 cell line with stable expression of human CD20 and human CD46. Generated by transfection of B16-hCD20 cells with the pCAG-Puro-P2A-hCD46-SMAR vector (Table 2).	Present thesis (see 4.7.2)
B16-hCD20-hCD46 (pCAG-Nano)	B16-F1 cell line with stable expression of human CD20 and human CD46. Generated by transfection of B16-hCD20 cells with the pCAG-Puro-P2A-hCD46-SMARter-NP vector (Table 2).	Present thesis (see 4.7.2)
B16-hCD20-hCD46 (pEF1-Nano)	B16-F1 cell line with stable expression of human CD20 and human CD46. Generated by transfection of B16-hCD20 cells with the pEF1-Puro-P2A-hCD46-SMARter-NP vector (Table 2).	Present thesis (see 4.7.2)
DC2.4 [160]	Immortalized murine dendritic cell line derived from bone marrow cells of a C57BL/6 mouse transduced with replication-defective retrovirus expressing murine GM-CSF and retrovirus encoding *myc* and *raf*.	H. Weyd (DKFZ, Heidelberg)

Table 10 (continued). Cell lines. CMV: cytomegalovirus.

Name	Description	Source
E.G7-OVA [161]	Murine lymphoma cell line expressing chicken ovalbumin. Generated by electroporation of EL4 cells with a plasmid encoding chicken ovalbumin. EL4 [162] is a murine lymphoma cell line derived from a lymphoma induced by 9,10-dimethyl-1,2-benzanthracene in a C57BL/6 mouse.	W. Osen and S. Eichmüller (DKFZ, Heidelberg)
FC1245 [163]	Murine pancreatic ductal adenocarcinoma cell line derived from a tumor in a KPC mouse. The KPC mouse model was generated by Hingorani *et al.* [164]	A. Nowrouzi (DKFZ, Heidelberg)
FC1245-hCD46 (lenti) [165]	FC1245 cell line with stable expression of human CD46. Generated by transduction of FC1245 cells with a lentiviral vector encoding human CD46 under the control of the human CMV promoter.	R. Veinalde (DKFZ, Heidelberg)
FC1245-hCD46 (pCAG-SMAR)	FC1245 cell line with stable expression of human CD46. Generated by transfection of FC1245 cells with the pCAG-Puro-P2A-hCD46-SMAR vector (Table 2).	Present thesis (see 4.7.2)
FC1245-hCD46 (pCAG-Nano)	FC1245 cell line with stable expression of human CD46. Generated by transfection of FC1245 cells with the pCAG-Puro-P2A-hCD46-SMARter-NP vector (Table 2).	Present thesis (see 4.7.2)
FC1245-hCD46 (pEF1-Nano)	FC1245 cell line with stable expression of human CD46. Generated by transfection of FC1245 cells with the pEF1-Puro-P2A-hCD46-SMARter-NP vector (Table 2).	Present thesis (see 4.7.2)
L929 [166]	Murine connective tissue cell line with fibroblast-like morphology, derived from a single cell (clone 929) of the parental cell line L. L is a murine cell line established from normal subcutaneous connective tissue (areolar and adipose) of a 100 day-old male C3H/An mouse. [167]	L. Vieira Codeco Marques and S. Eichmüller (DKFZ, Heidelberg)
MC38 [168]	Murine colon adenocarcinoma cell line derived from a tumor induced by 1,2-dimethylhydrazine (DMH) in a C57BL/6 mouse. Chemical induction of the tumor was conducted by Corbett *et al.* [169]	R. Cattaneo (Mayo Clinic, Rochester)
MC38-hCD46 (lenti) [154,155]	MC38 cell line with stable expression of human CD46. Generated by transduction of MC38 cells with a lentiviral vector encoding human CD46 under the control of the human CMV promoter.	J. Albert (DKFZ, Heidelberg)
MC38-hCD46 (pCAG-SMAR)	MC38 cell line with stable expression of human CD46. Generated by transfection of MC38 cells with the pCAG-Puro-P2A-hCD46-SMAR vector (Table 2).	Present thesis (see 4.7.2)
MC38-hCD46 (pCAG-Nano)	MC38 cell line with stable expression of human CD46. Generated by transfection of MC38 cells with the pCAG-Puro-P2A-hCD46-SMARter-NP vector (Table 2).	Present thesis (see 4.7.2)
MC38-hCD46 (pEF1-Nano)	MC38 cell line with stable expression of human CD46. Generated by transfection of MC38 cells with the pEF1-Puro-P2A-hCD46-SMARter-NP vector (Table 2).	Present thesis (see 4.7.2)

Table 10 (continued). **Cell lines.** **CMV:** cytomegalovirus.

Name	Description	Source
MC38cea [170]	MC38 cell line with stable expression of human carcinoembryonic antigen (CEA). Generated by transduction of MC38 cells with a gamma-retroviral vector encoding human CEA.	R. Cattaneo (Mayo Clinic, Rochester)
MC38cea-hCD46 (pCAG-SMAR)	MC38 cell line with stable expression of human CEA and human CD46. Generated by transfection of MC38cea cells with the pCAG-Puro-P2A-hCD46-SMAR vector (Table 2).	Present thesis (see 4.7.2)
MC38cea-hCD46 (pCAG-Nano)	MC38 cell line with stable expression of human CEA and human CD46. Generated by transfection of MC38cea cells with the pCAG-Puro-P2A-hCD46-SMARter-NP vector (Table 2).	Present thesis (see 4.7.2)
MC38cea-hCD46 (pEF1-Nano)	MC38 cell line with stable expression of human CEA and human CD46. Generated by transfection of MC38cea cells with the pEF1-Puro-P2A-hCD46-SMARter-NP vector (Table 2).	Present thesis (see 4.7.2)
OVA-CTL [171]	Chicken ovalbumin (OVA)-specific CD8+ cytotoxic T lymphocyte (CTL) line recognizing the H-2K^b-restricted OVA-derived epitope SIINFEKL ($OVA_{257-264}$). Cell line established from C57BL/6 mice immunized with SIINFEKL and a T-helper peptide.	W. Osen and S. Eichmüller (DKFZ, Heidelberg)
Vero	Epithelial cell line derived from the kidney of an adult African green monkey (*Cercopithecus aethiops*). Cell line initiated in 1962 at the Chiba University, Chiba, Japan. Vero cells are interferon-deficient. [172]	American Type Culture Collection (ATCC, Manassas), Ref. CCL-81™
Vero α-HIS [173]	Vero cell line with stable expression of a membrane-bound single-chain antibody against a six histidine peptide (α-HIS). Generated by transfection of Vero cells with a pDisplay™ vector encoding α-HIS. Allows rescue and propagation of retargeted MeVac using the STAR (six-his tagging and retargeting) system.	S. J. Russell (Mayo Clinic, Rochester)

3.1.11 Mouse Strains

Table 11. **Mouse strains.**

Strain	Description and Source
C57BL/6J	*Mus musculus* of C57BL/6J background, wild-type Source: Harlan Laboratories, Charles River, or Janvier Labs
MY II [174,175] Also known as B6.FVB-Tg(CD46)2Gsv/J	*Mus musculus* of C57BL/6J background expressing a transgene encoding human CD46 on all nucleated cells • Transgene-positive mice are known as CD46tg mice • Transgene-negative mice are known as non-carrier mice Source: The Jackson Laboratory, JAX stock #004971
OT-I	*Mus musculus* of C57BL/6 background expressing a T cell receptor that recognizes SIINFEKL ($OVA_{257-264}$) in the context of H-2K^b Source: DKFZ, Heidelberg

3.1.12 Buffers and Chemicals

Table 12. **Buffers and chemicals.**

Name	Manufacturer
2-mercaptoethanol for cell culture (50 mM)	Thermo Fisher Scientific, Ref. 31350010
2-mercaptoethanol for SDS-PAGE (14.3 M)	Sigma-Aldrich (Merck), Ref. M3148
3,3',5,5'-tetramethylbenzidine (TMB), soluble substrate system for ELISA	Thermo Fisher Scientific, Ref. 34028
3,3',5,5'-tetramethylbenzidine (TMB), precipitating substrate system for ELISpot	Mabtech, Ref. 3651-10
4',6-diamidino-2-phenylindole (DAPI)	Sigma-Aldrich (Merck), Ref. D8417
5-bromo-4-chloro-3-indolyl-phosphate / Nitro blue tetrazolium chloride (BCIP®/NBT), precipitating substrate system for ELISpot	Sigma-Aldrich (Merck), Ref. B1911
Accudrop Beads	BD FACS™, Ref. 345249
Agarose, molecular biology grade	Sigma-Aldrich (Merck), Ref. A9539
Ammonium-Chloride-Potassium (ACK) lysing buffer	Thermo Fisher Scientific, Ref. A1049201
Ampicillin	Carl-Roth, Ref. HP62.1
Antibiotic Antimycotic Solution for cell culture (100X) - Penicillin (10000 U/mL) - Streptomycin (10000 µg/mL) - Amphotericin B (25 µg/mL)	Sigma-Aldrich (Merck), Ref. A5955
CountBright™ absolute counting beads	Thermo Fisher Scientific, Ref. C36950
CutSmart® Buffer	NEB, Ref. B7204
Dako target retrieval solution (citrate buffer, pH = 6)	Agilent Technologies, Ref. S2369
Deoxynucleotide triphosphates (dNTPs)	Thermo Fisher Scientific, Ref. R0192
Dimethyl sulfoxide (DMSO)	Sigma-Aldrich (Merck), Ref. D2438
DirectPCR Lysis Reagent (Ear)	Viagen Biotech, Ref. 402-E
DNA gel loading dye (6X)	Thermo Fisher Scientific, Ref. R0611
Dulbecco's phosphate-buffered saline (D-PBS) without calcium and magnesium	Thermo Fisher Scientific, Ref. 14190-250
Eosin Y (yellowish)	Sigma-Aldrich (Merck), Ref. 115935
Ethanol	Carl-Roth (ROTIPURAN®), Ref. 9065
Ethidium bromide	AppliChem, Ref. 1239-45-8
Ethylenediaminetetraacetic acid (EDTA) disodium salt solution (0.5 M)	Sigma-Aldrich (Merck), Ref. E7889
Fetal calf serum (FCS)	PAN Biotech, Ref. P40-37500
FuGENE® HD transfection reagent	Promega, Ref. E2311

Table 12 (continued). **Buffers and chemicals.**

Name	Manufacturer
GeneRuler 100 bp Plus DNA ladder	Thermo Fisher Scientific, Ref. SM0321
GeneRuler 1 kb DNA ladder	Thermo Fisher Scientific, Ref. SM0311
Geneticin (G418 Sulfate) (50 mg/mL)	Thermo Fisher Scientific, Ref. 10131027
Hematoxylin solution modified according to Gill III	Sigma-Aldrich (Merck), Ref. 105174
HEPES buffer solution (1M)	Thermo Fisher Scientific, Ref. 15630056
Hydrochloric acid (HCl) fuming 37% (w/w)	Carl-Roth (ROTIPURAN®), Ref. 4625
Imperial™ Protein Stain (Coomassie Dye R-250)	Thermo Fisher Scientific, Ref. 24615
Incucyte® Cytotox Green Dye	Sartorius, Ref. 4633
Iodixanol (OptiPrep® Density Gradient Medium)	Sigma-Aldrich (Merck), Ref. D1556
Ionomycin calcium salt	Cayman Chemical, Ref. 11932
Kanamycin solution from *Streptomyces kanamyceticus*	Sigma-Aldrich (Merck), Ref. K0129
Laemmli sample buffer (4X)	Bio-Rad, Ref. 1610747
Lipofectamine™ 2000 transfection reagent	Thermo Fisher Scientific, Ref. 11668-030
Matrigel® Basement Membrane Matrix	Corning, Ref. 356234
Methyl α-D-mannopyranoside	Sigma-Aldrich (Merck), Ref. M6882
Mini-PROTEAN® TGX™ Precast Protein Gels	Bio-Rad, Ref. 4569034
Mitomycin C from *Streptomyces caespitosus*	Sigma-Aldrich (Merck), Ref. M4287
nCounter Mouse Immunology Panel (CodeSet Only)	NanoString Technologies, Ref. XT-CSO-MIM1-12
PageRuler™ Prestained Protein Ladder, 10 to 180 kDa	Thermo Fisher Scientific, Ref. 26616
Paraformaldehyde solution, 4% in D-PBS	Thermo Fisher Scientific, Ref. J19943.K2
Penicillin (5000 U/mL) and Streptomycin (5000 µg/mL)	Thermo Fisher Scientific, Ref. 15070063
Permanent AP-Red chromogenic substrate kit	Zytomed Systems, Ref. ZUC001
Phorbol 12-myristate 13-acetate (PMA)	Cayman Chemical, Ref. 10008014
Phosphate-buffered saline with Tween 20 (PBS-T)	Carl-Roth (Roti®Fair), Ref. 1115
Puromycin dihydrochloride	Thermo Fisher Scientific, Ref. A1113803
RNA*later*™ Stabilization solution	Thermo Fisher Scientific, Ref. AM7020
SDS-PAGE running buffer (10X)	Carl-Roth (Rotiphorese®), Ref. 3060
Sodium pyruvate (100 mM)	Thermo Fisher Scientific, Ref. 11360039
Staurosporine, protein kinase inhibitor	Abcam, Ref. ab120056
Stop Reagent for TMB (contains an organic acid)	Sigma-Aldrich (Merck), Ref. S5814
Sulphuric acid (H_2SO_4) (2N)	Carl-Roth, Ref. X873
SYBR® Safe DNA gel stain	Thermo Fisher Scientific, Ref. S33102

Table 12 (continued). Buffers and chemicals.

Name	Manufacturer
Tris(hydroxymethyl)aminomethane (Tris Base)	Sigma-Aldrich (Merck), Ref. 252859
Tris-borate-EDTA buffer, UltraPure™ (TBE) (10X)	Thermo Fisher Scientific, Ref. 15581044
Tris-buffered saline with Tween 20 (TBS-T) (10X)	Carl-Roth (Roti®Stock), Ref. 1061
Trypan blue solution	Sigma-Aldrich (Merck), Ref. T8154
Tween® 20	Carl-Roth, Ref. 9127
Water (H_2O), Aqua ad Iniectabilia, nuclease-free	B. Braun, Ref. 2351744
Water (H_2O), Milli-Q®	From the tap, purified using the Milli-Q® Direct Water Purification System (Merck)
Zombie Violet™ Fixable Viability kit	BioLegend, Ref. 423113

3.1.13 Consumables

Table 13. Consumables. Only specific consumables are indicated. In addition, general laboratory consumables were used throughout the study (refer to laboratory technicians for details).

Name	Manufacturer
96-well plate, flat bottom, transparent, high binding (ELISA plate)	Sarstedt, Ref. 82.1581.200
Biopsy punch, 1 mm diameter	pfmmedical, Ref. 48101
Cell strainer, 70 µm pore size	Sarstedt, Ref. 83.3945.070
Cell strainer, 100 µm pore size	Sarstedt, Ref. 83.3945.100
Cell scrapers	Santa Cruz Biotechnology, Ref. sc-395251
Filters, 0.22 µm pore size, PVDF membrane	Carl-Roth (ROTILABO®), Ref. P666.1
MultiScreen$_{HTS}$-IP, 0.45 µm filter, transparent, sterile (ELISpot plate)	Merck-Millipore, Ref. MSIPS4510
MultiScreen$_{HTS}$-IP, 0.45 µm filter, white, sterile (ELISpot plate)	Merck-Millipore, Ref. MSIPS4W10
Needles, diameter 0.45 x 12 mm, 26 G x ½ ”	B-Braun (Sterican®), Ref. 4665457
Scalpels	Teqler, Ref. T370610
Syringes, 1 mL	B-Braun (Injekt®-F), Ref. 9166017V
TC-Insert for 6-well plates, 0.4 µm pore size, PET membrane (membrane insert for the patient-derived *ex vivo* tumor slice cultures)	Sarstedt, Ref. 83.3930.041
Transwell®, 6.5 mm, 5.0 µm pore size, polycarbonate membrane insert, 24-well plate (transwell plate for the classical chemotaxis assay)	Corning, Ref. 3421
Transwell Incucyte® Clearview 96-well plate for chemotaxis (containing Incucyte® Clearview insert)	Sartorius, Ref. 4582
Ultracentrifuge tubes (5 mL, open-top, ultra-clear)	Beckman Coulter, Ref. 344057
Ultracentrifuge tubes (13.2 mL, open-top, ultra-clear)	Beckman Coulter, Ref. 344059

3.2 Methods

3.2.1 Cell Culture, Transfection, and Sorting

3.2.1.1 Culture of Cell Lines

General cell culture: I maintained all cell lines in humidified incubators at 37 ºC and 5% CO_2 and conducted all cell culture procedures in class II safety cabinets. The laboratory technicians routinely tested the cell lines for mycoplasma contamination using the Venor™ GeM mycoplasma detection kit. To determine the concentration of viable cells, I stained the cell suspension with trypan blue and counted the unstained (live) cells using a Neubauer hemocytometer (Marienfeld). Cell culture required different media depending on the cell line (Table 14). Fetal calf serum (FCS) was heat-inactivated (56 ºC, 30 min) and passed through a 0.22 µm pore size filter before addition to the culture medium. Media were warmed at room temperature (RT) before usage.

Table 14. Cell culture media. **α-MEM:** Minimum Essential Medium Eagle alpha modification; **DMEM:** Dulbecco's Modified Eagle medium with high glucose and GlutaMAX™ supplement; **FCS:** fetal calf serum; **HEPES:** 4-(2-Hydroxyethyl)piperazine-1-ethanesulfonic acid; **RPMI:** Roswell Park Memorial Institute 1640 medium with GlutaMAX™ supplement.

Adherent	Cell line: L929 Medium: DMEM + 5% FCS
	Cell line: Vero, MC38, MC38cea, MC38-hCD46(lenti) Medium: DMEM + 10% FCS
	Cell line: MC38/MC38cea derivatives harboring S/MAR or Nano-S/MAR vectors Medium: DMEM + 10% FCS + 7.5 µg/mL puromycin
	Cell line: B16-F1, B16-hCD20, B16-hCD20-hCD46(lenti), FC1245, FC1245-hCD46(lenti) Medium: RPMI + 10% FCS
	Cell line: B16-F1/B16-hCD20/FC1245 derivatives harboring S/MAR or Nano-S/MAR vectors Medium: RPMI + 10% FCS + 7.5 µg/mL puromycin
	Cell line: DC2.4 Medium: RPMI + 10% FCS + 10 mM HEPES
Suspension	Cell line: E.G7-OVA Medium: RPMI + 10% FCS + 0.8 µg/mL geneticin (G418)
	Cell line: OVA-CTL Medium: CTL medium [α-MEM + 10% FCS + 100 U/mL penicillin + 100 µg/mL streptomycin + 4 mM L-glutamine + 10 µM 2-mercaptoethanol] + weekly restimulation (see main text)

For maintenance of adherent cell cultures, I used Nunc® cell culture treated flasks with filter caps (Thermo Fisher Scientific). The cultures were split at a cell confluence of 80% to 100% by removing the old culture medium, washing the flask with Dulbecco's Phosphate Buffered Saline (D-PBS), detaching the cell monolayer with Trypsin (0.05%, w/v) – ethylenediaminetetraacetic acid (EDTA) for 15 min at 37 ºC. A 1:10 to 1:50 fraction (v/v) of the detached cell suspension was kept in the

flask and cultured further in fresh medium. The remaining cell suspension was discarded or used immediately in experiments.

Culture of E.G7-OVA cells: E.G7-OVA cells were cultured in suspension in non-tissue culture-treated (NTC) T75 flasks. The cultures were split weekly by washing the cells in D-PBS (300 x g, 5 min), resuspending the pellet in fresh medium, and transferring 1:10 (v/v) of the fresh cell suspension back to the flask, where fresh medium had been added.

Culture of OVA-CTLs: OVA-CTLs were cultured in suspension. For the first stimulation round, OVA-CTLs were thawed, adjusted to $1.7x10^5$ cells/mL in CTL medium (Table 14), distributed in wells of a NTC 24-well plate at 2 mL per well, and stimulated with irradiated feeder cells (E.G7-OVA cells and splenocytes) as previously described [176]. Briefly, E.G7-OVA cells were adjusted to $2x10^6$ cells/mL in RPMI + 10% FCS (without geneticin), irradiated at 200 Gy in a Gammacell® 1000 irradiator (Best Theratronics), and added onto the OVA-CTL cultures (100 µL, *i.e.*, $2x10^5$ irradiated E.G7-OVA cells, per well). Spleens were freshly isolated from C57BL/6J mice, irradiated at 33 Gy in a Gammacell® 1000 irradiator (Best Theratronics), and then processed into single-cell suspensions (see 3.2.6.3). Splenocyte suspensions were adjusted to $5x10^7$ cells/mL in CTL medium and added to the OVA-CTL + E.G7-OVA cultures ($5x10^6$ irradiated splenocytes per well). OVA-CTL cultures were split weekly at 1:2 (v/v) by centrifuging the cell suspension (pool of all wells), resuspending in double the volume of CTL medium, and distributing the fresh suspension into wells (2 mL/well, 24-well plates). Fresh stimuli (irradiated feeder cells) were added as outlined above. From the second restimulation onwards, the CTL medium also contained (i) 5% (v/v) supernatant of Concanavalin A-stimulated (5 µg/mL) rat splenocyte cultures as a source of IL-2 and (ii) 25 mM methyl α-D-mannopyranoside to neutralize the excess of Concanavalin A. Experiments were conducted on day 6 after restimulation.

3.2.1.2 Cryopreservation and Thawing of Cell Lines

For long-term storage, I cryopreserved the cell lines. Briefly, cell suspensions were prepared, adjusted to $2x10^6$ cells/mL in culture medium containing 5% (v/v) dimethyl sulfoxide (DMSO), and distributed into Nunc® CryoTubes® vials (Thermo Fisher Scientific) at 500 µL/vial. The vials were maintained in Stratagene Cryo 1 ºC Freezing Containers (Agilent) at -80 ºC during 24 h for progressive temperature decrease and subsequently stored in liquid nitrogen (Heidelberg storage) or at -150 ºC (Witten storage). For cell thawing, frozen vials were thawed in a 37 ºC water bath and the cell suspensions were transferred to the cell culture flasks, previously filled with the corresponding culture medium. After incubation (24 h, 37 ºC, 5% CO_2), the old medium was replaced by fresh medium. Cells harboring S/MAR or Nano-S/MAR vectors were thawed in puromycin-free medium. Unless otherwise indicated, puromycin was added on the following day and every time the culture was passaged.

3.2.1.3 Generation of hCD46(+) Murine Tumor Cell Lines Harboring S/MAR Vectors

To generate murine tumor cell lines with ectopic expression of human CD46 (hCD46), I transfected hCD46(-) parental cells with Plasmid-S/MAR (pCAG-SMAR) or Nano-S/MAR (pCAG-Nano, pEF1-Nano) vectors encoding the BC1 isoform of hCD46 (Table 2). Before transfection, I amplified the pCAG-SMAR vector in bacteria, purified it, and confirmed the hCD46 sequence via Sanger sequencing with the primers pCAG_P2A_hCD46_F and pCAG_ hCD46_R (Table 1) as described in 3.2.2.5 for other constructs. The Nano-S/MAR vectors cannot be amplified with conventional competent bacteria [152,153]. All S/MAR vectors were obtained from M. Bozza (DKFZ, Heidelberg).

One day before transfection, I seeded the parental cells (B16, B16-hCD20, FC1245, MC38, or MC38cea) into five wells of a 6-well plate per cell line ($2x10^5$ cells/well in 2 mL culture medium). On day 0 (transfection day), I prepared plasmid DNA – lipid complexes at a DNA (µg) to Lipofectamine™ 2000 (µL) ratio of 1:2.5. To this end, I added 1 µg DNA to 150 µL OptiMEM (tube A) and 2.5 µL Lipofectamine™ 2000 to 150 µL OptiMEM (tube B). After incubation (5 min, RT), I combined the contents of both tubes (ca. 300 µL) and incubated the mixture to allow complex formation (20 min, RT). The amounts and volumes were constant in all transfections, except for the transfection of MC38 cells with pCAG-SMAR, for which I used the double amount of DNA (2 µg) and double volume of Lipofectamine™ 2000 (5 µL), albeit keeping the total volume at ca. 300 µL. During the 20 min incubation, I replaced the medium from the seeded cells with 1.7 mL fresh culture medium (without puromycin). After DNA-lipid complex formation, I added 300 µL of the transfection mixture evenly onto the cell monolayer dropwise and incubated the cells (37 ºC, 5% CO_2). The five wells corresponded to different conditions: the cells from three wells were transfected with pCAG-SMAR, pCAG-Nano, and pEF1-Nano, respectively. The non-transfected two wells were used as positive and negative controls during puromycin selection (explained below). After 4 to 6 h incubation, I replaced the medium with 2 mL fresh culture medium (without puromycin) and incubated the cultures further (37 ºC, 5% CO_2).

On day 2, I replaced the medium with 2 mL fresh culture medium containing 7.5 µg/mL puromycin for selection of transfected cells. The puromycin concentration had been determined in cell line-specific puromycin sensitivity tests (not shown). Besides the three transfected conditions, I also added puromycin to the non-transfected positive control, where I expected all cells to die, thus confirming parental cell sensitivity to the selection antibiotic. The negative control was cultured without puromycin to monitor normal parental cell growth. All controls yielded the expected results. The cultures from the transfected wells were expanded to 10 cm plates on day 5 and subsequently to T75 flasks on day 10. For expansion, cells were detached with 0.05% Trypsin-EDTA and transferred to the larger container, previously filled with culture medium (without puromycin).

Two days after expansion (day 7, day 12), I replaced the old medium with fresh culture medium containing 7.5 µg/mL puromycin.

Around day 20 (day 18 to day 25), I bulk-sorted hCD46(+) cells from the transfected cultures using fluorescence-activated cell sorting (FACS). To that aim, I stained $6x10^6$ cells from each transfected population with a PE-conjugated anti-human CD46 antibody and 4',6-diamidino-2-phenylindole (DAPI) (see 3.2.7.2, Table 6). For sorting, I used the 100 µm nozzle and chose "purity" as precision, "4 tubes" as device, and "continuous" as target events. I adjusted the voltages and drop delay individually for each sort using unstained samples and BD FACS™ Accudrop Beads, respectively. After adjusting these settings, I bulk-sorted hCD46(+) cells into 15 mL tubes containing 2 mL DMEM or RPMI supplemented with 50% FCS using a BD FACSAria Fusion cell sorter (BD Biosciences) (B16-hCD46$_{[pCAG\text{-}SMAR]}$ cells) or a BD FACSAria™ II cell sorter (BD Biosciences) (all other cell lines) and the BD FACSDiva™ software (version 8.0.1, BD Biosciences). Afterwards, I centrifuged the sorted cells (300 x g, 5 min), resuspended them in 12 mL DMEM or RPMI supplemented with 20% FCS, 100 U/mL penicillin, and 100 µg/mL streptomycin, and cultured them in T75 flasks (37 ºC, 5% CO_2) until cryopreservation when reaching 90% confluence (see 3.2.1.2). One day after culture initiation, and upon each medium change, I added 7.5 µg/mL puromycin to the cultures. During culture, I changed the medium regularly for optimal nutrient availability. On the day of cryopreservation, I kept an aliquot of the cell suspension aside to assess, via flow cytometry, whether the cells were hCD46(+). Indeed, all generated cell lines were hCD46(+) (data not shown).

3.2.2 Cloning Methods

3.2.2.1. Generation of cDNA from Murine Splenocytes

To obtain cDNA from murine splenocytes, I prepared a single-cell suspension from the spleen of a C57BL/6J mouse (see 3.2.6.3) and extracted total RNA from the splenocytes using the RNeasy Protect Mini kit and QIAshredder kit according to the manufacturer's instructions. Next, I removed the genomic DNA contaminants using the RNase-Free DNase set following the manufacturer's guidelines and purified the RNA according to the protocol "RNA Cleanup" of the RNeasy Protect Mini kit. Subsequently, I determined the concentration and purity of the eluted RNA with a NanoDrop 1000 spectrophotometer (Thermo Fisher Scientific) by measuring the absorbance at 230 nm, 260 nm, and 280 nm wavelengths. Afterwards, I reverse transcribed polyadenylated RNAs to cDNA using the Maxima H Minus First Strand cDNA Synthesis kit following the manufacturer's instructions, employing oligo $(dT)_{18}$ as primer and 2 µg total RNA as template. After reverse transcription, I incubated the samples with RNase H (37 ºC, 20 min) for removal of RNA contaminants. The samples were stored at -20 ºC until further usage.

3.2.2.2 Polymerase Chain Reaction (PCR)

To amplify the coding sequence (CDS) of murine CCL5, CCL19, CCL21a, CXCL9, CXCL10, CXCL13, LT-α, LIGHT, and TNF-α (Table 3), I conducted polymerase chain reaction (PCR) with the Q5 High-Fidelity DNA polymerase using cDNA from C57BL/6J murine splenocytes (see 3.2.2.1) as template and primer pairs specific for the CDS of interest (Table 1). I designed the forward primers to bind the 3' end of the CDS and insert a MluI restriction site as well as a Kozak sequence upstream of the CDS. Similarly, I designed the reverse primers to bind the 5' end of the CDS and insert a PauI or BtgI restriction site downstream of the CDS. When required, the reverse primers also added an additional stop codon to the PCR product to comply with the rule of six [90]. To confirm insertion of DNA fragments into cloning vectors, I conducted PCR with the One*Taq*® DNA polymerase. As template, I used a colony of *Escherichia coli* transformed with the vector of interest, and as primer pair I used oligonucleotides binding to vector regions that flanked the insert (Table 1). I performed all PCR reactions in a T1 PCR thermocycler (Biometra). The PCR components and conditions are given in Tables 15 and 16, respectively.

Table 15. Polymerase chain reaction (PCR) components. Volumes or weights for each component of one PCR reaction with Q5 High-Fidelity DNA polymerase (Q5 PCR) and One*Taq*® DNA polymerase (One*Taq* PCR) are shown.

Q5 PCR		**One*Taq* PCR**	
5X Q5 Reaction Buffer	10 µL	5X One*Taq* Buffer	5 µL
10 mM dNTP	1 µL	10 mM dNTP	0.5 µL
5 µM Forward Primer	1.5 µL	30 µM Forward Primer	0.17 µL
5 µM Reverse Primer	1.5 µL	30 µM Reverse Primer	0.17 µL
DNA template	500 ng	DNA template	1 colony
Q5 DNA Polymerase	0.5 µL	One*Taq*® DNA Polymerase	0.125 µL
Nuclease-free water	Top to 50 µL	Nuclease-free water	Top to 25 µL

Table 16. Polymerase chain reaction (PCR) conditions. Conditions for PCR with Q5 High-Fidelity DNA polymerase (Q5) and One*Taq*® DNA polymerase (One*Taq*) are shown. The annealing temperature "a" was determined individually for each primer pair with the NEB Tm Calculator online tool (https://tmcalculator.neb.com/). The extension time "b" was calculated based on the size of the expected amplicon considering 60 s per kilo-base-pair (kbp).

	Q5 PCR			**One*Taq* PCR**		
	Temperature (ºC)	Time (s)	Cycles	Temperature (ºC)	Time (s)	Cycles
Initial denaturation	98	30	1x	94	30	1x
Denaturation	98	10		94	30	
Annealing	a	30	35x	a	30	30x
Extension	72	b		68	b	
Final extension	72	120	1x	68	300	1x

3.2.2.3 Agarose Gel Electrophoresis and DNA Purification

To separate and analyze DNA fragments, I conducted horizontal agarose gel electrophoresis using GeneRuler 100 bp Plus or GeneRuler 1 kb DNA ladders as molecular weight standards. I added DNA gel loading dye to the DNA samples and standards, and loaded them onto a 1% agarose in 1X Tris-borate-EDTA (TBE) gel containing ethidium bromide or SYBR® Safe for DNA visualization. After performing electrophoresis at 120 V for 90 min using 1X TBE as running buffer, I visualized the DNA fragments under ultraviolet light of 265 nm wavelength on a UV transilluminator (Herolab). To isolate DNA fragments from the agarose gel, I excised the bands of interest with a clean scalpel and purified the DNA using the QIAquick Gel Extraction kit according to the manufacturer's protocol. I determined the concentration of the eluted DNA by measuring absorbance at 260 nm wavelength with a NanoDrop 1000 spectrophotometer (Thermo Fisher Scientific).

3.2.2.4 DNA Fragment Cloning

As described above, I designed and generated cassettes encoding murine CCL5, CCL19, CCL21a, CXCL9, CXCL10, CXCL13, LT-α, TNF-α, and LIGHT. These cassettes consisted of a Kozak sequence and the CDS for the molecule of interest, and were flanked by MluI and either PauI or BtgI restriction sites. After generation, I analyzed these DNA fragments by agarose gel electrophoresis, purified them from the gel as indicated above, and ligated them into pJET1.2/blunt vectors using the CloneJET™ PCR Cloning kit, which employs T4 DNA ligase, following the manufacturer's instructions. These ligations yielded the plasmids pJET mCCL5, pJET mCCL19, pJET mCCL21a, pJET mCXCL9, pJET mCXCL10, pJET mCXCL13, pJET mLT-α, pJET mTNF-α, and pJET mLIGHT (Table 2).

The cassette encoding murine LT-β preceded by a Kozak sequence and flanked by MluI restriction sites was designed by me and obtained by gene synthesis in a pEX-A128 vector (pEX-A128 mLT-β) (Table 2) from Eurofins Genomics. The cassette encoding the Fc region from hamster (*Cricetulus migratorius*) immunoglobulin G (IgG-Fc *C.m.*) preceded by a Kozak sequence and flanked by MluI and AscI restriction sites was designed, generated, and cloned into the pJET1.2/blunt vector by R. Veinalde, yielding pJET IgG-Fc *C.m.* (Table 2) [150].

To generate pcMeVac P-ATU plasmids encoding murine chemokines, cytotoxic molecules, or a control transgene, I excised the DNA cassettes from pJET IgG-Fc *C.m.*, from pEX mLT-β, and from the newly generated pJET1.2/blunt-derived vectors as MluI-AscI, MluI-MluI, MluI-PauI, or MluI-BtgI fragments by restriction digest, and inserted them into the pcMeVac P-ATU vector, previously linearized and dephosphorylated. For vector linearization, I performed restriction digest with MauBI, which results in ends compatible with those yielded by MluI, AscI, PauI, and BtgI. For vector dephosphorylation and subsequent ligation with the excised fragments, I employed the Rapid DNA Dephos & Ligation Kit according to the manufacturer's protocol, and used a vector to insert molar

ratio of 1:3. These ligations yielded the plasmids pcMeVac P-mCCL5, pcMeVac P-mCCL19, pcMeVac P-mCCL21a, pcMeVac P-mCXCL9, pcMeVac P-mCXCL10, pcMeVac P-mCXCL13, pcMeVac P-mLT-α, pcMeVac P-mTNF-α, pcMeVac P-mLIGHT, pcMeVac P-mLT-β, and pcMeVac P-IgG-Fc *C.m* (Table 2).

3.2.2.5 Plasmid DNA Preparation and Quality Control

To amplify plasmid DNA, I transformed 50 µL suspension of chemically competent *Escherichia coli* (NEB 10-β strain, a derivative of the DH10B strain) (NEB, Ref. C3019) with 2-5 µL plasmid DNA by incubation for 30 min on ice followed by heat shock for 45 sec at 42 ºC and 5 min on ice. Next, I cultured the transformed bacteria in 950 µL antibiotic-free SOC liquid medium (Table 9) for 1 h at 37 ºC and 650 rpm in a Thermomixer comfort shaker (Eppendorf) to allow expression of the antibiotic resistance genes encoded in the plasmid. Afterwards, I plated 100 µL of the bacteria suspension onto LB-Agar plates containing selection antibiotics (100 µg/mL ampicillin or 50 µg/mL kanamycin) and incubated the plates overnight at 37 ºC. On the next day, I picked single colonies from the plates with a toothpick, and briefly submerged the tip of the toothpick in 25 µL nuclease-free water to release part of the colony, which I then used as template for the One*Taq* PCR (see 3.2.2.2). This PCR was run to analyze whether the plasmids transformed into the selected colonies contained the correct inserts. In parallel, I transferred the toothpicks into tubes containing 4 mL LB liquid medium with antibiotics, and incubated the cultures with positive PCR results overnight at 37 ºC and 150 rpm in an Innova 44 shaker (New Brunswick Scientific). Next, I isolated plasmid DNA from the cultures using the QIAprep Spin Miniprep kit following the manufacturer's instructions and determined the DNA concentration in the eluted samples using a NanoDrop 1000 spectrophotometer (Thermo Fisher Scientific) as described above. As quality control, I analyzed transgene insertion and plasmid integrity by restriction enzyme digest with HindIII and verified the sequence of the inserted transgenes via Sanger sequencing, conducted by GATC Biotech.

3.2.3 Virology Methods (I): Virus Rescue, Propagation, and Purification

I always manipulated recombinant measles viruses in class II safety cabinets and only worked with vaccine strains of measles virus.

3.2.3.1 Rescue of Recombinant Measles Viruses

To rescue recombinant measles viruses, I followed the system developed by Martin *et al.* [115], which relies on transfection of virus-producer cells with four plasmids: one plasmid encoding the MeVac antigenome under the control of an RNA polymerase II promoter and three helper plasmids encoding the components of the MeVac ribonucleoprotein complex: N, P, L (Table 2). In detail, I seeded Vero cells in 6-well plates at $2x10^5$ cells per well in 2 mL DMEM + 10% FCS one day before transfection. On the next day, I prepared the transfection mix by adding 5 µg of plasmid encoding the MeVac antigenome of interest, 500 ng pcDIMER-N, 100 ng pcDIMER-P, 500 ng pcDIMER-L,

100 ng pcDI dsRed, and 3 µL/µg DNA FuGENE HD transfection reagent to 180 µL DMEM. The pcDI dsRed plasmid, which encodes a red fluorescent protein, was added to monitor transfection efficiency. After gentle mixing, I incubated the transfection mix (25 min, RT) to allow formation of the transfection complexes. Meanwhile, I replaced the medium of the Vero cells by 1.8 mL DMEM + 2% FCS + 50 µg/mL kanamycin. After complex formation, I added the transfection mixture evenly onto the Vero cell monolayer dropwise and incubated the cells (37 ºC, 5% CO_2) for one week with regular monitoring of red fluorescence (correlating with transfection efficiency) and syncytia formation (indicative of virus production). Three days after transfection, I replaced the medium with 2 mL DMEM + 10% FCS.

3.2.3.2 Propagation of Recombinant Measles Viruses

To propagate recombinant measles viruses, I infected Vero cells with the MeVac variant of interest and harvested cell-associated viral progeny. I refer to the progeny of each propagation round as virus passage (VP), starting at VP0 with the rescue [vii].

To propagate a VP0 to a VP1, I harvested the rescues (VP0) one week after Vero cell transfection by scraping the cell monolayer with a cell lifter in the 2 mL medium. Next, I transferred the 2 mL suspension plus 3 mL DMEM + 2% FCS + 50 µg/mL kanamycin onto a 10 cm plate seeded with $1x10^6$ Vero cells on the previous day (cells were seeded in 10 mL DMEM + 10% FCS, the medium was removed before adding the scraped rescue). After incubation (3h, 37 ºC, 5% CO_2) I added 5 mL DMEM + 2% FCS + 50 µg/mL kanamycin to the 10 cm plate and cultured the cells for a maximum of 96 h. Once syncytia were observed across the monolayer, I removed all but 1 mL medium from the plate and scraped the cell monolayer with a cell lifter. To lyse the cells and release cell-associated virus, I subjected the scraped cell suspension to a freeze-thaw cycle consisting of freezing for 10 min in liquid nitrogen followed by overnight storage at -80 ºC and subsequent thawing in a 37 ºC water bath. After thawing, I clarified the cell suspension by centrifugation (5000 xg, 5 min) to remove the cell debris, transferred the supernatant into a Nunc® CryoTube® vial, taking a 100 µL aliquot aside for virus titer determination (see 3.2.3.3), and stored both samples at -80 ºC until further use.

To propagate a VP1 to a VP2, I seeded Vero cells in 15 cm plates ($5x10^6$ cells per plate in 13 mL DMEM + 10% FCS) and infected them on the next day with freshly thawed VP1 at a multiplicity of infection (MOI) of 0.03 in 8 mL OptiMEM. After 24 h incubation (37 ºC, 5% CO_2), I added 8 mL DMEM + 10% FCS to the plates and incubated the cultures further. Once syncytia were observed across the cell monolayers (ca. 48 h after infection), I harvested the new virus passage by completely removing

[vii] Virus propagation was conducted by myself and other members of our group (see Contributions).

the culture medium and scraping the cells with a cell lifter. After a freeze-thaw cycle and clarification as described above, I distributed the supernatant (containing the VP2 virus) into 100 µL – 1 mL aliquots, which I stored at -80 ºC until further use. To propagate viruses into VP3 or higher passages, I followed the same procedure, using a VP(X) aliquot to generate a VP(X+1) batch. See 3.2.3.5 for virus batches purified by ultracentrifugation.

3.2.3.3 Titration of Recombinant Measles Viruses

To determine functional titers of MeVac variants, I conducted titration assays on Vero cells. To that aim, I performed 10-fold serial dilutions of the stock virus suspension (thawed in a 37 ºC water bath) in technical quadruplicates (for growth curve assays) or octuplicates (for virus passaging and purification) for a total of six to twelve steps. The dilutions were established in 96-well plates in a total volume of 100 µL DMEM + 10% FCS per well. Subsequently, I added $2x10^4$ Vero cells in 100 µL DMEM + 10% FCS to each well. Forty-eight hours after incubation (37 ºC, 5% CO_2), I counted the number of syncytia in each well by light microscopy until reaching the dilution step that yielded no syncytia. One syncytia represented one cell infectious unit (ciu). Wells with more than 15 syncytia were considered too numerous to count. MeVac titers in ciu per 100 µL were determined by calculating the arithmetic mean number of syncytia in the dilution step yielding 0 to 15 syncytia per replicate and multiplying the result by the dilution factor. Subsequent multiplication by 10 yielded the titer in ciu per mL (ciu/mL). Sometimes, two dilution steps fulfilled the criteria of 0 to 15 syncytia per replicate. In that case, titers were calculated for both dilution steps independently, and the arithmetic mean of both was considered the titer of the tested virus suspension.

3.2.3.4 UV-C Inactivation of Recombinant Measles Viruses

When indicated, I inactivated the viruses with UV-C light. To that aim, I diluted virus suspensions to $4.1x10^6$ ciu in 2 mL OptiMEM and irradiated them with 0.5 J/cm^2 UV-C light using a UV Stratalinker 2400 (Stratagene). I confirmed virus inactivation by titration assays in quadruplicates (see 3.2.3.3).

3.2.3.5 Purification of Recombinant Measles Viruses

When indicated, I purified the virus suspensions by ultracentrifugation in a two-phase iodixanol gradient. To that aim, I produced a VP3 or VP4 batch as described in 3.2.3.2 (15 cm plates, MOI 0.03, harvest of cell-associated virus ca. 48 h after infection). After harvesting, I froze the 20 – 30 mL virus suspension for 10 min in liquid nitrogen and stored it at -80 ºC until purification. On the day of purification, I sterilized the ultracentrifugation tubes, buckets, bucket lids, and O-rings by submerging them in 70 % (v/v) ethanol in water and allowing them to dry under UV light for 30 min. Next, I prepared the two-phase iodixanol gradient by adding 0.5 mL or 1 mL of 20% (v/v) iodixanol in TE buffer (0.005 M Tris, 0.001 M EDTA, pH 7.4 adjusted with HCl) or in D-PBS, respectively, into the ultracentrifugation tubes and underlayering this phase with an equal volume of 54% (v/v)

iodixanol in the same solvent using a 1 mL syringe and a 26 G x ½ ” needle. The 20% and 54% iodixanol solutions were prepared in advance in batches of 30 mL, sterilized by passing through a 0.22 µm pore size filter (Merck Millipore), and stored at 4 ºC until usage. After establishing the gradient, I thawed the unpurified virus suspension in a 37 ºC water bath and clarified it by centrifugation (4000 – 4300 x g, 5 min, 4 ºC) (Table 17). The supernatant (consisting of clarified virus suspension) was maintained and the pellet was discarded. Next, I carefully layered the clarified virus suspension onto the 20% iodixanol phase, distributing it evenly across all tubes. When required, the tubes were filled up to the maximum volume by adding TE buffer or D-PBS onto the virus suspension. Subsequently, I transferred the tubes into the buckets and subjected the virus suspension to ultracentrifugation using a SW 50.1 or a SW 41 rotor (112000 x g, 2 h, 8 ºC, slow acceleration, no break) (Table 17). The ultracentrifugation speed was adapted from literature [177]. After ultracentrifugation, I collected the white interphase containing the purified virus suspension and distributed it into 100 µL or 200 µL aliquots, which I stored at -80 ºC until further use.

The clarification and ultracentrifugation procedures differed between research institutes (Table 17). Experiments shown in Figures 9, 10, 27 and 34 were conducted with virus suspensions purified at Universität Witten/Herdecke (UWH, Witten). Experiments shown in Figures 13, 14, and 15 were conducted with virus suspensions purified at Deutsches Krebsforschungszentrum (DKFZ, Heidelberg) [viii].

Table 17. Purification of recombinant measles viruses. Procedural differences between virus purifications at Deutsches Krebsforschungszentrum (DKFZ, Heidelberg) and Universität Witten/Herdecke (UWH, Witten) are indicated.

	DKFZ (Heidelberg)	UWH (Witten)
Clarification		
Centrifuge	5910R (Eppendorf)	Mega Star 1.6R (VWR)
Centrifuge settings	4300 x g, 5 min, 4 ºC	4000 x g, 5 min, 4 ºC
Ultracentrifugation		
Tubes (max. volume)	5 mL	13.2 mL
Gradient solvent	TE buffer	D-PBS
Gradient volume	0.5 mL per phase	1 mL per phase
Rotor	SW 50.1 (Beckman Coulter)	SW 41 (Beckman Coulter)
Ultracentrifuge	Optima™ LE-80K (Beckman Coulter)	Optima™ L-90K (Beckman Coulter)

[viii] The MeVac$_{Edm}$ suspension employed in Figure 35 was purified via a different method, consisting of two ultracentrifugation steps, as described by C. E. Engeland [146]. Briefly, I subjected the clarified virus suspension to ultracentrifugation in a two-phase iodixanol gradient. Next, I collected the interphase and subjected it to a second ultracentrifugation round for virus pelleting. Afterwards, I resuspended the virus pellet in 300 µL TE buffer and stored it at -80 ºC until further use.

To assess the performance of the ultracentrifugation process in terms of virus concentration and purification, I collected samples for downstream analyses before ultracentrifugation (200 µL input fraction) and after ultracentrifugation (300 µL interphase fraction, 2 mL top fraction). The top fraction corresponds to the fraction located above the interphase after ultracentrifugation. The samples were stored at -80 ºC until analysis by titration assay (see 3.2.3.3), bicinchoninic acid (BCA) assay (see 3.2.3.6), sodium dodecyl sulfate polyacrylamide gel electrophoresis (SDS-PAGE) (see 3.2.3.7), and, in the case of MeVac variants encoding chemokines, ELISA (see 3.2.4.6).

3.2.3.6 Bicinchoninic Acid (BCA) Assay

To determine the protein concentration in the fractions obtained at several steps of the virus purification protocol, L. Küther and I conducted BCA assays. This is a cuprous-based colorimetric assay that consists of two consecutive reactions: (i) reduction of Cu^{2+} to Cu^{1+} by proteins in an alkaline medium, and (ii) formation of BCA-Cu^{1+} complexes of purple color [178]. As protein standard, we prepared solutions of bovine serum albumin (BSA) in D-PBS at 2000 µg/mL, 1000 µg/mL, 500 µg/mL, 250 µg/mL, 125 µg/mL, 25 µg/mL, and 0 µg/mL. For the assay, we added 25 µL standard or sample (thawed in a 37 ºC water bath) to individual wells of a flat-bottom 96-well plate in duplicates. Samples were added at serial dilutions (v/v) prepared in D-PBS (undiluted, 1:10, 1:50, 1:100, 1:200). Next, we prepared the BCA working reagent by mixing 200 µL BCA solution with 4 µL 4 % cupric sulfate (per sample) using the BCA Protein Assay kit as per manufacturer's protocol, added 204 µL of the working reagent to each well, and incubated the samples (37 ºC, 30 min). Finally, we allowed the samples to cool down at RT and measured the absorbance at 562 nm wavelength using an Infinite® 200 PRO plate reader (M Plex configuration, Tecan) and the i-control™ software (version 2.0, Tecan). The protein concentrations were determined from the standard curves.

3.2.3.7 Sodium Dodecyl Sulfate Polyacrylamide Gel Electrophoresis (SDS-PAGE)

To assess the purity of the samples obtained at different steps of the virus purification protocol, L. Küther and I conducted SDS-PAGE using PageRuler™ prestained protein ladder as protein size standard covering a range from 10 kDa to 180 kDa. We thawed the samples in a 37 ºC water bath and diluted them in D-PBS to $1x10^7$ ciu/mL (input, interphase) or $1x10^4$ ciu/mL (top). To denature and reduce the proteins in the sample, we mixed the diluted samples with 4X Laemmli sample buffer containing 10% 2-mercaptoethanol (15 µL sample + 5 µL buffer) and incubated the mixture at 95 ºC for 5 min. Subsequently, we loaded 20 µL of the sample mixture or 5 µL of the protein ladder on Mini-PROTEAN TGX™ Precast gels. After performing electrophoresis at 120 V for 45 min using 1X Rotiphorese® SDS-PAGE as running buffer, we washed the gels thrice with 100 mL Milli-Q® water for 5 min per wash with constant shaking. Next, we stained the gels with 20 mL Imperial™ protein stain (Coomassie Dye R-250) for 2 h with constant shaking. This was followed by 4 washings

in 100 mL Milli-Q® water for 30 min each and a final washing in 100 mL Milli-Q® water overnight, always with constant shaking. Protein bands were visible by naked eye. Gel images were acquired on the next day with a cell phone camera (blue images) or a Universal Hood II instrument (Bio-Rad) (black/white images).

3.2.4 Virology Methods (II): Virus Characterization

3.2.4.1 Infection of Cells Grown in Monolayers

The details for the *in vitro* infections (plate format, cell number, infection volumes, medium change or medium addition, analysis timepoints) are indicated in Table S1. Briefly, I seeded the cells in the indicated plate format in cell line-specific culture medium and incubated the cultures overnight (37 ºC, 5% CO_2). On the next day, I replaced the medium by the virus inoculum, diluted in OptiMEM or DMEM to the indicated MOI (mock controls were exposed to OptiMEM or DMEM only). After incubation (37 ºC, 5% CO_2) for the indicated period of time, I either replaced the virus/mock inoculum by fresh medium, or added fresh medium to the wells without removing the inoculum. At the indicated timepoints, I (i) monitored the infection via microscopy (see 3.2.4.4), (ii) conducted metabolic cell viability assays on the infection plate (see 3.2.4.5), (iii) harvested the cells for further experiments, or (iv) harvested the viruses (in supernatants, cell lysates, or both) for further experiments.

3.2.4.2 Infection of Murine Bone Marrow Cells

To infect murine bone marrow cells, I centrifuged the bone marrow suspensions isolated from each mouse (see 3.2.6.4) (300 x g, 5 min, RT) and resuspended the pellet (one pellet per mouse) in 5 mL ammonium-chloride-potassium (ACK) lysis buffer for erythrocyte lysis. After incubation (5 min, RT), I added 5 mL D-PBS + 2% FCS to the cell suspension, passed it through a 70 µm cell strainer (Table 13), centrifuged it (300 x g, 5 min, RT), and resuspended the pellet in 5 mL culture medium (RPMI + 10% FCS + 100 U/mL penicillin + 100 µg/mL streptomycin + 1 mM sodium pyruvate + 1% (v/v) non-essential amino acids + 250 µM 2-mercaptoethanol + 10 mM HEPES). Next, I transferred $2.8x10^6$ cells to 1.5 mL tubes (2 tubes per mouse), centrifuged the cell suspensions (300 x g, 5 min, RT), and resuspended the pellet in 600 µL DMEM (mock) or 600 µL MeVac eGFP diluted in DMEM to an MOI of 3. After incubation (37ºC, 5% CO_2, 4 h), I washed the cells thrice with 1 mL D-PBS by centrifugation (300 x g, 5 min, RT). After the last wash, I adjusted the concentration to $3.3x10^6$ cells/mL in culture medium and transferred $5x10^5$ cells (150 µL) to individual wells of a 96-well U-bottom plate (4 wells per condition, one for each analysis timepoint). The cells were incubated (37 ºC, 5% CO_2) until flow cytometry analysis of eGFP signal 4 h, 24 h, 48 h, and 72 h after infection. For flow cytometry analysis, I stained the cells with Zombie Violet and fixed them in 1% paraformaldehyde (PFA) diluted in D-PBS (see 3.2.7.2).

3.2.4.3 Infection of Patient-Derived Tumor Slice Cultures

To assess MeVac spread in human tumor slices, I established tumor slice cultures on transwell membrane inserts (see 3.2.8.3). Next, I added $4.6x10^6$ ciu MeVac eGFP in 800 µL OptiMEM (or OptiMEM only as mock control) dropwise onto the membrane. After incubation (30 min, 37 ºC, 5% CO_2), I removed the virus/mock inoculum and replaced the old culture medium (underlayering the membrane) by 2 mL fresh culture medium. At the indicated timepoints, I monitored eGFP signal via fluorescence microscopy (see 3.2.4.4).

3.2.4.4 Fluorescence Microscopy (*In Vitro*, *Ex Vivo*)

To monitor infection via microscopy, I exposed cell monolayer cultures or patient-derived tumor slice cultures to MeVac eGFP (see 3.2.4.1 and 3.2.4.3). At the indicated timepoints, I monitored cell death and syncytia formation via bright-field light microscopy (cell monolayer cultures only) and eGFP signal as surrogate for viral gene expression via fluorescence microscopy (all cultures) using a ZEISS AxioVert 200 inverted fluorescence microscope (ZEISS) or a Nikon Eclipse TS2-FL inverted fluorescence microscope (Nikon) and the NIS-Elements BR software (version 5.21.03, Nikon).

3.2.4.5 Growth Curve

To assess the replication kinetics of MeVac vectors, I infected Vero cells and murine tumor cells with purified viruses at an MOI of 3 (one-step growth curve) or 0.03 (multi-step growth curve, Vero cells only) in triplicate per harvesting timepoint (see 3.2.4.1 and Table S1). At the indicated timepoints after infection, I pooled supernatants and cell lysates from triplicates and subjected them to a freeze-thaw cycle (10 min in liquid nitrogen followed by storage at -80 ºC for at least one week and subsequent thawing at 37 ºC). Next, I determined the viral titers in the thawed samples by titration assay on Vero cells in quadruplicates (see 3.2.3.3). In Figure 10 B-E, samples from the same cell line and timepoint were titrated in parallel. In Figure 32 A,B, samples from all timepoints were titrated in parallel per cell line.

3.2.4.5 Cell Viability Assay (XTT)

To analyze the cytotoxic potential of MeVac vectors, I infected murine tumor cells with OptiMEM (mock) or purified viruses at an MOI of 3 in triplicate per timepoint of analysis (see 3.2.4.1 and Table S1). At the indicated timepoints, I conducted cell viability assays (XTT assays) using the Colorimetric Cell Viability kit III following the manufacturer's protocol. This is a metabolic assay that measures conversion of a colorless substrate (tetrazolium) into a soluble orange-red product (formazan) by mitochondrial enzymes. Briefly, I mixed the XTT reagent with the activator at a 200:1 ratio and added 50 µL of the mixture per well without removing the cell culture supernatant. Once an intense orange-red color was visible in the mock controls, I measured the absorbance (Abs) of

each sample at 450 nm (main wavelength) and 630 nm (reference wavelength) using a SPECTROstar® *Nano* absorbance microplate reader (BMG Labtech) and the MARS software (version 5.50, BMG Labtech) set to the "spiral average" method (multiple areas of a well were scanned in a spiral trajectory and the average Abs was computed). I calculated the percent viability in each well as follows, regarding the arithmetic mean of mock controls as corresponding to 100% cell viability:

$$\text{Viability (\%)} = \frac{\text{Abs}_{450\text{nm}} \text{ (well of interest)}}{\text{Abs}_{450\text{nm}}\text{(arithmetic mean of mock controls)}} \times 100$$

3.2.4.6 Enzyme-Linked Immunosorbent Assay (ELISA) for Chemokine Detection

To assess (i) whether the chemokines encoded in MeVac vectors are expressed at protein level, (ii) whether murine tumor cells secrete specific chemokines (encoded in the murine genome) upon exposure to unmodified MeVac, and (iii) whether the MeVac purification protocol reduces the chemokine concentration in the virus suspension (in the case of chemokine-encoding viruses), I conducted ELISA. Accordingly, as samples I employed (i) supernatants from Vero cell cultures harvested 72 h after inoculation with DMEM (mock) or with the indicated purified viruses (see 3.2.4.1 and Table S1), (ii) supernatants from MC38-hCD46$_{[pCAG\text{-}SMAR]}$ cells harvested 72 h after inoculation with DMEM (mock) or purified MeVac$_{Schw}$ (see 3.2.4.1 and Table S1), and (iii) input, top, and interphase fractions from virus purifications (see 3.2.3.5), adjusted to the same virus titer. I conducted the ELISAs using commercially available kits (Table 7), following the manufacturers' protocols. Absorbance at the wavelengths indicated by the manufacturers was measured using an Infinite® 200 PRO plate reader (M Plex configuration, Tecan) and the i-control™ software (version 2.0, Tecan). Chemokine concentrations were determined using Microsoft 365 Excel (Microsoft) based on standard curves, generated individually for each ELISA plate as indicated in the manufacturers' instructions. Statistical analysis and data plotting were conducted using the Prism software (version 10.0.2, GraphPad).

3.2.4.7 Chemotaxis Assay with MeVac-Encoded Chemokines

To assess the chemotactic properties of MeVac-encoded chemokines, I conducted transwell migration assays in 24-well plates with 5 µm pore size polycarbonate membrane inserts (Table 13) (classical chemotaxis assay) or in Incucyte® Clearview 96-well plates with Incucyte® Clearview inserts (Table 13) (Incucyte chemotaxis assay). As chemoattractant, I employed supernatants from Vero cell cultures harvested 72 h after inoculation with OptiMEM (mock) or with the indicated MeVac variants (see 3.2.4.1 and Table S1). One day before the chemotaxis assay, I prepared single-cell suspensions from freshly resected murine spleens (C57BL/6J mice, male or female, see 3.2.6.3) and cultured the splenocytes at 37 ºC in RPMI supplemented with 10 % FCS, 100 U/mL penicillin, 100 µg/mL streptomycin, 50 U/mL murine IL-2 (cultures established in 6-well

plates, $5x10^6$ cells/well, 2 mL medium/well). On the next day, I harvested the splenocytes and adjusted them to the required concentration in serum-free RPMI + 100 U/mL penicillin + 100 µg/mL streptomycin. In parallel, I thawed the Vero cell culture supernatants (stored at -20 ºC) and sterilized them by passing through 0.22 µm pore size filters.

For the classical chemotaxis assay, I added $1x10^6$ splenocytes in 100 µL RPMI + 1 % Pen/Strep to the upper chamber and allowed the cells to settle for 10 min at RT. Next, I added 600 µL of the filtered supernatants to the lower chambers. After incubation (3 h, 37 ºC, 5% CO_2), I collected 500 µL from the bottom chamber (containing the cells that migrated) and determined the number of CD3(+) cells in this suspension by flow cytometry, adding 50 µL CountBright™ absolute counting beads to each sample for absolute quantification (see 3.2.7.2).

For the Incucyte chemotaxis assay, I coated both sides of the transwell membrane with 50 µg/mL Matrigel by adding 20 µL and 150 µL Matrigel diluted in RPMI to the upper and lower chambers, respectively. After 30 min incubation at 37 ºC, I aspirated the Matrigel, added $5x10^3$ splenocytes in 60 µL RPMI to the upper chambers, and allowed the cells to settle for 1 h at 37 ºC. Next, I added 200 µL of the filtered supernatants to the lower chambers of a fresh plate, and carefully transferred the upper chambers onto the fresh lower chambers (containing the supernatants) avoiding bubble formation. Subsequently, I monitored the cells via live-cell imaging using an Incucyte® SX5 instrument (Sartorius). Phase channel images of the top chamber (one image per well) were acquired with the 10x objective at a 1 h interval for a total of 24 h. Data were analyzed with the Incucyte® chemotaxis analysis software module (Sartorius) and plotted using the Prism software (version 10.0.2, GraphPad).

3.2.4.8 Cytotoxicity Assay with MeVac-Encoded Cytotoxic Molecules

To analyze the cytotoxic potential of MeVac-encoded murine LT-α and TNF-α, I conducted a cytotoxic assay in which I monitored target cell death via live-cell imaging. To that aim, I seeded L929 cells (target cells) in a 96-well plate ($2x10^4$ cells/well in 100 µL cell line-specific culture medium per well). On the next day, I replaced 80 µL medium with 70 µL treatment and 10 µL Incucyte® Cytotox Green Dye (DNA binding dye, concentration in the well = 250 nM) to label dying cells with disrupted cell membrane integrity. The dye suspension was vortexed and passed through a 0.22 µm pore-size filter before addition to the wells. As treatment, I employed supernatants from Vero cell cultures harvested 48 h or 72 h after inoculation with OptiMEM (mock) or with the indicated MeVac variants (see 3.2.4.1 and Table S1). The supernatants, which had been stored at -20 ºC, were thawed at a 37 ºC water bath and passed through a 0.22 µm pore size filter before addition to the wells for removal of infectious virus. As positive control, I treated the cells with 70 µL Staurosporine (concentration in the well = 10 µg/mL). Wells containing medium + target cells + dye (no treatment),

medium + dye (no treatment, no target cells), medium + target cells (no treatment, no dye), or medium only were employed as technical controls (data not shown). Each condition was analyzed in technical triplicates. After treatment addition, I monitored the cells via live-cell imaging using an Incucyte® SX5 instrument (Sartorius) set to the green/red optical module. Phase channel images (two per well) and green channel images (two per well) were acquired with the 10x objective at a 1 h interval for a total of 100 h. Data were analyzed with the Incucyte® base analysis software (Sartorius) and plotted using the Prism software (version 10.0.2, GraphPad).

3.2.4.9 RNA Extraction, Reverse Transcription, Quantitative PCR (qPCR) for MeVac *N* mRNA

When indicated, I assessed the levels of MeVac *N* mRNA in murine tissues (tumor or TDLN, see 3.2.6.1 and 3.2.6.2)) or *ex vivo* cultures of murine bone marrow-derived macrophages (BMDMs) (see 3.2.7.1). First, I extracted total RNA from the samples using the RNeasy® Plus Mini Kit according to the manufacturer's instructions and determined the concentration and purity of the eluted RNA by measuring the absorbance at 230 nm, 260 nm, and 280 nm wavelengths using a NanoDrop 1000 or a NanoDrop One spectrophotometer (both from Thermo Fisher Scientific). Next, I reverse transcribed polyadenylated RNAs to cDNA using the Maxima H Minus First Strand cDNA Synthesis kit following the manufacturer's instructions and employing oligo $(dT)_{18}$ as primer. As template, I used 1 µg total RNA (tumor samples, Figure 21 B), 2 µg total RNA (tumor samples, Figure 17 B), 900 ng total RNA (TDLN samples, Figure 17 B), or 400 ng total RNA (BMDM samples, Figure 26). After reverse transcription, I degraded the RNA with 1 µL RNase H (37 ºC, 20 min).

Subsequently, I performed qPCR for MeVac *N* on a C1000 Touch™ thermal cycler (Bio-Rad) harboring the CFX96™ real-time PCR detection system (Bio-Rad). As nucleic acid dye, I employed SYBR Green. Each qPCR reaction consisted of 0.13 µL forward primer at 33 µM, 0.13 µL reverse primer at 33 µM, 10 µL 2X *Power* SYBR™ Green PCR Master Mix, 1 µL template (cDNA or standard), and 8.74 µL nuclease-free water. As primers, I used MeV N-241 and MeV N-331+ to amplify MeVac *N* cDNA or mL13A_Fw and mL13A_Rv to amplify *Rpl13a* cDNA (Table 1). The reaction started with an initial denaturation (10 min, 95 ºC) and was followed by 45 cycles, each comprising three steps: denaturation (15 s, 95 ºC), annealing + extension (60 s, 62 ºC both for MeVac *N* and *Rpl13a*), and fluorescence detection (5 s, 78 ºC). Minus reverse transcriptase and non-template controls were included. Melting curve analysis was conducted from 60 ºC to 95 ºC to identify specific amplification. Amplification and melt peak plots were generated using the CFX Manager software (version 3.1, Bio-Rad).

For absolute quantification, samples with a known MeVac *N* copy number ("standards") were run in parallel to cDNA samples. The standards were generated by 10-fold serial dilutions of pCG-N, a plasmid containing the MeVac N gene (1 ng = 1.47×10^8 MeVac *N* copies) (Table 2), starting at a

plasmid concentration corresponding to $1x10^8$ MeVac *N* copies/µL. For data analysis, I obtained the quantification cycle (Cq) values of each sample from the CFX Manager software (version 3.1, Bio-Rad) and defined the lower limit of detection (LLOD) of the assay as "the lowest standard MeVac *N* copy number yielding a Cq value below that of mock samples". Using only the standards with a MeVac *N* copy number above the assay's LLOD, I correlated the standard Cq values with the $\log_{10}$(MeVac *N* copy number) via linear regression. This procedure yielded the equation of the standard curve, which I subsequently employed for absolute quantification. The fact that the standards were dsDNA while the experimental samples (cDNA) were ssDNA was taken into consideration during data analysis (*i.e.*, the MeVac *N* copy number calculated from the standard curve was multiplied by two to obtain the result displayed in Figures 17 B, 21 B, and 26 A).

For relative quantification (Figure 26 B), I employed *Rpl13a* as housekeeping gene. In this case, I calculated the MeVac *N* fold-change expression for each sample in relation to the mean of virus-exposed wild-type cultures using the $2^{-\Delta\Delta Cq}$ method.

3.2.5 *In Vivo* Methods

3.2.5.1 Ethics Statement and Mouse Husbandry

I conducted the animal experiments and breeding at the Center for Preclinical Research of the German Cancer Research Center (DKFZ, Heidelberg) or at the Animal Laboratory of Witten/Herdecke University (UWH, Witten). All animal experimental procedures were performed in compliance with the German Animal Protection Law and institutional guidelines. All experiments and breeding protocols were approved by the Animal Protection Officer of DKFZ or UWH and by the regional council, this being the Regierungspräsidium Karlsruhe for experiments and breeding conducted at DKFZ (protocols G-58/17, G-17/19, and EP-Z181I02) or the Landesamt für Natur, Umwelt und Verbraucherschutz Nordrhein-Westfalen for experiments and breeding conducted at UWH (protocol 81-02.04.2021.A263). For husbandry or experiments, mice were housed in groups of five or less in individually ventilated cages (IVC) under specific pathogen-free (SPF) conditions (at DKFZ) or in filter top cages (at UWH). For breeding, mice were housed in couples in the same type of cages as experimental mice. All mice were exposed to 12 h light / 12 h dark cycles and had permanent access to enrichment, food, and drinking water. Cages were changed at least once per week and each mouse was observed at least once per day.

3.2.5.2 Genotyping of MY II Mice

Mice from the B6.FVB-Tg(CD46)2Gsv/J strain (also known as MY II strain) (Table 11) were purchased in 2019 and bred at DKFZ or UWH. Ear punches were obtained upon weaning and lysed overnight in 150 µL Ear Direct PCR lysis reagent containing 4.5 µL of 800 U/mL Proteinase K. Lysis was conducted at 55 ºC and 600 rpm in a Thermomixer comfort shaker (Eppendorf). Presence of the

transgene (*CD46*, encoding hCD46) was assessed by PCR following the guidelines from The Jackson Laboratory (protocol #24513), using the primers oIMR3657, oIMR3658, oIMR7338, and oIMR7339 (Table 1). As template, 2 µL ear punch lysates were used. *CD46*(+) mice are referred to as CD46tg.

3.2.5.3 Tumor Cell Injection (First Challenge, Re-challenge)

To inject murine tumor cells into mice, I detached the cells from the culture flasks with trypsin, washed them thrice in 50 mL D-PBS, and adjusted them to 1 x 10^6 cells/mL or 1x10^7 cells/mL in D-PBS. In the first tumor challenge, I injected 1x10^6 cells in 100 µL D-PBS subcutaneously (s.c.) into the right flank of the mice. For tumor re-challenge, I injected 1x10^5 cells (Figures 18 and 19) or 1x10^6 cells (Figures 13, 14, and 15) in 100 µL D-PBS s.c. into the left flank of survivor mice and, when indicated, age-matched naïve mice. I conducted all tumor cell injections under class II safety cabinets using 1 mL syringes and 26 G x ½ '' needles (Table 13).

3.2.5.4 Monitoring and Termination Criteria

Mice were monitored daily for overall health status and signs of illness. After tumor cell implantation, body weight was measured at least once per week (in experiments conducted from 2019 onwards). Tumor growth was monitored at least every two days by measuring the longest diameter (L) and the shortest diameter (S) of the tumor with a digital caliper and calculating the tumor volume as follows:

$$\text{Tumor volume (mm}^3\text{)} = \text{L (mm)} \times \text{S (mm)} \times \text{S (mm)} \times 0.5$$

Mice were sacrificed by cervical dislocation when one of the following criteria was met: (i) experimental endpoint, (ii) tumor volume > 1000 mm^3, (iii) tumor diameter > 15 mm, (iv) bleeding or largely open tumor ulceration, (v) body weight loss of > 20% within one week, or (vi) other signs of morbidity (*e.g.* hunched posture, sunken eyes, reduced activity, abnormal respiration, ungroomed fur).

3.2.5.5 Treatment

When indicated, I treated the mice with virus, anti-PD-1 antibody, or carrier fluid. I initiated treatment once the tumors reached an arithmetic mean volume of 70 – 100 mm^3 (refer to figure legends). Before the first treatment dose, I allocated each mouse to a specific treatment group to ensure similar arithmetic mean tumor volume and standard deviation across groups. In experiments with CD46tg mice, I also considered similar sex and age distribution during mouse stratification, although these criteria could not always be fulfilled. After stratification, I was blinded until the experiment ended. I conducted all treatments under class II safety cabinets using 1 mL syringes and 26 G x ½ '' needles (Table 13).

For virus treatment, I administered $1x10^6$ ciu of the indicated MeVac variants in 100 µL carrier fluid intratumorally (i.t.) per mouse and treatment dose. Mock treatment consisted of 100 µL carrier fluid only. Mice received four virus doses on consecutive days or two virus doses at a two or three day interval (refer to figure legends). For each treatment dose, a new virus vial was thawed at 37 ºC and diluted to $1x10^7$ ciu/mL in OptiMEM (non-purified viruses), TE buffer (viruses purified at DKFZ), or D-PBS (MV-NIS or viruses purified at UWH). Diluted viruses were kept on ice until injection.

For antibody treatment, I administered 100 µg anti-mouse PD-1 antibody (clone J43) in 200 µL D-PBS intraperitoneally (i.p.) per mouse and treatment dose. Mock treatment consisted of 200 µL D-PBS only. Antibody treatment started on the day of the third virus dose and was repeated every third day for a maximum of four doses.

For the study depicted in Figure 17, I administered one dose of carrier fluid (100 µL) or virus ($1x10^6$ ciu $MeVac_{Hbl\alpha CEA}$ αmPD-1 in 100 µL carrier fluid) i.t. to mice bearing s.c. MC38cea tumors. Additionally, C. E. Engeland and I administered 100 µg anti-mouse PD-1 antibody (clone J43) in 200 µL D-PBS i.p. or intravenously (i.v.) to tumor-free mice.

3.2.6 Organ Extraction, Processing, and Culture

3.2.6.1 Tumor

To analyze murine tumors, I sacrificed the mice, explanted the tumors, and processed them differently according to the downstream analysis. For gene expression studies, I stored a piece of tumor at -20 ºC in 2 mL RNA*later* until RNA extraction (see 3.2.4.9 and 3.2.7.4). For histology and immunohistochemistry (IHC), I transferred a piece of tumor to an embedding cassette and stored it at 4 ºC in 4% formaldehyde (for fixation) until further processing (see 3.2.7.5). For flow cytometry and *ex vivo* monolayer cell culture, I prepared tumor single cell suspensions by cutting the tumors into pieces, digesting them in 10 mL RPMI + 10 % FCS + 200 U/mL collagenase type I (30 min, 37 ºC water bath), and meshing them through 100 µm cell strainers into 10 mL D-PBS. For flow cytometry staining, refer to 3.2.7.2. For *ex vivo* monolayer cell culture, I transferred $1x10^6$ cells from the dissociated tumor into a T25 flask containing 5 mL DMEM + 10% FCS + 100 U/mL penicillin + 100 µg/mL streptomycin. When indicated, I added 7.5 µg/mL puromycin to the cultures. At the indicated timepoints (see Figures 33 and S25), I analyzed hCD46 expression on the cell surface by flow cytometry (see 3.2.7.2).

3.2.6.2 Tumor Draining Lymph Node (TDLN)

To analyze TDLNs, I sacrificed the mice and explanted the TDLNs. For gene expression studies, I stored the entire TDLN at -20ºC in 2 mL RNA*later* until RNA extraction (see 3.2.4.9). For flow cytometry I prepared single cell suspensions by cutting the TDLNs in half, digesting them in 5 mL RPMI + 10% FCS + 200 U/mL collagenase type I (30 min, 37 ºC water bath), and meshing them through 100 µm cell strainers into 10 mL D-PBS. For flow cytometry staining, see 3.2.7.2.

3.2.6.3 Spleen

To obtain splenocytes, I sacrificed the mice, explanted the spleens, and processed them into single-cell suspensions by meshing them through 100 µm cell strainers into 10 mL D-PBS. Next, I centrifuged the cell suspension (300 x g, 5 min) and resuspended the pellet in 1 mL ACK lysis buffer for erythrocyte lysis. After incubation (10 min, RT), I washed the cells by adding 9 mL D-PBS and centrifuging (300 x g, 5 min). I resuspended the pellet in 10 mL D-PBS and kept the cells on ice until further processing. When indicated, T cells were isolated from the single-cell suspensions using the PAN T cell isolation kit II (mouse) according to the manufacturer's instructions.

3.2.6.4 Bone Marrow

To obtain bone marrow, I sacrificed the mice, dissected the hind limbs from the spinal cord, and cut them through the knee joint. Next, I removed the muscle and connective tissue from the bones (femur and tibia) and cut the bone ends. Afterwards, I inserted a 26 G x ½ " needle attached to a 5 mL syringe containing 5 mL low glucose DMEM + 10% FCS + 100 U/mL penicillin + 100 µg/mL streptomycin into one end of the bone and flushed the bone marrow out into a 50 mL tube. The cell suspension was then processed for infection (see 3.2.4.2) or for differentiation into macrophages (see 3.2.7.1).

3.2.6.5 Peripheral Blood and Peritoneal Wash

Murine peripheral blood (up to 100 µL) was collected from the saphenous vein into capillary tubes by C. E. Engeland (Figure 17). After incubation (20 min, RT), the blood was centrifuged (15000 rpm, 10 min, Eppendorf Centrifuge 5424R) and the supernatant (serum) was stored at 4 ºC until ELISA (see 3.2.7.8). Blood was collected at the following timepoints: before i.p. treatment (baseline), 30 min after i.p. treatment, 5-10 min and 24 h after i.v. treatment, and 24 h or 48 h after i.t. treatment. Mice were sacrificed by cervical dislocation after the last blood collection.

Murine peritoneal wash was obtained by C. E. Engeland 40 min after i.p. treatment (Figure 17). To that aim, mice were sacrificed by cervical dislocation and 500 µL D-PBS were injected into the peritoneal cavity. The cavity was massaged gently and the fluid was collected with the same syringe and needle used for injection. Samples were stored at 4 ºC until further processing.

3.2.7 Immunology Methods

3.2.7.1 Generation of Murine Bone Marrow-Derived Macrophages (BMDMs)

Differentiation of murine bone marrow cells into macrophages was conducted by B. Bognár and L. Vieira Codeço Marques. The bone marrow suspension isolated from each mouse (see 3.2.6.4) was passed through a 70 µm cell strainer, centrifuged (300 x g, 5 min, RT), and resuspended in 20 mL low glucose DMEM + 10% FCS + 100 U/mL penicillin + 100 µg/mL streptomycin (BMDM medium). The suspension was distributed in 2 x 15 cm plates (10 mL per plate) containing 10 mL BMDM medium and 10 mL filtered (0.2 µm) L929 cell culture supernatant as source of macrophage colony-stimulating factor (M-CSF). The cultures (30 mL per plate) were incubated at 37 ºC and 5% CO_2. Two and four days after bone marrow isolation, partial medium change was conducted by replacing 15 mL old medium with 10 mL BMDM medium and 5 mL filtered L929 cell culture supernatant. Seven days after bone marrow isolation, the macrophages (M0, unpolarized) were detached by incubation with trypsin followed by gentle scraping, washed in D-PBS, and seeded in 12-well plates. On the next day, the BMDM cultures (adherent cultures) were inoculated with MeVac eGFP or carrier fluid (see 3.2.4.1 and Table S1).

3.2.7.2 Flow Cytometry

The flow cytometry experiments included in my doctoral thesis follow different staining procedures. The general protocol and main modifications of specific experiments are described below.

General Protocol: To analyze cell suspensions by flow cytometry, I adjusted them to $1x10^7$ cells/mL in D-PBS and transferred $1x10^6$ cells (100 µL) to wells of a 96-well V-bottom plate. Next, I incubated each sample (15 min, RT) with 1 µL Mouse BD Fc Block™ to block the murine Fc receptors. Afterwards, I washed the cells as follows: addition of 100 µL D-PBS to each well, centrifugation (800 x g, 2 min), and supernatant removal by decantation followed by gentle tapping on a paper towel. Subsequently, I resuspended the cell pellets in 100 µL D-PBS and added the antibodies at the dilutions indicated in Table 6. After incubation with the antibodies (30 min, 4 ºC, dark), I washed the cells as outlined above, resuspended the cell pellets in 200 µL D-PBS, and transferred the samples to flow cytometry tubes with a filter lid (at DKFZ) or to 96-well flat-bottom plates (at UWH). The samples were stored at 4 ºC in the dark until data acquisition.

Controls: I always included (i) unstained controls to set the voltages (at DKFZ) or gains (at UWH), (ii) single-stained controls to determine and mathematically remove the spillover of a fluorophore into other detectors, and (iii) isotype controls to distinguish non-specific binding from specific binding.

Viability Staining: To assess viability, I stained the cell suspensions with DAPI or Zombie Violet. DAPI staining was conducted after antibody staining. Briefly, the cells were washed and resuspended with 200 µL of 0.2 µg/mL DAPI in D-PBS. After incubation (5 min, 4 ºC, dark), the cells were washed again, resuspended in 200 µL D-PBS, and transferred to the acquisition tubes or plates. Zombie Violet staining was conducted before antibody addition. In short, the cells were centrifuged in the 96-well V-bottom plate and resuspended in 100 µL Zombie Violet diluted 1:2000 in D-PBS (Zombie Violet was previously reconstituted according to the instructions from the manufacturer). After incubation (15 min, RT, dark), the cells were washed and resuspended in 100 µL D-PBS containing 1 µL Fc block. From this step onwards, the procedure followed the general protocol.

Fixation: Cell suspensions from infected cultures or from murine organs were fixed before acquisition. To that aim, after all stainings, I washed the cells and resuspended them in 100 µL D-PBS containing 1% PFA. After incubation (10 min, RT, dark), I washed the cells again, resuspended them in 200 µL D-PBS, and transferred them to the acquisition tubes or plates.

Chemotaxis Assay Readout: For the chemotaxis assay, I did not adjust the cell concentration to $1x10^7$ cells/mL before staining. Instead, I collected 500 µL from the bottom chambers, centrifuged these suspensions, resuspended the cells in 100 µL D-PBS, and transferred them to the V-bottom 96-well plates. From this step onwards, the staining followed the general protocol. Before data acquisition, I added 50 µL CountBright™ absolute counting beads for absolute quantification.

Flow Cytometry Without Antibodies: In flow cytometry experiments assessing only eGFP expression and cell viability, I did not employ antibodies. Thus, I did not include Fc block or isotype controls.

External Loading Assay (Murine Tumor Cells): For the external loading assay, MC38-hCD46$_{[lenti]}$ cells were exposed to MeVac variants and/or SIINFEKL peptide for 1 h (Table S1). After removing the inoculum and detaching the cells with 0.05% trypsin-EDTA, the cells were stained following the general protocol [ix].

External Loading Assay (Murine DCs): For the external loading assay with murine DCs, J. Albert and I exposed DC2.4 cells to clarified cell lysates from MC38-hCD46$_{[lenti]}$ cells previously exposed to MeVac variants for 24 h or pulsed with SIINFEKL peptide for 21 h (see Table S1 for infection and cell lysate generation). DC2.4 cells pulsed with SIINFEKL peptide or exposed to culture medium served as positive and negative controls, respectively. After 1 h incubation with cell lysates, SIINFEKL peptide, or culture medium, the medium was removed and the cells were detached with trypsin-EDTA (Table S1). Subsequently, the cells were stained following the general protocol.

[ix] J. Albert conducted this experiment. I analyzed the data.

Competitive Binding Assay: See section 3.2.7.3

Data Acquisition and Analysis: At DKFZ, I acquired the data using a BD FACSCanto™, a BD LSR II, or a BD LSRFortessa™ flow cytometer (all from BD Biosciences) and the BD FACSDiva™ software (version 8.0.1, BD Biosciences). At UWH, I acquired the data using a CytoFLEX flow cytometer (Beckman Coulter) and the CytExpert software (version 2.3.0.84, Beckman Coulter). I analyzed and plotted the data (dot plots, histograms) using the FlowJo™ software (versions 10.5.0 to 10.9.0, BD Biosciences). When indicated, I conducted statistical analysis and plotted the data (bar plots) using the Prism software (versions 8.4.3 to 10.0.2, GraphPad).

3.2.7.3 Competitive Binding Assay

To assess the binding specificity of anti-mouse PD-1 scFv-Fc molecules encoded in MeVac viruses, I conducted a competitive binding assay using PD-1(+) murine splenocytes as target cells. In detail, I prepared a single-cell suspension from the spleen of a C57BL/6J mouse (see 3.2.6.3) and cultured $4x10^6$ splenocytes in 2 mL RPMI supplemented with 10% FCS, + 100 U/mL penicillin + 100 µg/mL streptomycin, 50 µM β-mercaptoethanol, 10 ng/mL PMA, and 500 ng/mL ionomycin per well of a non-treated 6-well plate for 72 h (37 ºC, 5% CO_2) to induce PD-1 expression. Next, I harvested the splenocytes and incubated them (30 min, 4 ºC) with 10 µL clarified lysate from Vero-αHis cells infected with $MeVac_{H\alpha CEA}$ αmPD-1 (provided by R. Veinalde) plus 10 µL of 5-fold dilutions of a commercial anti-mouse PD-1 antibody (clone J43, stock concentration of 1 mg/mL) as competitor. Incubation in the absence of competitor was also included. Incubation with lysates from Vero-αHis cells infected with $MeVac_{H\alpha CEA}$ IgG-Fc *C.m.* served as negative control. After incubation, the cells were stained for flow cytometry analysis following the general protocol (see 3.2.7.2).

To assess the binding specificity of anti-mouse PD-L1 scFv-Fc molecules encoded in MeVac viruses, I conducted a competitive binding assay using PD-L1(+) $MC38\text{-}hCD46_{[lenti]}$ as target cells. To that aim, I infected MC38-hCD46 cells with MeVac eGFP (MOI = 3) for induction of PD-L1 expression and harvested the cells 48 h afterwards by detachment with trypsin-EDTA. Next, I incubated the cells (30 min, 4 °C) with 10 µL clarified lysate from Vero-αHis cells infected with $MeVac_{H\alpha CEA}$ αmPD-L1 (provided by R. Veinalde) plus 10 µL of 5-fold dilutions of a commercial anti-human/mouse PD-L1 antibody (Atezolizumab, stock concentration of 3.2 ng/mL) as competitor. Incubation in the absence of competitor was also included. Incubation with lysates from Vero-αHis cells infected with $MeVac_{H\alpha CEA}$ IgG1-Fc served as negative control. After incubation, the cells were stained for flow cytometry analysis following the general protocol (section 3.2.7.2).

3.2.7.4 Immune Gene Expression Analysis (NanoString)

Tumor immune gene expression was analyzed using the NanoString nCounter system. To that aim, R. Veinalde, J. P. W. Heidbuechel, and I extracted total RNA from murine tumor fragments using the RNeasy® Plus Mini Kit (see 3.2.4.9) [x]. Next, we submitted the samples to the nCounter Core Facility of Heidelberg University Hospital (Heidelberg) for further processing. There, sample quality was assessed using a 2100 Bioanalyzer instrument (Agilent) and RNA concentration was quantified with the Qubit™ RNA assay kit. After quality control, 25 ng RNA per sample were hybridized with the nCounter Mouse Immunology Panel (which contains probes for 561 endogenous genes in addition to positive and negative controls) and loaded into SPRINT cartridges. Raw data (RNA counts for each target gene) were obtained using an nCounter SPRINT Profiler instrument (NanoString Technologies). Data analysis was conducted by myself using the nSolver 4.0 software (for data normalization and heatmap generation) or Bioconductor software packages (for data normalization and differential gene expression analysis).

Using the nSolver 4.0 software, I normalized the raw data to a pre-defined set of reference genes included in the nCounter Mouse Immunology Panel. To generate the heatmap depicted in Figure 8, I analyzed grouped data using the Basic Analysis package from the nSolver 4.0 software. Grouped data contains the geometric mean of expression levels for each target gene within each treatment group. The geometric mean is computed using normalized data. In detail, once the grouped data was computed, I clustered it using agglomerative clustering, a bottom-up form of hierarchical clustering. Next, I generated heatmaps depicting Z-scores. These scores indicate the number of standard deviations a specific value is away from the mean. The Z-score transformation was based on target genes. That is, the Z-score of a gene in a treatment group was calculated by comparing its expression level in that treatment group to its expression level across all treatment groups. Additional parameters comprised “Euclidean distance” as distance metric and “average” as linkage method. To generate the heatmaps depicted in Figures S13 and S20, I analyzed the normalized data using the Custom Analysis option from the Advanced Analysis package of the nSolver 4.0 software, employing the mock-treated group as reference. This package scaled the normalized data to give all genes equal variance and generated the heatmaps and dendograms via unsupervised clustering.

For a more detailed analysis, I employed the Bioconductor software packages EDASeq, RUVSeq, and DESeq2, which use the R statistical programming language. First, I normalized the NanoString nCounter raw data using the upper quartile normalization method with the function betweenLaneNormalization() from the EDASeq package [179]. Next, I subjected the resulting data to

[x] RNA extraction was conducted by R. Veinalde (Figure 8: MC38cea and B16-hCD46 tumors, Figure 21: FC1245-hCD46 tumors), J. P. W. Heidbuechel (Figure 8: B16-hCD20-hCD46 tumors), and myself (Figure 28: B16-hCD20-hCD46 tumors).

a second normalization round using the remove unwanted variation (RUV) method with the function RUVg() from the RUVSeq package [180], choosing k = 1. As negative controls for RUV normalization, I used the negative control probes included in the nCounter Mouse Immunology Panel. These probes target sequences defined by the External RNA Controls Consortium (ERCC) that are absent in murine tumor RNA. After normalization, I conducted differential gene expression analysis with the function DESeq() from the DESeq2 package [181]. This analysis considers that the data follows a negative binomial distribution. To generate the volcano plots, I used the function EnhancedVolcano() from the EnhancedVolcano package.

3.2.7.5 Histology and Immunohistochemistry (IHC)

Study depicted in Figure 22: Tumor samples fixed in 4% formaldehyde (see 3.2.6.1) were submitted to A. Stenzinger and J. Leichsenring at the Institute of Pathology (Heidelberg University Hospital, Heidelberg). There, paraffin sections of tumor tissue were prepared. Deparaffinization and staining were conducted with a Benchmark Ultra IHC Staining module. Samples stained with hematoxylin/eosin and with an anti-mouse CD3 antibody (clone 2GV6, Roche) were evaluated by a specialist pathologist according to the guidelines of Rakaee *et al.* [182].

Study depicted in Figure 29: Tumor samples fixed in 4% formaldehyde (see 3.2.6.1) were submitted to the group of T. Poth at the Center for Model System and Comparative Pathology (CMCP, Heidelberg). There, the tissues were processed using a Tissue-Tek VIP® 5 Jr. vacuum infiltration processor (Sakura Finetek Germany) and embedded in paraffin using a HistoCore Arcadia H instrument (Leica). Formalin-fixed paraffin-embedded (FFPE) sections of 2-3 µm were cut using an Epredia™ HM 340E electronic rotary microtome (Thermo Fisher Scientific). Hematoxylin and eosin staining were conducted automatically using a Leica ST5020-CV5030 stainer integrated workstation (Leica Biosystems). For IHC, antigens were retrieved by immersing the FFPE sections in heated Dako target retrieval solution (citrate buffer, pH = 6). Next, the sections were stained with rabbit anti-mouse CD3 antibody (clone SP7, 1:100 dilution) (Table 6) and subsequently with anti-rabbit IgG antibodies conjugated to nanopolymers of alkaline phosphatase (AP) (Polyview® Plus AP reagent, anti-rabbit) (Table 6). The FFPE sections were then incubated with the chromogenic substrate (Permanent AP-Red kit) for 25 min, after which the reaction was stopped with tap water. The stained tumor samples were evaluated by a veterinarian pathologist (T. Poth). Virtual microscopy was conducted by V. Eckel using an Aperio AT2 digital pathology slide scanner (Leica) at the Tissue Bank of the National Center for Tumor Diseases (NCT, Heidelberg) in accordance with the regulations of the tissue bank and the approval of the ethics committee of Heidelberg University (Heidelberg). Slides were visualized using the QuPath software (version 0.4.4, open source) [183].

3.2.7.6 Enzyme-Linked Immunosorbent Spot (ELISpot) Assay for Murine IFN-γ

To assess immune cell reactivity to specific stimuli, I conducted IFN-γ ELISpot. Experiment-specific details are indicated in Table S2. In short, I established co-cultures of effector and target cells (or cultures of effector cells with peptides, proteins, or viruses) and detected IFN-γ spots 40 h afterwards. The co-cultures were set in sterile MultiScreen$_{HTS}$ IP filter plates with a 0.45 µm pore size hydrophobic polyvinylidene difluoride (PVDF) membrane. In detail, one day before co-culture set-up, I activated the plate membrane with 50 µL/well 35% ethanol (2 min, RT) and washed the plates five times with 200 µL/well H_2O as detailed below. Next, I coated the plates with 150 µL/well anti-mouse IFN-γ capture antibody diluted according to the manufacturer's instructions. The coated plates were incubated overnight at 4ºC. Plate washing was conducted as follows throughout the experiment: (1) discarding the volume by decanting the plate, (2) drying the plate by gently tapping it onto a pile of paper towels with a sterile gauze pad on top, (3) adding 200 µL/well wash buffer (H_2O or D-PBS), (4) incubating (2 min, RT), and (5) repeating the first two steps. On the day of (co-)culture set-up, I washed the ELISpot plates five times with 200 µL/well D-PBS and blocked them with 200 µL/well ELISpot medium (RPMI + 10% FCS + 1% Pen/Strep) for at least 2 h at RT. Next, I removed the blocking solution and established (co-)cultures in a total volume of 200 µL/well (see Table S2 for effector to target cell ratios and stimuli concentrations). Technical validation of each experiment was conducted with controls not shown in the figures, consisting of medium only, effector cells only, and effector cells cultured with 10 µg/mL concanavalin A. Three, six, or twelve replicates were tested per condition. After (co-)culture incubation (40 h, 37 ºC, 5% CO_2), IFN-γ detection was conducted as follows, diluting the antibodies and enzymes according to the manufacturer's instructions. First, I washed the plates seven times (3 x 200 µL/well D-PBS, 1 x 200 µL/well H_2O, 3 x 200 µL/well D-PBS). Next, I added 100 µL/well biotinylated rat anti-mouse IFN-γ detection antibody and incubated (2 h, RT). Afterwards, I washed the plates five times with 200 µL/well D-PBS and added 100 µL/well enzyme (AKP or HRP, Table S2) conjugated to streptavidin (SA). After incubation (90 min, RT, dark), I washed the plates five times with 200 µL/well D-PBS and added 100 µL/well substrate (BCIP/NBT or TMB, Table S2). Following substrate incubation (5 min, RT, dark), I washed the plates four times with 200 µL/well H_2O to stop the reaction and dried them overnight at RT.

At DKFZ, I counted the spots using a CTL ELISpot reader (CTL Europe) and the ImmunoSpot® software (version 7.0.24.1, CTL Europe). Quality control was conducted using the same software to remove falsely counted spots corresponding to artifacts. At UWH, I counted the spots using a Bioreader® 7000-E ELISpot reader (Biosys Scientific Devices) and the EazyReader® software (Biosys Scientific Devices). I also used the EazyReader® software for quality control. In all ELISpot experiments, I considered saturated samples to be "too numerous to count" (TNTC). Following the

recommendation from M. Bucur (DKFZ, Heidelberg), I set TNTC samples to a spot count of 450. Statistical analysis and data plotting were conducted using the Prism software (versions 8.4.3 to 10.0.2, GraphPad).

3.2.7.7 Enzyme-Linked Immunosorbent Assay (ELISA) for Murine IFN-γ

In tumor re-challenge experiments, I assessed antitumor immune memory by re-stimulating splenocytes *ex vivo* with mitomycin-C-treated tumor cells plus murine IL-2 and subsequently determining IFN-γ concentrations in culture supernatants via ELISA. To that aim, I prepared single-cell suspensions from the spleen of each mouse included in the re-challenge experiment (re-challenged mice and age-matched naïve mice) (see 3.2.6.3), adjusting the concentration to $4x10^6$ cells/mL (Figure 15) or $1x10^7$ cells/mL (Figure 19) in RPMI + 10% FCS + 100 U/mL penicillin + 100 µg/mL streptomycin + 20 U/mL murine IL-2. In parallel, I harvested MC38 tumor cells (cultured *in vitro*) via detachment with trypsin, washed them twice with 50 mL D-PBS (300 x g, 5 min), and resuspended them in RPMI + 10% FCS + 100 U/mL penicillin + 100 µg/mL streptomycin + 20 µg/mL mitomycin-C, adjusting the concentration to $4x10^5$ cells/mL (Figure 15) or $3.4x10^5$ cells/mL (Figure 19). After incubation (2 h, 37 °C, 500 rpm) in a Thermomixer comfort shaker (Eppendorf), I washed the tumor cells twice with D-PBS (300 x g, 5 min) and resuspended them in RPMI + 10% FCS + 100 U/mL penicillin + 100 µg/mL streptomycin + 20 U/mL murine IL-2, again adjusting the concentration to $4x10^5$ cells/mL (Figure 15) or $3.4x10^5$ cells/mL (Figure 19). Subsequently, I established *ex vivo* co-cultures of splenocytes (effector cells) and mitomycin-C-treated MC38 cells (target cells) at effector to target cell ratios of 10:1 ($2x10^6$ effector cells, $2x10^5$ target cells) (Figure 15) or 30:1 ($5x10^6$ effector cells, $1.7x10^5$ target cells) (Figure 19) in a total volume of 1 mL per well of 24-well plates. After incubation (37 ºC, 5% CO_2) for 5 days (Figure 15) or 48 h (Figure 19), I collected the culture medium, centrifuged it to remove the cells (300 x g, 5 min), and stored the resulting supernatant at -80 ºC until analysis.

For analysis, I thawed the culture supernatants at 4 ºC and determined the concentration of murine IFN-γ in each sample via ELISA using the IFN-γ Mouse Uncoated ELISA Kit according to the instructions provided by the manufacturer. Absorbance at 450 nm (main wavelength) and 570 nm (reference wavelength) was measured using an Infinite® 200 PRO plate reader (M Plex configuration, Tecan) and the i-control™ software (version 2.0, Tecan). Murine IFN-γ concentrations were determined using Microsoft 365 Excel (Microsoft) based on standard curves generated as indicated by the manufacturer. Statistical analysis and data plotting were conducted using the Prism software (versions 8.4.3 to 10.0.2, GraphPad).

3.2.7.8 Enzyme-Linked Immunosorbent Assay (ELISA) for Anti-Mouse PD-1 antibody/scFv-Fc molecule

The ELISA to detect anti-mouse PD-1 antibody or virus-encoded anti-mouse PD-1 scFv-Fc molecules was conceptualized by C. E. Engeland and conducted by L. Küther. In detail, high binding 96-well plates (Table 13) were coated with 500 ng/well His-tagged recombinant mouse PD-1 (100 µL/well of 5 µg/mL protein) and incubated (overnight, 4 ºC). On the next day, the wells were washed twice with 200 µL/well D-PBS and blocked (2 h, RT) with 200 µL/well blocking buffer (D-PBS + 5% FCS + 0.05% Tween 20). After washing the wells thrice in 200 µL/well D-PBS, 100 µL/well samples or standards were added and incubated (2 h, RT). Two-fold serial dilutions of anti-mouse PD-1 antibody (clone J43) in D-PBS, covering a range from 40 µg/mL to 0.3 µg/mL, were employed as standards. Following four washes with 200 µL/well wash buffer (D-PBS + 0.05% Tween 20), 100 µL/well biotinylated goat anti-hamster IgG (H+L) secondary antibody diluted 1:20000 in blocking buffer were added and incubated (1 h, RT). After five washes with 200 µL/well wash buffer, 100 µL/well HRP-Streptavidin diluted 1:500 in blocking buffer were added and incubated (10 min, RT, dark). Subsequently, the plates were washed five times with 200 µL/well wash buffer and 100 µL/well TMB substrate were added. After incubating the substrate (ca. 10 min, RT, dark), 100 µL/well stop solution (2 N sulfuric acid, H_2SO_4) were added. Absorbance at 450 nm wavelength was determined immediately using an Infinite® 200 PRO plate reader (M Plex configuration, Tecan) and the i-control™ software (version 2.0, Tecan).

3.2.8 *Ex Vivo* Methods with Primary Human Tumor Samples

3.2.8.1 Ethics Statement

I obtained human colorectal tumor samples from colorectal cancer patients undergoing surgical tumor resection at HELIOS University Hospital Wuppertal (Wuppertal). The sample collection complied with the World Medical Association Declaration of Helsinki. The patients consented to research usage of tumor material not required for diagnostic purposes by giving written informed consent before surgery. The study (project number 118/2021) was approved by the Ethics Committee of Witten/Herdecke University (UWH, Witten). The experiments were conducted at the Institute of Virology of UWH (Witten).

3.2.8.2 Sample Collection

Surgical resection of colorectal tumors was conducted at the Clinic of General, Visceral, and Oncological Surgery of HELIOS University Hospital Wuppertal by the team of F. Gebauer and H. Zirngibl, particularly by J. Dörner. A tumor sample obtained during surgery [xi] was immediately processed at the Institute of Pathology of HELIOS University Hospital Wuppertal by the team of H. M. Kvasnicka.

From the tumor material not required for diagnosis, I received one to three tumor fragments of ca. 1 cm^3 volume, which I transported to the Institute of Virology of UWH on ice in 40 mL RPMI + 10% FCS + 100 U/mL penicillin + 100 µg/mL streptomycin + 250 ng/mL amphotericin B. The antibiotics and antimycotics were provided by adding 1% (v/v) of the 100X stock antibiotic antimycotic solution for cell culture (Table 12) to RPMI + 10% FCS. Subsequent sample processing was conducted at the Institute of Virology of UWH in class II safety cabinets.

3.2.8.3 Establishment of Air-Liquid Interface (ALI) Tumor Slice Cultures

For the establishment of patient-derived *ex vivo* tumor slice cultures, I embedded the tumor fragments in 10% agarose (prepared in 1X TBE buffer) inside a tissue slicing device engineered by M. Hock (Heidelberg). This device moves the embedded material upwards at 1 mm intervals and thus allows the cutting of tumor slices of 1 mm thickness with a scalpel. After generating tissue slices, I cut circular tissue sections of 1 mm diameter from the tissue slices using a 1 mm circular biopsy punch (Table 13). Subsequently, I transferred the resulting tumor slices (circles of 1 mm thickness and 1 mm diameter) onto the membrane (PET membrane, 0.4 µm pore size) of transwell inserts (Table 13) placed into individual wells of a 6-well plate. Each insert was underlayered with 2 mL culture medium (RPMI + 10% FCS + 100 U/mL penicillin + 100 µg/mL streptomycin + 250 ng/mL amphotericin B). When possible, I placed three circular tumor slices (generated from different tumor sections) onto the membrane of the same transwell insert to represent tumor heterogeneity. This culture method is referred to as air-liquid interface (ALI) system and supports optimal gas exchange in all tumor slice areas as well as nutrient diffusion [184]. To assess whether this culture system supports MeVac spread, I exposed the tumor slices to MeVac eGFP (see 3.2.4.3) and monitored eGFP signal by fluorescence microscopy at the indicated timepoints (see 3.2.4.4).

[xi] More precisely, the tumor sample corresponded to a sample obtained during a histopathological rapid incision examination in the course of surgery. In German, this type of sample is known as a *Schnellschnitt*.

3.2.9 Data Analysis

I conducted all statistical analyses using the Prism software (versions 8.4.3 to 10.0.2, GraphPad).

ELISA, ELISpot, RT-qPCR, and flow cytometry data were analyzed using two-tailed unpaired t test (when two groups were compared) or one-way analysis of variance (ANOVA) (when more than two groups were compared). One-way ANOVA analysis was accompanied by Dunett's, Šidák's, or Tukey's correction for multiple comparisons. Dunnett's correction was employed when each group was only compared to a reference group (*e.g.*, Figure 11). Šidák's correction was employed for analyses restricted to pairwise comparisons of interest (as indicated in the corresponding figure legends, *e.g.*, Figure 6). Tukey's correction was employed for analyses comprising all possible pairwise comparisons (*e.g.*, Figure 19). Details on the analyses are indicated in the figure legends. The figures depict p values (for data analyzed using two-tailed unpaired t test) or multiplicity-adjusted p values (adj. p) (for data analyzed using one-way ANOVA). The difference between two groups was considered statistically significant if the p value (for two-tailed unpaired t test) or the adj. p value (for one-way ANOVA) was lower than 0.05.

Survival curves were analyzed using the Mantel-Cox (log rank) test with Bonferroni's correction for multiple comparisons. The difference between two groups was considered statistically significant if the p value was lower than the Bonferroni's-corrected significance level (α). The non-corrected α value was 0.05. The Bonferroni's-corrected α values were 0.008 (for 6 comparisons), 0.005 (for 10 comparisons), or 0.003 (for 15 comparisons).

Data acquired with the Incucyte® SX5 instrument (Sartorius) were analyzed using the Incucyte® base analysis software (Sartorius) to calculate the mean values and standard deviations (see 3.2.4.7 and 3.2.4.8). Subsequently, statistical analyses were conducted using the Prism software (version 10.0.2, GraphPad) as indicated above.

Data acquired with the flow cytometers (BD Biosciences or Beckman Coulter) were analyzed using the FlowJo™ software (versions 10.5.0 to 10.9.0, BD Biosciences) (see 3.2.7.2). When indicated, statistical analyses were conducted using the Prism software (versions 8.4.3 to 10.0.2, GraphPad) as described above.

Data acquired with the nCounter SPRINT Profiler instrument (NanoString Technologies) were analyzed using (i) the Basic Analysis or the Advanced Analysis packages of the nSolver 4.0 software (NanoString Technologies) or (ii) the EDASeq [179], RUVSeq [180], and DESeq2 [181] open-source software packages available from the Bioconductor Project (https://www.bioconductor.org/), which use the R programming language. In section 3.2.7.4, I provide a detailed description of these analyses.

4 Results

4.1 T Cell Priming and Activation

4.1.1 Contextualization – Aim – Hypothesis – Model System

T cell priming and activation are essential steps in the development of T cell mediated antitumor immunity. Therefore, my first aim was to study these phenomena in the context of MeVac virotherapy. However, these processes require antigen presentation, which is often limited at the tumor site due to low expression of tumor-associated antigens (TAAs) or defects in the antigen processing and presentation machinery of tumor cells. In this scenario, OVs encoding TAAs are a promising strategy to increase antigen availability in the tumor bed.

I hypothesized that MeVac vectors encoding TAAs or TAA-derived epitopes (MeVac TAA) could be employed to prime and activate cognate T cells. To test this hypothesis, I chose chicken ovalbumin (OVA) as model antigen and worked with murine co-culture systems. First, I monitored the direct effect of MeVac TAA on murine DCs (DC2.4 cells) in terms of viral permissiveness and antigen presentation. Next, I analyzed whether OVA-specific naïve T cells (OT-I T cells) and OVA-specific cytotoxic T lymphocytes (OVA CTLs) are primed and activated, respectively, by virus-exposed DCs. Given that OVs preferentially replicate in tumor cells, I conducted similar studies with murine colon adenocarcinoma cells instead of DCs. In this case, I did not perform the T cell priming assay, since tumor cells of epithelial origin are not professional APCs. As viruses, I used MeVac encoding the full-length antigen (MeVac OVA) or additional vectors designed to improve antigen presentation. These vectors encoded the OVA immunodominant epitope SIINFEKL (MeVac SIINFEKL), a secreted SIINFEKL variant (MeVac Igκ SIINFEKL), or epitope strings consisting of one, two, or six SIINFEKL copies targeted to the proteasome (MeVac Ub-AAY-[SIINFEKL-AAY]$_{1/2/6}$) (Table 8) [xii].

In my PhD thesis, I do not compare the MeVac variants in detail, since this has been described by K. D. Kubon [155] and will be discussed in the Medical Degree (M. D.) thesis of J. K. M. Mayer (unpublished). My focus is the usage of MeVac TAA variants as oncolytic vaccines.

4.1.2 T Cell Priming and Activation with Murine DCs Exposed to MeVac Variants

4.1.2.1 Permissiveness of DC2.4 Cells to MeVac

To determine whether murine DCs support MeVac gene expression, J. Albert and I inoculated DC2.4 cells with MeVac encoding eGFP (MeVac eGFP) and monitored eGFP fluorescence over time. Using fluorescence microscopy, we detected eGFP signal in very few DC2.4 cells distributed across the

[xii] J. Albert, E. Busch, K. D. Kubon, and J. K. M. Mayer generated and propagated the MeVac vectors that I employed in this section of the thesis.

monolayer 24 h and 48 h after virus inoculation, whereas no eGFP signal was present in mock controls (Figure S1 A). Consistent with these observations, flow cytometry analysis revealed eGFP signal in only 1 % of the DC2.4 population 24 h after virus inoculation (Figure S1 B). Therefore, I conclude that DC2.4 cells show limited permissiveness to MeVac.

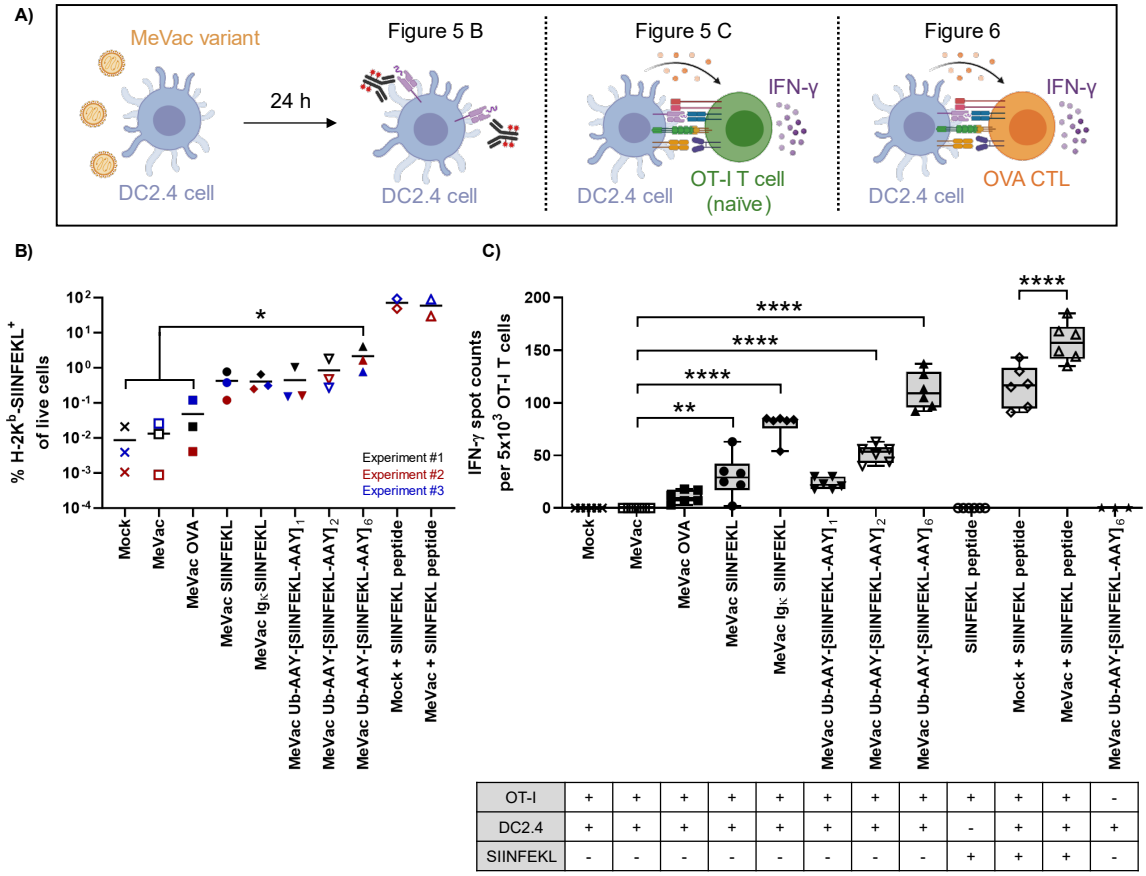

OT-I	+	+	+	+	+	+	+	+	+	+	+	-
DC2.4	+	+	+	+	+	+	+	+	-	+	+	+
SIINFEKL	-	-	-	-	-	-	-	-	+	+	+	-

Figure 5. Antigen presentation on DC2.4 cells and OT-I T cell priming. (A) Experiment schematic (created with BioRender.com). DC2.4 cells were inoculated with the indicated MeVac variants (MOI = 3) or medium (mock). Mock/MeVac + SIINFEKL conditions were pulsed with 10 µg/mL SIINFEKL peptide 1 h before cell harvest. 24 h after inoculation, the cells were harvested for downstream analyses. **(B)** For flow cytometry analysis, the DCs were stained with a PE-labelled antibody against SIINFEKL bound to H-2K^b. The percentage of H-2K^b-SIINFEKL+ (PE+) cells within live cells is shown for three independent experiments, with horizontal lines indicating mean values. Data were analyzed using one-way ANOVA with Tukey's correction for multiple comparisons. Technical controls (peptide-pulsed conditions) were excluded from the statistical analysis. **(C)** Naïve T cells from OT-I mice were co-cultured with the harvested DCs at a 10:1 DC to T cell ratio. After 40 h of co-culture, IFN-γ ELISpot was conducted. Biological controls (T cells + 10 µg/mL SIINFEKL [no DCs]; DCs only [exposed to a MeVac variant]) are shown. Technical controls (T cells [no stimulus]; T cells + 10 µg/mL ConA) are not shown. IFN-γ spot counts of six technical replicates per condition are depicted. Boxes indicate the 25th, 50th, and 75th percentiles. Whiskers depict minimum and maximum values. Data were analyzed using one-way ANOVA with Šidák's correction for multiple comparisons. Only pairwise comparisons of interest were analyzed, those being all conditions to mock, all peptide-pulsed conditions amongst themselves, and all virus-treated conditions amongst themselves. MeVac + SIINFEKL peptide was considered a peptide-pulsed condition. A selection of statistically significant differences that are referred to in the text is depicted. One representative of three independent experiments is shown. **(B-C)** *adj. $p < 0.05$; ***adj. $p < 0.001$; ****adj. $p < 0.0001$. adj. p: multiplicity-adjusted p value.

4.1.2.2 Presentation of Virus-Encoded SIINFEKL

To determine whether the MeVac vectors encoding OVA or epitope variants mediate SIINFEKL presentation on DCs, I exposed DC2.4 cells to the virus variants and analyzed SIINFEKL presentation on H-2K^b molecules 24 h afterwards by flow cytometry (Figure 5 A, Figure S1 D). Consistent with the limited permissiveness to MeVac, I detected low percentages of DC2.4 cells staining positive for H-2K^b-SIINFEKL upon exposure to any of the MeVac variants (Figure 5 B). MeVac encoding six epitope copies targeted to the proteasome led to the highest percentage of H-2K^b-SIINFEKL(+) cells (mean of 2%) and to the strongest signal intensity within the positive population. This indicates that, compared to the other variants, MeVac Ub-AAY-[SIINFEKL-AAY]$_6$ (i) mediates antigen presentation on more cells (higher percentage of positive events) (Figure 5 B) and (ii) increases the amount of antigen presented on the cell (higher signal intensity in a positive event) (Figure S1 C). Importantly, SIINFEKL presentation was abolished in DC2.4 cells exposed to UV-C-inactivated MeVac variants (*i.e.*, to non-replicating MeVac variants) and was not mediated by external peptide loading (Figure S2, Figure S3). Together, these data argue for presentation of virus-encoded SIINFEKL produced *de novo* during MeVac replication in DCs.

4.1.2.3 Priming of Naïve OT-I T Cells

To study the effect of MeVac encoding full-length antigens or epitope variants on T cell priming, I co-cultured naïve OT-I T cells with DC2.4 cells previously inoculated with the virus variants, and determined IFN-γ release by ELISpot 40 h afterwards (Figure 5 A). Remarkably, I detected significantly higher IFN-γ spot counts in most (four of five) conditions with DC2.4 cells exposed to MeVac vectors encoding SIINFEKL variants compared to inoculation with unmodified MeVac (Figure 5 C). In agreement with the higher levels of SIINFEKL presentation (Figure 5 B), DC2.4 cells inoculated with MeVac Ub-AAY-[SIINFEKL-AAY]$_6$ mediated the strongest priming of naïve OT-I T cells (Figure 5 C). Conversely, and consistent with the very low levels of SIINFEKL presentation detected by flow cytometry (Figure 5 B), DC2.4 cells exposed to MeVac encoding the full-length antigen (MeVac OVA) did not prime naïve OT-I T cells (Figure 5 C). Regarding peptide pulsing, I observed that co-cultures with DC2.4 cells pulsed with SIINFEKL peptide led to higher IFN-γ spot counts (*i.e.,* enhanced OT-I T cell priming) if DC2.4 cells were previously exposed to unmodified MeVac compared to mock exposure (Figure 5 C).

Overall, with these results I prove the concept of using MeVac vectors encoding TAA-derived epitopes for cognate T cell priming. Specifically, I conclude that DC2.4 cells exposed to MeVac vectors encoding SIINFEKL variants prime naïve OT-I T cells, and I show that DC exposure to MeVac encoding six epitope copies targeted to the proteasome is the most efficient strategy in terms of T cell priming among all tested approaches. Moreover, I report that the T cell priming capacity of

DC2.4 cells is enhanced by exposure to MeVac. Possible underlying mechanisms could include DC maturation triggered by virus sensing (see Discussion).

4.1.2.4 Activation of OVA-Specific Cytotoxic T Lymphocytes

Following the cancer-immunity cycle, primed CD8(+) T cells differentiate into antigen-experienced CTLs or memory T cells. CTLs migrate to the periphery and recognize target cells presenting cognate antigen. This recognition triggers CTL activation and cytotoxic effector functions comprising several mechanisms, one of which is IFN-γ release [19].

To study the role of the above-mentioned MeVac variants on CTL activation by DC2.4 cells, I co-cultured antigen-experienced OVA CTLs with DC2.4 cells exposed to active or UV-C-inactivated MeVac variants and conducted IFN-γ ELISpot 40 h afterwards (Figure 5 A, Figure 6). Compared to inoculation with unmodified MeVac, co-cultures of OVA CTLs with DC2.4 cells previously exposed to MeVac vectors encoding SIINFEKL variants led to significantly higher IFN-γ spot counts in four of five co-culture conditions, with DC2.4 cells exposed to MeVac Igκ SIINFEKL or MeVac Ub-AAY-[SIINFEKL-AAY]$_6$ mediating the strongest IFN-γ release. Remarkably, T cell activation was abolished in co-cultures with DC2.4 cells previously exposed to UV-C-inactivated MeVac variants. These data are in line with the flow cytometry analysis showing negligible levels of SIINFEKL presentation on DC2.4 cells exposed to UV-C-inactivated MeVac variants (Figure S2).

In summary, I show that DC2.4 cells exposed to most MeVac vectors encoding SIINFEKL variants activate antigen-experienced OVA CTLs. The lack of IFN-γ release in conditions employing UV-C-inactivated viruses suggests that, in this setting, viral replication in DCs is required for T cell activation.

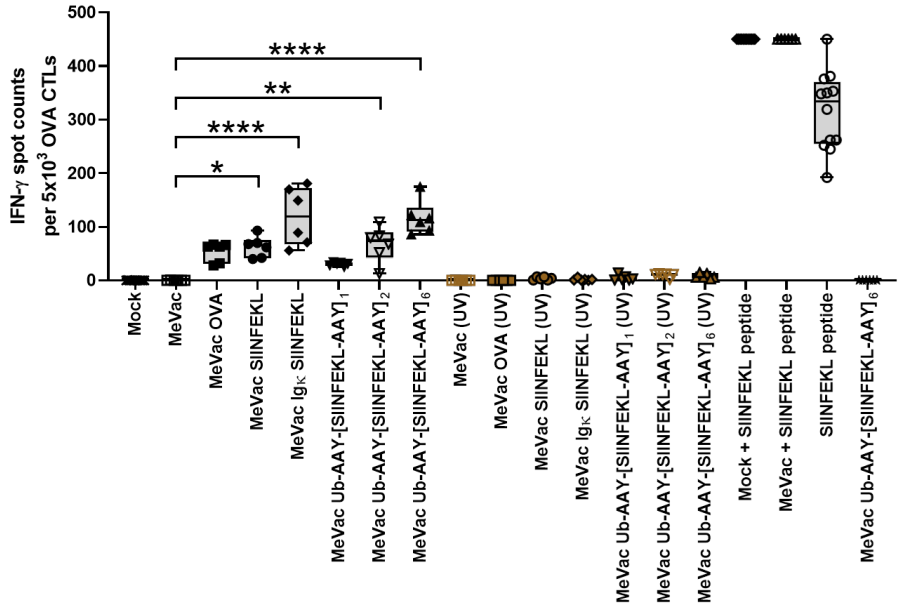

OVA-CTL	+	+	+	+	+	+	+	+	+	+	+	+	+	+	+	+	+	+	-
DC2.4	+	+	+	+	+	+	+	+	+	+	+	+	+	+	+	+	+	-	+
SIINFEKL	-	-	-	-	-	-	-	-	-	-	-	-	-	-	-	+	+	+	-

Figure 6. OVA CTL activation with DC2.4 cells exposed to MeVac encoding SIINFEKL variants. DC2.4 cells were inoculated with the indicated MeVac variants (MOI = 3) or medium (mock). Where indicated with "(UV)", viruses were inactivated by UV-C irradiation before inoculation. Mock/MeVac + SIINFEKL conditions were pulsed with 10 µg/mL SIINFEKL peptide 1 h before cell harvest. 24 h after inoculation, DCs were harvested and co-cultured with SIINFEKL-specific CTLs (OVA CTLs) at a 10:1 DC to T cell ratio. After 40 h of co-culture, IFN-γ ELISpot was conducted. The controls were equivalent to those described in Figure 5, but using OVA CTLs instead of naïve OT-I T cells. IFN-γ spot counts of six technical replicates per condition are depicted. Boxes indicate the 25th, 50th, and 75th percentiles. Whiskers depict minimum and maximum values. Data were analyzed using one-way ANOVA with Šidák's correction for multiple comparisons. Only pairwise comparisons of interest were analyzed, those being all conditions to mock, all peptide-pulsed conditions amongst themselves, all conditions with active MeVac variants amongst themselves, all conditions with UV-C- inactivated MeVac variants amongst themselves, and each condition with an active MeVac variant to the corresponding condition with the UV-C-inactivated MeVac counterpart. MeVac + SIINFEKL peptide was considered a peptide-pulsed condition. A selection of statistically significant differences that are referred to in the text is depicted. One representative of three independent experiments is shown. The other two experiments (not shown) did not include UV-C-inactivated viruses. **adj. $p < 0.01$; ****adj. $p < 0.0001$; adj. p: multiplicity-adjusted p value.

4.1.3 T Cell Activation with Murine Tumor Cells Exposed to MeVac Variants

4.1.3.1 Permissiveness of MC38-hCD46 Cells to MeVac

Next, I assessed whether MeVac TAA enhances CTL activation by promoting presentation of the encoded TAA-derived epitopes on tumor cells. To that end, I used OVA as model antigen and murine colon adenocarcinoma cells expressing the MeVac entry receptor human CD46 (MC38-hCD46 cells).

As for DC2.4 cells, I started by analyzing the permissiveness of MC38-hCD46 cells to MeVac together with J. Albert. Twenty-four hours after infection of tumor cells with MeVac eGFP, we measured eGFP signal in around 60 % of the cell population by flow cytometry, and observed a few eGFP(+)

cells distributed across the cell monolayer by fluorescence microscopy (Figure S4 A,B). The number of cells expressing eGFP increased 48 h after infection, suggesting that MC38-hCD46 cells support MeVac replication (Figure S4 A). At both timepoints, the number of eGFP(+) tumor cells was higher than the number of eGFP(+) DC2.4 cells (compare Figure S1 A,B to Figure S4 A,B). Thus, I conclude that MC38-hCD46 cells are more permissive to MeVac than murine DC2.4 cells.

4.1.3.2 Presentation of Virus-Encoded SIINFEKL

To assess presentation of virus-encoded SIINFEKL, I infected MC38-hCD46 cells with the MeVac variants and determined SIINFEKL presentation on H-2K^b molecules 24 h afterwards by flow cytometry (Figure 7 A, Figure S4 D). Compared to MeVac OVA, which led to epitope presentation on a very low percentage of tumor cells (mean of 0.26%), MeVac vectors encoding SIINFEKL variants mediated epitope presentation on a significantly higher percentage of tumor cells (mean of 5% to 41%) (Figure 7 B). Infection with MeVac Ub-AAY-[SIINFEKL-AAY]$_6$ mediated epitope presentation on the highest percentage of tumor cells. Moreover, compared to the other viruses, it increased the median abundance of H-2K^b-SIINFEKL complexes within H-2K^b-SIINFEKL(+) cells, as shown by the significant increase in the PE median fluorescence intensity within PE(+) cells (Figure S4 C). As observed with DC2.4 cells, epitope presentation was negligible in tumor cells exposed to UV-C-inactivated viruses, and was not mediated by external peptide loading (Figure S5, Figure S6). These findings suggest that H-2K^b molecules are loaded with SIINFEKL that was produced *de novo* during MeVac replication in tumor cells.

4.1.3.3 Activation of OVA-Specific Cytotoxic T Lymphocytes

To determine whether the levels of SIINFEKL presentation on MC38-hCD46 cells infected with the MeVac variants are sufficient to activate OVA CTLs, I repeated the experiment shown in Figure 6 with tumor cells instead of DCs (Figure 7 A,C). Overall, I detected significantly higher IFN-γ spot counts in co-cultures of OVA CTLs with MC38-hCD46 cells exposed to any of the engineered MeVac vectors compared to unmodified MeVac (Figure 7 C). This is in contrast with the ELISpot data from co-cultures of CTLs with vector-exposed DCs, where the effect of MeVac OVA or MeVac Ub-AAY-[SIINFEKL-AAY]$_1$ in terms of T cell activation was not significantly different to that of unmodified MeVac (Figure 6). Differences between both experiments might be explained by the better permissiveness of tumor cells to MeVac (compare Figure S1 A,B to Figure S4 A,B), which leads to transgene expression and SIINFEKL presentation on a larger percentage of cells (compare Figure 5 B to Figure 7 B). Importantly, OVA CTLs activation by vector-exposed tumor cells was significantly reduced in co-cultures with tumor cells exposed to UV-C-inactivated viruses compared to the active virus variant, suggesting that viral replication in tumor cells was required for T cell activation (Figure 7 C).

Overall, with these experiments I prove the concept of using MeVac vectors encoding TAAs or TAA-derived epitopes for activation of antigen-experienced cognate CTLs. Moreover, I show that CTL activation is not only triggered by virus-exposed DCs, but also by virus-exposed tumor cells.

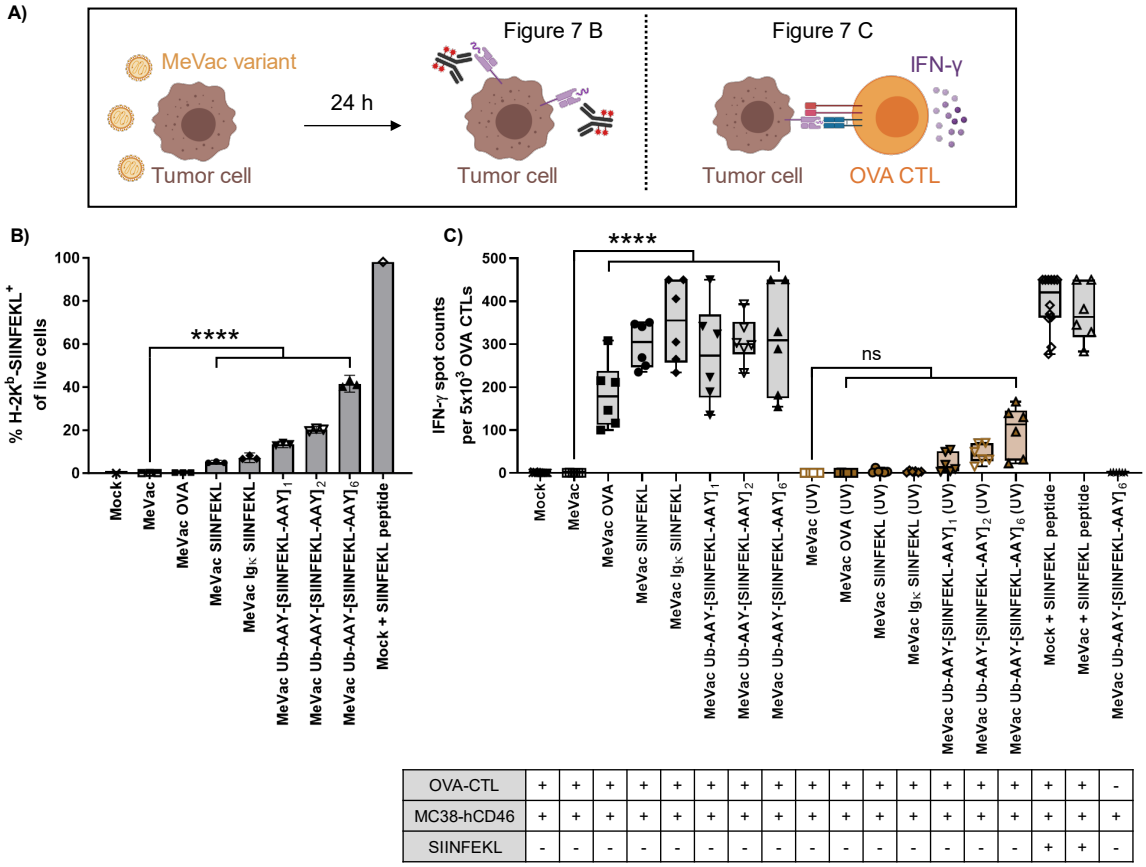

OVA-CTL	+	+	+	+	+	+	+	+	+	+	+	+	+	+	+	+	+	-
MC38-hCD46	+	+	+	+	+	+	+	+	+	+	+	+	+	+	+	+	+	+
SIINFEKL	-	-	-	-	-	-	-	-	-	-	-	-	-	-	-	+	+	-

Figure 7. Antigen presentation on MC38-hCD46 cells and OVA CTL activation. (A) Experiment schematic (created with BioRender.com). MC38-hCD46$_{[lenti]}$ cells were inoculated with the indicated MeVac variants (MOI = 3) or medium (mock). Where indicated with "(UV)", viruses were inactivated by UV-C irradiation before inoculation. Mock/MeVac + SIINFEKL conditions were pulsed with 2.5 µg/mL SIINFEKL peptide 1 h before cell harvest. 24 h after inoculation, the cells were harvested for downstream analyses. **(B)** For flow cytometry analysis, the cells were stained with a PE-labelled antibody against SIINFEKL bound to H-2K^b. The percentage of H-2K^b-SIINFEKL+ (PE+) cells within live cells is shown for one representative of three independent experiments conducted by J. Albert. Bars indicate mean values of technical triplicates and error bars show 95% confidence intervals. Data were analyzed using one-way ANOVA with Tukey's correction for multiple comparisons. Conditions with a single replicate (Mock, Mock + SIINFEKL peptide) were excluded from the statistical analysis. A selection of statistically significant differences that are referred to in the text is depicted. **(C)** SIINFEKL-specific CTLs (OVA CTLs) were co-cultured with the harvested MC38-hCD46$_{[lenti]}$ cells at a 10:1 tumor cell to T cell ratio. After 40 h of co-culture, IFN-γ ELISpot was conducted. The controls were equivalent to those described in Figure 5 but using OVA CTLs instead of naïve OT-I T cells and MC38-hCD46$_{[lenti]}$ cells instead of DC2.4 cells. IFN-γ spot counts of six technical replicates per condition are depicted. Boxes indicate the 25th, 50th, and 75th percentiles. Whiskers depict minimum and maximum values. Data were analyzed using one-way ANOVA with Šidák's correction for multiple comparisons. Only pairwise comparisons of interest were analyzed, as indicated in Figure 6. A selection of statistically significant differences that are referred to in the text is depicted. **(B-C)** **adj. p < 0.01; ****adj. p < 0.0001; adj. p: multiplicity-adjusted p value; ns: not significant.

4.2. T Cell Recruitment and Antitumor Cytotoxicity

4.2.1 Contextualization – Aim – Hypothesis – Model System

Following the cancer-immunity cycle, my next aim was to investigate how MeVac therapy promotes T cell recruitment into the tumor as well as antitumor cytotoxicity, and to elucidate whether the molecular mechanisms underlying these processes in the context of MeVac therapy are determinants of therapeutic efficacy. To address these questions, I identified several molecules as candidate drivers of the above-mentioned steps and assessed their contribution to MeVac therapeutic efficacy *in vivo* by gain of function (GOF) studies.

4.2.2 Candidate Identification

To identify molecular mechanisms driving intratumoral T cell recruitment and cytotoxic responses during MeVac therapy, I analyzed the expression of genes encoding T cell attractants or cytotoxic molecules using three gene expression datasets available in our research group (Figure 8). The three datasets comprised gene expression data from murine tumors treated with carrier fluid (mock), MeVac encoding a non-relevant transgene (control virus), or MeVac encoding an immunomodulator. However, these studies differed in the tumor model, the MeVac strain, and the transgenes encoded in the viral vectors. The therapeutic efficacy of the viruses had been previously assessed by P. Backhaus, R. Veinalde, T. Speck, and J. P. W. Heidbuechel, and was shown to be higher for MeVac encoding the immunomodulator than for the control virus [142,144].

The gene expression analysis that I conducted revealed upregulation of genes encoding the T cell attractants CCL5, CCL19, CXCL9, CXCL10, and CXCL13 as well as the cytotoxic molecules LT-α, LT-β, TNF-α, and LIGHT in murine tumors treated with control viruses compared to mock treatment, indicating that MeVac *per se* remodels the tumor microenvironment (TME) (Figure 8 B). Moreover, these genes were further upregulated in tumors treated with the more efficacious MeVac variant compared to control virus. Notably, the upregulation pattern of most of these genes was consistent between the three datasets. Thus, I conclude that upregulation of genes encoding chemokines and cytotoxic molecules is a general immunological effect of oncolytic MeVac therapy mediated by various MeVac strains, taking place across different tumor entities, and enhanced by different immunomodulators.

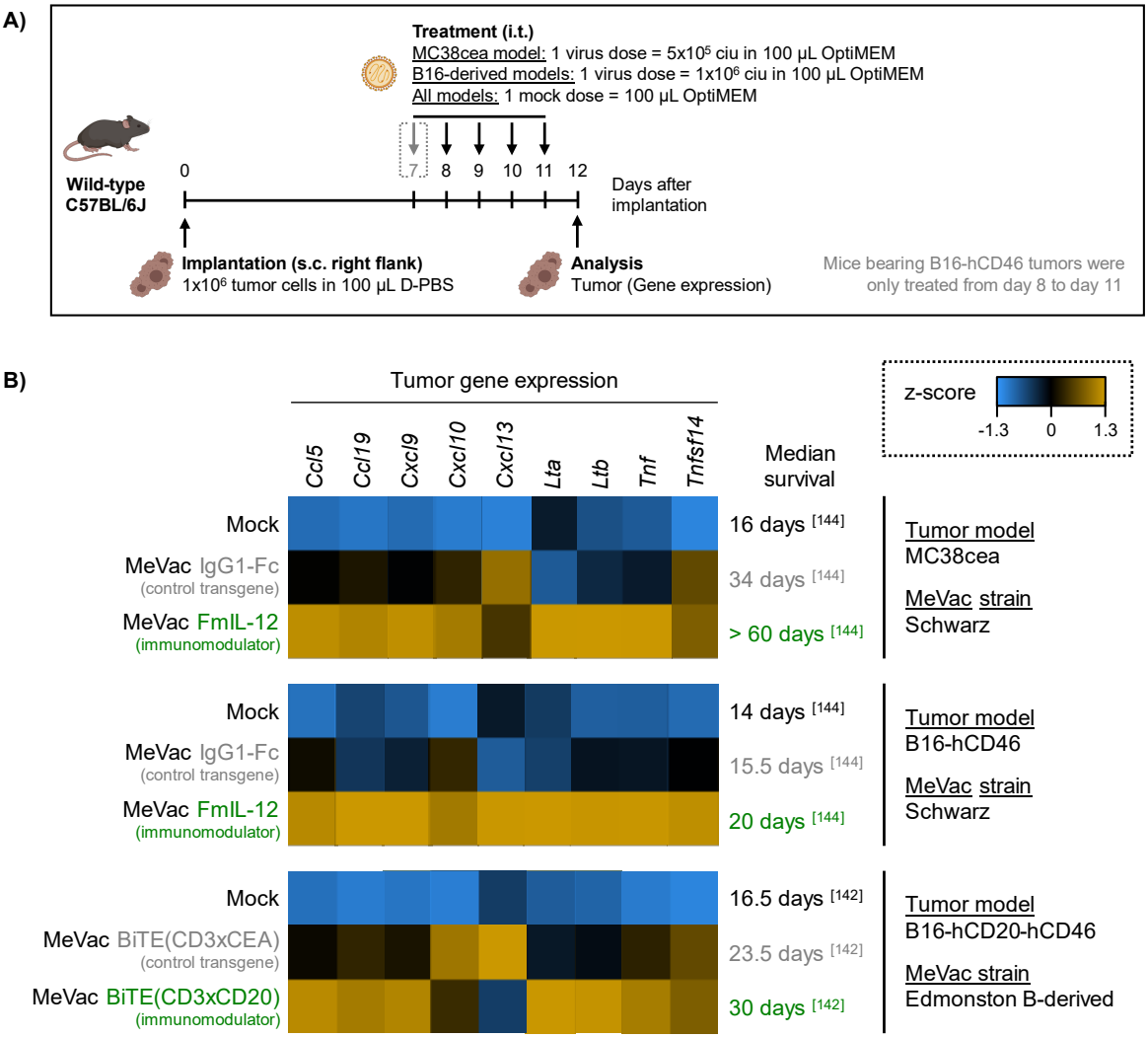

Figure 8. Tumor immune gene expression analysis after MeVac therapy, with focus on genes encoding chemokines or cytotoxic molecules. (A) Experiment schematic (created with BioRender.com). 1x10^6 MC38cea, B16-hCD46$_{[lenti]}$, or B16-hCD20-hCD46$_{[lenti]}$ cells were injected subcutaneously (s.c.) into the right flanks of 6-8 week-old wild-type C57BL/6J female mice (from Harlan Laboratories for the MeVac FmIL-12 studies; from Charles River for the MeVac BiTE study). After tumor establishment (average volume of 90 mm^3 for the MeVac FmIL-12 studies and 65 mm^3 for the MeVac BiTE study), the mice were treated intratumorally (i.t.) on four or five consecutive days with carrier fluid (mock) or MeVac variants as indicated in the diagram. MeVac IgG1-Fc and MeVac FmIL-12 were generated from MeVac$_{Schw}$. MeVac BiTE(CD3xCEA) and MeVac BiTE(CD3xCD20) were generated from MeVac$_{Edm}$. One day after the last treatment dose, tumors were resected and total tumor RNA was extracted for Nanostring gene expression analysis. These experiments were conducted by P. S. Backhaus and R. Veinalde (MeVac FmIL-12 studies) and by J. P. W. Heidbuechel (MeVac BiTE study). I performed the gene expression analysis shown in (B). n = 4 mice per treatment group (MeVac FmIL-12 studies) or 7-9 mice per treatment group (MeVac BiTE study). **(B)** Nanostring gene expression analysis from bulk tumor RNA obtained from (A). Heatmaps based on z-scores of normalized data grouped according to treatment were generated with the basic analysis package of the nSolver 4.0 software as described in Methods. Data from three independent experiments following similar treatment schedules but differing in the tumor model, MeVac strain, and immunomodulator are shown. Values on median survival were obtained from published efficacy studies employing the same mouse model, tumor model, and MeVac variants as the corresponding gene expression study [142, 144].

In subsequent *in vitro* studies, I found that MC38-hCD46 cells inoculated with MeVac secrete higher levels of murine (m)CCL5, mCXCL9, and mCXCL10 as compared to mock inoculation (Figure 9). These results suggest that the *Ccl5*, *Cxcl9*, and *Cxcl10* upregulation observed *in vivo* with the MC38cea model (Figure 8) took place, at least partly, in tumor cells. Conversely, MC38-hCD46 cells did not secrete mCCL19, mCCL21a, or mCXCL13 upon exposure to MeVac (Figure 9), suggesting that the *Ccl19* and *Cxcl13* upregulation detected *in vivo* took place in non-malignant cells from the TME. Despite not having gene expression data for *Ccl21a*, I included the chemokine encoded by this gene (mCCL21a) in the analysis because it is involved in the same signaling pathway as mCCL19.

Importantly, upregulation of the genes encoding the above-mentioned molecules correlated with the therapeutic efficacy of the MeVac vectors (Figure 8). This led me to hypothesize that the chemokines and cytotoxic molecules encoded by these genes are limiting factors of MeVac therapeutic efficacy. If that were the case, I reasoned that MeVac therapy would benefit from overexpressing these molecules in the tumor.

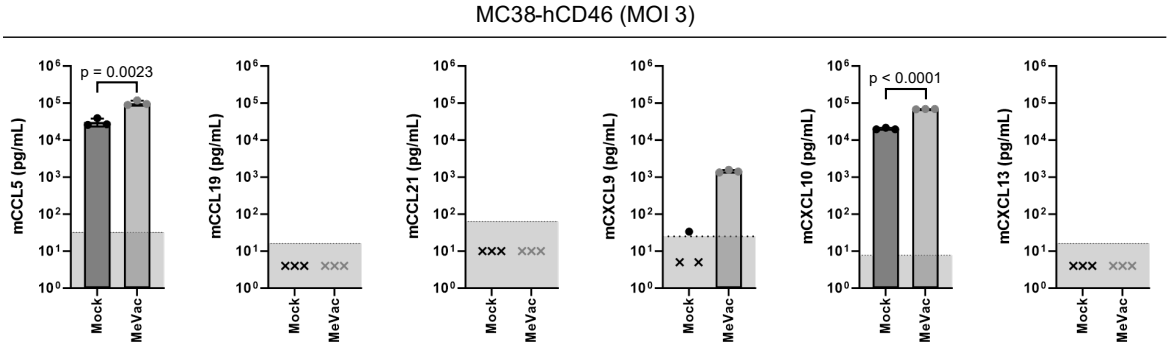

Figure 9. Chemokine expression by MC38-hCD46 cells upon exposure to MeVac. MC38-hCD46$_{[pCAG\text{-}SMAR]}$ cells were infected with purified MeVac (Schwarz strain, MOI = 3) or medium (mock) in triplicate. Culture supernatants were collected 72 h after infection and analyzed by ELISA to determine the concentration of the indicated murine chemokines. Bars indicate mean chemokine concentration of biological triplicates and error bars show standard deviation (not visible for most data points). The grey area under the horizontal dotted line corresponds to the range below the lower limit of detection of the assay. Concentrations below the dotted line could not be determined and are shown as "x". Data from the murine (m)CCL5 and mCXCL10 ELISAs were analyzed using two-tailed unpaired t test.

4.2.3 Generation of Recombinant MeVac Encoding Chemokines or Cytotoxic Molecules

To elucidate whether the identified chemokines and cytotoxic molecules are determinants of MeVac therapeutic efficacy, I conducted gain of function (GOF) efficacy studies in tumor-bearing mice. The GOF was achieved by encoding the candidate molecules in MeVac vectors. I reasoned that, in this setting, viral replication in the tumor should lead to transgene expression and therefore to local overexpression of the encoded candidate molecule.

Prior to conducting the *in vivo* experiments, I generated and characterized the MeVac viruses *in vitro*. To that aim, I constructed, rescued, and propagated eleven recombinant MeVac viruses of the Schwarz/Moraten strain, each encoding a candidate molecule or a control transgene in an additional transcription unit (ATU) downstream of the MeVac *P* gene (Figure 10 A). I chose this genomic position for transgene insertion to avoid virus attenuation, which may occur when large transgenes are inserted close to the MeVac leader sequence [102]. Nine of the encoded molecules corresponded to those identified in the gene expression analysis, that is, mCCL5, mCCL19, mCXCL9, mCXCL10, mCXCL13, mLT-α, mLT-β, mTNF-α, and mLIGHT. In addition, I generated a MeVac vector encoding murine CCL21a. Although the datasets that I analyzed did not provide expression data for the gene encoding this molecule (*Ccl21a*), the fact that CCL21a is involved in the same signaling pathway as CCL19 led me to speculate that *Ccl21a* might be upregulated in MeVac-treated tumors, as observed for *Ccl19*. Thus, I was also interested in investigating whether mCCL21a overexpression at the tumor site would contribute to MeVac therapeutic efficacy. As control, I generated a MeVac variant encoding IgG-Fc *C.m.*, which corresponds to the fragment crystallizable (Fc) region of hamster (*Cricetulus migratorius*) immunoglobulin G (IgG). Since IgG-Fc *C.m.* does not bind to murine Fc receptors, I did not expect therapeutic or immunological effects to be mediated by this transgene in mouse studies. Consistent with this reasoning, IgG-Fc *C.m.* has proven suitable as control molecule in a previous study from our research group [150].

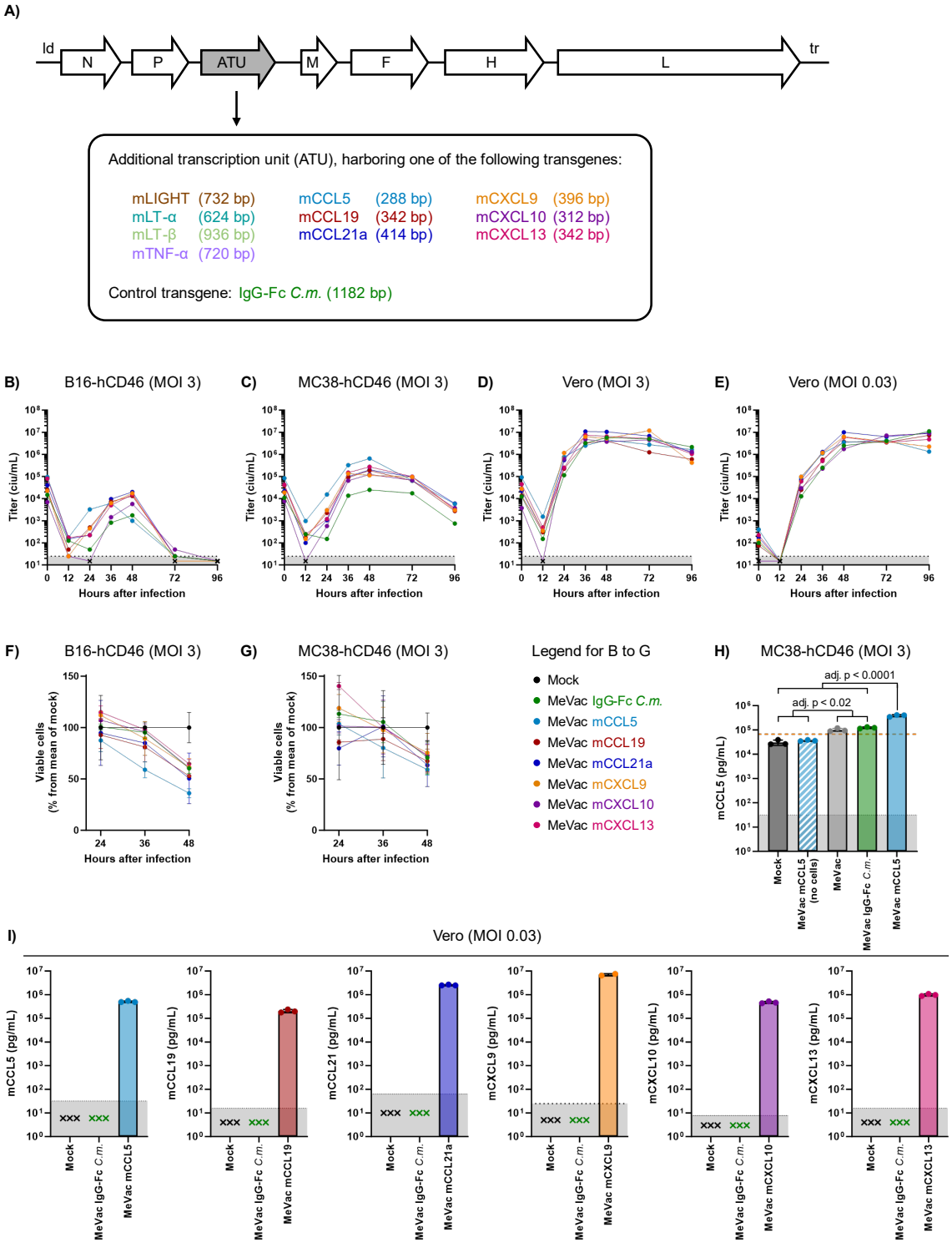

(Figure 10. Figure legend on the next page)

Figure 10. Generation of MeVac encoding murine chemokines or cytotoxic molecules and *in vitro* characterization of MeVac encoding murine chemokines. (A) Schematic of MeVac genome. Cassettes encoding murine cytotoxic molecules, murine chemokines, or the Fc region of hamster (*Cricetulus migratorius*) IgG (IgG-Fc *C.m.*) were cloned into an additional transcription unit (ATU) downstream of MeVac *P* (Schwarz strain). The size of the inserted cassettes is indicated in base pairs (bp). ld: MeVac leader region; tr: MeVac trailer region; *N*, *P*, *M*, *F*, *H*, *L*: genes encoding MeVac proteins. **(B-G)** Vero, B16-hCD46$_{[pCAG\text{-}SMAR]}$, or MC38-hCD46$_{[pCAG\text{-}SMAR]}$ cells were infected with purified MeVac encoding murine chemokines or a control transgene (MeVac IgG-Fc *C.m.*) at an MOI of 3 for one-step growth curves and XTT assays, or an MOI of 0.03 for multi-step growth curves. Cells exposed to medium served as mock controls for XTT assays. **(B-E)** At the indicated timepoints, cells were scraped into the supernatant. Viral progeny titers were determined in pooled samples from three biological replicates by titration assay on Vero cells. Titrations were performed in quadruplicates. Grey area: range below the lower limit of detection of the assay (25 ciu/mL). Titers below 25 ciu/mL could not be determined and are shown as "x". **(F-G)** At the indicated timepoints, cell viability was determined by XTT assay. Data are depicted as percent viability compared to the mean of mock controls (100% viability). Dots indicate the mean of biological triplicates and error bars show standard deviation (not visible for some data points). **(H-I)** MC38-hCD46$_{[pCAG\text{-}SMAR]}$ or Vero cells were infected with the indicated purified MeVac (Schwarz strain) variants (MOI = 3 for tumor cells, MOI = 0.03 for Vero cells) or exposed to medium only (mock). Culture supernatants were collected 72 h after infection and analyzed by ELISA to determine the concentration of the indicated murine chemokines. Bars indicate mean chemokine concentration of biological triplicates (or duplicates for MeVac mCXCL9) and error bars show standard deviation (not visible for most data points). The grey area under the horizontal dotted line corresponds to the range below the lower limit of detection of the assay. Concentrations below the dotted line could not be determined and are shown as "x". **(H)** Data were analyzed using one-way ANOVA with Tukey's correction for multiple comparisons. To control for the presence of mCCL5 in the virus suspension, the virus suspension employed for infection was also tested by ELISA (condition "MeVac mCCL5, no cells"). The value indicated by the dashed orange line (6.7×10^4 pg/mL) was calculated by adding the mean mCCL5 concentration of the "Mock" condition to the mean mCCL5 concentration of the "MeVac mCCL5, no cells" condition. Data from the "Mock" and "MeVac" conditions are also displayed in the mCCL5 ELISA results from Figure 9. adj. p: multiplicity-adjusted p value.

4.2.4 Growth Kinetics and Cytotoxic Effects

Following virus generation, I assessed the growth kinetics and cytotoxic effects of the MeVac variants encoding chemokines. In the future, I will conduct similar experiments with MeVac variants encoding the cytotoxic molecules.

To assess the growth kinetics of the recombinant viruses, I conducted one-step growth curves in murine tumor cells as well as one-step and multi-step growth curves in Vero cells. As murine tumor cells, I employed B16-hCD46 cells and MC38-hCD46 cells, which have ectopic expression of human CD46 as MeVac entry receptor. I generated these cell lines by transfecting parental hCD46(-) cells with the pCAG-SMAR vector (a plasmid-S/MAR vector encoding human CD46) (see 4.7.2). Before conducting the growth curve experiments, I purified the MeVac variants by ultracentrifugation following a methodology that I established during my doctoral studies (see 4.7.3).

One-step growth curves revealed productive infection of the three cell lines by all MeVac variants (Figure 10 B-D). The input titers differed between virus variants, presumably due to inaccuracy inherent to the titration method, with MeVac mCCL5 having the highest initial titers, and MeVac mCXCL10 the lowest initial titers in each cell line. Given that the MeVac replication cycle takes 24 h to 36 h in permissive cells [185], I expected that, at 12 h post infection (p.i.), most input viral particles would have already disassembled upon fusion with the membrane of target cells or degraded due to long exposure at 37 ºC, whereas viral particles generated *de novo* from ongoing viral replication would not be assembled yet. Consistent with these expectations, the titers of all MeVac variants decreased by at least 100-fold 12 h p.i. compared to the input titers in all cell lines.

Following the MeVac replication cycle, the viral progeny titers from all cell lines peaked between 36 h and 48 h p.i., with maximum titers ranging between $1.75x10^3$ and $2x10^4$ ciu/mL in B16-hCD46 cells, $2.5x10^4$ and $6.5x10^5$ ciu/mL in MC38-hCD46 cells, and $2.5x10^6$ and $1x10^7$ ciu/mL in Vero cells. Notably, the maximum titers obtained from MC38-hCD46 and B16-hCD46 cells were at least 10-fold and 100-fold lower compared to those from Vero cells, respectively. After peaking, the maximum titers obtained from MC38-hCD46 cells remained stable until 72 h p.i. and subsequently decreased, whereas the titers obtained from B16-hCD46 cells rapidly decreased to levels close to or below 25 ciu/mL (lower limit of detection of the assay). Since the viruses did not mediate complete lysis of the tumor cell cultures (Figure 10 F,G), these data indicate that murine tumor cells only support one or very few MeVac replication cycles. Compared to the other chemokine-encoding viruses, MeVac mCCL5 yielded higher viral progeny titers in MC38-hCD46 cells and showed faster replication kinetics in B16-hCD46 cells (Figure 10 B,C), whereas MeVac mCXCL10 yielded lower viral progeny titers in B16-hCD46 cells (Figure 10 B). I consider that the different input titers could explain these differences. Notably, MeVac IgG-Fc *C.m.* was attenuated in murine tumor cells,

perhaps due to the larger size of the transgene (1182 bp) compared to the transgenes inserted in the virus variants encoding chemokines (288 bp – 414 bp). Multi-step growth curves in Vero cells revealed similar replication kinetics for all viruses (Figure 10 E). Consistent with the lower MOI employed in this experiment, the initial titers were around 100-fold lower than those from the one-step growth curves in the same cell line. The viral progeny titers peaked later, between 48 h and 96 h p.i. in the range of $1.8x10^6$ to $1x10^7$ ciu/mL, and remained high up to 96 h p.i.

To assess the direct cytotoxic effect of the novel viruses on B16-hCD46 and MC38-hCD46 cells, I conducted XTT cell viability assays, which depend on cellular metabolism (Figure 10 F,G). Consistent with the peak of viral replication, the viability of murine tumor cells inoculated with the different viruses decreased to 40% - 70% compared to mock controls at 48 h p.i. A reduction of cell viability to 60% of mock was already detected at 36 h p.i. in B16-hCD46 cells exposed to MeVac mCCL5. This is in agreement with the faster replication kinetics of this virus in the murine melanoma cell line, and might be explained by the higher input titer. While these results confirm the cytotoxic effect of the virus variants on mouse tumor cells, they also suggest that direct oncolysis is insufficient to kill all tumor cells. This reinforces the rationale of exploiting the immunomodulatory properties of oncolytic MeVac in addition to the direct cytotoxic effects to improve therapeutic efficacy.

4.2.5 Transgene Expression and Functionality

4.2.5.1 Expression of MeVac-Encoded Chemokines

To assess transgene expression on the protein level, I infected Vero cells with chemokine-encoding MeVac variants or control virus (MeVac IgG-Fc *C.m.*) and determined the levels of the corresponding virus-encoded chemokine in culture supernatants by ELISA. Since Vero cells (primate cells) do not produce murine chemokines, chemokine detection in this setting is a direct proof of transgene expression. Indeed, whereas I did not detect murine chemokines in supernatants from mock-infected Vero cells or Vero cells infected with MeVac IgG-Fc *C.m.*, I detected high levels of the corresponding chemokines in supernatants from Vero cells infected with the MeVac variant encoding the chemokine of interest (Figure 10 I). Thus, with this experiment I confirm that the transgenes inserted in the MeVac variants are expressed and that the encoded chemokines are synthesized and secreted.

Given that *in vivo* studies are conducted with murine tumor cells, it is interesting to assess transgene expression in those. However, this is complex, since the virus-encoded chemokines cannot be distinguished from chemokines encoded in the murine cell genome, which might be expressed constitutively or in response to virus infection. Indeed, mCCL5 and mCXCL10 seem to be constitutively expressed in MC38-hCD46 tumor cells, since they are detected in supernatants from mock-infected cultures (Figure 9). Furthermore, in this cell line MeVac infection induces mCXCL9

expression and upregulates endogenous mCCL5 and mCXCL10 expression (Figure 9). Thus, as an indirect way of determining the production of virus-encoded chemokines in murine tumor cells, I compared the levels of a particular chemokine in supernatants from MC38-hCD46 cells exposed to control virus (either unmodified MeVac or MeVac IgG-Fc *C.m.*) to the levels of the same chemokine in supernatants from cells exposed to the MeVac variant encoding the chemokine of interest. In a pilot experiment, I performed this assay for mCCL5 (the other chemokines will be assessed in the future) (Figure 10 H). In this experiment, I detected higher levels of mCCL5 in supernatants from MC38-hCD46 cells exposed to MeVac mCCL5 compared to supernatants from mock-infected cells or cells infected with the control viruses, as determined by ELISA. This finding argues for the production of virus-encoded chemokines in murine tumor cells.

Determining whether the virus-encoded chemokines are produced *de novo* or already present in the virus suspension brings another layer of complexity. Indeed, although purified by ultracentrifugation, the stock suspension of MeVac mCCL5 contains mCCL5 (Figure 34 G). To control for this phenomenon, in the experiment described in the previous paragraph I also determined the levels of mCCL5 in the virus suspension employed for infection (diluted from the stock suspension to an MOI of 3). I refer to this suspension as “MeVac mCCL5 (no cells)”. This suspension contained levels of mCCL5 comparable to those in mock-infected cultures (Figure 10 H). Importantly, the levels of mCCL5 in supernatants from MC38-hCD46 cells infected with MeVac mCCL5 were higher than those from mock-infected cultures plus those from the virus suspension employed for infection (mock + “no cells” = 6.7×10^4 pg/mL, represented in Figure 10 H by a dashed orange line). Therefore, these results indirectly indicate that virus-encoded chemokines (in this example mCCL5) are produced *de novo* in murine tumor cells infected with the corresponding MeVac variant (in this example MC38-hCD46 cells infected with MeVac mCCL5).

4.2.5.2 Functionality of MeVac-Encoded Chemokines and Cytotoxic Molecules

To study the functionality of the chemokines and cytotoxic molecules encoded in MeVac vectors, I performed *in vitro* chemotaxis and cytotoxicity assays with supernatants from Vero cells infected with the different virus variants (Figure 11, Figure 12). I refer to these supernatants as SN, preceded by the virus variant employed to infect Vero cells.

To monitor cytotoxicity, I exposed L929 murine fibroblasts (target cells) to different supernatants and labelled dead cells in real-time with a green fluorescent dye. I monitored the labeling via fluorescence live-cell imaging. MeVac mTNF-α (SN) and MeVac mLT-α (SN) led to target cell death, whereas L929 cells remained viable upon treatment with mock (SN) or MeVac IgG-Fc *C.m.* (SN). Interestingly, MeVac mTNF-α (SN) mediated faster and stronger cytotoxic effects on L929 cells than MeVac mLT-α (SN) (Figure 11).

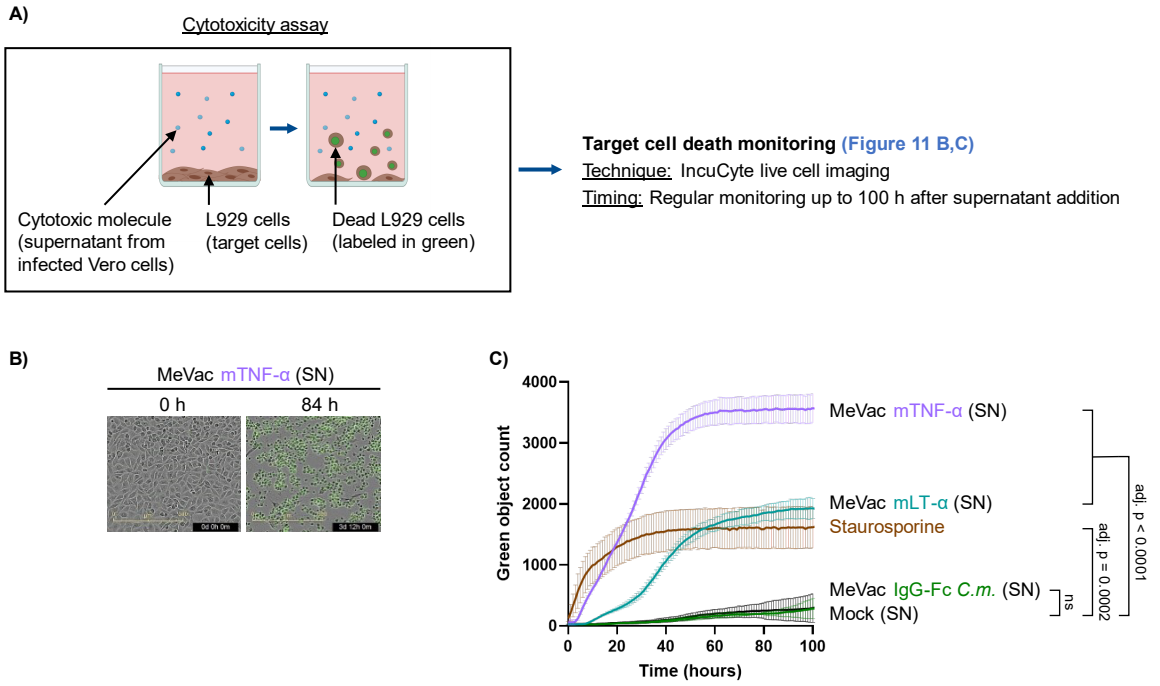

Figure 11. Functional characterization of MeVac-encoded murine cytotoxic molecules. (A) Experiment schematic (created with BioRender.com). Vero cells were infected with the MeVac (Schwarz strain) variants indicated in (C) at an MOI of 0.03 or exposed to medium only (mock). After 48 h or 72 h, filtered supernatants were transferred onto L929 target cells together with 250 nM Incucyte® Cytotox Green Dye for the labeling of dead cells. Target cell death was monitored at 1 h intervals for a total of 100 h via live cell imaging using the phase and green channels of an Incucyte® SX5 instrument. As positive control, L929 cells were exposed to 10 µg/mL Staurosporine. **(B)** Representative images of L929 cells exposed to supernatants from Vero cells infected with MeVac mTNF-α acquired at the time of (0 h) or 84 h after supernatant addition. Merged images from the phase and green channels are shown. Dead cells are labeled in green. Scale bar: 300 µm. **(C)** Target cell death quantification. The number of green objects (= dead L929 cells) per image and timepoint was determined with the Incucyte® base analysis software. The plot depicts the mean green object count of triplicates over time. Error bars show standard deviation. Data from the last timepoint were analyzed using one-way ANOVA with Dunnett's correction for multiple comparisons. Only pairwise comparisons of interest were analyzed, those being each condition to mock. adj. p: multiplicity-adjusted p value, ns: not significant.

To assess chemotaxis, I conducted transwell migration assays with murine splenocytes using flow cytometry as readout. Compared to mock (SN), these experiments revealed increased migration of murine CD3(+) cells towards MeVac mCXCL9 (SN), MeVac mCXCL10 (SN), MeVac mCCL19 (SN), and MeVac mCCL21a (SN), with MeVac mCCL21a (SN) mediating the strongest chemotactic effect (Figure 12 A,B). The remaining conditions did not promote significant migration of murine CD3(+) cells. Consistent with these results, MeVac mCXCL9 (SN), MeVac mCXCL10 (SN), MeVac mCCL19 (SN), and MeVac mCCL21a (SN) also increased migration of murine splenocytes in a second chemotaxis assay using live-cell imaging instead of flow cytometry as readout (Figure 12 A,C).

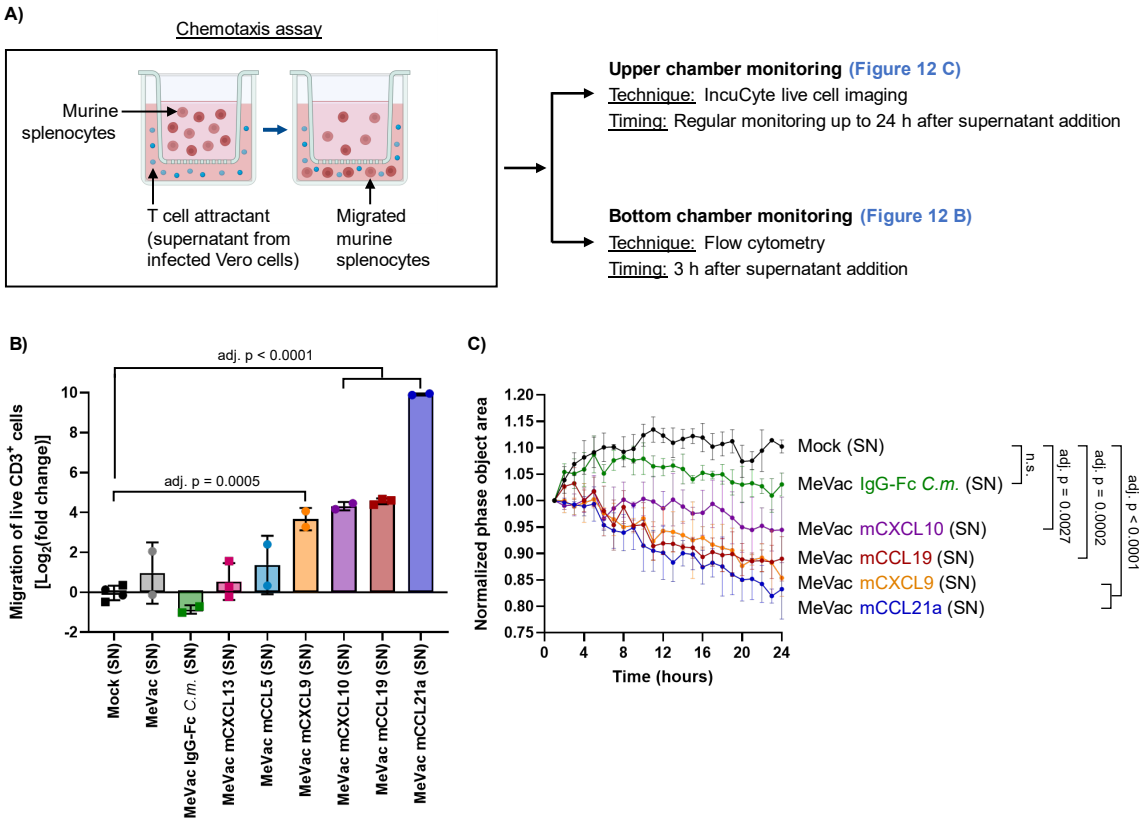

Figure 12. Functional characterization of MeVac-encoded murine chemokines. (A) Experiment schematic (created with BioRender.com). Vero cells were infected with the MeVac (Schwarz strain) variants indicated in (E) and (F) at an MOI of 0.03 or exposed to medium only (mock). After 72 h, filtered supernatants were transferred to the bottom chambers of 24-well plates (classical assay) or 96-well plates (Incucyte® assay) with membrane inserts. In parallel, murine splenocytes (isolated from C57BL/6J mice and stimulated for 24 h with 50 U/mL murine IL-2) were added onto the upper chambers. **(B)** Classical chemotaxis assay. Splenocyte migration was allowed for 3 h. Afterwards, the number of live CD3(+) cells that migrated to the bottom chamber was determined by flow cytometry using a viability dye and a PerCP-Cy5.5-labelled antibody against murine CD3. For absolute quantification, counting beads were added after staining. Two independent experiments were conducted, identified by circle and square symbols, respectively. Fold change migration of live CD3(+) cells was calculated for each replicate in relation to the mean of mock controls in the corresponding experiment. Bars indicate mean log_2(fold-change) values of biological duplicates or triplicates, and error bars show standard deviation. Data were analyzed using one-way ANOVA with Dunnetts's correction for multiple comparisons. Only pairwise comparisons of interest were analyzed, those being each condition to mock. adj. p: multiplicity-adjusted p value; SN: supernatant. **(C)** Incucyte® chemotaxis assay. Splenocyte migration was monitored at 1 h intervals for a total of 24 h via live cell imaging of the upper chamber using the phase channel of an Incucyte® SX5 instrument. The object area (= area occupied by cells) in the upper chamber was determined per phase image and timepoint using the Incucyte® chemotaxis analysis software module. Values were normalized to the object area in the corresponding upper chamber at the 1 h timepoint (*i.e.* after allowing the splenocytes to settle for 1 h). The plot depicts the mean normalized phase object area of triplicates over time. Error bars show standard deviation. Data from the last timepoint were analyzed using one-way ANOVA with Dunnett's correction for multiple comparisons. Only pairwise comparisons of interest were analyzed, those being each condition to mock. adj. p: multiplicity-adjusted p value; n.s.: not significant; SN: supernatant.

Overall, I conclude that MeVac-encoded murine TNF-α and LT-α mediate strong cytotoxic effects on L929 target cells, and MeVac-encoded murine CXCL9, CXCL10, CCL19, and CCL21a exert strong chemotactic effects on murine CD3(+) cells. In subsequent experiments addressing therapeutic efficacy I focus on the viruses encoding the four leading chemokines. The therapeutic efficacy of vectors encoding cytotoxic molecules will be assessed in the future.

4.2.6 Therapeutic Efficacy and Tumor-Specific Systemic Immunity

To determine whether, as hypothesized, intratumoral overexpression of murine CXCL9, CXCL10, CCL19, or CCL21a improves MeVac therapeutic efficacy, I conducted efficacy studies in C57BL/6J mice bearing subcutaneous tumors treated intratumorally with carrier fluid (mock), control virus (MeVac IgG-Fc *C.m.*), or MeVac encoding one of the above-mentioned chemokines (Figure 13, Figure 14). To distinguish the potentially beneficial effect of MeVac encoding chemokines over control virus, I followed a treatment schedule in which the control virus only confers a slight, statistically non-significant, therapeutic advantage compared to mock treatment. Overall, the treatment was well tolerated and did not induce major body weight changes (Figure S7, Figure S8).

Regarding the tumor model, I hypothesized that combining MeVac therapy with chemokine overexpression is particularly relevant in immune-desert and immune-excluded tumors, since this treatment combination might enhance intratumoral immune cell infiltration via chemotaxis. Thus, I conducted the first experiment in mice bearing B16-hCD20-hCD46 tumors. B16 tumors (murine melanoma) are characterized by low levels of chemokines and a low immune cell infiltrate [186].

Contrary to my hypothesis, median survival was similar between treatment groups, indicating that, in this tumor model and treatment setting, MeVac vectors encoding chemokines do not confer any clear therapeutic advantage over the control virus (Figure 13 B). Survival was not significantly different to that of the mock-treated group, either. Nevertheless, I observed signs of tumor regression in individual mice from most groups receiving MeVac variants. Compared to the mock group, tumor growth was delayed in most mice treated with MeVac mCCL19 or control virus (Figure S7 B,C). This delay could explain the slight, statistically non-significant increase in median survival from 18 days in the mock group to 23 days in the MeVac mCCL19 and control virus groups (Figure 13 B). Consistent with these observations, two mice treated with control virus showed a partial and a complete response, respectively (Figure 13 D). Moreover, five mice treated with MeVac mCCL19 experienced partial tumor regression after the second treatment dose (Figure 13 E). However, I did not identify them as partial responders because the tumor volumes were still larger than baseline. In addition to the mouse treated with control virus, I observed a partial tumor remission compared to baseline tumor volume in two other mice, treated with MeVac mCCL21a and MeVac mCXCL10, respectively (Figure 13 F,H).

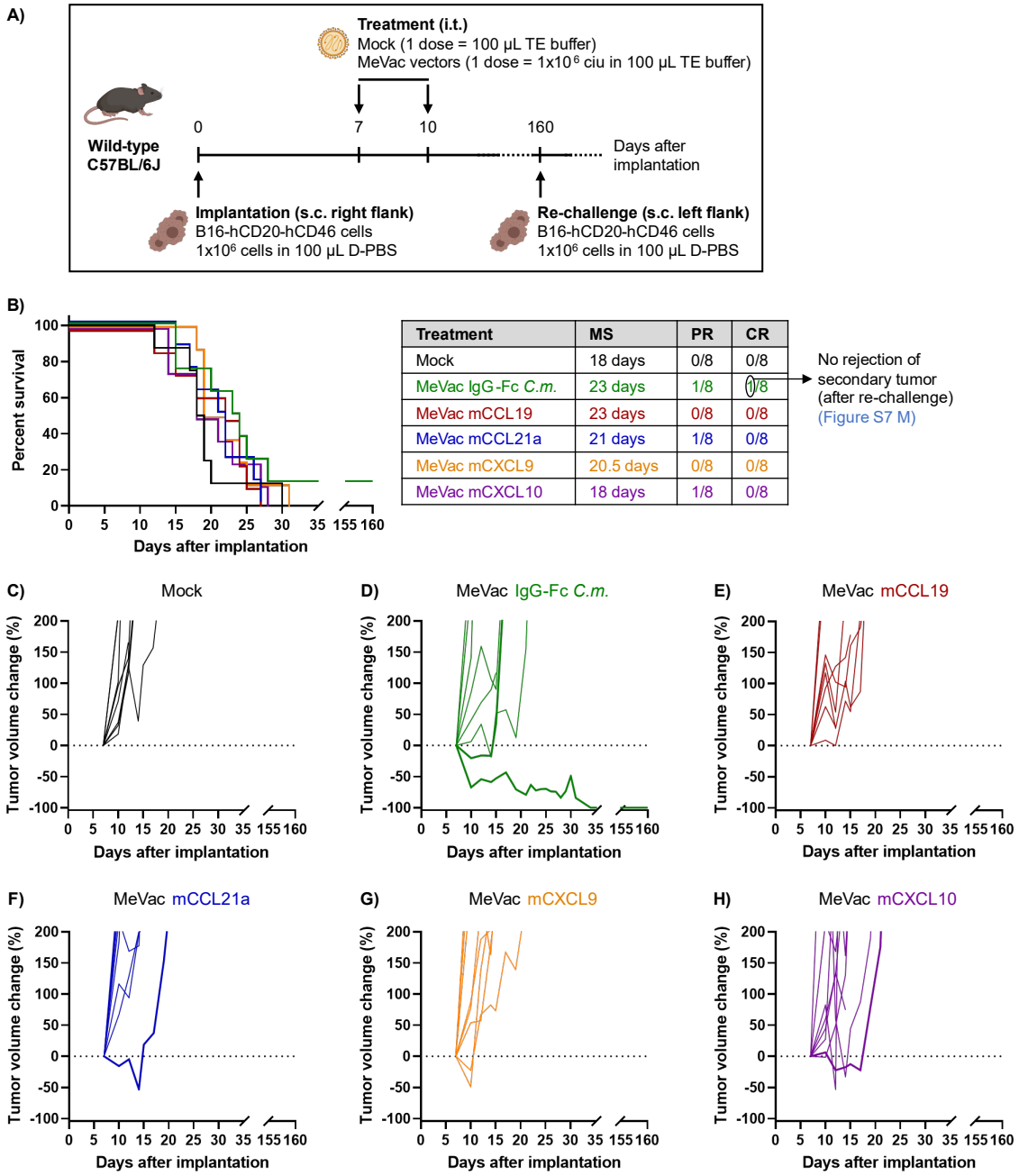

Figure 13. Therapeutic efficacy of MeVac encoding murine chemokines or a control molecule in murine melanoma. (A) Experiment schematic (created with BioRender.com). 1x10^6 B16-hCD20-hCD46$_{[pCAG-SMAR]}$ cells were injected subcutaneously (s.c.) into the right flank of wild-type C57BL/6J mice (from Janvier Labs). After tumor establishment (average volume of 60 mm^3), the mice received two intratumoral (i.t.) doses of TE buffer (mock) or the respective purified MeVac (Schwarz strain) variant (1x10^6 ciu per dose) at a three-day interval. On day 160 after initial tumor implantation, the long-term survivor was re-challenged as indicated in the diagram. ciu: cell infectious units. **(B)** Kaplan-Meyer survival analysis with Mantel-Cox (log rank) test. The significance level (α) after Bonferroni's correction for 15 comparisons was 0.003. P values are not shown because differences were not statistically significant. Median survival (MS) as well as rates for partial (PR) or complete (CR) remission of the primary tumor are indicated. Partial remission is defined as "tumor volume below pre-treatment tumor volume on two or more consecutive measurements". **(C-H)** Relative change in tumor volume as compared to pre-treatment tumor volume for individual mice. Y axis is cut at 200% for better visualization of PR and CR. Curves for mice experiencing PR or CR are thicker. **(A-H)** n = 8 female mice per treatment group, 6-8 weeks-old on the day of tumor implantation.

Strikingly, the complete responder from the group receiving control virus developed a tumor upon rechallenge with the same cell line, albeit with delayed kinetics compared to the growth of primary tumors in the other mice (Figure S7 M). These data show that the complete responder was not protected from secondary tumor engraftment and suggest that, in this mouse, the complete remission of the primary tumor was mediated by mechanisms other than systemic and memory antitumor immunity.

Overall, this efficacy experiment led me to conclude that encoding chemokines in MeVac vectors does not improve the therapeutic efficacy of the OV in B16-derived tumors. I then speculated that the novel viruses might show therapeutic advantage over the control virus in tumors with a baseline T cell infiltrate. I reasoned that, in these tumors, certain mechanisms of T cell recruitment might already be active, but might be insufficient to recruit a large number of T cells. Thus, I hypothesized that chemokine overexpression might enhance these mechanisms of T cell recruitment leading to increased intratumoral T cell abundance. Combined with the inflamed state triggered by oncolytic virotherapy, these mechanisms might trigger a strong antitumor immune response and thereby improve therapeutic efficacy.

To test this hypothesis, I repeated the efficacy study with mice bearing subcutaneous MC38-hCD46 tumors, which derive from the MC38 murine colon adenocarcinoma model, characterized by a higher baseline T cell infiltrate as compared with B16 tumors [186,187].

In this model, there were no statistically significant differences in survival between treatments, either. However, I noticed a trend towards prolonged survival in mice treated with MeVac mCCL19 and MeVac mCXCL10 (median survival of 26.5 days and 28.5 days, respectively) compared to mice receiving MeVac mCXCL9, control virus, or mock treatment (median survival of 18 days, 19 days, and 20 days, respectively) (Figure 14 B).

Interestingly, I observed two patterns of tumor growth: (i) rapid progression, with exponential tumor growth starting around day 10 post implantation and endpoint criteria reached around day 15 post implantation and (ii) slightly delayed progression, with exponential tumor growth starting around day 20 post implantation and endpoint criteria reached around day 25 post implantation (Figure S8 A-F). The fact that these two patterns were also observed in the mock group shows that tumor growth was heterogeneous despite working with inbred mice (Figure S8 A). Mice with tumor growth kinetics following the second pattern showed an equilibrium between tumor growth and tumor regression, including a short partial response in three mice, treated with carrier fluid, MeVac mCCL21a, and MeVac mCXCL10, respectively, that lasted until around day 20 after implantation and was followed by tumor progression (Figure 14 C-H).

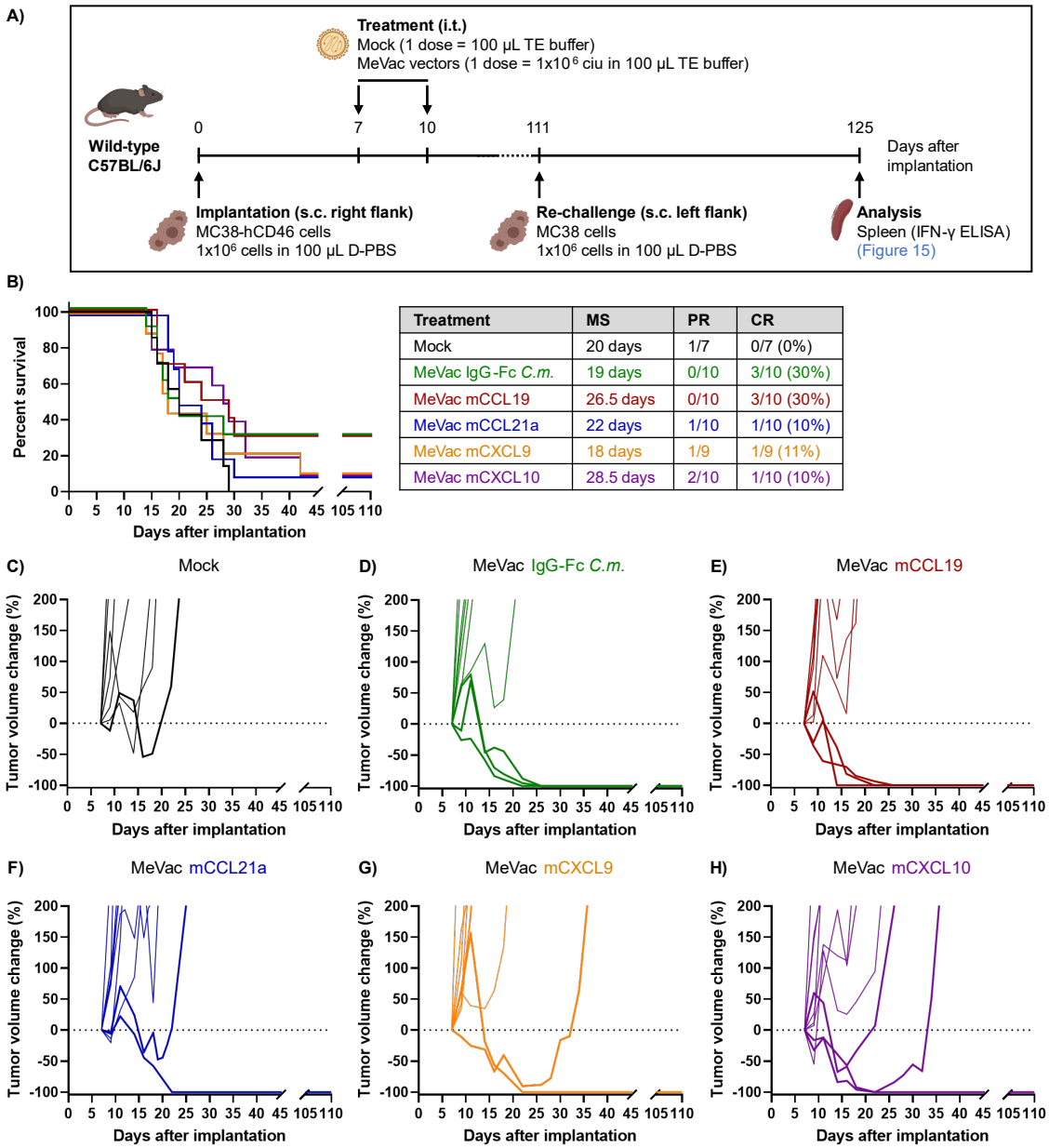

Treatment	MS	PR	CR
Mock	20 days	1/7	0/7 (0%)
MeVac IgG-Fc *C.m.*	19 days	0/10	3/10 (30%)
MeVac mCCL19	26.5 days	0/10	3/10 (30%)
MeVac mCCL21a	22 days	1/10	1/10 (10%)
MeVac mCXCL9	18 days	1/9	1/9 (11%)
MeVac mCXCL10	28.5 days	2/10	1/10 (10%)

Figure 14. Therapeutic efficacy of MeVac encoding murine chemokines or a control molecule in murine colon adenocarcinoma. (A) Experiment schematic (created with BioRender.com). 1x10^6 MC38-hCD46$_{[pCAG\text{-}SMAR]}$ cells were injected subcutaneously (s.c.) into the right flanks of wild-type C57BL/6J mice (from Janvier Labs). After tumor establishment (average volume of 70 mm^3), the mice received two intratumoral (i.t.) doses of TE buffer (mock) or the respective purified MeVac (Schwarz strain) variant (1x10^6 ciu per dose) at a three-day interval. Mice experiencing complete tumor remissions were re-challenged as shown in the diagram 3.5 months after initial tumor cell implantation and spleens were resected two weeks afterwards for immunological analysis (Figure 15). ciu: cell infectious units. **(B)** Kaplan-Meyer survival analysis with Mantel-Cox (log rank) test. The significance level (α) after Bonferroni's correction for 15 comparisons was 0.003. P values are not shown because differences were not statistically significant. Median survival (MS) as well as rates for partial (PR) or complete (CR) remission of the primary tumor are indicated. Partial remission is defined as "tumor volume below pre-treatment tumor volume on two or more consecutive measurements". **(C-H)** Relative change in tumor volume as compared to pre-treatment tumor volume for individual mice. Y axis is cut at 200% for better visualization of PR and CR. Curves for mice experiencing PR or CR are thicker. **(A-H)** n = 7 (mock) or 10 (MeVac variant) female mice per treatment group, 6-8 weeks-old on the day of tumor implantation. One mouse from the MeVac mCXCL9 group was sacrificed on day 10 due to an open ulceration and did not receive treatment dose #2. Data from this mouse (not shown) was excluded from the analysis.

Remarkably, while all mock mice reached endpoint criteria, in all groups receiving virus treatment 10% to 30% of mice experienced complete tumor remissions. Moreover, two mice treated with MeVac mCXCL9 and MeVac mCXCL10, respectively, experienced a partial tumor remission sustained for more than 20 days that led to a clear delay in tumor growth and prolonged survival compared to all other mice reaching endpoint criteria (Figure 14 C-H).

To investigate whether the mice experiencing complete tumor remission developed systemic antitumor immunity, I rechallenged them with parental MC38 cells in the contralateral flank and determined the rates of secondary tumor rejection (Figure 14 A, Figure 15). Notably, all long-term survivors rejected secondary tumor engraftment upon re-challenge, whereas tumors engrafted in 4 of 5 age-matched naïve mice (Figure 15 A). These results indicate that mice experiencing complete tumor remission upon treatment with any of the MeVac variants, including control virus, are protected from tumor recurrence at a distal site. The fact that tumors engrafted in 4 of 5 age-matched naïve mice (Figure 15 A) suggests that protection from tumor engraftment was mainly mediated by systemic and memory antitumor immunity.

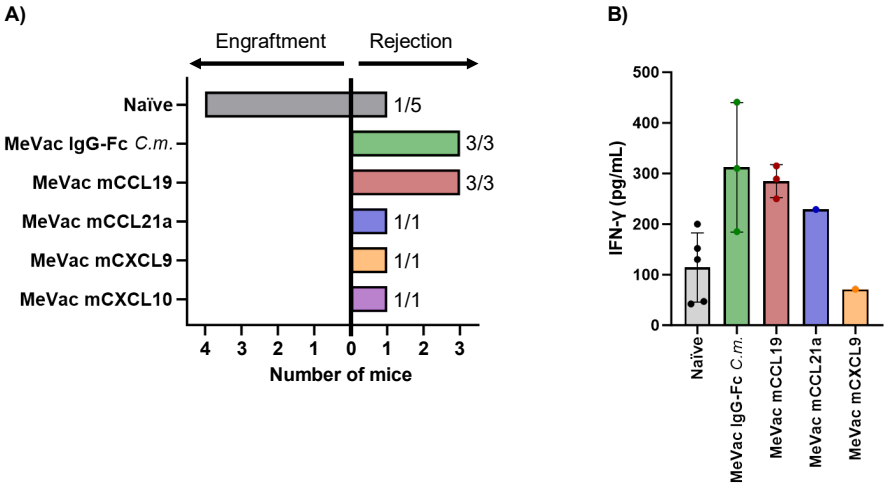

Figure 15. Antitumor immune memory upon virotherapy with MeVac encoding murine chemokines or a control molecule. Mice experiencing complete tumor remissions after treatment with the indicated MeVac variants (as shown in Figure 14) were re-challenged by injecting $1x10^6$ MC38 cells subcutaneously into the contralateral flank 3.5 months after initial tumor cell implantation (Figure 14 A). Age-matched naïve mice (wild-type C57BL/6J mice, from Janvier Labs) were included as controls. **(A)** Rates for rejection of secondary tumor engraftment (in re-challenged mice) or primary tumor engraftment (in naïve mice) are shown. **(B)** Two weeks after re-challenge (or primary challenge in naïve mice), spleens were extracted. Splenocytes were stimulated *ex vivo* with mitomycin-C-treated MC38 cells at a 10:1 splenocyte to tumor cell ratio plus 20 U/mL murine IL-2. After 5 days, culture supernatants were collected and the concentration of murine IFN-γ in the supernatants was determined by ELISA. Dots represent values for individual mice (mean of technical quintuplicates). Bars indicate mean values of all mice within a treatment group and error bars show standard deviation (for groups with more than one mouse). Sample size did not allow for statistical analysis with sufficient power. Moreover, there is not enough information in the data to make distributional assumptions. For technical reasons, the sample from the mouse belonging to the MeVac mCXCL10 group was not included in the ELISA.

To gain insights into the mechanisms underlying secondary tumor rejection, I stimulated splenocytes from rechallenged and naïve mice with parental MC38 cells *ex vivo* and determined the concentration of IFN-γ in supernatants from these cultures five days afterwards. In general, I found increased IFN-γ secretion in co-cultures of MC38 cells with splenocytes from rechallenged mice as compared to co-cultures with splenocytes from naïve mice (Figure 15 B). There were two exceptions: splenocytes from a mouse treated with the control virus and splenocytes from a mouse treated with MeVac mCXCL9 yielded IFN-γ levels similar to those from naïve mice. Consistent with the efficacy study, the ELISA results revealed no major differences between mice treated with the control virus and mice treated with chemokine-encoding virus variants. Thus, I conclude that MeVac virotherapy promotes antitumor immune memory but that encoding murine CXCL9, CCL19, or CCL21a in MeVac vectors does not increase the magnitude of the antitumor immune response.

4.2.7 Treatment Schedule for Loss of Function Efficacy Studies

The GOF efficacy studies showed that encoding murine CXCL9, CXCL10, CCL19, or CCL21a in the viral genome does not improve the efficacy of oncolytic MeVac, thereby suggesting that these chemokines are not limiting factors of MeVac virotherapy, at least in the tumor models that I investigated. Following up on these results, I hypothesized that, despite not being limiting, the identified chemokines are essential for therapeutic outcome. This reasoning is supported by the gene expression analysis shown in Figure 8, which revealed a correlation between MeVac therapeutic efficacy and intratumoral upregulation of chemokine-encoding genes.

To elucidate whether the candidate chemokines are essential determinants of MeVac therapeutic efficacy, I will conduct loss of function (LOF) efficacy studies in which tumor-bearing mice will receive intratumoral injections of MeVac (no transgene encoded) and intraperitoneal injections of antibodies blocking specific chemokine signaling pathways. However, to assess the potentially detrimental effect of blocking these signaling pathways, the experiments require a setting in which MeVac confers a strong therapeutic advantage over mock treatment. Since this was not the case in the treatment schedule employed for the GOF studies (Figures 13 B, Figure 14 B), before conducting the LOF studies it is necessary to modify the *in vivo* experimental system.

To that aim, I conducted a pilot experiment in which I compared the therapeutic efficacy of mock treatment to that conferred by two MeVac treatment regimens: (i) the one employed in the GOF studies (two virus doses, three days apart) and (ii) another one in which the number of virus doses was increased to four on consecutive days. Despite a trend towards prolonged survival in the two MeVac-treated groups compared to mock treatment, the differences in survival were statistically non-significant, indicating that the establishment of a treatment schedule suitable for *in vivo* LOF studies requires further optimization (data not shown, see Outlook).

4.3 Virotherapy Combined with PD-1/PD-L1 Immune Checkpoint Blockade in Murine Colon Adenocarcinoma

4.3.1 Contextualization – Aim – Hypothesis – Model System

Once at the tumor site, tumor-specific CTLs recognize and kill tumor cells presenting cognate antigen. However, this response is attenuated by immune checkpoint molecules such as PD-1 and PD-L1. Given that virotherapy induces PD-L1 upregulation on tumor cells [147], our research group hypothesized that MeVac therapy might benefit from combination with PD-1 or PD-L1 blockade.

To address this combination approach, R. Veinalde and I employed MeVac variants encoding antibody-like molecules targeting murine PD-1 or PD-L1. Following vector generation and characterization, we analyzed viral gene expression in tumors and tumor-draining lymph nodes (TDLNs), investigated the safety profile and therapeutic efficacy of our strategy, and determined whether it elicits an antitumor immune memory response [xiii].

4.3.2 Virus Generation and Characterization

To study MeVac virotherapy in combination with immune checkpoint blockade, R. Veinalde generated MeVac viruses encoding murine PD-1 or PD-L1 blockades ($MeVac_{H\alpha CEA}$ αmPD-1, $MeVac_{H\alpha CEA}$ αmPD-L1) or control molecules ($MeVac_{H\alpha CEA}$ IgG-Fc *C.m.*, $MeVac_{H\alpha CEA}$ IgG1-Fc) (Table 8). The PD-1 and PD-L1 blockades were scFv-Fc molecules. In detail, the PD-1 blockade consisted of a single-chain variable fragment (scFv) targeting murine PD-1 linked to the fragment crystallizable (Fc) region of hamster (*Cricetulus migratorius*) immunoglobulin G (IgG). The PD-L1 blockade consisted of an scFv targeting murine PD-L1 linked to the Fc region of human IgG subclass 1 (IgG1). The control transgenes only encoded the corresponding Fc region, and all transgenes encoded an HA tag for detection purposes. The H protein of these viruses was fully retargeted to human carcinoembryonic antigen (CEA) for infection of murine MC38cea cells, which express this antigen ectopically. Experiments conducted by R. Veinalde in MC38cea cells revealed similar growth kinetics and cytotoxic properties across the virus variants and confirmed transgene expression at the protein level (data not shown).

To assess the binding specificity of the αmPD-1 and αmPD-L1 scFv-Fc molecules encoded in MeVac vectors, I conducted competitive binding assays (Figure 16). In these experiments, I determined binding of MeVac-derived αmPD-1 and αmPD-L1 to target cells by flow cytometry in the presence of a competitor added at different concentrations. As target cells, I employed PD-1(+) murine

[xiii] R. Veinalde initiated this project and I developed it further until publication (see Contributions and Figure Legends). In this chapter, I describe the results from experiments that I conducted, and summarize the work of R. Veinalde when required.

splenocytes or PD-L1(+) MC38cea cells. Binding was detected with a PE-coupled antibody directed against the HA tag, which is present in virus-derived αmPD-1 or αmPD-L1 but not in the competitors. Detection of PE signal in cultures incubated with MeVac-derived αmPD-1 or αmPD-L1 but not in those incubated with MeVac-derived control molecules (which also contain the HA tag) showed that virus-derived αmPD-1 and αmPD-L1 bind to the target cells. Furthermore, I confirmed specific binding of MeVac-derived αmPD-1 to murine PD-1 by detecting a gradual decrease in PE signal on the target cell population with increasing competitor concentrations (Figure 16 A). Similarly, I confirmed specific binding of MeVac-derived αmPD-L1 to murine PD-L1, although in this case the effect of the competitor was less pronounced (Figure 16 B).

4.3.3 Viral Gene Expression and Treatment Safety

To assess whether viral gene expression, required for *de novo* production of MeVac-encoded αmPD-1, takes place *in vivo*, I determined the levels of MeVac *N* mRNA in tumor samples and TDLNs from mice bearing MC38cea tumors treated intratumorally with $MeVac_{H\alpha CEA}$ αmPD-1 or carrier fluid (mock) (Figure 17 A). One day after treatment I only detected MeVac *N* mRNA in 1 of 4 tumors from virus-treated mice. In contrast, two days after treatment MeVac *N* mRNA was detectable in all (3 of 3) tumors from virus-treated mice (Figure 17 B, Figure S9 B,C). Although a paired comparison between timepoints is not possible (since different mice were used per timepoint), these results argue for virus replication in the tumor. Importantly, I did not detect MeVac *N* mRNA in TDLNs from virus-treated mice at any of the tested timepoints. This suggests that viral replication, and therefore transgene expression and αmPD-1 secretion, is restricted to the virus injection site (Figure 17 B; Figure S9 B,D).

Next, I asked whether intratumoral virotherapy with $MeVac_{H\alpha CEA}$ αmPD-1 would result in the dissemination of virus-derived αmPD-1 to the blood, raising safety concerns. To address this question and assess the safety of our therapy, I compared the levels of MeVac-derived αmPD-1 (scFv-Fc molecule) in sera from the above-mentioned mice to the levels of anti-PD-1 antibody in sera and peritoneal washes from healthy mice receiving intravenous or intraperitoneal injections of J43, a commercially available antibody targeting murine PD-1 (Figure 17 A,C; Figure S9 A). Systemic antibody treatment increased anti-PD-1 antibody levels in sera and peritoneal washes compared to baseline. Conversely, despite detecting MeVac *N* mRNA in virus-treated tumors, intratumoral delivery of $MeVac_{H\alpha CEA}$ αmPD-1 yielded αmPD-1 serum levels similar to baseline both one and two days after treatment, suggesting that MeVac-derived αmPD-1 is produced locally and does not spread systemically (Figure 17 C). Therefore, I conclude that our intratumoral therapeutic approach has a better safety profile than systemic delivery of anti-PD-1 antibodies.

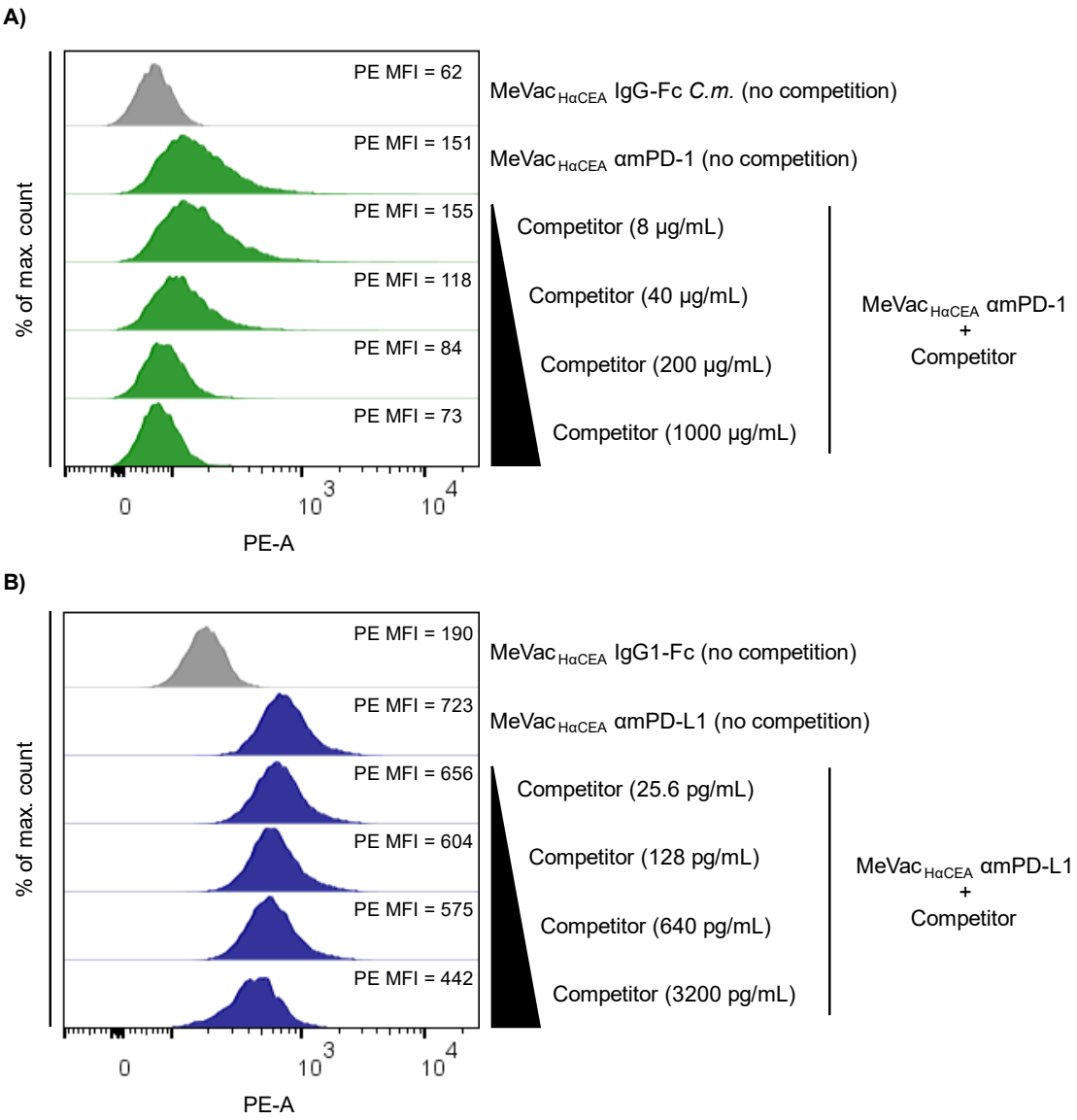

Figure 16. Binding of MeVac-derived αmPD-1 and αmPD-L1 to the respective target molecules. **(A)** Binding of αmPD-1 to murine PD-1. Splenocytes were freshly isolated from C57BL/6 mice and stimulated with 10 ng/mL PMA and 500 ng/mL ionomycin for 72 h to induce PD-1 expression. Subsequently, the splenocytes were incubated with 10 µL clarified lysate from Vero-αHis cells infected with MeVac$_{HαCEA}$ αmPD-1. When indicated, a commercial anti-mouse PD-1 antibody (clone J43) was added as competitor (10 µL of 5-fold dilutions, starting at the stock concentration of 1 mg/mL). Incubation with clarified lysates from Vero-αHis cells infected with MeVac$_{HαCEA}$ IgG-Fc *C.m.* served as negative control. **(B)** Binding of αmPD-L1 to murine PD-L1. MC38-hCD46$_{[lenti]}$ cells were infected with MeVac eGFP (MOI = 3) to induce PD-L1 expression. After 48h, the cells were incubated with 10 µL clarified lysate from Vero-αHis cells infected with MeVac$_{HαCEA}$ αmPD-L1. When indicated, a commercial anti-human/mouse PD-L1 antibody (Atezolizumab) was added as competitor (10 µL of 5-fold dilutions, starting at the stock concentration of 3.2 ng/mL). Incubation with clarified lysates from Vero-αHis cells infected with MeVac$_{HαCEA}$ IgG1-Fc served as negative control. **(A-B)** After incubation for 30 min, the cells were stained with a PE-labelled anti-HA tag antibody to detect MeVac-derived αmPD-1 (A) or αmPD-L1 (B) bound to target cells. Histograms depict the distribution of PE signal intensity in the live cell population as analyzed by flow cytometry. The PE median fluorescence intensity (PE MFI) of live cells is indicated per condition. **(B)** One representative of two independent experiments is shown.

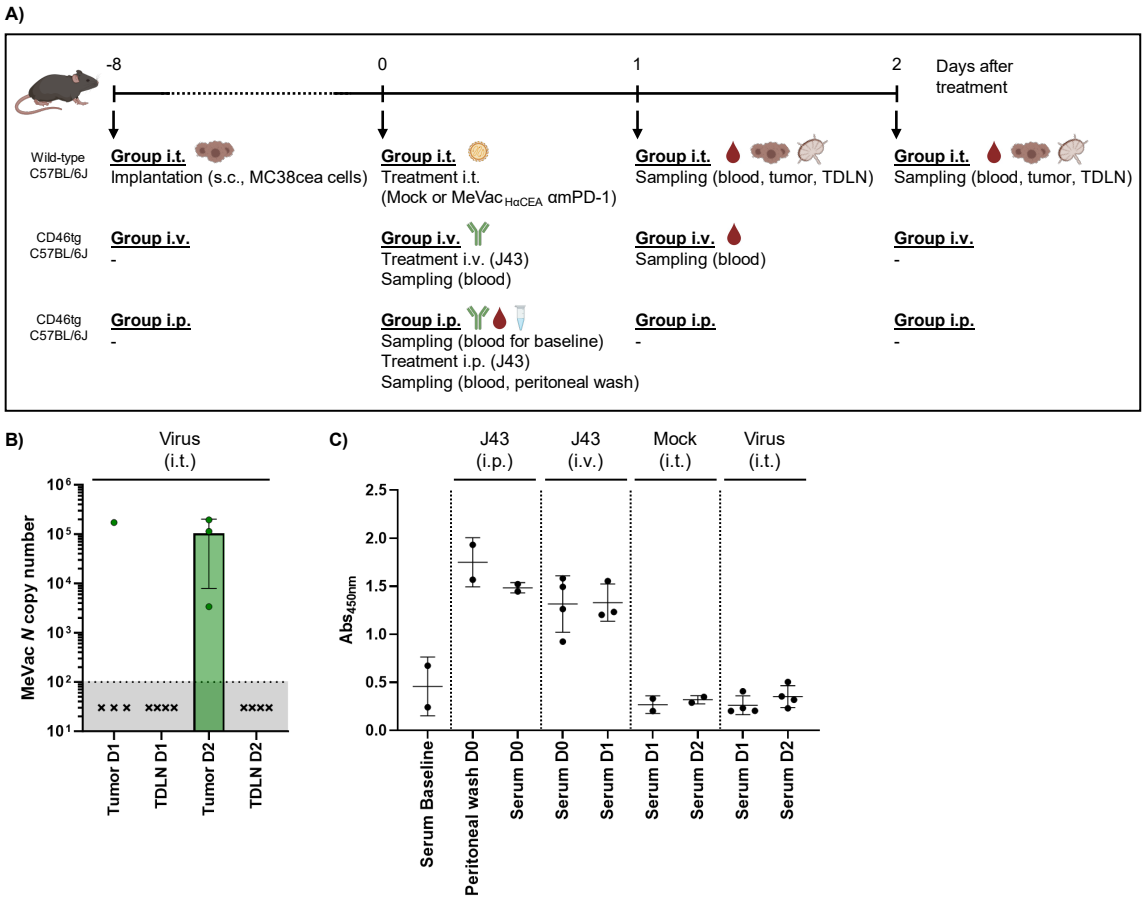

Figure 17. Detection of intratumoral MeVac *N* mRNA and systemic αmPD-1 antibody/scFv-Fc molecule. **(A)** Experiment schematic (created with BioRender.com). Mice were allocated to intratumoral (i.t.), intravenous (i.v.), or intraperitoneal (i.p.) treatment groups. i.t.: 1x10^6 MC38cea cells were implanted subcutaneously into the flank of wild-type C57BL/6J mice (non-carrier MY II mice). After tumor establishment (average volume of 87 mm^3), mice were treated i.t. with 100 µL D-PBS (mock, n = 4 mice) or 1x10^6 ciu MeVac$_{HαCEA}$ αmPD-1 in 100 µL D-PBS (virus, n = 7 mice). i.v./i.p.: CD46tg mice (C57BL/6J background) received 100 µg anti-mouse PD-1 antibody (clone J43) in 200 µL D-PBS i.v. (n = 4 mice) or i.p. (n = 2 mice). I conduced the *in vivo* procedures and organ resection together with C. E. Engeland. **(B)** Total RNA was extracted from tumors and tumor-draining lymph nodes (TDLNs) resected 1 or 2 days after i.t. treatment. The mRNA in 2 µg (tumor samples) or 900 ng (TDLN samples) of total RNA was reverse transcribed and 1 µL cDNA was analyzed by qPCR with primers specific for MeVac *N*. Dots indicate MeVac *N* copy number per µL of cDNA for individual mice (mean of technical duplicates). Standard curve, amplification plots, and melt peak plots are shown in Figure S9. Bars and error bars (shown only if all samples have a signal above background) depict mean values and standard deviation of all mice per group. The assay's lower limit of detection (LLOD) was 10^2 MeVac *N* copies (horizontal dotted line) (see Methods). MeVac *N* copy numbers below 10^2 could not be determined and are shown as "x" in the grey area (range below the assay's LLOD). **(C)** Peripheral blood was collected before i.p. injection (baseline), 30 min after i.p. injection (D0), 5-10 min (D0) plus 24 h (D1) after i.v. injection, and 24 h (D1) or 48 h (D2) after i.t. injection. Blood was withdrawn from different mice per timepoint (i.t. group) or from the same mice per timepoint (i.v./i.p. groups) and centrifuged to obtain serum. One mouse (i.v. group) was sacrificed before the second blood collection due to morbidity. Peritoneal washes were collected 40 min after i.p. injection. The presence of anti-mouse PD-1 antibodies/scFv-Fc molecules in serum and peritoneal wash was determined by ELISA. Within a group, each dot shows the absorbance at 450 nm wavelength for a different mouse, as determined after stopping the ELISA enzymatic reaction. Horizontal bars and error bars: mean + standard deviation of all mice per group. Known concentrations of J43 were used as positive control (Figure S9 A).

4.3.4 Therapeutic Efficacy

To investigate the therapeutic potential of the novel viruses, R. Veinalde and I conducted an efficacy study in immunocompetent mice bearing subcutaneous MC38cea tumors treated intratumorally with carrier fluid (mock) or one of the MeVac variants (Figure 18). In this experiment, MeVac encoding αmPD-1, αmPD-L1, or control IgG1-Fc led to a statistically significant improvement in survival compared to mock treatment, with MeVac encoding αmPD-L1 conferring the longest median survival (Figure 18 B). However, there were no statistically significant differences in survival between mice treated with the control viruses and mice treated with the viruses encoding αmPD-1 or αmPD-L1. Although statistically non-significant, the trend towards prolonged survival in mice treated with MeVac$_{H\alpha CEA}$ αmPD-L1 compared to the MeVac$_{H\alpha CEA}$ αmPD-1 group is an interesting observation, since I would expect both viruses to mediate similar effects, as they encode immunomodulators targeting the same signaling axis. Regarding tumor growth, most mice receiving any of the virotherapies showed a decrease in tumor volume after treatment completion (Figure 18 C-G, Figure S10 A-E). Several tumors continued to regress, resulting in 40% to 50% of mice experiencing complete remissions in all virus-treated groups. In other mice from the virotherapy groups, tumor volume remained stable for up to two weeks, but tumor growth eventually resumed.

4.3.5 Protective Antitumor Immunity

To determine whether the mice experiencing complete tumor remissions developed systemic antitumor immunity, I rechallenged them with parental MC38 cells in the contralateral flank and determined the rates of secondary tumor rejection (Figure 18 A, Figure 19 A). All mice experiencing complete tumor remissions after treatment with MeVac$_{H\alpha CEA}$ αmPD-L1, MeVac$_{H\alpha CEA}$ αmPD-1, or MeVac$_{H\alpha CEA}$ IgG1-Fc, and 3 of 4 mice experiencing complete tumor remissions after treatment with MeVac$_{H\alpha CEA}$ IgG-Fc *C.m.* rejected secondary tumor engraftment, indicating establishment of protective and systemic antitumor immunity. As opposed to 16 of 17 rechallenged mice (94.1%), only 1 of 6 age-matched naïve mice (16.7%) rejected tumor engraftment, suggesting that protection from tumor engraftment is mainly driven by memory immune responses.

To gain insights into the specificity of the observed antitumor response, I stimulated splenocytes from the mice employed in the rechallenge experiment with MC38 cells *ex vivo* and measured the concentration of IFN-γ in culture supernatants 48 h afterwards (Figure 19 B). The data revealed higher IFN-γ secretion in cultures containing splenocytes from mice treated with MeVac encoding αmPD-1 or αmPD-L1 compared to naïve splenocytes, whereas the levels of IFN-γ in cultures containing splenocytes from mice treated with control viruses were similar to those from naïve controls. However, the differences were statistically non-significant.

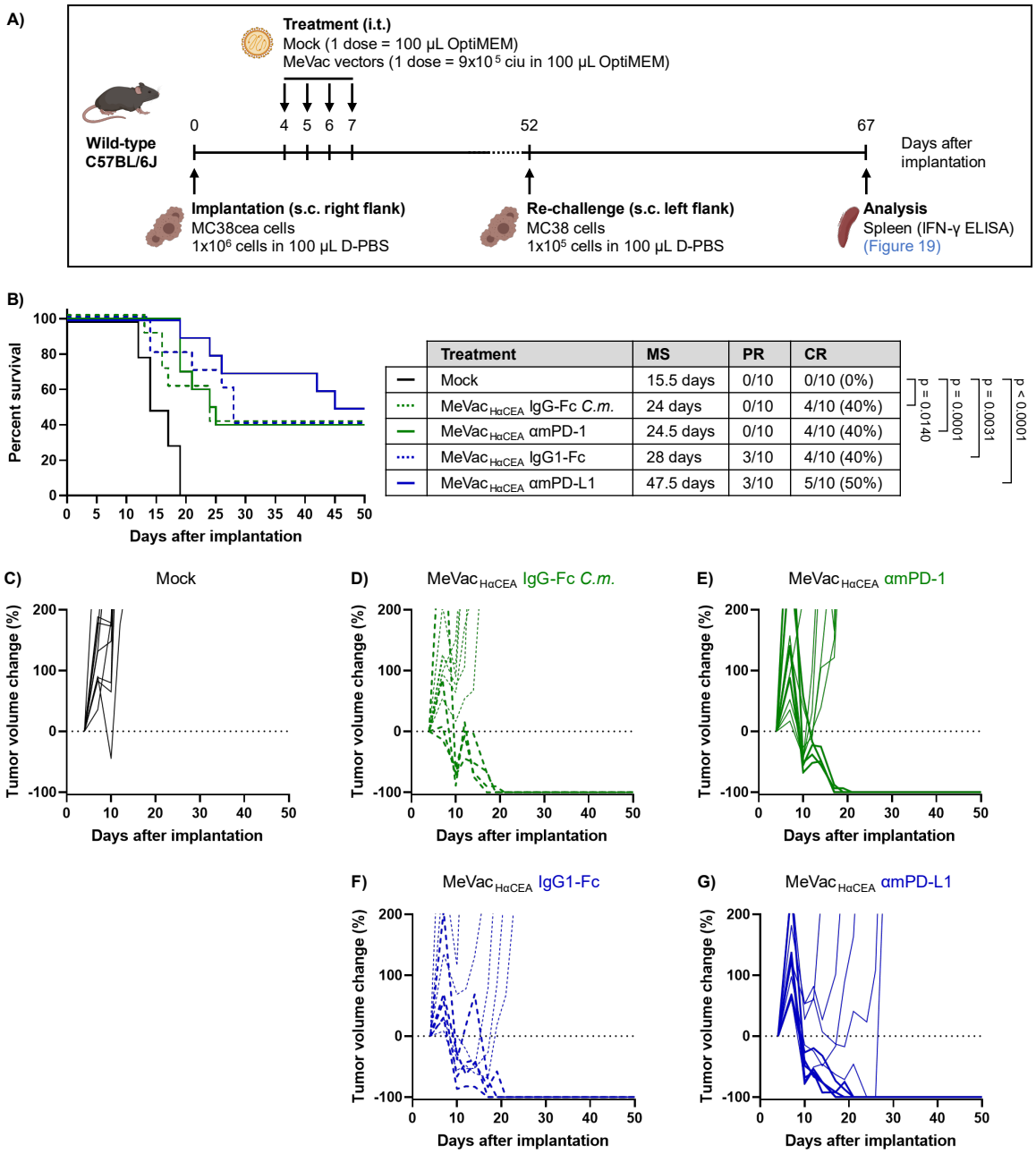

Figure 18. Therapeutic efficacy of MeVac encoding αmPD-1 scFv-Fc molecules, αmPD-L1 scFv-Fc molecules, or the corresponding Fc region in murine colon adenocarcinoma. (A) Experiment schematic (created with BioRender.com). 1x10^6 MC38cea cells were injected subcutaneously (s.c.) into the right flanks of wild-type C57BL/6J mice (from Janvier Labs). After tumor establishment (average volume of 45 mm^3), the mice received four intratumoral (i.t.) doses of OptiMEM (mock) or the respective MeVac (Schwarz strain) variant (9x10^5 ciu per dose) on consecutive days. Mice experiencing complete tumor remissions were re-challenged as shown in the diagram 52 days after initial tumor cell implantation and spleens were resected two weeks afterwards for immunological analysis (Figure 19). ciu: cell infectious units. **(B)** Kaplan-Meyer survival analysis with Mantel-Cox (log rank) test. The significance level (α) after Bonferroni's correction for 10 comparisons was 0.005. Median survival (MS) as well as rates for partial (PR) or complete (CR) remission of the primary tumor are indicated. Partial remission is defined as "tumor volume below pre-treatment tumor volume on two or more consecutive measurements". **(C-G)** Relative change in tumor volume as compared to pre-treatment tumor volume for individual mice. Y axis is cut at 200% for better visualization of PR and CR. Curves for mice experiencing CR are thicker. **(A-G)** n = 10 female mice per treatment group, 6-8 weeks-old on the day of tumor implantation. I conducted this experiment together with R. Veinalde.

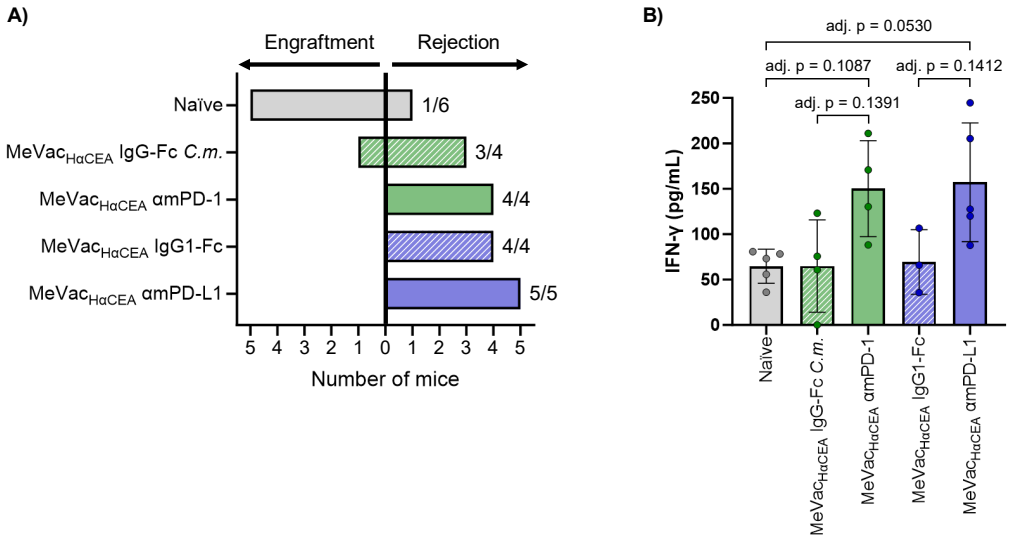

Figure 19. Antitumor immune memory upon virotherapy with MeVac encoding αmPD-1 scFv-Fc molecules, αmPD-L1 scFv-Fc molecules, or the corresponding Fc regions. Mice experiencing complete tumor remissions after treatment with the indicated MeVac variants (as shown in Figure 18) were re-challenged by injecting 1x10^5 MC38 cells subcutaneously into the contralateral flank 52 days after initial tumor cell implantation (Figure 18 A). Age-matched naïve mice (wild-type C57BL/6J mice, from Janvier Labs) were included as controls. **(A)** Rates for rejection of secondary tumor engraftment (in re-challenged mice) or primary tumor engraftment (in naïve mice) are shown. **(B)** Two weeks after re-challenge (or primary challenge in naïve mice), spleens were extracted. Splenocytes were stimulated *ex vivo* with mitomycin-C-treated MC38 cells at a 30:1 splenocyte to tumor cell ratio plus 20 U/mL murine IL-2. After 48 h, culture supernatants were collected and the concentration of murine IFN-γ in the supernatants was determined by ELISA. Dots represent values for individual mice. Bars indicate mean values of all mice within a treatment group and error bars show standard deviation. Data were analyzed using one-way ANOVA with Tukey's correction for multiple comparisons. All possible pairwise comparisons were included in the analysis. Multiplicity-adjusted p values (adj. p) for the pairwise comparisons that are referred to in the text are shown. **(A-B)** I conducted the re-challenge (day 52, Figure 18 A) together with R. Veinalde. The organ resection (day 67, Figure 18 A) and the ELISA were conducted by myself.

Taken together, these results suggest that, despite conferring similar therapeutic efficacy, treatment with MeVac encoding PD-1 or PD-L1 blockades induces a more potent tumor-specific immune memory response than treatment with control viruses. Moreover, the results from the splenocyte restimulation study show that the antitumor immune response triggered by MeVac$_{HαCEA}$ αmPD-1 and MeVac$_{HαCEA}$ αmPD-L1 is not restricted to the xenogeneic antigen CEA, of human origin, but rather directed to endogenous antigens of the MC38 cell line.

4.4 Virotherapy Combined with PD-1/PD-L1 Immune Checkpoint Blockade in Murine PDAC

4.4.1 Contextualization – Aim – Hypothesis – Model System

Having assessed the combination of virotherapy with immune checkpoint blockade (ICB) in an immunogenic tumor model partly responsive to MeVac monotherapy (Figure 18), R. Veinalde and I assessed whether immunologically cold tumors such as pancreatic ductal adenocarcinoma (PDAC), largely refractory to both monotherapies, would respond to the combination treatment.

To address this question and investigate correlates of response, we conducted efficacy and immunophenotyping studies in tumor-bearing immunocompetent mice. As tumor model, we chose FC1245 cells, which derive from PDAC developed in a *LSL-Kras*$^{G12D/+}$ *LSL-Trp53*$^{R172H/+}$ *Pdx-1-Cre* triple-mutant mouse (KPC mouse) [164]. Since KPC mice develop murine PDAC with features similar to those of human PDAC, such as intraepithelial neoplasia and exclusion of effector T cells, we reasoned that the KPC-derived FC1245 cell line is a relevant preclinical PDAC model (see Discussion).

Aiming at facilitating the clinical translation of our study and at resembling a prospective clinical trial for PDAC patients at the National Center for Tumor Diseases (Heidelberg, Germany), we chose a treatment strategy compliant with good manufacturing practices. This strategy consisted in combining systemic ICB with local virotherapy by treating mice intraperitoneally with J43, a commercially available anti-mouse PD-1 antibody, and intratumorally with MV-NIS, a clinical-grade MeVac of the Edmonston B-derived strain that encodes the human sodium/iodide symporter (NIS) and has proven safe in clinical trials [157,188,189] [xiv].

4.4.2 Therapeutic Efficacy

Before my involvement in this project, R. Veinalde evaluated the efficacy of the combination treatment (MV-NIS i.t. plus anti-PD-1 i.p.) and the corresponding monotherapies in mice bearing subcutaneous FC1245 tumors expressing human CD46 as MeVac entry receptor (FC1245-hCD46) (Figure 20). In this model, the combination therapy significantly prolonged survival compared to ICB monotherapy or mock treatment (Figure 20 B). Improved survival was also observed in mice treated with the combination approach compared to virotherapy alone, but the difference was statistically non-significant after correcting the significance threshold for multiple comparisons. Several mice receiving MV-NIS alone or in combination with anti-PD-1 experienced delayed tumor growth, which

[xiv] R. Veinalde initiated this project and I developed it further until publication (see Contributions and Figure Legends). In this chapter, I describe the results from experiments that I conducted as well as the results from an efficacy study performed by R. Veinalde. Moreover, I summarize additional work of R. Veinalde when required.

was sustained for a longer time in mice treated with the combination therapy compared to MV-NIS monotherapy (Figure 20 C-F; Figure S11). However, tumor growth eventually resumed in all mice, leading to no complete cures.

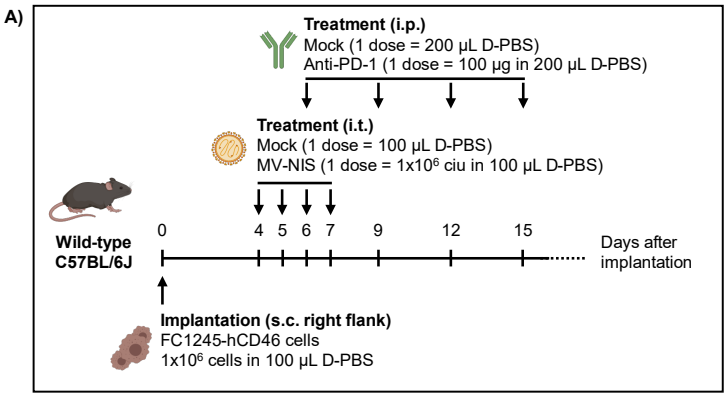

Treatment group	Treatment (i.t.)	Treatment (i.p.)
Mock	D-PBS	D-PBS
Anti-PD-1	D-PBS	Anti-PD-1
MV-NIS	MV-NIS	D-PBS
MV-NIS + Anti-PD-1	MV-NIS	Anti-PD-1

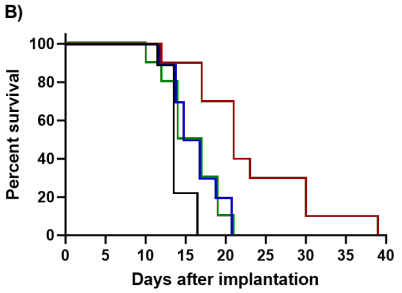

Treatment	MS	PR
Mock	14 days	0/10
Anti-PD-1	15.5 days	0/10
MV-NIS	16 days	0/10
MV-NIS + Anti-PD-1	21 days	1/10

p = 0.0008
p = 0.0050
p = 0.0011

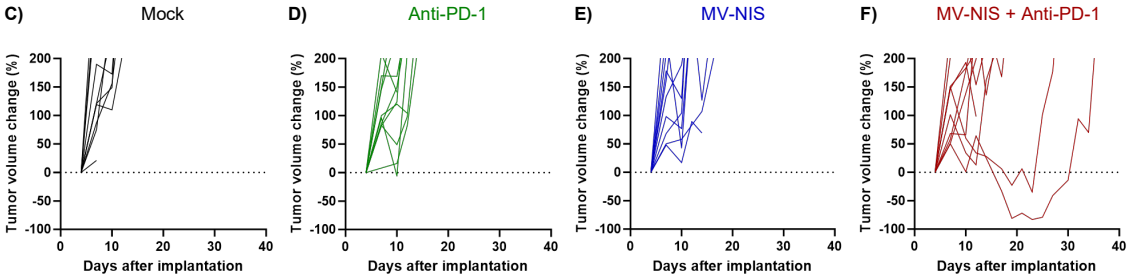

Figure 20. Efficacy of MV-NIS and/or anti-PD-1 treatment in murine pancreatic ductal adenocarcinoma. **(A)** Experiment schematic (created with BioRender.com). 1x10^6 FC1245-hCD46$_{[lenti]}$ cells were injected subcutaneously (s.c.) into the right flanks of wild-type C57BL/6J mice (from Janvier Labs). After tumor establishment (average volume of 75 mm^3), the mice were treated with four intratumoral (i.t.) doses of D-PBS (mock and anti-PD-1 groups) or MeVac$_{EdmB}$ encoding human sodium-iodide symporter (MV-NIS) (1x10^6 ciu per dose; MV-NIS and combination groups) on consecutive days. In addition, the mice received four intraperitoneal (i.p.) doses of D-PBS (mock and MV-NIS groups) or anti-PD-1 antibody (clone J43) (100 µg per dose; anti-PD-1 and combination groups) administered every three days starting on the day of third i.t. treatment. ciu: cell infectious units. **(B)** Kaplan-Meyer survival analysis with Mantel-Cox (log rank) test. The significance level (α) after Bonferroni's correction for 6 comparisons was 0.008. Median survival (MS) and rates for partial (PR) tumor remission are indicated. Partial remission is defined as "tumor volume below pre-treatment tumor volume on two or more consecutive measurements". **(C-F)** Relative change in tumor volume as compared to pre-treatment tumor volume for individual mice. Y axis is cut at 200% for better visualization of PR. **(A-F)** n = 10 female mice per treatment group, 6-8 weeks-old on the day of tumor implantation. This experiment was conducted by R. Veinalde.

4.4.3 Viral Gene Expression and Remodeling of the Tumor Microenvironment

To investigate whether the combined therapy reshapes the TME, R. Veinalde treated mice bearing subcutaneous FC1245-hCD46 tumors as detailed in Figure 21 A and resected tumors from all treatment groups at baseline (t0, before treatment), one week (t1), and two weeks (t2) after treatment onset. Subsequently, I analyzed viral gene expression in a selection of t1 tumor samples and characterized the immune environment of t1 and t2 tumors on the transcriptional level.

To assess viral gene expression, I quantified the levels of MV-NIS *N* mRNA (by RT-qPCR) in tumor samples resected at t1 from mock-treated mice as well as mice treated with MV-NIS monotherapy or MV-NIS plus anti-PD-1. Notably, in tumor samples from mice receiving MV-NIS, either alone or in combination with systemic anti-PD-1, I detected between $2x10^5$ and $2x10^6$ MV-NIS *N* copies per µL of cDNA (Figure 21 B; Figure S12). Importantly, these copies correspond to virus-derived mRNA, and not to virus genomes. With these results, I confirm the presence of virus-derived mRNA in tumor samples four days after the last virus dose, which is indicative of viral replication *in vivo*.

To gain insights into the local immunomodulatory effects of the combination treatment, I analyzed the expression of immune-related genes in tumor samples from all treatment groups using the Nanostring nCounter mouse immunology panel. Overall, using the advanced analysis package from the nSolver 4.0 software, I noticed a unique gene expression profile in tumors resected at t1 from mice receiving the combination treatment compared to t1 tumor samples from mice receiving mock treatment or a monotherapy. Hierarchical clustering supported this finding by showing that, at t1, the gene expression profile of combination-treated tumors clusters independently from that of mock-treated tumors and most monotherapy-treated tumors (Figure S13 A, left). However, this was not the case at t2 (Figure S13 A, right). Next, aiming at conducting a more refined analysis, I normalized the raw Nanostring nCounter data using a two-step approach (see Methods) and conducted differential gene expression analysis of the normalized data using the DESeq2 Bioconductor software package (see Methods) [xv]. The normalization process yielded relative log expression (RLE) plots with median close to zero across all samples, indicative of successful data normalization (Figure S13 B,C).

[xv] Initially, I analyzed the Nanostring data using the differential gene expression algorithm provided in the advanced analysis package of the nSolver 4.0 software. The results from this analysis have been published (doi: 10.3389/fimmu.2022.1096162). In my doctoral thesis, I show the results from a more refined analysis conducted with R using a script that I wrote after publishing the study.

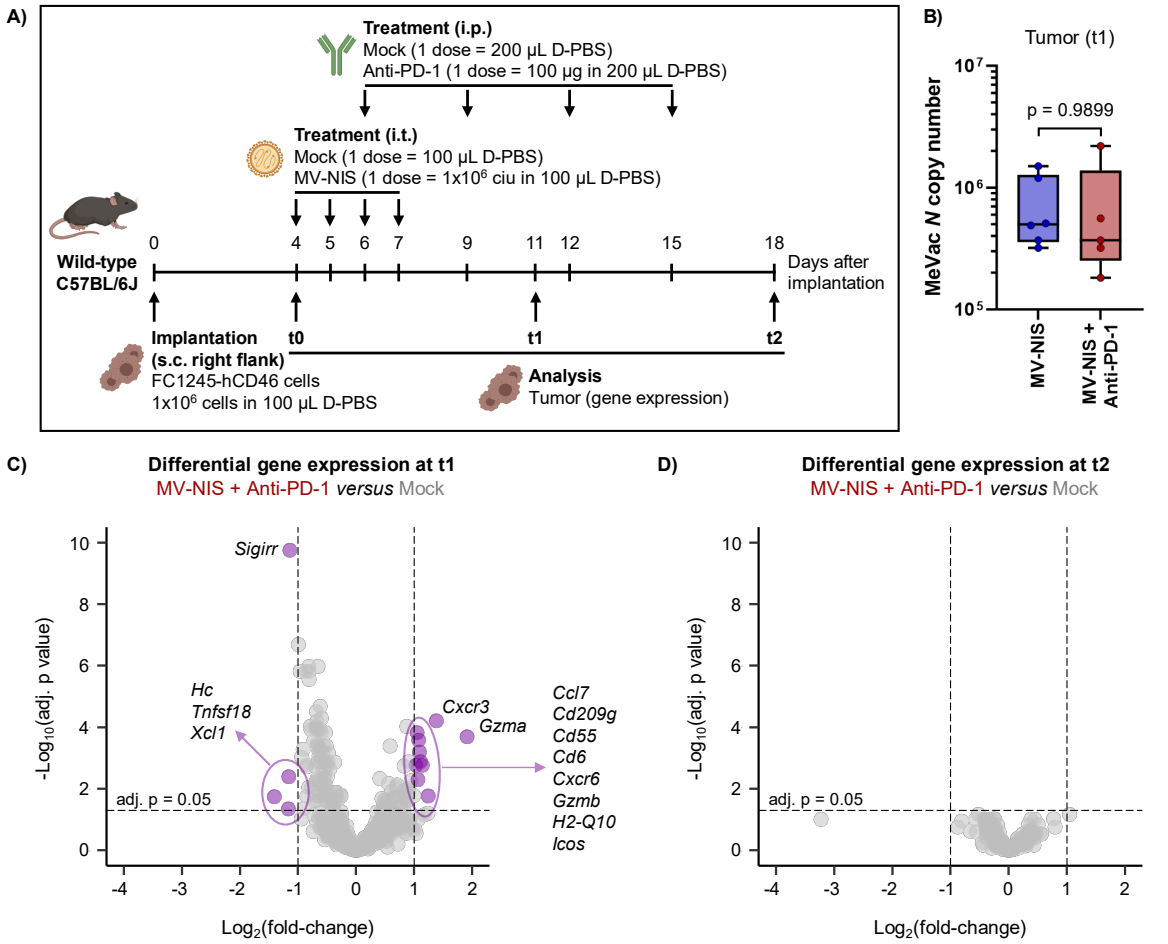

Figure 21. Detection of intratumoral MeVac *N* mRNA and tumor immune gene expression profiling after treatment of murine pancreatic ductal adenocarcinoma with MV-NIS and/or anti-PD-1. (A) Experiment schematic (created with BioRender.com). 1x10^6 FC1245-hCD46$_{[lenti]}$ cells were injected subcutaneously (s.c.) into the flank of wild-type C57BL/6J mice (from Janvier Labs). After tumor establishment (average volume of 65 mm^3), the mice were treated as shown in the schematic. At t0 (baseline, before treatment), t1, or t2, tumors were resected and total RNA was extracted. n = 3 – 4 mice per timepoint and treatment group. ciu: cell infectious units. **(B)** Experiment conducted with tumors resected at t1 from mice receiving mock treatment, MV-NIS monotherapy, or combination therapy. The mRNA in 1 µg of total tumor RNA was reverse transcribed and 1 µL cDNA was analyzed by qPCR with primers specific for MeVac *N*. Dots indicate MeVac *N* copy number per µL of cDNA for individual mice (mean of technical duplicates). Standard curve, amplification plots, and melt peak plots are shown in Figure S12. Boxes indicate the 25th, 50th, and 75th percentiles of all mice per group. Whiskers depict minimum and maximum values. The assay's lower limit of detection was 10^5 MeVac *N* copies (see Methods). All samples from virus-treated or combination-treated animals were above this limit. Data were analyzed with two-tailed unpaired t test. **(C-D)** Tumor immune gene expression was assessed using the mouse immunology panel from the Nanostring nCounter system. Data normalization and differential gene expression analysis of the normalized data were conducted with R using the Bioconductor packages EDASeq, RUVSeq, DESeq2, and Enhanced Volcano. Volcano plots depicting the differential expression of 561 genes between tumors from combination-treated mice and mock-treated mice at t1 **(C)** and t2 **(D)** are shown. Each dot represents one gene (most grey dots cannot be distinguished because the values overlap). A gene was considered to be differentially expressed if its expression showed a $|\log_2(\text{fold-change})| > 1$ between both groups and the difference had a $-\log_{10}(\text{adj. p value}) > 1.3$ (*i.e.* adj. p value < 0.05). Genes fulfilling these criteria are shown in purple. adj. p value: multiplicity-adjusted p value. **(A-D)** The *in vivo* procedures, organ resection, and RNA extraction were conducted by R. Veinalde. I performed the qPCR and differential gene expression analysis.

Evaluating the results from the DESeq2 analysis, I observed that monotherapy with MV-NIS or anti-PD-1 was insufficient to reshape the immune gene expression signature of PDAC at either timepoint (Figure S14). Consistently, I did not identify significant differences in immune gene expression between the two monotherapies at t1 or t2 (Figure S14). In contrast, at t1, the combined therapy resulted in a statistically significant intratumoral upregulation of several immune genes compared to mock treatment (Figure 21 C). Among those, the genes with the highest $\log_2$(fold-change) are involved in complement regulation (*Cd55*), antigen presentation (*H2-Q10*), costimulation (*Icos*), immune cell migration (*Ccl7*, *Cxcr3*, *Cxcr6*), lymphocyte activation (*Cd6*), and cytotoxic effector functions (*Gzma*, *Gzmb*). Some of these genes (*Cd55*, *Cd6*, *Cxcr6*, *Gzma*) were also significantly upregulated (adj. $p < 0.05$, $\log_2$[fold-change] > 1) at t1 in tumors from mice receiving the combination therapy compared to anti-PD-1 monotherapy, but not compared to virotherapy alone (Figure S14). Notably, the significant differences in immune gene expression identified at t1 were transient and not observed at t2 (Figure 21 D, Figure S14).

Overall, these data are in line with the efficacy experiment shown in Figure 20 and suggest that the transient remodeling of the tumor immune environment mediated by the combination treatment might contribute to the significantly prolonged survival detected in this treatment group compared to the mock and anti-PD-1 groups (Figure 20 B). Moreover, the transient nature of this remodeling might allow tumors to resume growth at later stages, as observed by R. Veinalde in 2 of 10 mice receiving the combination therapy (Figure 20 F).

To gain insights into TME remodeling at the cellular level, R. Veinalde conducted flow cytometry analysis of tumors resected at t0, t1, and t2, focusing on NK cells and T cells. However, she did not identify major differences in the intratumoral abundance of these cell populations across treatment groups (data not shown, published in [165]). In a subsequent experiment, we investigated the local distribution of T cells (as stained with the T cell lineage marker CD3) at the tumor site by immunohistochemistry (IHC). To that aim, R. Veinalde and I treated mice bearing subcutaneous FC1245-hCD46 tumors as detailed in Figure 22 A and resected tumors for histological analysis at baseline (t0, before treatment), one week (t1), and twelve days (t2) after treatment initiation. Histology and IHC were conducted by A. Stenzinger and J. Leichsenring. At t1, we detected higher CD3(+) cell abundance in 2 of 4 tumors from virus-treated mice and in 2 of 4 tumors from combination-treated mice as compared to tumors from mock-treated mice or mice treated with anti-PD-1 monotherapy (Figure 22 B,C). As observed in the transcriptional study, this phenomenon was transient and lost at t2 (Figure 22 B). Notably, in tumor samples with > 20% CD3(+) stroma, most CD3(+) cells were located at the tumor margin (circumferential location). This might explain why R. Veinalde did not detect increased T cell abundance in virus-treated and combination-treated tumors in the flow cytometry study. For the flow cytometry study, tumor tissue devoid of adjacent

skin was employed, and therefore peritumoral cells might not have been analyzed, whereas tumor samples submitted to IHC analysis contained a piece of adjacent skin to define the tumor margin and therefore allowed assessment of peritumoral cells.

In summary, these histological findings lead me to conclude that virotherapy, either alone or in combination with anti-PD-1, promotes T cell recruitment to PDAC tumors, at least early after treatment, but the recruited cells do not infiltrate into the tumor mass.

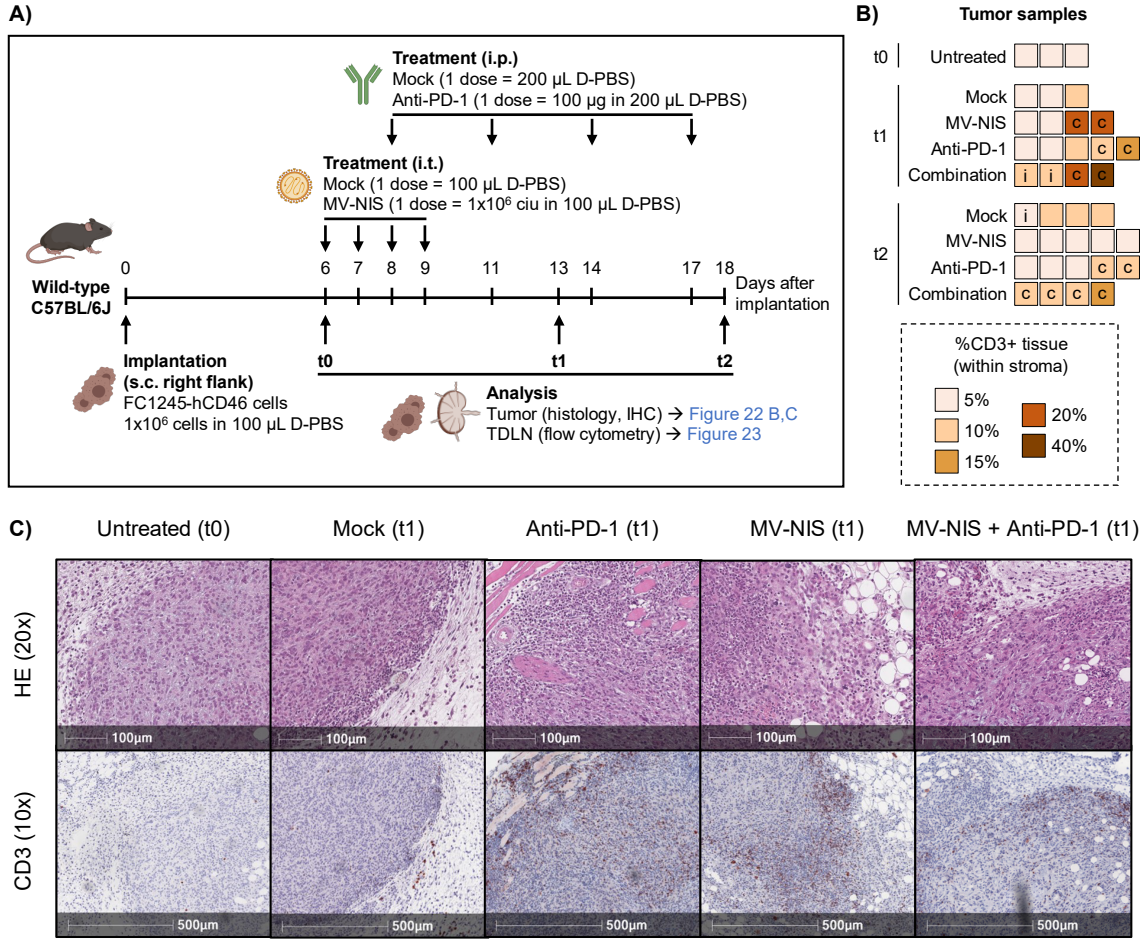

Figure 22. Histological assessment of murine pancreatic ductal adenocarcinoma after MV-NIS and/or anti-PD-1 treatment. (A) Experiment schematic (created with BioRender.com). 1x10^6 FC1245-hCD46$_{[lenti]}$ cells were injected subcutaneously (s.c.) into the flank of wild-type C57BL/6J mice (from Janvier Labs). After tumor establishment (average volume of 57 mm^3), the mice were treated as shown in the schematic. At t0 (baseline, before treatment), t1, or t2, tumors and tumor-draining lymph nodes (TLDNs) were resected. n = 5 mice per timepoint and treatment group (female, 6-8 weeks old on the day of tumor cell injection). ciu: cell infectious units. **(B)** Tumor sections were stained with hematoxylin/eosin (HE, refer to panel C) or an anti-mouse CD3 antibody. The percentage of CD3(+) tissue at the tumor stroma is shown, as determined by a pathologist following the guidelines from Rakaee *et al.* [182]. Each square corresponds to a section from a different tumor. c: circumferential (CD3[+] cells mainly located at the tumor margin); i: intratumoral (CD3[+] cells mainly located in the tumor mass). **(C)** Representative images of tumor sections stained with HE (top) or with an anti-CD3 antibody (bottom) are shown. Brown signal corresponds to CD3(+) cells. Scale bar: 100 µm (20x objective) or 500 µm (10x objective). **(A-C)** I conducted the *in vivo* procedures and organ resection together with R. Veinalde. Histology and immunohistochemistry were conducted by J. Leichsenring and A. Stenzinger.

4.4.4 Immunological Effects in Tumor-Draining Lymph Nodes

Following the cancer-immunity cycle, R. Veinalde and I hypothesized that, in addition to remodeling the TME, the combination treatment might also exert immune effects on TDLNs. To address this hypothesis, we analyzed the T cell compartment (by flow cytometry) of TDLNs resected at t0, t1, or t2 from the mice included in the histology experiment (Figure 22 A; Figure 23; Figure S15).

Overall, the total percentage of T cells within live cells remained stable across timepoints and treatment modalities (Figure 23 A), whereas the CD8(+) to CD4(+) T cell ratio decreased at t2 compared to the earlier timepoints (Figure 23 D). However, this decrease was not associated with any specific therapy, since it was detected in TDLNs from all treatment groups.

Despite no major shifts in T cell abundance, the memory phenotype of the T cell subpopulations differed between treatments. At t1, effector memory and central memory CD4(+) T cells were increased in TDLNs from the combination and MV-NIS groups compared to the anti-PD-1 and mock groups, with most differences being statistically significant (Figure 23 E,F). At the same timepoint, the naïve CD8(+) T cell population was increased in TDLNs from virus-treated mice but slightly decreased in TDLNs from combination-treated mice as compared to the other treatment groups (Figure 23 J). At t2, we detected higher abundance of CD4(+) and CD8(+) T cells with a central memory phenotype in TDLNs from mice receiving the combination therapy compared to either monotherapy (Figure 23 F,I).

Therefore, I conclude that virotherapy, either alone or in combination with anti-PD-1, modulates the memory phenotype of T cells in lymph nodes draining subcutaneous FC1245-hCD46 tumors.

4.4.5 Systemic Tumor-Specific and MeVac-Specific Immunity

To determine whether the combination treatment or the respective monotherapies elicit functional antitumor and antiviral immune responses at the systemic level in this very aggressive PDAC model, I treated mice bearing subcutaneous FC1245-hCD46 tumors as described in Figure 24 A and conducted IFN-γ ELISpot with splenocytes retrieved one week (t1) or thirteen days (t2) after treatment onset. Since MV-NIS was no longer commercially available, I performed this experiment with unmodified MeVac (Schwarz strain).

Consistent with virus exposure, I found reactivity to MeVac in splenocytes from MeVac-treated mice and mice treated with the combination approach (Figure 24 B, bottom panels). MeVac-specific immunity was detected at t1 and sustained at least until t2. Moreover, it was similar between both treatment groups, as shown by the comparable number of IFN-γ spot counts within a timepoint.

In agreement with the poor response of PDAC to ICB, anti-PD-1 monotherapy did not enhance systemic antitumor immunity at any timepoint compared to mock treatment. In contrast, at t1 splenocytes from mice receiving MeVac or the combination therapy reacted significantly stronger to FC1245-hCD46 cells than splenocytes from mock-treated mice or mice treated with anti-PD-1 alone (Figure 24 B, top left panel). This enhanced response was also detected at t2, although the differences to the mock and anti-PD-1 groups were no longer statistically significant (Figure 24 B, top right panel). Remarkably, within each timepoint, splenocytes from mice receiving MeVac monotherapy or combination treatment yielded similar IFN-γ spot counts in response to tumor cells, indicating that, in this model, systemic antitumor immunity is mainly mediated by virotherapy. As another interesting observation, in the MeVac and combination treatment groups I noticed a correlation between the strength of the antitumor immune response and the strength of the antiviral immune response, as most mice with higher tumor reactivity also showed a stronger MeVac-specific response (Figure S16).

To determine whether the antitumor response that I detected is independent of human CD46, expressed on FC1245-hCD46 cells, I conducted a similar animal experiment by treating mice bearing subcutaneous FC1245-hCD46 tumors with mock or the combination therapy and resecting spleens six days (t1) after treatment initiation for IFN-γ ELISpot (Figure S17 A). In this experiment, I assessed splenocyte reactivity to the implanted tumor cell line (FC1245-hCD46) and to the parental cell line (FC1245). Remarkably, while mock treatment did not elicit antitumor immunity, the combination treatment induced systemic IFN-γ responses against both cell lines (Figure S17 B). Within this treatment group, 3 of 4 mice developed a stronger response to FC1245-hCD46 cells than to the parental cell line, indicating that antitumor immunity was in part directed against the xenogeneic antigen human CD46. However, splenocytes from the same mice also reacted to parental FC1245 cells by yielding IFN-γ spot counts above baseline (baseline: 0-10 IFN-γ spot counts, as detected in cultures of splenocytes without stimulus [not shown]). These results show that antitumor immunity is not only directed against human CD46, but also against antigens endogenous to FC1245 cells.

All in all, I conclude that MeVac virotherapy, either alone or in combination with anti-PD-1, induces systemic antitumor and antiviral immunity in mice bearing subcutaneous PDAC, with antitumor immunity being not only directed against human CD46, but also against antigens expressed endogenously by FC1245 cells. Remarkably, as opposed to the local immune activation gene signature detected at t1 in tumors from combination-treated mice (Figure 21), systemic antitumor immunity is induced both upon MeVac monotherapy and combination treatment, and sustained for at least two weeks after treatment initiation. These results lead me to conclude that, in this setting, PD-1 blockade is dispensable for T cell priming but required at the periphery to support the cytotoxic effector function of the primed T cells.

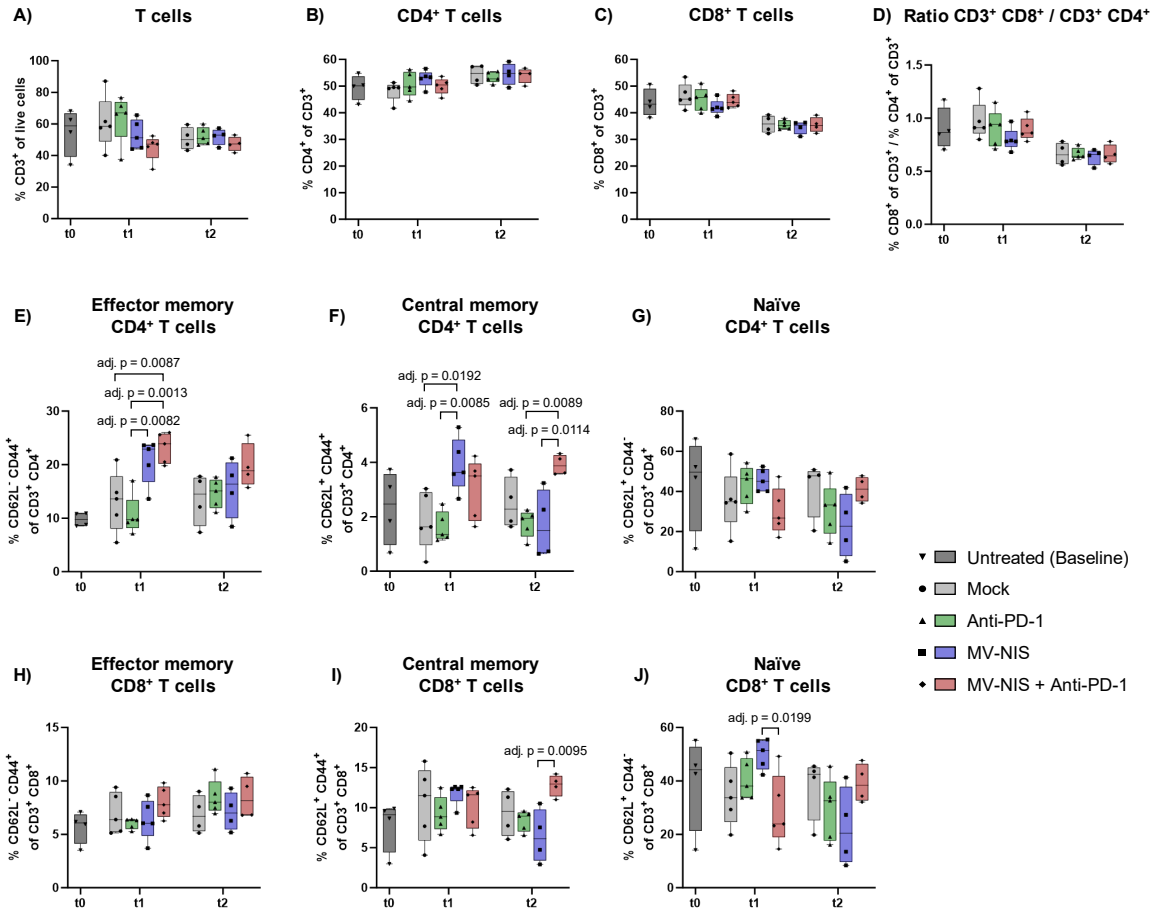

Figure 23. Flow cytometry of tumor-draining lymph nodes (TDLNs). The data refers to the experiment shown in Figure 22 A. TDLNs were resected, processed into single-cell suspensions, and analyzed by flow cytometry after staining with the following antibodies: PerCP-Cy5.5 anti-mouse CD3, APC anti-mouse CD8, APC-Cy7 anti-mouse CD4, PE anti-mouse CD44, and FITC anti-mouse CD62L. The gating strategy is shown in Figure S15. Percentage of CD3+ cells **(A)**, CD4+ cells **(B)**, CD8+ cells **(C)**, CD62L- CD44+ cells (effector memory) **(E, H)**, CD62L+ CD44+ cells (central memory) **(F, I)**, and CD62L+ CD44- cells (naïve) **(G, J)** from the indicated parental populations as well as ratios of CD8+ to CD4+ cells **(D)** from the CD3+ live cell population are shown. **(A-J)** Within a plot, symbols represent values for individual mice. Boxes indicate the 25th, 50th, and 75th percentiles per group. Whiskers depict minimum and maximum values. One group is shown for t0. Four groups are shown for t1 and t2. Data from t1 and t2 were analyzed using one-way ANOVA for each timepoint with Tukey's correction for multiple comparisons. adj. p: multiplicity-adjusted p value. I conducted the flow cytometry experiment together with R. Veinalde.

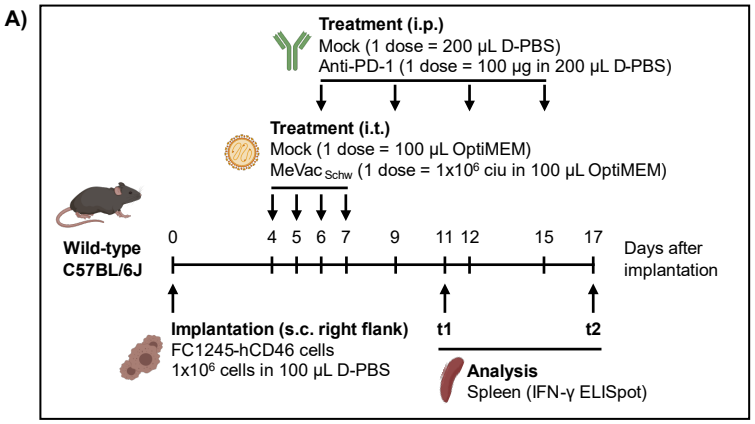

Treatment group	Treatment (i.t.)	Treatment (i.p.)
Mock	OptiMEM	D-PBS
Anti-PD-1	OptiMEM	Anti-PD-1
MeVac	MeVac Schw	D-PBS
MeVac + Anti-PD-1	MeVac Schw	Anti-PD-1

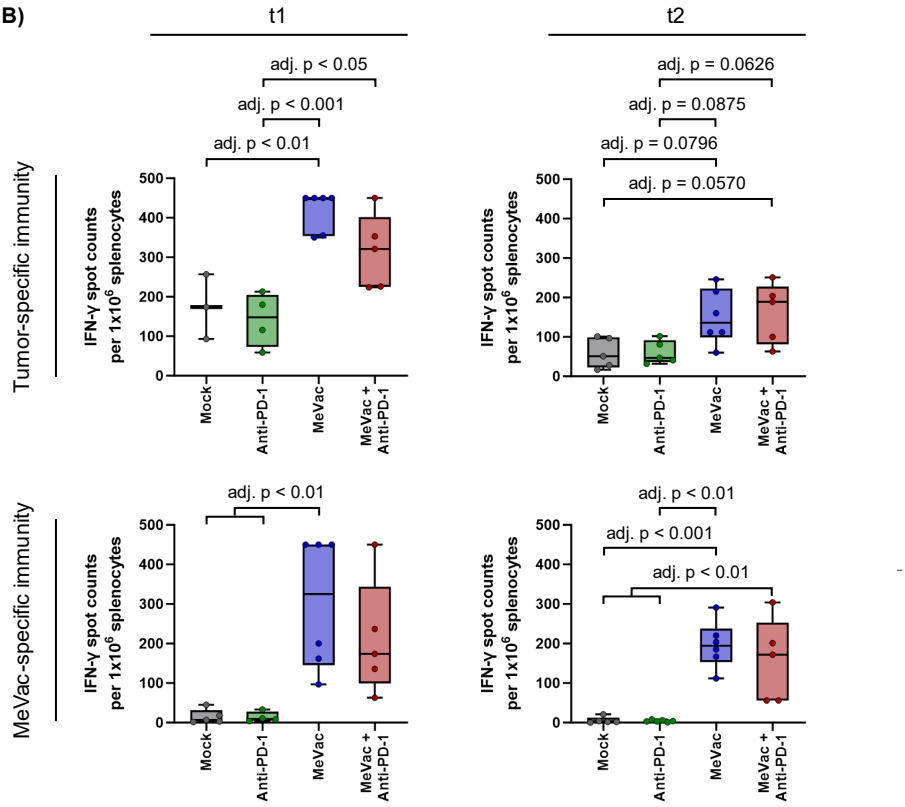

Figure 24. Systemic antitumor and antiviral immunity after treatment of murine pancreatic ductal adenocarcionma with MeVac and/or anti-PD-1. (A) Experiment schematic (created with BioRender.com). 1x10^6 FC1245-hCD46$_{[lenti]}$ cells were injected subcutaneously (s.c.) into the flank of wild-type C57BL/6J mice (from Janvier Labs). After tumor establishment (average volume of 75 mm^3), the mice were treated as shown in the schematic. Seven (t1) or thirteen (t2) days after treatment onset, the spleens were resected. n = 5-6 mice per timepoint and treatment group (female, 6-8 weeks-old on implantation day). Purity grade of MeVac$_{Schw}$: clarified lysates from infected Vero cells; ciu: cell infectious units. **(B)** IFN-γ ELISpot. 1x10^6 splenocytes were co-cultured with FC1245-hCD46 cells at a 10:1 splenocyte to tumor cell ratio. In parallel, 5x10^5 splenocytes were exposed to 7 µg/mL MeVac bulk antigen (t1) or incubated with MeVac$_{Schw}$ at an MOI of 0.5 (t2). As positive and negative controls, 5x10^5 splenocytes were stimulated with 10 µg/mL Concanavalin A or cultured without stimulation, respectively (not shown). After 40 h, IFN-γ ELISpot was conducted. IFN-γ spot counts are shown. Saturated wells were set to 450 counts. Within a group, each symbol corresponds to one mouse (mean of technical triplicates). Boxes show the 25th, 50th, and 75th percentiles. Whiskers depict minimum and maximum values. Data were analyzed using one-way ANOVA with Tukey's correction for multiple comparisons. Mice with less than 250 spot counts in the positive control are not shown and were excluded from the statistical analysis. adj. p = multiplicity-adjusted p value.

4.5 CD46tg Mice as a Novel Model of MeVac Virotherapy

4.5.1 Contextualization – Aim – Hypothesis – Model System

The experiments described in the previous sections of my thesis were conducted in wild-type mice, which do not express the MeVac entry receptor. In these studies, engineered tumor cells were the only cells susceptible to the virus. However, the clinical scenario is different, since in humans the MeVac entry receptor is expressed on all nucleated cells.

I hypothesize that, in a clinical setting, viral transduction of non-malignant cells during MeVac oncolytic virotherapy contributes to the remodeling of the TME and the induction of antitumor immunity. In agreement with this hypothesis, *ex vivo* studies ongoing in our research group show that MeVac reshapes the phenotype of human immune cells towards a mature, proinflammatory, and antitumoral state [190–192] [xvi]. Preliminary data suggest that these effects can be triggered by receptor-mediated fusion of MeVac particles with target immune cells [xvii].

Based on these data, I reasoned that a preclinical model in which all cells are susceptible to the virus would be more suitable for the *in vivo* study of MeVac oncolytic immunotherapy. To establish this model, I obtained CD46-transgenic (CD46tg) mice, which express human CD46 as MeVac entry receptor on all nucleated cells at levels comparable to humans[174,175]. These mice were purchased from the Jackson Laboratory (Table 11) and bred as well as genotyped at our research facilities (see 3.2.5.1 and 3.2.5.2). As an initial characterization, I conducted MeVac transduction experiments *ex vivo* using cells retrieved from wild-type and CD46tg mice. Next, I investigated the immunomodulatory properties of oncolytic MeVac in this refined mouse model.

4.5.2 MeVac Transduction of Cells from Wild-Type and CD46tg Mice

To compare MeVac transduction of hCD46(-) and hCD46(+) murine cells, I isolated cells from the bone marrow of wild-type and CD46tg mice, exposed them to MeVac eGFP (or mock treatment), and determined the percentage of eGFP(+) cells by flow cytometry 4 h, 24 h, 48 h, and 72 h after virus/mock inoculation (Figure 25). Given that eGFP molecules are present in the virus suspension used for inoculation (despite purification via ultracentrifugation), I employed eGFP signal as a surrogate for MeVac transduction. However, I could not employ it as a surrogate for viral replication, because I could not distinguish between eGFP molecules present in the virus suspension and eGFP molecules produced *de novo* during viral replication.

[xvi] In addition to the cited studies, M. S. C. Finkbeiner and L. Kuchernig (doctoral students in our group) are investigating the effects of MeVac on human monocyte-derived DCs and macrophages, respectively.
[xvii] Unpublished data from M. S. C. Finkbeiner (not shown).

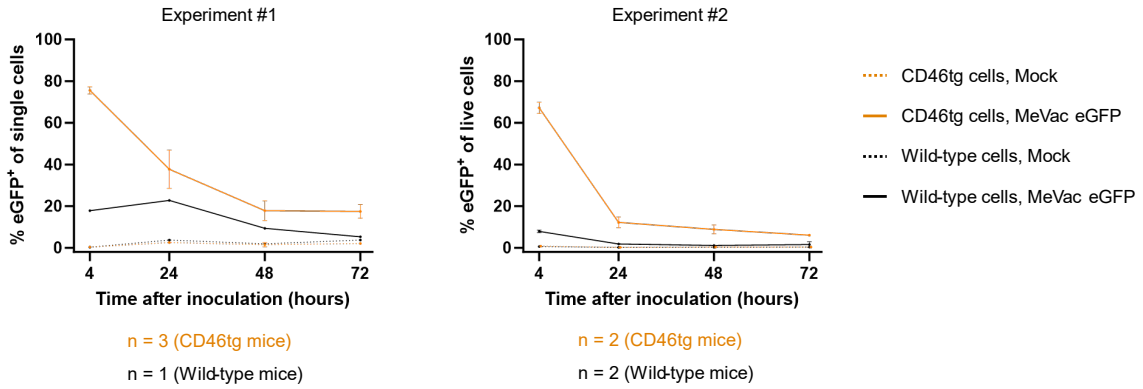

Figure 25. *Ex vivo* transduction of murine bone marrow cells with MeVac eGFP. Cells were isolated from the bone marrow of wild-type C57BL/6J mice or CD46tg mice (C57BL/6J background) and exposed to MeVac eGFP (MOI = 3) or medium (mock). At the indicated timepoints, the percentage of eGFP(+) cells within single or live cells was determined by flow cytometry. Data from conditions encompassing 2 or 3 mice are shown as mean (dots) + standard deviation (error bars, not visible for some data points). Data from conditions encompassing 1 mouse are depicted as single values without error bars. Two independent experiments conducted with cells from different mice are shown.

Throughout the experiments, I did not detect eGFP signal in mock controls, thus confirming the specificity of the eGFP signal detected in virus-exposed cultures. At the 4 h timepoint, I detected eGFP signal in 10% to 20% of the virus-exposed wild-type cell population, whereas the percentage of eGFP(+) cells was much higher (70% to 80%) in the virus-exposed CD46tg cell population (Figure 25). Given that the MeVac replication cycle has a duration of 24 h to 36 h [185], the signal detected at 4 h probably corresponds to eGFP molecules present in the virus suspension rather than eGFP produced *de novo* during viral replication. In this case, I consider that the detected eGFP signal corresponds to attachment (and perhaps entry) of eGFP(+) material to the cells. Detection of eGFP(+) cells in the virus-exposed wild-type cell population indicates that, at least in 10% to 20% of cells, the attachment (and potential entry) of eGFP(+) material is unspecific, *i.e.* independent of hCD46. Whether the eGFP(+) material consists of viral particles or extracellular vesicles co-purified with the virus (or both) remains unknown. The higher percentage of eGFP(+) cells in the virus-exposed CD46tg cell population compared to the virus-exposed wild-type cell population suggests that, at least in a fraction of CD46tg cells, the attachment (and potential entry) of eGFP(+) material to the cells is mediated by the interaction of MeVac H with hCD46. In this case, whether the attached eGFP(+) material consists of viral particles, extracellular vesicles, or both also remains unknown, since both viral particles and extracellular vesicles derived from virus-producer cells express MeVac H (and MeVac F) on the envelope/membrane.

Subsequent monitoring of the cultures at 24 h, 48 h, and 72 h after virus inoculation revealed different dynamics across two independent experiments. In experiment #1, I observed a gradual decrease in the percentage of eGFP(+) cells within the virus-exposed CD46tg cell population. This percentage remained stable at ca. 20% between the 48 h and the 72 h timepoints. In experiment #2, the percentage of eGFP(+) cells within the virus-exposed CD46tg cell population was drastically reduced from 70% (at 4 h) to 15% (at 24 h) and remained stable at this percentage thereafter, at least until the 72 h timepoint. As for the virus-exposed wild-type cell population, in experiment #1 the percentage of eGFP(+) cells remained stable at ca. 20% between the 4 h and the 24 h timepoint, and subsequently decreased to 5% – 10% at the later timepoints. In experiment #2, the percentage of eGFP(+) cells was almost negligible from the 24 h timepoint onwards. Whether the eGFP signal detected at the 24 h, 48 h, and 72 h timepoints corresponds to eGFP molecules already present in the virus suspension or to eGFP molecules produced *de novo* during viral replication remains unknown. Enhanced GFP (eGFP) is rather stable. Thus, it would not be surprising if the signal detected throughout the experiment, even at the 72 h timepoint, corresponds to eGFP molecules located inside viral particles or extracellular vesicles present in the initial virus suspension.

Whether the eGFP signal only corresponds to attachment of eGFP(+) material to the cells or also to entry remains unknown. Nevertheless, I expect eGFP(+) material (virus or vesicles) to have entered in ca. 20% of the virus-exposed CD46tg cells (the ones that are eGFP(+) at the 72 h timepoint), since I assume that virus/vesicle attachment would have been resolved by the 72 h timepoint, either by virus/vesicle detachment and degradation (eGFP[-] cells) or by virus/vesicle entry (eGFP[+] cells).

Overall, from this study I conclude that hCD46 expression on non-malignant murine cells improves the specific attachment of MeVac (and potentially of extracellular vesicles containing MeVac H) to the cells via the interaction of MeVac H with hCD46. Nevertheless, there is a certain degree of unspecific attachment. Further studies are required to assess whether the eGFP signal detected at the 4 h and 24 h timepoints corresponds to viral entry or only to attachment. In this regard, I plan to conduct similar experiments in the presence of antibodies blocking MeVac entry receptors (*e.g.* anti-hCD46 antibody) or of membrane fusion inhibitors (*e.g.* fusion inhibitory peptide [193]).

Viral replication should be analyzed by other means, for instance by comparing eGFP signal upon exposure to active and UV-inactivated viruses, or by assessing the levels of virus-derived mRNA in time course experiments. Towards this aim, I conducted a pilot experiment in which I analyzed the presence of MeVac *N* mRNA in hCD46(-) and hCD46(+) murine macrophages exposed to MeVac eGFP (Figure 26). The macrophages were derived from the bone marrow of wild-type or CD46tg mice (bone marrow-derived macrophages, BMDMs). Due to limited cell numbers, I only analyzed one timepoint which, based on the results from the MeVac growth curve experiments

(Figure 10 B,C), I chose to be 24 h after virus inoculation (one-step growth curves had shown that, in murine cells, the production of MeVac progeny peaks 36 h to 48 h after virus inoculation, at least in tumor cells; thus, I expected viral mRNA to reach its synthesis peak slightly earlier). Remarkably, by RT-qPCR, I found significantly higher levels of MeVac *N* mRNA in virus-exposed BMDMs from CD46tg mice compared to virus-exposed BMDMs from wild-type mice, both when performing absolute quantification (Figure 26 A) and when conducting relative quantification to account for inter-culture variability (Figure 26 B). However, whether the detected MeVac *N* mRNA corresponds to MeVac *N* mRNA synthesized *de novo* in BMDMs or to MeVac *N* mRNA molecules trapped in viral particles during virus passaging on Vero cells remains unknown. To answer this question, I plan to conduct time course experiments in the future.

Overall, although further studies are required, the experiments shown in my PhD thesis provide an initial indication that non-malignant murine cells expressing human CD46 react differently to MeVac exposure when compared to the hCD46(-) wild-type murine cell counterparts.

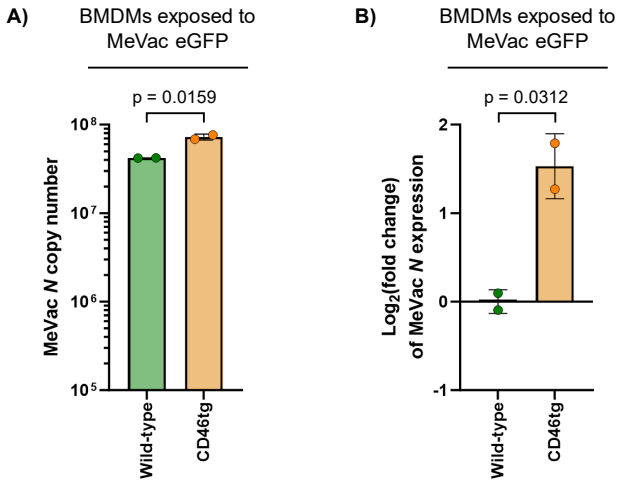

Figure 26. Detection of MeVac *N* mRNA in murine bone-marrow derived macrophages (BMDMs) inoculated with MeVac eGFP. Cells were isolated from the bone marrow of wild-type C57BL/6 mice (from Janvier Labs) or CD46tg mice (C57BL/6J background) and differentiated *ex vivo* into M0 macrophages. Upon differentiation, murine BMDMs were inoculated with MeVac eGFP (MOI = 3) or medium (mock). Total RNA was extracted from cells harvested 24 h after inoculation. The mRNA in 400 ng total RNA was reverse transcribed and 1 µL cDNA was analyzed by qPCR with primers specific for MeVac *N* and *Rpl13a*. Samples were assessed in technical triplicates per gene. Standard curve, amplification plots, and melt peak plots are shown in Figure S12. **(A)** Absolute quantification. Each dot shows the MeVac *N* copy number (mean of technical triplicates) per µL of cDNA in a BMDM culture. Bars depict mean values of biological duplicates (two mice per group). Error bars show standard deviation. The assay's lower limit of detection was 10^5 MeVac *N* copies (see Methods). All samples from virus-treated cultures were above this limit. Data were analyzed using two-tailed unpaired t test. **(B)** Relative quantification. MeVac *N* fold-change expression was calculated for each sample in relation to the mean of virus-exposed cultures from wild-type mice using the $2^{-\Delta\Delta Cq}$ method and *Rpl13a* as housekeeping gene. Dots indicate the $\log_2$(fold change) expression of MeVac *N* in individual cultures (mean of technical triplicates). Bars depict mean values of biological duplicates (two mice per group). Error bars show standard deviation. Data were analyzed using two-tailed unpaired t test.

4.5.3 Systemic Tumor-Specific and MeVac-Specific Immunity

To address whether MeVac therapy triggers systemic antitumor and antiviral immunity in the refined mouse model, I treated CD46tg mice bearing subcutaneous MC38-hCD46 tumors with carrier fluid (mock) or MeVac intratumorally and resected the tumors and spleens one week after treatment onset for flow cytometry analysis and IFN-γ ELISpot, respectively (Figure 27).

Flow cytometry analysis revealed increased T cell abundance in tumors from MeVac-treated mice compared to mock controls, although the difference was statistically non-significant (Figure 27 B, Figure S19). Regarding the systemic response, splenocytes from MeVac-treated mice reacted stronger to MeVac antigens and to MC38-hCD46 cells than splenocytes from mock-treated mice, as shown by the significantly higher number of IFN-γ spot counts (Figure 27 C,D). Importantly, splenocytes from MeVac-treated mice also reacted strongly to MC38 parental cells. This shows that the antitumor response triggered in these animals was not limited to human CD46. In fact, a response against human CD46 would be unexpected, since CD46tg mice should be tolerant to this molecule. Strikingly, splenocytes from MeVac-treated mice secreted IFN-γ in response to cells from a different tumor entity (B16 murine melanoma cells). However, the IFN-γ spot counts in these conditions were significantly lower than those detected upon splenocyte exposure to MC38 or MC38-hCD46 cells. Together, these results indicate that the antitumor immune response triggered in MeVac-treated mice was mainly directed against endogenous antigens of the tumor cells they had been exposed to. With this study, I conclude that MeVac therapy induces tumor-specific immunity (in my experiment mainly MC38-specific immunity) and MeVac-specific immunity at the systemic level in tumor-bearing CD46tg mice.

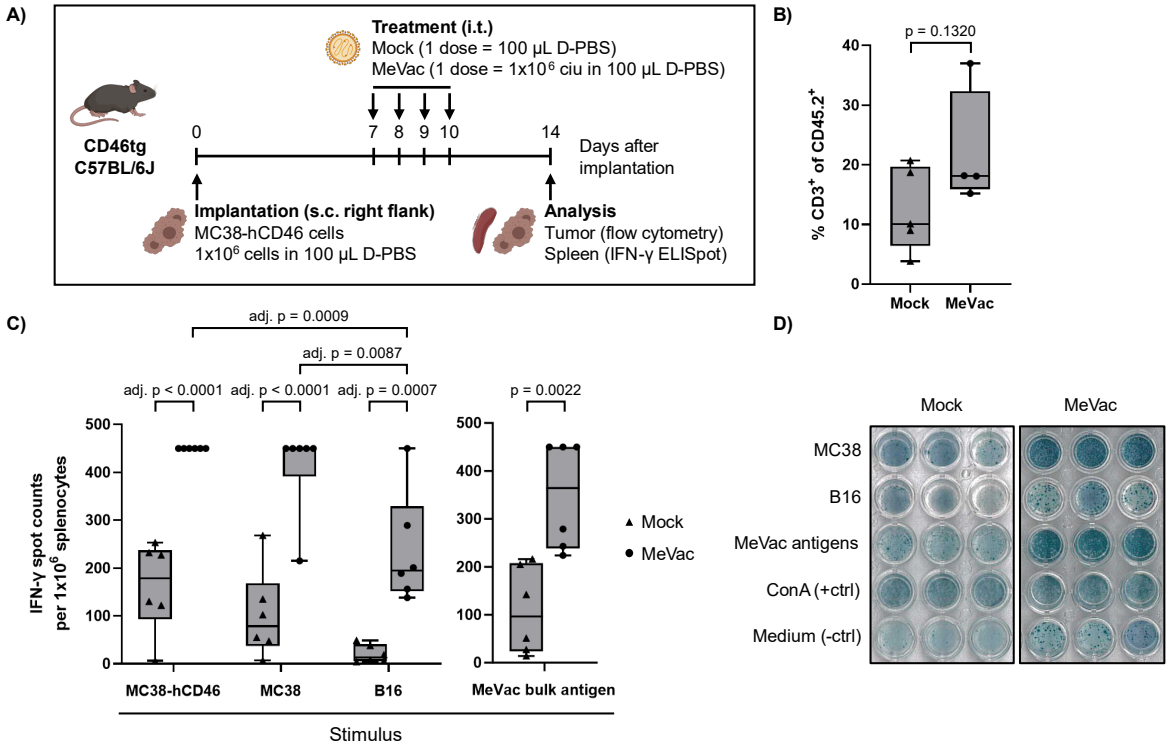

Figure 27. Systemic antitumor immunity and intratumoral T cell abundance in tumor-bearing CD46tg mice treated with MeVac virotherapy. (A) Experiment schematic (created with BioRender.com). 1x10^6 MC38-hCD46$_{[pCAG\text{-}SMAR]}$ cells were injected subcutaneously (s.c.) into the flank of CD46tg mice (C57BL/6J background). After tumor establishment (average volume of 117 mm^3), the mice received four intratumoral (i.t.) doses of D-PBS (mock) or purified MeVac$_{Schw}$ (1x10^6 ciu per dose) on consecutive days. One week after treatment initiation, tumors and spleens were resected for downstream analyses. n = 6-7 mice per treatment group (mock: 2 females, 4 males; MeVac: 3 females, 4 males). ciu: cell infectious units. **(B)** Tumors were dissociated and analyzed by flow cytometry after staining with PerCP-Cy5.5-conjugated anti-mouse CD45.2 and AF700-conjugated anti-mouse CD3 antibodies. The gating strategy is shown in Figure S19. The percentage of CD3(+) cells within the CD45.2(+) live cell population is shown for individual mice (1 dot = 1 mouse). Boxes indicate the 25th, 50th, and 75th percentiles per treatment group. Whiskers depict minimum and maximum values. Data were analyzed using two-tailed unpaired t-test. Tumors from three MeVac-treated mice and one mock-treated mouse (not shown) were excluded from the statistical analysis because less than 10000 single cells were recorded. **(C)** IFN-γ ELIspot. 1x10^6 splenocytes were co-cultured with MC38-hCD46$_{[pCAG\text{-}SMAR]}$, MC38, or B16 tumor cells at a 10:1 splenocyte to tumor cell ratio or incubated with 10 µg/mL MeVac bulk antigen. As positive and negative controls, 1x10^6 splenocytes were stimulated with 10 µg/mL Concanavalin A (ConA) or cultured without stimulation, respectively (not shown). After 40 h, IFN-γ ELISpot was conducted. IFN-γ spot counts of 6 mice per treatment group are shown. Saturated wells were set to 450 counts. Within a group, each symbol corresponds to one mouse (mean of technical triplicates). Boxes show the 25th, 50th, and 75th percentiles. Whiskers depict minimum and maximum values. Data were analyzed using two-tailed unpaired t test (splenocyte cultures stimulated with MeVac bulk antigen) or one-way ANOVA with Šidák's correction for multiple comparisons (splenocyte cultures stimulated with tumor cells). For one-way ANOVA, only pairwise comparisons of interest were analyzed, those being (i) cultures from mock-treated mice *versus* cultures from MeVac-treated mice exposed to the same stimulus, (ii) cultures from MeVac-treated mice exposed to a given tumor cell type *versus* cultures from the same mice exposed to another tumor cell type, and (iii) cultures from mock-treated mice exposed to a given tumor cell type *versus* cultures from the same mice exposed to another tumor cell type. adj. p values < 0.05 are shown. One MeVac-treated female mouse (not shown in the plots) was excluded from the statistical analysis because < 250 spots were counted in the positive control. adj. p = multiplicity-adjusted p value. **(D)** IFN-γ ELISpot images for one representative mouse per treatment group are shown.

4.5.4 Immunophenotyping Studies

Following up on the findings from the previous section, I was then interested in understanding the molecular mechanisms underlying MeVac-mediated systemic antitumor immunity. I hypothesized that the initial effects of local MeVac therapy, such as TME remodeling, might be decisive to induce antitumor immunity.

To gain insights into the remodeling of the tumor immune environment mediated by local MeVac therapy, I treated CD46tg mice bearing B16-hCD20-hCD46 tumors with carrier fluid (mock) or MeVac encoding a control molecule (MeVac IgG-Fc *C.m.*). I employed a B16-derived model because B16 tumors have a more immunosuppressed TME than MC38 tumors. Thus, I consider that B16 tumors are more suitable to address the immunological remodeling of the TME. At baseline (t0, before treatment), three days (t1), or one week (t2) after treatment onset, I resected tumors for gene expression profiling and histological assessment as well as TDLNs and spleens for flow cytometry analysis of the T cell compartment (Figure 28 A).

To analyze tumor immune gene expression, I used the Nanostring nCounter mouse immunology panel. Data analysis with the advanced analysis package from the nSolver 4.0 software revealed different gene expression signatures between mock-treated tumors and virus-treated tumors at t1 and t2, with most (at t1) and all (at t2) gene expression profiles from virus-treated tumors clustering independently from those of mock-treated tumors (Figure S20). At t1, the unique immune gene expression pattern of virus-treated tumors was associated with upregulation of genes involved in the type I IFN response and in MHC-I antigen presentation, as compared to mock-treated tumors (Figure S20 A). At t2, MeVac-treated tumors showed upregulation of genes involved in MHC-I and MHC-II antigen presentation, T cell receptor signaling, and lymphocyte activation, as compared to mock-treated tumors (Figure S20 B).

To conduct a more refined analysis, I normalized the raw Nanostring nCounter data in a two-step process (see Methods) and performed differential gene expression analysis of the normalized data using the DESeq2 Bioconductor software package (see Methods). The normalization approach resulted in relative log expression (RLE) plots with median close to zero in all samples, indicative of successful data normalization (Figure S21). Evaluating the results from the DESeq2 analysis, I found that, in the tumor, virotherapy induced statistically significant upregulation of genes involved in the innate antiviral immune response at t1, and in innate and adaptive immune responses at t2, with $\log_2$(fold change) values above 1.5 as compared to mock treatment (Figure 28 B,C).

In detail, and consistent with virus sensing, MeVac-treated tumors showed upregulation of *Ddx58* and *Ifih1* at t1, which encode the cytosolic receptors RIG-I and MDA-5, major sensors of RNA viruses

(Figure 28 B) [194]. Signaling through these receptors results in IRF3 and IRF7 activation, which are responsible for the transcription of genes encoding type I IFNs. Importantly, the gene encoding IRF7 (*Irf7*) showed the largest fold-change upregulation in virus-treated mice compared to mock controls. Type I IFNs trigger the type I IFN response, which leads to transcription of interferon-stimulated genes (ISGs). At t1, viral treatment led to upregulation of genes involved in this response (*Stat2*) as well as upregulation of numerous ISGs, including the above-mentioned genes *Ddx58*, *Ifih1*, *Irf7*, and *Stat2*. Other ISGs were also upregulated, namely (i) *Bst2* (at t1), the protein product of which (tetherin) is known to restrict MeV spread by inhibiting syncytia formation [195], (ii) *Ifi35* (at t1), which encodes a negative regulator of RIG-I [196], and (iii) *Ifi204* (at t2), which encodes a cytosolic DNA sensor [197] (Figure 28 B,C). Except for *Ifi204*, the upregulation of genes associated with virus sensing and type I IFN signaling was transient and not detected at t2 (Figure 28 C).

Differential gene expression analysis at t2 revealed upregulation of several genes involved in antigen processing and presentation in virus-treated tumors compared to mock controls, including genes encoding immunoproteasome subunits (*Psmb9*), MHC-II molecules (*H2-Aa*, *H2-Ab1*, *H2-Eb1*), the invariant chain involved in the assembly of MHC-II complexes (*Cd74*), and the MHC-II transactivator protein (*Ciita*) (Figure 28 C). At this timepoint, MeVac-treated tumors also showed upregulation of genes involved in immune cell migration (*Ccl5*, *Ccl8*, *Ccl24*, *Cxcl9*), T cell activation and differentiation (*Il12rb1*), T cell exhaustion (*Cd274*, encoding PD-L1), and cytotoxic responses (*Gzma*, *Gzmb*, *Prf1*) (Figure 28 C). In fact, *Gzma* and *Gzmb* were already upregulated at t1 (Figure 28 B), indicating the presence of cytotoxic responses at both early and late timepoints of the therapy.

Importantly, these findings are in agreement with concepts that I addressed in previous sections of the thesis, such as (i) the hypothesis that intratumoral upregulation of specific chemokines is an immunological determinant of MeVac therapeutic efficacy (see 4.2) and (ii) the hypothesis that MeVac therapy benefits from combination with ICB (see 4.3 and 4.4).

Consistent with the pro-inflammatory gene signature that I identified by gene expression analysis, histological and immunohistochemical assessment of tumor sections in collaboration with T. Poth revealed increased peritumoral inflammation as well as increased peritumoral and intratumoral CD3(+) cell abundance in tumors from virus-treated mice compared to baseline samples and mock controls (Figure 29). These observations, which were made both at t1 and t2, support the notion that MeVac virotherapy promotes T cell recruitment to the tumor margin (*e.g.*, Figure 29 G) and T cell infiltration into the tumor bed (*e.g.*, Figure 29 F).

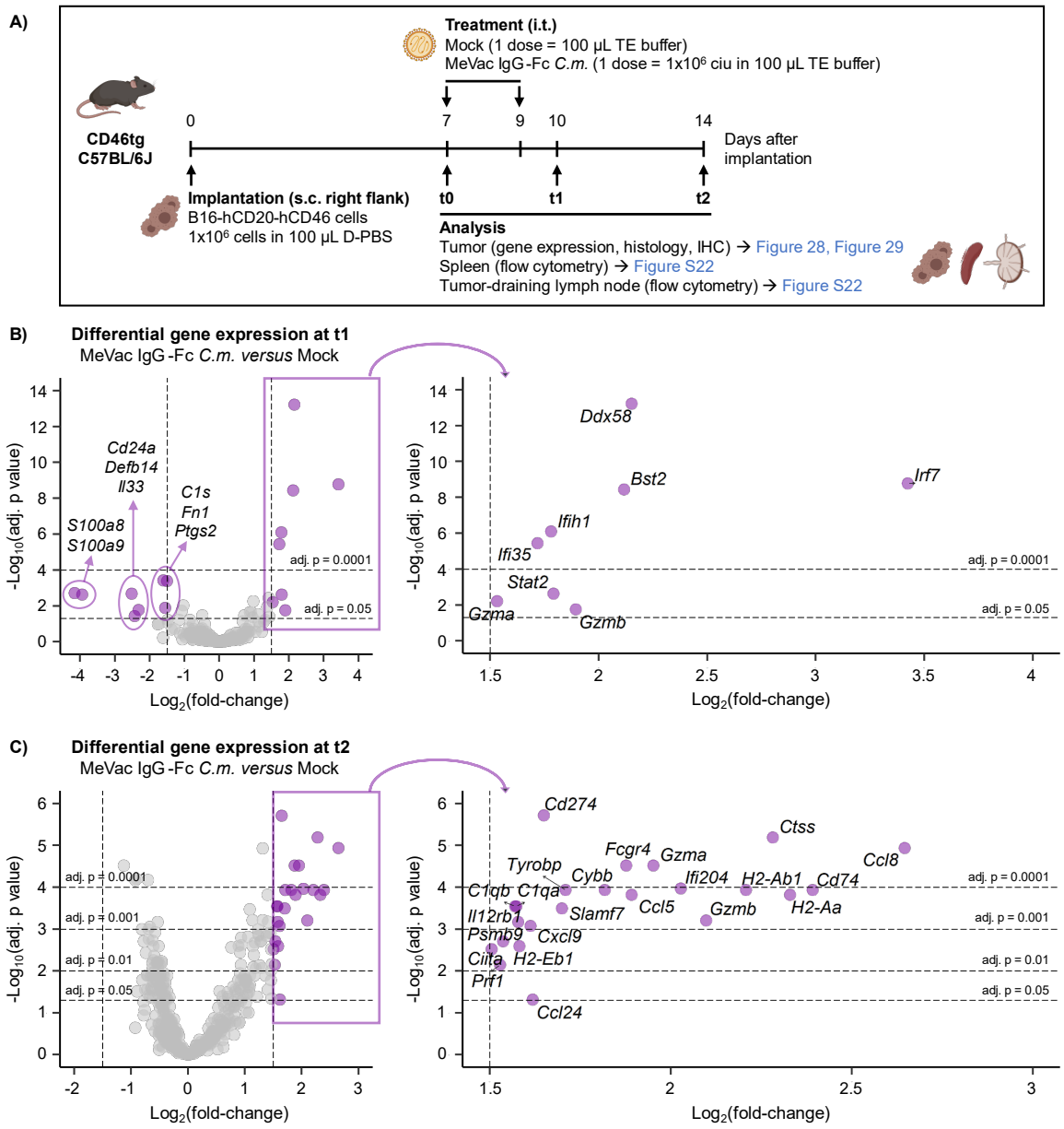

Figure 28. Tumor microenvironment remodeling after MeVac treatment of tumor-bearing CD46tg mice. **(A)** Experiment schematic (created with BioRender.com). 1x10^6 B16-hCD20-hCD46$_{[pCAG-SMAR]}$ cells were injected subcutaneously (s.c.) into the flank of CD46tg mice (C57BL/6J background). After tumor establishment (average volume of 114 mm^3), the mice were treated intratumorally (i.t.) as shown. Tumors, spleens, and tumor-draining lymph nodes (TDLNs) were resected at t0 (baseline, before treatment), t1, or t2. Tumors were sectioned as follows: ½ for flow cytometry (not shown, data not conclusive due to technical challenges), ¼ for gene expression analysis, and ¼ for histology. n = 6-7 mice per timepoint and treatment group (t0: 5F/1M; t1: 3F/3M per group; t2: 6F/1M [mock] or 5F/2M [virus]). F: female, M: male. **(B-C)** Tumor immune gene expression was assessed using the mouse immunology panel from the Nanostring nCounter system, employing 25 ng total tumor RNA as input. Data normalization and differential gene expression analysis were conducted with R using the Bioconductor packages EDASeq, RUVSeq, DESeq2, and Enhanced Volcano. Volcano plots depicting the differential expression of 561 genes between tumors from virus-treated mice and mock-treated mice at t1 **(B)** and t2 **(C)** are shown. Each dot represents one gene (most grey dots cannot be distinguished because the values overlap). A gene was considered to be differentially expressed if its expression showed a $|\log_2(\text{fold-change})| > 1.5$ between both groups and the difference had a $-\log_{10}(\text{adj. p value}) > 1.3$ (*i.e.*, adj. p value < 0.05). Genes fulfilling these criteria are shown in purple.
adj. p: multiplicity-adjusted p value.

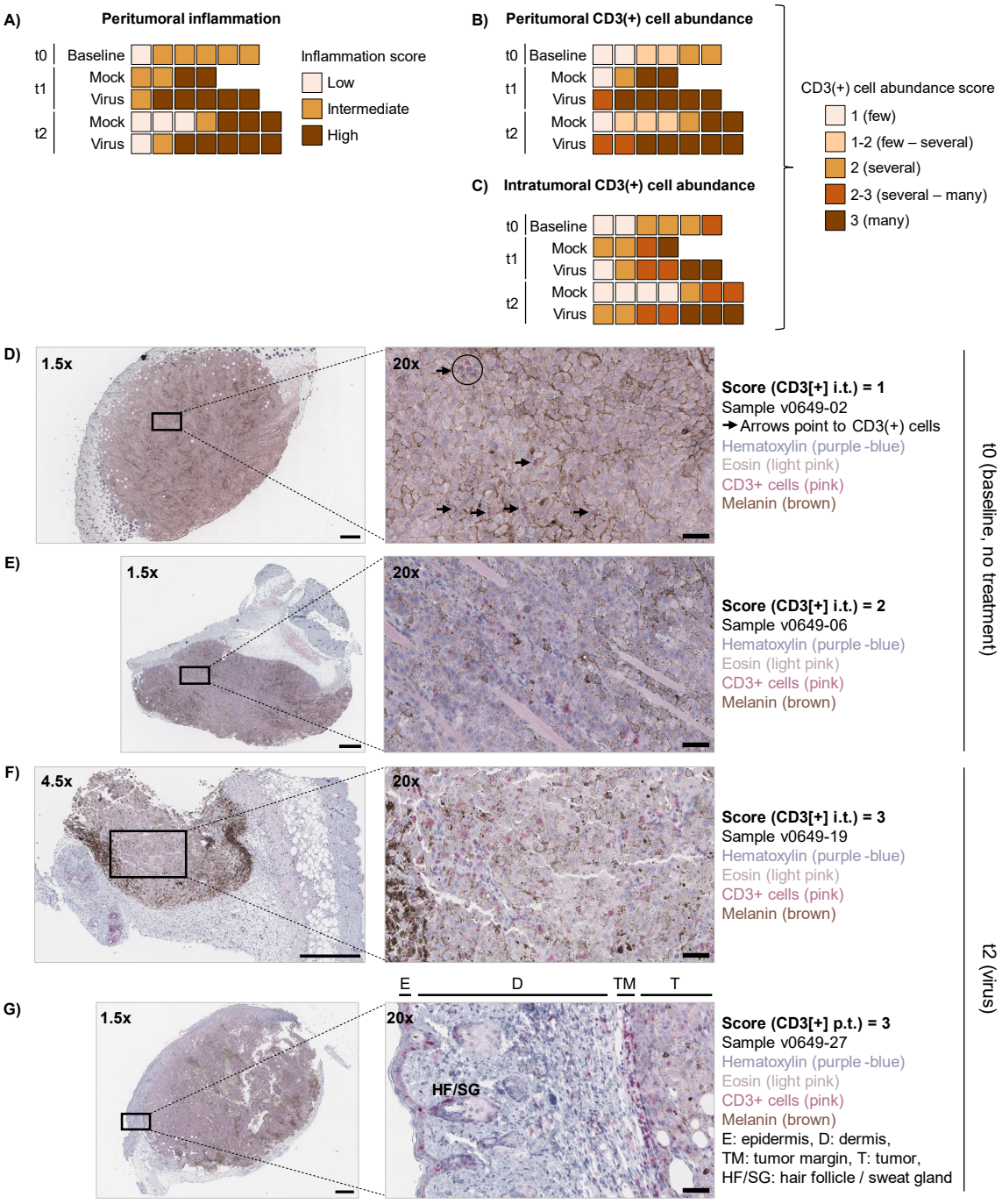

Figure 29. Tumor microenvironment remodeling after MeVac treatment of tumor-bearing CD46tg mice (continued). The data refers to the experiment described in Figure 28 A. **(A)** Tumor sections were stained with hematoxylin/eosin (HE). The degree of peritumoral inflammation was histologically assessed by a veterinarian pathologist and scored as low, intermediate, or high. Each square corresponds to a section from a different tumor. **(B-C)** Tumor sections were stained with HE and with an anti-mouse CD3 antibody. The abundance of peritumoral **(B)** and intratumoral **(C)** CD3(+) cells in each section was histologically assessed by a veterinarian pathologist and scored as 0 (none), 1 (few), 2 (several), or 3 (many). A total score of 1-2 indicates that some areas have a score of 1 and other areas a score of 2. The same reasoning applies to a total score of 2-3. Each square corresponds to a section from a different tumor. **(D-G)** Representative images of an intratumoral (i.t.) CD3(+) cell abundance score of 1 **(D)**, 2 **(E)**, or 3 **(F)** as well as a peritumoral (p.t.) CD3(+) cell abundance score of 3 **(G)** are shown. Images of the entire tumor slice were acquired at 40x with a Leica Aperio AT2 scanner. Scans were visualized with the QuPath software at 1.5x, 4.5x, or 20x, as indicated. **(A-D)** I conducted the *in vivo* procedures, organ resection, and QuPath analysis. Histology and IHC were performed by the team of T. Poth. Tumor slices were scanned by V. Eckel.

Regarding safety, flow cytometry analysis of spleens and TDLNs revealed that the T cell compartment remains stable in both organs at least until one week after treatment initiation, indicating no major systemic toxicities associated with the therapy (Figure S22). These data support the notion that MeVac virotherapy is safe and are in line with numerous vaccination studies reporting an excellent safety record for live-attenuated measles vaccines [108,198] as opposed to wild-type MeV, which induces transient lymphocyte depletion in blood and lymphoid tissues [199].

In summary, I conclude that local MeVac therapy in CD46tg mice is overall safe and remodels the TME towards a pro-inflammatory state characterized by induction of an antiviral response via the type I IFN pathway at early stages of the therapy as well as enhancement of antigen presentation, T cell recruitment, T cell activation, and cytotoxic effector functions at later stages. In follow-up studies, I will immunophenotype the TME with protein-based methods, such as ELISA or cytokine bead arrays, to elucidate whether the identified pathways remain differentially expressed on the protein level. Subsequently, I will address the relevance of these pathways, particularly that of the type I IFN response, to the overall efficacy of oncolytic MeVac therapy by gain and loss of function studies (see 5.4.5 and Outlook).

4.6 MeVac Spread in Patient-Derived *Ex Vivo* Tumor Slice Cultures

Besides studying MeVac oncolytic virotherapy *in vivo*, I also aimed at developing experimental models closer to the clinical setting. Towards this end, I established patient-derived gastrointestinal tumor cultures and assessed MeVac replication in this system. Given the large case numbers of colorectal cancer, I focused on this tumor entity because of sample availability.

To establish patient-derived tumor cultures preserving the three-dimensional tumor architecture, I obtained surgical samples of colorectal tumors, processed them into slices, and cultured them following the air-liquid interface (ALI) system (Figure 30 A). This culture approach preserves the patient-specific TME for at least six days and is therefore suitable to study viral replication and to profile cellular, molecular, and transcriptional changes in the TME at early stages of the therapy [200,201].

As initial proof-of-concept, I inoculated patient-derived tumor slices with MeVac eGFP or carrier fluid (control) and monitored eGFP signal 24 h, 48 h, and 72 h after virus inoculation as surrogate for viral gene expression. The surgical samples from patients #1 and #2 were only sufficient to derive two tumor slices, treated with MeVac eGFP and carrier fluid, respectively, whereas the surgical sample from patient #3 was larger and sufficient to obtain three slices per condition.

Remarkably, while there was no eGFP signal in control-treated slices, I detected eGFP fluorescence in virus-treated slices from two patients 24 h and 48 h (patient #3) or 72 h (patient #1) after virus inoculation (Figure 30 B, Figure S23). Interestingly, the eGFP signal was confined to a specific region of the tumor slice from patient #1, whereas it spread across the entire sample in the tumor slice from patient #3 (Figure 30 B). Although further studies are required, these results are an initial indication that patient-derived tumor slices support MeVac spread. However, despite these promising results, it should also be noted that I did not detect signs of virus spread in the virus-treated slice from patient #2 or in 2 of 3 slices from patient #3 (Figure S23) (see Discussion).

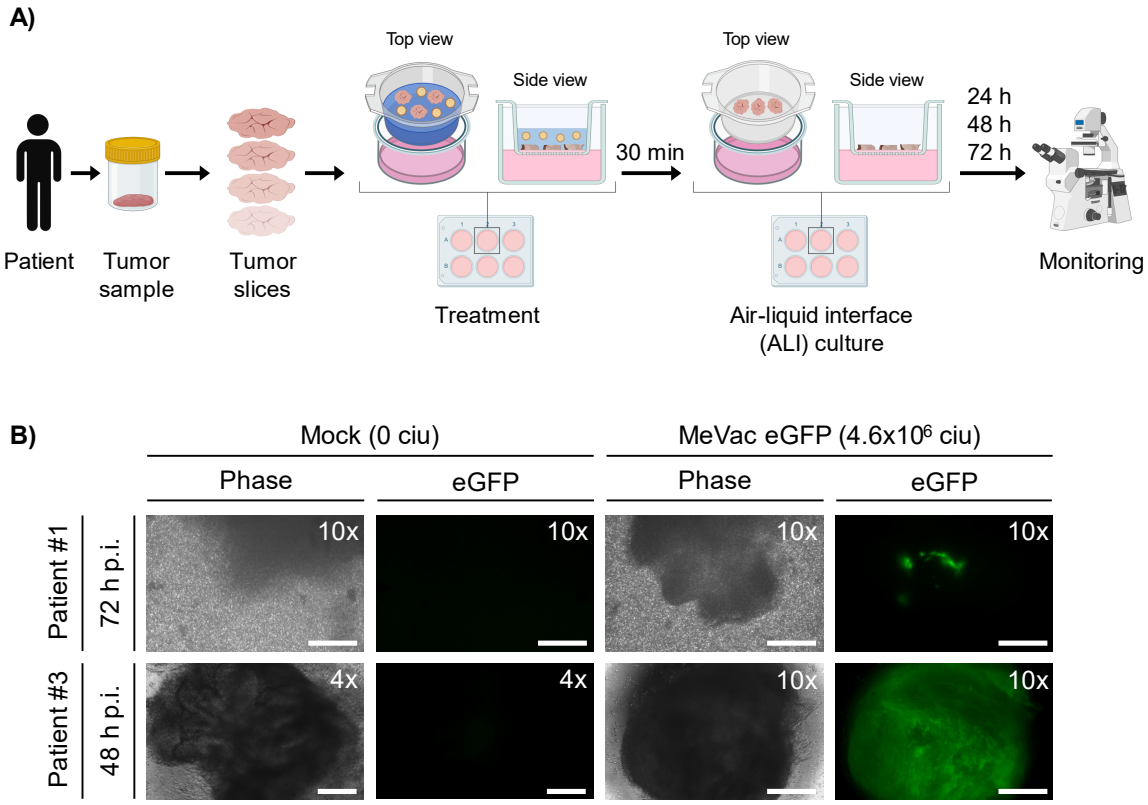

Figure 30. MeVac spread in patient-derived tumor slices. (A) Surgical colorectal cancer samples were obtained with the patient's informed consent and processed into slices. The slices were placed onto transwell membrane inserts (1-3 slices per insert), underlayered with culture medium (pink), and inoculated with $4.6x10^6$ ciu MeVac eGFP in 800 µL OptiMEM (blue). Exposure to OptiMEM alone was used as mock control. After 30 min, the inoculum was removed and the slices were cultured further on the membrane inserts, underlayered with fresh culture medium. This culture technique is referred to as air-liquid interface (ALI) culture system. **(B)** The ALI cultures were monitored by fluorescence microscopy 24 h, 48 h, and/or 72 h post inoculation (h p.i.). The slices were imaged with the phase contrast and eGFP fluorescence channels of a Nikon Eclipse TS2-FL microscope. Pictures were acquired using the NIS-Elements BR software (version 5.21.03, Nikon) and processed with ImageJ. A selection of images is displayed. The entire dataset is shown in Figure S22. Scale bar: 500 µm (4x objective) or 250 µm (10x objective). The tumor sample from patient #3 was processed jointly with J. Achberger. Images of patient #3-derived tumor slices were acquired by J. Achberger.

4.7 Technical Refinements of the Preclinical Model

4.7.1 Contextualization – Aims

During my doctoral studies, I aimed at refining the preclinical model employed in our research group. To this end, I generated and characterized MeVac-susceptible murine tumor cell lines and established a methodology for the purification of MeVac via ultracentrifugation.

4.7.2 Murine Tumor Cell Lines with Ectopic Expression of Human CD46

4.7.2.1 Cell Line Generation and Characterization

Our research group had previously generated MeVac-susceptible murine tumor cells ectopically expressing human CD46 by lentiviral transduction. However, some of the resulting cell lines failed to engraft in wild-type C57BL/6J mice. Reasoning that the immunogenicity of the lentiviral vector might have played a role in the *in vivo* rejection of these cells, I aimed at generating similar cell lines by transfection with less immunogenic vectors, such as non-viral DNA vectors.

To that aim, I transfected parental MC38, MC38cea, B16, B16-hCD20, and FC1245 cells with non-viral S/MAR DNA vectors encoding the BC1 isoform of human CD46 as MeVac entry receptor. In total, I tested three vectors per parental cell line, abbreviated as pCAG-SMAR, pCAG-Nano, and pEF1-Nano (Table 2). After antibiotic-based selection and fluorescence-activated bulk cell sorting, I obtained fourteen murine tumor cell lines with ectopic expression of human CD46 in more than 80% of the population (Figure 31 A, Figure S24). At that stage, human CD46 expression was sustained even in the absence of puromycin, indicating that antibiotic-based selection was no longer required for vector maintenance (Figure 31 A, Figure S24).

To determine the MeVac permissiveness of the newly generated cell lines, I inoculated them with MeVac eGFP at an MOI of 1 and monitored eGFP signal 24 h, 48 h, and 72 h after virus inoculation by fluorescence microscopy. As an example, I show the results for the MC38-derived cell lines 48 h after virus/mock inoculation (Figure 31 B). Whereas I only detected very few eGFP(+) cells in the parental population, I observed eGFP signal in many cells from the engineered populations 48 h (Figure 31 B) and 72 h (data not shown) after virus inoculation, indicating that, as opposed to the parental counterpart, the engineered cell lines support MeVac gene expression. Remarkably, I found that MeVac permissiveness varied between the three MC38-derived cell lines, with MC38-hCD46$_{[pCAG\text{-}SMAR]}$ cells being the most permissive.

Overall, the cell lines generated by transfection with the pCAG-SMAR vector showed the highest expression levels of human CD46 (Figure 31 A, Figure S24) as well as the highest MeVac permissiveness (Figure 31 B). Therefore, I chose these cell lines for further experiments.

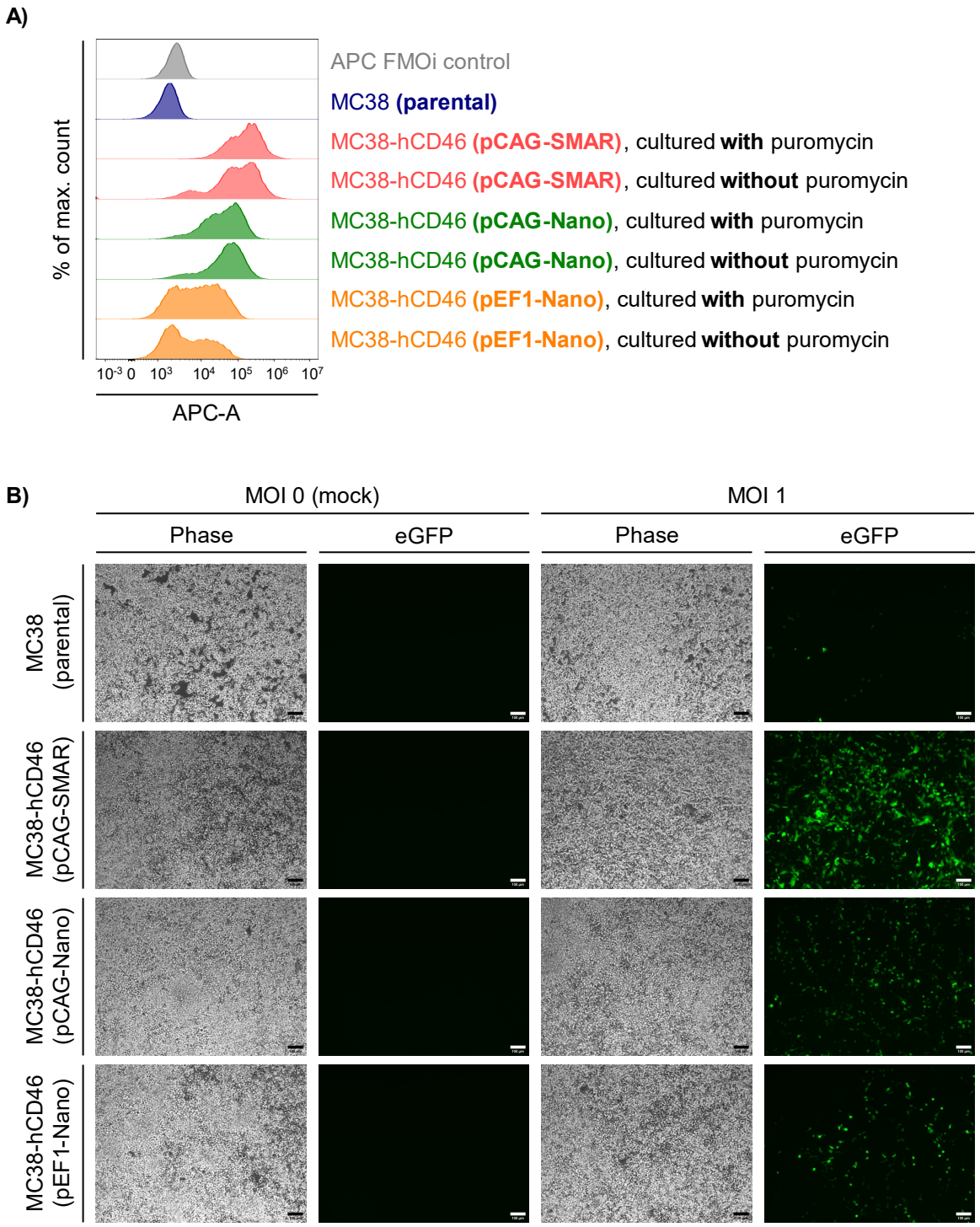

Figure 31. Generation of murine tumor cell lines with stable expression of human CD46 (hCD46). **(A)** The indicated cell lines were cultured in DMEM + 10% FCS with or without 7.5 µg/mL puromycin for two weeks. Afterwards, surface hCD46 expression was determined by flow cytometry with an APC-conjugated anti-hCD46 antibody. APC histograms of the live (Zombie Violet [-]) cell population are shown. FMOi staining was conducted on the pCAG-SMAR cell line variant, cultured with puromycin. FMOi: fluorescence minus one + isotype control. **(B)** The indicated cell lines were inoculated with MeVac eGFP (MOI = 3) or medium (mock). After 48 h, the cultures were monitored with the phase contrast and eGFP fluorescence channels of a Zeiss AxioVert 200 fluorescence microscope. Representative images, acquired with the AxioVision software and processed with ImageJ, are shown. Scale bar: 100 µm.

4.7.2.2 Growth Kinetics and Cytotoxic Effect of MeVac in MC38-hCD46 and B16-hCD46 cells

Next, I characterized the growth kinetics and cytotoxic potential of MeVac in the cell lines that I aimed to employ *in vivo*, those being B16-hCD46$_{[pCAG\text{-}SMAR]}$ and MC38-hCD46$_{[pCAG\text{-}SMAR]}$. By conducting one-step growth curves, I found that MeVac productively infects both cell lines, with viral progeny titers peaking 36 h and 48 h after virus infection at $9.25x10^3$ ciu/mL and $2.75x10^5$ ciu/mL in B16-hCD46$_{[pCAG\text{-}SMAR]}$ and MC38-hCD46$_{[pCAG\text{-}SMAR]}$ cells, respectively (Figure 32 A,B). Moreover, XTT cell viability assays revealed a reduction of cell viability to 80% and 50% of mock controls in B16-hCD46$_{[pCAG\text{-}SMAR]}$ and MC38-hCD46$_{[pCAG\text{-}SMAR]}$ cells 48 h after MeVac inoculation, indicating that MeVac exerts direct cytotoxic effects on both cell lines (Figure 32 C,D). These results were validated in later experiments addressing the growth kinetics and cytotoxic potential of MeVac vectors encoding chemokines in the same cell lines (Figure 10 B,C,F,G).

4.7.2.3 Tumor Cell Engraftment into CD46tg Mice

To determine whether B16-hCD46$_{[pCAG\text{-}SMAR]}$ cells and MC38-hCD46$_{[pCAG\text{-}SMAR]}$ cells are suitable for *in vivo* research, I conducted tumor engraftment experiments in CD46tg mice, which are of C57BL/6J background (Figure 32 E). After subcutaneous injection, both cell lines developed into tumors that grew until endpoint criteria, indicating that they are tolerated by CD46tg mice (Figure 32 F,G). B16-hCD46$_{[pCAG\text{-}SMAR]}$ tumors progressed rapidly and showed homogeneous growth kinetics, with mice reaching endpoint criteria between day 9 and day 12 after tumor cell injection (Figure 32 F). Conversely, MC38-hCD46$_{[pCAG\text{-}SMAR]}$ tumors followed heterogeneous growth kinetics, both in male and female mice (Figure 32 G,H). In this model, I observed a trend towards faster tumor progression in young mice (8 to 9 weeks-old on the day of tumor cell injection) compared to older mice (12 to 14 weeks-old on the day of tumor cell injection) (Figure 32 I). This heterogeneity should be taken into consideration in subsequent experiments, particularly in efficacy studies where tumor volume and survival are the main readout.

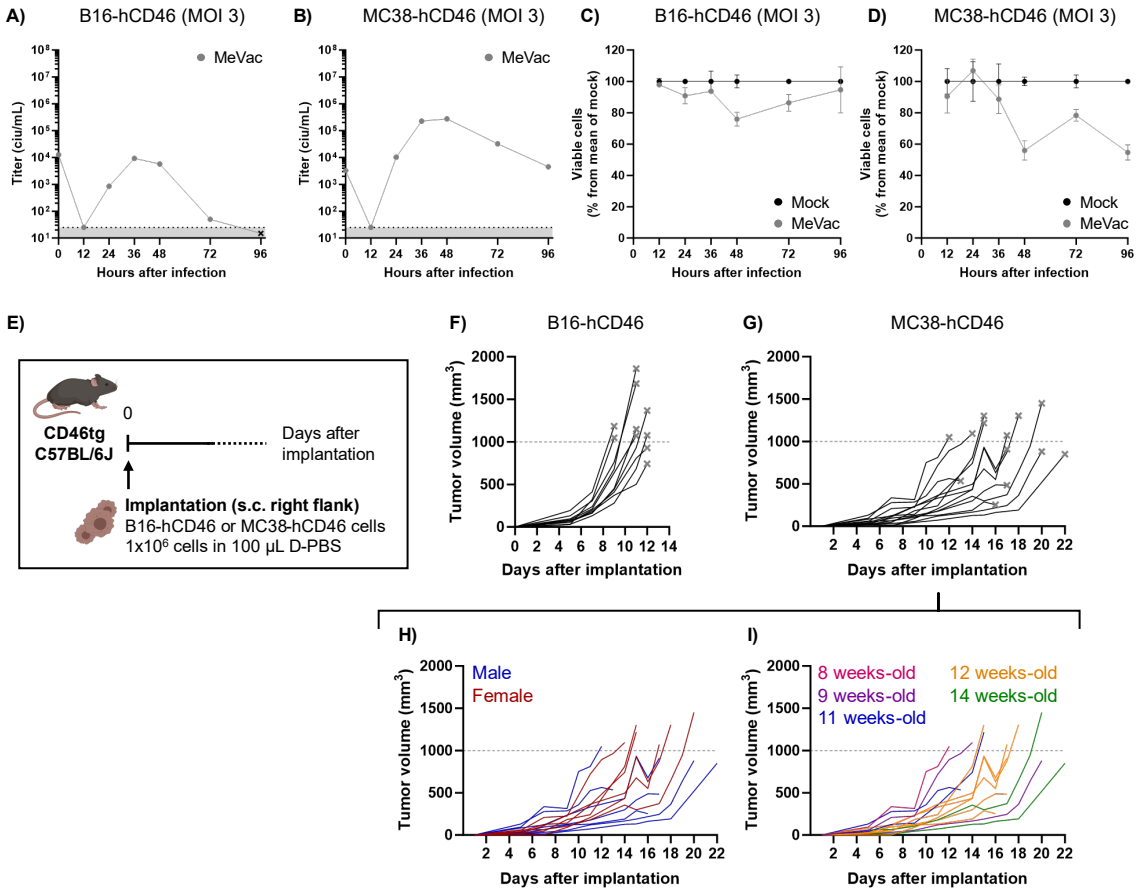

Figure 32. Characterization of B16-hCD46 [pCAG-SMAR] and MC38-hCD46 [pCAG-SMAR] cell lines. **(A-B)** B16-hCD46$_{[pCAG\text{-}SMAR]}$ or MC38-hCD46$_{[pCAG\text{-}SMAR]}$ cells were infected with purified MeVac$_{Schw}$ (MOI = 3). At the indicated timepoints, cells were scraped into the supernatant. Viral progeny titers were determined in pooled samples from biological triplicates by titration assay on Vero cells. Titrations were performed in quadruplicates. Grey area: range below the lower limit of detection of the assay (25 ciu/mL). Titers below 25 ciu/mL could not be determined and are shown as "x". **(C-D)** B16-hCD46$_{[pCAG\text{-}SMAR]}$ or MC38-hCD46$_{[pCAG\text{-}SMAR]}$ cells were infected with purified MeVac$_{Schw}$ (MOI = 3) or exposed to medium (mock). At the indicated timepoints, cell viability was determined by XTT assay. Data are depicted as percent viability compared to the mean of mock controls (100% viability). Dots indicate the mean of biological triplicates and error bars show standard deviation (not visible for some data points). **(E)** Experiment schematic for (F-I), created with BioRender.com. 1x10^6 B16-hCD46$_{[pCAG\text{-}SMAR]}$ or MC38-hCD46$_{[pCAG\text{-}SMAR]}$ cells were injected subcutaneously (s.c.) into the flank of CD46tg mice (C57BL/6J background). Tumor volume (F-G) and body weight (not shown) were monitored every two days. Mice were sacrificed when reaching endpoint criteria, as indicated in the methods section. **(F)** Tumor volume dynamics for individual mice injected with B16-hCD46$_{[pCAG\text{-}SMAR]}$ cells are shown. Dotted line represents one of the endpoint criteria (tumor volume > 1000 mm^3). Day of sacrifice is indicated with "x". n = 10 mice (all male), 11-13 weeks-old on the day of tumor cell injection. **(G)** Tumor volume dynamics for individual mice injected with MC38-hCD46$_{[pCAG\text{-}SMAR]}$ cells are shown. Dotted line represents one of the endpoint criteria (tumor volume > 1000 mm^3). Day of sacrifice is indicated with "x". n = 13 mice (6 females, 7 males), 8-14 weeks-old on the day of tumor cell implantation. **(H)** Plot shown in (G), color-coded according to the sex of each mouse. **(I)** Plot shown in (G), color-coded according to the age of each mouse on the day of tumor cell injection.

4.7.2.4 Human CD46 Expression on Murine Tumor Cells *In Vivo* and *Ex Vivo*

To assess whether the novel cell lines maintain ectopic expression of human CD46 (hCD46) *in vivo*, I injected MC38-hCD46$_{[pCAG\text{-}SMAR]}$ cells subcutaneously into wild-type or CD46tg mice and analyzed the tumors developing from these injections by flow cytometry at two timepoints: either when the tumors reached a volume of 100 mm^3 (t1, timepoint at which treatment is usually initiated) or ca. one week afterwards (t2) (Figure 33 A). To assess human CD46 expression on tumor cells, I excluded the CD45.2(+) cells present in the TME from the flow cytometry analysis and gated on CD45.2(-) cells according to the forward and side scatter profile of the tumor cells cultured *in vitro*. I refer to this gate as "tumor cell gate".

In tumors resected at t1, I detected hCD46 expression in > 70% of cells within the tumor cell gate, regardless of the mouse genotype (Figure 33 B [left panel]). Conversely, at t2, the tumors resected from 2 of 3 wild-type mice were hCD46(-) and the tumor from the remaining wild-type mouse only expressed hCD46 on ca. half (44%) of the cells within the tumor cell gate (Figure 33 C [left panel]). This contrasts with the tumors resected at t2 from CD46tg mice, which contained > 70% hCD46(+) cells within the tumor cell gate (Figure 33 C [left panel]). To monitor the dynamics of hCD46 expression even further, I established *ex vivo* monolayer cultures of tumor cells from the resected tumors and analyzed surface hCD46 expression in these cultures 4 weeks afterwards by flow cytometry (Figure 33 A). *Ex vivo* cultures established from tumors showing > 70% hCD46(+) cells on the day of tumor resection contained > 85% hCD46(+) cells, both when cultured with (data not shown) or without (Figure 33 B,C [right panels]) puromycin. Surprisingly, *ex vivo* cultures established from tumors showing < 50% hCD46(+) cells or almost no hCD46(+) cells on the day of tumor resection contained > 90% hCD46(+) cells, even when cultured without puromycin (Figure 33 C [right panel]). That is, hCD46 expression, which was largely lost in tumors growing in wild-type mice, was restored *ex vivo* even in the absence of antibiotic selection.

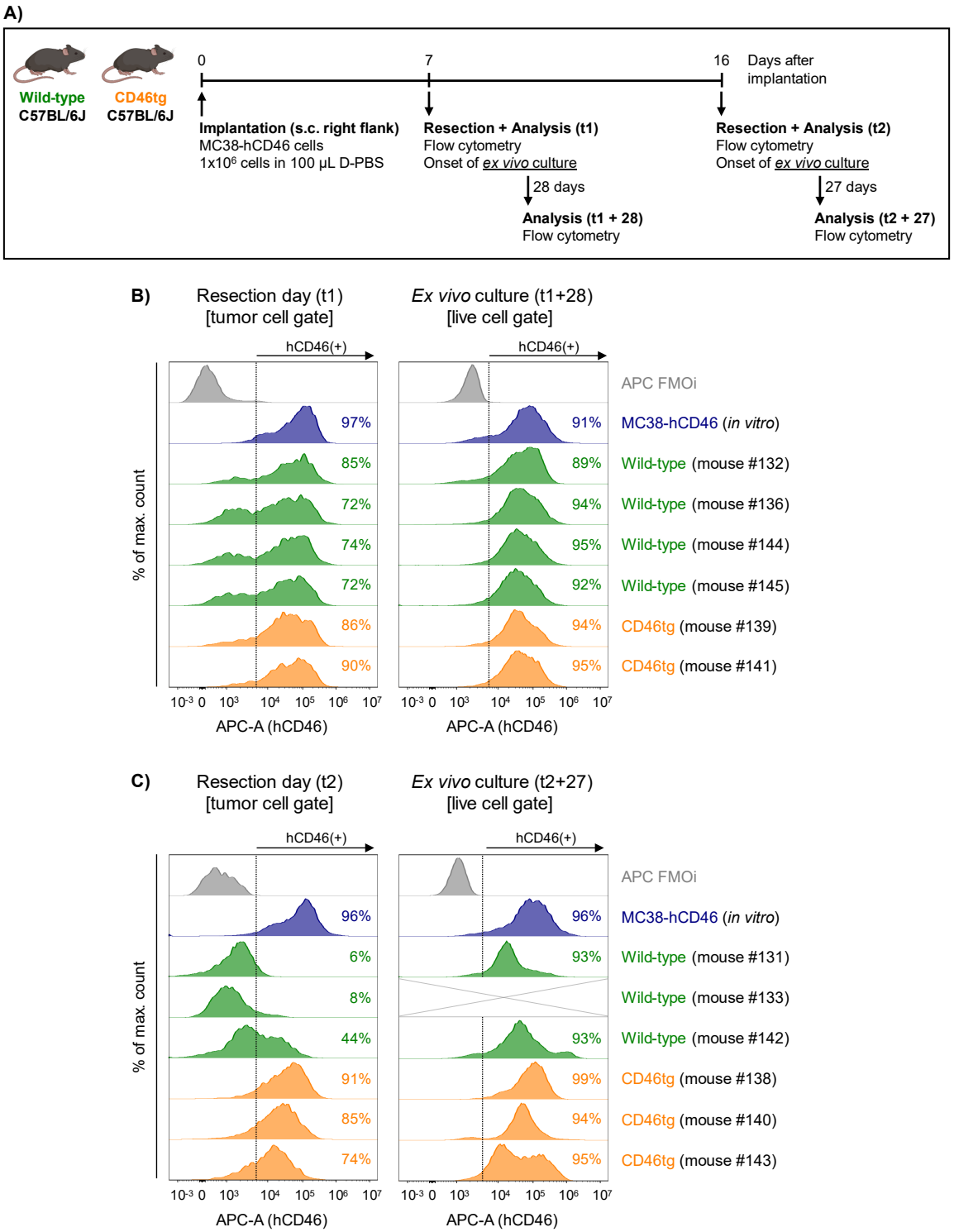

(Figure 33. Figure legend on the next page)

Figure 33. *In vivo* and *ex vivo* monitoring of human CD46 expression on MC38-hCD46 [pCAG-SMAR] cells injected into wild-type or CD46tg mice. (A) Experiment schematic (created with BioRender.com). $1x10^6$ MC38-hCD46$_{[pCAG\text{-}SMAR]}$ cells were injected subcutaneously (s.c.) into the flank of wild-type C57BL/6J mice (non-carrier MY II mice) or CD46tg mice. Tumors and spleens were resected seven (t1) or sixteen (t2) days after tumor cell injection (average tumor volume of 110 mm^3 and 395 mm^3, respectively) and processed into single-cell suspensions. On the day of organ resection, splenocytes and a fraction of each tumor cell suspension were stained with APC anti-human CD46 as well as PerCP-Cy5.5 anti-mouse CD45.2 antibodies and analyzed by flow cytometry. Splenocyte analysis confirmed the genotype of each mouse (data not shown). The remaining fraction of each tumor cell suspension was cultured *ex vivo* (without puromycin) as a monolayer. Two weeks afterwards, each *ex vivo* culture was expanded into two, from then onwards cultured with and without puromycin, respectively. Two weeks after culture expansion (*i.e.*, 27-28 days after tumor resection), the *ex vivo* cultures were harvested, stained with an APC-conjugated anti-human CD46 antibody, and analyzed by flow cytometry. Number of mice per timepoint, as well as genotype and sex, are indicated in the histograms. **(B-C)** APC histograms of tumors resected at t1 (B) and t2 (C) are shown. MC38-hCD46$_{[pCAG\text{-}SMAR]}$ cells cultured *in vitro* without puromycin were employed as positive control. FMOi: fluorescence minus one, plus isotype control. Left panels: flow cytometry results of the tumor single-cell suspensions analyzed on the tumor resection day. APC histograms are shown for the population within the tumor cell gate, defined as Zombie Violet(-) CD45.2(-) cells with a high FSC-A signal (*i.e.* large, non-immune live cells). Right panels: flow cytometry results of the tumor-derived *ex vivo* cultures analyzed 27-28 days after culture initiation. APC histograms of live (Zombie Violet[-]) cells are shown for *ex vivo* cultures without puromycin. *Ex vivo* cultures with puromycin yielded similar results (data not shown). The tumor from mouse #133 (t2) only had enough cells for flow cytometry on the resection day, *i.e.*, an *ex vivo* culture could not be established.

Following up on the flow cytometry data, I assessed whether the loss of hCD46 expression in tumors resected from wild-type mice alters the permissiveness of the tumor cells to MeVac. To that aim, I resected an MC38-hCD46$_{[pCAG\text{-}SMAR]}$ tumor from a wild-type mouse 44 days after subcutaneous tumor cell injection, processed it into a single-cell suspension for flow cytometry analysis, and established an *ex vivo* monolayer culture with the remaining tumor cell suspension. One week afterwards, I exposed the *ex vivo* cultures to MeVac eGFP or medium (mock) and monitored hCD46 expression as well as eGFP signal for three days. In parallel, I conducted the same infection test with *in vitro* cultures of MC38-hCD46$_{[pCAG\text{-}SMAR]}$ cells and parental MC38 cells (Figure S25 A).

On the day of tumor cell injection, most tumor cells were hCD46(+) (Figure S25 B [day 0]). In contrast, on the day of tumor resection most CD45.2(-) cells were hCD46(-) (Figure S25 B [day 44]), indicating that, as observed in the previous experiment, the tumor cells had lost (or silenced) hCD46 expression *in vivo*. Upon *ex vivo* culture for one week in the absence of puromycin, hCD46 expression was partly recovered and detected in ca. 50% of cells (Figure S25 B [day 51], Figure S25 C [(-)24 h timepoint]). This percentage remained stable for the subsequent three days independently of virus exposure (Figure S25 C). *In vitro* cultures of MC38-CD46$_{[pCAG\text{-}SMAR]}$ cells (employed as positive control) contained > 90% hCD46(+) cells throughout the infection experiment, also independently of virus exposure (Figure S25 C). Interestingly, in the previous experiment *ex vivo* culture of dissociated hCD46(-) tumors led to complete recovery of hCD46 expression (*i.e.* > 90% of cells staining positive for hCD46) (Figure 33 C [right panel]), whereas in the present study this recovery was only partial (Figure S25 B,C). Among other reasons, the timepoint of analysis might have accounted for this difference. In the previous experiment (Figure 33) the *ex vivo* cultures were analyzed four weeks after culture onset, whereas in the present experiment (Figure S25) the analysis was performed one week after culture onset.

Regarding MeVac gene expression, by fluorescence microscopy I found several eGFP(+) cells in the *ex vivo* cultures, particularly 48 h after virus inoculation (Figure S25 D). This indicates that at least a fraction of the *ex vivo* tumor cell population supported MeVac gene expression. In general, the abundance of eGFP(+) cells (Figure S25 D,F) and the eGFP signal intensity (Figure S25 E) of the *ex vivo* cultures was higher (although not always significantly) than that of the *in vitro* MC38 cell cultures (parental cells) and significantly lower than that of the *in vitro* MC38-hCD46$_{[pCAG\text{-}SMAR]}$ cultures. This finding correlates MeVac gene expression (as assessed by fluorescence microscopy and flow cytometry) (Figure S25 D-F) with the levels of hCD46 detected by flow cytometry (Figure S25 C), thereby indicating that hCD46 expression plays a role in the permissiveness of murine tumor cells to MeVac. However, it should be noted that this experiment was only conducted with one tumor. Biological replicates are required before drawing stronger conclusions.

All in all, I conclude that MC38-hCD46$_{[pCAG\text{-}SMAR]}$ cells maintain human CD46 expression *in vivo* in CD46tg mice, but not in wild-type mice. Moreover, I demonstrate that the loss of human CD46 expression in tumors resected from wild-type mice is time-dependent and partly (or completely) recovered *ex vivo*, even in the absence of the selection antibiotic. Further studies on the DNA and RNA level should elucidate whether the loss of hCD46 expression occurs on the genetic or epigenetic level. For instance, it would be interesting to investigate whether the recovery of hCD46 expression *ex vivo* results from the outgrowth of the very few hCD46(+) tumor cells remaining in the resected tumor, from reversion of epigenetic silencing, or from a different mechanism. Another factor to consider is tolerance to human CD46, which probably differs between both mouse strains (see 5.4.4.2).

4.7.3 MeVac Purification

Before my doctoral studies, the virus preparations employed *in vivo* by our research group consisted of clarified lysates from infected Vero cells. These virus suspensions contain several impurities, such as small cell debris, nucleic acids, proteins from virus-producer cells, and proteins expressed from the viral genome during virus propagation, including the encoded immunomodulators. Together, these impurities might act as adjuvants or immunogens and bias the immune response elicited by the OV *per se*. For instance, they might contribute to a more inflamed tumor milieu compared to the clinical scenario, where highly purified virus preparations are administered. Thus, to better resemble the clinical setting and to obtain more robust results regarding the immunological effects of OVs, I aimed at purifying the virus preparation.

To establish a protocol for the purification of oncolytic MeVac, I explored several strategies including cascade filtration, centrifugation, ultrafiltration, and ultracentrifugation together with A. Brunecker, V. Frehtman, B. Leuchs, and Ž. Modic. Table S3 summarizes the main approaches that we tested and the parameters that we optimized. Detailed information on multiple optimization rounds can be found in my laboratory notebooks and in the internship reports from Ž. Modic and A. Brunecker. The procedure yielding the highest virus recovery as well as a concentrated and purified virus suspension compared to the input material consisted of two steps: (i) clarification of the cell lysate by centrifugation, and (ii) concentration and purification of the clarified lysate by one-step ultracentrifugation with iodixanol fractionation.

To analyze the performance of the ultracentrifugation step, I determined the viral titer and protein concentration in the virus suspension before (input) and after (interphase) ultracentrifugation. In addition, I analyzed the fraction located above the interphase after ultracentrifugation (top). As representative examples, I show the results from the purification of MeVac (Figure 34 A-C) and MeVac mCCL5 (Figure 34 D-H). In both cases, ultracentrifugation of clarified cell lysates resulted in

three- to four-fold concentration of the virus suspension, with MeVac titers increasing from $7.75x10^7$ ciu/mL (input) to $3.38x10^8$ ciu/mL (interphase) (Figure 34 A), and MeVac mCCL5 titers increasing from $4.75x10^7$ ciu/mL (input) to $1.23x10^8$ ciu/mL (interphase) (Figure 34 D). Conversely, the viral titers were three to four log lower in the top fraction compared to the input suspension, indicating that most infectious virus locates at the interphase (Figure 34 A,D).

As an indicator of purity, I calculated the ratio between cell infectious units and micrograms of protein, which should increase when protein contaminants are removed and viral particles are maintained or even concentrated. Notably, this ratio was four to five times higher in the interphase fraction compared to the input suspension, thereby confirming virus purification. In detail, the ratio increased from $7.51x10^3$ to $3.69x10^4$ in the MeVac suspension (Figure 34 B), and from $4.09x10^3$ to $1.40x10^4$ in the MeVac mCCL5 suspension (Figure 34 E).

Consistent with these results, Coomassie-stained SDS-PAGE revealed more proteins in the input fraction compared to the interphase when normalizing to the same amount of cell infectious units, thus providing another indication of virus purification (Figure 34 C,F). Whereas the input lane was saturated, in the interphase lane I observed several bands, the most intense of which located at ca. 70 kDa. This band could correspond to MeVac N, which is the most abundant protein in the viral particle. However, techniques such as mass spectrometry would be required for a precise identification. Contrary to the interphase, the top fraction contained many proteins and had a staining pattern similar to the input fraction despite loading 1000 times less cell infectious units into the lane.

Importantly, in the top fraction from the MeVac mCCL5 purification I detected virus-encoded chemokine, as determined by ELISA (Figure 34 G). This shows that some of the virus-encoded chemokine (considered an impurity) is removed during the ultracentrifugation step. Interestingly, I also detected the chemokine in the interphase fraction, thus evidencing that not all mCCL5 is removed from the purified virus suspension. This is to be expected, as the ultracentrifugation step should remove free mCCL5 present in the virus suspension but cannot remove mCCL5 located inside extracellular vesicles (derived from the virus-producer cells) that are co-purified with the virus or inside viral particles (Vero cells produce mCCL5 during MeVac mCCL5 propagation; thus, some mCCL5 molecules are trapped inside the viral particles during budding). As an indicator of purity, I determined the ratio between cell infectious units and nanograms of mCCL5, which should increase if mCCL5 molecules are removed from the suspension but the amount of infectious virus is maintained or even concentrated. While the interphase had the highest ratio, the top fraction had the lowest (Figure 34 H). This indicates that the recovery of infectious virus at the interphase was larger than the recovery of mCCL5 in this fraction, and therefore shows that the ultracentrifugation

step succeeded in partly purifying the virus suspension from mCCL5. Therefore, ultracentrifugation is a suitable strategy to separate infectious MeVac from several protein contaminants, including the transgenic protein encoded in the viral vector.

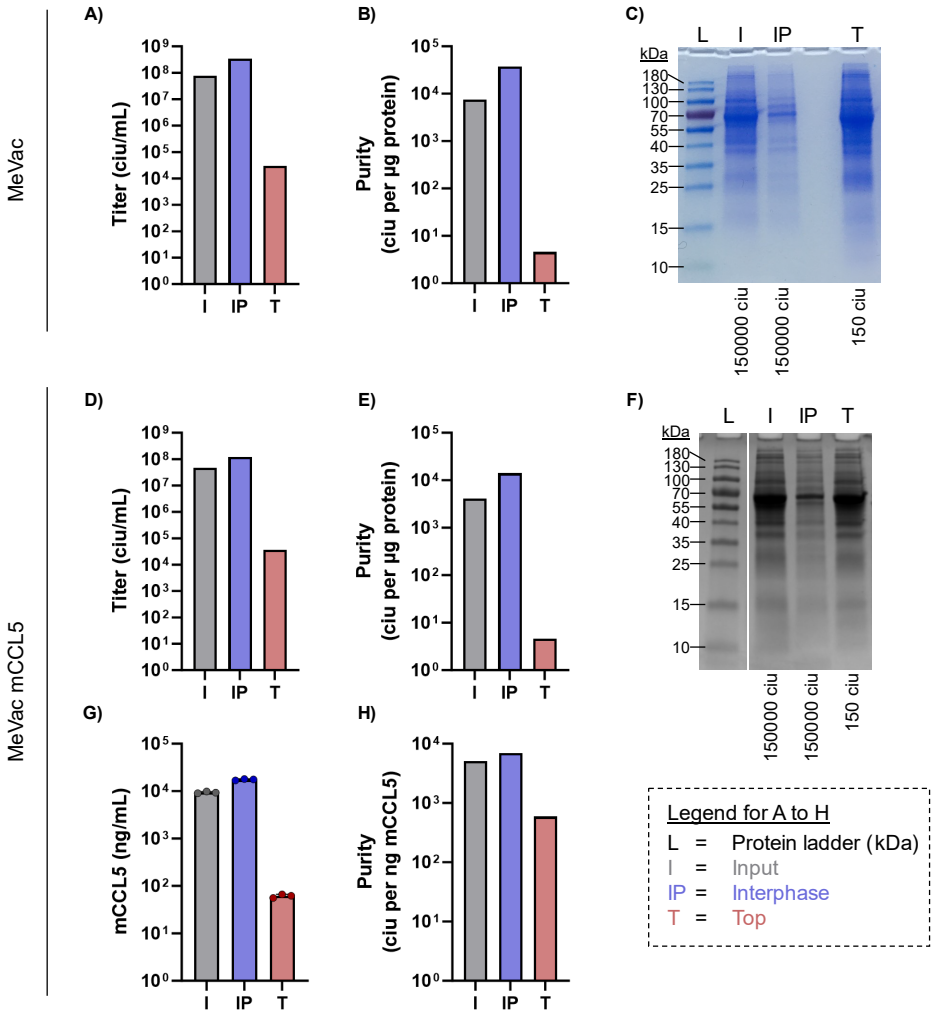

Figure 34. Purification of MeVac preparations. MeVac variants were purified as described in Methods. Briefly, the cell lysate from infected Vero cells was clarified by centrifugation. The resulting supernatant (referred to as input) was subjected to ultracentrifugation in a one-step iodixanol gradient. After ultracentrifugation, the interphase (fraction containing the purified virus suspension) was collected, aliquoted, and stored at -80 ºC until usage in experiments. Aliquots of the input, interphase, and top fractions (top: volume above interphase) were kept aside for analysis. Representative results of this analysis are shown for the purification of **(A-C)** $MeVac_{Schw}$ and **(D-H)** MeVac mCCL5 ($MeVac_{Schw}$ encoding murine CCL5). **(A,D)** The viral titer in each fraction was determined by titration assay on Vero cells. Titrations were performed in octuplicates. **(B,E)** The protein concentration in each fraction was determined by BCA assay with technical duplicates (see Methods). The ratio of viral titer (ciu/mL) to mean protein concentration (µg/mL) in each fraction is shown. This ratio (ciu per µg of protein) provides information on the purity of the virus suspension. **(C,F)** The three fractions were analyzed by sodium dodecyl sulfate polyacrylamide gel electrophoresis (SDS-PAGE). An image of the Coomassie-stained polyacrylamide gel is shown. The indicated cell infectious units (ciu) were loaded onto the corresponding lanes. **(G)** The concentration of murine CCL5 (mCCL5) in each fraction was determined by ELISA. Bars show mean values of technical triplicates and error bars depict standard deviation (not visible). **(H)** The ratio of viral titer (ciu/mL) to mean mCCL5 concentration (ng/mL) in each fraction is shown. This ratio (ciu per ng of mCCL5) provides information on the purity of the virus suspension. **(B)** L. Küther conducted the BCA assay. **(C)** L. Küther conducted the SDS-PAGE assay.

To determine whether the purity of the virus preparation affects therapeutic efficacy, I treated CD46tg mice bearing subcutaneous B16-hCD20-hCD46 tumors with two intratumoral doses of carrier fluid or virus suspensions prepared at three purity grades (laboratory, preclinical, and clinical) and monitored survival (Figure 35 A). For laboratory and preclinical grades, I employed suspensions of MeVac Edmonston B-derived strain ($MeVac_{Edm}$) produced by our research group. Laboratory grade purity consisted of clarified lysates from infected Vero cells. To achieve preclinical grade purity, the clarified lysates were concentrated and purified by ultracentrifugation (see 3.2.3.5). For clinical grade purity, I used commercially available MV-NIS, a derivate of $MeVac_{Edm}$ produced and purified in compliance with good manufacturing practice standards [202].

Overall, virotherapy prolonged the median survival of tumor-bearing mice from 14.5 days (mock treatment) to 16 or 17 days (virus treatment). Notably, there were no major differences between virus treatments, indicating that purified virus suspensions (both at preclinical and clinical grade) confer similar therapeutic efficacy than clarified lysates from infected Vero cells (Figure 35 B).

In conclusion, I have established a protocol that improves the concentration and purity of the virus suspension compared to the clarified cell lysates employed in previous studies, and I have validated this protocol in preparations of unmodified or chemokine-encoding MeVac variants. Moreover, I have shown that purified MeVac and MeVac suspensions consisting of clarified cell lysates mediate comparable therapeutic efficacy in a preclinical tumor model. However, since the efficacy study was only conducted with unmodified MeVac and MeVac encoding human sodium iodide symporter, whether the findings apply to MeVac encoding immunomodulators remains to be investigated.

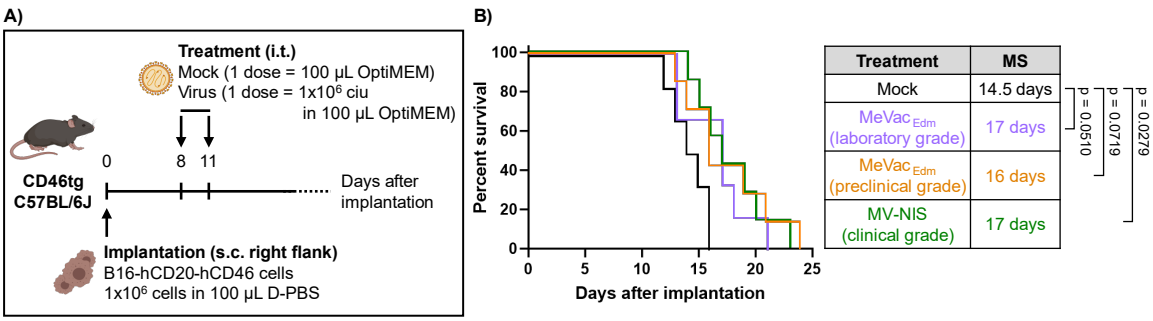

Figure 35. Effect of MeVac purity grade on therapeutic efficacy. (A) Experiment schematic (created with BioRender.com). $1x10^6$ B16-hCD20-hCD46[lenti] cells were injected subcutaneously (s.c.) into the flank of CD46tg mice (C57BL/6J background). After tumor establishment (average volume of 70 mm^3), the mice were treated as shown, either with carrier fluid (mock) or with viruses prepared at laboratory, preclinical, or clinical purity grades. Tumor volume and body weight were monitored every three days and once per week, respectively (data not shown). Mice were sacrificed upon reaching at least one endpoint criterion (see Methods). **(B)** Kaplan-Meyer survival analysis with Mantel-Cox (log rank) test. The significance level (α) after Bonferroni's correction for 6 comparisons was 0.008. p values < 0.1 are shown. Median survival (MS) is indicated. **(A-B)** n = 6-7 mice (2-3 females and 4-5 males) per treatment group. C. E. Engeland prepared the virus suspension at laboratory grade. C. E. Engeland and I prepared the virus suspension at preclinical grade. The virus suspension at clinical grade was purchased from Imanis Life Sciences (Rochester, U.S.A.).

5 Discussion

5.1 MeVac Encoding Tumor-Associated Antigens

Priming of naïve tumor-specific T cells is a key step in the development of adaptive antitumor immunity that requires three signals provided by professional APCs such as DCs: (i) TCR interaction with peptide::MHC complex, (ii) costimulation, and (iii) cytokines guiding the differentiation program of the primed cells [11]. However, in poorly immunogenic tumors or tumors expressing low TAA levels, the amount of antigen captured and presented by DCs might be insufficient to prime antitumor immunity [203]. In this scenario, OVs encoding TAAs (OV-TAA) have emerged as a promising strategy to increase antigen availability and presentation at the tumor site, thus facilitating the development of antitumor immunity. To develop effective OV-TAA vaccines, our group has generated measles virus vaccine strain (MeVac) vectors encoding full-length OVA (model antigen) or variants of the OVA-derived SIINFEKL epitope. In an *in vitro* murine system, I demonstrated that these vectors promote priming of SIINFEKL-specific naïve T cells and enhance SIINFEKL-specific CTL activation by mediating antigen presentation on murine DCs (important for T cell priming and activation) and murine tumor cells (relevant for CTL activation) [154].

5.1.1 Susceptibility of Murine Cells to MeVac

In my studies, antigen presentation and CTL activation were dependent on viral replication, as these processes were abrogated with UV-C-inactivated virus variants and were not mediated by external peptide loading. These results indicate that, despite limited, the permissiveness of murine DCs and tumor cells to MeVac was essential for *de novo* expression and presentation of the encoded epitopes. However, the mechanisms mediating MeVac entry into murine cells remain to be elucidated. MeVac infection of MC38-hCD46 cells could be explained by the ectopic expression of the MeVac entry receptor (human CD46). Conversely, given that murine cells do not express any of the known MeVac entry receptors (primate CD46, CD150, or Nectin-4), MeVac must have entered murine DCs in a manner independent of these receptors. There is the possibility that the virus was captured by phagocytosis or another endocytic route. In this scenario, a change in pH within endosomes could have disrupted the virus envelope, thereby releasing the ribonucleoprotein (RNP) and permitting viral replication. However, the change in pH could have also disrupted the RNP, in which case the virus would not replicate. As another hypothesis, MeVac entry into DCs might have been facilitated by DC-SIGN, a molecule involved in the dissemination of wild-type MeV in humans and non-human primates [204,205]. On the molecular level, MeV/MeVac binds to human DC-SIGN, although this interaction is insufficient to mediate virus entry [100]. Murine DC-SIGN is homologous to the human variant and highly expressed on DCs [206]. Thus, the interaction of MeVac with murine

DC-SIGN seems possible. However, whether and how this potential interaction would facilitate virus entry into murine cells remains unknown.

5.1.2 Tumor Cell Phagocytosis and Antigen Presentation

My studies employed a simplified model in which DC2.4 cells were exposed to MeVac variants in absence of other cell types. In this scenario, presentation of MeVac-encoded SIINFEKL on DCs required transgene expression within these cells. However, in more complex settings, OVs contribute to TAA presentation on DCs via additional mechanisms, such as enhanced tumor cell phagocytosis or uptake of TAAs released during virus-mediated tumor cell lysis (oncolysis). While these processes were not addressed in my experiments, they have been studied by Guillerme *et al.* and Gauvrit *et al.* in the context of MeVac virotherapy [125,130]. Using *in vitro* human co-culture systems, these studies have shown enhanced DC phagocytosis of MeVac-infected tumor cells as compared to non-infected cells. Importantly, these studies were conducted with unmodified MeVac instead of MeVac encoding tumor antigens. Indeed, provided that the tumor cells express the antigens of interest endogenously, TAA presentation on DCs via these additional mechanisms does not require the antigens to be encoded within the viral vector. Nevertheless, providing more antigen via MeVac vectors might still be beneficial, particularly in scenarios where low levels of endogenous TAAs fail to prime antitumor immunity. Moving one step further, M. S. C. Finkbeiner is currently investigating tumor cell phagocytosis and antigen presentation in co-cultures of human DCs with human tumor cells exposed to MeVac TAA instead of unmodified MeVac. My studies revealed that, among all virus variants tested, MeVac encoding six epitope copies targeted to the proteasome mediates the highest levels of antigen presentation and the strongest T cell priming. Thus, M. S. C. Finkbeiner focuses on this virus variant. Using the cancer testis antigen “Synovial Sarcoma X Chromosome Breakpoint 2” (SSX2) as model antigen, she analyses presentation of the SSX2-derived epitope KASEKIFYV on DCs co-cultured with SSX2(+) or SSX2(-) tumor cells infected with MeVac encoding six KASEKIFYV copies targeted to the proteasome. As a second model, she employs the cancer testis antigen “New York Esophageal Squamous Cell Carcinoma 1” (NY-ESO-1) as well as MeVac encoding six copies of the NY-ESO-1-derived epitope SLLMWITQC [xviii].

5.1.3 DC Maturation

Besides TAAs, oncolysis also results in the release of PAMPs and DAMPs into the TME, which are sensed by immune cells patrolling the tumor, including DCs. MeVac-infected DCs could also sense PAMPs and DAMPs resulting from viral replication within these cells. Overall, sensing PAMPs and DAMPs triggers DC maturation. Focusing on MeVac virotherapy, several mechanistic studies have

[xviii] Ongoing doctoral studies of M. S. C. Finkbeiner.

reported upregulation of the DC surface maturation markers CD40, CD80, CD83, CD86, and HLA-DR on monocyte-derived DCs (moDCs) or plamacytoid DCs (pDCs) co-cultured with MeVac-infected tumor cells compared to non-infected cells. These co-cultures also showed enhanced secretion of the pro-inflammatory molecules IL-1β, IL-6, TNF-α, and IFN-α [125,128,130,132]. Importantly, several of the surface markers upregulated on MeVac-exposed DCs provide co-stimulatory signals during T cell priming (*e.g.*, CD80, CD86) and several pro-inflammatory cytokines secreted by MeVac-exposed DCs contribute to the third signal required for T cell priming. This suggests that, in presence of the first signal (peptide::MHC complex), MeVac-mediated DC maturation supports T cell priming. Along this line, my studies showed that, in the presence of SIINFEKL, MeVac-exposed DCs mediate more efficient priming of naïve OT-I T cells compared to non-virus-exposed DCs. Based on the literature discussed above, MeVac-mediated DC maturation could be an explanation for this observation.

5.1.4 T Cell Priming

Using OVA as a model antigen, I proved the concept of employing MeVac encoding epitope variants to prime cognate naïve T cells by directly increasing epitope presentation on virus-exposed DCs. In particular, I showed that MeVac encoding six epitope copies targeted to the proteasome mediates the highest levels of antigen presentation on DCs and the strongest T cell priming among all the MeVac variants that I analyzed.

Interestingly, MeVac encoding the full-length antigen (MeVac OVA) instead of epitope variants failed to prime antigen-specific immunity (Figure 5 C). In contrast, Hutzler *et al.* reported priming of OVA-specific immunity in naïve mice vaccinated with MeVac encoding membrane-bound OVA (MV_{vac2} DisOva) [140]. The fact that this study was conducted in MeVac-permissive mice ($IFNAR^{KO}$-CD46Ge mice [207]) might explain these findings, since I expect the virus to replicate at significantly higher levels in cells from these transgenic mice than in the wild-type DC2.4 cells employed in my model, thus resulting in higher levels of transgene expression. Moreover, the MeVac transcriptional gradient [102] could have also accounted for enhanced transgene expression, since in this study the transgene was encoded downstream of the MeVac P gene [140] whereas in the virus variant that I employed (MeVac OVA) the transgene was encoded downstream of the MeVac H gene [154]. Higher levels of transgene expression could have led to more antigen processing and presentation, and thus to stronger T cell priming. Nevertheless, a direct comparison of my results to those from Hutzler *et al.* is difficult, since *in vitro* and *in vivo* systems are largely different.

While these projects employed a model antigen (OVA), similar studies could be conducted with clinically-relevant TAAs. In this regard, priming of tumor-specific immunity can be inferred from an *in vivo* vaccination study with MeVac encoding full-length claudin-6, an oncofetal antigen (MV_{vac2} CLDN6) [140]. In this study, naïve mice were vaccinated with MV_{vac2} CLDN6. Subsequently,

splenocytes were isolated and activated *ex vivo* with claudin-6-derived peptides, thereby confirming the development of claudin-6-specific immunity in vaccinated mice. While the splenocytes employed for the *ex vivo* restimulation experiment were already antigen-experienced, and therefore no longer naïve, the fact that they were isolated from vaccinated mice, which were naïve before vaccination, indicates that the vaccine primed antigen-specific immunity. However, experiments to directly address priming, for instance co-cultures of claudin-6-specific naïve T cells with virus-exposed DCs, similar to those conducted in my project, were not included in this study. Moreover, the mechanisms leading to T cell priming, such as MeVac-mediated antigen presentation on DCs, as elucidated in my experiments, were not discussed, either.

Besides tumor vaccination, MeVac variants encoding foreign antigens have also been developed to vaccinate against infectious diseases. In this case, the MeVac variants encode pathogen-derived antigens instead of TAAs and are administered intramuscularly or intravenously. For instance, MeVac vectors have been engineered to encode antigens from malaria parasites, Dengue virus, hepatitis B virus (HBV), or, as detailed in the addendum of my thesis, severe acute respiratory syndrome coronavirus 2 (SARS-CoV-2), among others[208]. Although these studies prove the concept of designing MeVac variants encoding foreign antigens to prime antigen-specific immunity, my approach is slightly different as it also exploits the oncotropic properties of the vector by promoting MeVac-mediated antigen presentation not only on DCs, but also on tumor cells. Moreover, despite not addressed in my studies, employing engineered MeVac in cancer immunotherapy has the added benefit of direct tumor reduction via oncolysis.

5.1.5 CTL Activation

Following the cancer immunity cycle, primed tumor-specific CD8+ T cells traffic to the tumor as CTLs and become activated upon TCR interaction with the cognate peptide::MHC-I complex without requiring additional co-stimulatory signals. The lower requirement for activation compared to naïve T cells, allows CTLs to become activated not only by antigen-presenting DCs, but also by other cells presenting cognate antigen, including tumor cells.

In this regard, I have demonstrated that MeVac encoding SIINFEKL variants promote epitope presentation on murine colorectal cancer cells (MC38-hCD46) and murine DCs at levels sufficient to activate SIINFEKL-specific CTLs (Figure 6, Figure 7). Interestingly, exposure of tumor cells to MeVac OVA led to very low levels of antigen presentation as compared with exposure to MeVac encoding epitope variants. The requirement for antigen processing, as opposed to pre-processed epitope variants, might explain this observation. Moreover, given the MeVac transcription gradient [102], the full-length antigen was probably expressed at lower levels than the epitope variants, as it was encoded further downstream within the MeVac genome [154].

Importantly, antigen presentation was dependent on viral replication (Figure S2, Figure S5). Consistently, CTL activation by DCs or tumor cells was abrogated when the DCs or tumor cells were exposed to UV-inactivated virus variants instead of active virus (Figure 6, Figure 7). Similarly, a vaccination study with MeVac encoding the surface antigen of HBV (MV HBsAg) reported induction of HBsAg-specific immunity in MeVac-susceptible mice immunized with active virus but not in those immunized with UV-inactivated virus [209].

Notably, my results from co-cultures of CTLs with tumor cells exposed to MeVac encoding epitope variants have been reproduced by our research group in an equivalent setting using tyrosinase-related protein-2 (TRP-2), a common melanoma TAA, as model antigen instead of OVA [154]. In addition to MeVac, the concept of activating antigen-specific CTL responses with OVs encoding TAAs has been proven with other viral platforms, including vaccinia virus, vesicular stomatitis virus, Maraba virus, and herpes simplex virus, although in some *in vivo* settings a heterologous prime-boost is required [210]. More complex strategies comprise repertoires of oncolytic vesicular stomatitis virus encoding cDNA libraries of specific tumor entities, such as melanoma and pancreatic cancer, and oncolytic adenoviruses coated with tumor antigen peptides [211–214]. Furthermore, OV TAAs are promising therapies to vaccinate against neoepitopes emerging from tumor immune evasion mechanisms, as recently demonstrated with an oncolytic vesicular stomatitis virus (VSV) encoding mutated CSDE1, a neo-epitope selected in tumor cells as a resistance mechanism to VSV-mediated oncolysis [215].

5.1.6 Conclusion

Overall, replication-competent viruses have been widely studied as antigen delivery vehicles in the context of oncolytic vaccination and vaccination against infectious diseases. My study provides mechanistic proof-of-concept for the employment of MeVac encoding antigen-derived epitope variants (in particular six epitope copies targeted to the proteasome) as oncolytic vaccines to enhance antigen presentation on DCs and tumor cells, promote priming of cognate naïve T cells, and trigger activation of cognate CTLs.

5.2 The Role of Chemokines in MeVac Virotherapy

5.2.1 MeVac-Mediated Increase in Peritumoral and Intratumoral T Cell Abundance

Previous *in vivo* studies in tumor-bearing immunocompetent mice have shown an increase in T cell abundance, as determined by staining with the T cell lineage marker CD3, at the tumor site upon intratumoral virotherapy with unmodified MeVac or MeVac encoding control molecules (eGFP, human IgG1-Fc, or hamster IgG-Fc) compared to mock treatment. These studies cover a wide variety of syngeneic murine tumor models, such as colon adenocarcinoma (MC38cea model, s.c.) [133,150], glioblastoma (GL261 and CT-2A models, both orthotopic) [147,216], lung carcinoma (LLC model, s.c.) [217], and melanoma (B16-hCD20 model, s.c.) [134], and as well as three MeVac strains (Edmonston B-derived, Schwarz, and Hu191). For instance, Grossardt *et al.* reported increased peritumoral and intratumoral abundance of CD3(+) cells in colon adenocarcinomas (MC38cea model, s.c.) treated with CEA-retargeted MeVac encoding eGFP compared to mock treatment [133]. Consistent with these results, I detected a higher percentage of CD3(+) cells among all CD45.2(+) cells in MeVac-treated MC38-hCD46 tumors (s.c.) compared to mock controls (Figure 27 B). Regarding more immunologically cold models, Engeland *et al.* found a higher percentage of CD8(+) cells among all CD3(+) cells and a higher CD8(+) to Foxp3(+) cell ratio in B16-hCD20 tumors (s.c.) treated with CD20-retargeted MeVac encoding human IgG1-Fc compared to mock treatment [134]. Using the same cell line, but with an additional surface receptor (human CD46), T. Poth and I observed increased intratumoral and peritumoral abundance of CD3(+) cells in B16-hCD20-hCD46 tumors (s.c.) treated with MeVac encoding hamster IgG-Fc compared to mock treatment (Figure 29). Similarly, together with R. Veinalde and J. Leichsenring, I found a higher percentage of CD3(+) cells in pancreatic ductal adenocarcinomas (FC1245-hCD46 model, s.c.) treated with MV-NIS monotherapy or MV-NIS plus PD-1 blockade compared to mock treatment (Figure 22) [165].

Overall, these studies show that MeVac therapy increases intratumoral and peritumoral T cell abundance. This phenomenon could result from several mechanisms, such as T cell recruitment into the tumor or proliferation of T cells already present at the tumor site. Follow up studies should elucidate which of these mechanisms play a role in the murine tumor models that I employed. For instance, I could assess the contribution of T cell recruitment to the overall increase in intratumoral T cell abundance by blocking lymphocyte egress from lymph nodes with the small molecule FTY720, which has previously been employed to block T cell recruitment into MC38 tumors [218].

5.2.2 MeVac-Mediated Upregulation of Chemokine-Encoding Genes

A major aim of my doctoral studies was to identify molecular mechanisms triggered by MeVac virotherapy playing a potential role in intratumoral T cell recruitment. Since chemokines are key mediators of cell trafficking, I focused on these molecules. Upregulation of genes encoding chemokines during oncolytic virotherapy has been investigated in several viral platforms, including Maraba virus, reovirus, and herpes simplex virus type 2 (HSV2). For instance, Bourgeois-Daigneault *et al.* reported increased *Ccl5* and *Cxcl10* upregulation as well as increased secretion of the encoded chemokines in 4T1 and E4T6 murine breast cancer cells exposed to oncolytic Maraba virus (MG1 strain) *in vitro*. This effect was abrogated in RIG-I knock-out cells, indicating that it was triggered by virus sensing [219]. In another study, four human melanoma cell lines showed increased secretion of CCL3, CCL4, CCL5, CCL11, CXCL10, and IL-8 in an NFκB-dependent fashion upon exposure to oncolytic reovirus [220,221]. While these studies were conducted *in vitro*, Fu *et al.* assessed the effect of an HSV2-derived OV in murine pancreatic ductal adenocarcinoma cells (Panc02-OVA model, s.c.) implanted into immunodeficient mice that later received adoptive transfer of OT-I T cells. In this setting, they detected increased levels of several chemokines, including CXCL9 and CXCL10 in virus-treated tumors compared to mock-treated tumors [222].

From this panel of chemokines, CXCL9 and CXCL10 are particularly known as chemoattractants of CD4(+) T_H1 cells, CD8(+) effector T cells, and NK cells [223]. Consistent with this role, intratumoral expression of CXCL9 and CXCL10 correlates with increased abundance of tumor-infiltrating lymphocytes and enhanced antitumor immunity [12]. CCL5 is involved in the recruitment of T cells with antitumor activity [224,225], but also in the recruitment of pro-tumorigenic immune cells, such as T_{REG} cells and tumor-associated macrophages [223]. This dual role suggests that the balance between chemokine-mediated recruitment of immune effector cells and immune regulatory cells is tightly orchestrated by the signaling networks within the TME and should be assessed in a per case basis in preclinical *in vivo* settings as well as in the clinical scenario.

Before my doctoral studies, knowledge on the mechanisms that could potentially increase intratumoral T cell abundance in the context of MeVac virotherapy was scarce. An *in vitro* study from 1997 reported *CXCL10* upregulation in MeVac-infected U373 human astrocytoma cells compared to mock infection [226]. Besides reproducing this observation, two years later Noe *et al.* reported *CCL5* upregulation in MeVac-infected U373 cells as well as increased CCL5 levels in supernatants from infected cultures [227]. These findings have recently been validated on the mRNA and protein level in a different human astrocytoma cell line (LNZ308 cells, *in vitro* study) and in a human hepatocellular carcinoma (HCC) xenograft model [126,127]. Besides *CCL5* and *CXCL10*, the HCC xenograft study also reported upregulation of *CCL3* and *CCL4* in MeVac-treated tumors compared

to mock controls. However, these genes showed a lower fold-change upregulation compared to *CCL5* and *CXCL10*.

Together, these results suggest that CCL3, CCL4, CCL5, and CXCL10 attract immune cells into the tumor during MeVac virotherapy. However, these studies are tumor-centric and do not consider the TME. This is a major limitation, since non-malignant cells located at the tumor site might also regulate the chemotactic environment of solid tumors. As an additional caveat, human tumors developed in immunodeficient mice lack infiltration of certain immune cell populations. Moreover, in preclinical studies, human tumor cells might not interact as efficiently as murine tumor cells with other murine cell populations present in the tumor bed.

To overcome these limitations, I conducted bulk gene expression analyses using total RNA from murine tumors developed subcutaneously in fully immunocompetent mice. Focusing on lymphocyte attractants, these analyses revealed intratumoral upregulation of *Ccl5*, *Ccl19*, *Cxcl9*, *Cxcl10*, and *Cxcl13* in MC38cea and B16-derived tumors treated with MeVac (Schwarz strain or Edmonston B-derived strain) compared to mock treatment (Figure 8). Thus, my results are in line with the *CCL5* and *CXCL10* upregulation reported in the previous studies that used human cells [126,127,226,227]. Importantly, the pattern of gene upregulation that I identified was shared across tumor entities (colon adenocarcinoma, melanoma) and MeVac strains (Schwarz, Edmonston B-derived). This suggests that intratumoral upregulation of *Ccl5*, *Ccl19*, *Cxcl9*, *Cxcl10*, and *Cxcl13* is a general immunological effect of MeVac virotherapy.

While my investigations focused on the RNA level, in subsequent studies I will conduct ELISA or cytokine bead arrays on total tumor lysates to determine whether the higher mRNA levels of the above-mentioned genes correlate with higher intratumoral expression of the encoded proteins. Moreover, I intend to identify the cell types upregulating each of these genes within the TME by conducting gene expression analyses at the single-cell level.

In vitro, I found that MeVac-infected MC38-hCD46 cells secrete higher levels of CCL5, CXCL9, and CXCL10 as compared to mock-infected cells (Figure 9). This suggests that the upregulation of *Ccl5*, *Cxcl9*, and *Cxcl10* detected in MeVac-treated MC38cea tumors could have taken place in tumor cells. In parallel, these genes might have been upregulated in other cell types from the TME, such as DCs [228], NK cells [229], and tumor-associated macrophages [225].

Conversely, MC38-hCD46 cells did not secrete CCL19, CCL21, or CXCL13 upon *in vitro* exposure to MeVac (Figure 9), although *Ccl19* and *Cxcl13* were upregulated at the tumor site in the animal experiments (Figure 8). Thus, I assume that, *in vivo*, MeVac-mediated upregulation of *Ccl19*, *Cxcl13*,

and perhaps *Ccl21* [xix] occurred in non-malignant cells. Importantly, in several human and murine tumor models increased levels of CCL19, CCL21, and CXCL13 correlate with the formation of tertiary lymphoid structures (TLS) at the tumor site, which are a good prognostic marker of response to immunotherapy in many tumor entities [230]. Current reviews in the field postulate that the cross-talk between immune cells and stromal cells via the lymphotoxin αβ signaling pathway drives the secretion of these chemokines by stromal cells at the tumor site [231]. Thus, stromal cells could have been the ones responsible for the increased levels of *Ccl19* and *Cxcl13* mRNA that I detected in my studies. Supporting this hypothesis, the data that I analyzed also revealed upregulation of genes involved in the lymphotoxin signaling pathway (*Lta*, *Ltb*, *Tnf*, *Tnfsf14*) in MeVac-treated tumors compared to mock controls (Figure 8).

Therefore, I speculate that MeVac virotherapy might trigger the development of TLS in B16 and MC38 tumors. In this regard, P. S. Backhaus from our research group recently observed lymphoid aggregates in histological sections from MeVac-treated B16-hCD46 melanomas (s.c.) (data not shown). Further studies could investigate whether these aggregates are organized into TLS, for instance by immunofluorescence [232]. In fact, the idea of studying whether OVs promote intratumoral TLS formation and, if so, investigating how this phenomenon modulates antitumor immunity, was recently proposed as a new research line in the field of oncolytic virotherapy [233]. Engineering OVs to enhance intratumoral TLS neogenesis is also under investigation [234].

Overall, my studies are in line with previous reports showing increased T cell abundance at the tumor site upon MeVac virotherapy. My findings validate previous results showing *CCL5* and *CXCL10* upregulation in MeVac-treated tumors, but using more physiologically-relevant models (syngeneic murine tumor models instead of *in vitro* cultures and xenograft models). Based on my findings and literature, I postulate that CCL5, CCL19, CXCL9, CXCL10, and CXCL13 play a relevant role in the antitumor immune response triggered by MeVac virotherapy. Finally, I discuss the cell types that might have upregulated the genes encoding the above-mentioned chemokines in the tumor bed and hypothesize that MeVac virotherapy might promote TLS neogenesis, a line of research which I will focus on in follow-up studies.

5.2.3 Correlation Between Chemokine-Encoding Genes and Therapeutic Efficacy

The gene expression analysis that I conducted showed that MeVac therapy leads to *Ccl5*, *Ccl19*, *Cxcl9*, *Cxcl10*, and *Cxcl13* upregulation at the tumor site compared to mock treatment (Figure 8). Remarkably, the extent of this upregulation was higher in tumors from mice treated with MeVac encoding an immunomodulator as compared to treatment with MeVac encoding a control

[xix] Gene expression data for *Ccl21* is missing, since this gene was not included in the NanoString panel.

molecule (control virus). Previous efficacy studies with the same viruses had shown that, although all virus variants are therapeutically better than mock treatment, MeVac encoding an immunomodulator confers better therapeutic efficacy compared to the control viruses [142,144]. Thus, the results from the gene expression analysis reveal a positive correlation between the therapeutic efficacy of MeVac variants and intratumoral upregulation of *Ccl5*, *Ccl19*, *Cxcl9*, *Cxcl10*, and *Cxcl13*: the stronger the upregulation, the higher the therapeutic outcome.

This correlation prompted me to hypothesize that the increase in intratumoral abundance of specific chemokines is a key mechanism of action of MeVac virotherapy. However, I also reasoned that MeVac virotherapy alone (*i.e.*, without immunomodulators) might not exploit the full potential of this mechanism, since the levels of chemokine-encoding genes and the therapeutic efficacy of the virus are further enhanced with the addition of an immunomodulator.

To address whether the chemokines encoded by *Ccl5*, *Ccl19*, *Cxcl9*, *Cxcl10*, and *Cxcl13* modulate MeVac therapeutic efficacy, I planned gain of function (GOF) and loss of function studies (LOF). The GOF approach was designed to elucidate whether the chemokines are limiting factors of MeVac therapy, *i.e.*, whether the therapy benefits from increasing the intratumoral abundance of CCL5, CCL19, CXCL9, CXCL10, or CXCL13 above the levels achieved with the virus alone. The LOF approach should unravel whether specific chemokines are essential for the therapeutic efficacy of the virus. During my doctoral studies, I focused on the GOF approach. In the future, I will conduct the LOF studies by treating tumor-bearing immunocompetent mice with unmodified MeVac (i.t.) and antibodies blocking specific chemokine pathways (i.p.). As readout, I will compare the therapeutic efficacy of these treatment approaches to that of MeVac monotherapy (MeVac treatment in the absence of blocking antibodies) and to mock treatment.

5.2.4 MeVac Variants Encoding Chemokines

Focusing on the GOF studies, to overexpress the candidate chemokines in the TME I generated and characterized several MeVac Schwarz strain vectors, each encoding a chemokine of interest (Figure 10). With this approach, I expected virotherapy to increase intratumoral chemokine concentrations via two mechanisms: (i) upregulation of endogenous chemokine-encoding genes, namely those identified in the gene expression analysis (*Ccl5*, *Ccl19*, *Cxcl9*, *Cxcl10*, and *Cxcl13*), and (ii) expression of the MeVac-encoded chemokine during viral replication. It should be noted that the second mechanism is restricted to the overexpression of a single chemokine. In future studies, I could expand this mechanism by generating novel MeVac variants, each encoding several chemokines, or by treating mice with several of the MeVac variants that I have generated, each encoding one chemokine. As control virus, I employed MeVac encoding the Fc region of hamster IgG (MeVac IgG-Fc *C.m.*). Since this virus does not encode any chemokine, it should only mediate

chemokine expression via the first mechanism. Although *Ccl21* was not included in the gene expression analysis, I also generated a MeVac variant encoding this chemokine, since its physiological role is similar to that of CCL19. From the two CCL21 isoforms, I chose to encode CCL21a, as this is the predominant isoform in lymphoid tissue and thus the one that I expect to be expressed in intratumoral lymphoid aggregates. All MeVac variants, including the control virus, showed similar replication kinetics and cytotoxic properties within a given cell line, as assessed in MC38-hCD46 and B16-hCD46 murine tumor cells (Figure 10).

To determine whether the identified chemokines (CCL5, CCL19, CCL21, CXCL9, CXCL10, and CXCL13) are limiting factors of MeVac therapy, I conducted *in vivo* GOF experiments employing therapeutic efficacy as readout in wild-type C57BL/6J mice bearing B16-hCD46 (s.c.) or MC38-hCD46 (s.c.) tumors. *In vitro*, MeVac-encoded murine CXCL9, CXCL10, CCL19, and CCL21a showed stronger T cell chemotactic properties compared to MeVac-encoded murine CCL5 and CXCL13 (Figure 12). Thus, I focused the *in vivo* studies on the viruses encoding these four chemokines, *i.e.*, MeVac mCXCL9, MeVac mCXCL10, MeVac mCCL19, and MeVac mCCL21a.

5.2.5 Contribution of Chemokine Overexpression to OV Therapeutic Efficacy

Contrary to my hypothesis, the GOF studies revealed similar therapeutic efficacy between MeVac encoding murine chemokines and the control virus (Figure 13, Figure 14). Therefore, I conclude that, in B16-derived and MC38-derived tumors, murine CXCL9, CXCL10, CCL19, and CCL21a do not limit the efficacy of MeVac virotherapy.

Supporting this conclusion, R. Veinalde found no therapeutic benefit in the treatment of subcutaneous MC38cea tumors with CEA-retargeted MeVac mCXCL10 compared to the control virus (CEA-retargeted MeVac, no chemokine encoded) [145]. In both studies (that of R. Veinalde and the present one, Figure 14), only 10 % of tumor-bearing mice treated with MeVac mCXCL10 (either retargeted or not) experienced complete tumor remission. Along the same line, an oncolytic adenovirus (AdV) encoding murine CXCL10 (AdV-CXCL10) conferred similar therapeutic efficacy compared to the control virus (AdV-Ctrl, no chemokine encoded) when administered intratumorally in mice bearing subcutaneous MC38 tumors that express the coxsackievirus and adenovirus receptor (MC38-CAR tumors) [235]. Neither AdV-CXCL10 nor the control virus mediated complete tumor remissions. These findings contrast with virotherapy studies employing oncolytic parvoviruses, since intratumoral delivery of a rodent parvovirus encoding CXCL10 (MVMp/IP-10) has proven more efficacious than parental MVMp in syngeneic models of murine sarcoma (H5V tumors, s.c.) and murine glioblastoma (GL261 tumors, s.c.) [236,237].

Using viral platforms other than MeVac, previous studies have also addressed the role of CXCL9, CCL19, and CCL21 in oncolytic virotherapy. In this regard, intratumoral administration of an oncolytic vesicular stomatitis virus (VSV) encoding murine CXCL9 (VSV-mCXCL9) conferred similar therapeutic efficacy compared to VSV encoding a control molecule (VSV-GFP) in syngeneic models of murine non-small cell lung cancer (LM2 tumors, s.c.) or plasmacytoma (5TGM1 tumors, s.c.) [238].

Regarding murine CCL21, also known as 6CK, intratumoral administration of oncolytic herpes simplex virus type 1 (HSV1) encoding this chemokine (rHsvQ1-m6CK) delayed the growth of orthotopic murine brain tumors (KR158B-Luc model) and murine metastatic brain tumors (4T1-Luc model) compared to the parental virus (rHsvQ1, no chemokine encoded) [239]. Oncolytic adenovirus encoding human CCL21 and IL-21, or human CCL21 alone, have also been described but only employed *in vitro* [240].

The contribution of the CCL19/CCL21/CCR7 axis to oncolytic virotherapy has also been explored by encoding CCL19 in OVs. Intratumoral delivery of oncolytic herpes simplex virus type 2 (HSV2) encoding CCL19 and IL-7 (oHSV2-IL7xCCL19) delayed the growth of subcutaneous CT26 tumors in BALB/c mice as compared to mock treatment [241]. Since this study did not include any control virus, it remains unknown whether encoding these molecules improved the therapeutic efficacy of the parental virus. In another study, intraperitoneal administration of oncolytic vaccinia virus (VACV) encoding murine CCL19 (vvCCL19) delayed the growth of subcutaneous MC38 tumors as compared to the control virus (vvDD, no chemokine encoded), but this effect was insufficient to reach complete tumor remissions [242]. Using a very similar tumor model (MC38-hCD46, s.c.), in my studies intratumoral delivery of MeVac mCCL19 led to complete tumor remission in three of ten mice (Figure 14). However, I observed the same rate of complete responders in the group receiving control virus, indicating that murine CCL19 does not limit the efficacy of MeVac virotherapy.

In summary, the role of chemokines in oncolytic virotherapy has been addressed using both DNA (HSV, VACV, AdV, parvovirus) and RNA (VSV, MeVac) viral platforms. The preclinical therapeutic efficacy of these viruses, as compared to the unmodified parental virus or the parental virus encoding a control molecule, ranges from no therapeutic difference to delayed tumor growth and prolonged survival. Among other factors, the viral platform, the tumor model, the treatment schedule, and the encoded chemokine probably contributed to the wide spectrum of therapeutic outcomes.

5.2.6 Modulation of Chemokine-Mediated Immune Cell Recruitment

As indicated above, the GOF efficacy studies that I conducted revealed that CXCL9, CXCL10, CCL19, and CCL21 do not limit MeVac therapeutic efficacy in syngeneic models of murine melanoma and murine colon adenocarcinoma, since overexpression of these chemokines did not improve the efficacy of the virotherapy. Various mechanisms might have prevented the overexpressed chemokines from enhancing MeVac therapeutic efficacy. In the following paragraphs, I elaborate on these mechanisms following the steps required for chemokine-mediated immune cell recruitment.

(i) Chemokine Expression

The first step required for chemokine-mediated immune cell recruitment is chemokine expression. Given that expression of virus-encoded molecules depends on viral replication, there is the possibility that in my studies the chemokines were not overexpressed because the viruses encoding them did not replicate *in vivo*. I consider this option unlikely, since I showed that B16-hCD46 and MC38-hCD46 cells support viral replication *in vitro* (Figure 10, Figure 32). Moreover, using supernatants from Vero cells infected with the different MeVac variants, I confirmed that the transgenes are expressed on the protein level and that the encoded chemokines are functional (Figure 10, Figure 12). In follow-up studies, I will repeat these *in vitro* experiments with supernatants from infected murine tumor cells instead of Vero cells. Regarding *in vivo* studies, others and I have detected intratumoral MeVac mRNA, indicative of MeVac replication, up to five days after treatment completion in similar preclinical models (Figure 17, Figure 21) [142]. To gain deeper insights into viral replication, I am establishing *ex vivo* tumor staining methodologies in collaboration with T. Poth, which include fluorescence *in situ* hybridization for MeVac *N* mRNA and immunohistochemistry for MeVac N protein. Moreover, I plan to assess transgene expression *in vivo* by conducting ELISA on total tumor lysates from mock-treated mice and mice treated with control MeVac or MeVac encoding chemokines.

(ii) Generation of a Tumor to Blood Chemokine Gradient

Aside from chemokine expression, the establishment of a chemokine gradient between the tumor and the bloodstream is another requirement for directed cell migration via chemotaxis.

In this regard, the first aspect to consider is chemokine availability. Typically, chemokines regulate cell migration by signaling through G protein-coupled receptors (GPCRs), mainly expressed on immune cells [223,243]. However, the overexpressed chemokines might have been scavenged by atypical chemokine receptors (ACKRs) such as ACKR4, shown to scavenge CCL19 and CCL21 in E0771 murine breast cancer tumors [244], or GPR182, shown to scavenge CXCL9 and CXCL10 in murine

melanoma models, including the B16 model [245]. Chemokine binding to these receptors, mainly expressed on non-immune cells, triggers internalization of the chemokine-receptor complex, thereby reducing chemokine availability and limiting the recruitment of immune effector cells into the site of chemokine production [243].

The establishment of a functional chemokine gradient might have also been impaired by chemokine cleavage. For instance, dipeptidylprotease 4 (DPP4), strongly expressed in B16 tumors, could have cleaved CXCL10 into an inactive product [246]. As another example, the strong expression of matrix metalloproteinase 3 (MMP3) in MC38 tumors [247] might have induced MMP9 secretion from tumor-associated macrophages [248], thereby promoting cleavage of CXCL9 and CXCL10 into inactive products [249]. To counteract these processes, protease inhibitors have been administered in combination with OVs or encoded in the viral genome [247,250].

Despite the above-mentioned mechanisms, the generation of tumor to blood gradients has been confirmed in previous studies with OVs encoding murine CXCL9 or CXCL10 [235,238]. To assess the establishment of these gradients in the context of my project, I will conduct ELISA on serum samples and total tumor lysates from mock-treated mice and mice treated with control MeVac or MeVac encoding chemokines.

(iii) Chemokine Sensing and Immune Cell Infiltration

Once the tumor to blood chemokine gradient is established, circulating immune cells expressing the cognate chemokine receptor sense the chemokine in the bloodstream (low chemokine concentration) and migrate along the gradient towards the tumor (high chemokine concentration).

However, the establishment of a chemokine gradient is no warrantee of intratumoral immune cell infiltration. This is exemplified by the VSV-mCXCL9 study, in which, despite mediating a stronger tumor to blood CXCL9 gradient, treatment with the chemokine-encoding virus did not increase intratumoral T cell abundance when compared to the control virus [238]. Regarding the underlying mechanisms, Eckert *et al.* hypothesized that the stronger CXCL9 gradient might have led to high CXCL9 concentrations in the blood. This might have saturated CXCR3 receptors on circulating T cells, making them unresponsive to the even higher chemokine concentrations at the tumor site.

Another factor to consider when discussing tumor-infiltrating immune cells is the extracellular matrix (ECM). In MC38 tumors, cancer-associated fibroblasts become more abundant as the tumor progresses and reticulin deposition increases over time [251]. These phenomena result in a denser ECM, which, in my studies, might have physically hampered immune cell recruitment into MC38 tumors even in the presence of a chemokine gradient strengthened by the virus-encoded chemokines. In the murine melanoma model, this is unlikely, since B16 tumors have a low stroma

content and minimal levels of collagen deposition [252]. Several therapeutic approaches aim at disrupting the ECM while limiting the risk of metastasis associated with this procedure. In the context of oncolytic virotherapy, the combination of chemotherapy with an oncolytic adenovirus encoding hyaluronidase [73], an enzyme that disrupts the ECM by degrading hyaluronic acid, is under clinical investigation for the treatment of patients suffering from pancreatic ductal adenocarcinoma (NCT05673811).

(iv) Phenotype of Chemokine-Recruited Immune Cells

Another phenomenon hampering the potential therapeutic benefit of chemokine overexpression could be the recruitment of tolerogenic immune cells. For instance, CXCL9 and CXCL10 could have attracted a subset of T_{REG} cells expressing the corresponding chemokine receptor (CXCR3), thereby limiting T cell-mediated antitumor immunity [253]. Indeed, in ovarian cancer patients intratumoral infiltration of CXCR3(+) T_{REG} cells has been documented and associated with disease progression[254]. Likewise, CCL19 and CCL21 could have recruited CCR7(+) T_{REG} cells and myeloid-derived suppressor cells (MDSCs) into the tumors, leading to immune escape [255].

However, although possible, these phenomena are rare. Typically, CXCL9 and CXCL10 recruit cells with antitumor activity, namely CD4(+) T_H1 cells, CD8(+) CTLs, and NK cells, whereas intratumoral CCL19 and CCL21 attract naïve T cells and DCs to the tumor site, thus promoting *in situ* T cell priming and activation [223]. In this line, two studies have reported increased abundance of immune effector cells in tumors treated with chemokine-encoding OVs compared to treatment with the control virus. In one of these studies, treatment with vaccinia virus encoding murine CCL19 (vvCCL19) increased the abundance of CD11c(+) cells, CD4(+) T cells other than CD4(+) T_{REG}, and CD8(+) T cells in MC38 tumors (s.c.) compared to treatment with the control virus [242]. These effects were detected between eight and twelve days after therapy with a single intraperitoneal virus dose. Using the same tumor model, but with ectopic expression of the coxsackievirus and adenovirus receptor (MC38-CAR tumors), Li *et al.* found higher percentages of CD4(+) and CD8(+) T cells expressing CXCR3 (the receptor for CXCL10) in tumors treated with AdV-CXCL10 compared to the control virus two to ten days after the last intratumoral virus dose [235]. These results suggest that AdV-encoded CXCL10 contributed to the increase in intratumoral T cell abundance by recruiting CXCR3(+) T cells to the tumor. However, the authors did not analyze the activation and differentiation phenotype of the recruited cells.

In the future, I will conduct flow cytometry analysis of mock-treated tumors and tumors treated with control MeVac or MeVac encoding chemokines to determine whether encoding chemokines in MeVac vectors increases the percentage of intratumoral immune cells. In these studies, I will also characterize the phenotype and activation state of several lymphoid and myeloid populations

within the tumor immune compartment and determine the percentage of intratumoral immune cells expressing the cognate receptors for the virus-encoded chemokines, those being CXCR3 (for CXCL9 and CXCL10) and CCR7 (for CCL19 and CCL21).

(iv) T Cell Exhaustion

Finally, in a scenario in which OV-mediated chemokine overexpression enhances intratumoral recruitment of immune effector cells, the increased abundance of cytotoxic immune cells at the tumor site might be insufficient to improve therapeutic efficacy, for instance due to immune cell exhaustion. As an example of this phenomenon, in the above-mentioned study from Li *et al.* AdV-CXCL10 conferred similar therapeutic efficacy compared to the control virus despite increasing the intratumoral abundance of CXCR3(+) T cells [235]. Mechanistically, the authors identified T cell exhaustion via the PD-1/PD-L1 axis as the main pathway mediating resistance to AdV-CXCL10 therapy. To tackle this resistance mechanism, Li *et al.* combined local AdV-CXCL10 with systemic anti-PD-1 antibody. Indeed, the combination treatment significantly prolonged survival compared to either monotherapy. Importantly, this combination also showed better therapeutic efficacy compared to anti-PD-1 plus control virus, indicating that, overall, the therapy benefited from encoding the chemokine in the viral vector. The underlying mechanisms of the triple therapy (AdV + CXCL10 [encoded in the viral vector] + anti-PD-1) comprised an increase in the intratumoral abundance of CXCR3(+) T cells (both CD4[+] and CD8[+]) as well as an increase in the levels of IFN-γ and granzyme B in tumors treated with the triple therapy compared to the dual therapies or monotherapies [235].

The combination of chemokine-encoding OVs with immune checkpoint blockade (ICB) might also prove efficacious in the context of MeVac virotherapy, particularly since MeVac therapy increases PD-L1 expression on tumor cells [150,216]. However, before testing this complex combination it is imperative to gain a better understanding of the mechanisms that led to similar therapeutic efficacy between the MeVac variants encoding chemokines and the control virus. Additionally, it is also necessary to gain mechanistic insights into the combination of ICB with MeVac virotherapy in the absence of virus-encoded chemokines (see 5.3).

Overall, several mechanisms might have hampered the expected therapeutic benefit of chemokine overexpression in the context of MeVac virotherapy, from chemokine availability to the phenotype and activation state of the attracted cells. The mechanistic studies planned for the near future will complement the results from the efficacy experiments shown in the present thesis and shed light into the main bottlenecks of this therapeutic approach, thereby providing the rationale for the preclinical assessment of novel (and probably more complex) treatment approaches.

5.3 The Role of PD-1/PD-L1 in MeVac Virotherapy

Oncolytic virotherapy induces PD-L1 upregulation in a wide range of tumor models. In the context of MeVac therapy, *in vitro* studies have confirmed higher PD-L1 expression on MeVac-treated murine tumor cells compared to mock controls [150,216]. This phenomenon has also been observed in a subset of patient-derived PDAC cultures [165] and patient-derived glioblastoma cultures[147,216]. Regarding preclinical studies, others and I have identified upregulation of *Pdcd1* and *Cd274* (encoding murine PD-1 and PD-L1, respectively) in MeVac-treated B16-derived tumors compared to mock-treated tumors (Figure 28) [142]. The PD-1/PD-L1 pathway is a key mediator of immunosuppression. Among its pleotropic roles, this axis promotes T cell exhaustion, MDSC generation and macrophage repolarization to a pro-tumorigenic phenotype [256]. Therefore, PD-L1 upregulation following MeVac therapy stands as a potential resistance mechanism to MeVac-mediated antitumor immunity. This provides a rationale for combining MeVac virotherapy with PD-1/PD-L1 checkpoint blockade. During my doctoral studies, R. Veinalde and I investigated this combination approach in fully immunocompetent murine models of colon adenocarcinoma (MC38cea tumors, s.c.) and pancreatic ductal adenocarcinoma (PDAC) (FC1245-hCD46 tumors, s.c.).

5.3.1 MeVac Combined with PD-1/PD-L1 Blockade in Murine Colon Adenocarcinoma

Recently, two MeVac (Schwarz strain) virotherapy studies showed that 40% of mice bearing colon adenocarcinoma (MC38cea model, s.c.) experience complete tumor remission upon virotherapy. However, tumors progressed in 60% of mice [135,144]. Since MC38 cells upregulate PD-L1 upon MeVac exposure [150], R. Veinalde and I hypothesized that, in these studies, immunosuppression induced by the PD-1/PD-L1 axis might have restricted the therapeutic potential of MeVac. To address this hypothesis, we combined MeVac virotherapy with PD-1/PD-L1 blockade by encoding scFv-Fc molecules targeting murine PD-1 (αmPD-1) or PD-L1 (αmPD-L1) in CEA-retargeted MeVac (Schwarz strain). As control, we generated MeVac variants encoding the corresponding Fc region. Similar viruses have been generated using the MeVac Edmonston B-derived strain [134].

In our study, MeVac encoding αmPD-1 or αmPD-L1 induced stronger antitumor immune memory compared to the control viruses, thus supporting the notion that the PD-1/PD-L1 axis reduces MeVac-mediated antitumor immunity (Figure 19). However, blocking the PD-1/PD-L1 pathway was insufficient to improve therapeutic efficacy, indicating that, in addition to PD-1/PD-L1, other pathways regulate the response to MeVac virotherapy (Figure 18). Indeed, various mechanisms might limit the immunotherapeutic effects of the virus. In this scenario, breaking resistance to MeVac virotherapy might require simultaneous targeting of several pathways. Supporting this idea, triple combination strategies consisting of OV, PD-1/PD-L1 blockade, and an additional

immunomodulator encoded in the viral vector, such as CXCL10 or IL-12, have proven more efficacious than the monotherapies and dual therapies in specific settings [235,257,258]. Local correlates of response include reduced immunosuppression, increased T cell abundance, and enhanced cytotoxicity at the tumor site.

Similar triple combinations could be investigated in the context of MeVac virotherapy, for instance by combining systemic PD-1/PD-L1 blockade with the MeVac mCXCL10 vector that I generated (Figure 10) or with MeVac encoding a murine IL-12 fusion protein (MeVac FmIL-12), a virus under preclinical investigation [135,144]. The triple combination of MeVac with PD-1/PD-L1 blockade and CXCL10 could be studied in the MC38 tumor model, where MeVac virotherapy does not benefit from single combination with CXCL10 or with PD-1/PD-L1 blockade (Figure 14, Figure 18). In this tumor model, MeVac therapeutic efficacy might be limited by insufficient intratumoral T cell recruitment and by exhaustion of the T cells that do infiltrate. In this case, the combined effect of a chemokine and PD-1/PD-L1 blockade might be required to counteract resistance to virotherapy. This tumor model, however, would not be suitable to study the triple combination of MeVac, PD-1/PD-L1 blockade, and IL-12, since the dual combination of MeVac plus IL-12 (MeVac FmIL-12) already mediates complete tumor remission in 90% to 100% of tumor-bearing mice [135,144]. Instead, this triple combination could be investigated in the B16 model, where the dual therapies (either MeVac plus IL-12 or MeVac plus PD-L1 blockade) are insufficient to cure the mice [134,144]. In agreement with this suggestion, 80% of mice bearing B16-derived tumors experienced complete tumor remission upon therapy with PD-1 blockade plus oncolytic Semliki Forest Virus encoding IL-12 (SFV IL-12), whereas tumors progressed in all mice receiving mock treatment, monotherapy, or dual therapy with SFV IL-12 or SFV plus PD-1 blockade [257].

5.3.2 MeVac Combined with PD-1/PD-L1 Blockade in Murine PDAC

Oncolytic virotherapy has limited efficacy in preclinical PDAC when administered alone [259]. The desmoplastic and immunosuppressive nature of these tumors, characterized by high abundance of PD-L1(+) stromal cells [260], prompted R. Veinalde and me to hypothesize that the PD-1/PD-L1 pathway might confer resistance to oncolytic virotherapy in this tumor entity. Focusing on MeVac, we addressed this hypothesis by comparing the immune response triggered by the virus in the presence or absence of PD-1 blockade. To that aim, we employed a syngeneic murine PDAC model that resembles the human disease.

5.3.2.1 FC1245-hCD46 as Preclinical PDAC Model

The contribution of PD-1/PD-L1 blockade to oncolytic virotherapy for the treatment of PDAC was recently studied in the Panc02 murine PDAC model (s.c.) using oncolytic adenovirus [259]. However, the Panc02 model, which was induced chemically [261], does not recapitulate the mutational landscape of human PDAC. For instance, it does not harbor *Kras* and *Trp53* mutations [262], which play a major role in the development of the human disease [263]. Moreover, despite widely employed as model for pancreatic adenocarcinoma of ductal origin, Panc02 cells do not express the ductal marker cytokeratin 19 (CK19) [264]. Therefore, the clinical relevance of this model is debatable, particularly nowadays when more refined PDAC models are available [265]. To overcome these limitations, we employed the FC1245-hCD46 (s.c.) transplantable murine PDAC model, which derives from PDAC developed in a *LSL-Kras*$^{G12D/+}$ *LSL-Trp53*$^{R172H/+}$ *Pdx-1-Cre* triple-mutant mouse (KPC mouse) [164]. Spontaneous PDAC development in KPC mice reproduces many key features of the human disease [264]. Consistently, KPC-derived PDAC cell lines harbor the *Kras*^{G12D} and *Trp53*^{R172H} mutations and express the ductal marker CK19 [264]. Therefore, R. Veinalde and I considered the transplantable KPC-derived FC1245-hCD46 model to be of clinical relevance.

5.3.2.2 Therapeutic Efficacy

Using the FC1245-hCD46 model, R. Veinalde investigated the therapeutic effect of systemic PD-1 blockade (anti-PD-1 antibody, i.p.) and local MeVac virotherapy (i.t.). While the model proved refractory to either monotherapy, animals receiving the combination treatment showed significantly prolonged survival (Figure 20). In terms of tumor progression, the therapeutic effect of the combination treatment was greater than the additive effect of each monotherapy, suggesting a synergistic interaction between MeVac virotherapy and PD-1 blockade in PDAC. Consistent with these data, the above-mentioned study conducted in the Panc02 model also reported a therapeutic advantage of the combination treatment over the monotherapies [259].

5.3.2.3 Immunological Correlates of Response

To gain insights into the mechanisms underlying the efficacy of the combination treatment, I investigated the development of systemic antitumor immunity. Indeed, I found that the combination treatment induces a systemic and tumor-specific immune response, whereas mock treatment and anti-PD-1 monotherapy do not. Remarkably, and consistent with the role of OVs as antigen-agnostic cancer vaccines [68], mice receiving the virus monotherapy developed a systemic and tumor-specific immune response as strong as those treated with the combination approach (Figure 24). This indicates that virotherapy was the main driver of the systemic antitumor response. However, despite triggering antitumor immunity, the virus monotherapy was insufficient to delay tumor growth (Figure 20), suggesting that later phases of the cancer-immunity cycle, namely

intratumoral immune cell recruitment and cytotoxic effector functions, might remain impaired upon virotherapy.

Given that the virus monotherapy, as well as the combination treatment, increased T cell abundance at the tumor site (Figure 22), R. Veinalde and I reasoned that resistance to virotherapy was not mediated by lack of T cell recruitment, but rather by impaired intratumoral infiltration of the recruited cells and/or impaired immune effector functions. In tumor immunophenotypting studies, we found that virotherapy required combination with PD-1 blockade to reshape the tumor immune environment towards a state of immune activation, characterized by upregulation of genes involved in complement regulation (*Cd55*), antigen presentation (*H2-Q10*), costimulation (*Icos*), immune cell migration (*Ccl7*, *Cxcr3*, *Cxcr6*), lymphocyte activation (*Cd6*), and cytotoxic effector functions (*Gzma*, *Gzmb*) (Figure 21). These results suggest that PD-1/PD-L1 was dispensable for priming a systemic antitumor immune response, but necessary at the periphery to counteract the immunosuppressive TME and support the effector phase of the primed response. Overall, this scenario is consistent with the physiological role of the PD-1/PD-L1 axis. While other immune checkpoints such as CTLA-4 regulate immune cell priming, the PD-1/PD-L1 pathway is mainly involved in peripheral immune tolerance and particularly studied in the field of cancer immunotherapy as a key mediator of intratumoral T cell exhaustion [28].

To my knowledge, no previous study has investigated immunological correlates of response to oncolytic virotherapy plus PD-1/PD-L1 blockade in fully immunocompetent PDAC models. Although this combination has entered clinical investigation for PDAC patients in the context of oncolytic adenovirus (NCT02705196) and reovirus [266,267], the corresponding preclinical studies were conducted in human PDAC xenografts or in syngeneic models of other tumor entities [268–271]. Kanaya *et al.* studied the combination of oncolytic adenovirus with PD-1/PD-L1 blockade in the Panc02 model, but focused only on therapeutic efficacy [259]. Two more studies have addressed this combination in the same tumor model, but employing a virus that encodes wild-type p53, a tumor suppressor protein [272,273]. In these studies, p53 overexpression might have influenced immunomodulation and therapeutic outcome. Thus, in the context of PDAC, whether our findings are translatable to other OV platforms and to the clinical scenario remains to be elucidated.

5.3.2.4 Antitumor and Antiviral Immunity

In our PDAC study, systemic antitumor immunity was maintained upon tumor progression (Figure 24). In contrast, the local pro-inflammatory effect of the combination treatment was transient and lost at later stages of the therapy (Figure 21). This loss could explain why tumor growth eventually resumed in mice receiving the combination treatment (Figure 20). In these mice,

tumor progression and loss of local immune activation was observed around two weeks after tumor implantation, coinciding with the withdrawal of anti-PD-1 therapy.

Future studies should therefore address whether prolonging the duration of PD-1 blockade by administering anti-PD-1 antibody for a longer period achieves durable TME remodeling and better therapeutic outcome. These studies should also address whether boosting the response with the OV is required. *A priori*, this seems unnecessary, since we detected a systemic antitumor immune response even after tumor progression (Figure 24). However, due to the aggressive nature of FC1245-hCD46 tumors, our studies only covered a period of two weeks from treatment onset, after which all mice had reached endpoint criteria. In other settings where long-term studies are possible, detection of a systemic antitumor immune response at early stages but absence of such a response at later stages (*e.g.* upon re-challenge of complete responders), would argue for boosting the antitumor response with additional OV doses. However, the boost schedule should be carefully considered, since the priming dose(s) could have triggered OV-specific immunity (as observed in our studies with measles-naïve mice, Figure 24). In this regard, heterologous prime-boost schedules might prove more effective than homologous prime-boost regimens [270]. Nevertheless, in the context of MeVac virotherapy, it should be noted that pre-existing immunity to the virus will be present even before the first dose, since most (if not all) patients eligible for MeVac virotherapy have been vaccinated against measles. The effect of pre-existing anti-OV immunity on the success of oncolytic virotherapy is currently under debate [71] (see 5.4.6).

5.3.3 MeVac Combined with PD-1/PD-L1 Blockade in Other Tumor Entities

Focusing on MeVac, previous studies have investigated the contribution of PD-1/PD-L1 blockade to oncolytic virotherapy in other tumor entities, namely murine melanoma [134] and murine glioblastoma [147,216]. In these studies, the combination treatment (MeVac + PD-1/PD-L1 blockade) also improved therapeutic efficacy as compared to either monotherapy. Therapeutic efficacy correlated with TME remodeling towards a state of immune activation, characterized by higher intratumoral ratios of CD8(+) T_{EFF} cells to Foxp3(+) T_{REG} cells, increased percentages of IFN-γ(+) CD8(+) T cells and GzmB(+) CD8(+) T cells among all intratumoral CD8(+) T cells, and decreased percentages of myeloid cells among all intratumoral immune cells. Consistent with these observations, in our PDAC study we detected upregulation of *Gzma* and *Gzmb* at the tumor site following treatment with the combination approach (Figure 21). Taken together, these results indicate that PD-1/PD-L1-mediated immunosuppression does not only confer resistance to MeVac therapy in PDAC, but rather in multiple tumor entities.

5.3.4 Concluding Remarks and Clinical Perspective

Overall, the role of PD-1/PD-L1 in MeVac virotherapy has been investigated in several syngeneic murine tumor models. Two patterns of response have been observed.

In tumor models partly responsive to the virus monotherapy (*e.g.*, MC38cea), blocking the PD-1/PD-L1 pathway has not improved the efficacy of the virotherapy despite strengthening antitumor immune memory. In these tumors, additional immunomodulation, for instance via triple combination approaches, might be required to break treatment resistance [235]. Alternatively, combining virotherapy with a strong immunomodulator, such as IL-12, might override the need for PD-1/PD-L1 blockade [135,144].

In contrast, in tumor models largely resistant to MeVac monotherapy (*e.g.*, FC1245, B16, GL261, CT-2A), the combination of MeVac with PD-1/PD-L1 blockade has significantly improved therapeutic efficacy compared to the monotherapies. In these tumors, TME remodeling towards a state of inflammation and immune activation has been identified as a major immune correlate of efficacy. Despite therapeutic improvement, this combination has been insufficient to achieve complete tumor remissions in most (if not all) mice, indicating that, while the PD-1/PD-L1 axis is a relevant mechanism of resistance to the virotherapy, additional processes are involved in immune evasion. Thus, these tumor models might benefit from more complex treatment combinations [257].

Based on these preclinical studies, I speculate that the combination of oncolytic MeVac with PD-1/PD-L1 blockade might prove efficacious in patients that do not respond to the respective monotherapies, particularly if the tumors have an immunosuppressive microenvironment. However, given that all preclinical models have limitations, the translational potential of the investigated therapies needs validation in clinical trials. Although MeVac is under clinical investigation as a single-agent treatment [149], to my knowledge no clinical trial has yet tested the combination of this OV with PD-1/PD-L1 blockade, with the exception of a trial assessing MeVac plus Atezolizumab in small cell lung cancer patients, which was terminated due to low recruitment (NCT02919449). Beyond the MeVac field, the combination of oncolytic virotherapy with PD-1/PD-L1 blockade is currently under clinical investigation for a wide range of tumor entities. OV platforms employed in these clinical trials include adenovirus (NCT03004183), herpes simplex virus (NCT03767348, NCT03866525, NCT04386967, NCT04616443, NCT04735978), reovirus (NCT03605719, NCT04445844), and vaccinia virus (NCT03206073, NCT04725331, NCT04787003), among others. Results from these studies, particularly those with an accompanying translational research program, are eagerly awaited and will provide valuable insights into the role of the PD-1/PD-L1 axis in oncolytic virotherapy.

5.4 Preclinical *In Vivo* Models of MeVac Oncolytic Immunotherapy

5.4.1 Current Models (Wild-Type Mice, IFNAR^{KO}-CD46Ge Mice)

To investigate the tumor vaccination effect of MeVac virotherapy, preclinical studies must be conducted in immunocompetent animals. However, these studies have long been hampered by the lack of small animal models that support MeVac infection of syngeneic tumor cells, especially since rodents do not express the MeVac entry receptors and are therefore not susceptible to MeVac. To circumvent this limitation, tumor cells have been rendered susceptible to the virus via two different approaches, discussed below.

i) MeVac Entry Via an Alternative Receptor (Human TAA, Murine TAA)

The first strategy to allow MeVac infection of murine tumor cells consisted in retargeting the virus to TAAs ectopically expressed on the tumor cell surface, such as human CEA or human CD20 [173]. This approach enabled MeVac to enter tumor cells via an alternative receptor, the human TAA. The first immunocompetent models of MeVac virotherapy were then developed by injecting murine tumor cells, expressing the TAA against which the virus had been retargeted, into wild-type mice and waiting for tumor establishment [134,135,274]. To date, these models are still in use. For instance, R. Veinalde and I followed this approach when treating wild-type mice bearing MC38cea tumors with CEA-retargeted MeVac (see 4.3) [150]. However, in this setting, the alternative MeVac entry receptor (human TAA) is only expressed on the engineered murine tumor cells, and not on host (murine) cells. The clinical situation would be different, as the alternative receptor would be a human molecule overexpressed on tumor cells, but potentially also expressed on non-malignant cells. To better resemble this situation, MeVac has been fully retargeted to the murine urokinase plasminogen activator receptor (uPAR), a murine antigen overexpressed on several murine tumor cell lines (*e.g.*, CT-2A, GL261, MC38) but also expressed at low levels on non-malignant cells [216,275]. Nevertheless, retargeted viruses do not represent the current clinical scenario, since all MeVac variants tested in clinical trials to date maintain the natural tropism.

ii) MeVac Entry Via a Natural Receptor (Human CD46)

To bypass the need for MeVac retargeting, others and I have generated murine tumor cells with ectopic expression of human CD46 and have confirmed the susceptibility and permissiveness of these cells to MeVac with natural tropism (see 4.7.2) [140,142,144,165,276]. We have then established novel models of MeVac virotherapy by injecting these cells into wild-type mice (*e.g.*, Figure 13, Figure 14, Figure 20) [142,144,165,276] or IFNAR^{KO}-CD46Ge mice [140] and waiting for tumor establishment. IFNAR^{KO}-CD46Ge mice are transgenic for human CD46 and express an inactive form of the murine

IFN-α/β receptor [207]. However, these mouse strains are not representative of the clinical situation. Wild-type mice are not susceptible to MeVac, whereas humans are, and IFNAR^{KO}-CD46Ge mice support extensive MeVac replication [277,278], whereas healthy human cells do not (see 5.4.3). Moreover, IFNAR^{KO}-CD46Ge mice do not have a functional type I IFN response, whereas humans do, at least in non-malignant cells.

In the next sections, I discuss how the susceptibility and limited permissiveness of non-malignant human cells to MeVac could influence the outcome of MeVac oncolytic immunotherapy.

5.4.2 Contribution of CD46 Expression on Non-Malignant Cells to MeVac Virotherapy

CD46 is constitutively expressed on all human nucleated cells [279]. Thus, while murine cells are not naturally susceptible to MeVac, all human cells (except erythrocytes) are. This susceptibility might therefore influence the safety, targeting, biodistribution, and antitumor efficacy of the MeVac variants under clinical investigation (all having natural tropism), potentially leading to results that differ from those observed in preclinical studies with wild-type mice. Before entering clinical trials, most of these aspects, particularly the pharmacodynamics, pharmacokinetics, safety, and toxicity of the measles virotherapeutic, are investigated in IFNAR^{KO}-CD46Ge mice [280,281], squirrel monkeys [280], or rhesus macaques [282], both susceptible to MeVac. However, since these studies are conducted in tumor-free animals, they do not address whether ubiquitous CD46 expression on host cells plays a role in antitumor efficacy and virus-host interactions at the tumor site in the context of MeVac oncolytic immunotherapy.

I hypothesize that ubiquitous CD46 expression contributes to the induction of an inflammatory response in the tumor bed by allowing MeVac infection of non-malignant cells located in the TME, subsequently leading to virus sensing by these cells and activation of pro-inflammatory signaling cascades. Consistent with my hypothesis, several *in vitro* and *ex vivo* studies have reported infection of various human cell types by MeVac of the Edmonston or Schwarz strain, including endothelial cells [283,284], B cells [285–287], T cells [285–288], DCs [190,191], monocytes/macrophages [191,287] (including M2 anti-inflammatory macrophages [191]) and, to a very limited extent, NK cells [192,287]. Subsequent *ex vivo* studies with human peripheral blood mononuclear cells (PBMCs) from healthy blood donors have shown that MeVac infection of DCs, NK cells, and monocyte-derived macrophages alters the phenotype of these cells by promoting DC maturation [125,130,132], NK cell activation [128], and macrophage repolarization from an M2 anti-inflammatory phenotype to an M1 pro-inflammatory phenotype [139,191]. Preliminary data from our research group suggest that these effects depend on receptor-mediated fusion of the MeVac envelope with the plasma membrane rather than

unspecific virus uptake via phagocytosis or other endocytic routes [191] [xx]. Since CD46 is the main MeVac entry receptor, these initial results argue for the involvement of CD46 in MeVac infection of non-malignant human cells. Consistent with this reasoning, infection of CD150(-) human endothelial cells by MeVac of the Edmonston strain was shown to be abrogated in the presence of anti-human CD46 antibodies [283].

Overall, these studies support my hypothesis that, in the context of MeVac oncolytic immunotherapy, ubiquitous CD46 expression contributes to tumor inflammation. This inflamed state might revert tumor immunosuppression and trigger subsequent steps of the cancer-immunity cycle, such as DC maturation and antigen presentation, thus contributing to the development of a T cell-mediated antitumor immune response.

5.4.3 Contribution of Virus Replication in Non-Malignant Cells to MeVac Virotherapy

The fact that MeVac infects non-malignant human cells raises the question on whether these cells support MeVac replication and productive infection. If that were the case, the interaction of MeVac with healthy host cells could modulate the outcome of MeVac virotherapy via several mechanisms. First, as discussed in the previous section, MeVac infection and virus sensing could modulate the phenotype of the non-malignant infected cells. Second, MeVac replication in these cells could contribute to *de novo* production of transgenes encoded in the recombinant viruses, such as immunomodulators. Third, productive MeVac infection would lead to the release of viral particles produced *de novo* in infected non-malignant cells, thus amplifying the initial virus dose and supporting multiple infection rounds. However, as observed in tumor cells, extensive MeVac replication could also result in death of the infected non-malignant cell.

It is therefore relevant to assess MeVac replication and production of viral progeny in non-malignant human cells. In this regard, our research group has detected MeVac replication in DCs and macrophages derived from primary human monocytes, albeit at lower levels compared to human tumor cells [190,191]. Importantly, human DCs and macrophages remain viable at least until 72 h after infection [191], whereas human tumor cells die [145,289]. In a previous study, Condack *et al.* infected human tonsil explants with MeVac *ex vivo*. Nine days after infection, they detected MeVac N protein in B cells, T cells, NK cells, and macrophages from these explants, thus arguing for viral replication [286]. Using a similar model system, Grivel *et al.* recovered infectious virus from *ex vivo* human tonsil explants up to twelve days after MeVac infection [285]. Thus, these results also

[xx] Ongoing doctoral studies of M. S. C. Finkbeiner.

argue for viral replication and production of viral progeny in non-malignant cells. However, the viral progeny titers remained low and infection only resulted in a modest cytopathic effect.

Together, these studies indicate that non-malignant human cells are permissive to MeVac, but only to a limited extent that does not result in cytotoxicity. Thus, expression of virus-encoded transgenes by infected non-malignant cells and *de novo* production of viral progeny by these cells do not seem to be major mechanisms contributing to MeVac virotherapy.

Overall, the data gathered to date support my hypothesis that, by infecting healthy cells without inducing cytotoxicity, MeVac induces a pro-inflammatory phenotype on non-malignant cells located at the tumor site and, at the same time, allows them to remain viable and therefore capable of interacting with other cells to trigger further steps of the cancer-immunity cycle. In agreement with my reasoning, Mosaheb *et al.* found that infection of DCs located at the tumor site promotes DC maturation and enhances antitumor immunity in the context of virotherapy with PVSRIPO, an oncolytic poliovirus-rhinovirus chimera [290]. Importantly, these findings argue for the *in vivo* study of oncolytic virotherapy in hosts susceptible to the virus under investigation.

5.4.4 CD46tg Mice as a Novel Model of MeVac Virotherapy

The studies discussed in the previous sections indicate that MeVac can infect non-malignant human cells and replicate in those cells to a low extent. To resemble this situation, preclinical *in vivo* studies of MeVac oncolytic immunotherapy should be conducted in hosts susceptible to MeVac, but showing limited permissiveness to the virus. However, the small animal models employed to date do not fulfil these criteria, since (i) wild-type mice are not susceptible to MeVac, and (ii) cells from IFNAR^{KO}-CD46Ge mice appear to be more permissive to MeVac than non-malignant human cells (as inferred from comparing [277,278] to [190,191]). The higher permissiveness is achieved by a targeted mutation in the *IFNAR* gene, resulting in the expression of an inactive form of the IFN-α/β receptor [207]. This mutation renders IFNAR^{KO}-CD46Ge mice immunodeficient, as they are unresponsive to type I IFNs, essential players of the antiviral immune response. Moreover, since the type I IFN response is also involved in antitumor immunity [291], IFNAR^{KO}-CD46Ge mice are not suitable to study the full potential of MeVac as oncolytic vaccines. To overcome these limitations, I propose studying MeVac virotherapy in immunocompetent mice transgenic for human CD46.

To that aim, I employed mice from the B6.FVB-Tg(CD46)2GsV/J strain (also known as MY II strain) [174,175]. This strain was generated by microinjection of a yeast artificial chromosome (YAC) harboring the complete *CD46* sequence (gene encoding human CD46) flanked by its endogenous regulatory elements (including the endogenous promoter) into fertilized murine oocytes [174]. Since the strain is usually maintained in hemizygosis, the gene encoding human CD46 might be

transferred or not to the offspring, resulting in non-carrier wild-type mice and in CD46-transgenic mice. I refer to the CD46-transgenic mice from this strain as "CD46tg". CD46tg mice are immunocompetent, have a C57BL/6 background, and express the different isoforms of human CD46 (BC1, BC2, C1, C2) on all nucleated cells at levels comparable to humans.

My thesis is the first one to report the usage of CD46tg mice in the field of MeVac virotherapy. Thus, before discussing the immunological effects of the therapy in these animals, I consider it relevant to elaborate on their susceptibility to MeVac and their tolerance to human CD46.

5.4.4.1 Susceptibility and Permissiveness to MeVac

The susceptibility and permissiveness of CD46tg mice to MeVac has only been investigated in one study [175]. However, three additional research groups have studied this aspect employing similar mouse strains, referred to as MBM-CD46, BAC-CD46, and CD46Ge [xxi]. These strains were generated by microinjection of a small (80 kb) DNA construct (MBM-CD46 strain [292]), a bacterial artificial chromosome (BAC-CD46 strain [293]), or a YAC (CD46Ge strain [207,294]) into fertilized murine oocytes. As for CD46tg mice, the microinjected construct carried *CD46* flanked by its regulatory elements. Thus, the mice from these strains are also immunocompetent and express the human CD46 isoforms at levels similar to humans. Given the similarity between the strains, I consider that the results obtained with MBM-CD46, BAC-CD46, and CD46Ge mice could be translatable to CD46tg mice. Therefore, in the next paragraphs I discuss findings made with any of the four mouse strains.

Overall, these studies investigated the susceptibility of transgenic mice to MeVac in two manners: (i) by establishing *ex vivo* cultures from transgenic mice and exposing these cultures to MeVac, or (ii) by administering MeVac into the mice and determining the presence or absence of infectious virus at specific timepoints.

Regarding the *ex vivo* experiments, Oldstone *et al.* detected viral antigens in MeVac-exposed peritoneal macrophages, skin fibroblasts, and kidney cells isolated from CD46tg mice, but not in those isolated from wild-type mice [175]. Similarly, Shingai *et al.* identified MeVac *H* RNA in virus-exposed DCs derived from the bone marrow of BAC-CD46 mice, but not in those derived from wild-type mice [293]. Consistent with these results, 24 h after MeVac exposure I detected higher levels of MeVac *N* mRNA in macrophages derived from the bone marrow of CD46tg mice compared to those derived from wild-type mice (Figure 26). In another *ex vivo* study, 48 h after MeVac exposure Blixenkrone-Møller *et al.* observed higher levels of MeVac N protein in lung cell cultures

[xxi] To my knowledge, the MBM-CD46 strain and the BAC-CD46 strain do not have official names. To distinguish them from the other strains, I employ the abbreviations MBM and BAC, respectively. MBM stands for "Model Blixenkrone-Møller" (referring to Blixenkrone-Møller, who is the first author of the publication describing the mouse strain). BAC stands for "Bacterial Artificial Chromosome" (referring to the methodology employed in the generation of the mouse strain).

established from MBM-CD46 mice compared to those established from wild-type mice [292]. All these findings contrast with a recent study by Mura *et al.*, who did not detect any signs of infection upon exposure of splenocytes from CD46-transgenic mice to MeVac [278]. However, Mura *et al.* employed the HMGCR-CD46 mouse strain [295] [xxii]. The splenocytes from these mice express much lower levels of CD46 compared to humans [279], CD46tg mice [174], BAC-CD46 mice [293], and CD46Ge mice [207] (no data reported for MBM-CD46 mice). Therefore, the results from the study by Mura *et al.* might not be translatable to the CD46tg mouse strain that I intend to employ as a novel *in vivo* model of MeVac virotherapy. As a side note, the difference in CD46 levels might have resulted from the fact that HMGCR-CD46 mice express the transgene under the control of a murine promoter instead of the endogenous *CD46* promoter [295].

Overall, the *ex vivo* studies discussed in the previous paragraph indicate that CD46tg mice, BAC-CD46 mice, and MBM-CD46 mice are susceptible to MeVac. Unfortunately, the studies from Oldstone *et al.* and Shingai *et al.* do not document the timepoint of analysis, so it remains unclear whether their findings only indicate virus infection, or also replication [175,293]. My study with murine macrophages (Figure 26) and that of Blixenkrone-Møller *et al.* [292] do not provide information on virus replication, either, as they only analyze one timepoint. In my study, there is the possibility that the MeVac mRNA detected 24 h after infection was not produced *de novo* in murine macrophages, but rather produced in Vero cells (virus producer cell line) and incorporated into the virions during budding. In that case, the mRNA would have been delivered into the murine macrophage upon infection and might have remained stable until the analysis timepoint. The same reasoning could apply to the MeVac N protein detected by Blixenkrone-Møller *et al.* 48 h after infection [292].

To investigate whether MeVac replicates in non-malignant murine cells expressing human CD46, time course experiments could be conducted (detecting more virus RNA/protein or more viral progeny over time would be indicative of viral replication). In this regard, I performed a pilot experiment by exposing bone marrow cultures from CD46tg mice or wild-type mice to MeVac eGFP and determining the percentage of eGFP(+) cells 4 h, 24 h, 48 h, and 72 h afterwards. Importantly, at all timepoints I detected a higher percentage of eGFP(+) cells in cultures established from CD46tg mice compared to those established from wild-type mice. The largest difference between both cultures was observed at the 4 h timepoint, suggesting that MeVac attaches to the surface of hCD46(+) murine cells more efficiently than to that of wild-type murine cells. However, the strong decrease in the percentage of eGFP(+) cells from the 4 h to the 24 h timepoint in cultures from CD46tg mice (Figure 25) suggests that most of the attached virus detaches rather than enters the

[xxii] I refer to this mouse strain as "HMGCR-CD46", where HMGCR stands for "Hydroxymethyl-glutaryl coenzyme A reductase" (the mice from this strain express human CD46 under the control of the murine *Hmgcr* promoter).

cells, or enters but does not replicate. In addition, whether the eGFP signal detected at the 24 h, 48 h, and 72 h timepoints corresponds to *de novo* eGFP production (thus arguing for viral replication) or to eGFP molecules present in the virus suspension employed for inoculation remains unknown. In the future, I will assess whether the signal detected at the 4 h and 24 h timepoints corresponds to MeVac entry. To that aim, I will conduct similar experiments in the presence of a receptor blockade (*e.g.*, anti-hCD46 antibody) or a fusion blockade (*e.g.*, FIP [193], a peptide that stabilizes MeVac F in the prefusion state). Moreover, I intend to study MeVac replication by determining the levels of MeVac-derived mRNA or protein in the cells at several timepoints after exposure to the virus, for instance by RT-qPCR or immunofluorescence. Another option would be to compare the levels of MeVac-derived mRNA or protein in cells infected with active virus to those in cells infected with UV-inactivated virus, which should not replicate. Productive infection could be assessed by determining the viral progeny titers at several timepoints after infection.

In fact, viral progeny was one of the readouts employed in the *in vivo* experiments that complement the above-mentioned *ex vivo* studies. In this regard, Oldstone *et al.* recovered infectious virus from PBMCs and splenic immune cells (namely CD4[+] T cells, CD8[+] T cells, B cells, and F4/80[+] macrophages) isolated from CD46tg mice two to five days after i.v. virus administration [175]. Using a different readout, in another *in vivo* study Roscic-Mrkic *et al.* detected MeVac H protein by flow cytometry on PBMCs isolated from CD46Ge mice three days after i.p. virus administration, but not on PBMCs isolated from MeVac-injected wild-type mice [294]. Importantly, MeVac H was no longer detected in PBMCs isolated at a later timepoint (six days after virus administration). These studies are in line with the *ex vivo* findings and suggest that the susceptibility of CD46tg mice and CD46Ge mice to MeVac is maintained *in vivo*. Recovery of infectious virus two to five days after virus administration argues for *de novo* production of viral particles, since the input virus should no longer be infectious at those timepoints (as it would have disassembled upon fusion with the plasma membrane of target cells or degraded if remaining outside the cell). However, the lack of MeVac H detection on the cell surface six days after virus administration suggests that, although the cells might be permissive to the virus, permissiveness is limited. While these studies were conducted in tumor-free mice, I am particularly interested in understanding whether non-malignant hCD46(+) cells from the TME support MeVac infection and replication in the context of MeVac virotherapy. To that aim, in future *in vivo* experiments I will analyze tumor sections obtained at different timepoints after i.t. virotherapy by fluorescence *in situ* hybridization (FISH) and IHC. These studies should determine the presence or absence of MeVac-derived RNA or protein, and elucidate the phenotype of the infected cells.

In summary, immunocompetent mice transgenic for human CD46 and expressing all isoforms of this molecule at levels comparable to humans (*i.e.*, CD46tg mice, MBM-CD46 mice, BAC-CD46 mice,

and CD46Ge mice) are susceptible to MeVac, since signs of viral infection have been detected in several cell populations from these mice. Although susceptible, the permissiveness of cells retrieved from these mice to the virus remains incompletely characterized. Preliminary data suggest that MeVac replication in hCD46(+) non-malignant murine cells is possible but limited. However, these initial findings have yet to be validated in mechanistic and time course studies. If confirmed, they will align with the results from the *ex vivo* studies conducted in non-malignant human cells (see 5.4.2 and 5.4.3), thereby supporting the notion that CD46tg mice are a more suitable model to study MeVac virotherapy compared to wild-type mice and IFNAR^{KO}-CD46Ge mice.

5.4.4.2 Tolerance to Human CD46

An additional difference between wild-type mice and CD46tg mice is that wild-type mice are not immunologically tolerant to hCD46, whereas humans and CD46tg mice are. Thus, in wild-type mice antitumor immunity might be partly directed to hCD46 (provided that the tumor cells express this antigen), whereas this should not be the case in humans and CD46tg mice.

Consistent with this reasoning, I observed that, *ex vivo*, splenocytes from CD46tg mice bearing MC38-hCD46 tumors (treated with MeVac) react similarly to MC38-hCD46 cells as to parental MC38 cells (Figure 27). This suggests that the antitumor immune response triggered in CD46tg mice does not target hCD46 epitopes.

In another study (see 4.4), I found that, *ex vivo*, splenocytes from wild-type mice bearing FC1245-hCD46 tumors (treated with MV-NIS and anti-PD-1) react stronger to FC1245-hCD46 cells than to parental FC1245 cells (Figure S17). This indicates that, in wild-type mice, hCD46 expression on tumor cells increases the magnitude of the antitumor immune response. I hypothesize that this is due to the priming of immune effector cells specific for hCD46 epitopes. However, my studies do not provide direct proof of hCD46-specific immunity, since I assessed reactivity to tumor cells rather than a defined set of antigens. To specifically study the immune response against hCD46, splenocytes could be re-stimulated *ex vivo* with hCD46-derived peptides instead of tumor cells.

I hypothesize that wild-type mice mount an immune response against hCD46 and that this response introduces selective pressure at the tumor site by eliminating hCD46(+) tumor cells (for instance, via CTL-mediated cytotoxicity), thereby favoring the outgrowth of hCD46(-) tumor cells, which are present at a very low percentage in the cell suspension injected into the mice (Figure S25 B). In agreement with this reasoning, I detected a strong reduction in the percentage of hCD46(+) cells in MC38-hCD46 tumors (not treated) resected from wild-type mice as compared to the cell suspension used for implantation (Figure 33, Figure S25 B). Recently, similar observations were made with other hCD46(+) tumor models, also established in wild-type mice [276,296]. Importantly, and consistent with my hypothesis that wild-type mice develop an immune response against hCD46

whereas CD46tg mice do not, I only detected this reduction in tumors resected from wild-type mice, and not in those resected from CD46tg mice (Figure 33).

Focusing on wild-type mice, it is interesting to notice that the reduction in the hCD46(+) population occurred during the second week after tumor cell injection, since it was observed 16 days after injection, but not at an earlier timepoint (7 days after injection). This supports the notion that adaptive immunity, which requires around one week to be primed against a new epitope, was involved in the specific elimination of hCD46(+) cells. Although these results were obtained with untreated mice, they show that, if wild-type mice bearing hCD46(+) tumors were to receive MeVac virotherapy, the tumor cells would remain susceptible to the virus during its administration. MeVac treatment usually starts 4 to 7 days after tumor cell implantation, at which time most tumor cells would still express hCD46. At later stages, tumor cells would lose the susceptibility to MeVac, but this should not affect the outcome of the virotherapy, since murine tumor cells, as observed in patient-derived tumor cell cultures [121,297], do not seem to support multiple rounds of MeVac infection and replication even when maintaining hCD46 expression (Figure 10, Figure 32). Therefore, I consider that the loss of the MeVac entry receptor on tumor cells does not limit the outcome of MeVac virotherapy in tumor-bearing wild-type mice. As previously discussed, this loss suggests that wild-type mice develop an immune response against hCD46 epitopes. However, it is important to mention that these mice also develop immunity against other tumor antigens. In my studies, this is evidenced by the fact that wild-type mice experiencing complete remission of MC38-hCD46 or MC38cea tumors (after virotherapy) reject the engraftment of MC38 parental cells (Figure 15, Figure 19). As another example, splenocytes from wild-type mice bearing FC1245-hCD46 tumors react to FC1245 parental cells *ex vivo* (Figure S17).

Overall, I consider that CD46tg mice are a more suitable small animal model for the study of MeVac virotherapy as compared to wild-type mice and IFNAR^{KO}-CD46Ge mice. As humans, CD46tg mice are immunocompetent, susceptible to MeVac, and immunologically tolerant to hCD46, whereas IFNAR^{KO}-CD46Ge mice are immunodeficient, and wild-type mice do not fulfill the two latter criteria. However, wild-type mice have been successfully employed to study antitumor immunity in the field of MeVac virotherapy. Thus, albeit suboptimal, these mice may still provide valuable mechanistic insights and may still be used when CD46tg mice are not available (as was the case for the studies described in sections 4.2, 4.3, and 4.4).

5.4.5 Immunological Effects of MeVac Virotherapy in CD46tg Mice

Before my doctoral studies, CD46tg mice had never been employed in oncology research. To determine whether they are suitable for the study of MeVac virotherapy, I first assessed whether they support tumor engraftment and whether MeVac treatment has an effect in the induction of

systemic antitumor immunity in these mice. Indeed, I found that CD46tg mice support subcutaneous engraftment of syngeneic tumors (Figure 32) and develop tumor-specific as well as MeVac-specific systemic immune responses upon MeVac treatment (Figure 27). Importantly, MeVac treatment enhanced antitumor immunity, since virus-treated mice showed a stronger antitumor immune response as compared to mock-treated mice. Thus, I conclude that CD46tg mice are suitable to study the immunological effects of MeVac virotherapy.

To investigate the local immunological effects of MeVac virotherapy in CD46tg mice, I focused on the remodeling of the TME both at early (t1) and late (t2) stages of the therapy. The early timepoint corresponds to three days after the first virus dose (one day after the last virus dose), and the late timepoint corresponds to one week after the first virus dose (five days after the last virus dose) (Figure 28). In the following paragraphs, I discuss the findings from this study.

5.4.5.1 Innate Antiviral Immune Response

At t1, I detected upregulation of *Bst2*, *Ddx58*, *Ifi35*, *Ifih1*, *Irf7*, and *Stat2* in MeVac-treated tumors compared to mock-treated tumors. Since all of these are interferon-stimulated genes (ISGs) [298], this pattern of gene expression indicates that MeVac virotherapy triggers a type I IFN response in the TME. Importantly, this response amplifies itself via a positive feedback loop, since some ISGs encode proteins involved in type I IFN production and type I IFN signal transduction.

In my studies this positive feedback loop is evidenced by the upregulation of *Ddx58* (encoding RIG-I), *Ifih1* (encoding MDA-5), *Irf7* (encoding IRF7), and *Stat2* (encoding STAT2). Briefly, RIG-I and MDA-5 are the main sensors of MeVac (and wild-type MeV) infection. Upon interaction with viral RNA, these receptors trigger a signaling cascade that activates the transcription factors IRF3 and IRF7. Together with NF-κB, these factors promote the transcription of genes encoding type I IFNs [124]. Thus, *Ddx58*, *Ifih1*, and *Irf7* upregulation suggests that MeVac is being sensed and that type I IFNs are being produced. The interaction of type I IFNs with type I IFN receptors, either in an autocrine or paracrine manner, triggers a signaling cascade via the JAK/STAT pathway. This leads to the formation of STAT1-STAT2-IRF9 complexes, which in turn promote transcription of numerous ISGs [124]. Thus, *Stat2* upregulation is indicative of enhanced type I IFN signal transduction.

Apart from these four genes, I detected upregulation of *Ifi35* and *Bst2*. The proteins encoded by these genes could also influence the innate antiviral response. IFI35 acts as a negative regulator of the antiviral response by promoting the proteasomal degradation of RIG-I [196]. Thus, detecting upregulation of *Ddx58* and *Ifi35* in the TME suggests that, upon MeVac therapy, there is an equilibrium between activation (*Ddx58* upregulation, RIG-I expression) and suppression (*Ifi35* upregulation, RIG-I degradation) of the signaling cascade initiated by virus sensing. BST2 (also known as tetherin) was shown to inhibit syncytia formation in cultures exposed to wild-type MeV

[195]. Thus, *Bst2* upregulation at the tumor site might restrict MeVac spread in the context of oncolytic virotherapy. The molecular mechanism underlying this phenomenon remains unknown, but recent data suggest that it involves the interaction of BST2 with the MeV H protein [195].

Overall, I consider that MeVac-mediated induction of a type I IFN response at the tumor site (together with direct oncolysis and immunogenic tumor cell death) induces an inflamed state in the TME that then supports immune cell activation and triggers the cancer-immunity cycle. Consistent with this reasoning, I detected increased peritumoral inflammation in MeVac-treated tumors (as compared to mock controls) already at t1 (Figure 29). Whether the type I IFN response is triggered in tumor cells or in non-malignant cells within the TME (or in both) remains to be elucidated, since I performed the gene expression analysis using total tumor RNA. Future studies at the single cell level should provide insights in this regard. In general, I expect IFN signaling to play a more important role in non-malignant cells than in tumor cells, since tumor cells commonly show defects in the type I IFN response, probably selected as a mechanism to evade its antiproliferative effect [59]. If future experiments confirm my expectations, those results would provide an additional argument for using CD46tg mice instead of IFNAR^{KO}-CD46Ge mice in preclinical studies.

5.4.5.2 Antigen Presentation and T Cell Migration

At t2, the pattern of gene expression detected in MeVac-treated tumors evolved towards an adaptive immune gene signature, characterized by upregulation of genes related to antigen processing and presentation (*Cd74*, *Ciita*, *H2-Aa*, *H2-Ab1*, *H2-Eb1*, *Psmb9*), immune cell migration (*Ccl5*, *Ccl8*, *Ccl24*, *Cxcl9*), T cell activation and differentiation (*Il12rb1*), T cell exhaustion (*Cd274*), and cytotoxic responses (*Gzma*, *Gzmb*, *Prf1*) (Figure 28 C).

Based on these results, I hypothesize that MeVac therapy enhances the presentation of tumor antigens on MHC-II molecules. My hypothesis is supported by the intratumoral upregulation of genes encoding MHC-II molecules (*H2-Aa*, *H2-Ab1*, *H2-Eb1*) and other proteins involved in the MHC-II antigen presentation pathway, such as the class II invariant chain Ii/CD74 (*Cd74*) and the class II transactivator protein CIITA (*Ciita*). Whether upregulation of these genes is sufficient to enhance antigen presentation in the context of MeVac therapy remains to be elucidated. Moreover, it would be interesting to investigate if the presented epitopes derive from TAAs. This could be assessed by flow cytometry with fluorochrome-conjugated antibodies targeted to MHC-II::peptide complexes. Taking B16 as an example (since this is the tumor model employed in my study), one option would be to use antibodies specific for H2-A^{b}::TRP-1$_{106\text{-}130}$ complexes [299]. Future studies should also investigate whether the MHC-II antigen presentation pathway is upregulated on tumor cells or on other cells from the TME. Detecting MHC-II upregulation in APCs, such as DCs, would argue for APC maturation.

At t2, I also detected upregulation of several chemokine-encoding genes (*Ccl5*, *Ccl8*, *Ccl24*, *Cxcl9*) (Figure 28 C). Importantly, two of these genes (*Ccl5*, *Cxcl9*) overlap with the immune gene expression pattern that I detected in MeVac-treated tumors resected from wild-type mice (Figure 8). Thus, using a refined preclinical model (CD46tg mice) I have validated some of the findings previously made with the suboptimal model (wild-type mice). The contribution of CCL5 and CXCL9 to MeVac virotherapy has been discussed in previous sections of this thesis (see 5.2). The other upregulated chemokines (CCL8 and CCL24) attract myeloid cells (monocytes, eosinophils) and lymphoid cells (CD4[+] T_{REG} cells, CD4[+] T_H2 cells), but only few studies have addressed their role in cancer, which has been related to immunosuppression and tumor cell migration [300,301].

5.4.5.3 IL-12 Signaling

Another gene upregulated in MeVac-treated tumors at t2 was *Il12rb1*, which encodes the beta 1 subunit of the high-affinity IL-12 receptor (Figure 28 C). Binding of IL-12 to the IL-12 receptor promotes the differentiation of CD4(+) naïve T cells into CD4(+) T_H1 cells as well as the activation of NK cells and CD8(+) CTLs [302]. Thus, these processes could have been enhanced in MeVac-treated mice compared to mock-treated mice. Importantly, IL-12 signaling has been identified as an immunological determinant of MeVac virotherapy in MC38 tumors. In fact, MeVac virotherapy combined with IL-12 was shown to mediate complete tumor remission in 90% to 100% of mice bearing MC38cea tumors (s.c.), whereas only 40% of mice experienced complete tumor remission when treated with virotherapy alone [135,144]. However, in the B16 tumor model, the combination of MeVac virotherapy with IL-12 has only shown modest improvements in terms of tumor progression and survival compared to mock treatment or MeVac monotherapy [144]. Thus, the role of IL-12 in MeVac virotherapy could be model- or context-dependent.

5.4.5.4 Lymphocyte Activation and Cytotoxic Effector Function

In addition to the above-mentioned genes, MeVac-treated tumors showed upregulation of genes encoding cytotoxic molecules, namely granzyme A (*Gzma*), granzyme B (*Gzmb*), and perforin (*Prf1*). This suggests that MeVac virotherapy triggers a cytotoxic immune response at the tumor site, which, for example, could have been mediated by CD8(+) CTLs and/or NK cells.

CD8(+) CTL-mediated effector functions might have been hampered by low levels of MHC-I molecules on tumor cells. In B16 cells, this phenomenon has been attributed to transcriptional suppression of the MHC-I antigen processing and presentation machinery, including subunits of the immunoproteasome [303]. In my study, MeVac virotherapy promoted *Psmb9* upregulation. Since *Psmb9* encodes an immunoproteasome subunit, its upregulation suggests that MeVac treatment contributes to the reversion of the transcriptional suppression. However, *Psmb9* upregulation

might have been insufficient to enhance antigen presentation on B16 cells via the MHC-I pathway, since other MHC-I-related genes might have remained transcriptionally suppressed.

Importantly, *Gzma* and *Gzmb* (but not *Prf1*) were already upregulated in MeVac-treated tumors at t1 (Figure 28 B). This is indicative of a cytotoxic innate immune response, probably mediated by NK cells. Upregulation of the type I IFN response at t1 and of *Il12rb1* at t2 is consistent with NK cell activation, a process triggered by type I IFNs and IL-12, among other cytokines [4]. Moreover, B16 cells are targetable by NK cells, since they express low surface levels of MHC-I molecules [303]. As indicated in the previous paragraph, *Psmb9* upregulation might have been insufficient to enhance MHC-I antigen presentation on B16 cells. In this case, B16 cells could have remained susceptible to NK cell-mediated killing at least until t2. In fact, an NK cell-mediated response, which does not induce immunological memory, could explain why the long-term survivor from the therapeutic efficacy study with B16-hCD46 cells experienced a complete remission of the primary tumor but was not protected from secondary tumor engraftment (Figure 13, Figure S7 M).

5.4.5.5 Lymphocyte Exhaustion

T cell-mediated and NK cell-mediated antitumor immune responses might have been dampened by PD-L1, as the gene encoding this molecule (*Cd274*) was upregulated in MeVac-treated tumors at t2 (Figure 28 C). In these tumors, PD-L1 could have been upregulated by B16 cells in response to MeVac infection, as observed *in vitro* [150]. Although the role of the PD-1/PD-L1 pathway is most studied in T cell-mediated immunity, where PD-1 expression represents a marker of T cell activation and exhaustion [304], this axis could also have modulated the magnitude of NK cell-mediated immune responses [305]. Of note, detecting intratumoral upregulation of *Cd274* in MeVac-treated tumors adds to the rationale for combining MeVac virotherapy with PD-1/PD-L1 checkpoint blockade, a treatment approach that I have studied and discussed in previous sections of this thesis (see 4.3, 4.4, and 5.3).

5.4.5.6 Conclusion and Future Studies

Overall, with the immunophenotyping study I show that CD46tg mice can be employed as a preclinical model of MeVac virotherapy to investigate the immunomodulation induced by the virus at the tumor site and predict immune correlates of response. The immune gene signature of MeVac-treated tumors identified at t1 and t2 (as compared to mock-treated tumors) indicates that MeVac virotherapy supports several stages of the cancer-immunity cycle, from local inflammation to cytotoxic effector functions. Consistent with the start of the cancer-immunity cycle, the immune genes upregulated in MeVac-treated tumors at t1 encode proteins involved in innate immune responses, such as nucleic acid sensors and components of the type I IFN response. At t2, the pattern of immune gene expression evolves towards an adaptive immune signature, including

upregulation of genes involved in antigen presentation as well as T cell differentiation, migration, activation, and exhaustion. Signs of cytotoxicity were identified at both timepoints, suggesting that CTLs and/or NK cells participate in the immune response triggered by MeVac therapy in B16-derived tumors. Correlative IHC analyses revealed enhanced abundance of CD3(+) cells in and at the margin of MeVac-treated tumors both at t1 and t2 (compared to mock-treated tumors), thereby supporting the notion that T cells contribute to the immune response triggered by MeVac virotherapy.

In future studies, I will investigate the hypotheses that I formulated based on the current results. To study the contribution of type I IFN signaling and elucidate whether this pathway is mainly triggered in tumor cells or other cells from the TME, F. V. Haas and I will conduct immunophenotyping studies in (i) CD46tg mice bearing IFNAR^{KO} tumors and (ii) IFNAR^{KO}-CD46Ge mice bearing IFN-competent tumors. Alternatively, we will treat tumor-bearing CD46tg mice with MeVac and antibodies blocking the type I IFN receptor. To gain deeper insights into local immunomodulation, I will analyze the maturation/activation state of intratumoral DCs, T cells, and NK cells as well as the antigen presentation capacity of tumor cells (MHC-I/II expression) upon MeVac virotherapy by flow cytometry. At the systemic level, immune cell depletion studies will contribute to unravel the main players of MeVac-mediated antitumor immunity. Since the immune correlates of response to MeVac virotherapy might differ between tumor models (mainly because of different stromal content, tumor immunosuppression, and basal intratumoral immune infiltrate), I plan to conduct these studies in two models: B16-hCD46 and MC38-hCD46. In addition, together with L. Küther, I am developing an E0771-derived breast cancer model (E0771-hCD46, data not shown), which we could implant orthotopically to better resemble the authentic tumor contexture.

5.4.6 Pre-Immunization as a Future Refinement of the CD46tg Mouse Model

Most cancer patients have been vaccinated against measles and therefore have pre-existing immunity to MeVac, which I assume will be recalled upon MeVac virotherapy. However, whether this response affects the development of antitumor immunity triggered by MeVac virotherapy remains unknown, since *in vivo* studies addressing the immunological effects of this OV have only been conducted in MeVac-naïve mice (with one exception [142], see below).

To address this question, and to better resemble the clinical situation, I propose refining the preclinical model by vaccinating CD46tg mice against measles before tumor implantation and virotherapy. Using an animal model similar to the one that I propose, Speck, Heidbuechel *et al.* reported that pre-immunization of wild-type mice against measles does not compromise the efficacy of MeVac virotherapy, at least when the virus is administered intratumorally [142]. However, this study only focused on therapeutic efficacy and did not investigate immune mechanisms of response to virotherapy in pre-immunized mice. Moreover, it employed wild-type mice instead of CD46tg mice.

From my perspective, the effects that pre-existing immunity to MeVac might have on the virotherapy are diverse. On the one hand, measles virus-specific neutralizing antibodies could neutralize the virus, thus preventing it from reaching the tumor or from spreading to metastatic sites [306]. MeVac-specific CD8(+) T cells could contribute to virus clearance by killing virus-infected cells [307]. On the other hand, antiviral immunity might be beneficial for the antitumor immune response [71,308]. For instance, it has been hypothesized that virus-specific CD4(+) T_H1 cells contribute to the priming of tumor-specific CD8(+) T cells by providing survival (IL-2) and co-stimulatory (CD40L/CD40) signals to these cells and by promoting DC maturation (and, therefore, enhanced presentation of MHC-I-restricted tumor epitopes to CD8[+] T cells) [71]. Moreover, pre-existing or virotherapy-induced antiviral immunity could be redirected to tumor cells. For example, virus-specific T cells recruited at the tumor site upon virotherapy have been harnessed as antitumor effector cells via bispecific T cell engagers (BiTEs) [309], also in the context of MeVac virotherapy [142]. Virus-specific antibodies can also be redirected to tumor cells by means of bispecific molecules, thus sensitizing tumor cells to antibody-dependent cellular cytotoxicity [310]. In future studies, our research group will explore these T cell and antibody redirection strategies and investigate the effect of pre-existing antiviral immunity on the antitumor immune response triggered by MeVac virotherapy.

5.5 Patient-Derived *Ex Vivo* Models of MeVac Oncolytic Immunotherapy

Immunocompetent mouse models are necessary to study how MeVac virotherapy triggers adaptive antitumor immunity. However, inbred mice are not representative of patient diversity and the tumors developed in these mice do not recapitulate intra- and intertumor heterogeneity, since they originate from the same cell line or the same driver mutations. Moreover, the microenvironment of murine tumors, particularly of those developed heterotopically (as was the case in my experiments), differs from that of human tumors.

To circumvent these limitations, I propose complementing the *in vivo* studies with patient-derived *ex vivo* tumor models. To date, several studies have investigated MeVac replication and virus-induced cytotoxicity in patient-derived cultures of melanoma [134,311], glioblastoma [121], colorectal adenocarcinoma [142,312], breast carcinoma [313], and PDAC [165,276,297]. However, although these cultures maintain intra- and intertumor heterogeneity, they do not preserve tumor integrity: the breast carcinoma model consists of organoids generated upon tumor dissociation, whereas the other models only contain tumor cells, passaged as monolayers or spheroids.

To better resemble the clinical scenario, patient-derived tumor models should preserve the native architecture of the TME. In this regard, I propose the employment of patient-derived *ex vivo* tumor slice cultures established on an air-liquid interphase (ALI) system [314]. Although common in the study of chemotherapeutic drugs [200,201,315], the ALI culture system has just entered the field of oncolytic virotherapy, where it has been employed to investigate the replication and cytotoxic potential of a vesicular stomatitis virus-derived OV [316]. Since this culture method maintains tissue integrity, viability, and heterogeneity for at least five days [200,201], I consider that, in addition to direct oncolysis, the ALI platform is also suitable to study early immunological effects of oncolytic virotherapy. Towards this aim, following the ALI culture system, I have established patient-derived *ex vivo* tumor slice cultures from surgical colorectal carcinoma samples. As initial proof-of-concept, I have shown that these cultures support MeVac gene expression, which is indicative of viral replication (Figure 30). Although only conducted with tumor samples from three patients, my results already revealed variability in the response to MeVac within and across tumors, suggesting that intra- and intertumor heterogeneity modulate permissiveness to oncolytic MeVac (Figure S23). This highlights the importance of identifying predictive biomarkers of response to MeVac virotherapy, which can then be integrated in patient stratification approaches [121,297,312]. However, in addition to biological differences between tumors, the variability that I observed might also arise from technical differences related to sample quality and processing.

Besides the ALI platform, patient-derived tumor slices have also been cultured following the free-floating (FF) system [184]. With this method, tumor slices are fully immersed in medium rather than cultured on an air-liquid interphase. In the context of MeVac virotherapy, the FF platform was employed to assess the permissiveness of patient-derived liver tumor slice cultures to different MeVac strains [317]. However, direct comparison between the ALI and FF models has identified the ALI platform as the one better preserving tissue morphology and providing optimal gas exchange [184]. Therefore, I chose the ALI method to study MeVac virotherapy in a model system closer to the clinical setting.

Recently, a novel methodology for the culture of patient-derived tumor samples was described. This new method consists of patient-derived tumor fragments (PDTFs) embedded into an artificial extracellular matrix that prevents immune cell efflux [318,319]. As with the ALI system, the PDTF platform preserves the patient-specific TME and maintains tissue integrity, viability, and heterogeneity *ex vivo* [318]. This culture system has been employed to assess the early immunological effects of immune checkpoint blockade in a near-clinical model and has successfully predicted clinical response to the tested treatments [318,320]. In light of these promising results, I consider that the PDTF platform could be suitable to study early immunological effects of oncolytic virotherapy and identify predictive biomarkers of clinical response.

Following up on my pilot experiments, I intend to develop a robust model for the *ex vivo* study of MeVac virotherapy using patient-derived samples preserving the three-dimensional tumor contexture. To that aim, I plan to establish patient-derived *ex vivo* tumor cultures following the ALI and PDTF methods. Upon culture establishment, I will compare the ALI and PDTF models regarding tissue composition, cell viability, MeVac replication, and MeVac-mediated oncolysis. The more suitable model, identified as the one better preserving tissue integrity and supporting higher levels of MeVac replication, will be chosen for immunophenotyping studies. In these studies, I will investigate how MeVac remodels the tumor immune environment by comparing MeVac-treated and mock-treated *ex vivo* tumor cultures on the cellular, protein, and transcriptional levels. On the cellular level, I intend to assess the abundance and phenotype of specific immune cell populations via flow cytometry and IHC. On the protein level, I aim at determining the concentration of certain cytokines/chemokines in total protein extracts as well as culture undernatants (ALI model) or supernatants (PDTF model) by means of cytokine bead arrays. On the transcriptional level, I plan to analyze the immune gene expression profile of the *ex vivo* cultures using total culture RNA. Overall, these studies will provide, for the first time, an initial dataset describing early immunomodulatory effects of MeVac virotherapy in a near-clinical model.

Moreover, I will compare the results from the patient-derived *ex vivo* tumor cultures to those from the *in vivo* murine tumor models (especially when both systems study the same tumor entity). This comparison will determine whether the immunological mechanisms of response to MeVac identified at early stages of the therapy in tumor-bearing mice are also triggered in the near-clinical setting. From my perspective, the immunological determinants of response overlapping between the *in vivo* and the *ex vivo* studies will be the most promising for clinical translation.

5.6 Perspectives on Clinical Translation

During my doctoral studies, I have investigated immune mechanisms of MeVac virotherapy. Using different preclinical models, I have shown that MeVac virotherapy primes systemic antitumor immunity and induces a pro-inflammatory gene signature at the tumor site. However, similar to the clinical situation, MeVac virotherapy alone was insufficient to achieve long-term responses in a large percentage of treated mice. This indicates that, in preclinical models, mechanisms other than (or acting downstream of) tumor-specific T cell priming limit the therapeutic potential of oncolytic MeVac.

On the clinical level, several early phase trials of MeVac virotherapy have been initiated, most of which are still ongoing. The trials completed to date have demonstrated the safety, feasibility, and tolerability of oncolytic MeVac administered via different routes (i.t., i.p., i.v.) and have provided evidence of viral gene expression in patients [188,189,321–324]. Since these trials focused on safety and tolerability, research on cellular and molecular correlates of clinical response is scarce. Functional analyses identified increased IFN-γ responses against tumor antigens in sera from individual patients after MeVac treatment, thus pointing towards T cell-mediated antitumor immunity. Overall, these trials showed moderate therapeutic efficacy, with several patients experiencing transient stable disease or partial tumor regression and only one exceptional responder (multiple myeloma patient) experiencing a complete tumor remission [323], which is still ongoing six years after virotherapy [324]. With the exception of this responder, the clinical data gathered to date indicate that, when administered as monotherapy, oncolytic MeVac does not mediate durable clinical responses in terms of long-term survival or complete remissions, at least in cancer patients with advanced disease. The application of MeVac virotherapy at earlier stages of the disease, for instance in an adjuvant or neoadjuvant setting, might be more appropriate to take full advantage of the oncolytic vaccination effect [325]. In this regard, a Phase I clinical trial investigating the tolerability and feasibility of neoadjuvant intravesical MV-NIS in patients with urothelial carcinoma was recently completed (NCT03171493), and the results are expected to be published in the coming months.

To improve clinical response, we must unravel the factors that limit the efficacy of MeVac virotherapy. This task requires the development of preclinical and near-clinical models in which potential cellular and molecular determinants of response can be identified and subsequently validated via mechanistic studies. It is on this level where I envision the clinical contribution of my doctoral work. The MeVac + anti-PD-1 study in preclinical PDAC (see 4.4) is a good example. In this study, identification of PD-L1 upregulation as a potential resistance mechanism to MeVac therapy provided the rationale for combining virotherapy with PD-1/PD-L1 blockade. Subsequently, preclinical efficacy studies confirmed the therapeutic benefit of the combination approach and preclinical mechanistic studies provided a biological explanation for the better efficacy of the combined therapy compared to either monotherapy. Whether the improved efficacy of this treatment combination translates to clinical practice remains to be elucidated. In this regard, a Phase I dose-escalation trial addressing the combination of MeVac virotherapy with the anti-PD-1 antibody Pembrolizumab in PDAC patients is currently in preparation at the National Center for Tumor Diseases (NCT, Heidelberg).

To predict clinical response, appropriate preclinical models must be chosen. Unfortunately, the preclinical studies setting the base for current clinical trials of MeVac virotherapy were conducted in human tumor xenografts, which neither allow the study of adaptive immunity nor resemble the human TME [112,326]. Nowadays, *in vivo* studies are conducted in wild-type mice or IFNAR^{KO}-CD46Ge mice, but those are not optimal models, either. Refining the current animal model is therefore essential to better resemble the clinical situation. The introduction of CD46tg mice as model organism for MeVac virotherapy, described in my thesis for the first time, is a major step in this direction (see 4.5 and 5.4).

Despite refinement, any model will, at its best, only be an approximation of clinical reality and as such present several limitations. Therefore, from my perspective, preclinical studies aiming at providing a solid foundation for clinical translation should be conducted in more than one model. These models should be complementary, *i.e.*, they should address different aspects of the therapy and circumvent the limitations of one another. In this regard, I propose studying MeVac virotherapy in two complementary systems: (i) an *in vivo* model (see 4.5 and 5.4), essential to study systemic effects, including antitumor and antiviral adaptive immunity, cell trafficking to and from the tumor, and adverse events, and (ii) a patient-derived *ex vivo* model (see 4.6 and 5.5) that preserves tumor heterogeneity and maintains the patient-specific TME, thereby providing a valuable platform to study the early and local effects of MeVac virotherapy (*e.g.* viral replication, oncolysis, initial TME remodeling) in the human context.

In the future, MeVac virotherapy studies using the refined *in vivo* model (perhaps optimized even further, for instance by pre-immunizing mice against measles, see 5.4.6) should provide insights into the interaction of oncolytic MeVac with non-malignant host cells, which could be relevant for the initiation of the cancer-immunity cycle (see 5.4.2). Efficacy and immunophenotyping studies in tumor-bearing CD46tg mice will broaden our knowledge on the immune mechanisms of oncolytic MeVac and may contribute to unravel the bottlenecks of MeVac virotherapy. Identifying these bottlenecks will guide the rational design of novel MeVac variants and the rational development of treatment combinations which might overcome treatment resistance and improve clinical response.

Ex vivo studies in patient-derived tumor cultures that preserve the native TME could be employed to elucidate whether and how the TME modulates viral replication and to understand how tumor heterogeneity affects permissiveness to MeVac. By correlating viral replication and direct oncolysis with the transcriptional profile of MeVac-resistant and MeVac-permissive tumors, we might find correlates of response that, upon validation, could be used as predictive biomarkers in patient screening and stratification strategies. Similar correlative studies with other OVs might unravel different predictive biomarkers for different OVs. This information could then be used to rationally predict which OV might be most effective in a particular patient.

Importantly, while preclinical studies should pave the way for translating investigational treatments to clinical research, clinical trials should be accompanied by robust translational research programs that inform on potential mechanisms of resistance that had not been identified at the preclinical level. The lack of these translational programs in early phase trials of MeVac virotherapy is unfortunate, since the field could have gained much knowledge from the enrolled patients. Encouragingly, this situation is now changing, since MeVac virotherapy trials initiated in the past few years include accompanying translational research programs (NCT01503177, NCT02364713, NCT02068794, NCT00390299, NCT04521764). Results from these trials are therefore eagerly awaited.

Overall, I envision the refined mouse model, the patient-derived *ex vivo* tumor cultures, and the translational research programs accompanying clinical trials as three complementary systems where basic research and clinical challenges converge to assess the translational potential of MeVac oncolytic immunotherapy as an additional treatment option for cancer patients.

6 Conclusions

During my doctoral studies, I have investigated immune mechanisms of response to MeVac virotherapy. In an *ex vivo* murine co-culture system, I have proven the concept of using MeVac vectors encoding antigen-derived epitope variants for naïve T cell priming. *In vivo*, I have shown that MeVac treatment induces systemic antitumor immunity. This was shown in wild-type mice bearing immunologically "hot" tumors (MC38-derived murine colon adenocarcinoma models, s.c.) but also in those bearing immunologically "cold" tumors (FC1245-hCD46 murine PDAC model, s.c.). However, despite triggering antitumor immunity, MeVac virotherapy only achieved 30% to 40% complete tumor remissions in the colon adenocarcinoma models and no complete remissions in the PDAC model, indicating that certain molecular mechanisms limit the efficacy of this therapeutic approach. To gain molecular insights into these mechanisms, I focused on phases of the cancer-immunity cycle downstream of T cell priming, namely T cell migration and effector functions.

Based on efficacy and tumor gene expression data from previous *in vivo* studies, I hypothesized that the full therapeutic potential of oncolytic MeVac is limited by insufficient intratumoral expression of specific chemokines (CCL5, CCL19, CCL21a, CXCL9, CXCL10, CXCL13) and cytotoxic molecules (LT-α, LT-β, TNF-α, LIGHT). To test this hypothesis, I planned *in vivo* gain of function (GOF) efficacy studies with several MeVac vectors, each encoding the murine variant of one candidate molecule. After generating these ten novel viruses, I refined the purity of the virus suspensions by establishing a protocol for MeVac purification via ultracentrifugation. Subsequently, I focused on the virus variants encoding chemokines. *In vitro*, I confirmed expression of MeVac-encoded chemokines on the protein level and found that, in murine tumor cells, the replication kinetics and direct cytotoxic effect of chemokine-encoding viruses is similar to that of MeVac encoding a control molecule (Fc region of hamster IgG). In transwell migration assays, MeVac-encoded murine (m) CXCL9, mCXCL10, mCCL19, and mCCL21a showed the strongest chemotactic effects. Thus, I chose the viruses encoding these molecules for the *in vivo* GOF studies, which I conducted in immunocompetent models of murine colon adenocarcinoma (MC38-hCD46, s.c.) and murine melanoma (B16-hCD20-hCD46, s.c.). Contrary to my hypothesis, these studies revealed similar therapeutic efficacy between control virus and MeVac vectors encoding chemokines. Thus, I conclude that, on its own, none of the tested chemokines (mCXCL9, mCXCL10, mCCL19, mCCL21a) limit the therapeutic efficacy of oncolytic MeVac in these tumor models. Whether simultaneous overexpression of the identified chemokines improves the therapeutic response to MeVac remains to be tested.

Virotherapy often leads to PD-L1 upregulation on tumor cells. Thus, I also hypothesized that the PD-1/PD-L1 pathway restricts the therapeutic efficacy of oncolytic MeVac. To address this hypothesis, I employed MeVac vectors encoding antibody-like molecules directed against murine PD-1 (αmPD-1) or PD-L1 (αmPD-L1), or the corresponding Fc region as control. In wild-type mice bearing MC38cea tumors (s.c.), all virus treatments conferred similar therapeutic efficacy and achieved 40% to 50% complete tumor remissions. Notably, all long-term survivors, except one, rejected contralateral tumor engraftment after rechallenge with MC38 parental cells, pointing towards the development of systemic antitumor immunity. In *ex vivo* restimulation experiments with splenocytes from the rechallenged mice, I showed that, in terms of IFN-γ secretion, MeVac encoding αmPD-1 or αmPD-L1 induce a stronger antitumor immune memory response compared to the control viruses. Therefore, I conclude that, in this preclinical model, the PD-1/PD-L1 axis restricts the strength of the antitumor immune memory response triggered by MeVac virotherapy. Blocking the PD-1/PD-L1 pathway enhances this response, but is insufficient to improve overall survival, suggesting that additional molecular mechanisms limit the efficacy of oncolytic MeVac in this tumor model.

In contrast to the MC38cea model, wild-type mice bearing murine PDAC tumors (FC1245-hCD46 model, s.c.) do not respond to local MeVac virotherapy or to systemic anti-PD-1 antibody treatment, but show delayed tumor growth and prolonged median survival when both therapies are combined. To gain insights into the immunological mechanisms underlying response to the combination treatment, I conducted immunophenotyping studies one week (t1) and two weeks (t2) after treatment initiation. By means of IFN-γ ELISpot assays, performed with restimulated splenocytes from treated mice, I showed that MeVac virotherapy, either alone or in combination with anti-PD-1, induces systemic antitumor and antiviral immunity, whereas anti-PD-1 monotherapy does not. The responses induced by MeVac monotherapy and combination treatment were of similar magnitude. At the tumor site, treatment with the combination approach reshaped the transcriptional profile towards an immune-activation state. Interestingly, this local immune gene signature, which I detected at t1, was transient and not observed at t2, whereas the systemic antitumor and antiviral responses triggered by MeVac virotherapy or combination treatment were detected at t1 and sustained, albeit at lower levels, at least until t2. Based on these results, I conclude that, in the FC1245-hCD46 tumor model, MeVac virotherapy is the main driver of systemic antitumor and antiviral immunity but is insufficient to reshape the tumor immune transcriptome. In this model, PD-1 blockade is dispensable for priming the systemic immune response but required at the tumor site in combination with virotherapy for transient induction of an immune activation gene signature.

In parallel to the projects outlined above, which were conducted in wild-type mice, I have established CD46tg mice as a novel animal model of oncolytic MeVac virotherapy. For the first time, I have shown that tumor-bearing CD46tg mice develop strong systemic antitumor and antiviral immune responses upon MeVac virotherapy. Local immunomodulation upon virotherapy comprised an increase in peritumoral and intratumoral T cell abundance as well as the induction of a particular immune gene signature at the tumor site, characterized by upregulation of genes associated with (i) virus sensing and type I IFN signaling, (ii) antigen processing and presentation, and (iii) immune cell recruitment, activation, cytotoxic effector function, and exhaustion. This pattern of gene expression warrants further investigation.

Finally, I worked towards the development of an *ex vivo* tumor model that maintains tumor heterogeneity and preserves the patient-specific tumor microenvironment, thereby complementing the *in vivo* study of MeVac virotherapy. In this regard, I started to establish patient-derived *ex vivo* tumor slice cultures and, in pilot experiments, showed that this *ex vivo* model supports MeVac spread.

Overall, I have contributed to the field of MeVac virotherapy by (i) investigating molecular determinants of response to this oncolytic virus, focusing on chemokines and immune checkpoints, (ii) characterizing the local and systemic immunological effects of the virotherapy, and (iii) establishing novel preclinical models, both *in vivo* and *ex vivo*. The results from my studies add to our knowledge on the immune mechanisms of action of (and resistance to) this complex biological therapy and, as outlined in the next section, set the foundation for further research in multiple directions.

7 Future Studies and Outlook

Based on the results from my doctoral studies, several research projects have been initiated.

The study of T cell priming and activation with MeVac vectors encoding antigen-derived epitope variants, which I conducted in murine co-culture systems, is currently continued in the human context with tumor cell lines and immune cells retrieved from healthy blood donors (M. S. C. Finkbeiner, N. Duus, C. E. Engeland, unpublished data). While my studies were restricted to co-cultures of two cell types, the current project investigates triple co-cultures of tumor cells, DCs, and T cells. Instead of the model antigen OVA, this project focuses on antigens endogenously expressed in tumor cells, in particular SSX2 and NY-ESO-1. In my study, antigen presentation on DCs was only mediated by direct interaction of DCs with the viruses encoding antigen-derived epitope variants. The optimizations introduced in the ongoing project, namely the triple co-culture system and the usage of TAAs, allow DCs to present TAA-derived epitopes via different routes, such as tumor cell phagocytosis, MHC-I cross-dressing, capture of antigens released upon MeVac-mediated tumor cell lysis, or, as in my project, direct interaction with the virus. Overall, this study aims at investigating the contribution of each of these routes to TAA presentation by DCs in the context of MeVac virotherapy and at elucidating whether MeVac-mediated tumor cell lysis enhances priming of TAA-specific human naïve T cells.

Regarding the MeVac variants encoding chemokines (G. Pidelaserra-Martí, Ž. Modic, R. Veinalde, J. P. W. Heidbuechel, C. E. Engeland, unpublished data), in follow-up studies I will determine whether, despite not improving therapeutic efficacy, chemokine overexpression enhances intratumoral immune cell infiltration in the context of MeVac virotherapy. If this is the case, I will subsequently explore potential mechanisms of resistance to the combination of MeVac and chemokines, for instance by assessing the phenotype of the recruited cells. Otherwise, I will investigate molecular mechanisms that could have hampered immune cell recruitment even in the presence of chemokines, such as desmoplasia or chemokine scavenging and degradation. Furthermore, I will address whether simultaneous overexpression of several chemokines, rather than a single one, improves the therapeutic efficacy of oncolytic MeVac. Importantly, I found that MeVac virotherapy alone enhances intratumoral T cell abundance and induces upregulation of chemokine-encoding genes at the tumor site compared to mock treatment. Thus, despite not being limiting factors, chemokines could play an essential role in the antitumor response triggered by MeVac monotherapy, for instance by recruiting primed T cells to the tumor. To address this, I will conduct loss-of-function studies by treating tumor-bearing mice with MeVac and antibodies blocking specific chemokine pathways. Furthermore, I will assess the relevance of T cell migration *in vivo* with studies combining MeVac virotherapy with blockade of lymphocyte egress from lymph

nodes. Together, these studies will provide mechanistic insights into the role of chemokines during MeVac virotherapy.

Besides chemokine signaling, I identified other molecular pathways transcriptionally upregulated at the tumor site upon MeVac virotherapy. The contribution of these pathways to the therapeutic efficacy of oncolytic MeVac will be explored in gain-of-function and loss-of-function studies similar to those conducted in the chemokine project. In this regard, two projects are ongoing. Those focus on the type I IFN pathway (F. V. Haas, G. Pidelaserra-Martí, C. E. Engeland, unpublished data) and on the lymphotoxin signaling network (G. Pidelaserra-Martí, C. E. Engeland, unpublished data), respectively. The latter will include histological assessment of murine tumor samples to determine whether MeVac virotherapy, either alone or in combination with lymphotoxin overexpression, promotes the formation of tertiary lymphoid structures at the tumor site.

Concerning the establishment of a refined small animal model for the study of MeVac virotherapy, head-to-head comparisons between wild-type and CD46tg mice are ongoing (G. Pidelaserra-Martí, C. E. Engeland, unpublished data). These studies comprise the *ex vivo* monitoring of MeVac entry and replication in different immune cell populations isolated from each mouse strain. In the human context, similar projects with immune cells retrieved from healthy blood donors are ongoing (M. S. C. Finkbeiner, B. Bognár, L. Kuchernig, C. E. Engeland, unpublished data) or have recently been published by Floerchinger *et al.* [192]. To determine whether CD46tg mice resemble the human scenario better than wild-type mice, the results from the murine studies will be compared to those from the human studies. In parallel, CD46tg mice are employed in a new project that addresses the effect of pre-existing MeVac-specific immunity on the antitumor response triggered by MeVac virotherapy (F. V. Haas, G. Pidelaserra-Martí, C. E. Engeland, unpublished data).

In addition, I have started a project to establish patient-derived *ex vivo* tumor models preserving the native tumor architecture and heterogeneity (G. Pidelaserra-Martí, M. S. C. Finkbeiner, F. V. Haas, J. Achberger, C. E. Engeland, unpublished data). These models will be employed to study local cytotoxic and immunological effects of oncolytic MeVac at early stages of the therapy in a patient-specific setting. Furthermore, they will be a valuable platform to identify potential biomarkers of permissiveness to MeVac, a topic of intense research in our group (N. Duus, Ž. Modic, S. Pernickel, and C. E. Engeland, unpublished; T. E. Schäfer *et al.*, in revision).

Moving towards clinical translation, the PDAC study described in my thesis supports the initiation of a Phase I dose-escalation trial that will assess the combination of MeVac virotherapy with Pembrolizumab in PDAC patients with liver metastasis. The basis for this trial does not solely arise from the study that R. Veinalde and I conducted, but also from many years of intense research, including the work of Grossardt *et al.* [133], who showed, for the first time in an immunocompetent

mouse model, that MeVac virotherapy induces systemic antitumor immunity, and the work of Engeland *et al.* [134], who, for the first time, reported on the therapeutic benefit of combining MeVac treatment with immune checkpoint blockade. The study that R. Veinalde and I conducted confirms the findings from Grossardt *et al.* (in murine colon adenocarcinoma) and Engeland *et al.* (in murine melanoma) in a clinically relevant murine PDAC model, thus supporting the enrollment of PDAC patients in the clinical trial. Yet, whether the findings from the preclinical studies will translate to the clinical setting remains unknown. In this regard, besides assessing the safety, tolerability, and feasibility of the treatment approach, the clinical trial, which is currently in preparation at the National Center for Tumor Diseases (NCT) Heidelberg, will be accompanied by a translational research program aiming at identifying immunological and molecular correlates of clinical response.

To conclude, in the course of my doctoral studies I have identified molecular mechanisms that can be exploited to increase the oncolytic vaccination effect of MeVac virotherapy. The development of MeVac variants encoding TAA-derived epitopes is currently being studied in the human context, whereas the combination of MeVac virotherapy with PD-1/PD-L1 blockade will soon enter clinical investigation. Furthermore, I have analyzed how MeVac virotherapy remodels the immune environment of several murine tumor entities (melanoma, colorectal adenocarcinoma, and PDAC). Based on these analyses, I have identified type I IFN signaling as well as specific chemokines and cytotoxic molecules as potential determinants of MeVac therapeutic efficacy. Besides continuing my research on the role of chemokines in MeVac virotherapy, future projects will address the contribution of type I IFNs and cytotoxic molecules, particularly lymphotoxins, to the efficacy of this treatment modality. The models that I have established, namely CD46tg mice and patient-derived *ex vivo* tumor slice cultures, will be employed in subsequent studies to increase the robustness of preclinical findings and assess early immunological effects of MeVac virotherapy in a near-clinical setting.

Overall, basic research in complementary settings, including *ex vivo* near-clinical systems and robust animal models, will improve understanding of cancer biology and contribute to unraveling cellular and molecular determinants of MeVac therapeutic efficacy, which may then be exploited therapeutically. Most importantly, preclinical and translational research will contribute to the rational prediction of a patient's response to certain (viro)therapeutics, thereby guiding personalized treatment decisions aimed at offering each patient the best possible treatment for their condition.

8 Supplementary Figures and Tables

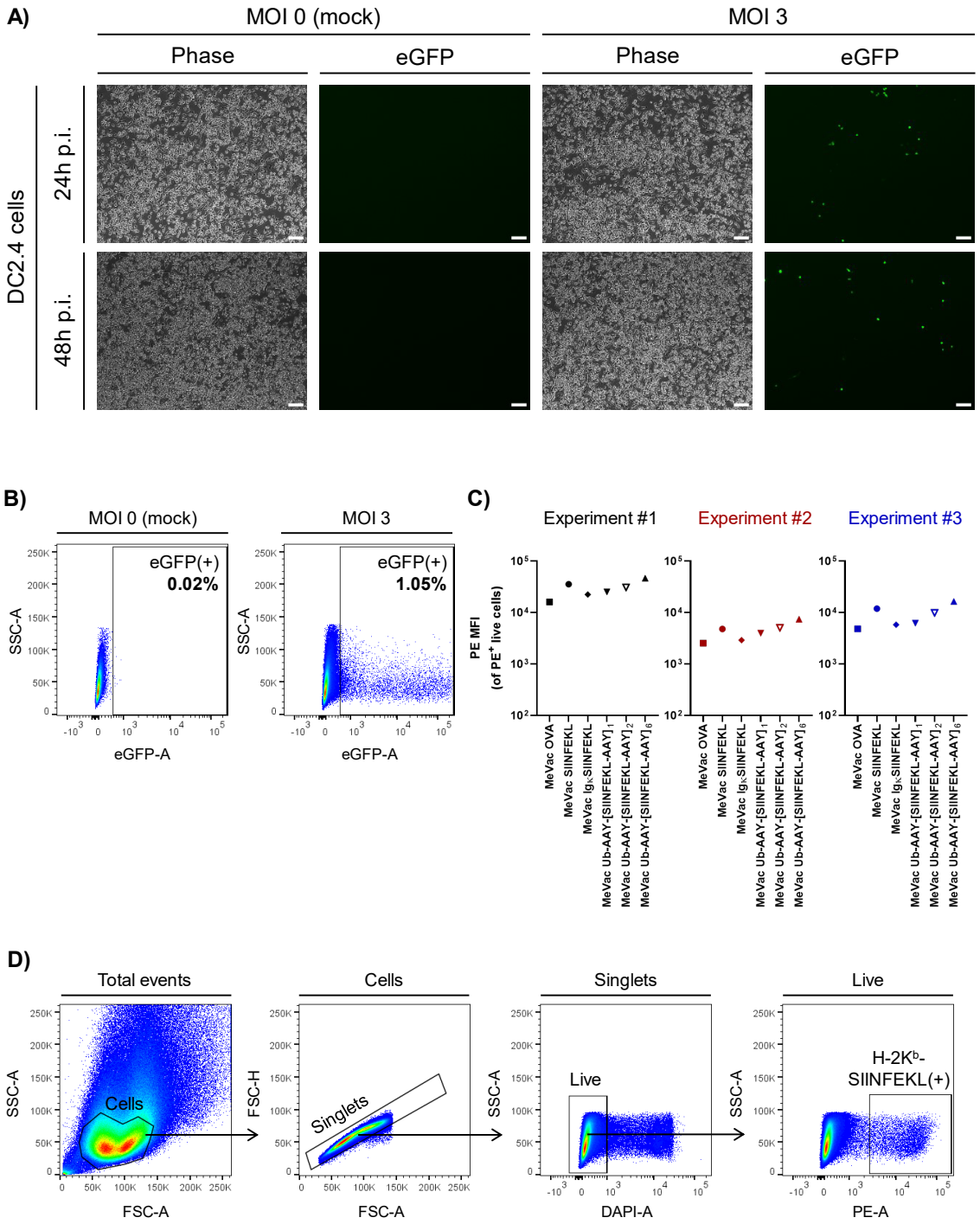

Figure S1. MeVac-encoded reporter gene expression and antigen presentation on DC2.4 cells exposed to MeVac variants. (A-B) DC2.4 cells were inoculated with MeVac eGFP (MOI = 3) or medium (mock). **(A)** After 24 h and 48 h, the cultures were monitored with the phase contrast and eGFP fluorescence channels of a Zeiss AxioVert 200 fluorescence microscope. Representative images, acquired with the AxioVision software and processed with ImageJ, are shown. Scale bar: 100 µm. **(B)** After 24 h, the percentage of eGFP(+) cells within live cells was determined by flow cytometry. Dotplots show live cells, with gate on eGFP(+) cells. **(C)** DC2.4 cells were inoculated with the indicated MeVac variants (MOI = 3). After 24h, the cells were analyzed by flow cytometry (see Figure 5 A,B). PE median fluorescence intensity (MFI) of PE(+) live cells per condition is shown. Three independent experiments were conducted. **(D)** Gating strategy for experiments depicted in Figures 5 B, Figure S1 C and Figure S3.

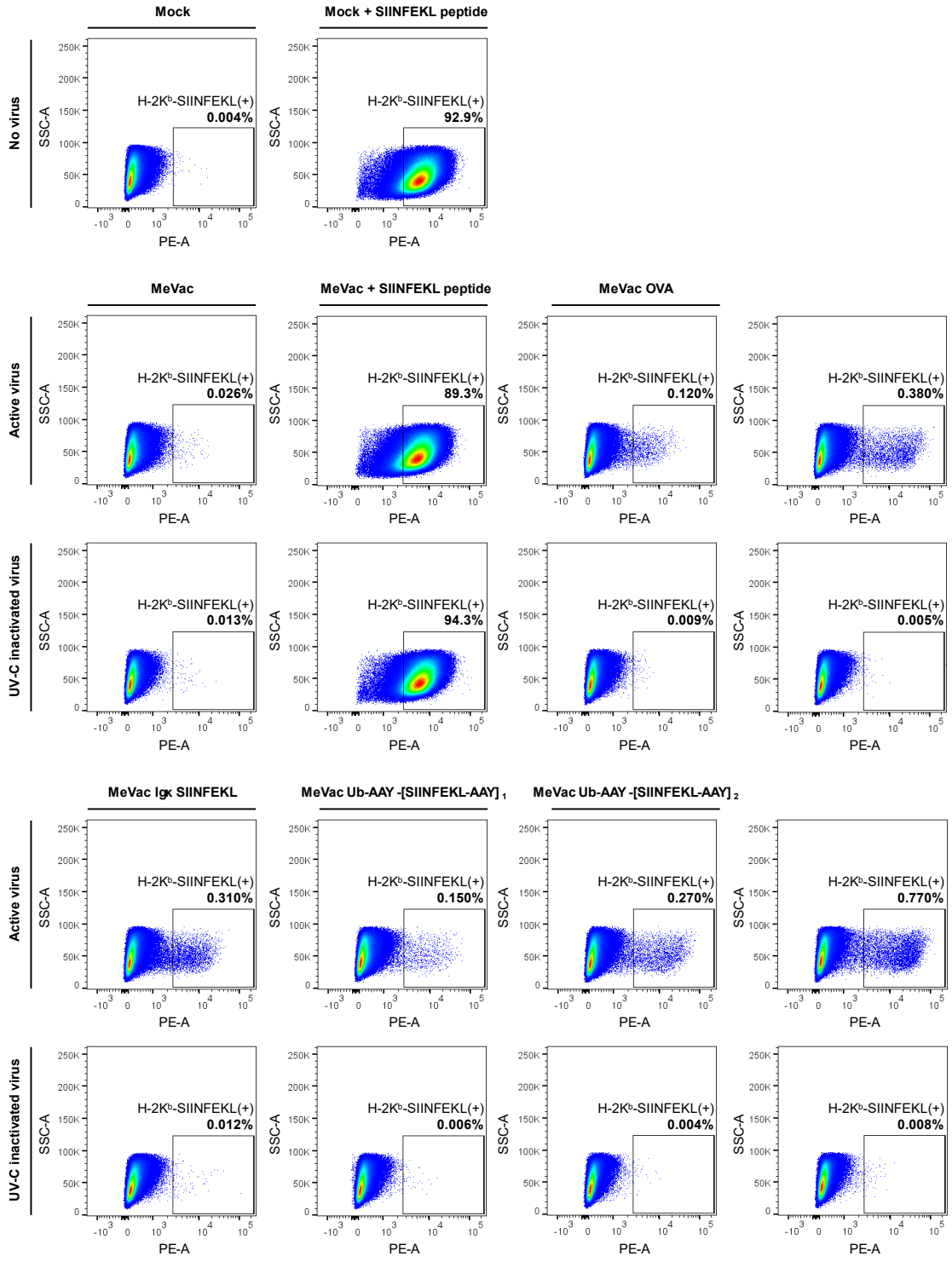

Figure S2. Antigen presentation on DC2.4 cells exposed to active or UV-C inactivated MeVac variants. DC2.4 cells were inoculated with the indicated MeVac variants (MOI = 3) or medium (mock). Where indicated, viruses were inactivated by UV-C irradiation before inoculation. Mock/MeVac + SIINFEKL conditions were pulsed with 10 µg/mL SIINFEKL peptide 1 h before cell harvest. 24 h after inoculation, the cells were harvested and flow cytometry for SIINFEKL bound to H-2K^b was performed with a PE-labelled antibody. Dotplots show live cells, with gate on H-2K^b-SIINFEKL+ (PE+) cells. Values indicate percentage of H-2K^b-SIINFEKL+ (PE+) cells within live cells.

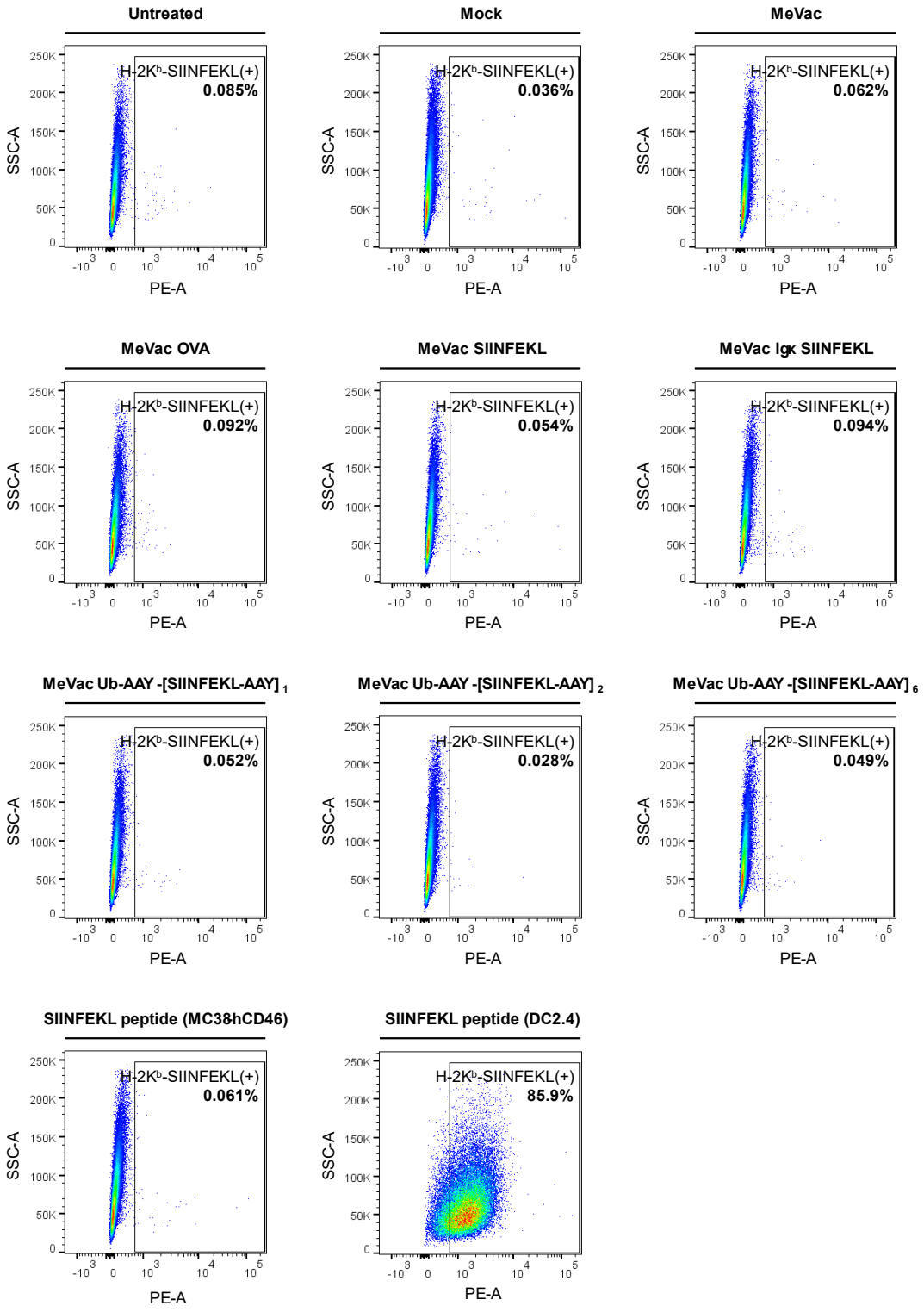

Figure S3. External peptide loading on DC2.4 cells. MC38-hCD46$_{[lenti]}$ cells were inoculated with the indicated MeVac variants (MOI = 3). Alternatively, the tumor cells were inoculated with medium (mock) or pulsed with 2.5 µg/mL SIINFEKL peptide. 24 h after inoculation or 21 h after peptide pulsing, tumor cell lysates were generated by one freeze-thaw cycle and clarified by centrifugation. Subsequently, DC2.4 cells were inoculated with 1 mL of the clarified tumor cell lysates. As controls, DC2.4 cells were left untreated (negative control) or pulsed with 2.5 µg/mL SIINFEKL peptide (positive control). After 1 h, flow cytometry for SIINFEKL bound to H-2K^b was performed with a PE-labelled antibody. Dotplots show live cells, with gate on H-2K^b-SIINFEKL+ (PE+) cells. Values indicate percentage of H-2K^b-SIINFEKL+ (PE+) DC2.4 cells within live cells.

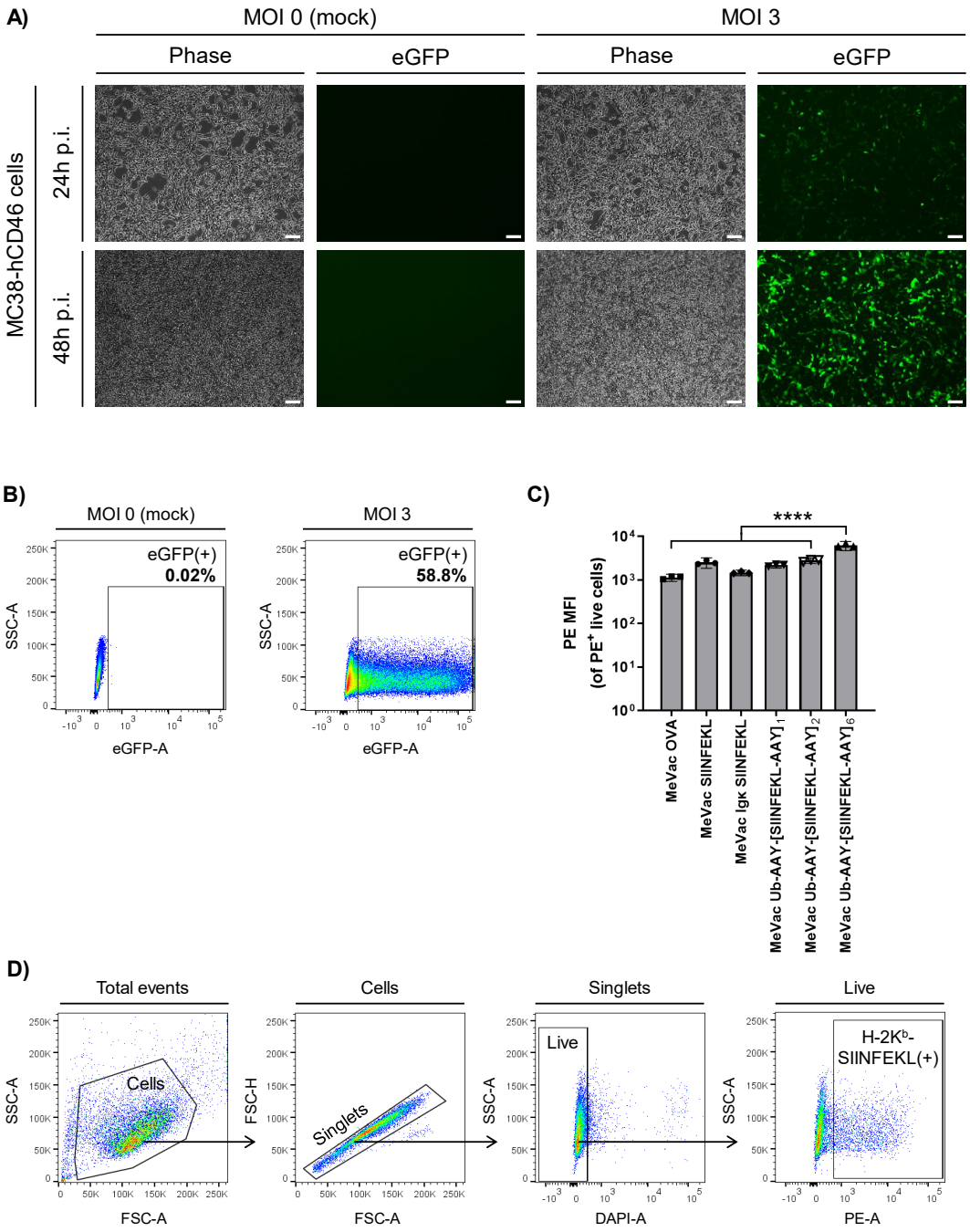

Figure S4. MeVac-encoded reporter gene expression and antigen presentation on MC38-hCD46 cells exposed to MeVac variants. (A-B) MC38-hCD46[lenti] cells were inoculated with MeVac eGFP (MOI = 3) or medium (mock). **(A)** After 24 h and 48 h, the cultures were monitored with the phase contrast and eGFP fluorescence channels of a Zeiss AxioVert 200 fluorescence microscope. Representative images, acquired by J. Albert with the AxioVision software and processed by myself with ImageJ, are shown. Scale bar: 100 µm. **(B)** After 24 h, the percentage of eGFP(+) cells within live cells was determined by flow cytometry. Dotplots show live cells, with gate on eGFP(+) cells. **(C)** MC38-hCD46[lenti] cells were inoculated with the indicated MeVac variants (MOI = 3). After 24h, the cells were analyzed by flow cytometry (see Figure 7 A,B). PE median fluorescence intensity (MFI) of PE(+) live cells is shown for one representative of three independent experiments conducted by J. Albert. Bars indicate mean values of technical triplicates and error bars show 95% confidence intervals. Data were analyzed using one-way ANOVA with Tukey's correction for multiple comparisons. A selection of statistically significant differences that are referred to in the text is depicted. ****: adj. $p < 0.0001$; adj. p: multiplicity-adjusted p value. **(D)** Gating strategy for experiments show in Figure 7 B and Figure S2 C.

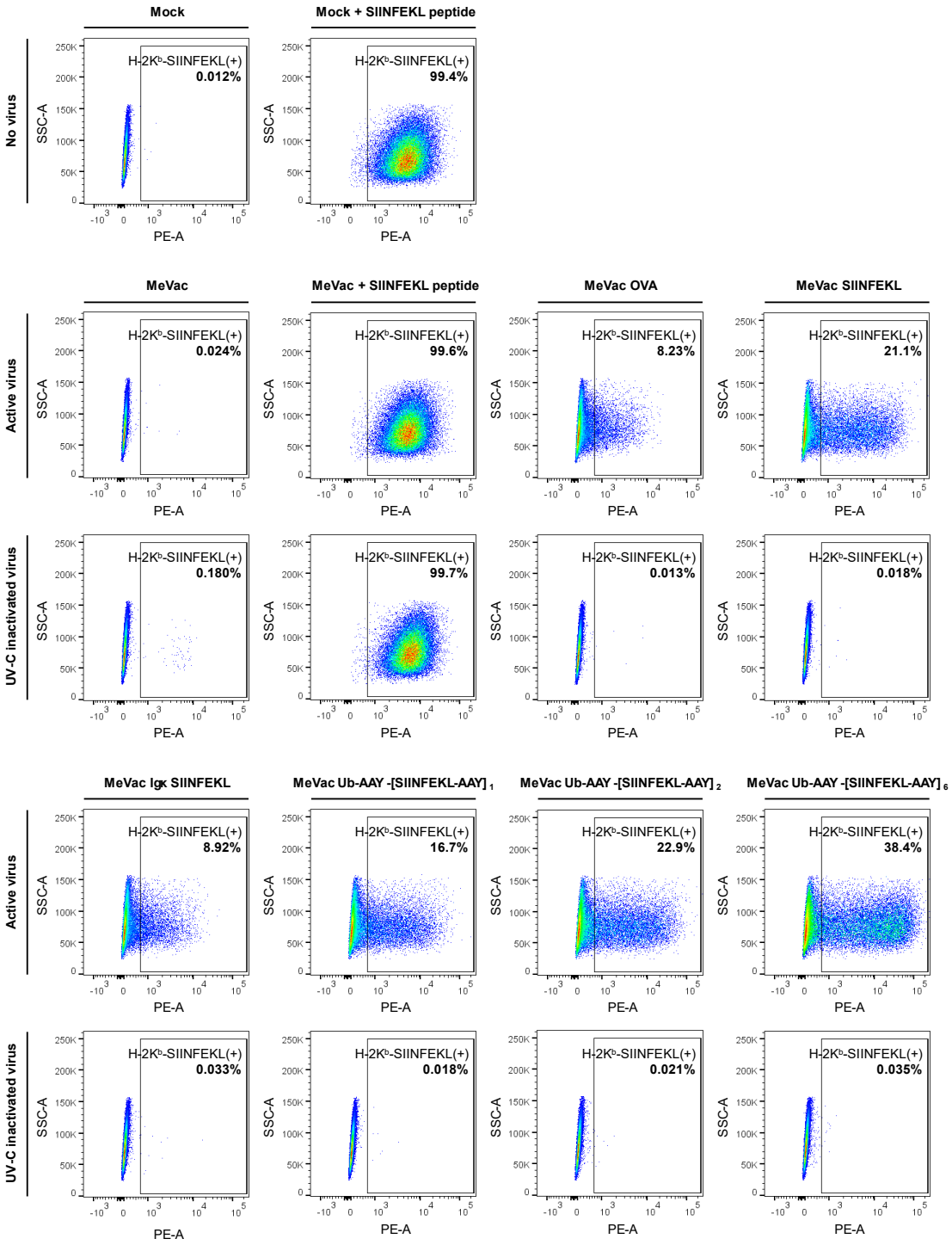

Figure S5. Antigen presentation on MC38-hCD46 cells exposed to active or UV-C inactivated MeVac variants. MC38-hCD46[lenti] cells were inoculated with the indicated MeVac variants (MOI = 3) or medium (mock). Where indicated, viruses were inactivated by UV-C irradiation before inoculation. Mock/MeVac + SIINFEKL conditions were pulsed with 2.5 µg/mL SIINFEKL peptide 1 h before cell harvest. 24 h after inoculation, the cells were harvested and flow cytometry for SIINFEKL bound to H-2K^b was performed with a PE-labelled antibody. Dotplots show live cells, with gate on H-2K^b-SIINFEKL+ (PE+) cells. Values indicate percentage of H-2K^b-SIINFEKL+ (PE+) cells within live cells.

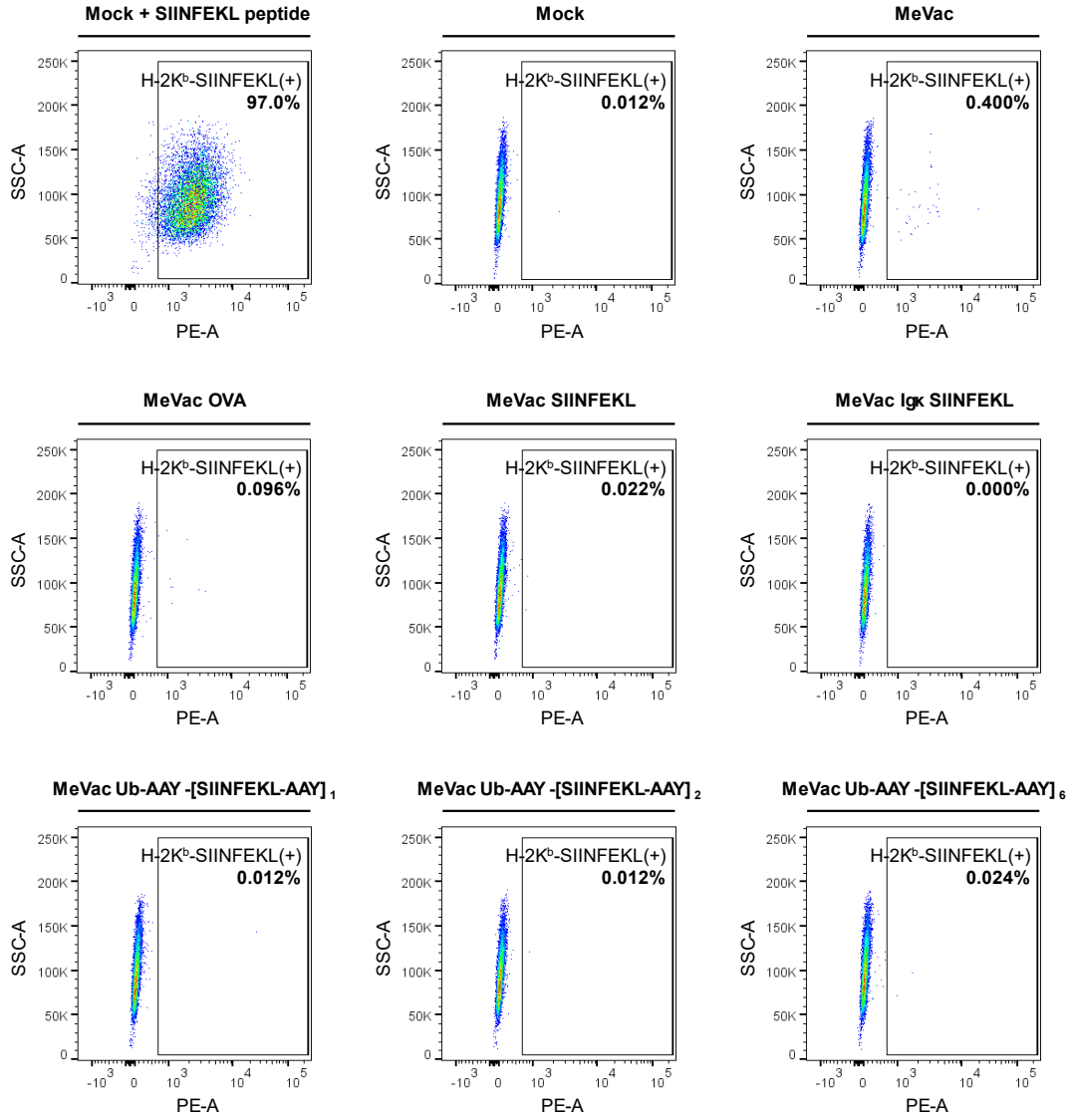

Figure S6. External peptide loading on MC38-hCD46 cells. MC38-hCD46$_{[lenti]}$ cells were inoculated with the indicated MeVac variants (MOI = 3) or medium (mock). As positive control, the tumor cells were pulsed with 2.5 µg/mL SIINFEKL peptide. One hour after inoculation or peptide pulsing, flow cytometry for SIINFEKL bound to H-2K^b was performed with a PE-labelled antibody. Dotplots show live cells, with gate on H-2K^b-SIINFEKL+ (PE+) cells. Values indicate percentage of H-2K^b-SIINFEKL+ (PE+) cells within live cells. Experiment conducted by J. Albert. Analysis using the FlowJo software conducted by myself.

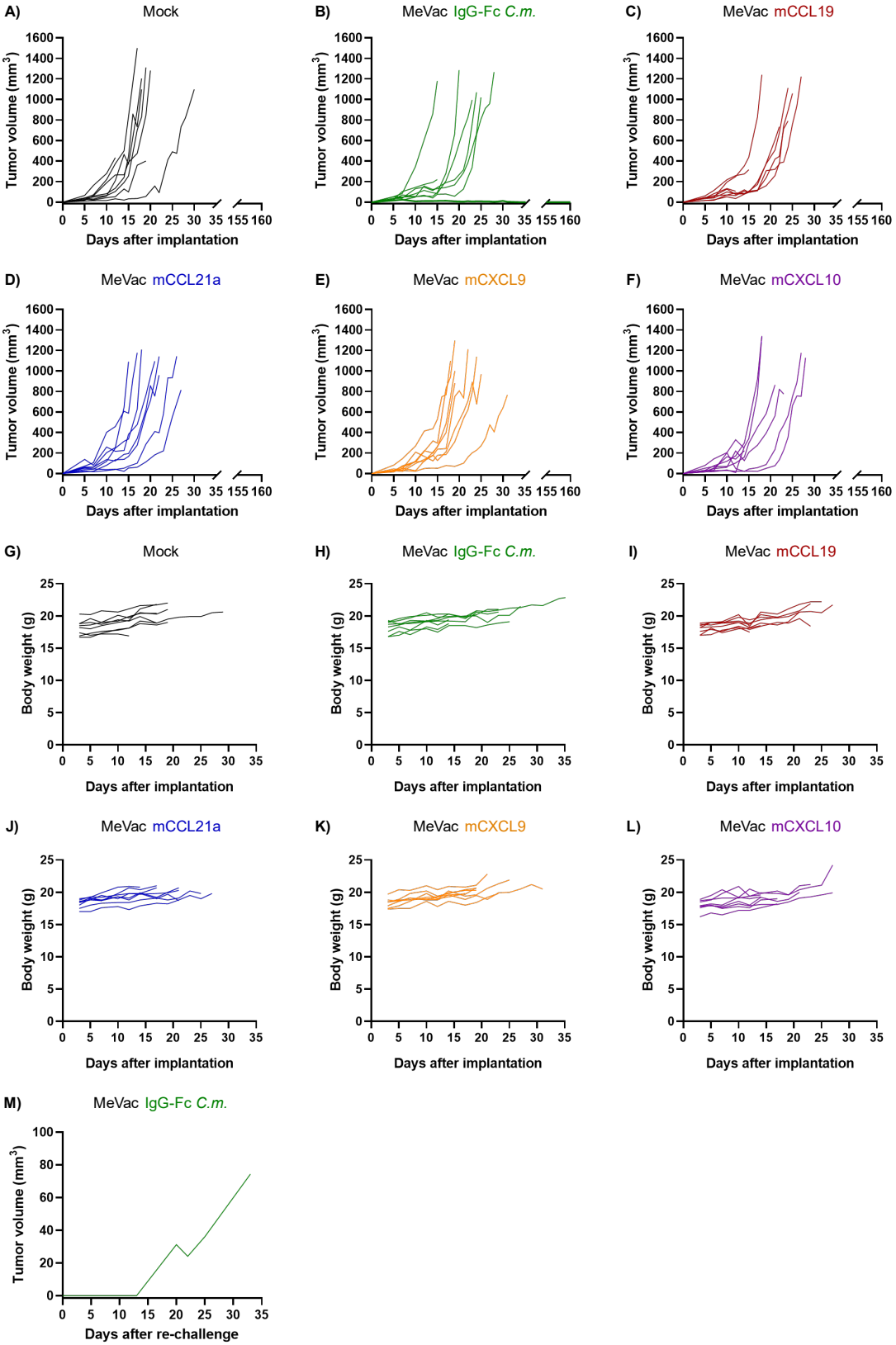

Figure S7. Therapeutic efficacy of MeVac encoding murine chemokines or a control molecule in murine melanoma (Supplementary). Data corresponds to the experiment described in Figure 13 A. **(A-L)** Tumor volume dynamics (A-F) and body weight dynamics (G-L) for individual mice in each treatment group. **(M)** Volume dynamics for the tumor developed in the left flank of the long-term survivor mouse (*i.e.*, the mouse that experienced a complete remission of the primary tumor) upon tumor re-challenge.

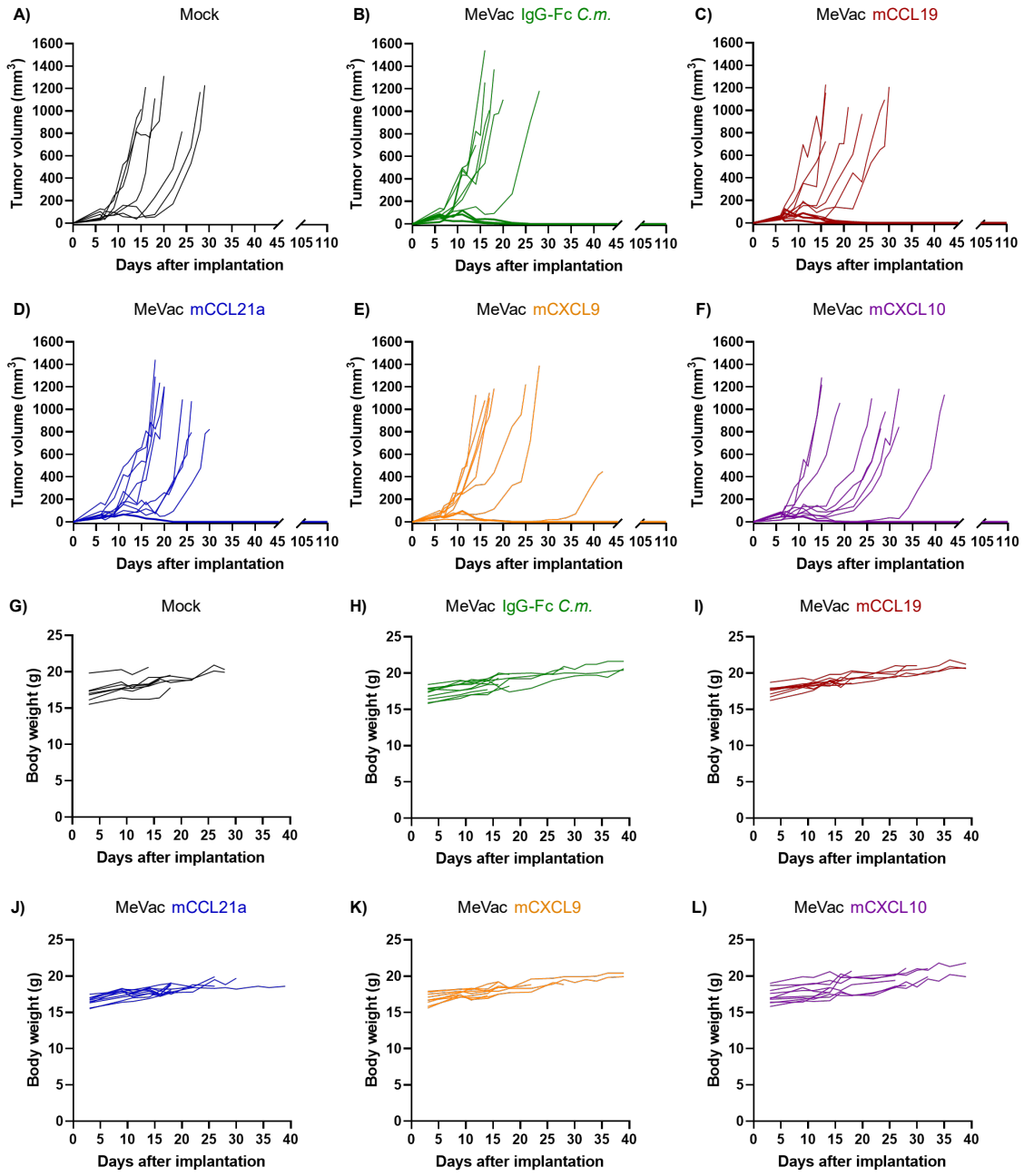

Figure S8. Therapeutic efficacy of MeVac encoding murine chemokines or a control molecule in murine colon adenocarcinoma (Supplementary). Data corresponds to the experiment described in Figure 14 A. **(A-L)** Tumor volume dynamics (A-F) and body weight dynamics (G-L) for individual mice in each treatment group.

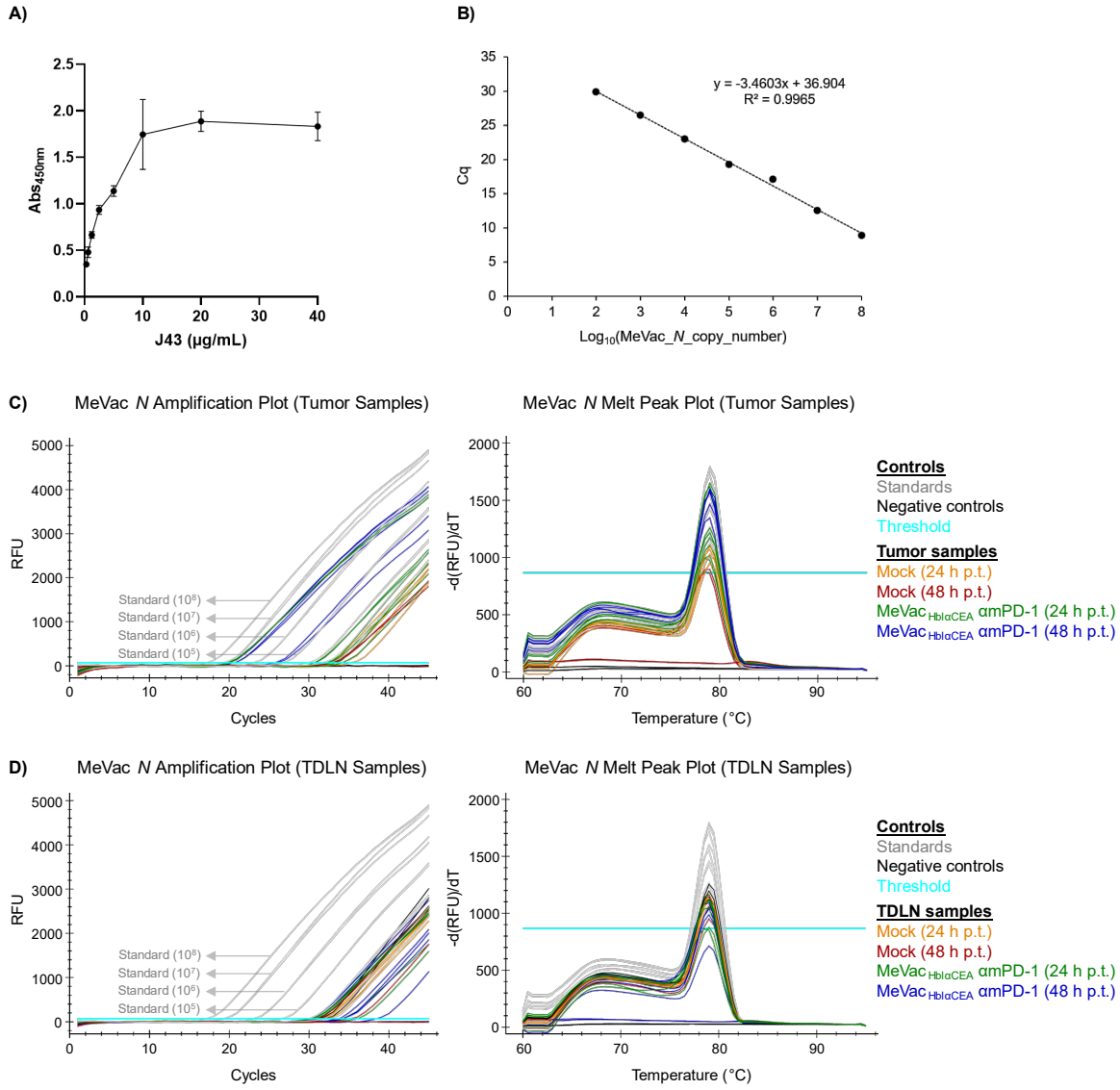

Figure S9. Detection of intratumoral MeVac *N* mRNA and systemic αmPD-1 antibody/scFv-Fc molecule (Supplementary). The data refers to the αmPD-1 ELISA and MeVac *N* qPCR experiment shown in Figure 18. **(A)** Positive control for the αmPD-1 ELISA. Absorbance values at 450 nm were determined for samples with the indicated concentrations of anti-mouse PD-1 antibody (clone J43) after stopping the ELISA enzymatic reaction. These samples were analyzed in the same ELISA experiment as those shown in Figure 18. **(B)** MeVac *N* qPCR standard curve. Dots show mean Cq values of technical duplicates per standard, as determined by qPCR with N-241 and N-331+ primers. Standards were generated by 10-fold serial dilutions of the pCG-N plasmid, starting at a plasmid concentration equivalent to $1x10^8$ MeVac *N* copies/µL. Standard Cq values below 31.2 (lowest Cq value of mock samples) were correlated with $\log_{10}$(MeVac *N* copy number) via linear regression, yielding the equation of the standard curve. **(C, D)** Amplification plots (left) and melt peak plots (right) for individual tumor **(C)** and tumor-draining lymph node (TDLN) **(D)** samples. All samples were analyzed in parallel, but the results are shown in two plots (one for tumors, one for TDLNs) for better visualization. Data for standards and negative controls are identical in the two plots. Each sample was assessed in technical duplicates. The threshold (light blue line) was defined by the Bio-Rad CFX Manager 3.1 software. RFU: relative fluorescence units; -d(RFU)/dT: negative derivative of fluorescence (RFU) with respect to temperature (T); h p.t.: hours post treatment.

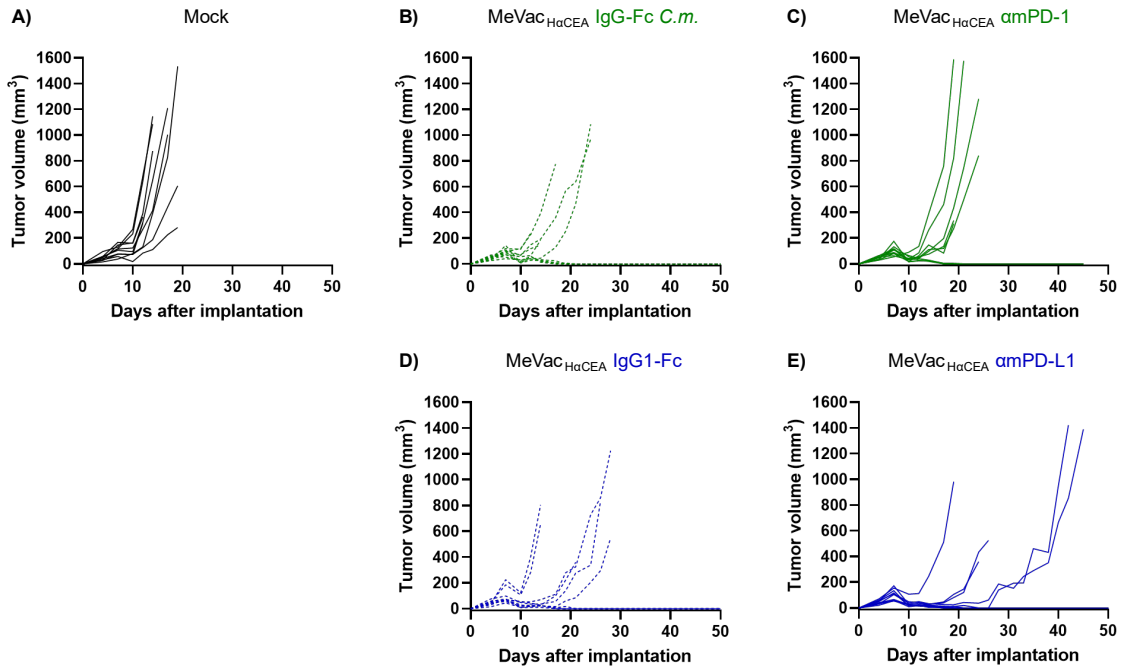

Figure S10. Therapeutic efficacy of MeVac encoding αmPD-1 scFv-Fc molecules, αmPD-L1 scFv-Fc molecules, or the corresponding Fc region in murine colon adenocarcinoma (Supplementary). (A-E) Tumor volume dynamics for individual mice in each treatment group. Data corresponds to the experiment described in Figure 18 A. I conducted this experiment together with R. Veinalde.

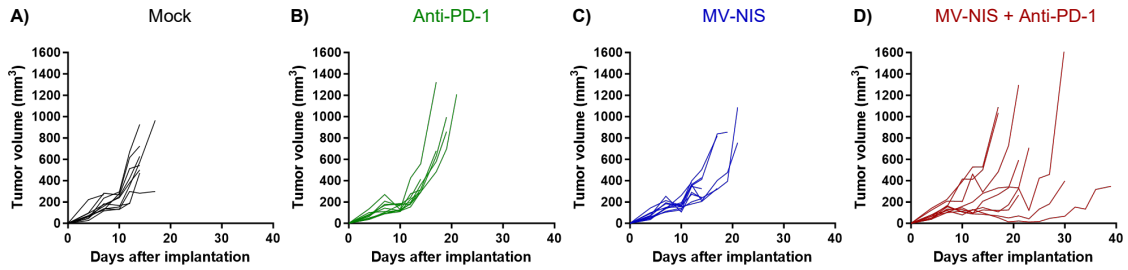

Figure S11. Efficacy of MV-NIS and/or anti-PD-1 treatment in murine pancreatic ductal adenocarcinoma (Supplementary). (A-D) Tumor volume dynamics for individual mice in each treatment group. Data corresponds to the experiment described in Figure 20 A. This experiment was conducted by R. Veinalde.

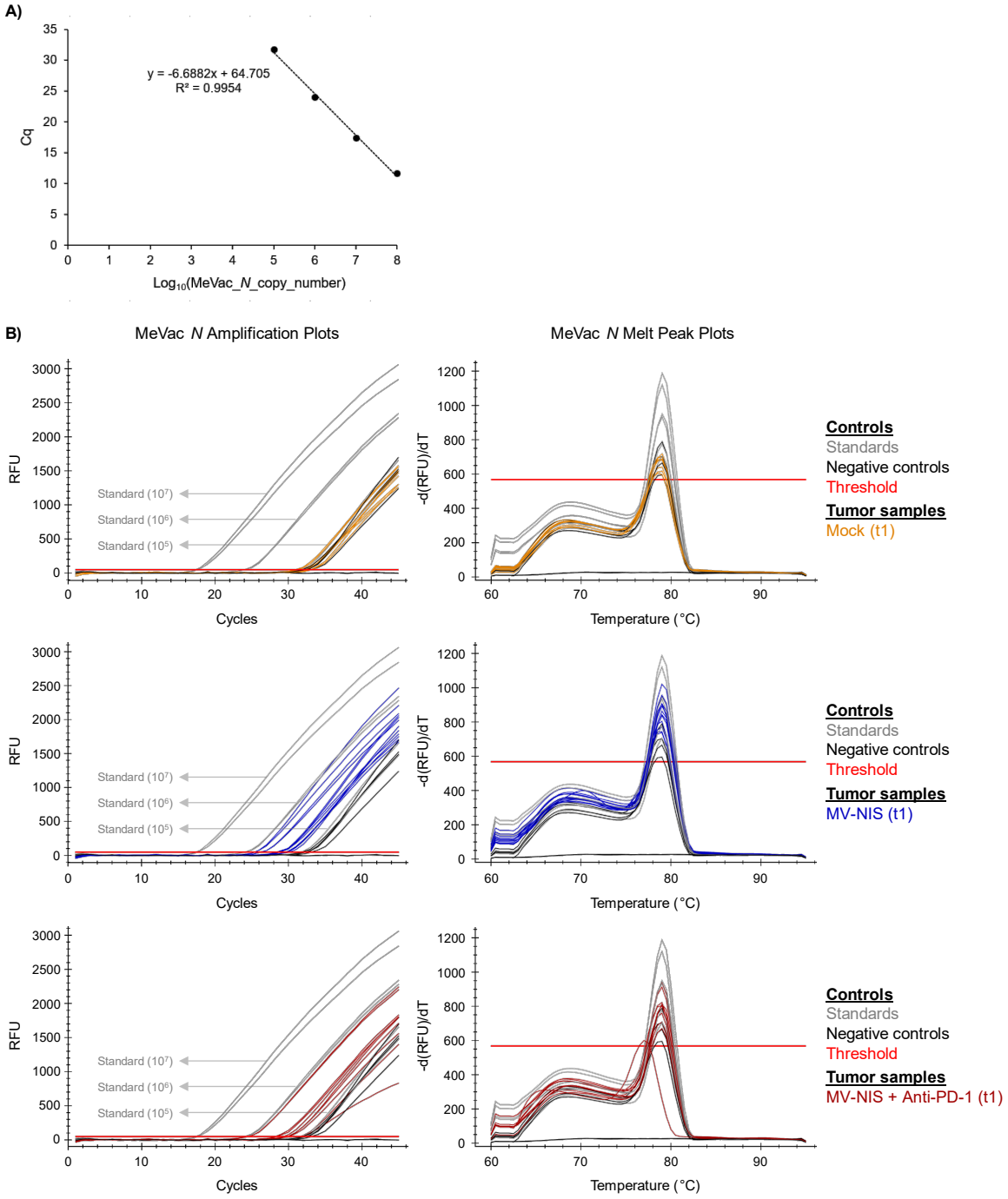

Figure S12. Detection of intratumoral MeVac *N* mRNA after treatment of murine pancreatic ductal adenocarcinoma with MV-NIS monotherapy or MV-NIS plus anti-PD-1 (Supplementary). The data refers to the MeVac *N* qPCR experiment shown in Figure 21. **(A)** MeVac *N* standard curve. Standards were generated as described in Figure S9. Dots show mean Cq values of technical duplicates per standard, as determined by qPCR with N-241 and N-331+ primers. Standard Cq values below 32 (mean Cq value of mock samples) were correlated with $\log_{10}$(MeVac *N* copy number) via linear regression, yielding the equation of the standard curve. **(B)** Amplification plots (left) and melt peak plots (right) for individual tumors. All samples were analyzed in parallel, but the results are shown in three plots (one per treatment group) for better visualization. Data for standards and negative controls are identical in the three plots. Each sample was assessed in technical duplicates. The threshold (red line) was defined by the Bio-Rad CFX Manager 3.1 software. RFU: relative fluorescence units; -d(RFU)/dT: negative derivative of fluorescence (RFU) with respect to temperature (T).

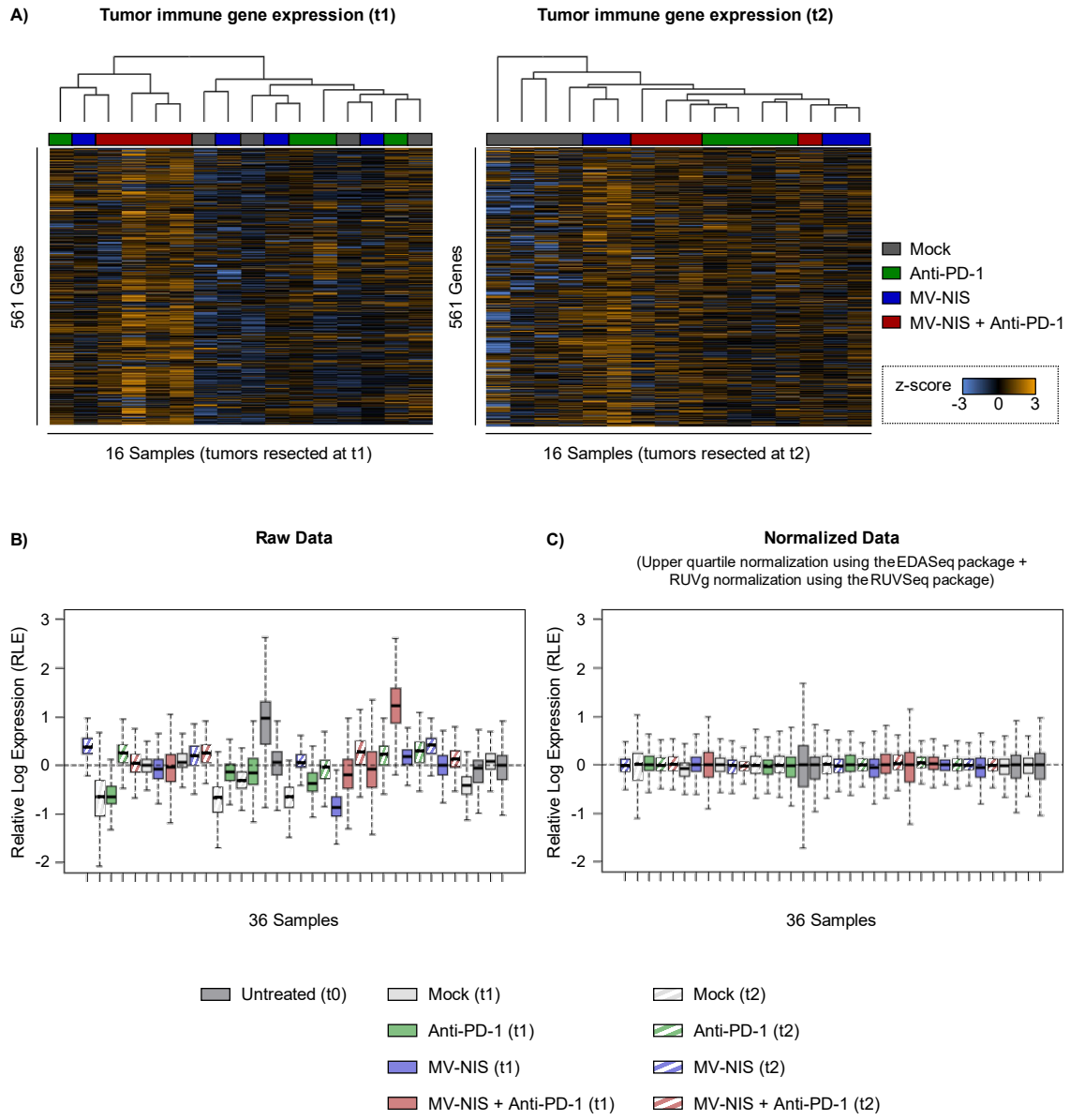

Figure S13. Tumor immune gene expression profiling after treatment of murine pancreatic ductal adenocarcinoma with MV-NIS and/or anti-PD-1 (Supplementary 1). The data refers to the tumor immune gene expression profiling experiment shown in Figure 21. Tumor immune gene expression was assessed using the mouse immunology panel from the Nanostring nCounter system. **(A)** Dendograms and heatmaps of normalized data from tumor samples resected at t1 (left) or t2 (right) are shown. Dendograms were generated by hierarchical clustering. Heatmaps depict the immune gene expression profiles of tumor samples from 4 mice per timepoint and treatment group. Data were normalized using the nSolver 4.0 software and analyzed using the Custom Analysis option from the Advanced Analysis package of the nSolver 4.0 software (see Methods). **(B-C)** Nanostring data normalization as conducted with R using the Bioconductor software packages EDASeq and RUVSeq (see Methods). Relative log expression (RLE) plots of all samples before **(B)** and after **(C)** data normalization are shown. Boxes depict the 25th, 50th, and 75th percentiles for each sample (1 box = 1 tumor sample). In a given sample, median RLE deviation from zero indicates the need for data normalization and/or the presence of outliers. The RLE plots were generated with the plotRLE() function from the EDASeq package.

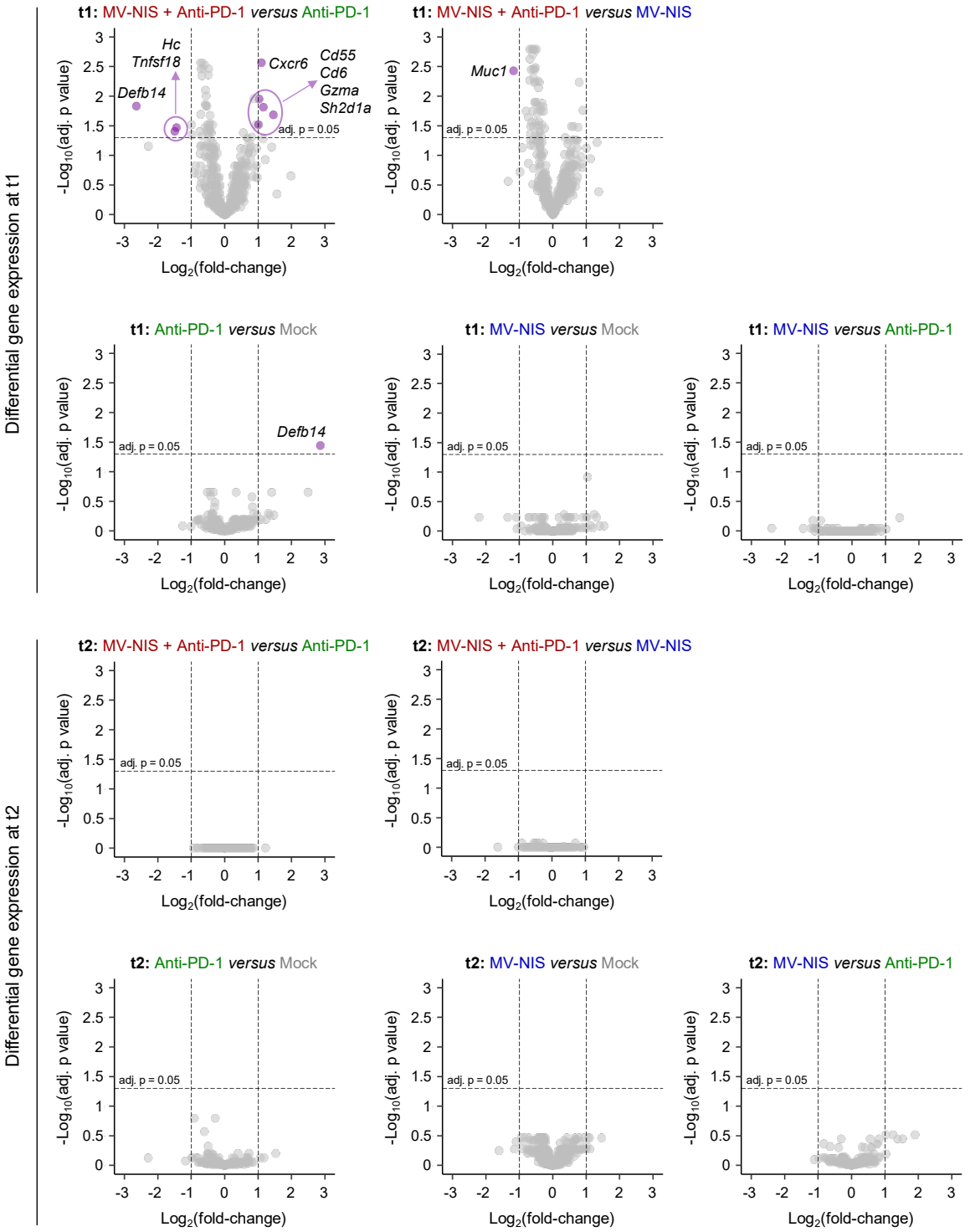

Figure S14. Tumor immune gene expression profiling after treatment of murine pancreatic ductal adenocarcinoma with MV-NIS and/or anti-PD-1 (Supplementary 2). The data refers to the tumor immune gene expression profiling experiment shown in Figure 21. Tumor immune gene expression assessment as well as data normalization and differential gene expression analysis are detailed in Figure 21 C-D. **(A-J)** Volcano plots depicting the differential expression of 561 genes between tumors from mice receiving the indicated treatments are shown. Tumors were resected at t1 **(A-E)** or t2 **(F-J)**. Each dot represents one gene (most grey dots cannot be distinguished because the values overlap). Differentially expressed genes (see criteria in Figure 21 C-D) are marked in purple. adj. p value: multiplicity-adjusted p value.

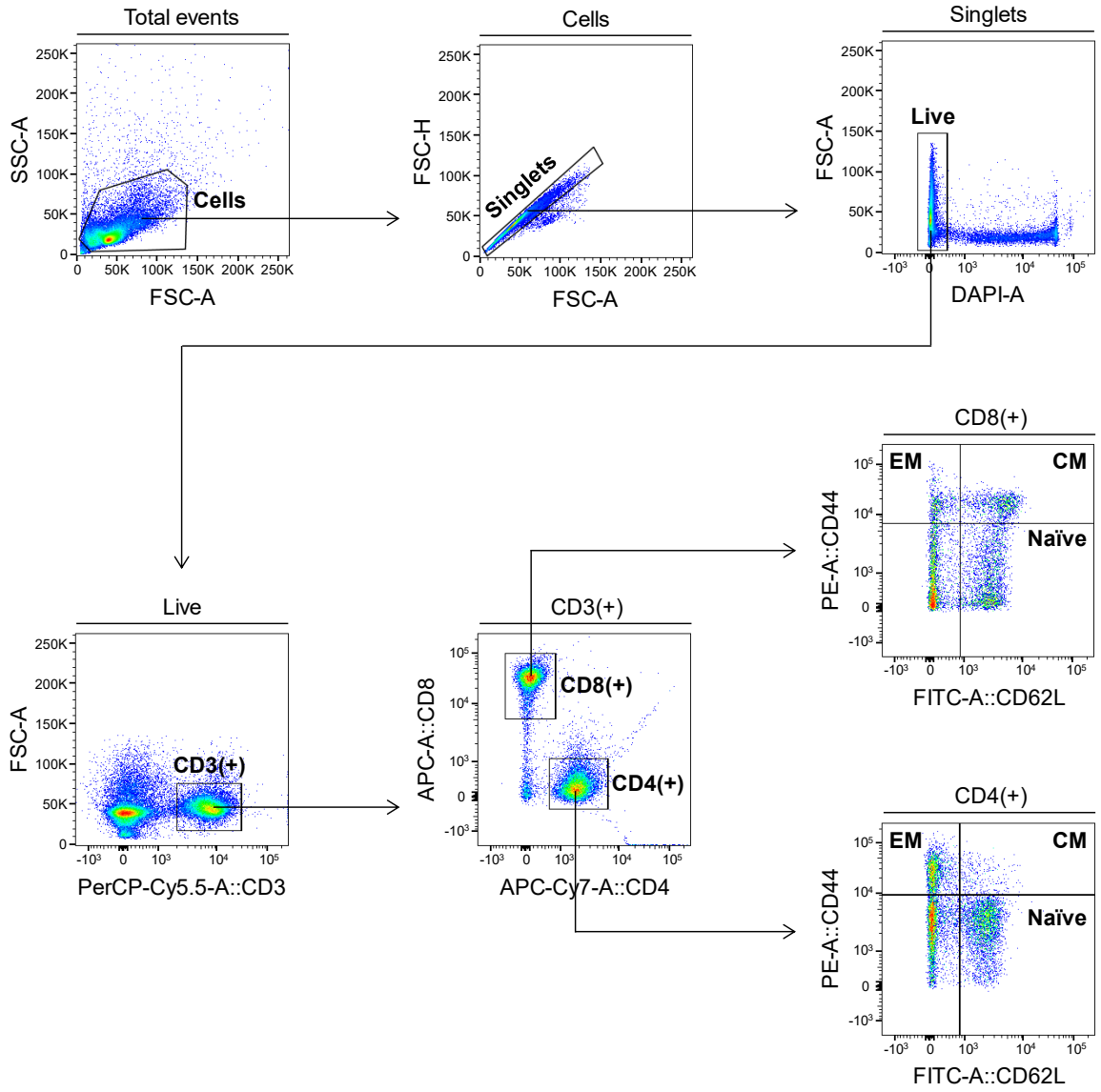

Figure S15. Flow cytometry of tumor-draining lymph nodes (Supplementary). The gating strategy for the flow cytometry analysis depicted in Figure 23 is shown. Dead cells were stained with DAPI. CM: central memory, EM: effector memory, N: naïve. I conducted the flow cytometry analysis together with R. Veinalde.

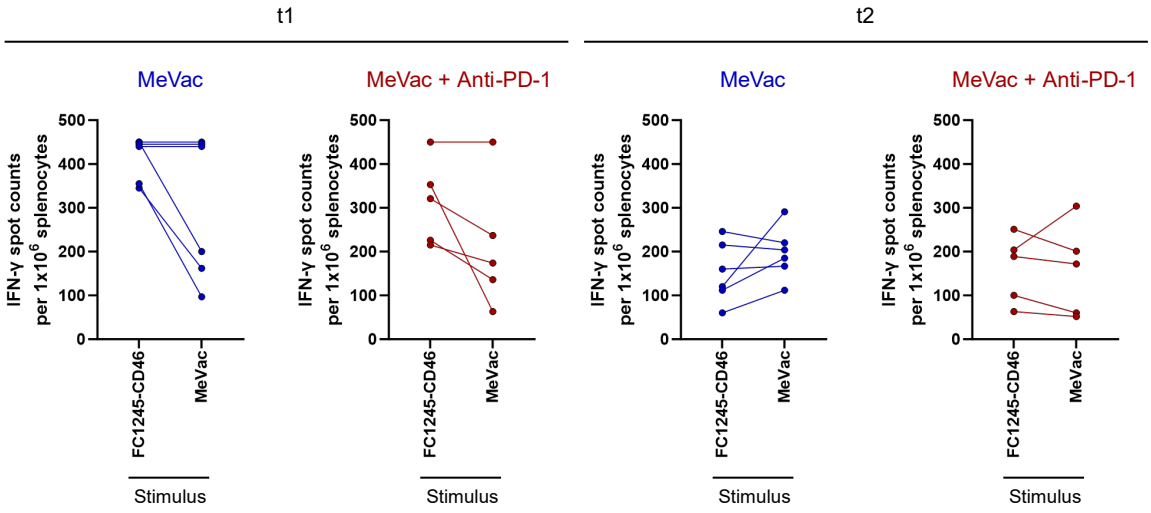

Figure S16. Systemic antitumor and antiviral immunity after treatment of murine pancreatic ductal adenocarcinoma with MeVac and/or anti-PD-1 (Supplementary). The data corresponds to the IFN-γ ELISpot shown in Figure 24. One plot is shown per treatment group (MeVac or combination treatment) and timepoint, with dots representing values for individual mice (mean of technical triplicates). Lines connect values obtained with splenocytes from the same mouse upon exposure to different stimuli.

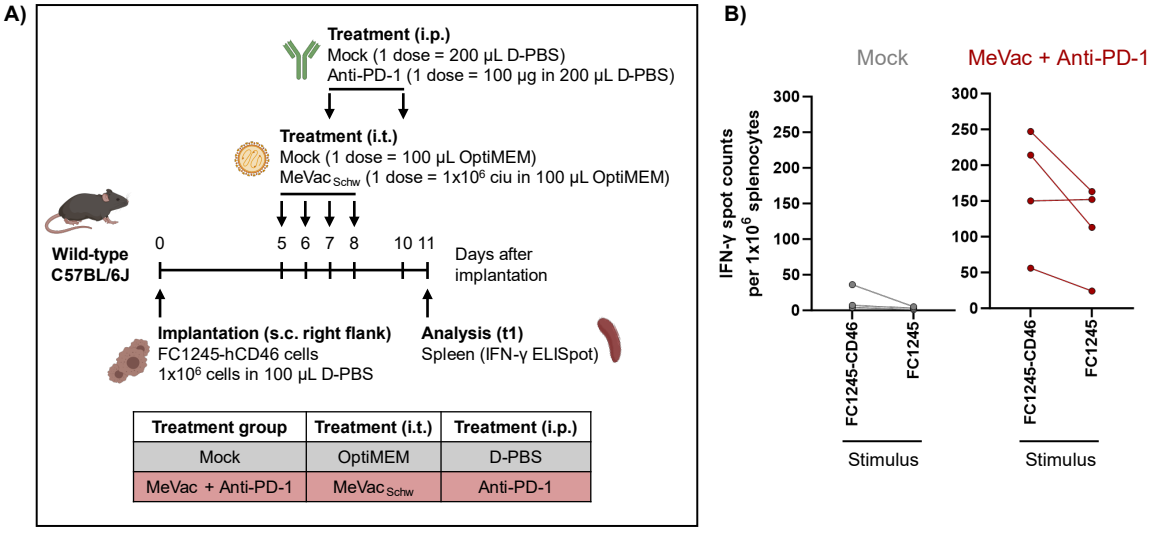

Figure S17. Role of hCD46 in the development of systemic immunity against hCD46+ tumors. **(A)** Experiment schematic (created with BioRender.com). 1x10^6 FC1245-hCD46$_{[lenti]}$ cells were injected subcutaneously (s.c.) into the flank of wild-type C57BL/6J mice (non-carrier MY II mice). After tumor establishment (average volume of 35 mm^3), the mice were treated as shown in the schematic. Six days (t1) after treatment onset, the spleens were resected. n = 3-5 mice per treatment group (mock: 3 females; combination: 3 females, 2 males). **(B)** IFN-γ ELISpot. 1x10^6 splenocytes were co-cultured with FC1245-hCD46 cells or parental FC1245 cells at a 10:1 splenocyte to tumor cell ratio. As positive and negative controls, 1x10^6 splenocytes were stimulated with 10 µg/mL Concanavalin A (ConA) or cultured without stimulation, respectively (not shown). After 40 h, IFN-γ ELISpot was conducted. IFN-γ spot counts are depicted. One plot is shown per treatment group, with dots representing values from individual mice (mean of technical triplicates). Lines connect values obtained with splenocytes from the same mouse upon exposure to different stimuli. Data from one combination-treated mouse was excluded from the corresponding plot because the splenocytes from this mouse did not respond to the positive control (*i.e.* no IFN-γ spots detected in splenocyte cultures stimulated with ConA).

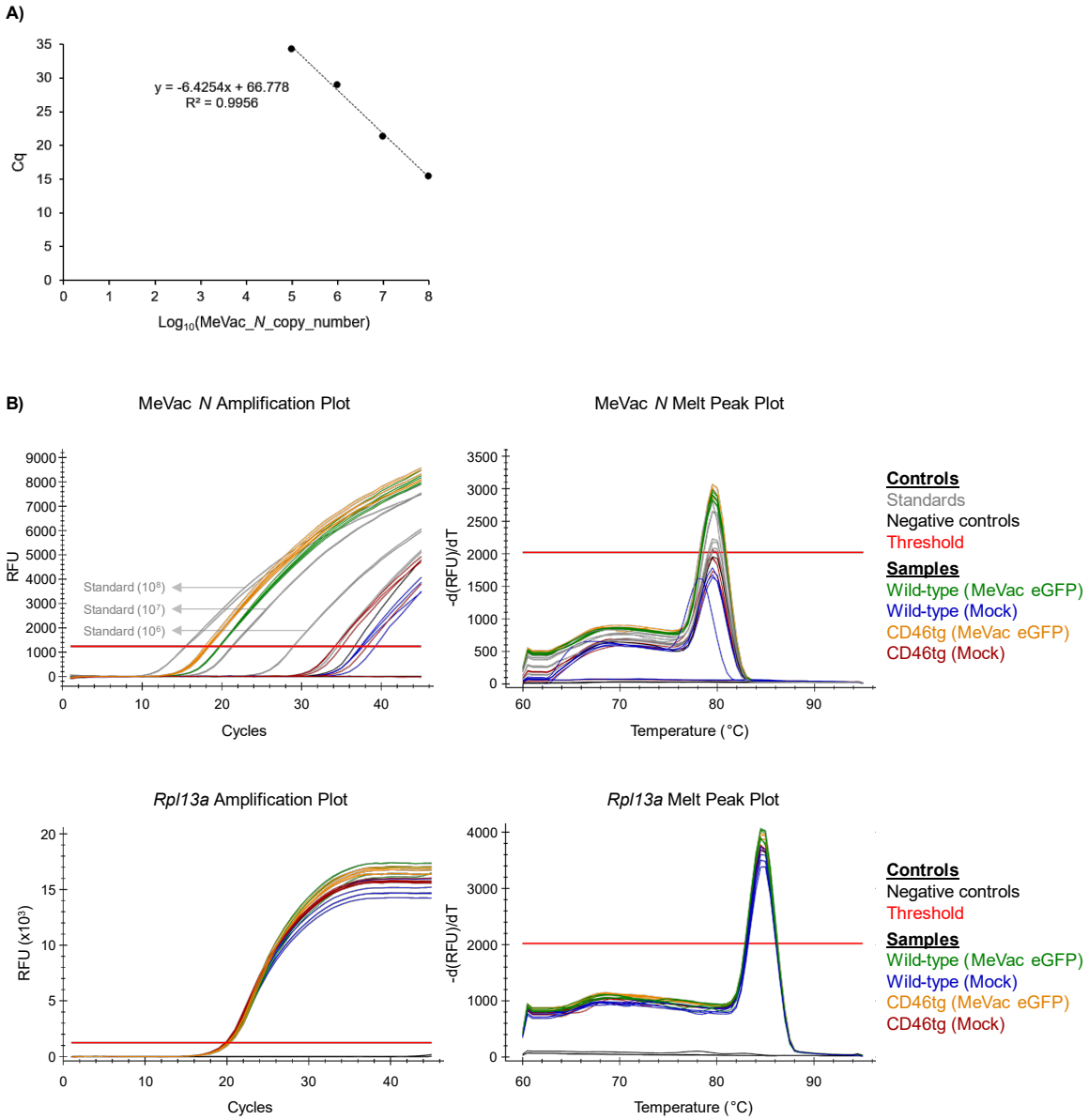

Figure S18. Detection of MeVac *N* mRNA in murine bone-marrow derived macrophages (BMDMs) transduced with MeVac eGFP (Supplementary). The data refers to the MeVac *N* qPCR experiment shown in Figure 26. **(A)** MeVac *N* standard curve. Standards were generated as described in Figure S9. Dots show mean Cq values of technical duplicates per standard, as determined by qPCR with N-241 and N-331+ primers. Standard Cq values below 36.7 (mean Cq value of mock samples) were correlated with the $\log_{10}$(MeVac *N* copy number) via linear regression, yielding the equation of the standard curve. **(B)** Amplification plots (left) and melt peak plots (right) for each sample (run in technical triplicates per gene). All samples were analyzed in parallel, but the results are shown in two plots (one for MeVac *N*, one for *Rpl13a*) for better visualization. The threshold (red line) was defined by the Bio-Rad CFX Manager 3.1 software. RFU: relative fluorescence units; -d(RFU)/dT: negative derivative of fluorescence (RFU) with respect to temperature (T).

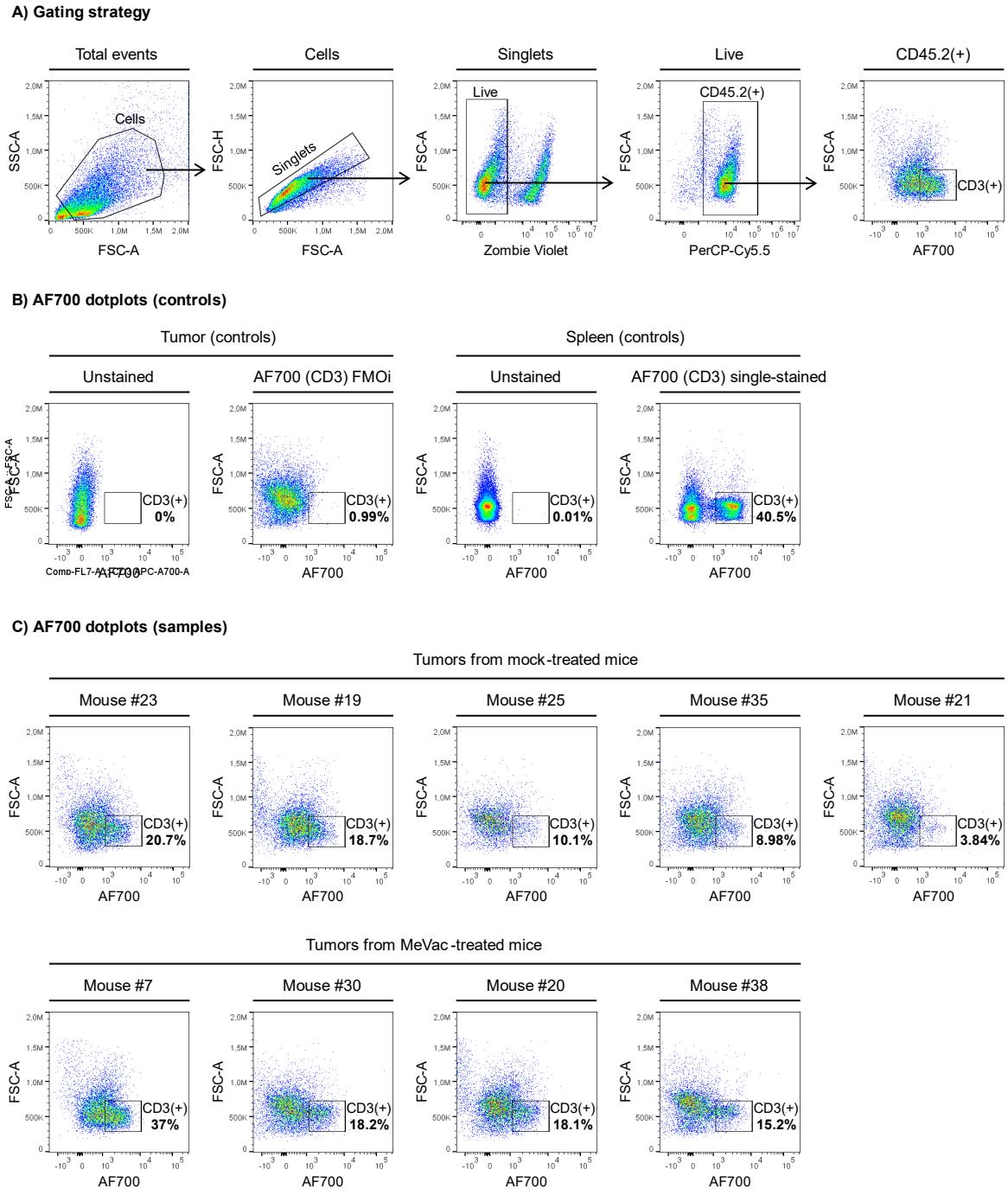

Figure S19. Flow cytometry of MC38-hCD46 tumors (Supplementary). (A) The gating strategy for the flow cytometry analysis depicted in Figure 27 is shown. Dead cells were stained with Zombie Violet. **(B)** Tumor single-cell suspensions were used for the FMOi controls, whereas splenocytes were used for the single-stained controls. The dotplots for the AF700 controls are shown as an example. Values indicate the percentage of AF700(+) [CD3(+)] cells within single-cells (unstained and single-stained controls) or within PerCP-Cy5.5(+) [CD45.2(+)] cells (FMOi control) as gated according to (A). Single-stained splenocyte controls were employed to generate the compensation matrix using FlowJo and to define the Zombie Violet(+), AF700(+), and PerCP-Cy5.5(+) gates, which were subsequently double-checked with the corresponding FMOi controls. FMOi: fluorescence minus one, plus isotype control. **(C)** AF700 dotplots depicting the PerCP-Cy5.5(+) population are shown for individual tumors, with gate on AF700(+) [CD3(+)] cells defined as explained in (B). The percentage of AF700(+) [CD3(+)] cells within PerCP-Cy5.5(+) [CD45.2(+)] cells, as gated according to (A), is indicated.

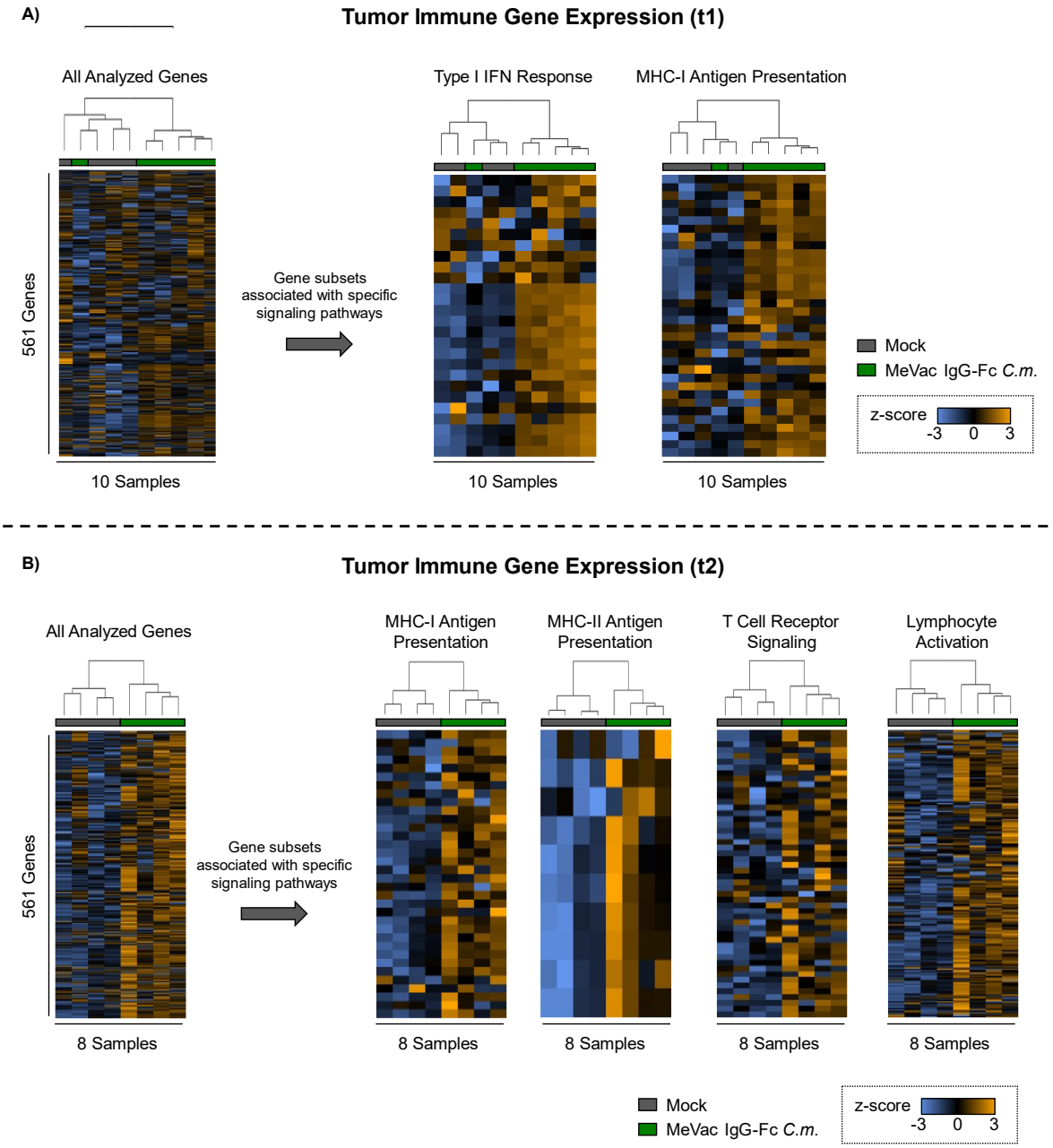

Figure S20. Tumor microenvironment remodeling after MeVac treatment of tumor-bearing CD46tg mice (Supplementary 1). The data refers to the tumor immune gene expression profiling experiment shown in Figure 28. Tumor immune gene expression was assessed using the mouse immunology panel from the Nanostring nCounter system. **(A-B)** Dendograms and heatmaps of normalized data from tumor samples resected at t1 **(A)** or t2 **(B)** are shown. Dendograms were generated by hierarchical clustering. The left-most heatmaps depict the expression profile of all analyzed genes across tumor samples from 4-6 mice per timepoint and treatment group. The other heatmaps show the expression profile of a selection of genes (from those displayed in the left-most heatmap) associated with specific signaling pathways, as indicated. Data were normalized using the nSolver 4.0 software and analyzed with the Custom Analysis option from the Advanced Analysis package of the nSolver 4.0 software (see Methods).

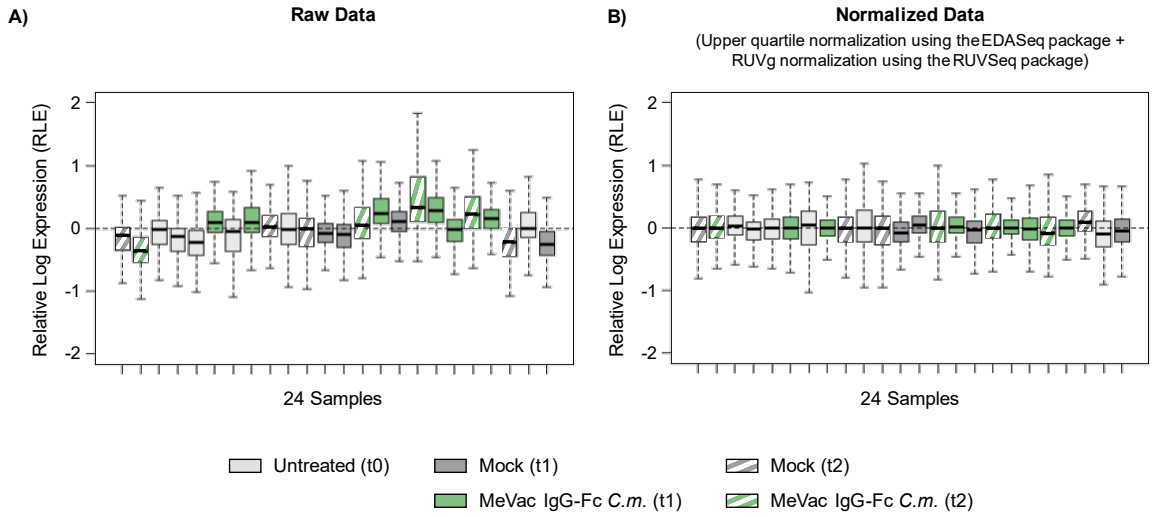

Figure S21. Tumor microenvironment remodeling after MeVac treatment of tumor-bearing CD46tg mice (Supplementary 2). The data refers to the tumor immune gene expression profiling experiment shown in Figure 28. Tumor immune gene expression was assessed using the mouse immunology panel from the Nanostring nCounter system. **(A-B)** Nanostring data normalization as conducted with R using the Bioconductor software packages EDASeq and RUVSeq (see Methods). Relative log expression (RLE) plots of all samples before **(A)** and after **(B)** data normalization are shown. Boxes depict the 25th, 50th, and 75th percentiles for each sample (1 box = 1 tumor sample). In a given sample, median RLE deviation from zero indicates the need for data normalization and/or the presence of outliers. The RLE plots were generated with the plotRLE() function from the EDASeq package.

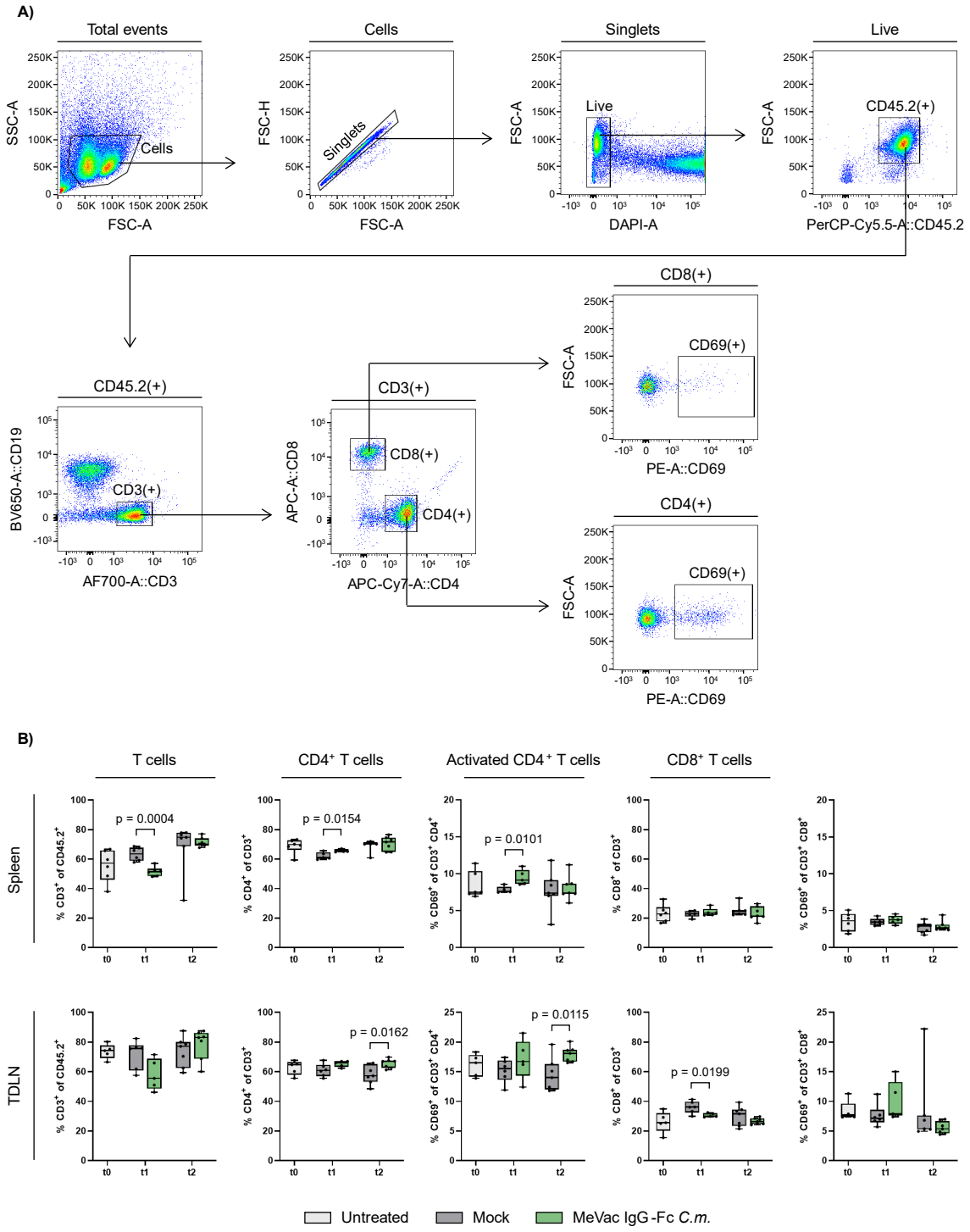

Figure S22. Flow cytometry of spleens and tumor-draining lymph nodes (TDLNs) after MeVac treatment of tumor-bearing CD46tg mice. The data refers to the experiment described in Figure 28 A. **(A-B)** Spleens and TDLNs were processed into single-cell suspensions and analyzed by flow cytometry after staining with the following antibodies: PerCP-Cy5.5 anti-mouse CD45.2, BV650 anti-mouse CD19, AF700 anti-mouse CD3, APC anti-mouse CD8, APC-Cy7 anti-mouse CD4, and PE anti-mouse CD69. Dead cells were stained with DAPI. **(A)** Gating strategy, identical for spleen and TDLN samples. **(B)** Percentages of CD3(+) cells, CD4(+) cells, CD8(+) cells, and CD69(+) cells from the indicated parental populations are shown for spleen and TDLN samples. Within a plot, dots represent values for individual mice. Boxes indicate the 25th, 50th, and 75th percentiles per group. Whiskers depict minimum and maximum values. One group is shown for t0. Two groups are shown for t1 and t2. Data from t1 and t2 were analyzed using two-tailed unpaired t test for each timepoint.

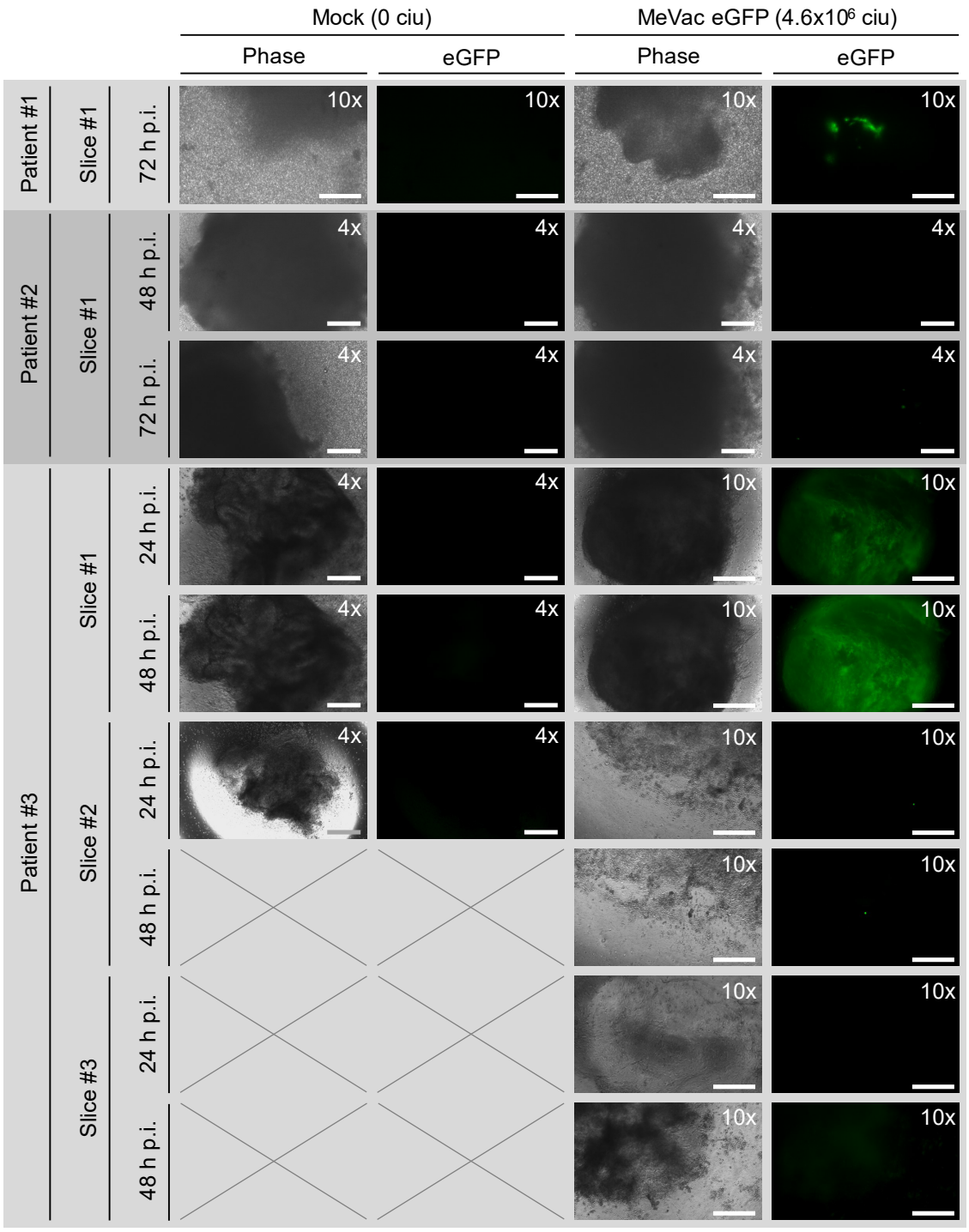

Figure S23. MeVac spread in patient-derived tumor slices (Supplementary). Surgical colorectal cancer samples were processed into slices, cultured following the air-liquid interface (ALI) system, and inoculated for 30 min with OptiMEM (mock) or 4.6x10^6 ciu MeVac eGFP as depicted in Figure 30 A. The cultures were monitored by fluorescence microscopy 24 h, 48 h, and/or 72 h post inoculation (h p.i.). Entire slices or representative slice sections were imaged with the phase contrast and eGFP fluorescence channels of a Nikon Eclipse TS2-FL microscope using the 4x or 10x objective, as indicated. The displayed images were acquired using the NIS-Elements BR software (version 5.21.03, Nikon) and processed with ImageJ. Cultures from patients #1 and #2 consisted of one slice per transwell. Cultures from patient #3 consisted of three slices per transwell, but only 2 of 3 slices (24 h p.i.) and 1 of 3 slices (48 h p.i.) were imaged from the mock group. Images of patient #1 (slice #1) and patient #3 (slice #1, 48 h p.i.) are also shown in Figure 30 B. The tumor sample from patient #3 was processed jointly with J. Achberger. Images of patient #3-derived tumor slices were acquired by J. Achberger. Scale bar: 500 µm (4x objective) or 250 µm (10x objective).

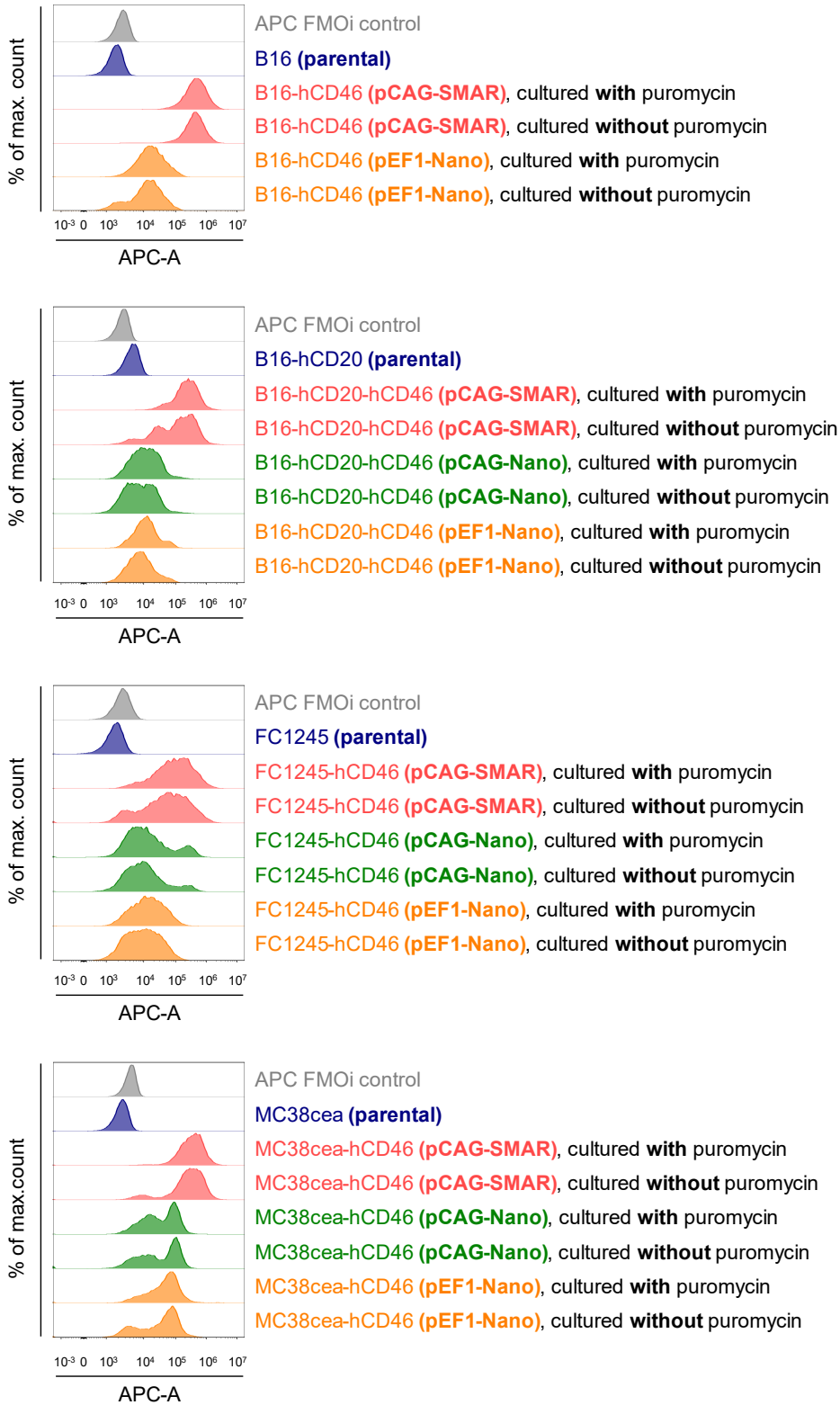

Figure S24. Generation of murine tumor cell lines with stable expression of human CD46 (hCD46) (Supplementary). The indicated cell lines were cultured in cell line-specific medium with or without 7.5 µg/mL puromycin for two weeks. Afterwards, surface hCD46 expression was determined by flow cytometry with an APC-conjugated anti-hCD46 antibody. APC histograms of the live [Zombie Violet (-)] cell population are shown. FMOi staining was conducted on the pCAG-SMAR cell line variant, cultured with puromycin. FMOi: fluorescence minus one + isotype control.

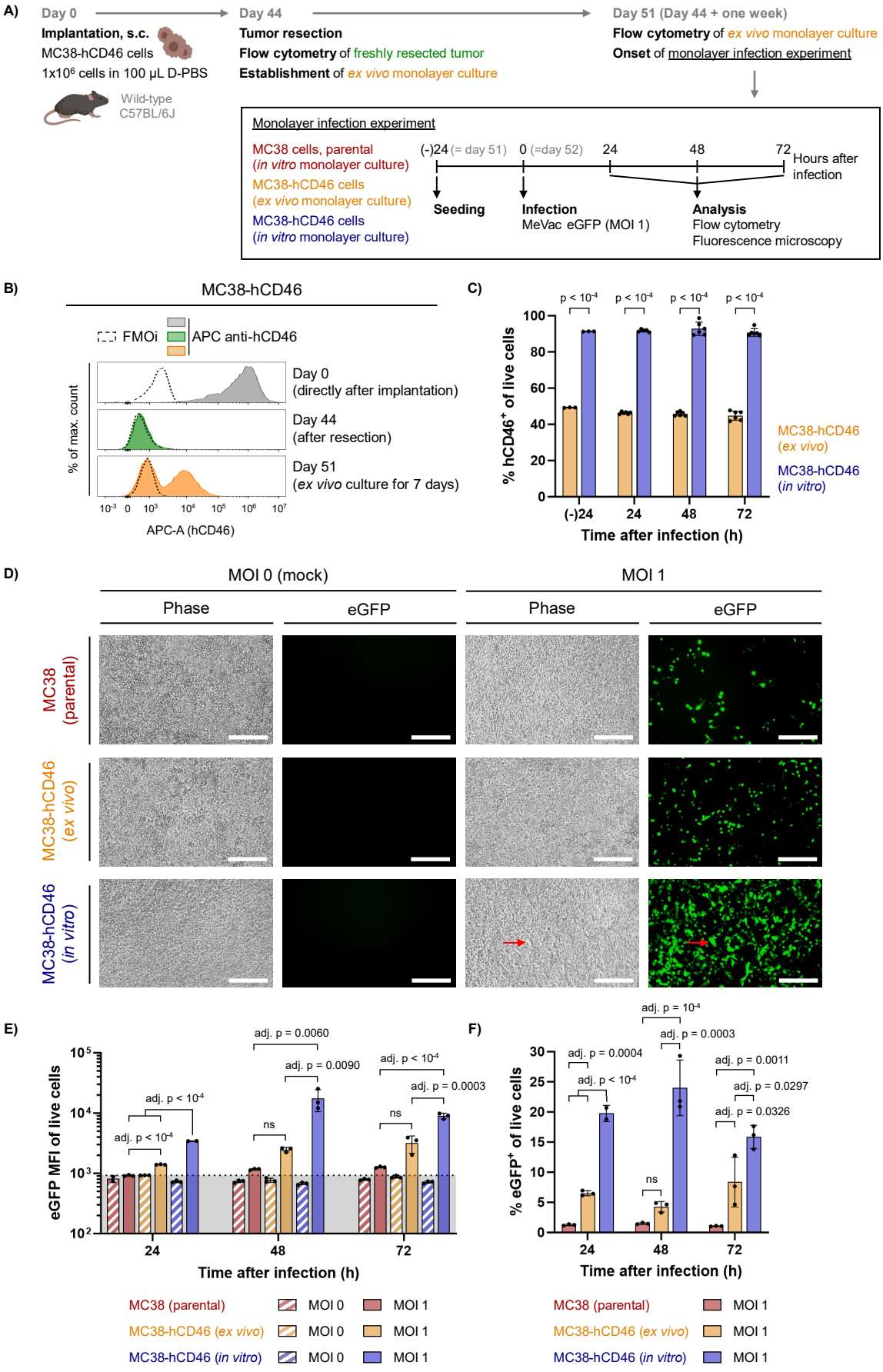

(*Figure S25. Figure legend on the next page*)

Figure S25. Human CD46 expression and MeVac reporter gene expression in MC38-hCD46 [pCAG-SMAR] cells retrieved from a tumor growing in a wild-type mouse. (A) Experiment schematic (created with BioRender.com). 1x10^6 MC38-hCD46$_{[pCAG\text{-}SMAR]}$ cells were injected subcutaneously (s.c.) into the flank of a wild-type C57BL/6J mouse (from Janvier Labs, female, 6-8 weeks-old on the day of tumor cell injection). Immediately afterwards, the extra volume of the cell suspension employed for injection was stained with an APC-conjugated anti-human CD46 (hCD46) antibody and analyzed by flow cytometry (B day 0). On day 44 after implantation (tumor volume of 928 mm^3), the tumor was resected and processed into a single-cell suspension. A fraction of this suspension was stained with APC anti-hCD46 as well as PerCP-Cy5.5 anti-mouse CD45.2 antibodies and analyzed by flow cytometry (B day 44). The remaining fraction was cultured *ex vivo* (without puromycin) as a monolayer. One week afterwards (day 51), the *ex vivo* culture as well as *in vitro* cultures of MC38-hCD46$_{[pCAG\text{-}SMAR]}$ cells and parental MC38 cells were harvested. A fraction of each culture was stained with the APC-conjugated anti-hCD46 antibody and analyzed by flow cytometry (B day 51 [data shown only for the *ex vivo* culture], C (-)24 h). The remaining fractions were seeded in 12-well plates for the monolayer infection experiment. On the next day (day 52), the seeded cultures were infected with MeVac eGFP (MOI = 1) or exposed to medium only (mock). 24 h, 48 h, and 72 h after infection, three wells per condition were monitored by fluorescence microscopy (D 48 h). The monitored cultures were subsequently harvested and stained with the APC-conjugated anti-hCD46 antibody. The eGFP and APC signals were analyzed by flow cytometry (C [24-72 h], E, F). **(B)** Histograms showing APC signal distribution of the live cell population (day 0, day 51) or the live CD45.2(-) large cell population (day 44). Each histogram depicts data from a different flow cytometry experiment. Full-stained samples (filled areas) and fluorescence minus one + isotype (FMOi) controls (dashed lines) are shown per experiment. Day 0: MC38-hCD46$_{[pCAG\text{-}SMAR]}$ cells cultured *in vitro*, analyzed directly after implantation. Day 44: tumor-derived single-cell suspension, analyzed on the day of tumor resection. Day 51: tumor-derived single-cell suspension, analyzed after being cultured *ex vivo* as a monolayer (without puromycin) for one week. **(C)** The percent of hCD46(+) cells within live cells, as assessed by flow cytometry, is shown for the indicated cultures. Parental MC38 cells, which are hCD46(-) (data not shown), were employed to define the hCD46(+) gate. Each dot corresponds to one culture. Bars show mean of six biological replicates (3 virus-treated, 3 mock-treated). Error bars indicate standard deviation (not visible for most datasets). Data were analyzed using two-tailed unpaired t test per timepoint. Data from B (*ex vivo* culture at day 51) and C (*ex vivo* culture at (-)24 h) are the same, but displayed differently (APC histogram in B, percent hCD46(+) cells within live cells in C). **(D)** Fluorescence microscopy. The indicated cultures were monitored with the phase contrast and eGFP fluorescence channels of a Nikon Eclipse TS2-FL microscope 24 h, 48 h, and 72 h after virus/mock inoculation. Representative images of the 48 h timepoint, acquired with the NIS-Elements BR software and processed with ImageJ, are shown. The red arrow points towards a syncytium. Scale bar: 250 µm. **(E)** The eGFP median fluorescence intensity (MFI) within the live cell population is shown for the indicated cultures, as assessed by flow cytometry. The threshold for specific eGFP signal (dotted line) was defined as the highest eGFP MFI of a mock-infected culture. An eGFP MFI below this value (*i.e.* within the grey area) was considered background signal. Data from virus-infected cultures (MOI = 1) were analyzed using one-way ANOVA for each timepoint with Tukey's correction for multiple comparisons. Data from mock-infected cultures (MOI = 0) were only employed to define the background signal, and thus excluded from the statistical analysis. adj. p: multiplicity-adjusted p value. **(F)** The percent of eGFP(+) cells within live cells, as assessed by flow cytometry, is shown for the indicated cultures. Mock-infected cells, which are eGFP(-) (data not shown), were employed to define the eGFP(+) gate. Each dot corresponds to one virus-infected culture. Bars show mean of biological triplicates. Error bars indicate standard deviation (not visible for some datasets). Data were analyzed using one-way ANOVA for each timepoint with Tukey's correction for multiple comparisons. adj. p: multiplicity-adjusted p value. **(C,E,F)** Within a timepoint, data from C, E, and F derive from the same flow cytometry experiment.

Table S1. Infection and cell/virus harvesting. The detailed parameters for MeVac infection of Vero cells or murine cells as well as sample harvesting procedures are indicated.

Experiment	Cell Lines	Plate Format	Seeding	Infection	MOI	Medium Change (MC) or Addition (MA)	Harvest (fraction, time)
Growth curves	Vero	96-well plate	$8x10^3$ cells/well in 100 µL/well	50 µL/well, OptiMEM	3 / 0.03	Samples collected at 0 h p.i. MA of 50 µL OptiMEM before harvest Samples collected at other timepoints MC to 100 µL culture medium (6-8 h p.i.)	Cell lysate + supernatant 0, 12, 24, 36, 48, 72, 96 h p.i.
	MC38-hCD46 B16-hCD46				3		
ELISA (chemokines)	Vero	96-well plate	$8x10^3$ cells/well in 100 µL/well	50 µL/well, DMEM	0.03	MA of 150 µL DMEM + 10% FCS (12 h p.i.)	Supernatant 72 h p.i.
	MC38-hCD46				3		
Chemotaxis & Cytotoxicity assays	Vero	6-well plate	$2x10^5$ cells/well in 2 mL/well	1 mL/well, OptiMEM	0.03	MC to 2 mL OptiPro SFM (7-10 h p.i.)	Supernatant 48 h p.i. (MeVac mTNF-α) 72 h p.i. (other conditions)
ELISpot & Flow cytometry (Figures shown in section 4.1)	DC2.4	15 cm dish	$5x10^6$ cells/dish in 13 mL/dish	8 mL/dish, OptiMEM	3	MC to 15 mL culture medium (3 h p.i.)	Cells (detached with trypsin) 24 h p.i. Note: 5 µg (well) or 150 µg (dish) SIINFEKL peptide were added to some mock- or MeVac-inoculated cultures 1 h before cell harvest Note: Where indicated in the Figure, the viruses were inactivated by UV-C irradiation before infection
	MC38-hCD46	6-well plate	$2x10^5$ cells/well in 2 mL/well	800 µL/well, OptiMEM	3	MC to 2 mL culture medium (3 h p.i.)	

Table S1 continues on the next page.

Table S1 (continued). Infection and cell/virus harvesting. The detailed parameters for MeVac infection of Vero cells or murine cells as well as sample harvesting procedures are indicated. **h p.i.:** hours post infection/inoculation.

Experiment	Cell Lines	Plate Format	Seeding	Infection	MOI	Medium Change (MC) or Addition (MA)	Harvest (fraction, time)
Flow cytometry for external peptide loading on DC2.4 cells (Figure S3)	MC38-hCD46	6-well plate	$2x10^5$ cells/well in 2 mL/well	800 µL/well, OptiMEM	3	MC to 2 mL culture medium (3 h p.i.) Note: 5 µg SIINFEKL peptide were added to some mock-inoculated cultures after the medium change	Cell lysate + supernatant 24 h p.i. (or 21 h after peptide pulsing) Note: Harvest was followed by 1 x freeze-thaw cycle, clarification (2500 x g, 5 min), and transfer of 1 mL clarified cell lysate to DC2.4 cells (seeded in 6-well plates on the previous day at $2x10^5$ cells per well in 2 mL per well)
Inoculation of murine bone marrow-derived macrophages (BMDMs) (Figure 26)	BMDMs	12-well plate	$3x10^5$ cells/well in 1 mL/well	300 µL/well, DMEM	3	MC to 1 mL DMEM low glucose + 5% FCS (2 h p.i.)	Cells, 24 h p.i. Procedure: remove medium, wash with 1 mL D-PBS, detach BMDMs with 500 µL trypsin/EDTA and gentle scraping, pellet and wash cells twice, keep cell pellets at -70 ºC until RNA extraction.

Table S2. ELISpot information. **MACS:** magnetic activated cell separation, **n.a.:** not applicable.

Experiment	Effector cells (per well)	Stimulus (per well)	Is this condition a control?	E:T	Reagents
OT-I priming by DC2.4 cells exposed to MeVac variants (Figure 5) or OVA-CTL activation by DC2.4 cells exposed to MeVac variants (Figure 6)	$5x10^3$ OT-I T cells (sorted from spleens of OT-I mice via MACS) or $5x10^3$ OVA-CTLs	$5x10^4$ DC2.4 cells, mock-infected	No	1:10	ELISpot plate PVDF membrane, white plate (Merck, Ref. MSIPS4W10) Coating antibody Rat anti-mouse IFN-γ (Clone R4-6A2, BD Pharmingen™, Ref. 551216) Detection antibody Biotin rat anti-mouse IFN-γ (Clone XMG1.2, BD Pharmingen™, Ref. 554410) Streptavidin-coupled enzyme Streptavidin-AKP (BD Pharmingen™, Ref. 554065) Substrate BCIP/NBT (Merck, Ref. B1911) ELISpot plate reader CTL ELISpot reader (CTL Europe)
		$5x10^4$ DC2.4 cells, infected with active MeVac variants			
		$5x10^4$ DC2.4 cells, infected with UV-C inactivated MeVac variants (only included in ELISpot with OVA-CTLs)			
		$5x10^4$ DC2.4 cells, mock-infected and exposed to SIINFEKL peptide for 1 h before harvesting (see Table S1)	Not a control for ELISpot with OT-I T cells, but positive control for ELISpot with OVA-CTLs		
		$5x10^4$ DC2.4 cells, infected with MeVac and exposed to SIINFEKL peptide for 1 h before harvesting (see Table S1)			
		10 µg/mL SIINFEKL peptide		n.a.	
		10 µg/mL ConA	Positive control		
		Medium	Negative control		
	Medium	Medium			
		$5x10^4$ DC2.4 cells, infected with MeVac Ub-AAY-$[SIINFEKL-AAY]_6$			
OVA-CTL activation by MC38-hCD46 cells exposed to MeVac variants (Figure 7)	$5x10^3$ OVA-CTLs	$5x10^4$ MC38-hCD46 cells, mock-infected	No	1:10	
		$5x10^4$ MC38-hCD46 cells, infected with active MeVac variants			
		$5x10^4$ MC38-hCD46 cells, infected with UV-C inactivated MeVac variants			
		$5x10^4$ MC38-hCD46 cells, mock-infected and exposed to SIINFEKL peptide for 1 h before harvesting (see Table S1)	Positive control		
		$5x10^4$ MC38-hCD46 cells, infected with MeVac and exposed to SIINFEKL peptide for 1 h before harvesting (see Table S1)			
		10 µg/mL SIINFEKL peptide		n.a.	
		10 µg/mL ConA			
		Medium	Negative control		
	Medium	Medium			
		$5x10^4$ DC2.4 cells, infected with MeVac Ub-AAY-$[SIINFEKL-AAY]_6$			

Table S2 (continued). ELISpot information. n.a.: not applicable.

Experiment	Effector cells (per well)	Stimulus (per well)	Control?	E:T	Reagents
Murine PDAC study (Figure S17)	$1x10^6$ murine splenocytes (from spleens resected at t1)	$1x10^5$ FC1245-hCD46 cells (cultured *in vitro*, no treatment)	No	10:1	*Horseradish peroxidase linked to streptavidin (HRP-SA) (Table 5) *Mouse IFN-γ ELISpot pair (coating and detection antibodies) (Table 6) *TMB substrate (Table 12) *While ELISpot plates (Table 13) *Plate scan with the CTL ELISpot reader (CTL Europe)
		$1x10^5$ FC1245 cells (cultured *in vitro*, no treatment)			
		10 µg/mL ConA	Positive control	n.a.	
		Medium	Negative control		
Murine PDAC study (Figures 24 & S16)	$1x10^6$ murine splenocytes (from spleens resected at t1 or t2)	$1x10^5$ FC1245-hCD46 cells (cultured *in vitro*, no treatment)	No	10:1	*Horseradish peroxidase linked to streptavidin (HRP-SA) (Table 5) *Mouse IFN-γ ELISpot pair (coating and detection antibodies) (Table 6) *TMB substrate (Table 12) *Transparent ELISpot plates (Table 13) *Plate scan with the Bioreader® 7000-E ELISpot reader (Biosys Scientific Devices)
	$5x10^5$ murine splenocytes (from spleens resected at t1 or t2)	*7 µg/mL MeVac bulk antigen (t1) *MeVac suspension (MOI = 5) (t2)	No	n.a.	
		10 µg/mL ConA	Positive control		
		Medium	Negative control		
CD46tg mouse study (Figure 27)	$1x10^6$ murine splenocytes	$1x10^5$ MC38-hCD46 cells (cultured *in vitro*, no treatment)	No	10:1	
		$1x10^5$ MC38 cells (cultured *in vitro*, no treatment)			
		$1x10^5$ B16 cells (cultured *in vitro*, no treatment)			
		10 µg/mL MeVac bulk antigen		n.a.	
		10 µg/mL ConA	Positive control		
		Medium	Negative control		

Table S3. Optimization of the MeVac purification protocol. The main strategies tested during optimization of the virus purification protocol are described. The procedures highlighted in green correspond to the optimized protocol, which is described in more detail in sections 3.2.3.2 and 3.2.3.5. I tested the different approaches shown in this table together with A. Brunecker, V. Frehtman, B. Leuchs, and Ž. Modic. Moreover, we tested purification via cation-exchange chromatography, but it wasn't feasible in the academic laboratory setting.

Step	Procedure	Details
Harvesting	Cell-free virus	Repetitive harvest of cell culture supernatant at several times between 22 h and 57 h after infection
	Cell-free virus	Harvest of cell culture supernatant at a single time (48 h after infection)
	Cell-associated virus	Removal of cell culture supernatant (except 1-2 mL) followed by scraping of the Vero cell monolayer
Cell Disruption	Freeze-thaw cycle	10 min in liquid nitrogen + 10 min at 37 ºC
	Ultrasonication	1 min, 140 W (Sonorex RK 100 H ultrasonic 5 homogenizer, Bandelin, Germany)
Clarification	Filtration	0.45 µm PVDF syringe filter or 5 µm CA syringe filter (Sartorius, Ref. S7594)
	Cascade Filtration	5 µm CA syringe filter (Sartorius, Ref. S7594) followed by 1.2 µm CA syringe filter (Sartorius, Ref. 17593)
	Centrifugation	Centrifuge settings: several speeds tested --> 4 ºC, 5 min, 2500/4000/5000 x g
Concentration	Ultrafiltration	Filtration unit: Pierce™ Protein Concentrator PES, 100K MWCO, 20-100mL (Thermo Fisher Scientific, Ref. 88537) Centrifuge settings: 2000 x g, 4ºC, 30 min
	Ultrafiltration	Filtration unit: Vivacell 100, 100000 MWCO PES (Sartorius, Ref. VC1041) Centrifuge settings: several times and speeds tested --> 4ºC, 5/10/30 min, 800/1000/1500/2500 x g
Concentration + Purification	Ultracentrifugation	Round #1: One-step sucrose cushion (Phases: 20% and 60% (w/v) sucrose in TE buffer) Settings: L8-55M ultracentrifuge (Beckman), SW50.1 rotor, 28000 rpm, 2 h, 4 ºC, no break Round #2: Step-wise sucrose gradient (Phases: 20%, 30%, 40%, 50%, and 60% (w/v) sucrose in TE buffer) Settings: L8-55M ultracentrifuge (Beckman), SW50.1 rotor, 28000 rpm, 4 h, 4 ºC, no break
	Ultracentrifugation	Round #1: One-step iodixanol cushion (Phases: 20% and 54% (w/v) OptiPrep in TE buffer) Settings: Beckman L8-55M ultracentrifuge, SW50.1 rotor, 28000 rpm, 2 h, 4 ºC, no break Round #2: Pelleting Settings: Beckman L8-55M ultracentrifuge, SW50.1 rotor, 28000 rpm, 4 h, 4 ºC, no break
	Ultracentrifugation [DKFZ, Heidelberg]	Round #1: One-step iodixanol cushion (Phases: 20% and 54% (w/v) OptiPrep in TE buffer) Settings: Beckman Optima™ LE-80K ultracentrifuge, SW50.1 rotor, 30600 rpm, 2 h, 8 ºC, no break
	Ultracentrifugation [UWH, Witten]	Round #1: One-step iodixanol cushion (Phases: 20% and 54% (w/v) OptiPrep in 1X D-PBS) Settings: Beckman Optima™ L-90K ultracentrifuge, SW41 rotor, 25600 rpm, 2 h, 8 ºC, no break

9 Addendum

9.1 Introduction

9.1.1 The COVID-19 Pandemic

In late 2019, the first cases of coronavirus disease 19 (COVID-19) were reported among patients suffering from severe respiratory syndrome in Wuhan, China [xxiii]. The causative agent of this disease, a coronavirus, was identified as severe acute respiratory syndrome coronavirus 2 (SARS-CoV-2) [327]. Following these clinical case reports, cases spread worldwide at a vertiginous speed, leading to the declaration of COVID-19 as a pandemic by the World Health Organization (WHO) on March 11, 2020 [xxiv]. Within just five months (as of May 31, 2020), over 5.9 million cases and over 360000 deaths were globally reported to the WHO [xxv]. By the end of 2020 (as of December 27, 2020), the numbers had increased to over 79.2 million cases and 1.7 million deaths, and within the subsequent year they triplicated to 278 million cases and 5.4 million deaths (as of December 26, 2021). These numbers are even more daunting when considering non-reported deaths and pandemic-related deaths not directly caused by COVID-19. In this regard, the WHO has estimated an excess mortality of 14.8 million associated with the COVID-19 pandemic between 2020 and 2021, 2.74 times higher than the reported 5.4 million deaths [328].

Back in 2020, knowledge about the disease and its causative agent was limited. Strict measures of disease control, including lockdowns, masks, and quarantines were established to slow down the spread of COVID-19, which was bringing the healthcare system of several countries to the border of collapse [xxvi]. Science communication and scientific counseling of governments responsible for the legislation of these countermeasures played an essential role in guiding public health decisions.

[xxiii] Risk assessment: Outbreak of acute respiratory syndrome associated with a novel coronavirus, Wuhan, China; first update (January 22, 2020). Available from: https://www.ecdc.europa.eu/en/publications-data/risk-assessment-outbreak-acute-respiratory-syndrome-associated-novel-coronavirus

[xxiv] WHO Director-General's opening remarks at the media briefing on COVID-19 (March 11, 2020). Available from: https://www.who.int/director-general/speeches/detail/who-director-general-s-opening-remarks-at-the-media-briefing-on-covid-19---11-march-2020

[xxv] The situation reports and weekly epidemiological updates cited in this paragraph are available from: https://www.who.int/emergencies/diseases/novel-coronavirus-2019/situation-reports

[xxvi] Wellcome Global Monitor: How COVID-19 affected people's lives and their views about science (2020). Available from: https://wellcome.org/reports/wellcome-global-monitor-covid-19/2020

With the development of the first SARS-CoV-2 diagnostic tests, meticulous screening of the population improved disease tracking and helped identify hotspots of virus transmission. In parallel, multiple research groups shifted the focus of their studies to investigate the biology of SARS-CoV-2, the pathogenicity of COVID-19, and the dynamics of the pandemic. Furthermore, numerous scientists and clinicians joined efforts to test potential treatment options and to develop effective vaccines against COVID-19. It is in this context that our research group participated in the preclinical assessment of a vaccine candidate against COVID-19 between October and December 2020.

9.1.2 MeVac-SARS2-S(H) – A MeVac-Based Vaccine Candidate Against COVID-19

The COVID-19 vaccine candidate that C. E. Engeland and I tested is a live attenuated vaccine based on MeVac as vector platform [208]. In detail, the vaccine consists of a MeVac vector (Schwarz vaccine strain, MeV_{vac2}) encoding the spike (S) glycoprotein of SARS-CoV-2 (Wuhan-Hu-1 isolate, GenBank accession number MN908947.1) in an additional transcription unit downstream of the MeVac H coding sequence. As opposed to other MeVac-based vaccination approaches (see 9.6), the inserted transgene encodes the full-length SARS-CoV-2 S protein in its native state. This vaccine candidate is referred to as MeV_{vac2}-SARS2-S(H) and was developed in 2020 by Hörner *et al.* at Paul-Ehrlich-Institut (Langen, Germany) [329]. *In vitro* studies by Hörner *et al.* confirmed that the vaccine replicates in permissive cells, leading to the expression of functional SARS-CoV-2 S protein. Subsequent preclinical studies were conducted by the same research group in MeVac-susceptible mice ($IFNAR^{KO}$-CD46Ge mice) immunized with the vaccine (or controls) via the intraperitoneal route according to a prime-boost schedule (two doses at a four-week interval). These studies revealed that MeV_{vac2}-SARS2-S(H) induces humoral and cellular immune responses against antigens endogenous to the viral vector (MeVac) and against the SARS-CoV-2 S protein. The humoral response was characterized by induction of MeVac-specific and SARS-CoV-2 S-specific antibodies of IgG1 and IgG2a subtypes. Higher levels of IgG2a were detected as compared to IgG1, indicating induction of a T_H1-type immune response [329]. The cellular immune response was characterized by systemic induction of SARS-CoV-2 S-specific CD8(+) T cells, which secreted IFN-γ, TNF-α, and/or IL-2 upon *ex vivo* restimulation with DC2.4-SARS2-S cells (murine DCs expressing SARS-CoV-2 S). IFN-γ ELISpot assays confirmed the induction of SARS-CoV-2 S-specific and MeVac-specific cellular immunity in vaccinated mice. Cytotoxic assays demonstrated that CTLs isolated from vaccinated mice and subsequently restimulated *ex vivo* with DC2.4-SARS2-S cells specifically kill target cells expressing the SARS-CoV-2 S protein [329]. Collectively, these findings showed that the vaccine is immunogenic and triggers a MeVac-specific as well as a SARS-CoV-2 S-specific immune response, thereby providing a solid base for further research.

9.2 Aim

Following up on the results of Hörner *et al.*, the next step in vaccine development was a preclinical dose-escalation study. Thus, in collaboration with Hörner *et al.*, C. E. Engeland and I aimed at characterizing the magnitude of the SARS-CoV-2 S-specific and MeVac-specific cellular immune response induced in IFNAR^{KO}-CD46Ge mice immunized with different doses of the MeV$_{vac2}$-SARS2-S(H) vaccine. Since Hörner *et al.* employed 1x10^5 median tissue culture infectious dose (TCID$_{50}$) of the virus per injection, we tested a lower (1x10^4 TCID$_{50}$) and a higher (1x10^6 TCID$_{50}$) dose in addition to the dose employed previously (1x10^5 TCID$_{50}$).

9.3 Materials and Methods

9.3.1 Materials

This section includes the materials exclusively used in the MeV$_{vac2}$-SARS2-S(H) vaccination study. The materials used in this and additional studies are detailed in section "3 Materials and Methods". The DC2.4 cell line is included in both sections because it was obtained from different sources.

Table A1. Cell lines. **PEI:** Paul-Ehrlich-Institut; **UMass Chan:** UMass Chan Medical School.

Name	Description	Source
DC2.4 [160]	Immortalized murine dendritic cell line derived from bone marrow cells of a C57BL/6 mouse transduced with replication-defective retrovirus expressing murine GM-CSF and retrovirus encoding *myc* and *raf*.	K. Rock (UMass Chan, Worcester), M. Mühlebach (PEI, Langen)
DC2.4-SARS2-S [329]	DC2.4 cell line with stable expression of SARS-CoV-2 spike (S) protein and GFP. Generated by transduction of DC2.4 cells with a lentiviral vector encoding SARS-CoV-2 S and GFP. Transduction was followed by bulk cell sorting of GFP(+) cells and subsequent generation of clonal cell lines by limiting dilution. The clonal cell line #P3:B8 (SARS-CoV-2 S[+] GFP[+]) was employed in the present thesis. These cells present SARS-CoV-2 S-derived peptides on MHC-I molecules.	M. Mühlebach (PEI, Langen)
JAWSII [330]	Immortalized murine dendritic cell line derived from bone marrow cells of a p53-knockout C57BL/6 mouse.	M. Mühlebach (PEI, Langen)
JAWSII-SARS2-S [329]	JAWSII cell line with stable expression of SARS-CoV-2 spike (S) protein and GFP. Generated by transduction of JAWSII cells with a lentiviral vector encoding SARS-CoV-2 S and GFP. Transduction was followed by bulk cell sorting of GFP(+) cells. SARS-CoV-2 S protein expression on cultures derived from the bulk-sorted cells was confirmed. These cells present peptides derived from the SARS-CoV-2 S protein on MHC-I molecules.	M. Mühlebach (PEI, Langen)

Table A2. Recombinant measles viruses (vaccine strain). **ATU:** additional transcription unit; **CDS:** coding sequence; **PEI:** Paul-Ehrlich-Institut; **SARS-CoV-2:** severe acute respiratory syndrome coronavirus 2.

Name	Description and Source
MeV_{vac2}-SARS2-S(H) [329]	MeVac (Schwarz vaccine strain) encoding the full-length spike (S) glycoprotein of SARS-CoV-2 (Wuhan-Hu-1 isolate, GenBank accession number MN908947.1) in an ATU downstream of the H CDS. The encoded SARS-CoV-2 S protein is expressed in its native form. NCBI GenBank accession number: MW090971.1 Source: M. Mühlebach (PEI, Langen)

Table A3. Proteins.

Name	Manufacturer
Murine granulocyte-macrophage colony-stimulating factor (GM-CSF), with carrier	R&D Systems, Ref. 415-ML

Table A4. Mouse strains. **PEI:** Paul-Ehrlich-Institut; **DKFZ:** Deutsches Krebsforschungszentrum.

Strain	Description and Source
$IFNAR^{KO}$-CD46Ge [207] Also known as B6.Ifnar1^{tm1Agt} Tg(CD46)373Zbz	*Mus musculus* of C57BL/6 background, expressing an inactive form of type I interferon receptor and expressing human CD46 on all nucleated cells at levels comparable to humans. Source: M. Mühlebach (PEI, Langen)

9.3.2 Methods

9.3.2.1 Cell Culture

I conducted all cell culture procedures in class II safety cabinets as described in 3.2.1.1. DC2.4 cells and DC2.4-SARS2-S cells were cultured in RPMI-GlutaMAX™ + 10% FCS + 1% non-essential amino acids + 10 mM HEPES + 50 µM 2-mercaptoethanol. JAWSII cells and JAWSII-SARS2-S cells were cultured in α-MEM + 20% FCS + 2 mM L-glutamine + 1 mM sodium pyruvate + 5 ng/mL murine GM-CSF. All cell lines were adherent and cultured as monolayers. The cells were maintained in humidified incubators at 37 ºC and 5% CO_2 or cryopreserved as described in 3.2.1.2.

9.3.2.2 Ethics Statement and Mouse Husbandry

C. E. Engeland and I conducted the animal experiment at the Center for Preclinical Research of the German Cancer Research Center (DKFZ, Heidelberg) in compliance with the German Animal Protection Law and institutional guidelines. The experiment was approved by the Animal Protection Officer of DKFZ and by the regional council (Regierungspräsidium Karlsruhe, amendment to the protocol G-17/19). $IFNAR^{KO}$-CD46Ge mice were bred at Paul-Ehrlich-Institut (PEI, Langen) and transferred to DKFZ for the experiment. Experimental procedures were conducted in the isolator unit, where mice were housed in groups of 1 to 4 animals per cage. Mice were exposed to light / dark cycles of 12 h / 12 h and had permanent access to enrichment, food, and drinking water. Each mouse was observed at least once per day by animal caretakers or investigators.

9.3.2.3 Vaccination and Sample Collection

C. E. Engeland and I vaccinated IFNAR^{KO}-CD46Ge mice via the intraperitoneal (i.p.) route with two doses of MeV$_{vac2}$-SARS2-S(H) at a four-week interval (prime dose: day 0, boost dose: day 28). Three treatment groups were established, in which mice received 1x10^4 TCID$_{50}$, 1x10^5 TCID$_{50}$, or 1x10^6 TCID$_{50}$ virus in 200 µL D-PBS (i.p.) per dose, respectively (n = 3 mice per treatment group, either male [1x10^4 TCID$_{50}$ and 1x10^6 TCID$_{50}$ groups] or female [1x10^5 TCID$_{50}$ group]). IFNAR^{KO}-CD46Ge mice receiving 200 µL D-PBS (i.p.) without virus served as mock controls (n = 2 male mice). The virus was obtained from M. Mühlebach (PEI, Langen) and passaged at DKFZ by S. Bossow and S. Sawall. The virus suspension employed for vaccination consisted of clarified lysates from infected Vero cells. Injections were conducted using 1 mL syringes and 26 G x ½ '' needles.

Five days, 28 days (before boosting), and 64 days (before sacrifice) after the first vaccine dose, C. E. Engeland collected peripheral blood from the saphenous vein of each mouse. The blood samples, collected into capillary tubes, were stored at room temperature (RT) for a minimum of 20 min and subsequently centrifuged at 15000 rpm for 10 min using a 5424R centrifuge (Eppendorf). The sera (3 µL to 60 µL) were then stored at 4 ºC until transfer to the Institute of Virology at Marburg University (Marburg). There, C. Rohde determined the SARS-CoV-2 neutralizing antibody titers in each serum sample (data not shown).

On day 64, *i.e.,* five weeks after the second vaccine dose, I sacrificed the mice by cervical dislocation (after blood sample collection by C. E. Engeland) and resected the spleens, which were subsequently processed into single cell suspensions as described in 3.2.6.3. The splenocytes were employed in the *ex vivo* restimulation experiment described in the next paragraph.

9.3.2.4 IFN-γ Enzyme-Linked Immunosorbent spot (ELISpot) Assay

To study the SARS-CoV-2 S-specific and MeVac-specific cellular immune responses elicited by vaccination, I assessed IFN-γ secretion (via ELISpot assay) in splenocytes from vaccinated or mock-vaccinated mice restimualted *ex vivo* with MeVac antigens or murine DCs expressing the SARS-CoV-2 S protein. I conducted this assay in MultiScreen immunoprecipitation (IP) 96-well filter plates with a 0.45 µm pore size hydrophobic PVDF membrane (Merck Millipore, Ref. MAIPS4510). In detail, one day before spleen resection I activated the plate membrane with 50 µL of 35% ethanol per well (2 min, RT), washed the plate five times with 200 µL/well H_2O (see 3.2.7.6 for the washing procedure), and coated each well with 100 µL anti-mouse IFN-γ capture antibody diluted 1:200 in D-PBS (BD ELISpot, Ref. 551881, RRID: AB_2868948, Part No. 51-2525KZ). After overnight incubation at 4 ºC, I washed and blocked the plates as described in 3.2.7.6. After removing the blocking solution, I established the splenocyte cultures of interest in a total volume of 200 µL/well. The splenocytes from each mouse (5x10^5 splenocytes per well) were restimulated with murine DCs

(DC2.4 cells, DC2.4-SARS2-S cells, JAWSII cells, or JAWSII-SARS2-S cells) at a 10:1 splenocyte to DC ratio or with 10 µg/mL MeVac bulk antigen. As positive control, I exposed $5x10^5$ splenocytes to 10 µg/mL concanavalin A (ConA). As negative control, I cultured $5x10^5$ splenocytes in the absence of stimuli. All these conditions were established in technical triplicates per mouse. In addition, each ELISpot plate contained technical triplicates of the following negative controls (no splenocytes added): medium only, $5x10^4$ JAWSII-SARS2-S cells only, $5x10^4$ DC2.4-SARS2-S cells only, or $5x10^4$ DC2.4 cells only. For culture establishment, splenocytes, DCs, MeVac bulk antigen, and ConA were diluted to the required concentrations in RPMI + 10% FCS + 1% Pen/Strep. After (co-)culture incubation for 36 h at 37 ºC and 5% CO_2, IFN-γ detection was conducted as described in 3.2.7.6. For detection, I employed a biotinylated rat anti-mouse IFN-γ antibody (BD ELISpot, Ref. 551881, RRID: AB_2868948, Part No. 51-1818KA, diluted 1:250 in D-PBS). As enzyme, I employed horseradish peroxidase conjugated to streptavidin (BD ELISpot, Ref. 557630, diluted 1:100 in D-PBS + 10% FCS). As substrate, I employed TMB (Table 12). I counted the IFN-γ spots using a CTL ELISpot reader (CTL Europe) and the ImmunoSpot® software (version 7.0.24.1, CTL Europe). Quality control was conducted using the same software to remove falsely counted spots corresponding to artifacts. Saturated wells were considered too numerous to count (TNTC) and set to a spot count of 700. Statistical analysis and data plotting were conducted using the Prism software (versions 8.4.3 to 10.0.2, GraphPad). The technical controls without splenocytes are not shown in the figure (no spots were detected). Data were analyzed using one-way ANOVA per stimulus, with Tukey's correction for multiple comparisons.

9.4 Results

To test the SARS-CoV-2 S-specific and MeVac-specific cellular immune response induced by the MeV_{vac2}-SARS2-S(H) vaccine, C. E. Engeland and I immunized $IFNAR^{KO}$-CD46Ge mice with different doses of the vaccine following the prime-boost schedule shown in Figure A1 A. Five weeks after the boost dose, we resected the spleens and restimulated the splenocytes *ex vivo* with (i) murine DCs (DC2.4 cells or JAWSII cells), (ii) murine DCs expressing the SARS-CoV-2 S protein (DC2.4-SARS2-S or JAWSII-SARS2-S), or (iii) MeVac bulk antigen. Next, we conducted an IFN-γ ELISpot assay on these cultures.

The IFN-γ ELISpot assay revealed a dose-dependent response to DC2.4-SARS2-S cells (Figure A1 B,C), with significantly higher IFN-γ spot counts in cultures with splenocytes from mice receiving the high vaccine dose ($1x10^6$ $TCID_{50}$/dose) as compare to splenocytes from mice receiving the low vaccine dose ($1x10^4$ $TCID_{50}$/dose) (Figure A1 B). This response was specific to the SARS-CoV-2 S protein, since the signal detected upon splenocyte exposure to parental DC2.4 cells was within background levels. Splenocytes from all vaccinated mice reacted stronger to JAWSII-SARS2-S cells than splenocytes

from mock-treated mice (Figure A1 B). Overall, vaccinated mice showed a stronger response to JAWSII-SARS2-S cells than to parental JAWSII cells, thus supporting the notion that vaccination triggers a SARS-CoV-2 S-specific immune response (Figure A1 B-G). However, in this case, the assay was not suitable to assess a potential dose-dependent effect of the vaccine, since the response to JAWSII-SARS2-S cells was beyond the assay's upper limit of detection in 2 of 3 mice from the low dose group and in all mice from the intermediate and high dose groups (Figure A1 B, E-G).

Of note, regardless of the treatment group, each mouse showed stronger reactivity to JAWSII-SARS2-S cells than to DC2.4-SARS2-S cells (Figure A1 B, D-G). The overall stronger response to parental JAWSII cells compared to parental DC2.4 cells (Figure A1 B, D-G) might account for this observation. Unexpectedly, vaccination seemed to increase splenocyte reactivity to endogenous antigens of JAWSII cells, since the response to these cells reached assay saturation in individual mice from the $1x10^5$ $TCID_{50}$ and $1x10^6$ $TCID_{50}$ groups, while remaining within background levels in mice from the mock and $1x10^4$ $TCID_{50}$ groups (Figure A1 B). Given the low number of animals employed in this pilot study as well as the wide spectrum of responses to JAWSII cells within a treatment group (from < 100 IFN-γ spots to assay saturation), my findings remain to be re-assessed in future studies employing a larger sample size.

Regarding MeVac-specific reactivity, splenocytes from 8 of 9 vaccinated mice responded stronger to stimulation with MeVac bulk antigens than splenocytes from the two mock-vaccinated mice (Figure A1 B,C). Although the differences were statistically non-significant, these results suggest that vaccination induced a MeVac-specific immune response. However, I did not detect differences in the magnitude of the response to MeVac between mice receiving the low, intermediate, or high vaccine dose (Figure A1 B).

9.5 Conclusion

Overall, with this pilot study I conclude that the MeV_{vac2}-SARS2-S(H) vaccine induces a SARS-CoV-2 S-specific cellular immune response, which is overall stronger in mice immunized with the intermediate ($1x10^5$ $TCID_{50}$/dose) or the high ($1x10^6$ $TCID_{50}$/dose) dose of MeV_{vac2}-SARS2-S(H) as compared to mice vaccinated with the low dose ($1x10^4$ $TCID_{50}$/dose). Furthermore, vaccination induces reactivity to MeVac bulk antigens. Nevertheless, future studies with a larger number of animals per treatment group should be conducted before drawing stronger conclusions, particularly since the magnitude of the response to certain stimuli (JAWSII cells, MeVac bulk antigens) varied considerably within mice from the same treatment group.

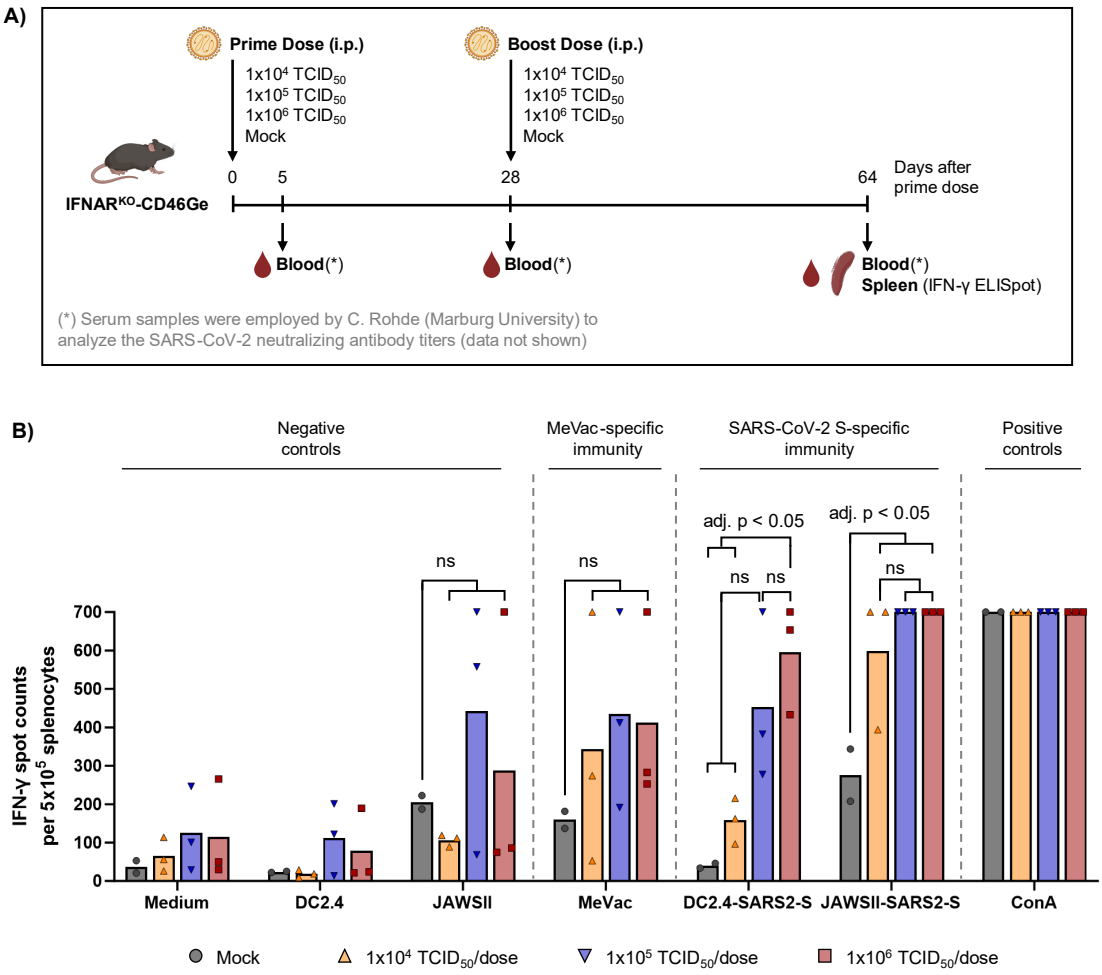

Figure A1 (continued on the next page). **MeVac-specific and SARS-CoV-2 S-specific cellular immune response after immunization with the MeV$_{vac2}$-SARS2-S(H) vaccine. (A)** Experiment schematic (created with BioRender.com). IFNAR^{KO}-CD46Ge mice (C57BL/6 background) were immunized by intraperitoneal (i.p.) injection of 1x10^4 TCID$_{50}$, 1x10^5 TCID$_{50}$, or 1x10^6 TCID$_{50}$ of MeV$_{vac2}$-SARS2-S(H) in 200 µL D-PBS on days 0 (prime dose) and 28 (boost dose). Mice receiving 200 µL D-PBS without virus were employed as mock controls. Blood was collected 5 days, 28 days (before boosting), and 64 days after the first immunization dose. Sera was analyzed in a neutralization assay conducted at Marburg University by C. Rohde (data not shown). On day 64 after the first immunization dose (*i.e.*, 5 weeks after boosting), spleens were collected. **(B-G)** 5x10^5 splenocytes were restimulated *ex vivo* with murine DCs (DC2.4 cells or JAWSII cells), murine DCs expressing the SARS-CoV-2 S protein (DC2.4-SARS2-S cells or JAWSII-SARS2-S cells), 10 µg/mL MeVac bulk antigen, or 10 µg/mL concanavalin A (ConA). Non-restimulated splenocytes ("medium" condition) were employed as negative controls. Co-cultures were established at a 10:1 splenocyte to DC ratio. After 36 h, IFN-γ ELISpot assay was conducted. Each condition was tested in technical triplicates per mouse. **(B)** IFN-γ spot counts of 2-3 mice per treatment group are shown. Saturated wells were set to 700 counts. Symbols correspond to individual mice (mean of technical triplicates). Bars show the mean value per group. Data were analyzed using one-way ANOVA per stimulus with Tukey's correction for multiple comparisons. adj. p = multiplicity-adjusted p value; n.s.: not significant. **(A-B)** I conducted the *in vivo* procedures and the IFN-γ ELISpot assay together with C. E. Engeland (see Contributions).

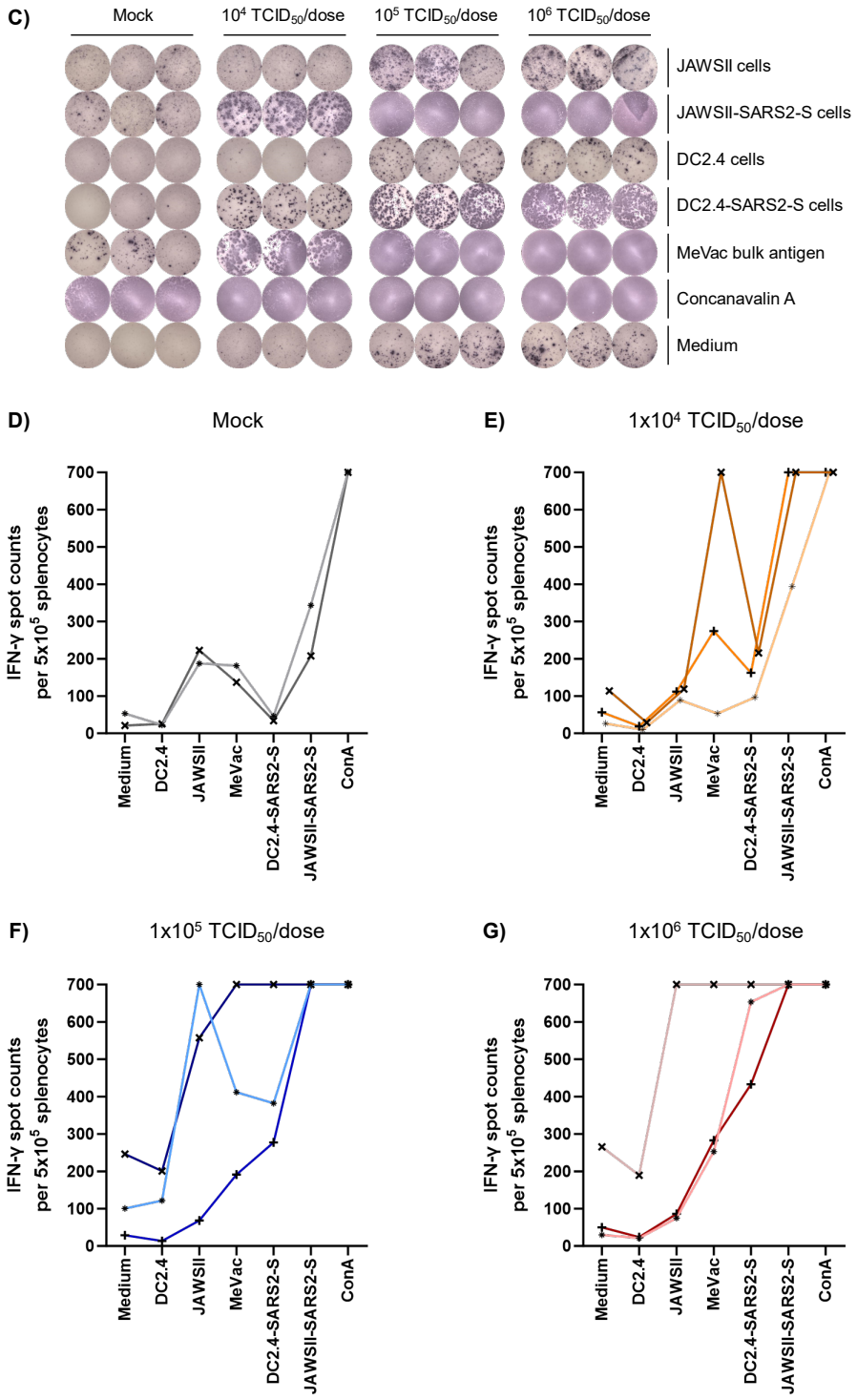

Figure A1 (continued). **MeVac-specific and SARS-CoV-2 S-specific cellular immune response after immunization with the MeV$_{vac2}$-SARS2-S(H) vaccine.** Mice were immunized as detailed in A (see previous page). IFN-γ ELISpot was conducted as described in B-G (see previous page). **(C)** IFN-γ ELISpot assay images for one representative mouse per treatment group are shown. The images correspond to the mice identified by the "x" symbol in D-G. **(D-G)** IFN-γ spot counts of 2-3 mice per treatment group are shown. Lines connect values obtained with splenocytes from the same mouse upon exposure to different stimuli. One plot is shown per treatment group. Within a plot, each mouse is identified by a different symbol. The values correspond to those shown in B. **(C-G)** I conducted the *in vivo* procedures and the IFN-γ ELISpot assay together with C. E. Engeland (see Contributions).

9.6 Discussion

At the beginning of the COVID-19 pandemic, research on MeVac-based vaccines against severe acute respiratory syndrome (SARS) and Middle East respiratory syndrome (MERS) was ongoing. These vaccines consisted of MeVac vectors encoding the S protein of the respective disease-causing agents: SARS-CoV-1 and MERS-CoV (both coronaviruses). In preclinical studies, these vaccines had proven immunogenic and conferred protection from disease [331–334]. Thus, in 2020, knowledge gained from these studies was rapidly applied to the development of vaccines against COVID-19.

Since then, several MeVac-based COVID-19 vaccines have been designed and investigated. These vaccines consist of MeVac vectors encoding different forms of the SARS-CoV-2 S protein: (1) the full-length protein in its native state (as was the case in my study) [329,335], (2) the protein in a stabilized pre-fusion state [336–339], (3) a soluble variant of the protein in a stabilized pre-fusion state [335,340,341], (4) the S1 or the S2 subunit of the protein [335,336], or (5) different lengths of the receptor-binding domain [335]. Direct comparison of several vaccine candidates in MeVac-susceptible mice and/or cotton rats has identified strategies 1, 2, and 3 as those inducing the highest levels of SARS-CoV-2-specific neutralizing antibodies as well as the strongest SARS-CoV-2 S-specific T cell-mediated immune responses [335,336]. In preclinical studies, immunization with the vaccines developed via any of these three strategies induced strong T_H1-biased immune responses against the SARS-CoV-2 S protein [335,336]. In general, these responses were characterized by higher levels of SARS-CoV-2 S-specific antibodies of IgG2a subtype compared to IgG1 subtype and by induction of T cells secreting typical T_H1 cytokines (IL-2, TNF-α, IFN-γ) upon *ex vivo* restimulation with SARS-CoV-2 S-expressing cells [329] or SARS-CoV-2 S-derived peptides [335,336]. The T_H1 nature of the response is an important finding, as it reduces the risk of vaccine-associated enhanced disease [342]. In vaccinated hamsters, high levels of SARS-CoV-2-specific neutralizing antibodies have also been detected (the cellular response has not been investigated) [329,335,336,339]. Remarkably, in two studies (both following strategy 2), the antibodies induced in vaccinated animals (either hamsters or MeVac-susceptible mice) neutralized different SARS-CoV-2 variants [336,339].

The protective capacity of several MeVac-based COVID-19 vaccines (developed following strategies 1, 2, or 3) has been assessed in vaccinated Syrian golden hamsters subsequently challenged with SARS-CoV-2. In these studies, vaccination protected hamsters from severe lung pathology upon SARS-CoV-2 challenge. Moreover, it reduced the viral genome load in lungs and nasal turbinates and decreased (in some animals to undetectable levels) the levels of infectious virus in lungs and nasal turbinates [329,335,336,339].

In parallel to these studies, a different MeVac-based COVID-19 vaccine candidate has been tested in two clinical trials (phase I and phase I/II) [337,338]. This vaccine, known as TMV-083 or V591, follows strategy 2 from those described above, *i.e.,* consists of a MeVac vector encoding the SARS-CoV-2 S protein in a stabilized pre-fusion state. To my knowledge, there are no publications on preclinical studies testing this vaccine. The clinical studies refer to preclinical research conducted with MeVac encoding the S protein of SARS-CoV-1. Overall, the results from the two clinical trials showed that TMV-083 is safe and well-tolerated. However, its immunogenicity was insufficient to support further investigation. Thus, the development of this vaccine has been discontinued.

The MeVac-based vaccine candidate employed in the clinical studies encodes a SARS-CoV-2 S protein stabilized in the pre-fusion state by the replacement of two amino acids with proline residues, among other modifications [337,338]. Recently, Zhang *et al.* found that MeVac vectors encoding soluble variants of the SARS-CoV-2 S protein (strategy 3) induce higher levels of SARS-CoV-2-specific neutralizing antibodies when the spike protein is stabilized in the pre-fusion state by six proline substitutions (preS-6P) instead of two (preS-2P) [340]. Thus, these results open the possibility to resume the clinical development of a MeVac-based COVID-19 vaccine with an optimized vaccine candidate (rMeV-preS-6P).

The continuous emergence of new SARS-CoV-2 variants hampers the induction of long-term protective immunity against COVID-19, since the new virus variants can potentially escape from the immune responses elicited by vaccination against previous variants. For instance, this was the case for the SARS-CoV-2 Omicron variant, which spread widely across individuals regardless of their COVID-19 vaccination status [343]. To protect from COVID-19 caused by different SARS-CoV-2 variants, Xu *et al.* developed a vaccine based on three vectors, each encoding the S protein of a different SARS-CoV-2 variant [341]. The three vectors derive from measles virus vaccine strains and mumps virus vaccine strains (MeVac, MuV JL1, MuV JL2). Importantly, these vaccines have demonstrated excellent safety and immunogenicity profiles across years of vaccination against measles and mumps within the MMR vaccine (which also vaccinates against rubella). In the study from Xu *et al.*, each of these vectors encoded the S protein (in a preS-6P soluble form) of a different SARS-CoV-2 variant or isolate, those being Omicron BA.1, Delta, and USA-WA1/2020. The vaccine was referred to as MMS (standing for measles virus, mumps virus, and SARS-CoV-2), and its immunogenicity was compared to that of the MeVac-based COVID-19 vaccine alone (rMeV-BA.1-preS-6P).

Importantly, this study assessed both mucosal and systemic immunity after vaccination via the intranasal route. In MeVac-susceptible mice, immunization with any of the vaccination strategies (MMS or MeVac-based vaccine alone) induced SARS-CoV-2 S-specific antibodies of IgA and IgG subtypes. The antibody response from mice immunized with the MMS vaccine showed stronger and

broader SARS-CoV-2-specific neutralizing activity compared to the MeVac-based vaccine alone. Of note, subcutaneous vaccination did not induce SARS-CoV-2 S-specific IgA responses, indicating that intranasal is the preferred route of immunization to induce mucosal immunity. Given that SARS-CoV-2 enters the host via the upper respiratory tract, mucosal immunity is crucial to limit viral spread to this region, thereby preventing severe respiratory syndrome associated with virus spread to the lower respiratory tract [344]. Regarding cellular immunity, both vaccination strategies (MMS or MeVac-based vaccine alone) induced SARS-CoV-2 S-specific T cell responses on the local (respiratory tissue) and on the systemic level. The systemic response was stronger in mice immunized with the MMS vaccine compared to the MeVac-based vaccine alone. In terms of efficacy, hamsters immunized with the MMS vaccine were completely protected from challenge with any of the three SARS-CoV-2 variants/isolates they had been immunized against (Omicron BA.1, Delta, and USA-WA1/2020) [341]. Based on these findings, the authors propose the development of an MMS vaccine that can be periodically adapted to encode the spike proteins of the three most common SARS-CoV-2 variants of concern in circulation.

An important aspect to consider when immunizing adult human individuals against a particular disease using MeVac-based vaccines is that most individuals will have pre-existing immunity to the viral vector (elicited by prior vaccination against measles). Unfortunately, this situation was not mimicked in the preclinical studies of MeVac-based COVID-19 vaccines, since those were conducted with measles-naïve animals. While most of these studies only focused on SARS-CoV-2 S-specific immune responses, two of them also assessed the immune response to the viral vector (as conducted in my study). The results revealed strong induction of MeVac-specific antibodies as well as MeVac-specific T cell responses in vaccinated mice [329,336]. Future preclinical studies in mice (or hamsters) vaccinated against measles before receiving the MeVac-based COVID-19 vaccine candidate should elucidate whether pre-existing immunity to MeVac alters the immunogenicity of the MeVac-based COVID-19 vaccine candidates, both in relation to MeVac-specific immune responses and to SARS-CoV-2 S-specific immune responses.

In this regard, results from MeVac-based vaccination studies conducted in the context of other infectious diseases can provide insightful information on the contribution of pre-existing MeVac-specific immunity to the overall immunogenicity of the vaccine. Indeed, MeVac-based vaccines are under development to protect against several diseases, particularly (but not limited to) those caused by viruses. For instance, MeVac vectors have been engineered to encode antigens from Dengue virus, hepatitis B virus (HBV), or West-Nile virus (WNV), among others [208]. In the meantime, several MeVac-based vaccine candidates are under clinical investigation for the prevention of HIV infection (NCT01320176), Zika virus infection (NCT02996890, NCT04033068), Lassa virus infection (NCT04055454), and Chikungunya virus infection. Among those, the

MeVac-based vaccine candidate against Chikungunya virus infection is the most advanced [345]. The results from phase I and phase II trials have shown that this vaccine is safe and immunogenic in humans, even in the presence of pre-existing MeVac-specific immunity [346–349]. Remarkably, these findings are in contrast with the low immunogenicity of the MeVac-based COVID-19 vaccine investigated in clinical trials (TMV-083 vaccine) [337,338]. The reasons underlying this difference remain to be elucidated. As one hypothesis, the low immunogenicity of the TMV-083 vaccine could have resulted from a suboptimal design of the heterologous antigen (SARS-CoV-2 S protein) encoded in the viral vector. Along this line, MeVac-based vaccines harboring improved antigen cassette variants (such as SARS-CoV-2 S in the preS-6P state rather than the preS-2P state [340]) might prove more immunogenic than TMV-083 in the clinical setting.

In summary, several MeVac-based COVID-19 vaccine candidates have been developed and investigated in preclinical models. One candidate has entered clinical research, but its development has been discontinued due to low immunogenicity in humans. In the meantime, millions of people have been immunized against COVID-19 with vaccines based on mRNA [350,351] or on non-replicating adenoviral vectors [352,353], which have proven efficacious against moderate to severe COVID-19 [354]. However, severe complications from vaccination have been reported in rare cases, namely myocarditis (upon administration of mRNA-based COVID-19 vaccines [355]) and thrombotic thrombocytopenia (upon administration of adenoviral vector-based COVID-19 vaccines, particularly in young women, with potentially fatal outcome [356,357]). Moreover, administration of mRNA-based vaccines to individuals living in developing countries is challenging, since the storage conditions of the vaccine (-70 ºC) are not always warranted. Thus, research on COVID-19 vaccination continues. Nowadays, studies aim at monitoring the safety profile of current vaccines, at developing novel vaccines that circumvent current limitations, and at adapting vaccines to new SARS-CoV-2 variants of concern. In this regard, MeVac vaccines have been very successful and therefore MeVac-based vaccines stand as promising candidates: they offer the advantage of an excellent safety profile associated to the viral vector (as extensively reported throughout decades of measles vaccination [108,198]), can be stored at 2 ºC to 8 ºC (thus facilitating vaccine distribution as compared to mRNA-based vaccines), and can be engineered via a reverse genetics system (thereby adapting the vaccine to the SARS-CoV-2 variants of concern in circulation at the time of vaccination).

Earlier this year (on May 5, 2023), the WHO announced that the COVID-19 pandemic no longer fits the definition of Public Health Emergency of International Concern (PHEIC)[xxvii]. This indicates that the emergency situation caused by the pandemic is considered to be over. While these are positive news, the WHO emphasizes that the pandemic itself is still ongoing. Therefore, at present, strategies for the long-term management of the COVID-19 pandemic, including vaccination policies, are under deliberation. While the unfolding of this pandemic remains uncertain, the lessons learned in the past three years, together with the extensive knowledge gained on the scientific and social levels, has hopefully prepared us for an effective global response shall new variants of concern arise.

[xxvii] *Statement on the fifteenth meeting of the IHR (2005) Emergency Committee on the COVID-19 pandemic* (May 5, 2023). Available from: https://www.who.int/news/

Bibliography

1. Hanahan, D. Hallmarks of cancer: New dimensions. *Cancer Discov* **12**, 31–46 (2022).

2. Sung, H. *et al.* Global cancer statistics 2020: GLOBOCAN estimates of incidence and mortality worldwide for 36 cancers in 185 countries. *CA Cancer J Clin* **71**, 209–249 (2021).

3. Dunn, G. P., Bruce, A. T., Ikeda, H., Old, L. J. & Schreiber, R. D. Cancer immunoediting: from immuno-surveillance to tumor escape. *Nat Immunol* **3**, 991–998 (2002).

4. Wolf, N. K., Kissiov, D. U. & Raulet, D. H. Roles of natural killer cells in immunity to cancer, and applications to immunotherapy. *Nat Rev Immunol* **23**, 90–105 (2023).

5. Raskov, H., Orhan, A., Christensen, J. P. & Gögenur, I. Cytotoxic CD8+ T cells in cancer and cancer immunotherapy. *Br J Cancer* **124**, 359–367 (2021).

6. Chen, D. S. & Mellman, I. Oncology meets immunology: The cancer-immunity cycle. *Immunity* **39**, 1–10 (2013).

7. Mellman, I., Chen, D. S., Powles, T. & Turley, S. J. The cancer-immunity cycle: Indication, genotype, and immunotype. *Immunity* **56**, 2188–2205 (2023).

8. Joffre, O. P., Segura, E., Savina, A. & Amigorena, S. Cross-presentation by dendritic cells. *Nat Rev Immunol* **12**, 557–569 (2012).

9. Kurts, C., Robinson, B. W. S. & Knolle, P. A. Cross-priming in health and disease. *Nat Rev Immunol* **10**, 403–414 (2010).

10. Liu, J., Zhang, X., Cheng, Y. & Cao, X. Dendritic cell migration in inflammation and immunity. *Cell Mol Immunol* **18**, 2461–2471 (2021).

11. Curtsinger, J. M. & Mescher, M. F. Inflammatory cytokines as a third signal for T cell activation. *Curr Opin Immunol* **22**, 333–340 (2010).

12. Nagarsheth, N., Wicha, M. S. & Zou, W. Chemokines in the cancer microenvironment and their relevance in cancer immunotherapy. *Nat Rev Immunol* **17**, 559–572 (2017).

13. Andersen, M. H., Schrama, D. & Becker, J. C. Cytotoxic T cells. *Journal of Investigative Dermatology* **126**, 32–41 (2006).

14. Tuomela, K., Ambrose, A. R. & Davis, D. M. Escaping death: How cancer cells and infected cells resist cell-mediated cytotoxicity. *Front Immunol* **13**, 867098 (2022).

15. Masson, D. & Tschopp, J. Isolation of a lytic, pore-forming protein (perforin) from cytolytic T-lymphocytes. *Journal of Biological Chemistry* **260**, 9069–9072 (1985).

16. Wohlleber, D. *et al.* TNF-Induced target cell killing by CTL activated through cross-presentation. *Cell Rep* **2**, 478–487 (2012).

17. Browning, J. L. *et al.* Signaling through the lymphotoxin beta receptor induces the death of some adenocarcinoma tumor lines. *Journal of Experimental Medicine* **183**, 867–878 (1996).

18. Rooney, I. A. *et al.* The lymphotoxin-β receptor is necessary and sufficient for LIGHT-mediated apoptosis of tumor cells. *Journal of Biological Chemistry* **275**, 14307–14315 (2000).

19. Gocher, A. M., Workman, C. J. & Vignali, D. A. A. Interferon-γ: Teammate or opponent in the tumour microenvironment? *Nat Rev Immunol* **22**, 158–172 (2022).

20. Hanahan, D. & Weinberg, R. A. Hallmarks of cancer: The next generation. *Cell* **144**, 646–674 (2011).

21. Schreiber, R. D., Old, L. J. & Smyth, M. J. Cancer immunoediting: integrating immunity's roles in cancer suppression and promotion. *Science (1979)* **331**, 1565–1570 (2011).

22. Junttila, M. R. & De Sauvage, F. J. Influence of tumour micro-environment heterogeneity on therapeutic response. *Nature* **501**, 346–354 (2013).

23. Chen, D. S. & Mellman, I. Elements of cancer immunity and the cancer-immune set point. *Nature* **541**, 321–330 (2017).

24. Binnewies, M. *et al.* Understanding the tumor immune microenvironment (TIME) for effective therapy. *Nat Med* **24**, 541–550 (2018).

25. Tie, Y., Tang, F., Wei, Y.-Q. & Wei, X.-W. Immunosuppressive cells in cancer: Mechanisms and potential therapeutic targets. *J Hematol Oncol* **15**, 61 (2022).

26. Groth, C. *et al.* Immunosuppression mediated by myeloid-derived suppressor cells (MDSCs) during tumour progression. *Br J Cancer* **120**, 16–25 (2019).

27. Chen, L. & Flies, D. B. Molecular mechanisms of T cell co-stimulation and co-inhibition. *Nat Rev Immunol* **13**, 227–242 (2013).

28. Waldman, A. D., Fritz, J. M. & Lenardo, M. J. A guide to cancer immunotherapy: from T cell basic science to clinical practice. *Nat Rev Immunol* **20**, 651–668 (2020).

29. Liu, C., Yang, M., Zhang, D., Chen, M. & Zhu, D. Clinical cancer immunotherapy: Current progress and prospects. *Front Immunol* **13**, 961805 (2022).

30. Propper, D. J. & Balkwill, F. R. Harnessing cytokines and chemokines for cancer therapy. *Nat Rev Clin Oncol* **19**, 237–253 (2022).

31. Weiner, G. J. Building better monoclonal antibody-based therapeutics. *Nat Rev Cancer* **15**, 361–370 (2015).

32. Kirtane, K., Elmariah, H., Chung, C. H. & Abate-Daga, D. Adoptive cellular therapy in solid tumor malignancies: Review of the literature and challenges ahead. *J Immunother Cancer* **9**, e002723 (2021).

33. Laskowski, T. J., Biederstädt, A. & Rezvani, K. Natural killer cells in antitumour adoptive cell immunotherapy. *Nat Rev Cancer* **22**, 557–575 (2022).

34. Saxena, M., van der Burg, S. H., Melief, C. J. M. & Bhardwaj, N. Therapeutic cancer vaccines. *Nat Rev Cancer* **21**, 360–378 (2021).

35. Lin, D., Shen, Y. & Liang, T. Oncolytic virotherapy: basic principles, recent advances and future directions. *Signal Transduct Target Ther* **8**, 156 (2023).

36. Kantoff, P. W. *et al.* Sipuleucel-T immunotherapy for castration-resistant prostate cancer. *New England Journal of Medicine* **363**, 411–422 (2010).

37. Hodi, F. S. *et al.* Improved survival with Ipilimumab in patients with metastatic melanoma. *New England Journal of Medicine* **363**, 711–723 (2010).

38. Andtbacka, R. H. I. *et al.* Talimogene laherparepvec improves durable response rate in patients with advanced melanoma. *Journal of Clinical Oncology* **33**, 2780–2788 (2015).

39. Maude, S. L. *et al.* Tisagenlecleucel in children and young adults with B-Cell lymphoblastic leukemia. *New England Journal of Medicine* **378**, 439–448 (2018).

40. Huang, P. W. & Chang, J. W. C. Immune checkpoint inhibitors win the 2018 Nobel Prize. *Biomed J* **42**, 299–306 (2019).

41. Maloney, D. G. *et al.* IDEC-C2B8: Results of a Phase I Multiple-Dose Trial in Patients With Relapsed Non-Hodgkin's Lymphoma. *J Clin Oncol* **15**, 3266–3274 (1997).

42. Topp, M. S. *et al.* Targeted therapy with the T-cell-engaging antibody blinatumomab of chemotherapy-refractory minimal residual disease in B-lineage acute lymphoblastic leukemia patients results in high response rate and prolonged leukemia-free survival. *Journal of Clinical Oncology* **29**, 2493–2498 (2011).

43. Hiraga, J. *et al.* Down-regulation of CD20 expression in B-cell lymphoma cells after treatment with rituximab-containing combination chemotherapies: its prevalence and clinical significance. *Blood* **113**, 4885–4893 (2009).

44. Choi, Y. *et al.* T-cell agonists in cancer immunotherapy. *J Immunother Cancer* **8**, e000966 (2020).

45. Morad, G., Helmink, B. A., Sharma, P. & Wargo, J. A. Hallmarks of response, resistance, and toxicity to immune checkpoint blockade. *Cell* **184**, 5309–5337 (2021).

46. Tawbi, H. A. *et al.* Relatlimab and Nivolumab versus Nivolumab in untreated advanced melanoma. *New England Journal of Medicine* **386**, 24–34 (2022).

47. Mirza, M. R. *et al.* Dostarlimab for primary advanced or recurrent endometrial cancer. *New England Journal of Medicine* **388**, 2145–2158 (2023).

48. Robert, C. *et al.* Pembrolizumab versus Ipilimumab in advanced melanoma. *New England Journal of Medicine* **372**, 2521–2532 (2015).

49. Herbst, R. S. *et al.* Pembrolizumab versus docetaxel for previously treated, PD-L1-positive, advanced non-small-cell lung cancer (KEYNOTE-010): A randomised controlled trial. *The Lancet* **387**, 1540–1550 (2016).

50. Bachmann, M. The UniCAR system: A modular CAR T cell approach to improve the safety of CAR T cells. *Immunol Lett* **211**, 13–22 (2019).

51. Feldmann, A. *et al.* Versatile chimeric antigen receptor platform for controllable and combinatorial T cell therapy. *Oncoimmunology* **9**, 1785608 (2020).

52. Zheng, L. *et al.* Vaccine-induced intratumoral lymphoid aggregates correlate with survival following treatment with a neoadjuvant and adjuvant vaccine in patients with resectable pancreatic adenocarcinoma. *Clinical Cancer Research* **27**, 1278–1286 (2021).

53. Biavati, L. *et al.* An allogeneic multiple myeloma GM-CSF-secreting vaccine with lenalidomide induces long-term immunity and durable clinical responses in patients in near complete remission. *Clinical Cancer Research* **27**, 6696–6708 (2021).

54. Keam, S., Gill, S., Ebert, M. A., Nowak, A. K. & Cook, A. M. Enhancing the efficacy of immunotherapy using radiotherapy. *Clin Transl Immunology* **9**, e1169 (2020).

55. Fumet, J. D., Limagne, E., Thibaudin, M. & Ghiringhelli, F. Immunogenic cell death and elimination of immunosuppressive cells: A double-edged sword of chemotherapy. *Cancers (Basel)* **12**, 1–13 (2020).

56. Bierman, H. R. *et al.* Remissions in leukemia of childhood following acute infectious disease. Staphylococcus and streptococcus, varicella, and feline panleukopenias. *Cancer* **6**, 591–605 (1953).

57. Kelly, E. & Russell, S. J. History of oncolytic viruses: genesis to genetic engineering. *Molecular Therapy* **15**, 651–659 (2007).

58. Gao, J., Zheng, Q., Xin, N., Wang, W. & Zhao, C. CD155, an onco-immunologic molecule in human tumors. *Cancer Sci* **108**, 1934–1938 (2017).

59. von Locquenghien, M., Rozalén, C. & Celià-Terrassa, T. Interferons in cancer immunoediting: Sculpting metastasis and immunotherapy response. *Journal of Clinical Investigation* **131**, e143296 (2021).

60. Stojdl, D. F. *et al.* Exploiting tumor-specific defects in the interferon pathway with a previously unknown oncolytic virus. *Nat Med* **6**, 821–825 (2000).

61. Martuza, R. L., Malick, A., Markertt, J. M., Ruffner, K. L. & Coen, D. M. Experimental therapy of human glioma by means of a genetically engineered virus mutant. *Science (1979)* **252**, 854–856 (1991).

62. Fueyo, J. *et al.* A mutant oncolytic adenovirus targeting the Rb pathway produces anti-glioma effect in vivo. *Oncogene* **19**, 2–12 (2000).

63. Yaiw, K. C. *et al.* CD20-targeted measles virus shows high oncolytic specificity in clinical samples from lymphoma patients independent of prior rituximab therapy. *Gene Ther* **18**, 313–317 (2011).

64. Lanson, N. A., Friedlander, P. L., Schwarzenberger, P., Kolls, J. K. & Wang, G. Replication of an adenoviral vector controlled by the human telomerase reverse transcriptase promoter causes tumor-selective tumor lysis. *Cancer Res* **63**, 7936–7941 (2003).

65. Lee, C. Y. F., Rennie, P. S. & Jia, W. W. G. MicroRNA regulation of oncolytic herpes simplex virus-1 for selective killing of prostate cancer cells. *Clinical Cancer Research* **15**, 5126–5135 (2009).

66. Lichty, B. D., Breitbach, C. J., Stojdl, D. F. & Bell, J. C. Going viral with cancer immunotherapy. *Nat Rev Cancer* **14**, 559–567 (2014).

67. Palanivelu, L., Liu, C. H. & Lin, L. T. Immunogenic cell death: The cornerstone of oncolytic viro-immunotherapy. *Front Immunol* **13**, 1038226 (2023).

68. Russell, S. J. & Barber, G. N. Oncolytic viruses as antigen-agnostic cancer vaccines. *Cancer Cell* **33**, 599–605 (2018).

69. Andtbacka, R. H. I. *et al.* Patterns of clinical response with Talimogene Laherparepvec (T-VEC) in patients with melanoma treated in the OPTiM phase III clinical trial. *Ann Surg Oncol* **23**, 4169–4177 (2016).

70. Mealiea, D. & McCart, J. A. Cutting both ways: the innate immune response to oncolytic virotherapy. *Cancer Gene Ther* **29**, 629–646 (2022).

71. Gujar, S., Pol, J. G., Kim, Y., Lee, P. W. & Kroemer, G. Antitumor benefits of antiviral immunity: An underappreciated aspect of oncolytic virotherapies. *Trends Immunol* **39**, 209–221 (2018).

72. Rivadeneira, D. B. *et al.* Oncolytic viruses engineered to enforce leptin expression reprogram tumor-Infiltrating T cell metabolism and promote tumor clearance. *Immunity* **51**, 548-560.e4 (2019).

73. Guedan, S. *et al.* Hyaluronidase expression by an oncolytic adenovirus enhances its intratumoral spread and suppresses tumor growth. *Molecular Therapy* **18**, 1275–1283 (2010).

74. Garber, K. China approves world's first oncolytic virus therapy for cancer treatment. *J Natl Cancer Inst* **98**, 298–300 (2006).

75. Liu, B. L. *et al.* ICP34.5 deleted herpes simplex virus with enhanced oncolytic, immune stimulating, and anti-tumour properties. *Gene Ther* **10**, 292–303 (2003).

76. Chesney, J. A. *et al.* Randomized, double-blind, placebo-controlled, global phase III trial of Talimogene Laherparepvec combined with Pembrolizumab for advanced melanoma. *Journal of Clinical Oncology* **41**, 528–540 (2023).

77. Todo, T., Ino, Y., Ohtsu, H., Shibahara, J. & Tanaka, M. A phase I/II study of triple-mutated oncolytic herpes virus G47Δ in patients with progressive glioblastoma. *Nat Commun* **13**, 4119 (2022).

78. Todo, T. *et al.* Intratumoral oncolytic herpes virus G47Δ for residual or recurrent glioblastoma: a phase 2 trial. *Nat Med* **28**, 1630–1639 (2022).

79. Frampton, J. E. Teserpaturev/G47Δ: First approval. *BioDrugs* **36**, 667–672 (2022).

80. Laksono, B. M., de Vries, R. D., Duprex, W. P. & de Swart, R. L. Measles pathogenesis, immune suppression and animal models. *Curr Opin Virol* **41**, 31–37 (2020).

81. Mina, M. J. *et al.* Long-term measles-induced immunomodulation increases overall childhood infectious disease mortality. *Science (1979)* **348**, 694–699 (2015).

82. Griffin, D. E. Measles virus persistence and its consequences. *Curr Opin Virol* **41**, 46–51 (2020).

83. Griffin, D. E. Measles vaccine. *Viral Immunol* **31**, 86–95 (2018).

84. Dowling, P. C. *et al.* Transcriptional map of the measles virus genome. *Journal of General Virology* **67**, 1987–1992 (1986).

85. Hall, W. W. & Martin, S. J. Purification and characterization of measles virus. *Journal of General Virology* **19**, 175–188 (1973).

86. Bellini, W. J., Englund, G., Rozenblatt, S., Arnheiter, H. & Richardson, C. D. Measles virus P gene codes for two proteins. *J Virol* **53**, 908–919 (1985).

87. Cattaneo, R., Kaelin, K., Baczko, K. & Billeter', M. A. Measles virus editing provides an additional cysteine-rich protein. *Cell* **56**, 759–764 (1989).

88. Parks, C. L. *et al.* Analysis of the noncoding regions of measles virus strains in the Edmonston vaccine lineage. *J Virol* **75**, 921–933 (2001).

89. Ruigrok, R. W. H., Crépin, T. & Kolakofsky, D. Nucleoproteins and nucleocapsids of negative-strand RNA viruses. *Curr Opin Microbiol* **14**, 504–510 (2011).

90. Kolakofsky, D. *et al.* Paramyxovirus RNA synthesis and the requirement for hexamer genome length: the rule of six revisited. *J Virol* **72**, 891–899 (1998).

91. Cox, R. & Plemper, R. K. The paramyxovirus polymerase complex as a target for next-generation anti-paramyxovirus therapeutics. *Front Microbiol* **6**, 459 (2015).

92. Brindley, M. A. & Plemper, R. K. Blue native PAGE and biomolecular complementation reveal a tetrameric or higher-order oligomer organization of the physiological measles virus attachment protein H. *J Virol* **84**, 12174–12184 (2010).

93. Plemper, R. K., Hammond, A. L. & Cattaneo, R. Measles virus envelope glycoproteins hetero-oligomerize in the endoplasmic reticulum. *Journal of Biological Chemistry* **276**, 44239–44246 (2001).

94. Iwasaki, M. *et al.* The matrix protein of measles virus regulates viral RNA synthesis and assembly by interacting with the nucleocapsid protein. *J Virol* **83**, 10374–10383 (2009).

95. Sviben, D. *et al.* Mass spectrometry-based investigation of measles and mumps virus proteome. *Virol J* **15**, 160 (2018).

96. Mühlebach, M. D. *et al.* Adherens junction protein nectin-4 is the epithelial receptor for measles virus. *Nature* **480**, 530–533 (2011).

97. Noyce, R. S. *et al.* Tumor cell marker PVRL4 (nectin 4) is an epithelial cell receptor for measles virus. *PLoS Pathog* **7**, e1002240 (2011).

98. Tatsuo, H., Ono, N., Tanaka, K. & Yanagi, Y. SLAM (CDw150) is a cellular receptor for measles virus. *Nature* **406**, 893–897 (2000).

99. Dörig, R. E., Marcil, A., Chopra, A. & Richardson, C. D. The human CD46 molecule is a receptor for measles virus (Edmonston strain). *Cell* **75**, 295–305 (1993).

100. de Witte, L., Abt, M., Schneider-Schaulies, S., van Kooyk, Y. & Geijtenbeek, T. B. H. Measles virus targets DC-SIGN to enhance dendritic cell infection. *J Virol* **80**, 3477–3486 (2006).

101. Plattet, P., Alves, L., Herren, M. & Aguilar, H. C. Measles virus fusion protein: Structure, function and inhibition. *Viruses* **8**, 112 (2016).

102. Cattaneo, R., Rebmann, G., Baczko, K., Ter Meulen, V. & Billeter, M. A. Altered ratios of measles virus transcripts in diseased human brains. *Virology* **160**, 523–526 (1987).

103. Wild, T. F., Malvoisin, E. & Buckland, R. Measles virus: both the haemagglutinin and fusion glycoproteins are required for fusion. *Journal of General Virology* **72**, 439–442 (1991).

104. Fontana, J. M., Bankamp, B. & Rota, P. A. Inhibition of interferon induction and signaling by paramyxoviruses. *Immunol Rev* **225**, 46–67 (2008).

105. Enders, J. F. & Peebles, T. C. Propagation in tissue cultures of cytopathogenic agents from patients with measles. *Proc Soc Exp Biol Med* **86**, 277–286 (1954).

106. Bankamp, B., Hodge, G., McChesney, M. B., Bellini, W. J. & Rota, P. A. Genetic changes that affect the virulence of measles virus in a rhesus macaque model. *Virology* **373**, 39–50 (2008).

107. Bankamp, B., Takeda, M., Zhang, Y., Xu, W. & Rota, P. A. Genetic characterization of measles vaccine strains. *J Infect Dis* **204**, S533–S548 (2011).

108. Minta, A. A. *et al.* Morbidity and mortality weekly report progress toward regional measles elimination-worldwide, 2000-2021. *MMWR Morb Mortal Wkly Rep* **71**, 1489–1495 (2022).

109. Bluming, A. Z. & Ziegler, J. L. Regression of Burkitt's lymphoma in association with measles infection. *Lancet* **2**, 105–106 (1971).

110. Gross, S. Measles and leukaemia. *Lancet* **1**, 397–398 (1971).

111. Mota, H. C. Infantile Hodgkin's disease: remission after measles. *Br Med J* **2**, 421 (1973).

112. Engeland, C. E. & Ungerechts, G. Measles virus as an oncolytic immunotherapy. *Cancers (Basel)* **13**, 1–19 (2021).

113. Zuniga, A. *et al.* Attenuated measles virus as a vaccine vector. *Vaccine* **25**, 2974–2983 (2007).

114. Radecke, F. *et al.* Rescue of measles viruses from cloned DNA. *EMBO J* **14**, 5773–5784 (1995).

115. Martin, A., Staeheli, P. & Schneider, U. RNA polymerase II-controlled expression of antigenomic RNA enhances the rescue efficacies of two different members of the mononegavirales independently of the site of viral genome replication. *J Virol* **80**, 5708–5715 (2006).

116. Anderson, B. D., Nakamura, T., Russell, S. J. & Peng, K. W. High CD46 receptor density determines preferential killing of tumor cells by oncolytic measles virus. *Cancer Res* **64**, 4919–4926 (2004).

117. Peng, K. W. *et al.* Intraperitoneal therapy of ovarian cancer using an engineered measles virus. *Cancer Res* **62**, 4656–4662 (2002).

118. Phuong, L. K. *et al.* Use of a vaccine strain of measles virus genetically engineered to produce carcinoembryonic antigen as a novel therapeutic agent against glioblastoma multiforme. *Cancer Res* **63**, 2462–2469 (2003).

119. Blechacz, B. *et al.* Engineered measles virus as a novel oncolytic viral therapy system for hepatocellular carcinoma. *Hepatology* **44**, 1465–1477 (2006).

120. Achard, C. *et al.* Sensitivity of human pleural mesothelioma to oncolytic measles virus depends on defects of the type I interferon response. *Oncotarget* **6**, 44892–44904 (2015).

121. Kurokawa, C. *et al.* Constitutive interferon pathway activation in tumors as an efficacy determinant following oncolytic virotherapy. *J Natl Cancer Inst* **110**, 1123–1132 (2018).

122. Delaunay, T. *et al.* Frequent homozygous deletions of type I interferon genes in pleural mesothelioma confer sensitivity to oncolytic measles virus. *Journal of Thoracic Oncology* **15**, 827–842 (2020).

123. Pidelaserra-Martí, G. & Engeland, C. E. Mechanisms of measles virus oncolytic immunotherapy. *Cytokine Growth Factor Rev* **56**, 28–38 (2020).

124. Ayasoufi, K. & Pfaller, C. K. Seek and hide: the manipulating interplay of measles virus with the innate immune system. *Curr Opin Virol* **41**, 18–30 (2020).

125. Gauvrit, A. *et al.* Measles virus induces oncolysis of mesothelioma cells and allows dendritic cells to cross-prime tumor-specific CD8 response. *Cancer Res* **68**, 4882–4892 (2008).

126. Rajaraman, S. *et al.* Measles virus-based treatments trigger a pro-inflammatory cascade and a distinctive immunopeptidome in glioblastoma. *Mol Ther Oncolytics* **12**, 147–161 (2018).

127. Chen, A. *et al.* Oncolytic measles virus enhances antitumour responses of adoptive CD8+NKG2D+ cells in hepatocellular carcinoma treatment. *Sci Rep* **7**, 5170 (2017).

128. Donnelly, O. G. *et al.* Measles virus causes immunogenic cell death in human melanoma. *Gene Ther* **20**, 7–15 (2013).

129. Galluzzi, L., Buqué, A., Kepp, O., Zitvogel, L. & Kroemer, G. Immunogenic cell death in cancer and infectious disease. *Nat Rev Immunol* **17**, 97–111 (2017).

130. Guillerme, J. B. *et al.* Measles virus vaccine-infected tumor cells induce tumor antigen cross-presentation by human plasmacytoid dendritic cells. *Clinical Cancer Research* **19**, 1147–1158 (2013).

131. Fonteneau, J. F., Guillerme, J. B., Tangy, F. & Grégoire, M. Attenuated measles virus used as an oncolytic virus activates myeloid and plasmacytoid dendritic cells. *Oncoimmunology* **2**, e24212 (2013).

132. Achard, C. *et al.* Oncolytic measles virus induces tumor necrosis factor-related apoptosis-inducing ligand (TRAIL)-mediated cytotoxicity by human myeloid and plasmacytoid dendritic cells. *Oncoimmunology* **6**, e1261240 (2016).

133. Grossardt, C. *et al.* Granulocyte-macrophage colony-stimulating factor-armed oncolytic measles virus is an effective therapeutic cancer vaccine. *Hum Gene Ther* **24**, 644–654 (2013).

134. Engeland, C. E. *et al.* CTLA-4 and PD-L1 checkpoint blockade enhances oncolytic measles virus therapy. *Molecular Therapy* **22**, 1949–1959 (2014).

135. Veinalde, R. *et al.* Oncolytic measles virus encoding interleukin-12 mediates potent antitumor effects through T cell activation. *Oncoimmunology* **6**, e1285992 (2017).

136. Grote, D., Cattaneo, R. & Fielding, A. K. Neutrophils contribute to the measles virus-induced antitumor effect : enhancement by granulocyte macrophage colony-stimulating factor expression. *Cancer Res* **63**, 6463–6468 (2003).

137. Li, H., Peng, K. W., Dingli, D., Kratzke, R. A. & Russell, S. J. Oncolytic measles viruses encoding interferon B and the thyroidal sodium iodide symporter gene for mesothelioma virotherapy. *Cancer Gene Ther* **17**, 550–558 (2010).

138. Zhang, Y. *et al.* Attenuated, oncolytic, but not wild-type measles virus infection has pleiotropic effects on human neutrophil function. *The Journal of Immunology* **188**, 1002–1010 (2012).

139. Tan, D. Q. *et al.* Macrophage response to oncolytic paramyxoviruses potentiates virus-mediated tumor cell killing. *Eur J Immunol* **46**, 919–928 (2016).

140. Hutzler, S. *et al.* Antigen-specific oncolytic MV-based tumor vaccines through presentation of selected tumor-associated antigens on infected cells or virus-like particles. *Sci Rep* **7**, 16892 (2017).

141. Iankov, I. D., Haralambieva, I. H. & Galanis, E. Immunogenicity of attenuated measles virus engineered to express helicobacter pylori neutrophil-activating protein. *Vaccine* **29**, 1710–1720 (2011).

142. Speck, T. *et al.* Targeted BiTE expression by an oncolytic vector augments therapeutic efficacy against solid tumors. *Clinical Cancer Research* **24**, 2128–2137 (2018).

143. Dey, A. *et al.* The role of neutrophils in measles virus-mediated oncolysis differs between B-cell malignancies and is not always enhanced by GCSF. *Molecular Therapy* **24**, 184–192 (2016).

144. Backhaus, P. S. *et al.* Immunological effects and viral gene expression determine the efficacy of oncolytic measles vaccines encoding IL-12 or IL-15 agonists. *Viruses* **11**, 914 (2019).

145. Veinalde, R. Unraveling determinants of efficacy in measles immunovirotherapy. PhD thesis. (Ruperto-Carola University of Heidelberg, 2017).

146. Engeland, C. E. Immune checkpoint modulation enhances oncolytic virotherapy. PhD thesis. (Ruperto-Carola University of Heidelberg, 2014).

147. Hardcastle, J. *et al.* Immunovirotherapy with measles virus strains in combination with anti-PD-1 antibody blockade enhances antitumor activity in glioblastoma treatment. *Neuro Oncol* **19**, 493–502 (2017).

148. Leber, M. F. *et al.* Engineering and combining oncolytic measles virus for cancer therapy. *Cytokine Growth Factor Rev* **56**, 39–48 (2020).

149. Msaouel, P. *et al.* Clinical trials with oncolytic measles virus: current status and future prospects. *Curr Cancer Drug Targets* **18**, 177–187 (2018).

150. Veinalde, R. *et al.* Oncolytic measles vaccines encoding PD-1 and PD-L1 checkpoint blocking antibodies to increase tumor-specific T cell memory. *Mol Ther Oncolytics* **24**, 43–58 (2021).

151. Weiland, T. *et al.* Enhanced killing of therapy-induced senescent tumor cells by oncolytic measles vaccine viruses. *Int J Cancer* **134**, 235–243 (2014).

152. Bozza, M. *et al.* Novel non-integrating DNA Nano-S/MAR vectors restore gene function in isogenic patient-derived pancreatic tumor models. *Mol Ther Methods Clin Dev* **17**, 957–968 (2020).

153. Bozza, M. *et al.* A nonviral, nonintegrating DNA nanovector platform for the safe, rapid, and persistent manufacture of recombinant T cells. *Sci. Adv* **7**, 1333–1347 (2021).

154. Busch, E. *et al.* Measles vaccines designed for enhanced CD8+ T cell activation. *Viruses* **12**, 242 (2020).

155. Kubon, K. D. Personalized oncolytic vaccination: Tumor antigen encoding measles viruses for malignant melanoma. MD thesis. (Ruperto-Carola University of Heidelberg, 2020).

156. Singh, M. & Billeter, M. A. A recombinant measles virus expressing biologically active human interleukin-12. *Journal of General Virology* **80**, 101–106 (1999).

157. Dingli, D. *et al.* Image-guided radiovirotherapy for multiple myeloma using a recombinant measles virus expressing the thyroidal sodium iodide symporter. *Blood* **103**, 1641–1646 (2004).

158. Fidler, I. J. Selection of successive tumour lines for metastasis. *Nat New Biol* **242**, 148–149 (1973).

159. Grossardt, C. Engineering targeted and cytokine-armed oncolytic measles viruses. PhD thesis. (Ruperto-Carola University of Heidelberg, 2013).

160. Shen, Z., Reznikoff, G., Dranoff, G. & Rock, K. L. Cloned dendritic cells can present exogenous antigens on both MHC class I and class II molecules. *Journal of Immunology* **158**, 2723–2730 (1997).

161. Moore, M. W., Carbone, F. R. & Bevan, M. J. Introduction of Soluble Protein into the Class I Pathway of Antigen Processing and Presentation. *Cell* **54**, 777–785 (1988).

162. Gorer, P. A. Studies in antibody response of mice to tumour inoculation. *Br J Cancer* **4**, 372–379 (1950).

163. Roy, I. *et al.* Pancreatic cancer cell migration and metastasis is regulated by chemokine-biased agonism and bioenergetic signaling. *Cancer Res* **75**, 3529–3542 (2015).

164. Hingorani, S. R. *et al.* Trp53R172H and KrasG12D cooperate to promote chromosomal instability and widely metastatic pancreatic ductal adenocarcinoma in mice. *Cancer Cell* **7**, 469–483 (2005).

165. Veinalde, R. *et al.* Virotherapy combined with anti-PD-1 transiently reshapes the tumor immune environment and induces anti-tumor immunity in a preclinical PDAC model. *Front Immunol* **13**, 1096162 (2023).

166. Sanford, K. K., Earle, W. R. & Likely G D. The growth in vitro of single isolated tissue cells. *J Natl Cancer Inst* **9**, 229–246 (1948).

167. Earle, W. R. *et al.* Production of malignancy in vitro. IV. The mouse fibroblast cultures and changes seen in the living cells. *J Natl Cancer Inst* **4**, 165–212 (1943).

168. Tan, M. H., Holyoke, E. D. & Goldrosen, M. H. Murine colon adenocarcinomas: methods for selective culture in vitro. *J Natl Cancer Inst* **56**, 871–873 (1976).

169. Corbett, T. H., Griswold Jr, D. P., Roberts, B. J., Peckham, J. C. & Schabel Jr, F. M. Tumor induction relationships in development of transplantable cancers of the colon in mice for chemotherapy assays, with a note on carcinogen structure. *Cancer Res* **35**, 2434–2439 (1975).

170. Robbins, P. F. *et al.* Transduction and expression of the human carcinoembryonic antigen gene in a murine colon carcinoma cell line. *Cancer Res* **51**, 3657–3662 (1991).

171. Zhao, F. *et al.* Activation of p38 mitogen-activated protein kinase drives dendritic cells to become tolerogenic in Ret transgenic mice spontaneously developing melanoma. *Clinical Cancer Research* **15**, 4382–4390 (2009).

172. Emeny, J. M. & Morgan, M. J. Regulation of the interferon system: Evidence that Vero cells have a genetic defect in interferon production. *Journal of General Virology* **43**, 247–252 (1979).

173. Nakamura, T. *et al.* Rescue and propagation of fully retargeted oncolytic measles viruses. *Nat Biotechnol* **23**, 209–214 (2005).

174. Yannoutsos, N. *et al.* A membrane cofactor protein transgenic mouse model for the study of discordant xenograft rejection. *Genes to Cells* **1**, 409–419 (1996).

175. Oldstone, M. B. A. *et al.* Measles virus infection in a transgenic model: Virus-induced immunosuppression and central nervous system disease. *Cell* **98**, 629–640 (1999).

176. Samorski, R., Gissmann, L. & Osen, W. Codon optimized expression of HPV 16 E6 renders target cells susceptible to E6-specific CTL recognition. *Immunol Lett* **107**, 41–49 (2006).

177. Navaratnarajah, C. K. *et al.* Dynamic interaction of the measles virus hemagglutinin with its receptor signaling lymphocytic activation molecule (SLAM, CD150). *Journal of Biological Chemistry* **283**, 11763–11771 (2008).

178. Smith, P. K. *et al.* Measurement of protein using bicinchoninic acid. *Anal Biochem* **150**, 76–85 (1985).

179. Risso, D., Schwartz, K., Sherlock, G. & Dudoit, S. GC-content normalization for RNA-Seq data. *BMC Bioinformatics* **12**, 480 (2011).

180. Risso, D., Ngai, J., Speed, T. P. & Dudoit, S. Normalization of RNA-seq data using factor analysis of control genes or samples. *Nat Biotechnol* **32**, 896–902 (2014).

181. Love, M. I., Huber, W. & Anders, S. Moderated estimation of fold change and dispersion for RNA-seq data with DESeq2. *Genome Biol* **15**, 550 (2014).

182. Rakaee, M. *et al.* Evaluation of tumor-infiltrating lymphocytes using routine H&E slides predicts patient survival in resected non–small cell lung cancer. *Hum Pathol* **79**, 188–198 (2018).

183. Bankhead, P. *et al.* QuPath: Open source software for digital pathology image analysis. *Sci Rep* **7**, 16878 (2017).

184. Davies, E. J. *et al.* Capturing complex tumour biology in vitro: Histological and molecular characterisation of precision cut slices. *Sci Rep* **5**, 17187 (2015).

185. Plumet, S., Duprex, W. P. & Gerlier, D. Dynamics of viral RNA synthesis during measles virus infection. *J Virol* **79**, 6900–6908 (2005).

186. Yu, J. W. *et al.* Tumor-immune profiling of murine syngeneic tumor models as a framework to guide mechanistic studies and predict therapy response in distinct tumor microenvironments. *PLoS One* **13**, e0206223 (2018).

187. Taylor, M. A. *et al.* Longitudinal immune characterization of syngeneic tumor models to enable model selection for immune oncology drug discovery. *J Immunother Cancer* **7**, 328 (2019).

188. Galanis, E. *et al.* Oncolytic measles virus expressing the sodium iodide symporter to treat drug-resistant ovarian cancer. *Cancer Res* **75**, 22–30 (2015).

189. Dispenzieri, A. *et al.* Phase I trial of systemic administration of Edmonston strain of measles virus genetically engineered to express the sodium iodide symporter in patients with recurrent or refractory multiple myeloma. *Leukemia* **31**, 2791–2798 (2017).

190. Finkbeiner, M. S. C. Dendritic cell and T cell activation during measles virus oncolysis. Master's thesis. (Ruperto-Carola University of Heidelberg, 2021).

191. Bognár, B. Reprogramming tumor-associated macrophages with oncolytic measles vaccines. Master's thesis. (IMC Fachhochschule Krems, 2023).

192. Floerchinger, A. *et al.* A vector-encoded bispecific killer engager to harness virus-activated NK cells as anti-tumor effectors. *Cell Death Dis* **14**, 104 (2023).

193. Hashiguchi, T. *et al.* Structures of the prefusion form of measles virus fusion protein in complex with inhibitors. *Proc Natl Acad Sci U S A* **115**, 2496–2501 (2018).

194. Kell, A. M. & Gale, M. RIG-I in RNA virus recognition. *Virology* **479–480**, 110–121 (2015).

195. Kelly, J. T. *et al.* BST2/Tetherin overexpression modulates morbillivirus glycoprotein production to inhibit cell–cell fusion. *Viruses* **11**, 692 (2019).

196. Das, A., Dinh, P. X., Panda, D. & Pattnaik, A. K. Interferon-inducible protein IFI35 negatively regulates RIG-I antiviral signaling and supports vesicular stomatitis virus replication. *J Virol* **88**, 3103–3113 (2014).

197. Unterholzner, L. *et al.* IFI16 is an innate immune sensor for intracellular DNA. *Nat Immunol* **11**, 997–1004 (2010).

198. Kuter, B. J., Marshall, G. S., Fergie, J., Schmidt, E. & Pawaskar, M. Prevention of measles, mumps and rubella: 40 years of global experience with M-M-RII. *Hum Vaccin Immunother* **17**, 5372–5383 (2021).

199. Griffin, D. E. Measles immunity and immunosuppression. *Curr Opin Virol* **46**, 9–14 (2021).

200. Koerfer, J. *et al.* Organotypic slice cultures of human gastric and esophagogastric junction cancer. *Cancer Med* **5**, 1444–1453 (2016).

201. Lim, C. Y. *et al.* Organotypic slice cultures of pancreatic ductal adenocarcinoma preserve the tumor microenvironment and provide a platform for drug response. *Pancreatology* **18**, 913–927 (2018).

202. Langfield, K. K., Walker, H. J., Gregory, L. C. & Federspiel, M. J. Manufacture of measles viruses. *Methods in Molecular Biology* **737**, 345–366 (2011).

203. Spiotto, M. T. *et al.* Increasing tumor antigen expression overcomes 'ignorance' to solid tumors via crosspresentation by bone marrow-derived stromal cells. *Immunity* **17**, 737–747 (2002).

204. De Witte, L. *et al.* DC-SIGN and CD150 have distinct roles in transmission of measles virus from dendritic cells to T-Lymphocytes. *PLoS Pathog* **4**, e1000049 (2008).

205. Mesman, A. W. *et al.* A prominent role for DC-SIGN+ dendritic cells in initiation and dissemination of measles virus infection in non-human primates. *PLoS One* **7**, e49573 (2012).

206. Park, C. G. *et al.* Five mouse homologues of the human dendritic cell C-type lectin, DC-SIGN. *Int Immunol* **13**, 1283–1290 (2001).

207. Mrkic, B. *et al.* Measles virus spread and pathogenesis in genetically modified mice. *J Virol* **72**, 7420–7427 (1998).

208. Ebenig, A., Lange, M. V. & Mühlebach, M. D. Versatility of live-attenuated measles viruses as platform technology for recombinant vaccines. *NPJ Vaccines* **7**, 119 (2022).

209. Singh, M., Cattaneo, R. & Billeter, M. A. A recombinant measles virus expressing hepatitis B virus surface antigen induces humoral immune responses in genetically modified mice. *J Virol* **73**, 4823–4828 (1999).

210. Aitken, A. S., Roy, D. G. & Bourgeois-Daigneault, M. C. Taking a stab at cancer: Oncolytic virus-mediated anti-cancer vaccination strategies. *Biomedicines* **5**, 3 (2017).

211. Kottke, T. *et al.* Broad antigenic coverage induced by vaccination with virus-based cDNA libraries cures established tumors. *Nat Med* **17**, 854–859 (2011).

212. Pulido, J. *et al.* Using virally expressed melanoma cDNA libraries to identify tumor-associated antigens that cure melanoma. *Nat Biotechnol* **30**, 337–343 (2012).

213. Feola, S. *et al.* Peptides-coated oncolytic vaccines for cancer personalized medicine. *Front Immunol* **13**, 826164 (2022).

214. Feola, S. *et al.* A novel immunopeptidomic-based pipeline for the generation of personalized oncolytic cancer vaccines. *Elife* **11**, e71156 (2022).

215. Kottke, T. *et al.* Oncolytic virotherapy induced CSDE1 neo-antigenesis restricts VSV replication but can be targeted by immunotherapy. *Nat Commun* **12**, 1930 (2021).

216. Panagioti, E. *et al.* Immunostimulatory bacterial antigen-armed oncolytic measles virotherapy significantly increases the potency of anti-PD1 checkpoint therapy. *Journal of Clinical Investigation* **131**, e141614 (2021).

217. Zhao, D. *et al.* Live attenuated measles virus vaccine induces apoptosis and promotes tumor regression in lung cancer. *Oncol Rep* **29**, 199–204 (2013).

218. Tang, H. *et al.* Facilitating T cell infiltration in tumor microenvironment overcomes resistance to PD-L1 blockade. *Cancer Cell* **29**, 285–296 (2016).

219. Bourgeois-Daigneault, M.-C. *et al.* Neoadjuvant oncolytic virotherapy before surgery sensitizes triple-negative breast cancer to immune checkpoint therapy. *Sci. Transl. Med* **10**, 1641 (2018).

220. Errington, F. *et al.* Inflammatory tumour cell killing by oncolytic reovirus for the treatment of melanoma. *Gene Ther* **15**, 1257–1270 (2008).

221. Steele, L. *et al.* Pro-inflammatory cytokine/chemokine production by reovirus treated melanoma cells is PKR/NF-κB mediated and supports innate and adaptive anti-tumour immune priming. *Mol Cancer* **10**, 20 (2011).

222. Fu, X., Rivera, A., Tao, L. & Zhang, X. An HSV-2 based oncolytic virus can function as an attractant to guide migration of adoptively transferred T cells to tumor sites. *Oncotarget* **6**, 902–914 (2015).

223. Ozga, A. J., Chow, M. T. & Luster, A. D. Chemokines and the immune response to cancer. *Immunity* **54**, 859–874 (2021).

224. González-Martín, A., Gómez, L., Lustgarten, J., Mira, E. & Mañes, S. Maximal T cell-mediated antitumor responses rely upon CCR5 expression in both CD4+ and CD8+ T cells. *Cancer Res* **71**, 5455–5466 (2011).

225. Dangaj, D. *et al.* Cooperation between constitutive and inducible chemokines enables T cell engraftment and Immune attack in solid tumors. *Cancer Cell* **35**, 885–900 (2019).

226. Nazar, A. S. *et al.* Induction of IP-10 chemokine promoter by measles virus: comparison with interferon-g shows the use of the same response element but with differential DNA-protein binding profiles. *J Neuroimmunol* **77**, 116–127 (1997).

227. Noe, K. H., Cenciarelli, C., Moyer, S. A., Rota, P. A. & Shin, M. L. Requirements for measles virus induction of RANTES chemokine in human astrocytoma-derived U373 cells. *J Virol* **73**, 3117–3124 (1999).

228. Spranger, S., Dai, D., Horton, B. & Gajewski, T. F. Tumor-residing Batf3 dendritic cells are required for effector T cell trafficking and adoptive T cell therapy. *Cancer Cell* **31**, 711–723 (2017).

229. Böttcher, J. P. *et al.* NK cells stimulate recruitment of cDC1 into the tumor microenvironment promoting cancer immune control. *Cell* **172**, 1022-1037.e14 (2018).

230. Fridman, W. H. *et al.* Tertiary lymphoid structures and B cells: An intratumoral immunity cycle. *Immunity* **56**, 2254–2269 (2023).

231. Kang, W. *et al.* Tertiary lymphoid structures in cancer: The double-edged sword role in antitumor immunity and potential therapeutic induction strategies. *Front Immunol* **12**, 689270 (2021).

232. Rodriguez, A. B., Peske, J. D. & Engelhard, V. H. Identification and characterization of tertiary lymphoid structures in murine melanoma. *Methods in Molecular Biology* **1845**, 241–257 (2018).

233. Houel, A., Foloppe, J. & Dieu-Nosjean, M. C. Harnessing the power of oncolytic virotherapy and tertiary lymphoid structures to amplify antitumor immune responses in cancer patients. *Semin Immunol* **69**, 101796 (2023).

234. He, T. *et al.* Oncolytic adenovirus promotes vascular normalization and nonclassical tertiary lymphoid structure formation through STING-mediated DC activation. *Oncoimmunology* **11**, 2093054 (2022).

235. Li, X. *et al.* CXCL10-armed oncolytic adenovirus promotes tumor-infiltrating T-cell chemotaxis to enhance anti-PD-1 therapy. *Oncoimmunology* **11**, 2118210 (2022).

236. Giese, N. A. *et al.* Suppression of metastatic hemangiosarcoma by a parvovirus MVMp vector transducing the IP-10 chemokine into immunocompetent mice. *Cancer Gene Ther* **9**, 432–442 (2002).

237. Enderlin, M. *et al.* TNF-α and the IFN-γ-inducible protein 10 (IP-10/CXCL-10) delivered by parvoviral vectors act in synergy to induce antitumor effects in mouse glioblastoma. *Cancer Gene Ther* **16**, 149–160 (2009).

238. Eckert, E. C. *et al.* Generation of a tumor-specific chemokine gradient using oncolytic vesicular stomatitis virus encoding CXCL9. *Mol Ther Oncolytics* **16**, 63–74 (2019).

239. Terada, K., Wakimoto, H., Tyminski, E., Chiocca, E. A. & Saeki, Y. Development of a rapid method to generate multiple oncolytic HSV vectors and their in vivo evaluation using syngeneic mouse tumor models. *Gene Ther* **13**, 705–714 (2006).

240. Li, Y. *et al.* CCL21/IL21-armed oncolytic adenovirus enhances antitumor activity against TERT-positive tumor cells. *Virus Res* **220**, 172–178 (2016).

241. Hu, H. *et al.* A novel cocktail therapy based on quintuplet combination of oncolytic herpes simplex virus-2 vectors armed with interleukin-12, interleukin-15, GM-CSF, PD1v, and IL-7 × CCL19 results in enhanced antitumor efficacy. *Virol J* **19**, 74 (2022).

242. Li, J. *et al.* Expression of CCL19 from oncolytic vaccinia enhances immunotherapeutic potential while maintaining oncolytic activity. *Neoplasia* **14**, 1115–1121 (2012).

243. Torphy, R. J., Yee, E. J., Schulick, R. D. & Zhu, Y. Atypical chemokine receptors: Emerging therapeutic targets in cancer. *Trends Pharmacol Sci* **43**, 1085–1097 (2022).

244. Whyte, C. E. *et al.* ACKR4 restrains antitumor immunity by regulating CCL21. *Journal of Experimental Medicine* **217**, e20190634 (2020).

245. Torphy, R. J. *et al.* GPR182 limits antitumor immunity via chemokine scavenging in mouse melanoma models. *Nat Commun* **13**, 97 (2022).

246. Barreira Da Silva, R. *et al.* Dipeptidylpeptidase 4 inhibition enhances lymphocyte trafficking, improving both naturally occurring tumor immunity and immunotherapy. *Nat Immunol* **16**, 850–858 (2015).

247. Liang, M. *et al.* Targeting matrix metalloproteinase MMP3 greatly enhances oncolytic virus mediated tumor therapy. *Transl Oncol* **14**, 101221 (2021).

248. Steenport, M. *et al.* Matrix Metalloproteinase (MMP)-1 and MMP-3 Induce Macrophage MMP-9: Evidence for the Role of TNF-α and Cyclooxygenase-2. *The Journal of Immunology* **183**, 8119–8127 (2009).

249. Van Den Steen, P. E., Husson, S. J., Proost, P., Van Damme, J. & Opdenakker, G. Carboxyterminal cleavage of the chemokines MIG and IP-10 by gelatinase B and neutrophil collagenase. *Biochem Biophys Res Commun* **310**, 889–896 (2003).

250. Mahller, Y. Y. *et al.* Tissue inhibitor of metalloproteinase-3 via oncolytic herpesvirus inhibits tumor growth and vascular progenitors. *Cancer Res* **68**, 1170–1179 (2008).

251. Shields, N. J. *et al.* Late-stage MC38 tumours recapitulate features of human colorectal cancer – implications for appropriate timepoint selection in preclinical studies. *Front Immunol* **14**, 1152035 (2023).

252. Gupta, A. *et al.* Isoform specific anti-TGFβ therapy enhances antitumor efficacy in mouse models of cancer. *Commun Biol* **4**, 1296 (2021).

253. Moreno Ayala, M. A. *et al.* CXCR3 expression in regulatory T cells drives interactions with type I dendritic cells in tumors to restrict CD8+ T cell antitumor immunity. *Immunity* **56**, 1613-1630.e5 (2023).

254. Redjimi, N. *et al.* CXCR3+ T regulatory cells selectively accumulate in human ovarian carcinomas to limit type I immunity. *Cancer Res* **72**, 4351–4360 (2012).

255. Shields, J. D., Kourtis, I. C., Tomei, A. A., Roberts, J. M. & Swartz, M. A. Induction of lymphoidlike stroma and immune escape by tumors that express the chemokine CCL21. *Science (1979)* **328**, 749–752 (2010).

256. Kim, M. J. & Ha, S. J. Differential role of PD-1 expressed by various immune and tumor cells in the tumor immune microenvironment: expression, function, therapeutic efficacy, and resistance to cancer immunotherapy. *Front Cell Dev Biol* **9**, 767466 (2021).

257. Quetglas, J. I. *et al.* Virotherapy with a Semliki forest virus-based vector encoding IL12 synergizes with PD-1/PD-L1 blockade. *Cancer Immunol Res* **3**, 449–454 (2015).

258. Xie, X. *et al.* The combination therapy of oncolytic HSV-1 armed with anti-PD-1 antibody and IL-12 enhances anti-tumor efficacy. *Transl Oncol* **15**, 101287 (2022).

259. Kanaya, N. *et al.* Immune modulation by telomerase-specific oncolytic adenovirus synergistically enhances antitumor efficacy with anti-PD1 antibody. *Molecular Therapy* **28**, 794–804 (2020).

260. Rahn, S. *et al.* POLE Score: a comprehensive profiling of programmed death 1 ligand 1 expression in pancreatic ductal adenocarcinoma. *Oncotarget* **10**, 1572–1588 (2019).

261. Corbett, T. H. *et al.* Induction and chemotherapeutic response of two transplantable ductal adenocarcinomas of the pancreas in C57BL/6 mice. *Cancer Res* **44**, 717–726 (1984).

262. Wang, Y. *et al.* Genomic sequencing of key genes in mouse pancreatic cancer cells. *Curr Mol Med* **12**, 331–341 (2012).

263. Bardeesy, N. & DePinho, R. A. Pancreatic cancer biology and genetics. *Nat Rev Cancer* **2**, 897–909 (2002).

264. Torres, M. P. *et al.* Novel pancreatic cancer cell lines derived from genetically engineered mouse models of spontaneous pancreatic adenocarcinoma: Applications in diagnosis and therapy. *PLoS One* **8**, e80580 (2013).

265. Pham, T. N. D. *et al.* Preclinical models of pancreatic ductal adenocarcinoma and their utility in immunotherapy studies. *Cancers (Basel)* **13**, 1–22 (2021).

266. Mahalingam, D. *et al.* Pembrolizumab in combination with the oncolytic virus Pelareorep and chemotherapy in patients with advanced pancreatic adenocarcinoma: A phase Ib study. *Clinical Cancer Research* **26**, 71–81 (2020).

267. Collienne, M. *et al.* P-49 GOBLET: A phase 1/2 multiple indication signal finding and biomarker study in advanced gastrointestinal cancers treated with Pelareorep and Atezolizumab - safety and preliminary response results. *Annals of Oncology* **33**, S264 (2022).

268. Eriksson, E. *et al.* Shaping the tumor stroma and sparking immune activation by CD40 and 4-1BB signaling induced by an armed oncolytic virus. *Clinical Cancer Research* **23**, 5846–5857 (2017).

269. Rajani, K. *et al.* Combination therapy with reovirus and Anti-PD-1 blockade controls tumor growth through innate and adaptive immune responses. *Molecular Therapy* **24**, 166–174 (2016).

270. Ilett, E. *et al.* Prime-boost using separate oncolytic viruses in combination with checkpoint blockade improves anti-tumour therapy. *Gene Ther* **24**, 21–30 (2017).

271. Mostafa, A. A. *et al.* Oncolytic reovirus and immune checkpoint inhibition as a novel immunotherapeutic strategy for breast cancer. *Cancers (Basel)* **10**, 205 (2018).

272. Araki, H. *et al.* Oncolytic virus-mediated p53 overexpression promotes immunogenic cell death and efficacy of PD-1 blockade in pancreatic cancer. *Mol Ther Oncolytics* **27**, 3–13 (2022).

273. Kajiwara, Y. *et al.* Oncolytic virus-mediated reducing of myeloid-derived suppressor cells enhances the efficacy of PD-L1 blockade in gemcitabine-resistant pancreatic cancer. *Cancer Immunology, Immunotherapy* **72**, 1285–1300 (2023).

274. Ungerechts, G. *et al.* An immunocompetent murine model for oncolysis with an armed and targeted measles virus. *Molecular Therapy* **15**, 1991–1997 (2007).

275. Jing, Y. *et al.* Tumor and vascular targeting of a novel oncolytic measles virus retargeted against the urokinase receptor. *Cancer Res* **69**, 1459–1468 (2009).

276. Derani, J. M. Combining radiation and oncolytic measles virus for the treatment of refractory tumors. (2023).

277. Peng, K. W. *et al.* Biodistribution of oncolytic measles virus after intraperitoneal administration into Ifnar^{TM} -CD46Ge transgenic mice. *Hum Gene Ther* **14**, 1565–1577 (2003).

278. Mura, M. *et al.* hCD46 receptor is not required for measles vaccine Schwarz strain replication in vivo: Type-I IFN is the species barrier in mice. *Virology* **524**, 151–159 (2018).

279. Johnstone, R. W., Loveland, B. E. & McKenzie, F. C. Identification and quantification of complement regulator CD46 on normal human tissues. *Immunology* **79**, 341–347 (1993).

280. Myers, R. M. *et al.* Preclinical pharmacology and toxicology of intravenous MV-NIS, an oncolytic measles virus administered with or without cyclophosphamide. *Clin Pharmacol Ther* **82**, 700–710 (2007).

281. Viker, K. B. *et al.* Preclinical safety assessment of MV-s-NAP, a novel oncolytic measles virus strain armed with an H. pylori immunostimulatory bacterial transgene. *Mol Ther Methods Clin Dev* **26**, 532–546 (2022).

282. Myers, R. *et al.* Toxicology study of repeat intracerebral administration of a measles virus derivative producing carcinoembryonic antigen in rhesus macaques in support of a phase I/II clinical trial for patients with recurrent gliomas. *Hum Gene Ther* **19**, 690–698 (2008).

283. Andres, O., Obojes, K., Kim, K. S., ter Meulen, V. & Schneider-Schaulies, J. CD46- and CD150-independent endothelial cell infection with wild-type measles viruses. *Journal of General Virology* **84**, 1189–1197 (2003).

284. Abdullah, H., Brankin, B., Brady, C. & Louise Cosby, S. Wild-type measles virus infection upregulates poliovirus receptor-related 4 and causes apoptosis in brain endothelial cells by induction of tumor necrosis factor-related apoptosis-inducing ligand. *J Neuropathol Exp Neurol* **72**, 681–696 (2013).

285. Grivel, J.-C., García, M., Moss, W. J. & Margolis, L. B. Inhibition of HIV-1 replication in human lymphoid tissues ex vivo by measles virus. *Journal of Infectious Diseases* **192**, 71–78 (2005).

286. Condack, C., Grivel, J. C., Devaux, P., Margolis, L. & Cattaneo, R. Measles virus vaccine attenuation: Suboptimal infection of lymphatic tissue and tropism alteration. *Journal of Infectious Diseases* **196**, 541–549 (2007).

287. Soliman, N. Crosstalk of oncolytic measles virus, peripheral blood mononuclear cells and neutralizing antibodies. Master's thesis. (Ruperto-Carola University of Heidelberg, 2019).

288. Ong, H. T., Hasegawa, K., Dietz, A. B., Russell, S. J. & Peng, K. W. Evaluation of T cells as carriers for systemic measles virotherapy in the presence of antiviral antibodies. *Gene Ther* **14**, 324–333 (2007).

289. Floerchinger, A. Harnessing natural killer cell activation in oncolytic measles virotherapy. Master's thesis. (Ruperto-Carola University of Heidelberg, 2021).

290. Mosaheb, M. M. *et al.* Genetically stable poliovirus vectors activate dendritic cells and prime antitumor CD8 T cell immunity. *Nat Commun* **11**, 524 (2020).

291. Zitvogel, L., Galluzzi, L., Kepp, O., Smyth, M. J. & Kroemer, G. Type I interferons in anticancer immunity. *Nat Rev Immunol* **15**, 405–414 (2015).

292. Blixenkrone-Moller, M. *et al.* Role of CD46 in measles virus infection in CD46 transgenic mice. *Virology* **249**, 238–248 (1998).

293. Shingai, M. *et al.* Wild-type measles virus infection in human CD46/CD150-transgenic mice: CD11c-positive dendritic cells establish systemic viral infection. *The Journal of Immunology* **175**, 3252–3261 (2005).

294. Roscic-Mrkic, B. *et al.* Roles of macrophages in measles virus infection of genetically modified mice. *J Virol* **75**, 3343–3351 (2001).

295. Horvat, B. *et al.* Transgenic mice expressing human measles virus (MV) receptor CD46 provide cells exhibiting different permissivities to MV infection. *J Virol* **70**, 6673–6681 (1996).

296. Wenthe, J. *et al.* Immune priming using DC- and T cell-targeting gene therapy sensitizes both treated and distant B16 tumors to checkpoint inhibition. *Mol Ther Oncolytics* **24**, 429–442 (2022).

297. Schäfer, T. E. Molecular stratification for the optimization of oncolytic virotherapy in pancreatic ductal adenocarcinoma. MD thesis. (Ruperto-Carola University of Heidelberg, 2023).

298. Rusinova, I. *et al.* INTERFEROME v2.0: An updated database of annotated interferon-regulated genes. *Nucleic Acids Res* **41**, D1040-6 (2013).

299. Muranski, P. *et al.* Tumor-specific Th17-polarized cells eradicate large established melanoma. *Blood* **112**, 362–373 (2008).

300. Korbecki, J. *et al.* CC chemokines in a tumor: A review of pro-cancer and anti-cancer properties of the ligands of receptors CCR1, CCR2, CCR3, and CCR4. *Int J Mol Sci* **21**, 1–29 (2020).

301. Lim, S.-J. CCL24 signaling in the tumor microenvironment. in *Tumor microenvironment: The role of chemokines (Part B)* (ed. Birbrair, A.) vol. 1302 91–98 (Springer Nature, 2021).

302. Trinchieri, G. Interleukin-12 and the regulation of innate resistance and adaptive immunity. *Nat Rev Immunol* **3**, 133–146 (2003).

303. Seliger, B. *et al.* Characterization of the major histocompatibility complex class I deficiencies in B16 melanoma cells. *Cancer Res* **61**, 1095–1099 (2001).

304. Sharpe, A. H. & Pauken, K. E. The diverse functions of the PD1 inhibitory pathway. *Nat Rev Immunol* **18**, 153–167 (2018).

305. Quatrini, L. *et al.* The immune checkpoint PD-1 in natural killer cells: Expression, function and targeting in tumour immunotherapy. *Cancers (Basel)* **12**, 1–21 (2020).

306. de Swart, R. L., Yüksel, S. & Osterhaus, A. D. M. E. Relative contributions of measles virus hemagglutinin- and fusion protein-specific serum antibodies to virus neutralization. *J Virol* **79**, 11547–11551 (2005).

307. Ota, M. O. *et al.* Hemagglutinin protein is a primary target of the measles virus-specific HLA-A2-restricted CD8+ T cell response during measles and after vaccination. *Journal of Infectious Diseases* **195**, 1799–1807 (2007).

308. Groeneveldt, C., van den Ende, J. & van Montfoort, N. Preexisting immunity: Barrier or bridge to effective oncolytic virus therapy? *Cytokine Growth Factor Rev* **70**, 1–12 (2023).

309. Heidbuechel, J. P. W. & Engeland, C. E. Oncolytic viruses encoding bispecific T cell engagers: a blueprint for emerging immunovirotherapies. *J Hematol Oncol* **14**, 63 (2021).

310. Niemann, J. *et al.* Molecular retargeting of antibodies converts immune defense against oncolytic viruses into cancer immunotherapy. *Nat Commun* **10**, 3236 (2019).

311. Kaufmann, J. K. *et al.* Chemovirotherapy of malignant melanoma with a targeted and armed oncolytic measles virus. *Journal of Investigative Dermatology* **133**, 1034–1042 (2013).

312. Modic, Ž. Tumor cell determinants of measles virus oncolysis in patient-derived tumor models. Master's thesis. (Ruperto-Carola University of Heidelberg, 2020).

313. Carter, M. E. *et al.* A three-dimensional organoid model of primary breast cancer to investigate the effects of oncolytic virotherapy. *Front Mol Biosci* **9**, 826302 (2022).

314. Vaira, V. *et al.* Preclinical model of organotypic culture for pharmacodynamic profiling of human tumors. *Proc Natl Acad Sci U S A* **107**, 8352–8356 (2010).

315. Sönnichsen, R. *et al.* Individual susceptibility analysis using patient-derived slice cultures of colorectal carcinoma. *Clin Colorectal Cancer* **17**, e189–e199 (2018).

316. Runge, A. *et al.* Patient-derived head and neck tumor slice cultures: a versatile tool to study oncolytic virus action. *Sci Rep* **12**, 15334 (2022).

317. Zimmermann, M. *et al.* Human precision-cut liver tumor slices as a tumor patient-individual predictive test system for oncolytic measles vaccine viruses. *Int J Oncol* **34**, 1247–1256 (2009).

318. Voabil, P. *et al.* An ex vivo tumor fragment platform to dissect response to PD-1 blockade in cancer. *Nat Med* **27**, 1250–1261 (2021).

319. Roelofsen, L. M. *et al.* Protocol for ex vivo culture of patient-derived tumor fragments. *STAR Protoc* **4**, 102282 (2023).

320. Kaptein, P. *et al.* Addition of interleukin-2 overcomes resistance to neoadjuvant CTLA4 and PD1 blockade in ex vivo patient tumors. *Sci. Transl. Med* **14**, 9779 (2022).

321. Heinzerling, L. *et al.* Oncolytic measles virus in cutaneous T-cell lymphomas mounts antitumor immune responses in vivo and targets interferon-resistant tumor cells. *Blood* **106**, 2287–2294 (2005).

322. Galanis, E. *et al.* Phase I trial of intraperitoneal administration of an oncolytic measles virus strain engineered to express carcinoembryonic antigen for recurrent ovarian cancer. *Cancer Res* **70**, 875–882 (2010).

323. Russell, S. J. *et al.* Remission of disseminated cancer after systemic oncolytic virotherapy. *Mayo Clin Proc* **89**, 926–933 (2014).

324. Packiriswamy, N. *et al.* Oncolytic measles virus therapy enhances tumor antigen-specific T-cell responses in patients with multiple myeloma. *Leukemia* **34**, 3310–3322 (2020).

325. Thomas, R. J. & Bartee, E. The use of oncolytic virotherapy in the neoadjuvant setting. *J Immunother Cancer* **10**, e004462 (2022).

326. Robinson, S. & Galanis, E. Potential and clinical translation of oncolytic measles viruses. *Expert Opin Biol Ther* **17**, 353–363 (2017).

327. Wu, F. *et al.* A new coronavirus associated with human respiratory disease in China. *Nature* **579**, 265–269 (2020).

328. Msemburi, W. *et al.* The WHO estimates of excess mortality associated with the COVID-19 pandemic. *Nature* **613**, 130–137 (2023).

329. Horner, C. *et al.* A highly immunogenic and effective measles virus-based Th1-biased COVID-19 vaccine. *Proc Natl Acad Sci U S A* **117**, 32657–32666 (2020).

330. MacKay, V. L. & Moore, E. E. Immortalized dendritic cells. *Patent number US5648219* (1997).

331. Liniger, M. *et al.* Induction of neutralising antibodies and cellular immune responses against SARS coronavirus by recombinant measles viruses. *Vaccine* **26**, 2164–2174 (2008).

332. Escriou, N. *et al.* Protection from SARS coronavirus conferred by live measles vaccine expressing the spike glycoprotein. *Virology* **452–453**, 32–41 (2014).

333. Malczyk, A. H. *et al.* A highly immunogenic and protective middle east respiratory syndrome coronavirus vaccine based on a recombinant measles virus vaccine platform. *J Virol* **89**, 11654–11667 (2015).

334. Bodmer, B. S., Fiedler, A. H., Hanauer, J. R. H., Prüfer, S. & Mühlebach, M. D. Live-attenuated bivalent measles virus-derived vaccines targeting Middle East respiratory syndrome coronavirus induce robust and multifunctional T cell responses against both viruses in an appropriate mouse model. *Virology* **521**, 99–107 (2018).

335. Lu, M. *et al.* A safe and highly efficacious measles virus-based vaccine expressing SARS-CoV-2 stabilized prefusion spike. *Proc Natl Acad Sci U S A* **118**, e2026153118 (2021).

336. Frantz, P. N. *et al.* A live measles-vectored COVID-19 vaccine induces strong immunity and protection from SARS-CoV-2 challenge in mice and hamsters. *Nat Commun* **12**, 6277 (2021).

337. Vanhoutte, F. *et al.* Safety and immunogenicity of the measles vector-based SARS-CoV-2 vaccine candidate, V591, in adults: results from a phase 1/2 randomised, double-blind, placebo-controlled, dose-ranging trial. *EBioMedicine* **75**, 103811 (2022).

338. Launay, O. *et al.* Safety and immunogenicity of a measles-vectored SARS-CoV-2 vaccine candidate, V591 / TMV-083, in healthy adults: results of a randomized, placebo-controlled phase I study. *EBioMedicine* **75**, 103810 (2022).

339. Kwak, H. W. *et al.* Recombinant measles virus encoding the spike protein of SARS-CoV-2 efficiently induces Th1 responses and neutralizing antibodies that block SARS-CoV-2 variants. *Vaccine* **41**, 1892–1901 (2023).

340. Zhang, Y. *et al.* Recombinant measles virus expressing prefusion spike protein stabilized by six rather than two prolines is more efficacious against SARS-CoV-2 infection. *J Med Virol* **95**, e28687 (2023).

341. Xu, J. *et al.* A next-generation intranasal trivalent MMS vaccine induces durable and broad protection against SARS-CoV-2 variants of concern. *Proc Natl Acad Sci U S A* **120**, e2220403120 (2023).

342. Munoz, F. M. *et al.* Vaccine-associated enhanced disease: Case definition and guidelines for data collection, analysis, and presentation of immunization safety data. *Vaccine* **39**, 3053–3066 (2021).

343. Dejnirattisai, W. *et al.* SARS-CoV-2 Omicron-B.1.1.529 leads to widespread escape from neutralizing antibody responses. *Cell* **185**, 467–484 (2022).

344. Russell, M. W. & Mestecky, J. Mucosal immunity: The missing link in comprehending SARS-CoV-2 infection and transmission. *Front Immunol* **13**, 957107 (2022).

345. Brandler, S. *et al.* A recombinant measles vaccine expressing chikungunya virus-like particles is strongly immunogenic and protects mice from lethal challenge with chikungunya virus. *Vaccine* **31**, 3718–3725 (2013).

346. Ramsauer, K. *et al.* Immunogenicity, safety, and tolerability of a recombinant measles-virus-based chikungunya vaccine: A randomised, double-blind, placebo-controlled, active-comparator, first-in-man trial. *Lancet Infect Dis* **15**, 519–527 (2015).

347. Reisinger, E. C. *et al.* Immunogenicity, safety, and tolerability of the measles-vectored chikungunya virus vaccine MV-CHIK: a double-blind, randomised, placebo-controlled and active-controlled phase 2 trial. *The Lancet* **392**, 2718–2727 (2019).

348. Tschismarov, R. *et al.* Antibody effector analysis of prime versus prime-boost immunizations with a recombinant measles-vectored chikungunya virus vaccine. *JCI Insight* **6**, e151095 (2021).

349. Schmitz, K. S. *et al.* A measles virus-based vaccine induces robust chikungunya virus-specific CD4+ T-cell responses in a phase II clinical trial. *Vaccine* **41**, 6495–6504 (2023).

350. Thomas, S. J. *et al.* Safety and efficacy of the BNT162b2 mRNA COVID-19 vaccine through 6 months. *New England Journal of Medicine* **385**, 1761–1773 (2021).

351. Baden, L. R. *et al.* Efficacy and safety of the mRNA-1273 SARS-CoV-2 vaccine. *New England Journal of Medicine* **384**, 403–416 (2021).

352. Falsey, A. R. *et al.* Phase 3 safety and efficacy of AZD1222 (ChAdOx1 nCoV-19) COVID-19 vaccine. *New England Journal of Medicine* **385**, 2348–2360 (2021).

353. Sadoff, J. *et al.* Safety and efficacy of single-dose Ad26.COV2.S vaccine against COVID-19. *New England Journal of Medicine* **384**, 2187–2201 (2021).

354. Feikin, D. R. *et al.* Duration of effectiveness of vaccines against SARS-CoV-2 infection and COVID-19 disease: results of a systematic review and meta-regression. *The Lancet* **399**, 924–944 (2022).

355. Wong, H.-L. *et al.* Risk of myocarditis and pericarditis after the COVID-19 mRNA vaccination in the USA: a cohort study in claims databases. *The Lancet* **399**, 2191–2199 (2022).

356. Greinacher, A. *et al.* Thrombotic thrombocytopenia after ChAdOx1 nCov-19 vaccination. *New England Journal of Medicine* **384**, 2092–2101 (2021).

357. Muir, K.-L., Kallam, A., Koepsell, S. A. & Gundabolu, K. Thrombotic thrombocytopenia after Ad26.COV2.S vaccination. *New England Journal of Medicine* **384**, 1964–1965 (2021).

Publications, Presentations, Awards

Publications During to the Doctoral Studies

Veinalde, R.*; **Pidelaserra-Martí, G.***; Moulin, C.; Leng Tan, C.; Schäfer, T. E.; Kang, N.; Ball, C. R.; Leichsenring, J.; Stenzinger, A.; Kaderali, L.; Jäger, D.; Ungerechts, G.; Engeland, C. E. **Virotherapy combined with anti-PD-1 transiently reshapes the tumor immune environment and induces anti-tumor immunity in a preclinical PDAC model.** *Frontiers in Immunology* 13, 1096162 (2023) doi.org/10.3389/fimmu.2022.1096162

- * = **shared first authorship**
- The main findings of **section 4.4** from the present thesis are published in this manuscript.

Veinalde, R.; **Pidelaserra-Martí, G.**; Moulin, C.; Jeworowski, L. M.; Küther, L.; Buchholz, C. J.; Jäger, D.; Ungerechts, G.; Engeland, C. E. **Oncolytic measles vaccines encoding PD-1 and PD-L1 checkpoint blocking antibodies to increase tumor-specific T cell memory.** *Molecular Therapy – Oncolytics* 24, 43-58 (2021) doi: 10.1016/j.omto.2021.11.020

- The main findings of **section 4.3** from the present thesis are published in this manuscript.

Pidelaserra-Martí, G. & Engeland, C. E. **Mechanisms of measles virus oncolytic immunotherapy.** *Cytokine & Growth Factor Reviews* 56, 28-38 (2020) doi: 10.1016/j.cytogfr.2020.07.009

- **Figure 3** from the present thesis is published in this review.

Busch, E.*; Kubon, K. D.*; Mayer, J. K. M.*; **Pidelaserra-Martí, G.***; Albert, J.; Hoyler, B.; Heidbuechel, J. P. W.; Stephenson, K. B.; Lichty, B. D.; Osen, W.; Eichmüller, S. B.; Jäger, D.; Ungerechts, G.; Engeland, C. E. **Measles vaccines designed for enhanced CD8+ T cell activation.** *Viruses* 12, 242 (2020) doi: 10.3390/v12020242

- * = **shared first authorship**
- The main findings of **section 4.1** from the present thesis are published in this manuscript.

Publications Prior to the Doctoral Studies

Imkeller, K.; Scally, S. W.; Bosch, A.; **Pidelaserra Martí, G.**; Costa, G.; Triller, G.; Murugan, R.; Renna, V.; Jumaa, H.; Kremsner, P. G.; Sim, B. K. L.; Hoffman, S. L.; Mordmüller, B.; Levashina, E. A.; Julien, J.-P.; Wardemann, H. **Antihomotypic affinity maturation improves human B cell responses against a repetitive epitope.** *Science* 360, 1358-1362 (2018)
doi: 10.1126/science.aar5304

Murugan, R.; Buchauer, L.; Triller, G.; Kreschel, C.; Costa, G.; **Pidelaserra Martí, G.**; Imkeller, K.; Busse, C. E.; Chakravarty, S.; Sim, B. K. L.; Hoffman, S. L.; Levashina, E. A.; Kremsner, P. G.; Mordmüller, B.; Höfer, T.; Wardemann, H. **Clonal selection drives protective memory B cell responses in controlled human malaria infection.** *Science Immunology* 3, eaap8029 (2018) doi: 10.1126/sciimmunol.aap802

Pidelaserra Martí, G.; Isdahl Mohn, K. G.; Cox, R. J.; Brokstad, K. A. The influence of tonsillectomy on total serum antibody levels. Scandinavian Journal of Immunology 80, 377-379 (2014). doi.org/10.1111/sji.12213

Internship Reports and Master's Theses

During my doctoral studies, I have supervised three master internships and one master thesis, the results of which are detailed in the following documents, written by the respective master student:

Finkbeiner, M. S. C. Dendritic cell and T cell activation during measles virus oncolysis. **Master's thesis** (Ruperto-Carola University of Heidelberg, 2021)

Brunecker, A. Optimizing the oncolytic measles virus manufacturing process: Preparing the process stream for cation exchange chromatography. **Master's internship report** (Technical University of Munich, 2020)

Finkbeiner, M. S. C. Oncolytic immunotherapy with measles vaccines. **Master's internship report** (Ruperto-Carola University of Heidelberg, 2019)

Modic, Ž. Immunomodulatory oncolytic measles vaccines. **Master's internship report** (Ruperto-Carola University of Heidelberg, 2019)

Presentations at Scientific Conferences

Poster Presentations

G. Pidelaserra-Martí, M. S. C. Finkbeiner, Ž. Modic, R. Veinalde, J. P. W. Heidbuechel, M. Bozza, T. Poth, J. Doerner, H. M. Kvasnicka, G. Ungerechts, C. E. Engeland.
Immunological Determinants of Oncolytic Measles Virotherapy.
14th International Oncolytic Virotherapy Conference (IOVC)
October 23 – 26, 2022, Karuizawa, Nagano, Japan.

Oral Presentations

G. Pidelaserra-Martí, M. S. C. Finkbeiner, Ž. Modic, R. Veinalde, J. P. W. Heidbuechel, M. Bozza, T. Poth, J. Doerner, H. M. Kvasnicka, R. Hardbottle, D. Jäger, G. Ungerechts, C. E. Engeland. **Immunological Determinants of Measles Virus Oncolysis.**
15th International PhD Student Cancer Conference (IPSCC)
June 8 – 10, 2022, Heidelberg, Germany

Scientific Awards

Universität Witten/Herdecke Interne Forschungsförderung 2024 (2023)
Awarded to pursue my research further, particularly with regards to the patient-derived *ex vivo* tumor models.

14th International Oncolytic Virotherapy Conference – Travel Award (2022)
Awarded for outstanding poster presentation.

The Company of Biologists' DMM Conference Travel Grant (2022)
Awarded to attend the 14th International Oncolytic Virotherapy Conference.

Helmholtz Graduate School for Cancer Research – Doctoral Fellowship (2018)
Awarded to conduct my doctoral studies.

Contributions

The studies described in my thesis would not have been possible without the dedication of many researchers, laboratory technicians, and animal caretakers who have supervised and assisted me throughout more than five years. Below I detail their individual contribution, organized according to the Figures. You all deserve immense credit for your help and support!

Figure	Contributions
Figure 3	C. E. Engeland and I created this figure together.
Figures 5 to 7 Figures S1 to S6	J. Albert, E. Busch, K. Kubon, and J. Mayer generated and propagated the virus variants.
Figure 7 B	J. Albert conducted the flow cytometry experiment. I analyzed the data.
Figure 8	P. Backhaus and R. Veinalde (MeVac FmIL-12 studies) or J. P. W. Heidbuechel (MeVac BiTE studies) conducted the in vivo procedures and RNA extraction. I performed the gene expression analysis.
Figure 11, Figure 12 C	M. Benkisser-Petersen supervised and assisted me in the analysis of the IncuCyte data.
Figure 15 B	C. E. Engeland and J. P. W. Heidbuechel collected the supernatants from the ex vivo cultures.
Figure 16	R. Veinalde generated and propagated the viruses.
Figure 17	C. E. Engeland performed the intraperitoneal injections and collected the blood samples as well as the peritoneal wash samples. Moreover, she assisted me in the conduction of all other *in vivo* procedures. L. Küther performed the ELISA depicted in Figure 17 C.
Figure 18, Figure 19 A	R. Veinalde supervised me in the conduction of all in vivo procedures. Moreover, she generated and propagated the virus variants.
Figure 19 B	J. Albert and I resected the spleens. J. Albert, J. P. W. Heidbuechel, and J. Klein prepared single-cell suspensions from the spleens. C. E. Engeland assisted me in setting the co-culture.
Figure 20	R. Veinalde conducted this experiment before the start of my doctoral studies. I was not involved in any procedure.
Figure 21	R. Veinalde conducted the in vivo procedures and RNA extraction. A. Benner assisted me in writing the R script for the differential gene expression analysis.
Figure 22, Figure 23	R. Veinalde and I resected the tumors and tumor-draining lymph nodes. R. Veinalde supervised me in the conduction of all in vivo and ex vivo procedures and assisted me in the analysis of the flow cytometry data. J. Leichsenring and A. Stenzinger conducted the histological and immunohistochemical procedures (Figure 22 C), including the evaluation of the results (Figure 22 B).
Figure 24	J. Albert propagated the virus. C. E. Engeland and L. Kuther prepared single-cell suspensions from the spleens.

Figure	Contributions
Figure 25	L. Vieira Codeço Marques supervised me in the isolation of cells from murine bone marrow.
Figure 26	L. Vieira Codeço Marques isolated cells from murine bone marrow and, together with B. Bognár, differentiated them into macrophages.
Figure 27	C. E. Engeland and I resected the spleens and tumors. L. Kuther prepared single-cell suspensions from the spleens.
Figure 28, Figure 29	C. E. Engeland and I resected the spleens, tumor-draining lymph nodes, and tumors. J. Albert and S. Sawall prepared single-cell suspensions from the spleens. C. E. Engeland and I prepared single-cell suspensions from the tumor-draining lymph nodes. J. P. W. assisted me in the flow cytometry staining procedure. T. Poth conducted the histology and immunohistochemical procedures, including the evaluation of the results. V. Eckel scanned the slides.
Figure 30	M. S. C. Finkbeiner assisted me in obtaining the patient-derived tumor samples. J. Achberger assisted me in generating tumor slices from patient #3 and acquired the images of the cultures derived from this patient.
Figure 34 B,C	L. Küther performed the BCA assay and the SDS-PAGE assay.
Figure 35	C. E. Engeland produced the laboratory grade virus suspension. C. E. Engeland and I produced the preclinical grade virus suspension.
Figure 36	S. Bossow and S. Sawall propagated the virus variant. C. E. Engeland and I immunized the mice. C. E. Engeland collected the blood samples.

Besides the specific contributions detailed above, I would also like to acknowledge the following:

- J. Albert, B. Hoyler, and S. Sawall (at DKFZ, Heidelberg) as well as L. Küther (at UWH, Witten) assisted me in the conduction of the following procedures:
    - In vivo monitoring of mice (tumor volume, body weight)
    - Flow cytometry staining
    - General cell culture
- J. Albert, B. Hoyler, and S. Sawall (at DKFZ, Heidelberg) as well as L. Küther (at UWH, Witten) conducted the following procedures:
    - Propagation of MeVac variants encoding chemokines or cytotoxic molecules from VP2 to VP3
    - Genotyping of MY II mice
- M. Eich, S. Martin, and D. Sanzio Gimenes da Cruz supervised me during cell sorting.

Finally, I would like to state that I created all the schematics shown in this thesis with BioRender.com.

Acknowledgments

First and foremost, I would like to express my most sincere gratitude to Prof. Dr. Dr. Christine E. Engeland. Thank you, Christine, for welcoming me into your research group and for your excellent guidance, supervision, and mentoring throughout my doctoral studies. I am particularly grateful for your constant support and the scientific discussions, from the most spontaneous ones to the big picture sessions. Thank you for your constructive feedback, wise advice, scientific input, and challenging questions. Thank you, also, for evaluating my doctoral studies as Supervisor and for participating in my Thesis Advisory Committee meetings. Most especially, thank you for sharing your enthusiasm and dedication with me in every project we are involved in. I feel very privileged to have you as scientific mentor and I am looking very much forward to working on the many projects we have in mind.

I would like to express my gratitude to Prof. Dr. Ralf Bartenschlager for evaluating my doctoral studies as Faculty Supervisor and for the valuable scientific input provided during the Thesis Advisory Committee meetings, which certainly contributed to the development of the projects described in my thesis.

I am grateful to Prof. Dr. Martin Müller and PD Dr. Karin Müller-Decker for agreeing to participate in my Disputation as members of the Examination Commission. I am looking forward to an inspiring scientific discussion on December 15, 2023.

I would like to thank Prof. Dr. Stefan Eichmüller and Prof. Dr. Michael Hundemer for evaluating the progress of my doctoral studies as members of my Thesis Advisory Committee. Thank you for the inspiring discussions and for your scientific input. Your expertise in Immunology definitely helped me optimize several assays in the context of my work. Furthermore, I thank Prof. Eichmüller for giving me the opportunity to participate in the Journal Club “Cancer Immunotherapy”.

I thank Prof. Dr. Dr. Guy Ungerechts as Head of the Clinical Cooperation Unit Virotherapy (DKFZ) for allowing me to conduct my research in this Division and for giving me the chance, together with Prof. Engeland, of investigating a MeVac-based COVID-19 vaccine candidate.

I am grateful to Dr. Poth, for the histological evaluation of the murine melanoma samples and for the fascinating virtual microscopy sessions, to Veronika Eckel, for scanning the slides, and to Prof. Stenzinger as well as Dr. Leichsenring, for the histological evaluation of the murine PDAC samples. I thank Prof. Kaderali, for the support with the analysis of the NanoString data and Dr. Benner for the assistance in writing the R script for the differential gene expression analyses.

Furthermore, I am grateful to the following people, who have helped me at specific stages of my doctoral studies: Thank you, Markus Eich, Sylvia Martin, and Daniel Sanzio Gimenes da Cruz, for your assistance and supervision at the cell sorter. Thank you, Barbara Leuchs and Veronika Frehtman, for your advice and supervision on virus purification. Thank you, Pascal Mutz, for your help with the first virus ultracentrifugation rounds. Thank you, Matthias Hock, for designing and producing the tissue slicing device and the ultracentrifuge-tube-friendly rack. Thank you, Mariana Bucur and Wolfram Osen for your suggestions on the optimization of the ELISpot assays. Thank you, Marco Benkisser-Petersen, for your support with the IncuCyte data analysis. Thank you, Luisa Vieira Codeço Marques, for teaching me how to isolate cells from murine bone marrow. Thank you, Matthias Bozza and Claudia Hagedorn, for our discussions on the S/MAR vectors.

I am extremely thankful to Dr. Rūta Veinalde and Dr. Johannes P. W. Heidbuechel for their scientific input and discussions. Several projects described in my thesis were initiated by them or are based on their findings. Thank you for sharing these projects with me and for trusting me in continuing the research. Thank you, Rūta, for teaching me so much in my first three months, for supervising my first animal experiments (you are so patient!), for helping me with the first flow cytometry analyses, for providing me with protocols I have treasured through more than five years, and for kindly answering many of my initial questions. Thank you, Hanno, for your help with large experiments, for being there when I needed a senior PhD/PostDoc to talk to, and for cheering me up in moments of slight frustration. To both of you – thank you for being fantastic colleagues!

I would like to thank the three master students who contributed to the projects: Živa Modic, Maximilliane S. C. Finkbeiner, and Adrian Brunecker. Thank you, Živa, for your motivation and morning energy, for your help with the first virus purification rounds, the first transwell assays, and the first ELISAs. Thank you, Adrian, for your help with the virus purification protocol, particularly with the chromatography tests. Thank you, Maxi, for committing to your master internship and master thesis with such motivation and dedication, that they became the foundation of your current doctoral studies. I am very glad you stayed in the research group, and I am delighted to witness your scientific maturity on a daily basis. Thank you for your scientific input on all the projects, for following up on the T cell priming and activation studies, for your help with the patient samples, for your support on long experiment days, and, most importantly, for your friendship.

Thank you Jesse, Steffi, Birgit, and Linda, for being the backbone of the lab. Your support throughout these years has been essential to manage several projects in parallel while keeping my sanity. Jesse and Steffi, you are the masters of VP3 production! Birgit and Linda, mice like being transgenic when you genotype them! I especially thank all of you for your help at the animal facility and your crucial involvement in the long ELISpot and FACS days. Thank you, also, for your admirable organization

skills. No matter what I need, you know where to find it! And, of course, thank you for the many delicious chocolate/cake/cookie breaks, including self-made brownies and blondies!

I would like to thank all members of the Clinical Cooperation Unit Virotherapy (Heidelberg) and Experimental Virology Department (Witten) I have had the pleasure to work with, particularly the Measles Club. Thank you Alessia, Adrian, Bianka, Birgit, Christine, Ferdi, Gwendolin, Hannah, Hanno, Jesse, Jessica, Johanna, Johannes, Jonny, Judith, Julie, Katia, Kinam, Kristina, Lara, Linda, Lukas, Maxi, Nardine, Natalie, Nicolas, Paul, Rūta, Sophie, Steffi, Teresa, Theresa, Ugo, Viola, and Živa for creating an enjoyable and friendly working atmosphere!

Likewise, I thank all friends and colleagues at Witten/Herdecke University. Thank you, Anja, for the warm welcoming to the Institute, for the discussions at the Department seminars, and for your constant motivation through the writing of this thesis. Thank you, Eric, for the very entreating lunch discussions (you always have a funny story to tell!) and for your help with protocols on how to process patient-derived material. Thank you Erwan, for challenging me with out-of-the-box questions, your knowledge is very impressive! Thank you, Wenli and Montaha, for helping me adapt the virus purification strategy to the facilities in Witten. Thank you Katrin S., Katrin B., and Montaha, for joining Linda and me during the monitoring of mice. Thank you Basti, for your help with ImageJ, for being my PhD-thesis-writing buddy, and for introducing me to another Catalan in Germany. Thank you Maike, for your expertise with mouse breeding and husbandry, your support has been essential in the establishment of the CD46tg mouse colony! In this regard, I would like to acknowledge all mice that have been involved in the projects and thank them for their contribution to science. It is in my to-do list to visit the monument to the laboratory mouse.

I thank Prof. Kvasnicka and Dr. Doerner at HELIOS University Hospital for their essential contribution to the pilot experiments with patient-derived tumor samples. I am grateful to the patients that participate in this study, and I am looking forward to many months of successful collaboration.

I also thank the DKFZ Graduate School for organizing an exciting program for doctoral students. I am thankful to the Center for Biomedical Research and Education (ZBAF in German) at Witten/Herdecke University for the financial support to attend conferences, and I thank the Company of Biologists' for awarding me a grant to attend (finally in person!) a fantastic scientific conference on the most recent highlights in oncolytic virotherapy.

Besides the scientific support that I have had through these years, I would like to thank several friends. Thank you, Alba, Alejandra, Amanda, Andrés, Bernat, Dani, David, Espe, Joan, Judit, Maru, Núria, and Sheila for the many enjoyable moments during my visits in Barcelona. It is always a pleasure to catch up with you! Thank you Lopa, for accompanying me through the doctoral studies

from the very first day. You have given me so much energy when I needed it most and you are someone I can always count on. Thank you Anke, Annika, Daniel, and Iunia, for your friendship, I am looking forward to visiting you soon!

Finally, I would like to thank my family for their support. Thank you for fostering my curiosity as a child, for understanding my decisions, for your advice in numerous topics, for being so close despite the physical distance. Thank you, uncles Jordi and Antonio, and aunts Rosa Maria and Teresa, for your support and interest in my studies. Thank you, Xavier and Hannah, for the relaxing evenings during my visits, for sharing your experiences on your many trips around the world with me, and introducing me into the Corean culture. I hope to visit you in Corea next year! Thank you, Brigitte, Gerhard, and Jens Kamlage, and Eva Weber, for the nice weekends we have spent together. Thank you (Danke!), Tobias, for understanding me so well, for your support and patience on the most critical phases, and for the very-much-needed outdoor activities to disconnect a bit from writing! Your emotional support has been crucial in the writing of my thesisThank you, mum, and thank you, dad, for your daily "Good mornings", for your warm letters, your virtual hugs, the happiness transmitted by your eyes in each videocall – this is a classic, but there are things one cannot put into words. This thesis is dedicated to you.

[Below I repeat the last paragraph in Catalan]

Finalment, voldria agrair el suport de la meva família. Gràcies per promoure la meva curiositat de petita, per entendre les meves decisions, pels consells en nombrosos temes, per estar tan a prop malgrat la distància física. Gràcies, tiets Jordi i Antonio, i tietes Rosa Maria i Teresa, pel vostre suport i l'interès en els meus estudis. Gràcies, Xavier i Hannah, pels vespres relaxants durant les meves visites, per compartir les vostres experiències en els nombrosos viatges pel món amb mi, i per introduir-me en la cultura coreana. Espero visitar-vos a Corea l'any que ve! Gràcies, Brigitte, Gerhard, i Jens Kamlage, i Eva Weber, pels bons caps de setmana que hem passat junts. Gràcies (Danke!), Tobias, per entendre'm tan bé, pel suport i la paciència en les fases més crítiques, i per les sortides tan necessàries a l'exterior per desconnectar una mica del procés d'escriure! El teu suport emocional ha estat essencial durant l'escriptura de la tesi. Gràcies mama, i gràcies, papa, pels vostres "Bon dia" diaris, per les cartes tan agradables, per les abraçades virtuals, i per la felicitat transmesa pels vostres ulls en cada videotrucada – això és un clàssic, però hi ha coses que no es poden posar en paraules. Aquesta tesi està dedicada a vosaltres.

To all of you – A tots vosaltres

Thank you! – Gràcies! – Danke!

Thesis Dedication

I dedicate my PhD thesis to my parents, Miquel Pidelaserra Mas and Maria Mercè Martí Campaña, for their love, support, and strength throughout the exciting yet challenging process of completing a PhD.

I dedicate the results of my thesis and the knowledge I have gained in these five and a half years to my scientific mentor, Prof. Dr. Dr. Christine E. Engeland, for guiding me along the path of becoming a scientist.

I dedicate the experiments conducted at Witten/Herdecke University to my partner, Tobias Kamlage, whom the transition to Witten allowed me to meet.

I wrote my thesis in tribute to my grandparents: Esteve Pidelaserra Surià, Eulàlia Mas Cortés, Joan Martí Fortuny, and Montserrat Campaña Castellano, who would have certainly been very proud of their granddaughter.

I dedicate my contribution to the development of novel therapies against cancer to my grandmother, Montserrat Campaña Castellano, whom I would have loved to meet. Unfortunately, she left us at the young age of 39 after a four-year fight against ovarian and endometrial cancer.

I dedicate section 4.4 to my grandmother, Eulàlia Mas Cortés, who left us 20 years ago due to pancreatic cancer. *Iaia*, you were very present in my mind during the PDAC experiments. I miss you.

I dedicate section 4.6 to my granduncle, Josep Serrahima Perelló, and my grandaunt, Maria Assumpta Martí Fortuny, who left us due to cancer.

I dedicate the addendum to my grandaunt, Maria Puig Sellarés, whom the COVID-19 pandemic took away from us.

As you set out for Ithaka
hope your road is a long one,
full of adventure, full of discovery.
(Fragment from the poem “Ithaka” by C. P. Cavafy)

Dedicatòria de la Tesi

Dedico la meva tesi doctoral als meus pares, Miquel Pidelaserra Mas i Maria Mercè Martí Campaña, per la seva estima, el seu suport, i la força que m'envien durant el procés emocionant però a la vegada difícil de completar el doctorat.

Dedico els resultats de la meva tesi i el coneixement que he adquirit en aquests cinc anys i mig a la meva mentora científica, Prof.ª Dra. Dra. Christine E. Engeland, per guiar-me en el camí de convertir-me en científica.

Dedico els experiments duts a terme a la Universitat de Witten/Herdecke a la meva parella, el Tobias Kamlage, a qui la mudança a Witten m'ha permès conèixer.

He escrit la meva tesi en homenatge als meus avis: Esteve Pidelaserra Surià, Eulàlia Mas Cortés, Joan Martí Fortuny, i Montserrat Campaña Castellano, que de ben segur s'haguessin sentit molt orgullosos de la seva neta.

Dedico la meva contribució al desenvolupament de noves teràpies contra el càncer a la meva àvia, Montserrat Campaña Castellano, a qui m'hagués encantat conèixer. Malauradament, ens va deixar a la jove edat de 39 després de quatre anys de lluita contra el càncer d'ovari i el càncer d'endometri.

Dedico la secció 4.4 a la meva àvia, Eulàlia Mas Cortés, que ens va deixar fa 20 anys a causa de càncer de pàncrees. Iaia, et tenia molt present durant els experiments amb aquest model tumoral. Et trobo a faltar.

Dedico la secció 4.6 al meu tiet-avi, Josep Serrahima Perelló, i a la meva tieta-àvia, Maria Assumpta Martí Fortuny, que ens van deixar a causa càncer.

Dedico l'apèndix a la meva tieta-àvia, Maria Puig Sellarés, de qui la pandèmia de la COVID-19 ens va separar.

Quan surts per fer el viatge cap a Ítaca,
has de pregar que el camí sigui llarg,
ple d'aventures, ple de coneixences.
(Fragment del poema "Ítaka" de C. P. Cavafy)

Thesis Declaration

I hereby declare that I have written the submitted dissertation myself and in this process I have used no other sources or materials than those expressly indicated. I hereby declare that I have not applied to be examined at any other institution, nor have I used the dissertation in this or any other form at any other institution as an examination paper, nor submitted it to any other faculty as a dissertation.

Heidelberg, October 19th, 2023

Gemma Pidelaserra Martí